ISSI Scientific Report 10

Niklaus Kämpfer *Editor*

Monitoring Atmospheric Water Vapour

Ground-Based Remote Sensing and In-situ Methods

INTERNATIONAL SPACE SCIENCE INSTITUTE

Springer

ISSI Scientific Report Series

For further volumes:
http://www.springer.com/series/10151

Niklaus Kämpfer
Editor

Monitoring Atmospheric Water Vapour

Ground-Based Remote Sensing and In-situ Methods

Vol. No. 10

Springer

Editor
Niklaus Kämpfer
lnstitute of Applied Physics
University of Bern
Bern
Switzerland

ISBN 978-1-4614-3908-0 ISBN 978-1-4614-3909-7 (eBook)
DOI 10.1007/978-1-4614-3909-7
Springer New York Dordrecht Heidelberg London

Library of Congress Control Number: 2012946036

Cover illustration: Detail from Tryptichon Schwarzwasser, Xylography by Franz Gertsch

Printed on acid-free paper

Springer is part of Springer Science+Business Media (www.springer.com)

Preface

Recognizing the important role of water vapour for atmospheric processes and in climate issues the steering committee of the Network for the Detection of Atmospheric Composition Change (NDACC) set up a task group to carefully analyse the different measuring and retrieval techniques for water vapour. This working group on water vapour met in 2006 for the first time at the University of Bern in Switzerland. Different measurement techniques for water vapour, in situ and remote, have been discussed. Special emphasis has been put on strengths and weaknesses of the different techniques, on the aspect of validation and inter-comparison of data obtained by different instruments and on detailed specifications of the different methods. It soon turned out that too many aspects remained unanswered and that a thorough investigation of the different issues asked for an in depth analysis.

It turned out that this could ideally be achieved in the frame of a so called science team of the International Space Science Institute, ISSI (www.issibern.ch). ISSI is an Institute of Advanced Studies where scientists from all over the world meet in a multi- and interdisciplinary setting to reach out for new scientific horizons. The main function is to contribute to the achievement of a deeper understanding of the results from different space missions, ground based observations and laboratory experiments, and adding value of those results through multidisciplinary research in the framework of International Teams, Workshops, Working Groups, Forums or as individual Visiting Scientists. The program of ISSI covers a widespread spectrum of disciplines from the physics of the solar system and planetary sciences to astrophysics and cosmology, and from Earth sciences to astrobiology. A dozen of experts in water vapour measurement techniques met three times as a so called ISSI international team at the ISSI facility in Bern discussing in detail above mentioned issues.

It has been decided to summarize the outcome of these discussion in the form of a book in the ISSI series of scientific reports. Individual chapters have been written by the team members and sent out to external experts in the field for a critical review. Special thanks goes to these reviewers (S. Bekki, B. Connor, J. Hannigan, D. Kley, M. Kurylo, J. Langen, N. Livesey, L. Miloshevich, S. Oltmans, A. Parrish, D. Whiteman, J.R. Russell III) who helped a lot to improve the quality of the book.

In parallel to the activities in the frame of the ISSI project also a working group of the COST project WAVACS (Atmospheric Water Vapour in the Climate System)

dealt with the topic of water vapour measurement. Discussions between the team members of this COST project and particularly discussions during workshops of this COST project stimulated some of the authors from the ISSI project and had direct influence on the content of some of the book chapters. Particularly the interactive tables about information of the cross validation of different sensors are accessible through www.watervapour.org is the outcome of this joint effort.

Last but not least very special thanks go to René Bleisch from the Institute of Applied Physics, University of Bern, who did the complete compilation of the book in LATEX based on the material that has been submitted in the most different and exotic forms of typesetting.

Bern Niklaus Kämpfer
August 2011

Contents

Chapter 1
Introduction

Niklaus Kämpfer

1.1 Importance of Water Vapour

Water vapour is an important climate variable and it plays a key role in several issues of atmospheric processes from the ground to the upper atmosphere. It is the most important natural greenhouse gas accounting for about 60 % of the natural greenhouse effect and it provides the largest positive feedback in model projections of climate change (Solomon et al. 2007). In the troposphere it plays a role in air quality and oxidation efficiency, it influences the size and composition of hygroscopic aerosol particles and, through the equilibration between the vapour and liquid phases, it has impacts on the optical properties of aerosols and, hence, on visibility and radiative forcing, as well as the heterogeneous reactions of gases with aerosols. Further, water vapour is a source of clouds and precipitation, which directly affect the climate, and which disperse, transform and remove soluble gases and aerosols in the atmosphere. Increasing concentrations of water vapour in the upper troposphere and lower stratosphere are of growing concern because of its influence on the radiation balance in this climate-sensitive region, and the potential changes in the homogeneous and heterogeneous chemistry affecting ozone.

1.1.1 Stratospheric and Mesospheric Water Vapour

Water vapour in the middle atmosphere plays a multiple role. It is active chemically, radiatively, and physically. As a consequence any change in its abundance may have different impacts. H_2O is the primary source of the OH radical and thus is involved in a large number of chemical processes. The oxidation of methane is an important source of water in the middle and upper stratosphere. Despite the dryness of the stratosphere temperatures can be low enough for water to condense into polar

N. Kämpfer (✉)
Institute of Applied Physics, University of Bern, Sidler str. 5, CH-3012 Bern, Switzerland
e-mail: niklaus.kaempfer@iap.unibe.ch

N. Kämpfer (ed.), *Monitoring Atmospheric Water Vapour,*
ISSI Scientific Report Series 10,
DOI 10.1007/978-1-4614-3909-7_1, © Springer Science+Business Media, LLC 2013

stratospheric clouds, PSCs. Heterogeneous reactions on such clouds play a key role in the formation of the ozone hole. There are indications that increasing H_2O alters the radiation budget of the atmosphere resulting in a cooler stratosphere. A change in temperature would affect the circulation of the middle atmosphere, the stratosphere and mesosphere and also may affect the tropospheric circulation as has recently been shown by studies of (Joshi et al. 2006).

It is widely accepted that air enters the stratosphere in the tropics and it is agreed that the water vapour mixing ratio of air entering the stratosphere is limited to a few parts per million by volume by the extremely low temperatures at the tropical tropopause (Mote et al. 1996; Fueglistaler et al. 2009). Exactly how long-term changes in tropical tropopause temperatures relate to the amount of water vapour that makes it into the stratosphere is under debate.

There is some evidence for a long-term positive trend in lower stratospheric water vapour until about 2000 (Rosenlof et al. 2001; Nedoluha et al. 2003). However this trend has not continued since then and even a decrease of stratospheric water vapour after 2001 is reported (Randel et al. 2006) that might be explained by a change in the Brewer-Dobson circulation. Latest studies by Hurst et al. (2011) show evidence for a new increase after 2005.

Increases in stratospheric water vapour act to cool the stratosphere but to warm the troposphere, whereas the reverse is true for stratospheric water vapour decreases. Studies have suggested that stratospheric water vapour changes might contribute to climate change, but there has been debate about the magnitude of the effect. Solomon et al. (2010) investigated in detail the effect of such a change in stratospheric H_2O at different altitudes on surface climate change and showed by combining data and models that stratospheric water vapour very likely made substantial contributions to the flattening of the global warming trend since about 2000. The findings of Solomon et al. (2010) show that stratospheric water vapour is an important driver of decadal global surface climate change.

The distribution of water vapour in the mesosphere is determined by the effects of global-scale, net transport processes and by photolysis from Lyman-alpha radiation. The largest periodic variations of H_2O in the upper mesosphere are found at higher latitudes and on seasonal and solar cycle time scales. Thus, observed variations of H_2O at these altitudes can be a useful diagnostic tool of the performance of radiative chemical transport models and of global change in the mesosphere (Lastovicka 2009). Water vapour measurements in the mesosphere over the whole solar cycle 23 by ground based microwave radiometry at Mauna Loa by Nedoluha et al. (2009), allowed to estimate to which extent the early 1990s increase of H_2O in the upper mesosphere is related to the solar cycle. The strongest mode of annual variability in tropical regions above 35 km is the semi-annual oscillation. Observations of the mesospheric semi annual oscillations in water vapour have been investigated by Lossow et al. (2008) using data from the ODIN satellite. They found a phase shift in the maxima of the water vapour distribution. Below approx. 75 km maxima occur around equinoxes whereas above more around solstices.

Remsberg (2010) analysed observed seasonal to decadal responses in mesospheric water vapour based on satellite data for different latitudes and report a marked difference for the 11 year and trend terms of the two hemispheres. This is an indicator of the differences for the seasonal exchanges of air between the middle and high latitudes. During winter there is descent of air having low H_2O values in the polar vortex. The degree to which that air is transported and/or mixed to lower latitudes depends on the extent to which the vortex remains intact through the winter/spring period, and generally there is more wintertime wave activity propagating to the mesosphere from below in the northern hemisphere (Sato et al. 2009). Northern hemisphere, midwinter warming events in the upper stratosphere are accompanied by a cooling in the mesosphere, a weakening or breakdown of the polar night jet, and an enhanced meridional transport and mixing of the air. Such sudden warming events have been more frequently observed in recent winters even at midlatitudes. They are of particular interest as they couple all layers of the atmosphere from the troposphere up to the mesosphere. However such coupling processes between the mean flow, planetary waves, tides, and gravity waves during a sudden stratospheric warming event are rather unexplored yet.

1.1.2 Tropospheric Humidity

Global, regional and local studies all indicate increases in moisture in the atmosphere near the surface, but highlight differences between regions and between day and night and the seasons. Excellent reviews of water vapour and climate change are given e.g. in Schneider et al. (2010) and Sherwood et al. (2010). The variability in water vapour is closely tied to changes in surface temperatures, possibly due to greenhouse warming. There remains considerable uncertainty concerning the magnitude of the temperature response to a given increase in greenhouse gases. Because convectivity in the troposphere is affected by the temperature of the underlying ocean, a connection exists between the sea surface temperature and the temperature in the lower stratosphere and thus in the water vapour content as has been shown by Rosenlof and Reid (2008).

There are a number of climatic responses that are tightly coupled to such a temperature response. Most of these are related, directly or indirectly, to lower tropospheric water vapour. In the lower troposphere, condensation of water vapour provides latent heating that dominates the structure of tropospheric diabatic heating. A number of important aspects of the hydrological response to warming are a direct consequence of the increase in lower tropospheric water vapour. The increase in column integrated water vapour (Trenberth et al. 2005), the decrease in convective mass fluxes, the increase in horizontal moisture transport, the enhancement of the pattern of evaporization minus precipitation and the decrease in horizontal sensible heat fluxes are responses to the increase in temperature and the saturation vapour pressure (Held and Soden 2006). One consequence of the change of the hydrological cycle due to atmospheric warming is amplification of precipitation extremes. It has been recognized

that the observed amplification is found to be larger than predicted by models, implying that projections of future changes in rainfall extremes due to anthropogenic global warming may be underestimated (Allen and Soden 2008). Observational evidence supports the findings that moist regions are becoming wetter and dry regions drier. The overall response of the models to the current warming trend appears underestimated and the cause of this discrepancy may impact the fidelity of climate predictions. The relation between specific humidity and the longwave downward radiation has been investigated (e.g. Ruckstuhl et al. 2010). In the upper troposphere a detectable trend in relative humidity has not been confirmed. However there is now evidence for global increases in upper tropospheric specific humidity over the past two decades, which is consistent with the observed increases in tropospheric temperatures. Clear sky outgoing longwave radiation is also highly sensitive to upper tropospheric water vapour. This radiation has been detected by several instruments (e.g. Palchetti et al. 2007).

1.1.3 Observations

The state of present knowledge about water vapour is well summarized by a statement from Sherwood et al. (2010): *Despite its central importance, work to date has not led to a universally accepted picture of the factors controlling water vapour amount, a solid understanding of the mechanisms by which it influences atmospheric processes, or even precise knowledge of its concentrations in many parts of the atmosphere, to say nothing of its trends over time. On the other hand, there has been considerable progress in recent years on some key issues, not all of it broadly appreciated, driven by new ideas and by new observing techniques*.

A core aspect in understanding atmospheric water vapour definitely are observations. Unfortunately, accurate, height-resolved global-scale measurements of atmospheric humidity are difficult to obtain. In the troposphere, the water vapour distribution is extremely variable on almost all scales, and the change in concentration of five orders of magnitude from the ground to the mesopause explains why there is no standard instrument that will measure everywhere. This has led to different measuring techniques, all with strengths and weaknesses, which need to be inter compared carefully under different conditions if progress is to be made on understanding the water vapour distribution.

Routine measuring instruments, such as radio-sondes, suffer from a variety of systematic errors (Miloshevich et al. 2006). Remote sensing can offer both accuracy and coverage, but at the price of reduced resolution which in the upper troposphere is a serious drawback. Global coverage of water vapour measurements are provided by satellites where the most advanced instruments are MLS (Waters et al. 2006) on the Aura Satellite, and the Odin satellite (Urban et al. 2007). Middle atmospheric water vapour measurements on a routine basis from the ground are thus far only performed by microwave radiometry instruments in the frame of the Network for the Detection of Atmospheric Composition Change, NDACC.

1.2 Aim and Structure the Book

The aim of the presented work is to assess in detail in situ and remote sensing techniques presently used to monitor on a regular basis the distribution of atmospheric water vapour. The basics of the different measurement methodologies are reviewed on a level that is considered helpful for the non expert to obtain insight and sufficient knowledge to make most out of available data in a sense that also limitations, caveats and problem areas of the corresponding technique are mentioned. The authors felt it extremely helpful also to point out weaknesses in order to understand what realistically can be expected from a certain type of sensor. A special weight was also put on the retrieval aspects of the sensor types as most sensors do not directly measure humidity itself but a signature of humidity such as emission or absorption spectra, backscattered signals etc. In many cases the signal of interest can be retrieved only after complex mathematical treatment and by using additional information that might falsify in the worst case the data product or that in minimum must be considered when properly interpreting data.

As stated only techniques used so far on an *operational basis* are covered in the book. Therefore the topic covered is far from being complete with respect to measurement techniques of humidity in general. Techniques that are on an experimental level and so far not used on a regular basis are thus not covered though they might be promising in the future. Also it has been decided not to cover aspects of humidity measurements as used mainly for numerical weather forecast such as microwave radiometry of integrated water vapour or liquid amount. Also not covered for the same reason are GPS based measurements of the column density of water vapour.

It also has to be mentioned that it is not the aim of the book to review any water vapour data sets or the present state of knowledge in water vapour research. This topic is covered elsewhere, e.g. in special reports of SPARC.

The book is structured in three sections plus appendices. A first section is devoted to *in situ methods* as normally used on balloons or on aircraft. Thin film capacitive sensors and frost point hygrometry is covered as well as fluorescence methods. Section two is devoted to *remote sensing techniques* operated from the ground and covers passive microwave radiometry, infrared Fourier transform spectrometry using the sun as a background source and lidar where the two approaches, Raman lidar and differential absorption lidar are covered. The third section approaches the topic from the point of view of *networks and measurements on more global frame from satellites*. The value of networks to probe the atmosphere with a special weight on water vapour is highlighted. A detailed overview over the different concepts used from satellite is given. A special chapter is devoted to the difficulties encountered when combining data from different platforms with different viewing geometries, different altitude resolutions and different sampling schemes. These aspects too often are neglected when using data from different sources and resources. A last chapter finally is devoted to the aspect of validation and inter-comparison of different techniques. The chapter essentially covers all the different techniques and the multitude of performed inter-comparisons. Most use of this chapter can however be made in the interactive pdf-version available at www.watervapour.org.

The book ends with several appendices that the authors consider to provide useful information in a concise way. Appendix A is built up of so called fact sheets about the different techniques. They summarize the basic facts about the corresponding technique such as accuracy, resolution etc. but also problem areas and what has to be kept in mind when using data from the respective methodology. The same appendix also provides fact sheets of individual instruments such as used in the frame of NDACC. Appendix B covers an overview of many available equations for water vapour saturation pressure over liquid water and over ice.

References

R. Allan, B. Soden, Atmospheric warming and the amplification of precipitation extremes. Science Express. **7**, (2008). doi:10.1126/science.1160787

S. Fueglistaler, A. Dessler, T. Dunkerton, J. Folkins, Q. Fu, P. Mote, Tropical tropopause layer. Rev. Geophys **47**, (2009)

I. Held, B. Soden, Robust response of the hydrological cycle to global warming. J. Climate. **19**, 5686–5699 (2006)

D.F. Hurst, S.J. Oltmans, H. Vömel, K.H. Rosenlof, S.M. Davis, E.A. Ray, E.G. Hall, A.F. Jordan, Stratospheric water vapor trends over Boulder, Colorado: Analysis of the 30 year Boulder record. J. Geophys. Res. **116**, (2011). doi:10.1029/2010JD015065

M. Joshi, A. Charlton, A. Scaife, On the influence of stratospheric water changes on the tropospheric circulation. Geophys. Res. Lett. **33**, (2006). doi:10.1029/2006GL025983

J. Lastovicka, Global pattern of trends in the upper atmosphere and ionosphere: Recent progress. JASTR. **71**, 1514–1528 (2009)

S.J.U. Lossow, J. Gumbel, P. Eriksson, D. Murtagh, Observations of the mesospheric semi-annual oscillation (MSAO) in water vapour by Odin/SMR. Atmos. Chem. Phys. **8**, 6527–6540 (2008)

L. Miloshevich, H. Vömel, D.N. Whiteman, B.M. Lesht, F.J. Schmidlin, F. Russo, Absolute accuracy of water vapor measurements from six operational radiosonde types launched during AWEX-G and implications for AIRS validation. J. Geophys. Res. **111**, (D09S10) (2006). doi:10.1029/2005JD006083

P.W. Mote, K.H. Rosenlof, M.E. Mclntyre, E.S. Carr, J.C. Gille, J.R. Holton, J.S. Kinnersley, H.C. Pumphrey, J.M. Russell III, J.W. Waters, An atmospheric tape recorder: The imprint of tropical tropopause temperatures on stratospheric water vapor. J. Geophys. Res. **101**, 3989–4006 (1996)

G. Nedoluha, R.M. Bevilacqua, R.M. Gomez, B.C. Hicks, J.M. Rusell III, B.J. Connor, An evaluation of trends in middle atmospheric water vapor as measured by HALOE, WVMS, and POAM. J. Geophys. Res. **108** (2003) doi:10.1029/2002JD003332

G.E. Nedoluha, R.M. Gomez, B.C. Hicks, J.E. Wrotny, C. Boone, A. Lambert, Water vapor measurements in the mesosphere from Mauna Loa over solar cycle. J. Geophys. Res. **114**(D23), 1–9 (2009). doi:10.1029/2009JD012504

L. Palchetti, G. Bianchini, B. Carli, U. Cortesi, S. DelBianco, Measurement of the water vaporvertical profile and of the earth's outgoing far infrared flux. Atmos. Chem. Phys. Discuss **7**, 17741–17767 (2007)

W. Randel, F. Wu, H. Vömel, G.E. Nedoluha, P. Forster, Decreases in stratospheric water vapor after 2001: Links to changes in the tropical tropopause and the Brewer-Dobson circulation. J. Geophys. Res. **111** (2006). doi:10.1029/2005JD006744

E. Remsberg, Observed seasonal to decadal scale responses in mesospheric water vapor J. Geophys. Res. **115** (D06 306) (2010). doi:10.1029/2009JD012904

K. Rosenlof, G. Reid, Trends in the temperature and water vapor content of the tropical lower stratosphere: sea surface connection. J. Geophys. Res, **113** (2008). doi:10.1029/2009GL039908

K. Rosenlof, S. Oltmans, D. Kley, J. Rusell III, E.-W. Chiou, W. Chu, D. Johnson, K. Kelley, H. Michelsen, G. Nedoluha, E. Remsberg, G. Toon, M. McCormick, Stratospheric water vapor increases over the past half-century Geophys. Res. Lett. **28**, 1195–1198 (2001)

C. Ruckstuhl, R. Philipona, J. Morland, A. Ohmura, Observed relationship between surface speci_c humidity, integrated water vapor, and longwave downward radiation at di_erent altitude. J. Geophys. Res, **112** (2010). doi:10.1029/2006JD007850

K. Sato, S. Watanabe, Y. Kawatani, Y. Tomikawa, K. Miyazaki, M. Takahashi, On the origin of mesospheric gravity waves. Geophys. Res. Lett **36** (2009). doi:10.1029/2009GL039908

T. Schneider, P.A. O'Gorman, X.J. Levine, Water vapor and the dynamics of climate changes. Rev. Geophys. **48**, (RG3001) (2010). doi:10.1029/2009RG000302

S. Sherwood, R. Roca, T.M. Weckwerth, N.G. Andronova, Tropospheric water vapor, convection, and climate. Rev. Geophys. **48**, (RG2001) (2010). doi:10.1029/2009RG000301

S. Solomon, D. Qin, M. Manning, Z. Chen, M. Marquis, K. Averyt, M. Tignor, H. Miller (eds.), Climate Change 2007: The Physical Science Basis. *Contribution of working group I to the fourth Assessment, report of the intergovernmental panel on climate change* (Cambridge University Press, Cambridge, 2007)

S. Solomon, K Rosenlof, R. Portmann, J. Daniel, S. Davis, T. Sanford, G. Plattner, Constributions of stratospheric water vapor to decadal changes in the rate of global warming. Science **237**, 1219–1223 (2010)

K. Trenberth, J. Fasullo, L. Smith, Trends and variability in column-integrated atmospheric water vapor. Climate Dynamics **24**, 741–758 (2005). doi:10.1007/s00382-005-0017-4

J. Urban, N. Lautie, D. Murtagh, P. Eriksson, Y.K.S. Loßow, E. Dupuy, J. de La Noe, U. Frisk, M. Olberg, E.L. Flochmoen, P. Ricaud, Global observations of middle atmospheric water vapor by the odin satellite: an overview. Planet space Sci **55** (2007)

J. Waters, L. Froidevaux, R. Harwood, R. Jarnot, H. Pickett, W. Read, P. Siegel, R. Cofield, M. Filipiak, D. Flower, J. Holden, G. Lau, N. Livesey, G. Manney, H. Pumphrey, M. Santee, D. Wu, D. Cuddy, R. Lay, M. Loo, V. Perun, M. Schwartz, P. Stek, R. Thurstans, M. Boyles, S. Chandra, M. Chavez, G.-S. Chen, B. Chudasama, R. Dodge, R. Fuller, M. Girard, J. Jiang, Y. Jiang, B. Knosp, R. LaBelle, J. Lam, K. Lee, D. Miller, J. Oswald, N. Patel, D. Pukala, O. Quintero, D. Scaff, W. Snyder, M. Tope, P. Wagner, M. Walch, The earth observingsystem microwave limb sounder (EOS MLS) on the aura satellite, IEEE Trans. Geosci. Remote Sens. **44**, 1075–1092 (2006) doi:10.1109/TGRS.2006.873771

Part I
In Situ Sensors

Chapter 2
Thin Film Capacitive Sensors

Herman Smit, Rigel Kivi, Holger Vömel and Ari Paukkunen

2.1 Introduction: Principle of Operation

Achievements in microtechnology have encouraged the development of a large variety of very small humidity sensors for miscellaneous applications to measure the water vapour content in gaseous systems. Today, more than 75 % of these miniaturised humidity sensors in the market use a capacitive technique (Rittersma 2002). Most of these capacitive sensors are based on dielectric changes of thin films upon water vapour uptake as a measure of the water vapour content. The porous polymer material acts as a hydroactive sponge whereby the water molecules within the polymer material are in thermodynamic equilibrium with the gas phase, i.e. the rate of adsorption of molecules onto the surface is exactly counterbalanced by the rate of desorption of molecules into the gas phase (Anderson 1995). The water adhesion is characterized by physical hydrogen bonds through the "weak" Van der Waals interaction of water molecules with the hydrophilic groups of the polymer molecules (Matsuguchi et al. 1998, e.g.).

The capacitive thin-film moisture sensor responds to changes of relative, rather than absolute humidity in the surrounding air as well as to changes of temperature. It is, therefore, commonly calibrated in terms of relative humidity (RH). The response time of the humidity sensor is dependent on the polymer's ability to adsorb and desorb water vapour and on the sensor design, whereby it is strongly dependent on the temperature of the sensor. The sensor is sensitive to chemical contamination by

H. Smit (✉)
Research Center Jülich (IEK-8), 52425 Jülich, Germany
e-mail: h.smit@fz-juelich.de

R. Kivi
Finnish Meteorological Institute, Sodankylä, Finland

H. Vömel
Deutscher Wetterdienst, Am Observatorium 12, 15848 Lindenberg, Germany
e-mail: holger.voemel@dwd.de

A. Paukkunen
Vaisala Oy, Helsinki, Finland

N. Kämpfer (ed.), *Monitoring Atmospheric Water Vapour,*
ISSI Scientific Report Series 10,
DOI 10.1007/978-1-4614-3909-7_2, © Springer Science+Business Media, LLC 2013

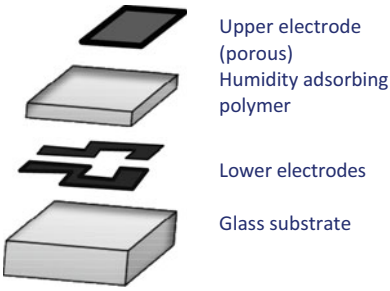

Fig. 2.1 The basic principle of the Humicap technology

either additional bonding of the non-water molecules or reducing the ability of the polymer to adsorb water molecules, which may cause either a dry bias or reduce the sensitivity of the sensor.

The best known meteorological application is the Humicap sensing element developed by Vaisala (Finland) in 1970's (Salasmaa and Kostamo1975), which is being used on their radiosondes since 1980. Based on thin-film technology the sensor consists of a hydroactive polymer film as dielectric between two electrodes applied on a glass substrate (see Fig. 2.1). Two types of polymer materials have been developed, the A-type and the H-type polymer. The newer H-polymer (introduced in 1990) is more stable and less hydrophilic compared to the A-type polymer. An additional airborne application of capacitive sensors is their deployment on board of commercial aircraft to measure the water vapour concentration between the surface and up to 13 km altitude in the context of the MOZAIC (Measurement of Ozone and Water Vapour by AIRBUS In Service Aircraft). The performance of the humidity sensors made by Vaisala and used on their radiosondes as well as by MOZAIC onboard commercial aircraft are described in this chapter.

2.2 Radiosondes

2.2.1 Introduction

For nearly 80 years, balloon-borne radiosondes have been the primary source for vertical profiles of atmospheric parameters used in operational weather forecasting and, more recently for climate studies. During balloon ascent, pressure, temperature, humidity and wind are measured from the surface to the lower stratosphere and transmitted to a ground receiving station for further data processing and archiving. A comprehensive overview of radiosondes instruments is given in (WMO 2008). Radiosondes are provided by various manufacturers and deploy different types of relative humidity sensors, such as goldbeater's skin sensors, lithium chloride sensors, carbon hygristors, and thin-film capacitors.

In the early decades of upper air soundings goldbeater's skin (the outer membrane of cattle intestine, which varies in length with changes in relative humidity) and films of lithium chloride on strips of plastic (whose electrical resistance varies with

relative humidity) were most commonly used. These sensor types perform poorly at temperatures below −20 °C and suffer from significant hysteresis effects and biases (WMO 2008). Later, plastic or glass strip coated with a hygroscopic film containing carbon particles that changes electrical resistance with relative humidity, called carbon hygristors, were used. However, carbon hygristors suffer from a moist bias at relative humidities above 60 % (Schmidlin and Ivanov 1998) and reveal a pronounced hysteresis after exiting clouds. In general, its performance is unreliable at temperatures below −40 °C or at low relative humidities (WMO 2008). Thin film capacitors, consisting of a hydroactive polymer film between two electrodes are faster and more reliable than carbon hygristors and are the most common type of humidity sensors on radiosondes today. Much of the archived upper tropospheric humidity data for the past several decades are not reliable for climate studies, possibly with the exception of upper tropospheric humidity data from thin-film capacitors (Kley et al. 2000).

The most widely used radiosondes in the global upper-air sounding network have been developed by Vaisala. Since 1980 Vaisala has produced radiosondes using Humicap sensors. These sensors were first integrated into RS80 radiosondes and later into RS90 and RS92 radiosondes. This section provides an overview for each of the Vaisala humidity sensors since the early 1980s including a description of the main changes affecting the long-term humidity data continuity.

2.2.2 RS80 Radiosonde

RS80 radiosondes were introduced in 1980. These sondes were first equipped with an A-Humicap sensor. Later these sondes were also available with H-Humicap sensors. The factory calibration procedure relates the measured capacitance to relative humidity with respect to liquid water at +20 °C. RH is calculated from the measured capacitance in two processing steps. First, RH is calculated from the individual calibration curve derived from the calibration of each sensor at +20 °C and at 0 % and 75 % RH. Second, RH is then adjusted for the measured ambient temperature on the basis of a sensor-type specific temperature-dependence (TD) calibration model, which consists of RH and temperature dependent curve fits derived from a large set of sensors tested at the calibration facility of the manufacturer (Miloshevich et al. 2001).

Most meteorological sensors are calibrated in terms of relative humidity over liquid water (WMO 2008), which is defined as:

$$RH \equiv RH_w = 100 \cdot \frac{e}{e_w\,(p, T)} \tag{2.1}$$

No data exist for the saturation vapour pressure over liquid water $e_w(T)$ at low temperatures and theoretical equations describing the saturation vapour pressure over liquid water differ significantly at temperatures less than −40 °C. Therefore it is essential to know the vapour pressure equation used by the manufacturer in their calibration process when using RH measurements at low temperatures. Vaisala uses the formulation by (Wexler 1976) for $e_w(T)$. However, other saturation water

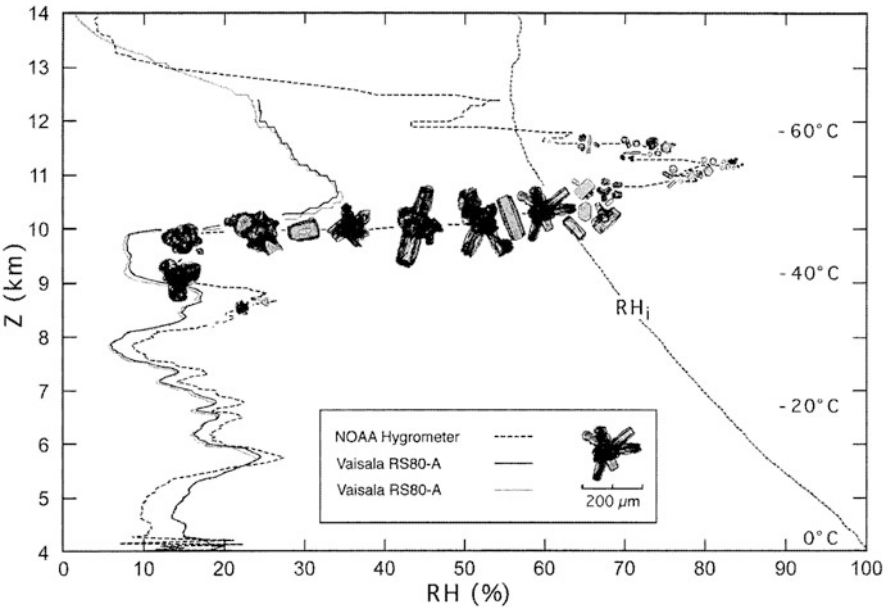

Fig. 2.2 Altitude profiles of RH (with respect to liquid water) measured simultaneously by the NOAA frostpoint hygrometer and two Vaisala RS80-A radiosondes in a cirrus cloud on 10 Nov 1994 near Boulder, Colorado. Superimposed are simultaneously observed ice crystals. The ice-saturation curve (RH_i) and several reference temperatures are also shown. (From Miloshevich et al. 2001, used with permission)

vapour pressure equations for temperature below 0 °C exist (see Appendix B) and were reviewed by for example by (Murphy and Koop 2005).

Production calibration of the RS80 radiosonde A-Humicap sensor relies on the A-type specific calibration model and on linear temperature dependence. Calibration and related corrections have been unchanged between October 1985 and the end of production in 2008. Production calibration of the RS80 radiosonde H-Humicap sensor uses an H-type specific calibration model, including a nonlinear temperature dependence, which have been unchanged between 1990 and the end of the RS80 production.

Measurements have shown that the temperature dependence of the A-Humicap is, in fact, nonlinear. As a result, the linear correction is insufficient at temperatures below −20 °C (Miloshevich et al. 2001; Wang et al. 2002), leading to a significant dry bias in RH measurements especially at high humidities. An example of this dry bias inside a cirrus cloud is shown in Fig. 2.2. From a statistical analysis of simultaneous RH measurements from RS80-A radiosondes and the NOAA cryogenic frost point hygrometer (Miloshevich et al. 2001) derived a multiplicative dry bias correction factor of about 1.3 at −35 °C, 1.6 at −50 °C, 2.0 at −70 °C. Thus, the inadequate temperature-dependence (TD) correction is the dominant systematic error in A-type Humicap measurements.

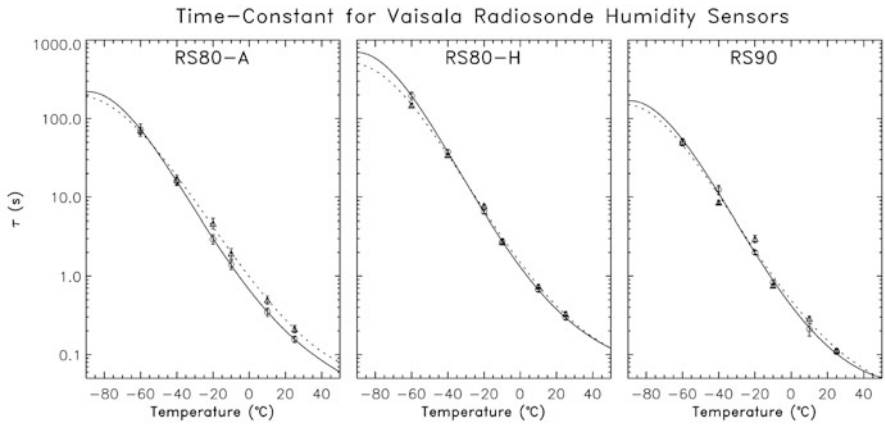

Fig. 2.3 Response time as function of temperature for the Vaisala RS80-A, RS80-H and RS90 humidity sensors. (From Miloshevich et al. 2004, used with permission)

The nonlinear TD correction for H-type RS80 sensors removed large parts of the humidity dry bias found in the A-type Humicap; however a significant dry bias at low temperatures remained: 4 % of the measured RH at −40 °C, 13 % at −60 °C, and 32 % at −80 °C (Wang et al. 2002). Despite the improved calibration, some issues in RS80-H production remained, causing biases and additional batch variations (Turner et al. 2003; Revercomb 2003; Verver et al. 2006).

An additional source of measurement error is caused by sensor lag, i.e. strong smoothing of the RH-profile at lower temperatures. The response time of the RS80 Humicap is mainly dependent on the characteristics of the polymer, sensor and sensor boom design. Laboratory measurements by Vaisala (Miloshevich et al. 2004), adopted from (Paukkunen 2002) show that the response time (63 %) of the Humicap sensor increases approximately exponentially with decreasing temperature, exceeding 1 min. at temperatures colder than about −50 °C (Fig. 2.3). Depending on the sign of the vertical RH-gradient the time lag error can be positive or negative. Statistically, the time lag is expected to produce on the average a zero overall bias if at a given altitude the distribution of increasing and decreasing relative humidity would be symmetric. In reality, the time lag error may contribute a systematic bias at levels with pronounced increasing or decreasing relative humidity, such as at the tropopause.

A time lag correction has been developed by (Miloshevich et al. 2004). A statistical analysis of the difference between time lag corrected RS80-H and simultaneous NOAA-cryogenic frostpoint hygrometer (CFH) shows that the corrections reduced the mean radiosonde dry bias to 4 % RH at −20 °C and 10 % RH at −70 °C to about ±2 % RH at all temperatures (Miloshevich et al. 2004).

In addition to time lag for both Humicap sensors and an inappropriate temperature-dependence for the A-Humicap sensor some issues in RS80-H production remained, causing biases and additional batch variations (Turner et al. 2003; Revercomb 2003; Verver et al. 2006). Chemical contamination was found to be an additional

source of systematic bias. A major source of contaminating chemical molecules is the radiosonde packaging material, which outgases after the radiosonde has been vacuum-sealed in its foil bag. Contamination may cause a dry bias depending on sensor type, storing time and storage conditions. The A-Humicap polymer is more selective to water and thereby less sensitive to chemical contamination. The contamination correction for the A-Humicap sensor is estimated to be approximately 2–5 RH %. For RS80-H the contamination correction is estimated in the range of 5–10 RH %, depending on storing time and storage conditions (Wang et al. 2002). RS80 radiosondes produced after June 2000 are not expected to exhibit this error due to a change in packaging using an absorbing material (gradually phased into production starting in September 1998) and a mechanical shield around the sensor boom, which is removed before radiosonde use (in production starting in June 2000). Several studies reported a significant decrease of the dry bias after the introduction of new packaging materials (Wang et al. 2002; Nakamura et al. 2004).

RS80 humidity sensors are shielded with an aluminized protective cap to prevent the impact of solar radiation and precipitation. Despite the shielding, the sensor exhibits a daytime radiation dry bias, which was noted as a sensor arm heating before launch and for a certain time after launch (Wang et al. 2002) and a dry bias in the integrated precipitable water (Turner et al. 2003; Cady-Pereira et al. 2008; Ciesielski et al. 2009).

Condensation and sublimation on the surface of the sensor or on the surrounding mechanical surfaces may also contribute to a microclimate around the sensor. In saturated conditions or in rain a sensor may become contaminated or coated with ice or liquid water and may no longer measure the true ambient RH correctly. RH values that are obviously too high and a lack of sensitivity in fast changes of ambient RH are an indication for sensor icing.

2.2.3 RS90 Radiosonde

The RS90 radiosonde, which was manufactured from 1997 to 2005 introduced a heated H-polymer twin sensor design (Antikainen and Paukkunen 1994; Paukkunen 1995) to make measurements less vulnerable to sensor icing. Due to the smaller sensor size the time response was significantly faster compared to the RS80 sensors. The humidity sensors of this sonde were alternately heated at regular time intervals using a heating resistor integrated into the glass substrate of the sensor. In heating mode a sensor's temperature was raised above the boiling point of water to remove any condensation. After cooling down to ambient temperature, the sensor then continued operating in measurement mode, at which moment the second sensor started its heating cycle. Alternating heating cycles extended down to −40 °C and were not done at lower temperatures. Due to the smaller sensor size the time response was significantly faster compared to the RS80 sensors (see Fig. 2.3).

With the introduction of the RS90 radiosonde a new calibration facility and a new calibration model (Paukkunen 1998) were introduced as well. The calibration was now fitted to several calibration points, directly traceable to reference standards.

Batch dependent variations and basic calibration model based biasing (as in RS80 radiosondes) were reduced. Accuracy and performance of RS90 radiosonde have been described by Paukkunen et al. (2001), who also introduced a new method for the evaluation of uncertainties of radiosonde measurements.

Initially the temperature dependence correction for the humidity sensor was based on the RS80 H-Humicap model. An updated temperature dependence correction was introduced on 25 June 2001. In contrast to the RS80 radiosondes, a contamination protection shield (boom cover) was not used for RS90 radiosonde packages. As a result, increased variations and a possible dry bias in RS90 humidity measurements may have been caused by storage time and conditions (Miloshevich et al. 2006). Also due to the geometry of the sensor, the RS90 humidity sensor does not have a protective rain cap over it. Although this may be considered advantageous with respect to sensor ventilation, the lack of a cap leads to increased sensitivity of the RS90 sensor to solar radiation.

Few detailed comparisons have been done using the RS90 radiosonde. Comparisons of integrated precipitable water from sondes and microwave radiometers showed that the RS90 exhibited a significant daytime dry bias in the lower troposphere (Van Baelen et al. 2005). This relative dry bias was found to be between 6–8 % (Miloshevich et al. 2006), using a smaller sample 2–9 % (Cady-Pereira et al. 2008), and using a number of different stations 5–7 % (Wang and Zhang 2008). This daytime dry bias has not been vertically resolved for the RS90 radiosonde; however, (Vömel et al. 2007a) noted that in a very limited sample the vertically resolved dry bias might not be as large as that for the RS92. However, (Rowe et al. 2008) investigated the RS90 dry bias over Antarctica at lower pressures compared to the other studies and found a dry bias consistent with that by (Vömel et al. 2007a) for the RS92. The radiation error is larger than that for the RS80 (Smout et al. 2000) because of the absence of a protective cap, which had been part of the RS80 humidity sensor. The absence of this protective cap exposes the sensing elements to direct sunlight allowing the sensor temperature to rise significantly above ambient temperature. Furthermore, a larger batch-to-batch variability in the production of RS90 radiosondes may increase the overall uncertainty of humidity measurements using RS90 sondes (Smout et al. 2000).

2.2.4 RS92 Radiosonde

The latest Vaisala radiosonde model, the RS92, is in use since 2004 and uses a heated dual H-Humicap sensors design similar to that of the RS90. The heating cycles were optimized to prevent sensor icing by tuning the heating parameters and extending the heating cycles from −40 °C to down to −60 °C (introduced since March 2005). In addition the coating of the sensor arm has been improved (Vaisala 2007), which was tested in the Mauritius radiosonde intercomparison (Nash et al. 2006) and entered production in September 2006 and modified in June 2008. The RS92 incorporates a reconditioning cycle before a sounding using the ground check device (model GC25) to remove chemical contamination. The time response of the RS92 humidity sensor is assumed to be the same as the RS90, and time lag errors may still be seen in fast

humidity changes at cold temperatures. At the beginning of the RS92 production, the temperature dependence correction for the radiosonde humidity sensor was based on the RS90 H-Humicap model. A new temperature-dependent (TD) calibration model was implemented in production since April 2004. Changes in the RS92 design have been documented by Vaisala and can be identified with the help of the radiosonde serial number (Vaisala 2009).

First RS92 radiosondes were tested during radiosonde campaigns in 2003–2004 (Miloshevich et al. 2006; Vömel et al. 2007a, b; Suortti et al. 2008). The sondes participated in the WMO radiosonde intercomparison campaign at Mauritius in 2005 (Nash et al. 2006) and later in a number of field campaigns (Suortti et al. 2008; Vömel et al. 2007a, b; Miloshevich et al. 2006, 2009; Nuret et al. 2008). Similar to previous studies the following sources of RS92 humidity measurement uncertainty should be considered (Miloshevich et al. 2009): mean calibration bias, solar radiation error in daytime measurements, random production variability, sensor time-lag error, ground check related uncertainty, and round off error in the standard RS92 processed data files. Time-lag and empirical bias corrections are expected to improve the humidity measurements of operationally launched RS92 sondes.

In daytime measurements the radiation dry bias is the dominant systematic error. It is strongly altitude dependent due to the decrease in convective cooling of the sensor and may reach up to 50 % of the measured relative humidity in the tropical upper troposphere (Vömel et al. 2007a; Yoneyama et al. 2008).

In nighttime soundings the radiation error does not play a role and only calibration and measurement errors of the sensor itself contribute. (Miloshevich et al. 2009) found that in the lower troposphere the RS92 shows a moist relative bias between 3 % for moist conditions and up to 20 % for dry conditions (both at 700 hPa). The moist bias is also indicated in pre-launch ground tests under saturated conditions, and shows a strong dependence on the production-batch. In the upper troposphere this changes to a dry relative bias between 5 % for moist conditions and up to 20 % for dry conditions (Miloshevich et al. 2009).

The time lag smoothes out sharp vertical features and only leads to systematic biases in climatological records, where the RH profile is always decreasing, i.e. above the tropopause. However, the time lag will reduce the measurement uncertainty for individual profiles and increase the significance in larger data sets.

During the ground check the RH sensors are sealed in a small chamber filled with a desiccant and assumed to be at 0.0 % RH. Laboratory tests of different desiccants indicate that the best desiccant may only achieve an RH of 0.5 % (Gorman 2002), which coincidentally is near the average correction applied with well-maintained ground check units. Great care has to be taken that the desiccant has been properly dried, since the ground check value may represent the largest source of measurement uncertainty at low RH values.

After the correction of all systematic biases and time lag error RS92 data may have a bias uncertainty which is independent of height or RH and is estimated to be ± 4 % RH for nighttime soundings and ± 5 % for daytime soundings, plus an RH offset uncertainty of ± 0.5 % RH that is significant for dry conditions (Miloshevich et al. 2009). The uncertainty in the reference observations is one of the contributions to these uncertainty estimates and already included in these estimates.

2.2.5 Summary

Radiosondes deploying thin film capacitive sensors have the ability to provide humidity data that may be used for long term climate studies. The most widely used capacitive sensor is the Humicap (A- or H-type) developed by Vaisala and integrated in their radiosondes. Since 1980 the RS80 sondes have been equipped with the A-type (RS80-A) and the more stable and less hydrophilic H-type polymers, while the RS90 and RS92 sondes have been equipped only with the H-type polymer. The Humicap sensor responds to changes of relative humidity with respect to liquid water with a precision of ±1 % RH for Humicap-A and ±0.5 % RH for Humicap-H. An overview of factors affecting humidity measurements using Vaisala RS80-A, RS80-H, RS90 and RS92 sondes is shown in Table 2.1. The differences and correction methods of the humidity measurements by these widely used radiosondes have been described by (Suortti et al. 2008) and (Miloshevich et al. 2009).

The Humicap sensors are calibrated at the factory applying different temperature dependent (TD) calibration models for the RS80-A, RS80-H, RS90 and RS92 sondes, respectively. Due to an inadequate linear TD-calibration model RS80-A humidity measurements show a strongly increasing dry bias with decreasing temperature. Although, the use of a non-linear TD-calibration model for the Humicap-H type sensors have reduced large part of these dry bias effects at lower temperatures, a significant dry bias remains. The most often used dry bias corrections for the RS80 humidity measurements are given by (Leiterer et al. 2005) and by (Miloshevich et al. 2001, 2004).

The response time of the Humicap sensor is increasing exponentially with decreasing temperature (∼0.5–1 s at +20 °C; ∼2–8 s at −20 °C; ∼60–200 s at −60 °C), such that vertical structures in atmospheric humidity profiles are increasingly smoothed with decreasing temperature (i.e. increasing altitude). Vertical RH-profiles may be corrected for this time-lag effect by applying algorithms developed by (Miloshevich et al. 2004). A time lag correction will reduce the measurement uncertainty for individual profiles, increase the significance in larger data sets, and may reduce systematic biases in regions of the atmosphere, where the vertical RH gradient has a climatological preference.

For RS80-sondes manufactured before June 2000 outgasing of packaging material contaminated the Humicap sensors causing a dry bias of 2 % and 10 % of measured RH for 1-yr old RS80-A and RS80-H sondes, respectively. For RS90 and RS92 daytime measurements solar radiation can be the dominant systematic error source causing a dry bias, however, this can be corrected for.

After correction of all identified systematic biases and time lag effects Vaisala radiosondes may measure relative humidity with a relative uncertainty of about ±(3–5) % at ambient temperatures above −20 °C for RS80-A/H and RS90/92 radiosondes. However, at lower temperatures the relative uncertainty is increasing to ±10 % for RS80-A and ±(5–10) % for RS80-H or RS90. RS92 sensors may achieve a relative uncertainty of ±5.5 % for night time observations and ±6.5 % for day time observations (incl. ±1.5 % uncertainty contribution due to production variability), plus an RH-offset uncertainty of ±0.5 % RH (Miloshevich et al. 2009).

Table 2.1 Factors affecting humidity measurements by the RS80, RS90 and RS92 radiosondes

Factor	RS80-A	RS80-H	RS90	RS92
Batch variation in basic calibration at room temperature	Yes	Yes	No (direct multi point calibration against references)	No
Calibration model error (mainly at low temperatures)	Yes (large, due to linear model, last change in 1985)	Yes (smaller, TD correction model improved since 1990)	Yes (improved May 2001)	Yes (improved April 2004)
Chemical contamination of sensor	Yes (corrected by using drying agent in September 1998 and a protection shield in May 2000)	Yes (larger than for the RS80-A, corrected by using drying agent in September 1998 and a protection shield in May 2000)	Yes (minimized)	No (corrected by using reconditioning cycle in ground check unit)
Sensor wetting or icing	Yes	Yes	Yes (minimized by heated twin sensor)	Yes (minimized by heated twin sensor and extended heating cycles)
Humidity time lag (at cold)	Yes	Yes (larger than RS80-A)	Yes (smaller than RS80-A)	Yes (smaller than RS80-A)
Solar radiation heatings	Yes	Yes	Yes (larger than RS80)	Yes (larger than RS80)

Fig. 2.4 Airbus A340 equipped with MOZAIC-humidity device. Inlet system is mounted at the outside skin of the aircraft close to the cone

To reduce the estimated uncertainties of operational radiosondes as well as for reference instruments large efforts have been started in the scope of the Global Climate Observing System (GCOS) Reference Upper Air Network (GRUAN), (Seidel et al. 2009) as well the development of a new humidity sensor for balloon borne radiosonde measurements (Vaisala et al. 2010).

2.3 Humidity Monitoring from Aboard Commercial Aircraft: MOZAIC-Program

2.3.1 Introduction to MOZAIC-Program

MOZAIC (Measurements of ozone and water vapour by Airbus in-service aircraft) is an European project funded by the European Union for the measurement of the large scale distribution of trace gases like ozone, water vapour, nitrogen oxides and carbon monoxide from board of commercial Airbus A340-aircraft (Fig. 2.4) during scheduled "in-service" flights (Marenco et al. 1998), http://mozaic.aero.obs-mip.fr/web/.

Since 1994 compact light weighted humidity devices are flown on five A340-aircraft operated by several European airlines (Lufthansa: 2 aircraft; Air France, Austrian Airlines and Sabena each 1 aircraft). The MOZAIC-flight routes cover a large extent of the northern hemisphere and parts of the southern hemisphere (Fig. 2.5). Every flight includes vertical profiles during takeoff/landing and continuous data at cruise altitude. Particularly the recording at cruise altitude between 9 and

Fig. 2.5 Overview of major flight routes with MOZAIC humidity measurements since August 1994. The numbers give the percentage of individual flight routes out of all flight

12 km altitude covers large areas of the upper troposphere and lower stratosphere, an important region with the largest climate sensitivity. Data from more than 25000 flights (comprised of two vertical profiles and about 8 hours of data in the UTLS per flight) have been collected since 1994. The data are stored in a scientific data base at CNRM (Toulouse, France) (http://mozaic.aero.obs-mip.fr/web).

Presently, three of the MOZAIC-aircraft (2 Lufthansa and 1 Air Namibia) are still in service. However, MOZAIC is entering a new phase as part of the IAGOS (In-service Aircraft for a Global Observing System) project (http://www.iagos.org/). IAGOS aims to fly instruments on a larger fleet of about 20 aircraft with a long term mission over the next 10–20 years and a better global coverage in both hemispheres. The first two IAGOS aircraft have started their mission in 2011 and 2012, respectively.

2.3.2 MOZAIC Humidity Device (MHD)

Relative humidity and temperature are measured with a compact airborne sensing device AD-FS2 (Aerodata, Braunschweig, Germany), as shown in Fig. 2.6 and described in detail by (Helten et al. 1998). The sensing element consists of a capacitive sensor (Industrial version Humicap-H, Vaisala, Finland) with a hydroactive polymer film as dielectric whose capacitance depends on the relative humidity (Anderson et al.1995) plus a platinum resistance sensor (PT100) for the direct measurement of the temperature at the humidity sensing surface. The humidity and temperature signals are linearized by a microprocessor controlled transmitter unit (HMP-230, Vaisala, Finland), which passes the relative humidity (RH) and the temperature signal to the automated data acquisition system of MOZAIC located in the avionic bay of the aircraft (Marenco et al. 1998). The humidity sensing element, together with

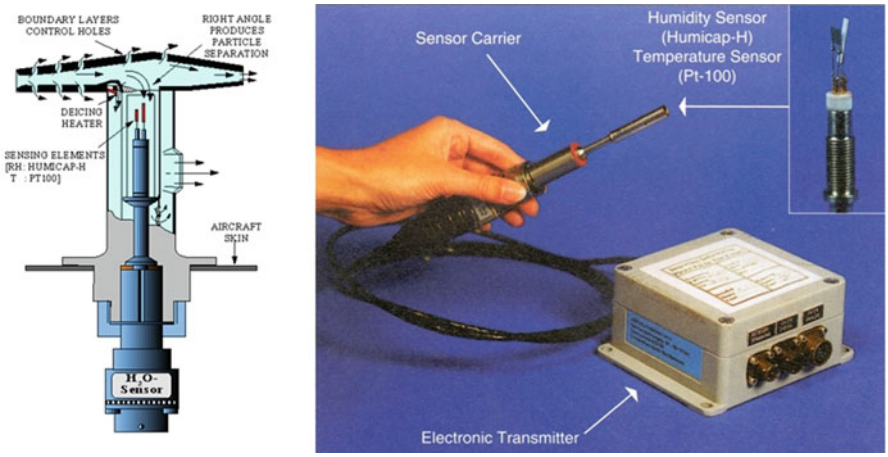

Fig. 2.6 Left panel: Cross section of the airborne MOZAIC humidity sensor mounted in air sampling housing (Rosemount, Model 102 BX). Right panel: MOZAIC Humidity Device (MHD) consisting of the sensor carrier (including sensing element of Humicap-H and Pt100) to be installed in the Rosemount housing mounted on the outside skin of the Airbus A340 aircraft (Fig. 2.4) and a microprocessor-controlled transmitter unit (H × L × W = 120 × 180 × 130 mm, Total weight ~1.5 kg, Power consumption 5 VA at 28 VDC)

the PT100-resistor, are mounted at the top of an axisymmetric body, which is designed for installation in an appropriate housing (Model 102 BX, Rosemount Inc., Aerospace Division, USA). The sensor housing (Fig. 2.6) is known to derive accurate ambient air temperatures (Stickney et al. 1994).

The housing with both sensors is positioned outside the fuselage, 7 m backwards from the aircraft nose on the left side just below the cockpit. Air sampling occurs at a distance of 7 cm from the aircraft skin, well outside the local boundary layer (thickness only 3 cm) of the aircraft, thus avoiding contaminating interferences that might originate from the aircraft skin. The sampled air flow is divided into two sub flows inside the inlet of the housing. The main flow traverses straight through the housing. The minor flow makes a sharp right angle turn to a smaller channel, perpendicular to the main channel, passing over the sensor elements before reaching a small outlet, located at the lower back side of the housing. The right angle turn of the secondary air flow protects the sensors against dust, hydrometeors and particles. The internal boundary layer air is sucked off through small holes in the side walls of the housing, minimising internal boundary-layer effects. This protects the core of the sampled air flow from thermal or humidity influences as might originate from contact of the outer parts of the sampled flow with the walls of the housing.

The air entering the Rosemount housing is subject to adiabatic compression caused by the strong speed reduction in the inlet part of the housing. The conversion of the kinetic energy of the sampled air into heat leads to a significant temperature increase of the air sampled by the sensor. The thermal recovery process at the sensing element is well defined (Stickney et al.1994). In flight, Static Air Temperature (*SAT*) is the

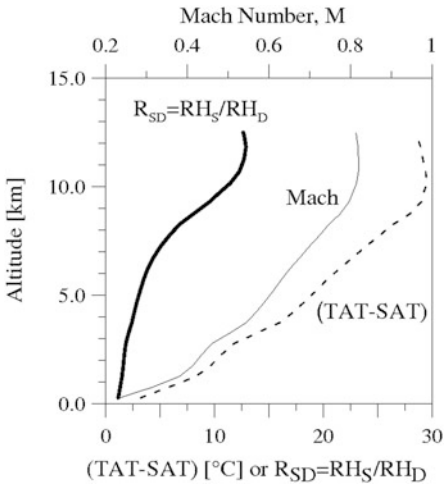

Fig. 2.7 Mean values of the speed of the MOZAIC aircraft (Mach number, *thin solid line, upper scale*) as a function of altitude. The *broken line* (*lower scale*) gives the corresponding difference between the temperature measured by the sensor and the ambient temperature (*TAT-SAT*) and the *thick solid line* gives the ratio between ambient and measured relative humidity (RH_S/RH_D)

temperature of the undisturbed air through which is about to fly. Total Air Temperature (*TAT*) is the maximum temperature that can be attained by 100 % conversion of the kinetic energy into heat of the air sample. The relation between total and static air temperature is:

$$TAT = SAT\left(1 + \left(\frac{c_p - c_V}{2c_V}\right) M^2\right) \tag{2.2}$$

In Eq. 2.2, c_p and c_V are the specific heats of dry air at constant pressure and volume, respectively, and M is the Mach number, i.e. ratio of the aircraft speed (relative to air) relative to the speed of sound. M is available in flight from the avionic system of the aircraft. M typically increases from values of about 0.2 near ground to 0.81±0.01 at cruise altitude (Fig. 2.7). The conversion of kinetic energy inside the housing is not exactly 100 %. Therefore, the temperature measured by PT100 inside the housing, the total recovery temperature (*TRT*), is lower than the total air temperature (*TAT*), expected after a complete conversion of the kinetic energy. The housing manufacturer provides an empirical recovery factor η to determine the real *TAT* from *TRT* by the relation

$$TAT = \frac{TRT}{1 - \eta} \tag{2.3}$$

The recovery factor η, determined from a series of wind channel experiments, is a function of the Mach number and given by a function table (Stickney et al. 1994). Even at large Mach numbers the recovery factor is smaller than 0.004 such that corrections of *TRT* to *TAT* are always smaller than 1 K.

The adiabatic compression produces an appreciable temperature rise relative to the ambient static air temperature (*SAT*) if the aircraft speed is comparable to the speed of sound (Fig. 2.7). The resulting difference between total and static air temperature (*TAT-SAT*) increases from 2 K near ground to approximately 30 K at 10–12 km cruise

altitude. Because of the strong temperature increase, the relative humidity RH_D detected by the sensing element in the Rosemount housing is appreciably lower than the static relative humidity of the ambient air, RH_S (Helten et al. 1998).

$$RH_S = RH_D \left(\frac{SAT}{TAT}\right)^{\frac{c_p}{c_p - c_V}} \frac{E_W\,(TRT)}{E_W\,(SAT)} \tag{2.4}$$

The first factor in Eq. 2.4 describes the adiabatic compression, while the second term accounts for the different water vapour saturation pressures E_W at SAT and TRT, respectively.

For the evaluation of the water vapour data we follow the formulation of E_W by (Goff and Gratch 1946) over a plane surface of pure liquid water, as recommended by the World Meteorological Organisation (WMO 1983) and adapted to the International Temperature Scale 1990 (ITS-90; Sonntag 1994):

$$E_W\,(T) = exp\left(\frac{a}{T} + b + c \cdot T + d \cdot T^2 + e \cdot ln\,(T)\right) \tag{2.5}$$

where E_W is in Pa and T in K. For a liquid water surface, the constants are: $a = -6096.9385\,\mathrm{K}$, $b = 21.2409642$, $c = -2.711193 \times 10^{-2}\,\mathrm{K}^{-1}$, $d = 1.673952 \times 10^{-5}\ \mathrm{K}^{-2}$, $e = 2.433502$.

At cruise altitude, RH_D is a factor of 12–13 lower than RH_S (Fig. 2.7). Therefore, the humidity sensor usually works within the lowest 10 % of its dynamic range. This fact is not adequately covered by the factory calibration provided with the transmitter unit and hence requires regular individual recalibration of each sensor, in particular of the sensor bias.

2.3.3 *Pre- and Post-Flight Calibration in Environmental Simulation Chamber*

Each MOZAIC humidity sensor that is used for the MOZAIC project is individually calibrated in the laboratory at Jülich before installation in the aircraft and again after 500 flight hour intervals. Prior to a preflight calibration the sensor is rinsed with ethanol and then reformed by heating it to 130 °C. Postflight calibrations are done without prior cleaning. The laboratory calibration is executed in an environmental simulation chamber (Fig. 2.8; http://www2.fz-juelich.de/icg/icg-2/esf). The chamber is a stainless steel vacuum chamber with a volume of 500 l (80 × 80 × 80 cm) (Smit et al. 2000). Pressure, temperature, and relative humidity are computer controlled to simulate atmospheric flight conditions, which are typically encountered in the troposphere, including tropopause, and lower stratosphere. Typical tropospheric conditions of water vapour concentrations, temperatures, and pressures up to altitudes of 15 km can be simulated. Frost point temperatures down to −80 °C can be reached.

A Lyman(α) fluorescence hygrometer (Kley and Stone 1978) is installed in the simulation chamber as reference instrument for the measurement of low water vapour

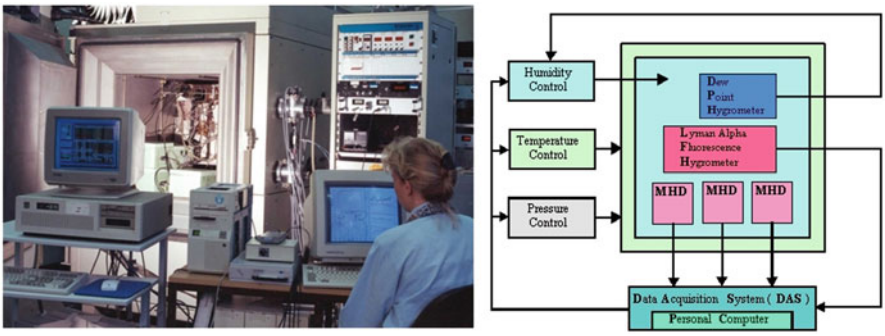

Fig. 2.8 Environmental simulation facility at Forschungszentrum Juelich (IEK-8) to calibrate MOZAIC-Humidity Devices at typical pressure, temperature and humidity conditions encountered during flight

mixing ratios (1–1000 ppmv) with a relative accuracy of ±4 % (Helten et al. 1998). At water vapour mixing ratios above 1000 ppmv serves a dew/frost point hygrometer (General Eastern, Type D1311R) with an accuracy of ±0.5 K. Up to three water vapour sensors can be simultaneously calibrated. They are positioned in the outlet duct flow of the Lyman(α) hygrometer and sample the air just after it has passed the hygrometer.

The calibrations revealed that the relative humidity of a calibrated sensor (RH_C) for a constant temperature can be expressed by a linear relation

$$RH_C = a + b \cdot RH_{UC} \tag{2.6}$$

where RH_{UC} is the uncalibrated output from an individual sensor, while the offset (a) and slope (b) are determined as a function of temperature (Helten et al. 1998). At a fixed sensor temperature, three different levels of humidity are set which correspond to typical conditions encountered at the sensing element during in-flight operation in the troposphere.

To derive the coefficients a and b as function of temperature calibrations were executed at three temperatures, −20 °C, −30 °C, and −40 °C while at higher temperatures an interpolation between the chamber calibration at −20 °C and the nominal calibration of the manufacturer at 20 °C has been applied (Helten et al. 1998). However, since 1999 additional calibrations at 0 °C and 20 °C have become standard in the calibration process to improve the accuracy of the measurements made in the corresponding altitude region between 0 and 5 km (Fig. 2.9). The pressure at −40 °C and −30 °C is set to 180 hPa and increased to 400 hPa at higher temperatures. From investigations made at constant temperature but at different pressures between 100 and 1000 hPa, no significant pressure dependence of the sensitivity of the humidity sensor had been observed (Helten et al. 1998).

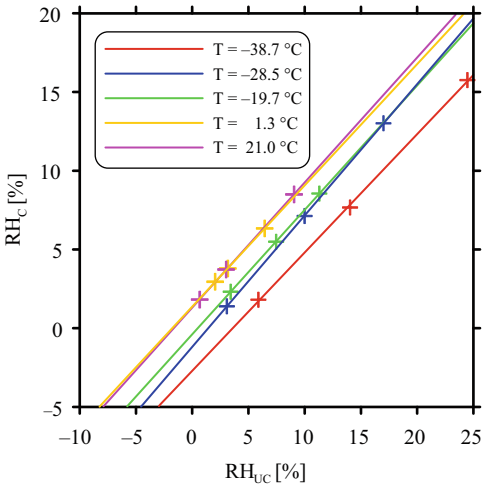

Fig. 2.9 Calibration of a MOZAIC humidity sensor at 5 temperature levels: Reference hygrometer (Lyman Alpha & Dew/Frost point) as a function of the sensor measurement (*crosses*) together with corresponding linear regression fits

2.3.4 Assessment of In-Flight Uncertainties

It is recalled that the analysis of the MOZAIC measurement is performed with the averages of the individual preflight and postflight calibration coefficients a and b for each interval of 500 hours of flight operation. RH_S of the ambient air is determined from the measured RH_D, TRT, TAT, and SAT by Eq. 2.4. The uncertainty of RH_S is deduced by the law of error propagation with the uncertainty of these parameters. The uncertainty of RH_D is a composite of the following contributions: uncertainty of the Lyman-α hygrometer calibration and half of the absolute value of the differences of the individual preflight and postflight calibration coefficients, a and b. To convert to the uncertainty of RH_S, the uncertainties of TAT and TRT (equal to $\pm 0.25\,^{\circ}$C) and SAT (equal to $\pm 0.5\,^{\circ}$C) have to be included. The contribution of uncertainty of the air speed measurement by the aircraft to the uncertainty of temperature determination is below $\pm 0.01\,^{\circ}$C and was excluded from the error propagation determination. The uncertainty of the recovery factor η of the Rosemount probe housing contributes to the uncertainties of the temperature measurements and, thus, RH_S recovery. One determines then the total uncertainty of RH_S. The analysis show that the major contribution comes from the differences of calibration coefficients a and b between preflight and postflight calibration (Helten et al. 1998). If these differences are small, then this contribution is of the same order of magnitude as the uncertainty caused by the temperature uncertainty. The MOZAIC database contains estimates of the total uncertainty of RH_S for each individual humidity data point based on the pre- and post-flight calibration of the flown humidity sensor.

The mean of the pre- and post-flight calibration coefficients of each flight period are used to evaluate the average uncertainty of the measurements. The differences between both sets of these calibration coefficients give the main contribution to the uncertainty of the measurement (Helten et al. 1998). The variations of the uncertainties

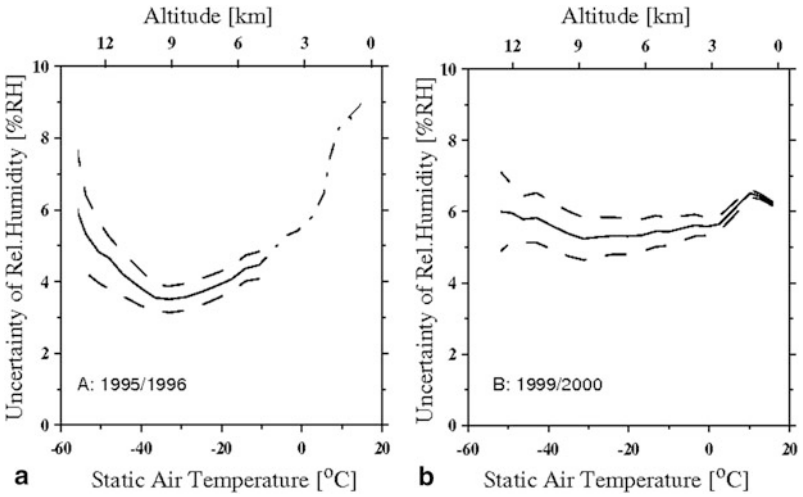

Fig. 2.10 Mean uncertainty in percent *RH* of all MOZAIC relative humidity measurements (*solid curve*) as a function of static air temperature (bottom x-axis) made over 1995 & 1996 (left diagram **a**; calibration at (−20 °C, −30 °C, and −40 °C) and 1999 & 2000 (right diagram **b**; calibration including 0 °C and 20 °C). The standard deviation of the mean is marked by the *dashed curves*. For 1995/1996 (**a**) the region not covered by preflight and postflight calibrations (lower troposphere, see text) is indicated with an estimated mean uncertainty (*dashed/dotted line*). The corresponding altitude is indicated as the top x-axis

of the *RH* measurements were determined as the mean of all individual total uncertainties over all MOZAIC data as a function of *SAT* for 1996/1997 and 1999/2000, representive for calibrations made at the three lower temperatures (−20 °C, −30 °C, and −40 °C) and inclusion of higher temperatures (0 °C and 20 °C), respectively (Fig. 2.10). The standard deviation is also shown. For 1994–1998 data (left diagram) the uncertainty ranges from ±7 % *RH* at −55 °C (≈13 km) down to ±4 % *RH* at −40 °C (≈10 km). At lower altitude, for SAT ranging between −40 °C (≈9 km) and −20 °C (≈6 km) the uncertainty is within ±(4–6) % *RH*, increasing above 0 °C (near ground level) to ±8 % *RH*. For the region below 5 km altitude, only an interpolation between the sensor calibration made in the chamber at −20 °C and the nominal calibration of the sensor manufacturer is used, indicated as a dashed dotted line in Fig. 2.10. However, since 1999 after inclusion of sensor calibration at 0 °C and 20 °C the accuracy below 5 km has increased significantly. From the regular pre- and post-flight calibration of each flown sensor typical 1σ-uncertainties of ±(4–6) % relative humidity between surface and 12 km altitude are obtained. It is to be noticed that the relative uncertainties of the measurements are rapidly increasing in dry air. For measurements of stratospheric humidity, where relative humidities well below 5 % prevail, the uncertainty of the MOZAIC humidity device is insufficient for quantitative water vapour measurements.

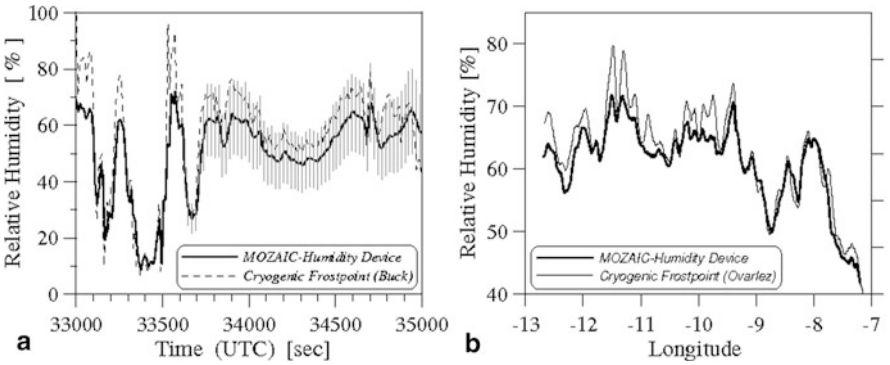

Fig. 2.11 (**a**) Relative humidity measured by MHD and cryogenic frostpoint hygrometer (Busen and Buck 1995) as function of flight time during intercomparison flight on board the DLR Falcon aircraft in March 1995 (Helten et al. 1998). (**b**) Relative humidity measured by MHD on the MOZAIC-Airbus aircraft and cryogenic frostpoint hygrometer (Ovarlez and Velthoven 1997) on the DLR Falcon aircraft as a function of longitude during a dedicated comparison flight in September 1997. The Falcon followed the Airbus at a distance of 7 to 35 km. (Source: Helten et al. 1999)

2.3.5 In-Flight Comparison of MHD With Other Hygrometer: Time Response and Spatial Resolution

The in-flight performance of the MOZAIC-humidity device had been assessed by intercomparison with reference instrumentation during dedicated research aircraft missions. Fig. 2.11 shows results from two missions with a Fanjet Falcon E research aircraft of the Deutsches Zentrum für Luft- und Raumfahrt (DLR), the in-flight performance of the MHD was assessed by intercomparison with reference instrumentation. The first in-flight comparison of the MHD against reference instrumentation was conducted in 1995 with the MHD mounted aboard the Falcon aircraft (Helten et al. 1998). As reference served an airborne cryogenic frostpoint hygrometer, with a relative accuracy of $\pm 10\,\%$ (Busen and Buck 1995). The second mission took place in 1997 whereby the Falcon aircraft approached the flight path of the MOZAIC-aircraft at 13° W longitude and followed until 7° W longitude (Helten et al. 1999). The Falcon aircraft was equipped with a cryogenic frostpoint hygrometer developed for airborne water vapour mixing ratio measurements with a relative accuracy of about 5 % (Ovarlez and van Velthoven 1997). Both aircraft missions confirmed the results yielded from pre- and post-flight calibrations (Helten et al. 1998). Similar results (Fig. 2.12) were obtained more recently in 2006 during an in-flight comparison of the MHD with the Jülich Lyman-α fluorescence hygrometer, FISH (relative accuracy $\pm 5\,\%$; (Zöger et al. 1999) made from aboard a Learjet 35 aircraft (Kunz et al. 2008).

The structures measured with the reference instruments are smoothed by the MHD. This is caused by the response time of the MHD which increases with decreasing sensor temperature due to the adsorption and diffusion of water molecules into the

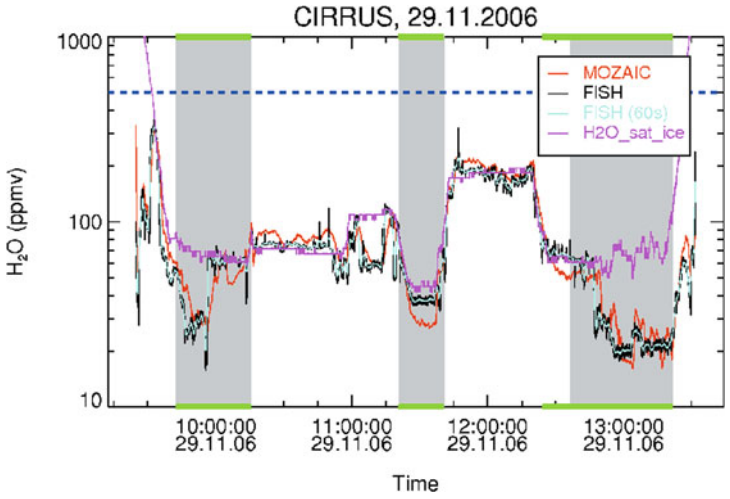

Fig. 2.12 In-flight comparison of water vapour mixing ratio measured by MHD and FISH as function of flight time during one flight mission on board the Learjet 35 A aircraft in November 2006. (Source: Kunz et al. 2008)

sensor material (Antikainen and Paukkunen 1994). It is inferred from Fig. 2.11 that at sensor temperatures (equal to *TRT*) of about −30 °C the response time is several minutes. Above −10 °C the MHD tracks fine structures in the humidity field well, but measures drier values compared to the frost point hygrometer. This is most likely due to the fact that before 1999 the MOZAIC sensor was not calibrated at these relative high sensor temperatures.The response time of the MOZAIC sensor during ascent and descent is well below 10 s near ground and below 1 min around 9 km altitude (Helten et al. 1998). This means that at an ascent/descent rate of the MOZAIC aircraft of about 8 m/s, the vertical resolution of measured vertical humidity profiles is better than 100 m in the lower troposphere and around 500 m in the upper troposphere. At cruise altitude the response time is about 1–3 min such that at a horizontal aircraft speed of 250 m/s, the horizontal resolution is about 15–50 km which is sufficient to record large-scale distributions of upper tropospheric water vapour.

2.3.6 Performance at High Relative Humidities: Ice Super Saturation

In the upper troposphere (Z = 9 − 12 km) a substantial fraction (0.1–0.3) of the MOZAIC-relative humidity measurements show supersaturation with respect to ice (e.g. Gierens et al. 2000; Luo et al. 2007). A common phenomena common observed from other measurement platforms in the upper troposphere, both in clear and cloudy regions (e.g. Heymsfield et al. 1998; Jensen et al. 1998; Vay et al. 2000; Comstock

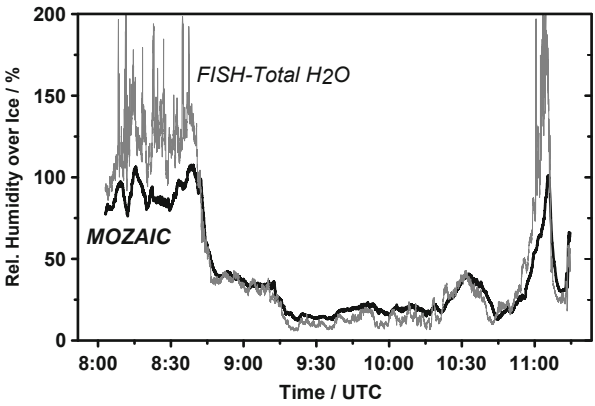

Fig. 2.13 In-flight comparison of relative humidity with respect to ice measured by MHD (*thick black*) and FISH-Total H_2O (*thin grey*) as function of flight time during a research flight on board the Learjet 35 A aircraft in April 2003. Cruise altitude 11–12 km and air temperature 215–220 K

et al. 2004). An important feature suggesting that water vapour in the upper troposphere is for a significant fraction of time not in thermodynamical equilibrium with the ice phase. However, in how far these *RH* measurements are artifacts (e.g. evaporation of ice crystals in inlet system due to adiabatic heating) or real atmospheric features? At low temperatures it is very unlikely that the contamination of evaporating ice crystals is a significant error source for the following reasons:

1. In wind tunnel experiments with true air speed (*TAS*) ∼100 m/s it was shown that only particles smaller than 1 μm have a considerably high chance to get to the *RH*-sensing element in the Rosemount housing (O. Reynolds, UK Met Office, 2003, personal communication). However, the *TAS* in real flights is rather ∼250 m/s, thus reducing additionally the probability of incoming ice crystals. These small ice crystals have masses on the order of 10^{-15} kg and for usual ice crystal number concentrations ($N < 10\,cm^{-3}$) the net effect is probably negligible.
2. In situ comparisons of the MHD with the FISH-total water vapour instrument (Schiller et al. 2008) on board a Learjet 35A aircraft show no evidence of contamination of the gas phase water vapour measurement of MOZAIC inside cirrus (Fig. 2.13). Below ice saturation the MHD tracks the FISH very well. However, at saturation levels above 100 % *RH* with respect to ice the behavior of both instruments is very different. Although the MHD stays close to 100 % *RH* with respect to ice, the FISH detects excesses of water vapour because it measures total water vapour, i.e. gaseous phase plus contribution of liquid/ice phase which has been forced to evaporate by heating before detection.
3. Only a very small fraction of 0.5 % of all MOZAIC measurements (complete data base) show *RH* values in excess of 100 % with respect to liquid water, whereas more than 30 % of the data in the tropopause region show ice supersaturation (Fig. 2.14). In case of massive contamination due to evaporating ice crystals the frequency of occurrence for $RH > 100\,\%$ "values" should be enhanced.

In the lower and middle troposphere at warmer temperatures, relative humidity values in excess of 100 % to liquid water are occasionally observed. This contamination is

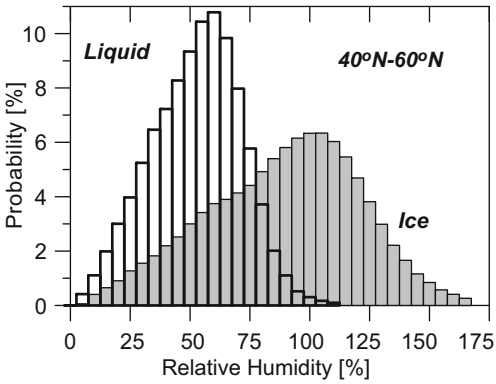

Fig. 2.14 Probability distribution function of relative humidity with respect to liquid water (*thick black*) and ice (*thin black, grey shaded area*) in UT between 40°–60° N obtained over the Atlantic (10°–70° W) over more than 1000 flights made in 1998

most likely caused by partial or complete evaporation of liquid droplets after entering the Rosemount inlet. In contrast to ice particles, the strong shear flow forces caused by the strong speed reduction, can atomize liquid droplets into a large number of very small droplets that evaporize much faster than ice particles with the same water content.

2.3.7 New Developments: In-Flight Calibration Method

While MOZAIC has demonstrated the large potential of in-service aircraft as a cost efficient platform for obtaining high quality humidity data in the free and upper troposphere, a larger fleet of aircraft is required for obtaining a truly global picture. This calls for a measurement system that is (i) compact, light-weight, and quasi maintenance-free and (ii) reliable, precise, and sufficiently accurate. The MOZAIC humidity sensor has shown to fulfill these criteria (Kley et al. 2000). However, the method of pre- and post-flight calibration in the laboratory every 500 hours of operation, as applied in MOZAIC, is not suitable for real-time data provision, a pre-requisite for operational use in meteorological networks. Therefore, based on the experience gained on instrument characteristics at different temperatures during 10 years of MOZAIC-operation a novel method for automatic in-flight calibration (IFC) of the sensors has been developed and described in detail by (Smit et al. 2008).

The IFC method corrects the potential drift of the sensor offset at zero relative humidity, which is the critical parameter in determining the uncertainty of the measurements. Any drift of the sensor offset is caused by additional bonding of non-water molecules originated from polluted air. However, praxis has shown that the offset drifts slowly and only significant changes have been first observed after 4–8 weeks of flight operation. The sensor offset is determined from the measurements themselves as obtained during periods when the aircraft is flying in the lower stratosphere at or above the hygropause where the H_2O mixing ratio reaches well defined minimum values of about 5 ppmv and the contribution of atmospheric H_2O to the sensor signal

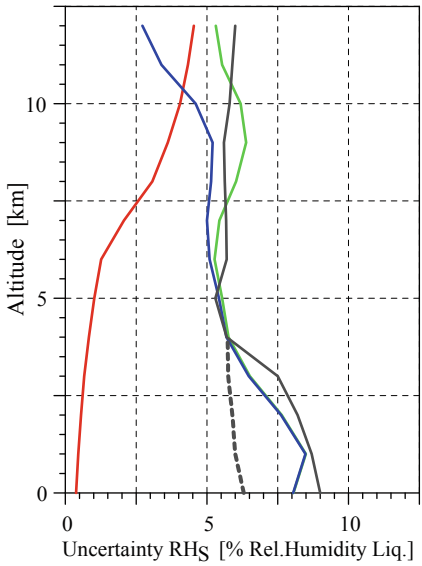

Fig. 2.15 Total uncertainty of the relative humidity profile (*green curve*) calculated from the uncertainty of the average slope *b* (*blue curve*) and the uncertainty of the offset *a* (*red curve*) obtained from the IFC-method. For comparison, the average uncertainty of the MOZAIC calibrations is also shown (*black solid curve*: based on calibrations between 235 K and 260 K as reported by (Helten et al. 1998); dashed black curve: valid since 1999, after extending the calibrations at sensor temperatures of 270–290 K. (Source: Smit et al. 2008))

is minimal. The selection of stratospheric data is achieved with the help of potential temperature that can be calculated in-situ from measured temperature and pressure.

The IFC method is capable of providing humidity measurements in near real time with an uncertainty of ±8 % *RH* at the surface and ±7 % *RH* in the upper troposphere (Fig. 2.15). For validation, the IFC method was applied to five years of archived raw signals from the MOZAIC aircraft. The resulting humidity data are in good agreement (within 2 % *RH*) with the original MOZAIC data that used monthly pre- and post flight calibrations of the sensor. The standard deviation of the differences varies with altitude between ±4 % and ±6 % RH which is comparable to the accuracy of the MOZAIC laboratory calibrations (Fig. 2.15).

At the typical cruise altitude of longhaul aircraft (9–12 km), the IFC method is most efficient and accurate at higher latitudes where dry stratospheric air coincides with relatively high ambient temperatures (220–230 K), hence providing the lowest contribution to the signal of the sensor, which measures relative humidity. At these conditions the a priori assumption of 5 ppmv for the water vapour mixing ratio at the hygropause is not critical for the accuracy of the method. Compared to MOZAIC-operation based on monthly calibrations in the laboratory the use of IFC will substantially reduce the efforts for maintenance and thus will enable to operate the sensor on a large fleet of in-service aircraft for near real time measurements of humidity in the troposphere. The IFC method will not work, however, on aircraft that never enter the lower stratosphere, e.g. aircraft that fly exclusively regional routes or in the tropics. Regular offline calibrations will remain important for such aircraft.

2.3.8 Summary and Conclusions

The MOZAIC project features more than 15 years of continuous measurements of water vapour from board commercial Airbus A340 aircraft during scheduled flights. Thereby capacitive humidity sensing devices are used to measure tropospheric relative humidity together with temperature from aboard aircraft, if the sensors are carefully calibrated before their installation and after deinstallation. After an operation time of 4–6 weeks (∼500 flight hours) the differences between preflight and postflight calibration result in uncertainties ±(4–6) % *RH* for measurements between surface and 12 km altitude. For dry regions with low relative humidities (e.g. stratosphere) the uncertainty of ±(4–6) % *RH* is getting limited for accurate humidity measurements.

The installation of the humidity sensor in an appropriate housing (Rosemount Model 102 BX), normally used in aviation to measure accurate ambient air temperature, has the advantage of protection against the impact of particles or dust. Also, wall contact of the sampled air, which would influence temperature and humidity, is avoided. Adiabatic compression causing a temperature increase of the sampled air leads to a reduction of the dynamic range of the sensor, but also provides for sufficient time response at low static air temperatures. There are no indications that MOZAIC-observations of ice super saturation in the upper troposphere are interfered by evaporation of ice crystals in the Rosemount inlet. In the lower and middle troposphere at higher temperatures in the presence of liquid droplets contamination from evaporation can occur because at the inlet droplets might atomize into a large number of very small droplets which evaporate much faster.

In-flight intercomparisons with a Lyman-α fluorescence hygrometer and a frost point hygrometer showed good agreement within ±(5–10) % *RH* for measurements in the middle/upper troposphere. The deviations of the Humicap sensor observed during this in-flight intercomparison is in agreeent with the uncertainty obtained from the estimated overall uncertainty which is dominated by contribution of the differences observed between preflight and postflight calibrations. The time response of the sensor in the lower/middle troposphere is good, but increases at lower temperatures to values of about 1 min at cruise altitude. Vertical resolution of humidity profiling during ascent and descent of the MOZAIC aircraft is better than 100 m in the lower part of the profile and around 200 m in the upper part of the profile. At cruise altitude the horizontal resolution of humidity measurements is around 15 km which is sufficient for climatological purposes.

A new method for in-flight calibration (IFC) has been developed, whereby the sensor offset is quasi-continuously monitored and adjusted in flight, while the less critical sensor sensitivity can be determined at longer (yearly) intervals. Through the use of the IFC-method the sensor needs only to be recalibrated on much longer time intervals (yearly) compared to the monthly calibrations as applied in MOZAIC. This enables operating the sensors on a larger fleet of aircraft with about the same amount of calibration efforts. Consequently, the IFC method will reduce maintenance drastically that make the sensor a serious candidate for real time humidity measurements

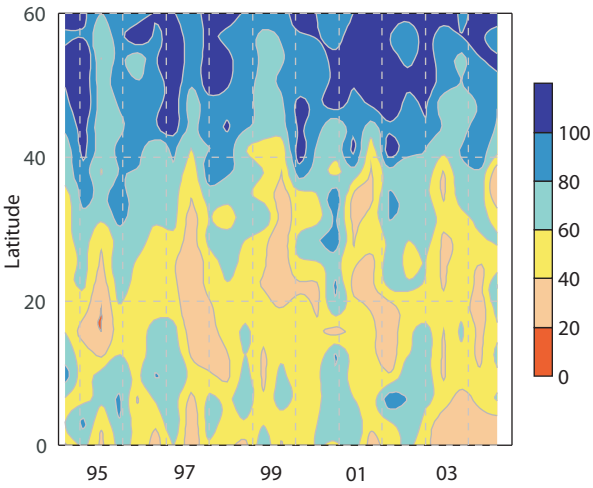

Fig. 2.16 10 year climatology of the latitudinal (averaged over 10–70 °W longitude) distribution of upper tropospheric relative humidity (in % with respect to ice) obtained from MOZAIC-measurements between August 1994 and December 2004

in synoptical networks for weather forecasting. The IFC method is capable of providing humidity measurements in near real time with an uncertainty of ±8 % *RH* at the surface and ±7 % *RH* in the upper troposphere.

MOZAIC has demonstrated the large potential of in-service aircraft as a cost efficient platform for obtaining high quality humidity data in the free and upper troposphere. MOZAIC has provided the first measured climatology of upper tropospheric humidity. The observations showed that the UT at cruise altitude (9–12 km) is much more wet than has been assumed before (Fig. 2.16) and that 15-30 % of the UT is ice super-saturated (relative humidity in excess of 100 % with respect to ice) (Gierens et al. 2000). However, to obtain a truly global picture the measurements will be expanded on larger fleet of aircraft in the scope of the IAGOS (In-service Aircraft in a Global Observing System).

References

P.S. Anderson, Mechanism for the behaviour of hydroactive materials used in humidity sensors. J. Atmos. Ocean. Tech. **12**, 662–667 (1995)

V. Antikainen, A. Paukkunen, Dies on improving humidity measurements in radiosondes, in instruments and observing methods. Tech. Rep. **57** (1994), WMO, Geneva

R. Busen, A. Buck, A high-performance hygrometer for aircraft use: Description, installation, and flight data. J. Atmos. Ocean. Tech. **12**, 73–84 (1995)

K.E. Cady-Pereira, M.W. Shephard, D.D. Turner, E.J. Mlawer, S.A. Clough, T.J. Wagner, Improved daytime column-integrated precipitable water vapor from Vaisala radiosonde humidity sensors. J. Atmos. Ocean. Tech. **25**, 873–883 (2008)

P.E. Ciesielski, R.H. Johnson, J. Wang, Correction of humidity biases in Vaisala RS80-H Sondes during NAME. J. Atmos. Ocean. Tech. **26**, 1763–1780 (2009)

J.M. Comstock, T.P. Ackerman, D.D. Turner, Evidence of high ice supersaturation in cirrus clouds using ARM Raman lidar measurements. Geophys. Res. Lett. **31**, L11106 (2004) doi:10.1029/2004GL019705

K. Gierens, U. Schumann, M. Helten, H. Smit, P. Wang, Ice-supersaturated regions and subvisible cirrus in the northern midlatitude upper troposphere. J. Geophys. Res. **105**, 22743–22753 (2000)

J.A. Goff, S. Gratch, Low-pressure properties of water from −160 to 212 F, in Transactions of the American society of heating and ventilating engineers. Paper presented at the 52nd annual meeting of the American society of heating and ventilating engineers, New York, 95–122, 1946

J. Gorman, 2002, Evaluation of desiccants, Instrum. test rep. 2002 664, Aust. Bur. of Meteorol., Melbourne, Victoria, Australia, available at www.wmo.int/pages/prog/www/IMOP/WebPortal-AWS/Tests/ITR664.pdf

M. Helten, H.G.J. Smit, W. Straeter, D. Kley, P. Nedelec, M. Zöger, R. Busen, Calibration and performance of automatic compact instrumentation for the measurement of relative humidity from passenger aircraft. J. Geophys. Res. **103**, 25643–25652 (1998)

M. Helten, H. Smit, D. Kley, J. Ovarlez, H. Schlager, R. Baumann, U. Schumann, P. Nedelec, A. Marenco, In-ight intercomparison of MOZAIC and POLINAT water vapour measurements. J. Geophys. Res. **104**, 26087–26096 (1999)

A.J. Heymsfield, L.M. Miloshevich, C. Twohy, G Sachse, S. Oltmans, Upper tropospheric relative humidity observations and implications for cirrus ice nucleation. Geophys. Res. Lett. **25**, 1343–1346 (1998)

E. Jensen, O.B. Toon, A. Tabazadeh, G.W. Sachse, B.E. Anderson, K.R. Chan, C.W. Twohy, B. Gandrud, S.M. Aulenbach, A. Heymsfield, J. Hallett, B. Gary, Ice nucleation processes in upper tropospheric wave-clouds observed during SUCCESS. Geophys. Res. Lett. **25**, 1363–1366 (1998)

D. Kley, E. Stone, Measurement of water vapor in the stratosphere by photodissociation with Lyα (1216 Å) light. Rev. Sci. Instrum. **49**, 691–874 (1978)

D. Kley, J.M. Russell III, C. Phillips, SPARC Assessment of upper tropospheric and stratospheric water vapour, SPARC Report 2, SPARC Water Vapour Working Group, 2000

A. Kunz, C. Schiller, F. Rohrer, H.G.J. Smit, P. Nedelec, N. Spelten, Statistical analysis of water vapour and ozone in the UT/LS observed during SPURT and MOZAIC. Atmos. Chem. Phys. **8**, 6603–6615 (2008)

U. Leiterer, H. Dier, D. Nagel, T. Naebert, D. Althausen, K. Franke, A. Katz, F. Wagner, Correction method for RS80-A Humicap humidity profiles and their validation by lidar backscattering profiles in tropical cirrus clouds. J. Atmos. Ocean. Tech. **22**, 18–29 (2005)

Z. Luo, D. Kley, R.H. Johnson, H. Smit, Ten years of measurements of tropical uppertropospheric water vapor by MOZAIC. Part I: Climatology, variability, transport, and relation to deep convection. J. Clim., **20**, 418–435 (2007). doi:10.1175/JCLI3997.1

A. Marenco, V. Thouret, P. Nedelec, H. Smit, M. Helten, D. Kley, F. Karcher, P. Simon, K. Law, J. Pyle, G. Poschmann, R.V. Wrede, C. Hume, T. Cook, Measurement of ozone and water vapour by Airbus in-service aircraft: The MOZAIC airborne program, An Overview. J. Geophys. Res. **103**, 25631–25642 (1998)

M. Matsuguchi, S. Umeda, Y. Dadaoka, Y. Sakai, Characterization of polymers for a 24 capacitive type humidity sensor based on water absorption behavior. Sensors and Actuators **49**, 179–185 (1998)

L.M. Miloshevich, H. Vömel, A. Paukkunen, A. Heymsfield, S.J. Oltmans, Characterization and Correction of relative humidity measurements from Vaisala RS80-A radiosondes at cold temperatures. J. Atmos. Ocean. Tech. **18**, 135–156 (2001). doi:10.1175/1520-0426(2001)018h0135:CACORHi2.0.CO; 2

L.M. Miloshevich, A. Paukkunen, H. Vömel, S.J. Oltmans, Development and validation of a time lag correction for Vaisala radiosonde humidity measurements. J. Atmos. Ocean. Tech. **21**, 1305–1327 (2004)

L.M. Miloshevich, H. Vömel, D.N. Whiteman, B.M. Lesht, F.J. Schmidlin, F. Russo, Absolute accuracy of water vapor measurements from six operational radiosonde types launched during AWEX-G and implications for AIRS validation. J. Geophys. Res. **111**, D09S10 (2006). doi:10.1029/2005JD006083

L.M. Miloshevich, H. Vömel, D.N. Whiteman, T. Leblanc, Accuracy assessment and correction of Vaisala RS92 radiosonde water vapor measurements. J. Geophys. Res. **114**, D11305 (2009). doi:10.1029/2008JD011565

D.M. Murphy, T. Koop, Review of the vapour pressures of ice and supercooled water for atmospheric applications. Quart. J. Royal Met. Soc **131**, 1539–1565 (2005)

H. Nakamura, H. Seko, Y. Shoji, Dry biases of humidity measurements from the Vaisala RS80-A and Meisei RS2-91 radiosondes and from Ground-Based GPS (1.Ground-Based GPS Meteorology). J. Meteorological Society of Japan. Ser. II, **82**, 277–299, ISSN 00261165, URL (2004) http://ci.nii.ac.jp/naid/110001803074/en/

J. Nash, R. Smout, T. Oakley, B. Pathack, S. Kurnosenko, WMO Intercomparison of high quality radiosonde systems. Vacoas, Mauritius, 2-25 February 2005. Final report. Tech. rep. (2006) WMO Instruments and Methods of Observation Programme, Geneva, Switzerland

M. Nuret, J.-P. Lafore, O. Bock, F. Guichard, A. Agusti-Panareda, J.-B. N'gamini, J.-L. Redelsperger, Correction of humidity bias for Vaisala RS80-A sondes during the AMMA 2006 observing period. J. Atmos. Ocean. Tech. **25**, 2152–2158 (2008)

J. Ovarlez, van P. Velthoven, Comparison of water vapor measurements with data retrieved from ECMWF analyses during the POLINAT experiment. J. Appl. Meteorol. **36**, 1329–1335 (1997)

A. Paukkunen, Sensor heating to enhance reliability of radiosonde humidity measurement, in Proceedings of 11th AMS Conference, Dallas, 103–106 (1995)

A. Paukkunen, New calibration procedure optimizes RS90 radiosonde performance, Vaisala News 147. (1998)

A. Paukkunen, V. Antikainen, H. Jauhiainen, Accuracy and performance of the new Vaisala RS90 radiosonde in operational use, in Proceedings of 11th AMS Symposium on Meteorological Observations and Instrumentation, Albuquerque, New Mexico, 14–18 January 2001

A. Paukkunen, e.a., Measurement accuracy and repeatability of Vaisala RS90 radiosonde, Vaisala News 159, pp 11–13. (2002)

H.E. Revercomb, e. a., The ARM program's water vapor intensive observation periods. Overview, initial accomplishments, and future challenges, Bull. Am. Met. Soc. **84**, 217–236 (2003)

Z.M. Rittersma, Recent achievements in minitiarised humidity sensors-a review of transduction techniques. Sensors and Actuators A **96**, 196–210 (2002)

P.M. Rowe, L.M. Miloshevich, D.D. Turner, V.P. Walden, Dry bias in Vaisala RS90 radiosonde humidity profiles over Antarctica. J. Atmos. Ocean. Tech. **25**, 1529–1541 (2008)

E. Salasmaa, P. Kostamo, New thin film humidity sensor, in Proceedings of Third Symposium on Meteorological Observations and Instrumentation, Amer. Meteorol. Soc., Washington DC 33–38 1975

C. Schiller, M. Krämer, A. Afchine, N. Spelten, N. Sitnikov, Ice water content of arctic, midlatitude, and tropical cirrus. J. Geophys. Res. **113**, D24208, (2008). doi:10.1029/2008JD010342

F.J. Schmidlin, A. Ivanov, editors, Radiosonde relative humidity sensor performance: The WMO intercomparison Sept. 1995. Preprint volume. 10th Symposium on Meteorological Observations and Instrumentation. Amer. Meteorol. Soc. **68** 71.25 (1998)

D. Seidel, F. Berger, H. Diamond, J. Dykema, D. Goodrich, F. Immler, W. Murray, T. Peterson, D. Sisterson, M. Sommer, P. Thorne, H. Vömel, J. Wang, Reference upper-air observations for climate: Rationale, progress, and plans, Bull. Amer. Meteorol. Soc. **90**, 361–369 (2009). doi:10.1175/2008BAMS2540.1

H. Smit, W. Sträter, M. Helten, D. Kley, Environmental simulation facility to calibrate airborne ozone and humidity sensors. Tech. Rep. Juel. Berichte Nr. 3796, Forschungszentrum Jülich (2000)

H. Smit, A. Volz-Thomas, M. Helten, H. Pätz, D. Kley, An in-ight calibration method for near real-time humidity measurements with the airborne MOZAIC sensor. J. Atmos. Ocean. Tech. **25**, 656–666, (2008). doi:10.1175/2007JTECHA975.1

R. Smout, J. Elms, D. Lyth, J. Nash, New technology in upper-air observations., in Proceedings TECO-2000 Conference, WMO/TD-1028, Beijing, China, World Meteorological Organization 179–182 (2000)

D. Sonntag, Advancements in the field of hygrometry, Meteorol. Zeitschrift, N. F., 51–66 (1994)

T. Stickney, M. Shedlov, D. Thompson, Rosemount total temperature sensors, Tech. Rep. 5755, Revision C, Aerosp. Div. Rosemount Inc., Eagan, Minn. (1994)

T. Suortti, A. Kats, R. Kivi, N. Kämpfer, U. Leiterer, L. Miloshevich, R Neuber, A. Paukkunen, P. Ruppert, H. Vömel, V Yushkov, Tropospheric Comparisons of Vaisala Radiosondes and Balloon-Borne Frost-Point and Lyman-a Hygrometers during the LAUTLOS-WAVVAP Experiment. J. Atmos. Ocean. Tech. **25**, 149–166, (2008) doi:10.1175/2007JTECHA887.1

D.D. Turner, B.M. Lesht, S.A. Clough, J.C. Liljegren, H.E. Revercomb, D.C. Tobin, Dry bias and variability in Vaisala RS80-H radiosondes: The ARM experience. J Atmos. Ocean. Tech **20**, 117–132 (2003)

Vaisala, Improved coating of vaisala radiosonde RS92 humidity sensor contact (2007)

Vaisala, Data continuity (2009), URL http://www.vaisala.com/weather/products/datacontinuity.html.

Vaisala, Reference radiosonde program (2010) URL http://www.vaisala.com/weather/applications/referenceradiosondeprogram.html

J. Van Baelen, J.-P. Aubagnac, A. Dabas, Comparison of near-real time estimates of integrated water vapor derived with GPS, radiosondes, and microwave radiometer. J. Atmos. Ocean. Tech. **22**, 201–210 (2005)

S.A. Vay, B.E. Anderson, E.J. Jensen, G.W. Sachse, J. Ovarlez, G.L. Gregory, S.R. Nolf, JR. Podolske, T.A. Slate, C.E. Sorenson, Tropospheric water vapor measurements over North Atlantic during Subsonic Assessment Ozone and Nitrogen Oxide Experiment (SONEX) J. Geophys. Res. **105**, 3745–3756 (2000)

G. Verver, M. Fujiwara, P. Dolmans, C. Becker, P. Fortuin, L. Miloshevich Performance of the Vaisala RS80A/H and RS90 Humicap Sensors and the Meteolabor "Snow White" Chilled-Mirror Hygrometer in Paramaribo, Suriname. J. Atmos. Ocean. Tech. **23**, 1506–1518 (2006)

H. Vömel, H. Selkirk, L. Miloshevich, J. Valverde-Canossa, J. Valdes, E. Kyrö, R. Kivi, W. Stolz, Peng, G. Diaz, J.A., Radiation dry bias of the Vaisala RS92 humidity sensor. J. Atmos. Ocean. Tech. **24**, 953–963, (2007a) doi:10.1175/JTECH2019.1

H. Vömel, V. Yushkov, S. Khaykin, L. Korshunov, E. Kyrö, R. Kivi, Intercomparisons of stratospheric water vapor sensors: FLASH-B and NOAA/CMDL Frost-Point Hygrometer. J. Atmos. Ocean. Tech. **24**, 941–952 (2007b) doi:10.1175/JTECH2007.1

J. Wang, L. Zhang, systematic errors in global radiosonde precipitable water data from comparisons with ground-based GPS measurements. J. Clim. **21**, 2218–2238 (2008). doi:10.1175/2007JCLI1944.1

J. Wang, H.L. Cole, D.J. Carlson, E.R. Miller, K. Beierle, A. Paukkunen, T.K. Laine, Corrections of Humidity Measurement Errors from the Vaisala RS80 Radiosonde - Application to TOGA COARE Data J. Atmos. Ocean. Tech. **19**, 981–1002 (2002)

A. Wexler, Vapor pressure formulation for water in range 0 to 100˚C: A revision. J. Res. Natl. Bur. Stand. U. S., Sect. A. **80**, 775–785 (1976)

WMO, *Measurement of atmospheric humidity, in guide to meteorological instruments and methods of observation*, 5th edn. (Tech. Rep. WMO Rep.8, World Meteorological Organization. 1983)

WMO, *Measurements of upper air temperature, pressure, and humidity. Guide to Meteorological Instruments and Methods of Observation chap. 12*, 7th edn. (WMO No.8, Geneva, 2008)

K. Yoneyama, M. Fujita, N. Sato, M. Fujiwara, Y. Inai, F. Hasebe, Correction for radiation dry bias found in RS92 radiosonde data during the MISMO field experiment, SOLA, **4**, 13–16 (2008)

M. Zöger, A. Afchine, N. Eicke, M.-T., Gerhards, E. Klein, D. S. McKenna, U. Moerschel, U. Schmidt, V. Tan, F. Tuitjer, T. Woyke, C. Schiller, Fast in-situ stratospheric hygrometers: A new family of balloon-borne and airborne Lyman photofragment uorescence hygrometers. J. Geophys. Res. **104**, 1807–1816 (1999)

Chapter 3
Balloon-Borne Frostpoint-Hygrometry

Holger Vömel and Pierre Jeannet

3.1 Introduction

Balloon borne frostpoint hygrometers have been used for 50 years and although they have gone through many technological advances, the measurement principle has remained the same. An important feature of this technique is that it is an absolute measurement. This means that a property of water vapour can be related to another fundamental quantity—in this case temperature—which is easier to measure. The technique therefore does not require a calibration to a laboratory standard of water vapour, rather it only requires an accurate temperature calibration, which is much easier to achieve than a water vapour calibration. Frostpoint hygrometry is well suited for in situ profiling using small sounding balloons covering the range between the lower troposphere and the middle stratosphere. However, many differences exist between different frostpoint hygrometers, which limit the use of each particular implementation. This chapter describes the basic principle of frostpoint hygrometers used in profiling, the limitations and some possible artifacts, which may impact the interpretation of frostpoint measurements.

3.2 Fundamental Principle

Frostpoint hygrometry has its foundation in equilibrium thermodynamics of a two phase system. The Clausius Clapeyron equation describes the relation between the vapour pressure and the temperature of a two phase system, which is in thermodynamic equilibrium. If the temperature can be measured at which the vapour

H. Vömel (✉)
Deutscher Wetterdienst, Am Observatorium 12, 15848 Lindenberg, Germany
e-mail: holger.voemel@dwd.de

P. Jeannet
MeteoSwiss, Payerne, Switzerland

N. Kämpfer (ed.), *Monitoring Atmospheric Water Vapour,*
ISSI Scientific Report Series 10,
DOI 10.1007/978-1-4614-3909-7_3, © Springer Science+Business Media, LLC 2013

phase of water and its condensed phase are in equilibrium, then the partial pressure can be calculated based on the measured frostpoint (or dewpoint) temperature using a formulation of the Clausius Clapeyron equation. Frostpoint or dewpoint hygrometers actively maintain the equilibrium of a two phase system consisting of water ice (or liquid) and water vapour by continuously adjusting the temperature of the condensed phase such that it remains stable and constant, i.e. the condensed phase neither grows nor shrinks. If this active control is successful, then the temperature variations of the condensed phase needed to maintain the equilibrium are small and the mean temperature approximates the frostpoint or dewpoint temperature, which is then used to calculate the partial pressure of the vapour phase.

Frostpoint and dewpoint hygrometers only differ in the phase of the condensate and therefore in the temperature range for which they are intended. For frostpoint hygrometers the phase of the water condensate is ice, and for dewpoint hygrometers it is liquid that means the measurement range is generally above 0 °C. To calculate the partial pressure of water the vapour pressure equation belonging to the proper condensate phase has to be used. For practical purposes the description here is limited to frostpoint hygrometers and most arguments and descriptions apply to dewpoint hygrometers as well. A temperature range of ambiguous condensate phase exists, which will be described in more detail below.

Implementations of the frostpoint principle vary significantly and most limitations of the technique are a result of the individual implementation. Therefore, not all frostpoint or dewpoint hygrometers are equivalent and some understanding about the technical realization of the principle is needed to properly interpret the reported frostpoint temperature.

For the detection of the condensed phase two different approaches have been used. The first and most common uses optical detection to sense a frost layer on a small mirror, the second uses a quartz crystal as substrate and detects the accumulated mass deposit through a change in the oscillation frequency. Most problems are common to either implementation and therefore we will mostly focus on optical frostpoint hygrometers.

Common to all frostpoint hygrometers is the feedback loop that actively regulates the mirror temperature. In this feedback loop a detector senses the frostlayer on the substrate and quantifies the amount of ice that makes up this frostlayer. The feedback controller then regulates the temperature of the substrate such that the amount of ice (depending on how it was determined), remains constant within preset limits. If this feedback controller is operating properly, then the frost layer does remain constant (by definition) and the substrate temperature is used as an approximation of the frost point temperature.

The degree of success for all frostpoint hygrometers lies in the stability of this feedback controller, the ability to maintain a stable amount of condensate and the ability to exclude external influences (Fig. 3.1).

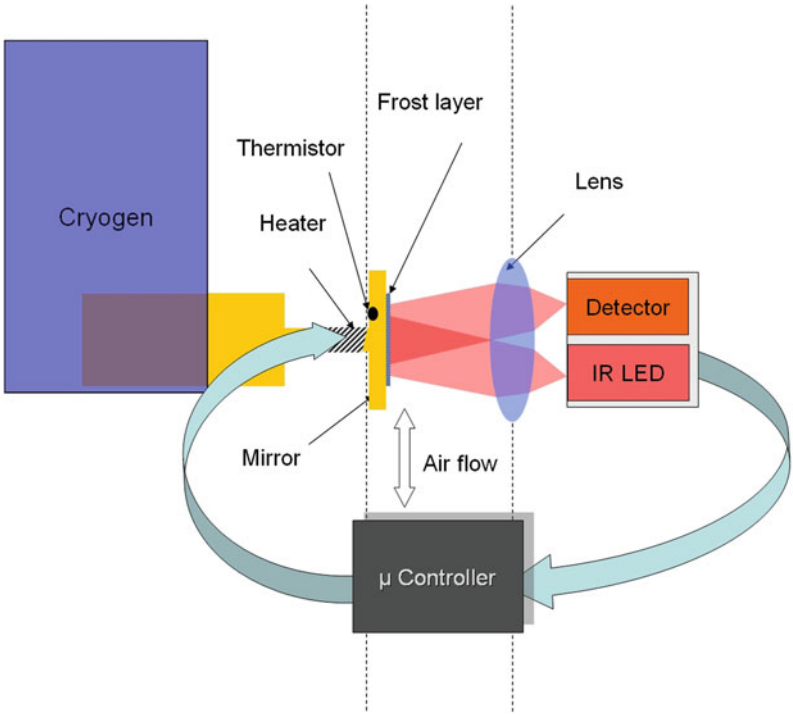

Fig. 3.1 Schematic diagramm of a frostpoint hygrometer. Key components are the *frost layer* detector, the feedback *controller*, the substrate (*mirror*) temperature control (*heater*) and the *frost layer*. The substrate temperature measurement is independent of the feedback controller

3.3 The Optical Detector

For optical frostpoint hygrometers, a mirror, usually a small plated metal disk, serves as substrate and a detector monitors a light source that is reflected off this mirror. The amount of condensate is measured as bulk reflectivity, referring to the amount by which frost covering the mirror reduces the reflected light. This measured signal is scaled by the signal measured on a clear mirror, giving a consistent quantity across different instruments. It is impossible to translate this quantity into mass, density, or number of molecular layers; however, for the test of thermodynamic stability the bulk reflectivity is a suitable approximation of the amount of condensate on the mirror. A frostpoint hygrometer, which is in stable control, interprets any change in bulk reflectivity as a change in partial pressure, for which it has to readjust the mirror temperature to re-establish equilibrium. It is of utmost importance that other influences that may cause changes in the reflectivity measurement are excluded, since the feedback controller cannot discern the cause for changes in reflectivity. The output signal of most low cost optical detectors (photodiodes or phototransistors) is highly temperature sensitive and instrument designers control the temperature of

the detector, monitor the output of the light source, or match the optical components with a second pair showing a similar temperature drift, thus canceling the temperature influence in the measured signal. Any failure in effectively canceling the temperature influence automatically leads to measurement artifacts, which are difficult to detect.

Sunlight causes significant problems for optical detectors and instrument designers have come up with several ways to shield the detector from sunlight or to filter out sunlight electronically. An effective elimination of sun light in the detector signal is essential for daytime measurements.

3.4 The Surface Acoustic Wave Detector

Surface acoustic wave detectors create the frost layer on top of a piezoelectric crystal. In these devices an acoustic wave through a particular electrode pattern, which is confined to the surface of the crystal. The velocity and amplitude of this wave is influenced by deposition of material on the surface and a measure for the amount of condensate on the mirror. This scheme has the advantage that it is insensitive to sunlight. It also may allow distinguishing the phase of the condensate on the mirror.

3.5 The Feedback Controller

The experience of many designers building frostpoint hygrometers is that it is very difficult building a well tuned feedback controller for a frostpoint hygrometer. Simple proportional controllers use the difference of the measured frost layer amount from a preset value to control the mirror temperature. This implementation is simple and works under some conditions. However, these instruments struggle with controller stability, common to all proportional controllers and cover only a certain range of frostpoint temperatures. A further limitation of proportional controllers is that they only approximate the assumption of a constant frost layer, since the deviation from the constant value is required to drive the mirror temperature controller. Proportional Integrating (PI) controllers do not intrinsically violate the assumption of a constant frost layer, since they always reduce the difference from the setpoint to zero. In instruments using PI controllers it is more difficult to find the proper controller parameters, but once these parameters have been established, observations using PI controllers are superior. Ideal solutions implement PID controllers, which have a superior dynamic response and also support the assumption of a constant frost layer. PID (Proportional, Integrating, Differentiating) controllers are very common in a large multitude of applications; however, frostpoint hygrometers at times operate with simpler controller implementations, since tuning over the large range of parameter space proves to be a challenge. However, these implementations are more sensitive to noise and other spurious influences and may be useful only if all spurious influences can be excluded or where spurious influences do not impact the overall controller stability. Therefore large difference between different frostpoint hygrometers can be found in their implementation of the feedback controller.

3.6 Mirror Temperature Control

Two main technologies have been implemented to actively control the mirror temperature. The techniques are described in this section together with the limitations that result form the particular cooling method.

3.6.1 Peltier Cooler

Most common are Peltier coolers, which use an electrical current to create a temperature gradient based on the Peltier effect. In these instruments the cold side of a Peltier device is thermally connected to the mirror or substrate holding the frost layer and the warm side is either cooled convectively by the outside air or connected to a cold sink. The range of measurements using such a cooling device is limited, since Peltier elements can create only a limited temperature gradient between the warm and cold side of the device and since this gradient itself is temperature dependent. These instruments also face the challenge of efficiently cooling the warm side of the Peltier element, since (usually convective) cooling of the warm side determines the temperature that can be achieved on the cold side. Pre-cooling the warm side of the Peltier element can extend the measurement range significantly, but is not done in upper air applications.

3.6.2 Cryogenic Cooling

Cryogenic or refrigeration cooling combined with an electrical heater of the mirror allows a much larger temperature range that can be controlled. The lowest frostpoint temperatures that can be measured using this technique depend on the type of cryogen or refrigeration that is being used. Instruments using liquid cryogens are the only frostpoint technique used for stratospheric frostpoint observations and are currently the only instruments capable of measuring water vapour between the surface and the middle stratosphere.

3.7 Airflow

For proper measurement, all frostpoint hygrometers need airflow over a surface. In still air, the measured mirror temperature represents only the vapour pressure in the boundary layer above the frost layer, not the vapour pressure in free air. Furthermore, in the absence of airflow across the frost layer the feedback controllers do not operate within their range of parameters, leading to controller instability and unpredictable artifacts. Rapid mixing across this boundary layer is essential for a representative

measurement of water vapour of the free atmosphere in all instruments, which is only achieved with sufficient airflow.

3.8 Artifacts of Frostpoint Hygrometers

The water vapour partial pressure is derived only from the measured mirror or substrate temperature. Therefore, the calculation of the vapour pressure is only valid if the feedback controller is properly maintaining a constant condensate layer. A number of artifacts may occur, in which the instrument is responding properly, but violate the assumption of constant condensate layer. In this case the substrate or mirror temperature has no relation to the ambient frostpoint temperature.

3.8.1 Controller Tuning

In some instruments it is difficult to determine whether the feedback controller is stable or unstable. An oscillating or unstable feedback controller may cause structures in a sounding profile that appear reasonable, but are an artifact due to controller instability. A poorly tuned controller can only be identified if additional instrument parameters, notably the frost layer signal are available. Large oscillations are more readily detectable without this additional piece of information, but small scale instabilities or a slow response may go undetected. A poorly tuned feedback controller may also lead to a poor time response and to extreme smoothing of the measured water vapour signal. This is also not easily detected from the instrument response itself.

3.8.2 Air Temperature Variations

At any moment the mirror temperature is determined by the heat that flows from the mirror either into the Peltier element or into the heater moderated cryogenic cooler. Air flowing across the mirror provides a heat source that needs to be considered in the feedback control loop. Changes in air temperature lead to changes in heat input into the mirror, to which the instrument needs to respond. This happens through a transient change in condensate coverage, followed by readjustment of the cooling power through the feedback controller. In a fast responding instrument, air temperature changes do not cause significant disturbances in the mirror temperature. However, in slow responding instruments, these air temperature changes may be interpreted as large frostpoint changes and may even lead to controller instabilities.

3.8.3 Liquid/Ice Ambiguity

In the region between 0 °C and −38 °C supercooled liquid water instead of ice may be present as condensate. Most frostpoint hygrometers do not have the means to detect the difference. However, it is essential to know the correct phase of the condensate, since it determines the vapour pressure equation that has to be used to calculate the vapour pressure. This substrate temperature region is called the region of liquid/ice ambiguity. For all practical purposes this region exists for condensate temperatures between −15 °C and −33 °C. This temperature must not be confused with air temperatures, since the air temperature has no relevance for the condensate phase. Only the substrate temperature (mirror or crystal) determines the condensate phase. In profiling instruments the condensate layer is most often (although by no means guaranteed) still liquid above −18 °C, whereas below −33 °C it is almost always solid. Within this region it is extremely difficult to determine the proper condensate phase. A liquid layer will spontaneously begin to freeze generally within −20 °C and −30 °C and it is not possible to predict the precise temperature at which this process will start. The most challenging problem of the force freezing is that although the process is called spontaneous, it may take several minutes to more than 10 minutes to complete, depending on the variations of the water vapour partial pressure. While the freezing of the condensate layer occurs, the feedback controller no longer responds to changes in water vapour, but rather to changes in the condensate phase. During this time the instrument output is neither a frostpoint nor dewpoint measurement, but rather a meaningless quantity (see Fig. 3.2).

3.8.4 Cloud Influences

Within clouds a frostpoint hygrometer is by design only sensitive to water vapour, not the condensed phase. However, the presence of condensed phase (liquid drops or ice crystals), poses two source of artifacts. In instruments, where the sampling volume or the inlet system is heated, evaporation of the condensed phase will occur. Such instruments will measure the vapour phase plus the amount of condensed phase that has been evaporated. Instruments that achieve complete evaporation of all cloud particles are considered total water instruments, which report the combined amount of water substance in the vapour and condensed phase. If it can't be assured that the evaporation is complete, then the instrument output will be at an undetermined measurement above the frostpoint of the air depending on the amount of evaporation that took place within the instrument. With these instruments it is not possible to study supersaturation within clouds.

Cloud particles may also be detected as a change in reflectivity. In some cases this may lead to increased noise or apparent controller instability, since cloud particles pass the optical path quickly. In liquid clouds, in particular in supercooled liquid or mixed clouds, the optical detector itself may get wet. Again the instrument cannot distinguish the source of reflectivity reduction and responds to the condensate on

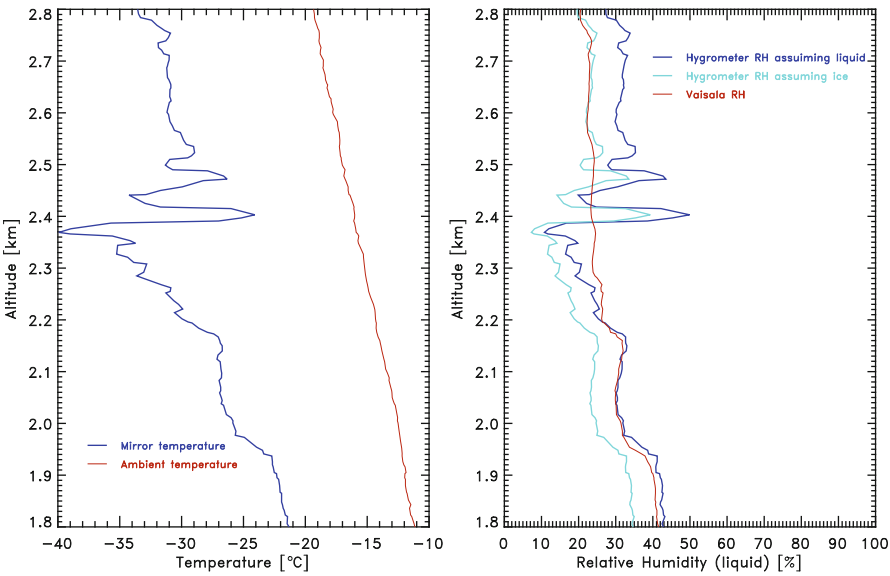

Fig. 3.2 *Left* Measured mirror (frostpoint) temperature (*blue*) and air temperature (*red*) of a frostpoint sounding. The vertical structures in the mirror temperature around 2.5 km are indicative of the liquid to ice transition. *Right* Comparison of the relative humidity derived from the frostpoint sounding with the relative humidity measured simultaneously by the Vaisala radiosonde. The frostpoint relative humidity was computed assuming liquid water on the mirror (*dark blue*) and ice on the mirror (*light blue*). In this example the liquid to ice transition region extends from about 2.2 km altitude to about 2.6 km altitude. The instrument took about 1.5 min for the liquid to ice transition to complete and to regain proper frost layer control

the detector with a complete loss of control. This artifact is usually quite apparent. If water vapour gets adsorbed or even condenses within the inlet system of any hygrometer, then subsequent measurements may be impacted by the evaporation of this excess amount of water vapour and contaminate the water vapour measurement. Although the instrument itself is still measuring correctly, the measured value no longer represents the water vapour concentration in the free atmosphere. The risk of contamination is particularly large in the passage through liquid clouds.

Instruments that rely on mechanical blocking of sunlight are generally more susceptible to contamination than those using open sampling volumes with few surfaces in the inlet system.

3.8.5 Radio Frequency Interference

The instruments described here are used as part of an in situ sounding package, where the signals are measured onboard a balloon payload and transmitted to the ground via radio telemetry. In some instruments radio frequency interference has been observed,

which can lead to offsets in either the control loop or in the measurement of the mirror temperature. These offsets may be indistinguishable in a sounding profile and the instrument manufacturer may need to be extremely careful in avoiding these problems through proper electronic design.

3.9 Time Response

The time response of a frostpoint hygrometer depends critically on the PID controller that it is based on. A fast instrument may show a response time on the order of a second in the lower troposphere to 10 seconds or more in the middle stratosphere. A slow instrument may show a response time of several tens of seconds in the troposphere and be unresponsive in the stratosphere, despite having the temperature capabilities. For stratospheric measurements, a stable controller is essential, since the time to accumulate a frost layer to amount expected for the set point may be several hours and may exceed the duration of a typical stratospheric measurement. A loss of the frost layer above the tropopause due to any reason usually implies a complete loss of stratospheric measurements.

3.10 Specific Instrument Implementations

A number of instruments have been built for observations of upper air water vapour. Some laboratory instruments have been adapted to aircraft use and a number of instruments have been designed specifically for balloon borne sounding applications. The description here focuses on instruments that were or are still used in balloon borne observations.

3.10.1 The Naval Research Laboratory Frostpoint Hygrometer

The first balloon borne frostpoint hygrometers were built at the University of Chicago (Barrett et al. 1950; Suomi and Barrett 1952). These instruments were capable of measuring stratospheric water vapour, but were too large for wide spread used. The New York University in cooperation with the Naval Research Laboratory in Washington, DC built a new instrument based on the earlier experiences that was able to be used on a large scale (Slater 1953; Nathan 1954; Mastenbrook and Dinger 1961).

This instrument used a mirror that was thermally connected to a cryogenic liquid combined with a heater around the edge of the mirror to control the mirror temperature. The location of the heater created a temperature gradient across the mirror leading to frost covering only the center area of the mirror. The instrument was adjusted such that the edge of the frost coverage was located on top of the thermistor measuring the mirror temperature. In this case the temperature at the edge of

the frost layer was assumed to best represent the frostpoint temperature. Variations in the adjustment of the frost area before flight lead to variations in the measured frostpoint temperatures and to a larger sounding to sounding variability compared to later instruments. This instrument was used between 1960 and 1979 at Washington, DC and participated in a number of significant campaigns, in particular in tropical campaigns at Hyderabad in 1961, Kwajalein in 1963 (Mastenbrook 1965), and Trinidad between 1964 and 1965 (Mastenbrook 1966).

3.10.2 NOAA Frostpoint Hygrometer

The balloon borne frostpoint hygrometer of NOAA's Earth System Research Laboratory (NOAA/ ESRL) is based on the NRL instrument with several important improvements (Vömel et al. 1995). It is being used in Boulder, CO since 1980 and has provided the longest stratospheric water vapour record. It has also been the basis of a number of tropical, mid latitude and polar campaigns. In contrast to the NRL instrument, the NOAA hygrometer uses a mirror design with center cooling and heating, leading to a uniform mirror temperature. The location of the thermistor no longer plays a critical role, which is reflected by the significantly reduced sounding to sounding variability. It uses a proportional controller with a two step parameter adjustment, which in addition to stratospheric observations allows for some observations in the middle and upper troposphere. It has not been designed to provide good observations in the lower troposphere and the controller is generally unstable for liquid condensate. The measurement uncertainty for this instrument is limited by the controller stability and under optimal performance is around 0.5 K in frostpoint temperature. This translates to about 10 % uncertainty in mixing ratio. This instrument has been key to the long term trend of stratospheric water vapour observed at Boulder, CO (Oltmans and Hofmann 1995; Oltmans et al. 2000), and has been used in sonde intercomparisons (Kley et al. 1997; Miloshevich et al. 2001).

3.10.3 CFH

The Cryogenic Frostpoint Hygrometer (CFH) has been developed at the University of Colorado and is loosely based on the NOAA instrument, with a number of significant improvements (Vömel et al. 2007). The most important difference is the design of the feedback controller, which uses a continuously variable PID parameter schedule, which allows observations between the surface and the middle stratosphere under all conditions. It is equipped with a phase sensitive optical detector to eliminate sun light, avoiding the use of baffles or light traps during daytime observations. This reduces the risk of contamination significantly and allows observations on balloon ascent between the surface and typically up to 25 km. The instrument is capable of running as dew point hygrometer and force freezes the liquid condensate in the region

of liquid/ice ambiguity. This largely eliminates the uncertainty of the condensate phase in the temperature range below 0 °C, allowing continuous profiles over the largest frostpoint temperature range of all instruments currently available. It suffers no artifacts in cirrus clouds and may only be limited in wet precipitating clouds with the detector lens getting wet.

The measurement uncertainty of the CFH is less than 0.5 K throughout the entire profile, which translates to about 4 % in the lower troposphere and about 9 % in the stratosphere. Intensive measurement campaigns have shown that the uncertainty is generally better than this estimate (Vömel et al. 2007). Monitors of the optics signal and optics temperature generally support the stability of the controller.

The CFH has been used in a number of intercomparison experiments (e.g. Whiteman et al. 2006; Miloshevich et al. 2006; Vömel et al. 2007a) in stratospheric as well as tropospheric satellite validation observations (Read et al. 2007; Shephard et al. 2008; Vömel et al. 2007b; Fetzer et al. 2008) and at a large number of scientific observational campaigns (e.g. Corti et al. 2006; Hasebe et al. 2007; Shibata et al. 2007; Yang et al. 2008) and is currently in routine operation at Sodankylä, Finland; Alajuela, Costa Rica; and Lindenberg, Germany.

3.10.4 Snow White

The Snow White chilled-mirror hygrometer is a commercial dewpoint/frostpoint instrument developed by Meteolabor AG, Switzerland. It uses an optical detector and a single stage Peltier cooler. The mirror is directly attached to the cold side of the Peltier cooler and made of a copper and a gold plated constantan layer, which form part of a thermocouple. In this configuration the mirror also acts as temperature sensor. The instrument uses an adjustable gain schedule which operates over the entire temperature range for the instrument. The Peltier element achieves an effective maximum temperature depression of 36.5 K at 0 °C, 27.5 K at −30 °C and 12.6 K at −80 °C, which translates to a lower detection limit in relative humidity of about 3 % to 6 % RH (Vömel et al. 2003).

Two versions of Snow White are produced, one for daytime and one for nighttime operation. In the daytime version the sensor and the cooling fins attached to the Peltier hot side are mounted inside the instrument Styrofoam box. This arrangement protects the detector from stray light and the cooling fins from solar heating. This configuration leads to some limitations of performance in and above thick clouds due to contamination issues within the enclosed sampling and sensor system.

In the nighttime version, the sensor is almost completely exposed and mounted either on top or on the side of the box. The cooling surfaces are exposed and painted black to increase radiative cooling. This arrangement improves cooling of the Peltier hot side and reduces contamination issues caused by outgassing of water vapour from the instrument.

The Snow White sensor housing has a heater that is switched on in saturated layers to avoid icing of the sensor. In such situations water droplets or ice crystals

evaporate and the instrument becomes partially a total water instrument. Snow White mirror temperature measurements sometimes exhibit spikes when going through ice clouds, in parts because of rapid ice crystal evaporation upsetting the controller stability. The uncertainty in mirror temperature measurement is stated as 0.1 K; however, the total measurement uncertainty including the controller stability has not been documented. Under optimal conditions it is believed to be comparable to that of the CFH for tropospheric measurements, except for the temperature range of the liquid ice transition.

Intercomparison campaigns with different hygrometers measuring simultaneously on the same balloon represent the best way of qualifying the uncertainty of radiosonde hygrometer measurements. Snow White took part in several research field campaigns (Fujiwara et al. 2003; Verver et al. 2006; Fortuin et al. 2007; Hasebe et al. 2007; Mattioli et al. 2007) as well as in instrument intercomparisons (Wang et al. 2003; Behrendt et al. 2007; Sapucci et al. 2005; Nash et al. 2006; Ferrare et al. 2004; Miloshevich et al. 2006; Suortti et al. 2008).

3.10.5 The LMD-CNRS Frost Point Hygrometers

Balloon borne optical frostpoint hygrometers were also built by the Laboratoire de Météorologie Dynamique (LMD) of the Centre National De Recherche Scientifique (CNRS). One earlier version used a multistage thermoelectric cooler, which was later changed to cryogenic cooling using liquid nitrogen. Both versions were used for stratospheric and upper tropospheric observations. Due to their relatively large size and the capability to do observations during balloon float, these instruments only flew on larger research balloons. Their accuracy is estimated to be 0.5 K in frostpoint temperature for the thermoelectric instrument and 0.3 K for the cryogenic instruments. These instruments have participated in a number of scientific experiments (Ovarlez 1985, 1991; Ovarlez and Ovarlez 1994, 1995; Ovarlez et al. 1999).

3.10.6 Surface Acoustic Wave Hygrometers

Hygrometers based on the surface acoustic wave principle have been in existence for nearly thirty years. A balloon-borne Surface Acoustic Wave (SAW) frostpoint hygrometer has been developed at the Jet Propulsion Laboratory during the 1990s and has flown onboard meteorological balloons as well as several research aircraft (Hoenk et al. 2000). No data have been published and the capabilities of this instrument have not been evaluated. A SAW frostpoint hygrometer has also been developed at the University of Cambridge (Hansford et al. 2006). This instrument uses two-stage and three-stage Peltier elements and a gold resistance thermometer. The calibration of the gold thermometer proved to be difficult and an accuracy of 0.3 K has been reported, which is the lower limit for the measurement uncertainty. Nine soundings have been reported, but data have not yet been published.

3.10.7 Others

Several other balloon borne frostpoint instruments have been built such as one by the Sandia National Laboratories (Brown and Lichfield 1988), who built a cryogenically cooled instrument for upper tropospheric and stratospheric observations and by Yankee Environmental Systems (Stein et al. 2001), who tested a thermoelectrically cooled instrument for tropospheric measurements. However, these instruments did not transit into large scale use and data are not available from these instruments.

References

E.W. Barrett, L.R. Herndon, H.J. Carter, Some measurements of the distribution of water vapor in the stratosphere. Tellus. **2**, 302–311 (1950)

A. Behrendt, V. Wulfmeyer, P. Girolamo, C. Kiemle, H.-S. Bauer, T. Schaberl, D. Summa, D. Whiteman, B. Demoz, E. Browell, S. Ismail, R. Ferrare, S. Kooi, G. Ehret, J. Wang, Intercomparison of water vapor data measured with lidar during IHOP 2002. Part I: Airborne to ground-based lidar systems and comparisons with chilled-mirror hygrometer radiosondes. J. Atmos. Ocean. Tech. **24**, 3–21 (2007). doi:10.1175/JTECH1924.1

G.S. Brown, E.W. Lichfield, *A balloon-borne frost point hygrometer for tropospheric and stratospheric water vapor concentration measurements* (Tech. Rep. SAND88-2467, Sandia National Laboratories, Albuquerque, USA, 1988)

T. Corti, B.P. Luo, Q. Fu, H. Vömel, T. Peter, The impact of cirrus clouds on tropical troposphere-to-stratosphere transport. Atmos. Chem. Phys. **6**, 2539–2547 (2006)

R.A. Ferrare, E.V. Browell, S. Ismail, S.A. Kooi, L.H. Brasseur, V.G. Brackett, M.B. Clayton, J.D.W. Barrick, G.S. Diskin, J.E.M. Goldsmith, B.M. Lesht, J.R. Podolske, G.W. Sachse, F.J. Schmidlin, D.D. Turner, D.N. Whiteman, D. Tobin, L.M. Miloshevich, H.E. Revercomb, B.B. Demoz, P.D. Girolamo, Characterization of upper-troposphere water vapor measurements during AFWEX using LASE. J. Atmos. Oceanic Tech. **21**, 1790–1808 (2004)

E. Fetzer, W.G. Read, D. Waliser, B.H. Kahn, B. Tian, H. Vömel, F.W. Irion, H. Su, A. Eldering, M. de la Torre Juarez, J. Jiang, V. Dang, Comparison of upper tropospheric water vapor observations from the microwave limb sounder and atmospheric infrared sounder. J. Geophys. Res. **113**(D22), 110 (2008). doi:10.1029/2008JD010000

J. Fortuin, C.R. Becker, M. Fujiwara, F. Immler, H. Kelder, M.P. Scheele, O. Schrems, G. Verver, Origin and transport of tropical cirrus clouds observed over Paramaribo station, Surinam (5.8°N, 55.2°W). J. Geophys. Res. **112**(D09), 107 (2007)

M. Fujiwara, M. Shiotani, F. Hasebe, H. Vömel, S.J. Oltmans, P.W. Ruppert, T. Horinouchi, T. Tsuda, Performance of the meteolabor snow white chilled-mirror hygrometer in the tropical troposphere: comparisons with the Vaisala RS80 A/H-Humicap sensors. J. Atmos. Ocean. Tech. **20**, 1534–1542 (2003). doi:10.1175/1520-0426(2003)020

G.M. Hansford, R.A. Freshwater, L. Eden, K.F.V. Turnbull, D.E. Hadaway, V.P. Ostanin, R.L. Jones, Lightweight dew-/frost-point hygrometer based on a surface-acoustic-wave sensor for balloon-borne atmospheric water vapor profile sounding. Rev. Sci. Instrum. **77**(14) 502 (2006)

F. Hasebe, M. Fujiwara, N. Nishi, M. Shiotani, H. Vömel, S. Oltmans, H. Takashima, S. Saraspriya, N. Komala, Y. Inai, In situ observations of dehydrated air parcels advected horizontally in the tropical tropopause layer of the western Pacific. Atmos. Chem. Phys. **77**, 803–813 (2007)

M.E. Hoenk, G. Cardell, F. Noca, R.K. Watson, A surface acoustic wave hygrometer for high-resolution measurements of atmospheric humidity. J. Acoust. Soc. Am. vol 108 p. 2495, Acoustical Society of America, 2000

D. Kley, H.G.J. Smit, H. Vömel, H. Grassl, V. Ramanathan, P.J. Crutzen, S. Williams, J. Meywerk, S.J. Oltmans, Tropospheric water-vapour and ozone cross-sections in a zonal plane over the central equatorial Pacific Ocean, Quart. J. R. Meteorol. Soc. **123**, 2009–2040 (1997)

H.J. Mastenbrook, *The vertical distribution of water vapor over Kwajalein Atoll, Marshall Islands* (Tech. Rep. NRL 6367, Naval Research Laboratory, Washington D.C., U.S.A., 1965)

H.J. Mastenbrook, *Water vapor observations at low, middle and high latitudes during 1964 and 1965* (Tech. Rep. NRL 6447, Naval Research Laboratory, Washington D.C., U.S.A., 1966)

H.J. Mastenbrook, J.E. Dinger, Distribution of water vapor in the stratosphere. J. Geophys. Res. **66**, 1437–1444 (1961)

V. Mattioli, E.R. Westwater, D. Cimini, J.C. Liljegren, B.M. Lesht, S.I. Gutman, F.J. Schmidlin, Analysis of radiosonde and ground-based remotely sensed PWV data from the 2004 north slope of Alaska arctic winter radiometric experiment. J. Atmos. Ocean. Tech. **24**, 415–431 (2007)

L. Miloshevich, H. Vömel, A. Paukkunen, A. Heymsfield, S.J. Oltmans, , Characterization and correction of relative humidity measurements from Vaisala RS80-A radiosondes at cold temperatures. J. Atmos. Ocean. Tech. **18**, 135–156 (2001). doi:10.1175/1520-0426(2001)018h0135:CACORHi2.0.CO;2

L.M. Miloshevich, H. Vömel, D.N. Whiteman, B.M. Lesht, F.J. Schmidlin, F. Russo, Absolute accuracy of water vapor measurements from six operational radiosonde types launched during AWEX-G and implications for AIRS validation. J. Geophys. Res. 111(D09S10) (2006). doi:10.1029/ 2005JD006083

J. Nash, R. Smout, T. Oakley, B. Pathack, S. Kurnosenko, 2006, WMO intercomparison of high quality radiosonde systems. Vacoas, Mauritius, Final report, Tech. rep., WMO Instruments and methods of observation programme, Geneva, Switzerland, 2–25 February 2005

A.M. Nathan, *Dew-point hygrometer development* (Tech. Rep. 272.03, N.Y. Univ. Coll. Eng.1954)

S.J. Oltmans, D.J. Hofmann, Increase in lower-stratospheric water vapour at a mid-latitude northern hemisphere site from 1981 to 1994, Nature. **374**, 146–149 (1995). doi:10.1038/374146a0

S.J. Oltmans, H. Vömel, D.J. Hofmann, K.H. Rosenlof, D. Kley, The increase in 38 stratospheric water vapor from balloonborne, frostpoint hygrometer measurements at Washington, DC, and Boulder, Colorado. Geophys. Res. Lett. **27**, 3453–3456 (2000)

J. Ovarlez, A two temperature calibration system, measurement and control in science and industry, in *Proceeding of 1985 International Symposium on Moisture and Humidity*, Washington, D.C., pp. 235–241, Instrument Society of America 1985

J. Ovarlez, Stratospheric water vapor measurement in the tropical zone by means of a frost point hygrometer on board long-duration balloons. J. Geophys. Res. **96**, 15541–15545 (1991)

J. Ovarlezand, H. Ovarlez, Stratospheric water vapor content evolution during EASOE. Geophys. Res. Lett. 21, 1235–1238 (1994)

J. Ovarlez, H. Ovarlez, *Water vapour and aerosols measurements during sesame, and the observation of low water vapour content layers* (Tech. rep., CEC Publ., Air Pollution report No 56, Polar Stratospheric Ozone, 1995)

J. Ovarlez, P. van Velthoven, H. Schlager, Water vapor measurements from the troposphere to the lowermost stratosphere: some signatures of troposphere to stratosphere exchanges. J. Geophys. Res. **104**, 16973–16978 (1999)

W.G. Read, A. Lambert, J. Bacmeister, R.E. Cofield, L.E. Christensen, D.T. Cuddy, W.H. Daffer, B.J. Drouin, E. Fetzer, L. Froidevaux, R. Fuller, R. Herman, R.F. Jarnot, J.H. Jiang, Y.B. Jiang, K. Kelly, B.W. Knosp, L.J. Kovalenko, N.J. Livesey, H.-C. Liu, G.L.Manney, H.M. Pickett, H.C. Pumphrey, K.H. Rosenlof, X. Sabounchi, M.L. Santee, M.J. Schwartz, W.V. Snyder, P.C. Stek, H. Su, L.L. Takacs, R.P. Thurstans, H. Vömel, P.A. Wagner, J.W. Waters, C.R. Webster, E.M. Weinstock, D.L. Wu, Aura microwave limb sounder upper tropospheric and lower stratospheric H_2O and relative humidity with respect to ice validation. J. Geophys. Res. **112**(D24S35) (2007), doi:10.1029/2007JD008752

L.F. Sapucci, L.A.T. Machado, R.B. da Silveira, G. Fisch, J. Monico, Analysis of relative humidity sensors at the WMO radiosonde intercomparison experiment in Brazil. J. Atmos. Ocean. Tech. **22**, 664–678 (2005)

M.W. Shephard, R.L. Herman, B.M. Fisher, K.E. Cady-Pereira, S.A. Clough, V.H. Payne, D.N. Whiteman, J.P. Comer, H. Vömel, L.M. Miloshevich, R. Forno, M. Adam, G.B. Osterman, A. Eldering, J.R. Worden, L.R. Brown, H.M. Worden, S.S. Kulawik, D.M. Rider, A. Goldman, R. Beer, K.W. Bowman, C.D. Rodgers, M. Luo, C.P. Rinsland, M. Lampel, M.R. Gunson, Comparison of tropospheric emission spectrometer nadir water vapor retrievals with in situ measurements. J. Geophys. Res. **113**(D15S24) (2008). doi:10.1029/2007JD008822

T. Shibata, H. Vömel, S. Hamdi, S. Kaloka, F. Hasebe, M. Fujiwara, M. Shiotani, Tropical cirrus clouds near cold point tropopause under ice supersaturated conditions observed by lidar and balloon-borne cryogenic frost point hygrometer. J. Geophys. Res. **112**(D03 210) (2007). doi:10.1029/2006JD007361

D. Slater, *Dew-point hygrometer development* (Tech. Rep. 170.03, N. Y. Univ. Coll. Eng. 1953)

W.M. Stein, A. Bisberg, D. Beaubien, Flight test results of a low-cost balloon borne chilled mirror hygrometer, in 81st AMS Annual Meeting, Albuquerque, NM, 16 January 2001

V.E. Suomi, W.E. Barrett, An experimental radiosonde for the investigation of the distribution of water vapor in the stratosphere. Rev. Sci. Instr. **23**, 272–292 (1952)

T. Suortti, A. Kats, R. Kivi, N. Kämpfer, U. Leiterer, L. Miloshevich, R. Neuber, A. Paukkunen, P. Ruppert, H. Vömel, V. Yushkov, Tropospheric comparisons of Vaisala radiosondes and balloon-borne frost-point and Lyman-α Hygrometers during the LAUTLOS-WAVVAP Experiment. J. Atmos. Ocean. Tech. **25**, 149–166 (2008). doi:10.1175/2007JTECHA887.1

G. Verver, M. Fujiwara, P. Dolmans, C. Becker, P. Fortuin, L. Miloshevich, Performance of the Vaisala RS80A/H and RS90 humicap sensors and the meteolabor snow white chilled-mirror hygrometer in Paramaribo, Suriname. J. Atmos. Ocean. Tech. **23**, 1506–1518 (2006)

H. Vömel, S.J, Oltmans, D.J. Hofmann, T. Deshler, J.M. Rosen, The evolution of the dehydration in the antarctic stratospheric vortex. J. Geophys. Res. **100**, 13919–13926 (1995)

H. Vömel, M. Fujiwara, M. Shiotani, F. Hasebe, S.J. Oltmans, J.E. Barnes, The behavior of the snow white chilled-mirror hygrometer in extremely dry conditions. J. Atmos. Ocean. Techn. 39 20, 1560–1567(2003). doi:10.1175/15200426(2003)020h1560:TBOTSWi2.0.CO;2

H. Vömel, D.E. David, K. Smith, Accuracy of tropospheric and stratospheric water vapor measurements by the cryogenic frost point hygrometer: Instrumental details and observations. J. Geophys. Res. 112 (2007). doi:10.1029/2006JD007224

H. Vömel, H. Selkirk, L. Miloshevich, J. Valverde-Canossa, J. Valdés, E. Kyrö, R. Kivi, W. Stolz, G. Peng, J.A. Diaz, Radiation dry bias of the Vaisala RS92 humidity sensor. J. Atmos. Ocean. Tech. **24**, 953–963 (2007a). doi:10.1175/JTECH2019.1

H. Vömel, J.E. Barnes, R.N. Forno, M. Fujiwara, F. Hasebe, S. Iwasaki, R. Kivi, N. Komala, E. Kyrö, T. Leblanc, B. Morel, S.-Y. Ogino, W. Read, S. Ryan, S. Saraspriya, H. Selkirk, M. Shiotani, J.V. Canossa, D. Whiteman, Validation of aura microwave limb sounder water vapor by balloon-borne cryogenic frost point hygrometer measurements. J. Geophys. Res., **112**(D24S37) (2007b). doi:10.1029/2007JD008698

J. Wang, D. Carlson, D. Parsons, T. Hock, D. Lauritsen, H. Cole, K. Beierle, E. Chamberlain, Performance of operational radiosonde humidity sensors in direct comparison with a chilled mirror dew-point hygrometer and its climate implication. Geophys. Res. Lett. **30**, 1680 (2003). doi:10.1029/ 2003GL016985

D.N. Whiteman, F. Russo, B. Demoz, L.M. Miloshevich, I. Veselovskii, S. Hannon, Z. Wang, H. Vömel, F. Schmidlin, B. Lesht, P.J. Moore, A.S. Beebe, A. Gambacorta, C. Barnet, Analysis of Raman lidar and radiosonde measurements from the AWEX-G field campaign and its relation to aqua validation. J. Geophys. Res. **111**(D09S09) (2006). doi:10.1029/2005JD006429

Q. Yang, Q. Fu, J. Austin, A. Li, F. Gettelman, H. Vömel, Observationally derived and general circulation model simulated tropical stratospheric upward mass uxes. J. Geophys. Res. **113**(D00B07) (2008). doi:10.1029/2008JD009945

Chapter 4
Application of Fluorescence Method for Measurements of Water Vapour in the Atmosphere

Vladimir Yushkov

4.1 Method Description

The method used to measure H_2O by a fluorescence technique was developed by (Kley and Stone 1978) and (Bertaux and Delannoy 1978). The photodissociation of H_2O molecules by radiation at wavelengths $\lambda < 137$ nm produces electronically excited OH:

$$H_2O + h\nu(\lambda < 137\,\text{nm}) \rightarrow OH(A^2\Sigma^+) + H(^2S) \tag{4.1}$$

The electronically excited OH relaxes to the ground state by fluorescence or by collisions with other molecules M:

$$OH(A^2\Sigma^+) \rightarrow OH(X^2\Pi) + h\nu(\lambda = 305 - 325\,\text{nm}) \tag{4.2}$$

$$OH(A^2\Sigma^+) + M \rightarrow OH(X^2\Pi) + M \tag{4.3}$$

By measuring the intensity of the emitted fluorescence, the H_2O abundance can be determined. The number of fluorescence photons N_f is given by

$$N_f = \frac{[H_2O]J\Phi}{[\text{air}]k_q + A_0} \tag{4.4}$$

$[H_2O]$ and [air] denote respectively the concentration of H_2O and air molecules, J the photodissociation rate of reaction 4.1, Φ the quantum efficiency for excited state OH production via 4.1, A_0 the Einstein coefficient of reaction 4.2, and k_q the quenching coefficient of the OH radical in air (reaction 4.3). In the UT/LS, that is, for altitudes below 20 km, $k_q[\text{air}] >> A_0$, and Eq. 4.4 can be approximated by

$$N_f = C\frac{[H_2O]}{[\text{air}]} \tag{4.5}$$

V. Youshkov (✉)
Central Aerological Observatory, Pervomayskaya str. 3, Dolgoprudny,
Moscow Region 141700, Russia
e-mail: vladimir@caomsk.mipt.ru

N. Kämpfer (ed.), *Monitoring Atmospheric Water Vapour,*
ISSI Scientific Report Series 10,
DOI 10.1007/978-1-4614-3909-7_4, © Springer Science+Business Media, LLC 2013

The factor C includes molecular coefficients from the literature as well as instrument specific quantities. If C is a constant, the number of detected fluorescence photons is proportional to the H_2O mixing ratio $[H_2O]/[air]$ for measurements in the UT/LS. For measurements at higher altitudes, Eq 4.4 has to be used to obtain correct water vapour mixing ratios.

In reality, C is a function of J and thus depends on the photon flux in the fluorescence volume, which in turn depends on variations of the lamp intensity and absorption by atmospheric gases. In the vacuum UV (VUV) spectral region, absorption by oxygen and water vapour has to be taken into account. The Lyman-α line at $\lambda = 121.6$ nm coincides with a narrow deep minimum in the oxygen absorption cross section and thus enables measurements with the fluorescence technique down to the middle troposphere. Measurement of the absorption of Lyman-α radiation at higher concentrations can be used for quantification of H_2O abundances in the troposphere as well (e.g. Tillman 1965). Such instruments (e.g. Buck 1976) are used on several research aircraft as part of the basic instrumentation.

The most advanced Lyman-α fluorescence hygrometers have been developed in the laboratories at NOAA in Boulder, at Harvard, in Jülich (Germany) and in Dolgoprudny (Russia). Though they are based on the same technique, they differ in several experimental details, and also in their calibration procedure. The instruments are employed on different aircraft and balloons from the UT up to 35 km altitude. Rocket borne measurements in the mesosphere using this technique have been reported by (Khaplanov et al. 1996).

One of the advantages of this technique is the large dynamic range for measurements from the UT at several hundred ppmv to dry stratospheric air masses where changes of the order of 0.1 ppmv can still be detected. Large flow rates through the hygrometers can be achieved for contamination-free measurement together with integration times on the order of 1 s for detection of small-scale features in the atmosphere.

4.2 Fluorescence Lyman-α Hygrometers

4.2.1 The NOAA Fluorescence Lyman-α Hygrometers

The NOAA balloon-borne Lyman-α fluorescence hygrometer was developed by (Kley and Stone 1978). The actual flight instrument for use in the stratosphere has been described and characterized by (Kley et al. 1979). This was an open-cell design with a radio-frequency discharge Lyman-α light source. The stray light intensity across the cell and the intensity in the fluorescence region were monitored by nitric oxide ionization cells. The instrument was flown at night to eliminate solar scatter.

A characteristic of this and successive NOAA Lyman-α fluorescence hygrometers both balloon and air-borne ones is their method of in situ calibration through the simultaneous measurement of water vapour concentration by absorption and OH fluorescence. The main sources of error of the present aircraft instrument are the

accuracy of the water Lyman-α absorption cross section and the Poisson counting statistics of the signal and background. The total 2σ error is 10 % at 4 ppmv for 1 s data and 6.6 % at 4 ppmv and 10 s data.

4.2.2 The Harvard Fluorescence Lyman-α Hygrometers

The Harvard balloon-borne Lyman-α has been described by (Weinstock et al. 1990). Briefly, Lyman-α radiation from a RF discharge lamp photodissociates water vapour in a 6 inch duct. The OH fluorescence is collected at right angles to the lamp and airflow through an interference filter and detected with a photomultiplier tube. A large fan is used to aid in the airflow through the duct. The quoted accuracy of these 2-σ data is 40 % in 1987 for a 2-min. average and 30 % in 1988 and 1989 for a 30-s average.

The Harvard Lyman-α instrument for the NASA ER-2 aircraft was described in detail by (Weinstock et al. 1994), with an update in (Hintsa et al. 1999). Flow velocities in the duct are typically 30–70 m/sec for fast time response and to avoid (and directly test for) contamination from walls. The calibration is checked in-flight by comparing Lyman-α photofragment fluorescence with direct absorption measurements of water vapour, similar to the method of (Kley et al. 1979), using the atmosphere to provide a wide range of H_2O concentrations. Based on laboratory calibrations and in-flight calibration checks, the instrument is accurate to ± 5 %, with an additional systematic uncertainty of 0.1 ppmv.

4.2.3 The Jülich Fluorescence Lyman-α Hygrometers (FISH)

The Fast In situ Stratospheric Hygrometer (FISH) developed at the Forschungszentrum Jülich (Germany) is described in detail by (Zöger et al. 1999). Today, three different hygrometers exist, one for employment on large stratospheric balloons, and two for use on different aircraft platforms.

FISH consists of a closed, vacuum-tight fluorescence cell, a Lyman-α radiation source, a PMT in photon-counting mode, detectors to monitor the VUV radiation output of the Lyman-α lamp, and a mirror drive that controls the measuring cycle: determination of the fluorescence and background count rate and of the lamp intensity.

FISH is calibrated between flights in the laboratory using a calibration bench (Zöger et al. 1999) under realistic conditions. FISH can also be calibrated during in-flight operation by measuring the absorption of Lyman-α radiation whenever the optical depth of H_2O is sufficient. Including an error of the pressure measurement in the calibration bench, the H_2O mixing ratio can be determined with an accuracy better than 5 %.

4.2.4 The CAO Fluorescence Lyman-α Hygrometers (FLASH)

The Fluorescence Advanced Stratospheric Hygrometer (FLASH) is developed at the Central Aerological Observatory of Roshydromet (Russia). At present, two different instruments exist, one is employed on board M55-Geophysica aircraft and the other one (FLASH-B) is designed for use on board small balloons. FLASH-B appears to be the smallest fluorescence hygrometer worldwide, however its technical characteristics, accuracy and performance do not differ much from the other, more sophisticated Lyman-α instruments. The following section describes in detail the FLASH-B design, its applications and performance assessment.

4.3 The FLASH-B Instrument

The FLASH-B instrument was developed at Central Aerological Observatory, Russia for balloon-borne water vapour measurements in the upper troposphere and stratosphere (Yushkov et al. 1998, 2001). The source of Lyman-α radiation (λ=121.6 nm) is a hydrogen discharge lamp while the detector of OH fluorescence at 308–316 nm is a HAMAMATSU R647-P photomultiplier run in photon counting mode with an narrowband interference filter for selecting the fluorescence spectral region. The intensity of the fluorescent light sensed by the photomultiplier is directly proportional to the water vapour mixing ratio under stratospheric conditions (30–150 hPa) with small oxygen absorption (3 % at 50 hPa).

The precursor of FLASH-B instrument, optical hygrometer (Khaplanov et al. 1992) designed for use onboard both stratospheric balloons and rockets had a weight of about 5 kg. It participated in EASOE field campaign in 1991/1992 (Khattatov et al. 1994)as well as in Arctic field balloon campaign in Russia.

The modified version of the optical hygrometer named FLASH-B (Fluorescent Advanced Stratospheric Hygrometer for Balloon) had significantly reduced dimensions and weight. It was successfully applied for water vapour measurements on board of long and short duration balloons (Yushkov et al. 2001). Based on this experience the recent version of FLASH-B has been developed for regular balloon soundings.

The instrument uses the open layout, where the optics is looking directly into the outside air. This arrangement is suitable only for nighttime measurements with a solar zenith angle larger than 98°, at which sun light no longer reaches the detector. The co-axial optical layout allows reducing the size of the instrument to $106 \times 156 \times 242$ mm with a total weight of 0.5 kg.

The accuracy of the FLASH-B instrument is determined by the calibration error estimated as 4 % in the 3–100 ppmv range. The measurement precision is 5.5 % calculated for 4 seconds integration time at stratospheric conditions. The total uncertainty of the measurement is less than 10 % at the stratospheric mixing ratios greater than 3 ppmv increasing to about 20 % at mixing ratios less than 3 ppmv.

The source of vacuum UV (VUV) radiation used in the FLASH-B instrument is a hydrogen glow-discharge lamp filled with a mixture of hydrogen and helium at the total pressure of 10 hPa with VUV flux amounting to 10^{14} quanta per second. Unlike the more sophisticated hygrometers based on the fluorescence technique, FLASH-B doesn't use VUV photon flux control. However the hydrogen glow-discharge lamps used in the FLASH-B instrument have been proved to have very stable intensity of the Lyman-α emission over both operation and storage time. Every lamp is subjected to continuous laboratory tests for stability of the emission intensity which is checked before the flight.

An indicator of lamp emission stability is the hygrometer conversion factor, which is determined through calibration of the instruments using reference frost point hygrometer. Repeatability of calibrations is the proof of lamp emission stability. The intensity of Lyman-α radiation in the lamp applied is in linear relation with the discharge current value. The lamp power supply scheme provides direct current stabilization better than 0.1 %. An important indirect evidence of stable lamp performance during flight is the precise match of ascent and descent measurements in the stratosphere below 70 mBar, where the water outgassing from balloon and payload does not affect the ascent measurements, while the spatial and temporal variability of water vapour is negligible between stratospheric ascent and descent measurements.

The VUV light sources containing the mixture of hydrogen and helium are known to have the stray helium line emission which overrides the spectrum of hydroxyl fluorescence and thus may cause spurious signal from backscattering of this emission. The FLASH-B instrument uses the hydrogen lamp in which the 270–320 nm emission is suppressed by a special window-filter. This window-filter is made using monocrystalline magnesium fluoride with an absorbing layer vacuum-deposited on its inner surface. In this way, up to 50 % transmission at the 121.6 nm line and selective absorption at 300 nm are achieved. In addition the instrument uses the narrowband interference filter centered at 310 nm with 8 nm bandwidth and out-of-band extinction of 10^{-5} thus reducing the possible effect of the stray light backscattering.

Temperature of the lamp can vary during the flight experiment, however the laboratory studies have shown that the temperature drift of the lamp flux does not exceed 0.016 %/°C, meaning that the error introduced by the lamp temperature variations is negligible.

The background signal caused by the night sky emissions in the absence of fluorescence light is detected using lamp modulation with 1 kHz square wave with 1/8 or 1/16 duty cycle and synchronous demodulation of the signal received. The background signal is detected while the lamp is off and then subtracted from the fluorescence signal (Table 4.1).

Table 4.1 FLASH-B technical characteristics

Range of water vapour measurements	0.5–1000 ppmv
Detection limit	0.1 ppmv
Response time	0.2 s
Integration time	4 s
Measurement precision	5.5 %
Total uncertainty	<10 % (1σ) at $\mu > 3$ ppmv
Temperature range	95 °C − +40 °C
Height range	7–35 km
Required power	9–30 V, 1 W max
Weight w/out batteries	0.5 kg
Dimensions (incl. flight box)	150 mm × 200 mm × 350 mm
Interface card	Built-in (T-MAX type)
Radiosonde	Vaisala RS80-15 A(L), SRS-C34, Vaisala RS-92

4.3.1 Instrumental Layout

In Fig 4.1 the optical layout of the hygrometer is sketched. A system of three lenses is concentrically arranged around the lamp. The lenses are made from U-Viol glass. The front lens has a diameter of 50 mm and is sealed to the lamp body. A modification of FLASH-B employs Fresnel plastic lens, which replaces two inner glass lenses. The analyzed volume is located outside the instrument 24 mm off the window of Vacuum UV (VUV) lamp. This separation largely prevents the effect of the desorption of water vapour (contamination) from the instrument's technological surfaces and communication lines, inherent in closed-type hygrometers using aspiration system. This compact open layout is suitable only for nighttime measurements with a solar zenith angle larger than 98°, at which sun light no longer reaches the detector.

After passing the interference filter with bandwidth 306 nm the fluorescence light hits the cathode of the photomultiplier (PMT). The photomultiplier is the HAMAMATSU R647P run in photon counting mode with bialkali cathode. The PMT unit is maintained at constant temperature of 33 °C, while PMT supply voltage is precisely stabilized. The interference filter centered at 310 nm with 6 nm bandwidth and out of band extinction of 10^{-5} is used to select the spectral region coincident with the emission from the upper rotational levels of the (0→0) band of the A→X system of OH. Filter is designed as a system of multilayer (35 layers) dielectric hafnium and silicon sheets on a quartz substrate. Use of these materials allows producing filters with high transmission (not less than 50 %). The filter design ensures performance stability and safety from mechanical damage.

The electronic part provides lamp modulation, PMT signal processing and demodulation, PMT heat setting and transmission of the data over telemetry channel. The essential feature of signal detection is lamp modulation with 1 kHz square wave with 1/16 duty cycle (OSC) and synchronous demodulation of the signal received. Such setup allows increasing signal-to-noise ratio several-fold, improving the sensitivity, and widening the dynamic range of the hygrometer. Output data format is a

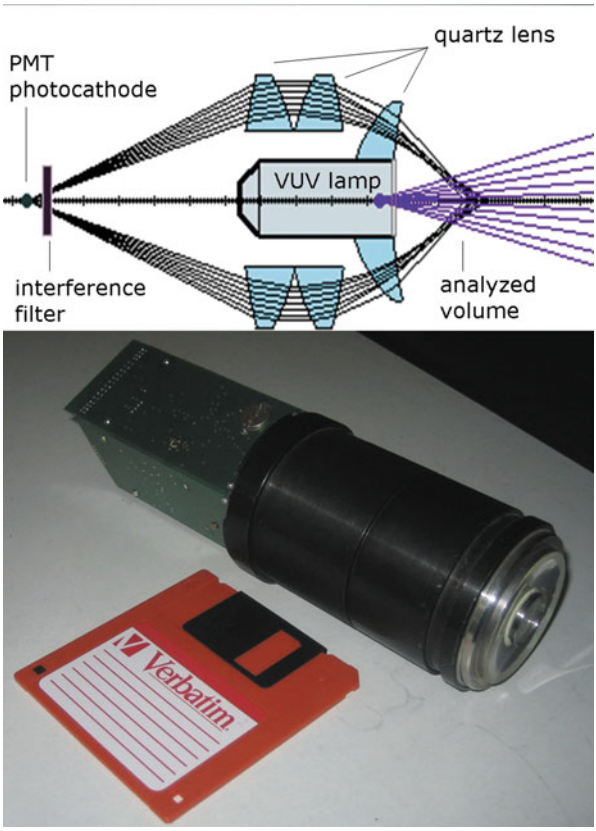

Fig. 4.1 *Upper Panel* Schematics of the optical arrangement of the FLASH-B. *Lower Panel* Basic view of the FLASH-B

300-baud Bell-103 standard. The ground receiving equipment consists of a 400 MHz ground receiver, modem and PC. FLASH-B controller is equipped with an internal rewritable flash memory capable of storing up to 8 hours of sounding data. FLASH-B has electronic interface with Vaisala RS-80, Meteolabor SRS-C34 and Vaisala RS-92.

4.3.2 FLASH-B Calibration

Each hygrometer has to be calibrated in the laboratory before the flight. The laboratory studies showed that calibration coefficients remain constant in time. The lamp flux intensity, being the most influencing factor for calibration, is checked directly before the flight by direct measurement of VUV flux using special CuI_2 VUV sensor.

For calibration a laboratory facility capable of simulating atmospheric conditions is used. In particular, the large range of water vapour mixing ratios (1-1000 ppmv), pressure from 1000 to 3 hPa and temperature down to 190 K can be generated by the calibration setup. A description of the procedure can be found in (Vömel et al. 2007).

The calibration fit function is linear in the pressure range of 30–150 hPa and water vapour mixing range of 1–300 ppmv. At higher pressures the VUV absorption by oxygen and water vapour is taken into account. The lamp stray light being constant doesn't affect the calibration since the calibration coefficients are determined as the slope of the regression line.

The total uncertainty of the calibration is determined by the following factors: uncertainty of the frost point measurement (0.1 K), uncertainty of the temperature dependence of the water vapour partial pressure, error in pressure determination, error accounting for inconsistency of the air sampled by the reference dew point hygrometer and the air inside the chamber, instability of the VUV intensity of the lamp. The total relative error of the calibration amounts to 4 %.

4.3.3 FLASH-B Operational Layout

The FLASH-B hygrometer being a very compact and light-weight sonde can be flown on small rubber balloons equipped with a parachute for a slow descent and a 50 m unwinder for holding the hygrometer away from balloon. The instrument is placed into a styrofoam box covered with metal foil to prevent water desorption from the styrofoam. The flight box has battery compartment embedded. The flight configuration of FLASH-B is such that the analyzed volume is located beneath the downward looking optics about 24 mm away from the lens. The measurements during balloon ascent in the stratosphere above 90 hPa are affected by contamination due to water outgassing from the instrument surfaces and the balloon. The measurements during the descent below parachute in undisturbed air can be considered contamination-free as shown by the drop of water vapour immediately after the burst of balloon at ceiling altitude. Total weight of the flight payload including Vaisala RS-80 or RS-92 radiosonde and batteries amounts to 1.3 kg and 2.4 kg when using SRS-C34 with Snow White. The vertical resolution of the measurements depends on the descent rate, that is around 50 m in the lower stratosphere provided normal parachute performance.

The aircraft version of FLASH instrument is employed on the M55-Geophysica high altitude aircraft of MDB. It uses a closed aspiration system with backward air inlet for measuring gas phase water vapour. The fluorescence chamber is opened when the aircraft reaches 8 km to avoid chamber contamination. The airborne FLASH was used within a number of M55-Geophysica campaigns, e.g. TROCCINOX, SCOUT-O3, SCOUT-AMMA. The detailed description of the instrument is given by (Sitnikov et al. 2007).

FLASH-B has an electronic and mechanical interface to the CNES long-duration balloon gondola ISBA flown onboard CNES super pressure balloon (SPB). FLASH-B was flown on board SPB from Zinder, Niger in August 2006 and from Esrange, Sweden in March 2007. In a long-duration balloon experiment FLASH-B is suspended beneath the gondola on a 10 m long cable. FLASH-B power is triggered by the light sensor to restrict the hygrometer operation to the night time. During the

measurements cycle of 15 min. long the data are recorded into internal hygrometer memory, and when the measurement cycle is over, the data are uploaded onto the ISBA gondola memory via RS485 protocol with digital acknowledgement line. The interval between measurement cycles is 2 h. The detailed description of the long-duration balloon instrument and the experiments is given in (Lykov et al. 2009).

4.4 FLASH-B Performance: Comparison with Other Sensors

The quoted total uncertainty of FLASH-B measurements is < 10 %. While this estimate is based primarily on the theoretical computations, field intercomparisons fully confirm the estimated uncertainty level of FLASH-B instrument.

During LAUTLOS-WAVVAP Intercomparison campaign held in Sodankyla, Finland in January-February 2004 (http://fmiarc.fmi.fi/LAUTLOS_web/index_lautlos.html) FLASH-B was flown a number of times on the same balloon payload with NOAA-CMDL frost point hygrometer (Vömel et al. 1995). The simultaneous measurements from 7 soundings show good agreement between both instruments, with a mean deviation of -2.4 % ± 3.1 % (one standard deviation) for data between 15 and 25 km. The comparison between NOAA/CMDL and FLASH-B, including the low-temperature correction and a 5-s time-lag correction for NOAA/CMDL hygrometer, gives a mean deviation of -1.3 % ± 2.7 % (one standard deviation) for data between 15 and 25 km. The FLASH-B during LAUTLOS was found to measure water vapour reliably above 7 km. This lower altitude limit is determined by the absorption of Lyman-α radiation by oxygen and water vapour and can be lower in a dry atmosphere, which was seen in some profiles (Vömel et al. 2007a). The results of comparison are shown in Fig. 4.2 (left).

The balloon soundings during LAUTLOS were accompanied with microwave remote measurements of water vapour in the 20–70 km range using Middle Atmospheric Water Vapour Radiometer (MIAWARA) of University of Bern. Comparison between FLASH-B and MIAWARA in the overlapping region (20–26 km) showed very good agreement with difference of -0.33 % ± 7.66 % (one standard deviation) (Deuber et al. 2005).

Within SCOUT-AMMA balloon campaign held in Niamey, Niger in August, 2006 FLASH-B was flown 7 times together with Vaisala RS-92 radiosonde. The comparison between FLASH-B and Vaisala RS-92 night time ascents shows good agreement in the overlapping region (150–350 hPa) with the relative difference 0.44 % $\pm$ 5.89 % (one standard deviation). The results of comparison are shown in Fig. 4.2 (right).

During NASA TC4 campaign held in Alajuela, Costa-Rica in August 2007 (http://www.espo.nasa.gov/tc4/) FLASH-B was flown five times on the same balloon payload with CFH (Cryogenic Frost point Hygrometer) (Vömel et al. 2007b), the successor of NOAA/CMDL frost point hygrometer. Comparison showed that the difference between FLASH-B and CFH smoothed data is 1.1 % ± 4.74 % (one standard deviation) in the 9–28 km range. The results of comparison are shown in

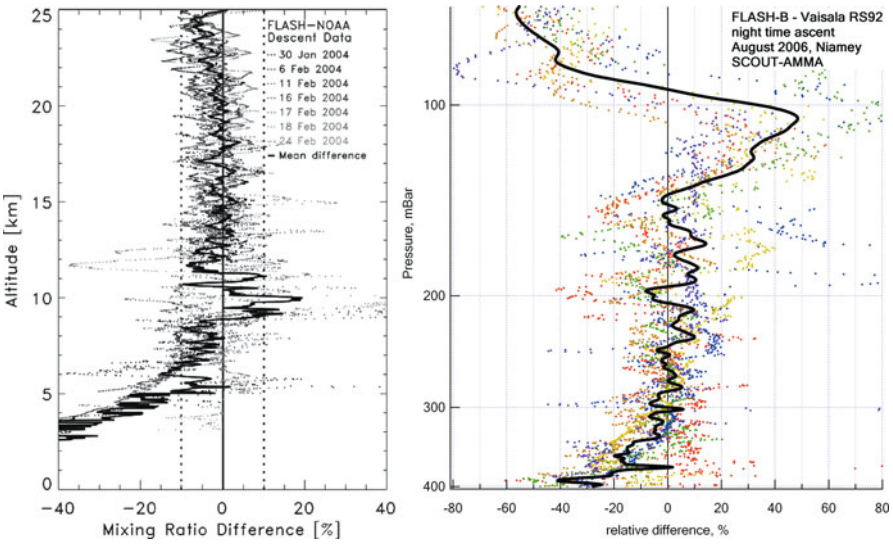

Fig. 4.2 Comparison of *Left* the FLASH-B and NOAA/CMDL water vapour observations during descent after time-lag and low-temperature calibration correction. LAUTLOS-WAVVAP campaign, Sodankylä, Finland, Jan–Feb 2004. *Right* FLASH-B and Vaisala RS-92 during night-time ascents. SCOUT-AMMA, Niger, August 2006

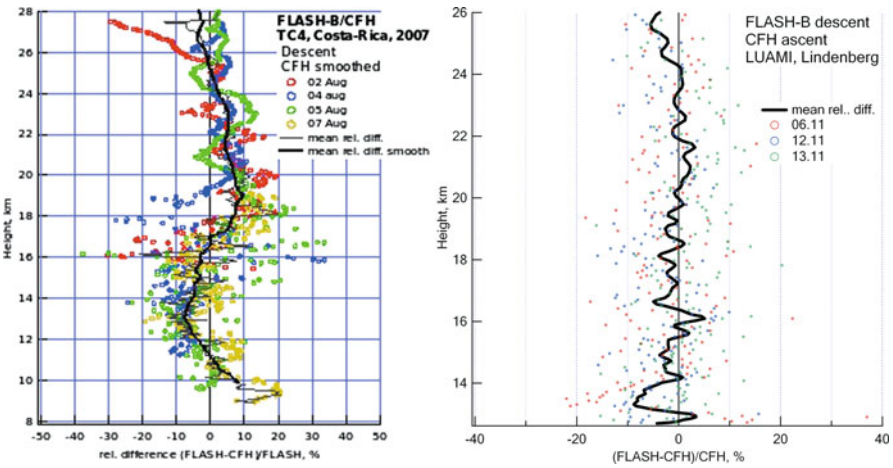

Fig. 4.3 Comparison of the FLASH-B and CFH water vapour observations during descent. *Left* NASA TC4 campaign, Alajuela, Costa-Rica, August 2007. *Right* LUAMI campaign, Lindenberg, Germany, November 2008

Fig. 4.3 (left). Another comparison of FLASH-B and CFH was carried out after the LUAMI campaign held in Lindenberg, Germany during November 2008. Comparison of FLASH-B and CFH based on 3 simultaneous soundings showed very good

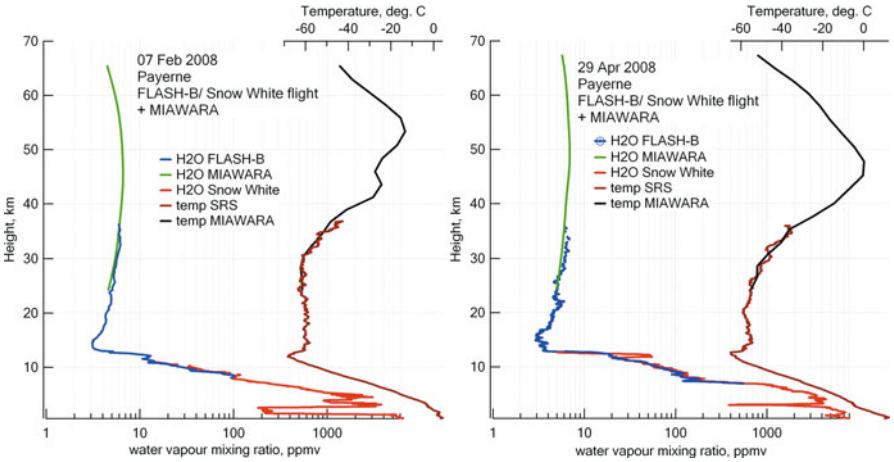

Fig. 4.4 Merged water vapour and temperature profiles obtained using combination of Snow White, FLASH-B and MIAWARA measurements at Payerne station on 07.02.2008 *(left)* and 29.04.2008 *(right)*. The observations were carried out in the frame of SHOMING project of IAP/University of Bern

agreement with the mean relative difference of 1.46 % ±3.88 % (one standard deviation) in the 13–26 km range. The results of comparison are shown in Fig. 4.3 (right).

Soundings of FLASH-B interfaced with SRS/Snow White sonde from Payerne were accompanied with microwave remote measurements by MIAWARA from Bern. Combination of different techniques for water vapour measurements enables acquiring a single water vapour profile from the surface up to 70 km as shown in Fig. 4.4.

4.5 Water Vapour Observations Using FLASH-B

During 2004–2009 periods FLASH-B sondes were flown over 90 times on board small and medium sized balloons in the frame of various projects and campaigns.

The longest sounding data record refers to AWI Koldewey station at Ny-Alesund (79 °N), where 5–6 FLASH-B sondes were flown every winter since 2004 in the frame of EU FP6 SCOUT-O3 project. During the winter periods FLASH-B was also flown from another arctic station—FMI-ARC in Sodankylä (67.4 °N) and SSC Esrange (67.9 °N). The obtained data set allowed comprehensive case studies and detailed characterization of stratospheric water vapour vertical distribution within different conditions in the Arctic Polar stratosphere such as presence of PSCs (Maturilli and Dörnbrack 2006), subsidence within Polar vortex (Yushkov et al. 2005), lamination of water vapour profile in the vicinity of vortex edge (Maturilli et al. 2006; Yushkov et al.

2005) and troposphere-stratosphere exchange (Karpechko et al. 2007; Lukyanov et al. 2009).

At mid-latitude FLASH-B measurements were conducted at two European stations: Lindenberg (Richard Assman observatory) and Payerne of MeteoSwiss.

At the tropical region FLASH-B was employed within the SCOUT-AMMA campaigns held in Niamey, Niger in August 2006 and September 2008; within the NASA TC4 campaign in Alajuela, Costa-Rica in August 2007 and in Biak, Indonesia in January 2009 within the SOWER campaign. The obtained series of water vapour vertical profiles reveal various processes occurring within the TTL such as hydration of LS by ice geysers (Khaykin et al. 2009, 2010), lagrangian dehydration and vertical mixing (Khaykin et al. 2008).

4.6 Summary and Conclusions

Fluorescence method has been used for measurements of atmospheric water vapour since 1978. The advantage of this technique is the large dynamic range for measurements from the UT at several hundred ppmv to dry stratospheric air masses where changes of the order of 0.1 ppmv can still be detected. The most advanced Lyman-α fluorescence hygrometers have been developed in the laboratories at NOAA in Boulder, at Harvard, in Jülich, Germany (FISH) and in Dolgoprudny, Russia (FLASH). Though they are based on the same technique, they differ in several experimental details, and also in their calibration procedure. The instruments are employed on different aircraft and balloons from the UT up to 35 km altitude. Rocket borne measurements in the mesosphere using this technique have been also reported.

This overview focuses on the Russian Lyman-α instrument FLASH-B, a compact and light-weight fluorescence hygrometer. The essential features of FLASH-B design are open-cell co-axial optical layout and the hydrogen Lyman-α lamp with highly stable VUV flux intensity, which does not require in-flight monitoring. Such design allows reducing the hygrometer to the size of a meteorological sonde. While operation of FLASH-B sonde is rather easy, its design restricts the measurements to night time and introduces the problem of water contamination during balloon ascent in the stratosphere, therefore parachuted payload descent is required. For calibration of FLASH-B instruments a laboratory facility capable of simulating atmospheric conditions is used. The laboratory studies showed that calibration coefficients remain constant in time.

The total uncertainty of FLASH-B measurements is $<10\,\%$ while the precision amounts to 5.5 %. Field intercomparisons fully confirm the instrument stated accuracy. The intercomparison campaigns with FLASH-B were carried out at a wide latitude range and include comparisons with NOAA/CMDL frost point hygrometer, its successor - CFH and various commercial radiosondes, particularly Vaisala RS-92. The results of comparisons against independent sensors point out stable performance and data quality of the FLASH-B instrument.

During 2004–2009 period FLASH-B sondes were flown over 90 times on board small and medium sized balloons in the frame of various projects and campaigns. FLASH-B can be used as a reference for validation of the radiosonde humidity sensors, for satellite validation and for long-term water vapour trends monitoring.

References

J.-L. Bertaux, A. Delannoy, Vertical distribution of H_2O in the stratosphere as determined by UV uorescence in situ measurements. Geophys. Res. Lett. **5**, 1017–1020 (1978)

A. L. Buck, The variable-path Lyman-α hygrometer and its operating characteristics. Bull. Am. Meteorol. Soc. **57**, 1113–1118 (1976)

B. Deuber, A. Haefele, D.G. Feist, L. Martin, N. Kämpfer, G.E. Nedoluha, V. Yushkov, S. Khaykin, R. Kivi, H. Vömel, Middle atmospheric water vapour radiometer (MIAWARA): Validation and first results of the LAPBIAT upper tropospheric lower stratospheric water vapour validation project (LAUTLOS-WAVVAP) campaign. J. Geophys. Res. **110**(D13), 306 (2005)

E. Hintsa, E. Weinstock, J. Anderson, R. May, D. Hurst, On the accuracy of in situ water vapor measurements in the troposphere and lower stratosphere with the Harvard Lyman-α hygrometer. J. Geophys. Res. **104** 8183–8189 (1999)

A. Karpechko, A. Lukyanov, E. Kyrö, S. Khaikin, L. Korshunov, R. Kivi, H. Vömel, The water vapour distribution in the Arctic lowermost stratosphere during the LAUTLOS campaign and related transport processes including stratosphere-troposphere exchange. Atmos. Chem. Phys. **7**, 107–119 (2007)

M. Khaplanov, V. Astakhov, A. Lukjanov, M. Kretova, V. Yushkov, Fluorescent hygrometer for middle atmosphere measurements, in *Proceedings 19th Annual European Meeting on Atmospheric Studies by Optical Methods*, pp. 540–545 (1992)

M. Khaplanov, J. Gumbel, N. Wilhelm, G. Witt, A direct measurement of water vapor in the stratosphere and mesosphere. Geophys. Res. Lett. **23** 1645–1648 (1996)

V. Khattatov, V. Yushkov, M. Khaplanov, I Zaitzev, J. Rosen, N. Kjome, Some results of water vapor, ozone, and aerosol balloon borne measurements during EASOE. Geophys. Res. Lett. **21**, 1299–1302 (1994)

S. Khaykin, J. Pommereau, H. Vömel, L. Korshunov, V. Yushkov, J. Nielsen, Water vapour in the tropical UT/LS from balloon observations with FLASH-B hygrometer. Geophys. Res. Abstracts. **10**, EGU2008-A-00444 (2008)

S. Khaykin, J.-P. Pommereau, L. Korshunov, V. Yushkov, J. Nielsen, N. Larsen, T. Christensen, A. Garnier, A. Lukyanov, E. Williams, Hydration of the lower stratosphere by ice crystal geysers over land convective systems. Atmos. Chem. Phys. **9**, 2275–2287 (2009)

S. Khaykin, V. Yushkov, L. Korshunov, A. Lukyanov, J.-P. Pommereau, J. Nielsen, H. Vömel, Water vapour in the tropical lower stratosphere: Observations and analysis. Izv. RAN. Atmo. Ocean. Phys. **46**, 76–84 (2010)

D. Kley, E. Stone, Measurement of water vapor in the stratosphere by photodissociation with Lyman-α (1216 å) light. Rev. Sci. Instrum. **49**, 691–697 (1978)

D. Kley, E. Stone, W. Henderson, J. Drummond, W. Harrop, A. Schmeltekopf, T. Thompson, R. Winkler, In situ measurements of the mixing ratio of water vapor in the stratosphere. J. Atmos. Sci. **36**, 2513–2524 (1979) doi:10.1175/1520-0469(1979)036h2513:SMOTMRi2.0.CO;2

A. Lukyanov, A. Karpechko, V. Yushkov, L. Korshunov, S. Khaykin, E. Kyro, R. Kivi, M. Maturilli H. Vömel, Transport of water vapour and ozone in the upper troposphere and lower stratosphere and stratosphere-troposphere exchange during LAUTLOS campaign. Izv. RAN. Atmo. and Ocean. Phys. in press (2009)

A. Lykov, S. Khaykin, V. Yushkov, L. Korshunov, P. Cocquerez, Observations of water vapour on board long-duration super pressure balloon using FLASH-B lyman-α hygrometer., in *Proceedings of the 19th ESA Symposium on European Rocket and Balloon programmes and Related Research*, Bad Reichenhall—Germany, 7–11 June 2009, (in press)

M. Maturilli, A. Dörnbrack, Polar stratospheric ice cloud above Spitsbergen. J. Geophys. Res. **111**(D18), 210 (2006). doi:10.1029/2005JD006967

M. Maturilli, F. Fierli, V. Yushkov, A. Lukyanov, S. Khaykin, A. Hauchecorne, Stratospheric water vapour in the vicinity of the Arctic polar vortex. Ann. Geophys. **24**, 1511–1521 (2006)

N.M. Sitnikov, V.A. Yushkov, A.A. Afchine, L.I. Korshunov, V.I. Astakhov, A.E. Ulanovskii, M. Kraemer, A. Mangold, C. Schiller, F. Ravegnani, The FLASH instrument for water 50 vapor measurements on board the high-altitude airplane, Instruments and Experimental Techniques, **50**, 113–121 (2007). doi:10.1134/S0020441207010174

J. Tillman, Water vapor density measurements utilizing the absorption of vacuum ultraviolet and infrared radiation, in *Humidity and Moisture, I: Principles and methods of measuring humidity in gases, Proc. 1963 Int. Symp. on Humidity and Moisture*, Washington, D.C, 1965 ed. by A. Wexler, R. Ruskin, (Reinhold Publishing Corporation, New York) pp. 428–443

H. Vömel, S.J. Oltmans, D.J. Hofmann, T. Deshler, J.M. Rosen, The evolution of the dehydration in the antarctic stratospheric vortex. J. Geophys. Res. **100**, 13919–13926 (1995)

H. Vömel, H. Selkirk, L. Miloshevich, J. Valverde-Canossa, J. Valdés, E. Kyrö, R. Kivi, W. Stolz, G. Peng, J.A. Diaz, Radiation dry bias of the Vaisala RS92 humidity sensor. J. Atmos. Ocean. Tech. **24**, 953–963 (2007a). doi:10.1175/JTECH2019.1

H. Vömel, D.E. David, K. Smith, Accuracy of tropospheric and stratospheric water vapor measurements by the cryogenic frost point hygrometer: Instrumental details and observations. J. Geophys. Res. **112** D08305 (2007b). doi:10.1029/2006JD007224

E. Weinstock, J. Schwab, J. Nee, M. Schwab, J. Anderson, A cryogenically cooled photofragment uorescence instrument for measuring stratospheric water vapor. Rev. Sci. Instrum. **61**, 1413–1432 (1990)

E. Weinstock, E. Hintsa, A. Dessler, J. Oliver, N. Hazen, J. Demusz, N. Allen, L. Lapson, J. Anderson, New fast response photofragment uorescence hygrometer for use on the NASA ER-2 and the Perseus remotely piloted aircraft. Rev. Sci. Instrum. **65**, 3544–3554 (1994)

V. Yushkov, S. Merkulov, V., A., Optical balloon hygrometer for upper stratosphere and stratosphere water vapour measurements, in *Optical remote sensing of the atmosphere and clouds*, *Proceedings of SPIE*, SPIEInternational Society for Optical Engine, **3501**, pp. 439–445 1998, ed by J. Wang, B. Wu, T. Ogawa, Z.-H. Guan

V. Yushkov, N. Sitnikov, I. Zaitzev, J.-P. Pommereau, A. Garnier, Stratospheric water vapor measurements in the winter arctic with optical uorescence hygrometer on short and long duration balloons, in *Proceedings of the 15th ESA Symposium on European Rocket and Balloon programmes and Related Research*, Biarritz, France, ESA SP-471, 28–31 May 2001 ed. by B. Warmbein, pp. 263–268

V. Yushkov, A. Luk'yanov, S. Khaikin, L. Korshunov, R. Neuber, M. Muller, E. Kuro, R. Kivi, H. Vömel, Y. Sasano, H. Nakane, Vertical distribution of water vapor in the arctic stratosphere in january-february 2004 from data of the LAUTLOS field campaign. Izv. Atmo. Ocean. Phys. **41**, 622–630 (2005)

M. Zöger, A. Afchine, N. Eicke, M.-T. Gerhards, E. Klein, D. S. McKenna, U. Mörschel, U. Schmidt, V. Tan, F. Tuitjer, T. Woyke, C. Schiller, Fast in situ stratospheric hygrometers: A new family of balloon-borne and airborne Lyman-α photofragment uorescence hygrometers. J. Geophys. Res. **104**, 1807–1816 (1999)

Part II
Remote Sensing Sensors

Chapter 5
Microwave Radiometry

Niklaus Kämpfer, Gerald Nedoluha, Alexander Haefele and Evelyn De Wachter

5.1 Introduction

Water vapour profiles in the atmosphere can be retrieved from spectral measurements obtained by microwave radiometers. These instruments observe the pressure broadened emission lines of rotational transitions by water vapour at specific frequencies in the microwave part of the spectrum. Transitions of water vapour that are used for remote sensing of the atmosphere are located e.g. at 22.235 GHz, 183.310 GHz, 448.001 GHz and at 556.936 GHz. However, not all of these lines can be observed from the ground as the line strength at some frequencies is too high to allow instruments to look through the troposphere where most water vapour resides. Opacity of the troposphere allows mainly to use the transition at 22.235 GHz for ground based observations. From very dry places such as on high mountains or operated from an aircraft it is possible to make measurements using the much stronger line at 183.310 GHz. Such measurements could provide superior signal-to-noise as compared to 22 GHz measurements, but because of the larger tropospheric attenuation a small fractional error in estimating tropospheric attenuation could lead to a significant error in the middle atmospheric water vapour retrieval. In Fig. 5.1 we show calculated typical spectra for observations taken from a range of altitudes.

Measurements by microwave receivers at 22.235 GHz can be made from the ground nearly continuously, including under cloudy conditions, however there may be some degradation in the quality of the measurements. During rain or snow reliable observations are not possible. Microwave radiometers operated on satellites that observe the Earth atmosphere from the limb often use the transitions in the submillimeter part of the spectrum, i.e. at 448.001 GHz or at 556.936 GHz. (see also

N. Kämpfer (✉)
Institute of Applied Physics, University of Bern, Sidlerstr. 5, CH-3012 Bern, Switzerland
e-mail: niklaus.kaempfer@iap.unibe.ch

G. Nedoluha
Naval Research Laboratory, Washington, D.C., USA

A. Haefele · E. De Wachter
Institute of Applied Physics, University of Bern, Bern, Switzerland

N. Kämpfer (ed.), *Monitoring Atmospheric Water Vapour,*
ISSI Scientific Report Series 10,
DOI 10.1007/978-1-4614-3909-7_5, © Springer Science+Business Media, LLC 2013

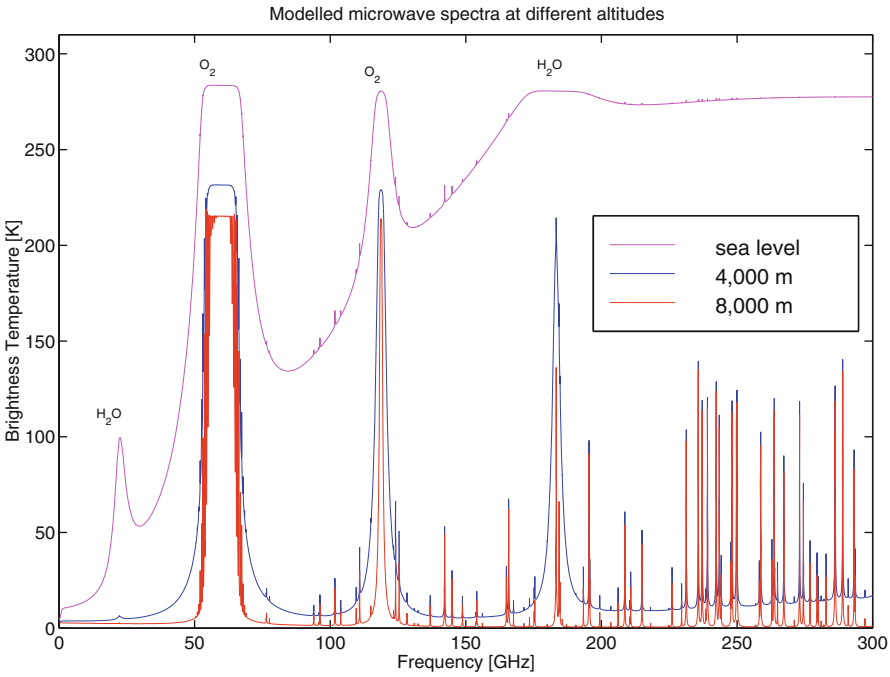

Fig. 5.1 Modeled emission spectra as observed from the ground for altitudes at sea level, a high mountain (4,000 m) or from an aircraft at 8,000 m

Chap. 9 about satellite observations.) For a basic treatise of microwave radiometry we refer e.g. to (Janssen 1993).

5.2 Spectroscopy and Forward Modeling

In microwave radiometry it is common to express the signal intensity as a brightness temperature, T_b, in units of Kelvin according to the Rayleigh-Jeans approximation of Planck's law. The frequency-dependent signal strength $T_b(\nu, s_0)$ at the ground contains contributions from different emission altitudes according to the radiative transfer equation

$$T_b(\nu, s_0) = T_0 e^{-\tau(\nu,\, s_1)} + \int_{s_0}^{s_1} T(s')\, \alpha(\nu, s')\, e^{-\tau(\nu,\, s')} ds'. \tag{5.1}$$

$T_b(\nu, s_0)$ is the brightness temperature at the place of observation s_0, in our case on the earth surface, s_1 is an upper boundary of the atmosphere, $T(s)$ is the physical temperature along the integration path s and ν is the frequency. The opacity $\tau(\nu, s)$

Table 5.1 Spectroscopic parameters of the 6_{16}–5_{23} transition of H_2O for $T = 296$ K

	ν_0 [GHz]	S [m^{2}Hz]	E'' [J]	γ_{air} [Hz/Pa]	n_{air} [–]	γ_{self} [Hz/Pa]	n_{self} [–]
Parameter	22.2350800	1.3206e-18	8.86970e-21	28110	0.690	134928	1

ν_0 resonant frequency, S line intensity, γ_{air} (γ_{self}) air (self) broadening parameter, n_{air} (n_{self}) temperature dependence of γ_{air} (γ_{self})
ν_0, S and E'' from (Pickett et al. 1998) other parameters from (Liebe et al. 1989)

is the integral of the absorption coefficient $\alpha(\nu, s)$ that depends on frequency and the amount of molecules along the observing path.

$$\tau(\nu, s) = \int_{s_0}^{s} \alpha(\nu, s')ds'. \tag{5.2}$$

It is evident that in order to compute the atmospheric spectrum for a given transition of a given molecule according Eq. (5.1) the absorption coefficient, the temperature and pressure profiles as well as the density profiles of the relevant molecules (in this case H_2O) have to be known. Typical sources for the needed profiles are climatologies, operational analyses (NCEP, ECMWF) or observations. A proper forward model does not only consider the radiative transfer in the atmosphere but takes into account as well the sensor, like the antenna pattern, sideband suppression, down-conversion and filter characteristics, in order to provide a spectrum that is comparable with the measurement. Actually there are several codes in use to do the forward calculation. Many groups make use of the ARTS/QPack software package (Buehler et al. 2005), (Eriksson et al. 2005).

A key parameter in these calculation is the absorption coefficient $\alpha(\nu, s)$ as a function of frequency. The essential spectroscopic parameters for such a calculation are the resonant frequency, ν_0, the line intensity, $S(T)$, the line width, $\Delta\nu(p, T)$ and the energy of the lower quantum state, E''. The line-width must account for the Doppler and pressure broadening of the spectral line (the natural linewidth can be neglected at microwave frequencies).

The calculation of pressure broadening includes both self broadening and air broadening parameters. The pressure broadened line halfwidth $\Delta\nu(p, T)$ for a gas at pressure p, temperature T and partial pressure p_s is given by:

$$\Delta\nu(p, T) = \left(\frac{T_{ref}}{T}\right)^{n_{air}} \gamma_{air}(p - p_s) + \left(\frac{T_{ref}}{T}\right)^{n_{self}} \gamma_{self}\, p_s. \tag{5.3}$$

Values of the relevant parameters base on measurements or calculations or both and are provided by spectral line catalogues like JPL[1] or HITRAN[2] and by a wealth of publications. Some of the commonly used values for the transition at 22.235 GHz are shown in Table 5.1.

As shown in Fig. 5.2, the width of the line in the upper mesosphere is determined primarily by Doppler broadening, while below this the lineshape is dominated by

[1] http://spec.jpl.nasa.gov/ftp/pub/catalog/catform.html

[2] http://www.cfa.harvard.edu/hitran/

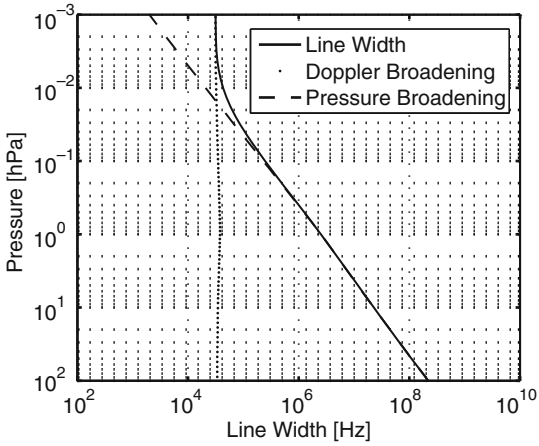

Fig. 5.2 Line width as function of pressure altitude in case of pressure and Doppler broadening for a line frequency of 22 GHz

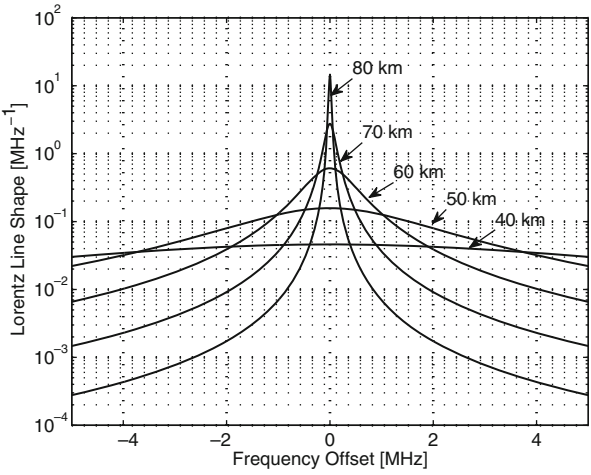

Fig. 5.3 Pressure broadened line shape for different altitudes

the pressure broadening term. In the region where Doppler broadening dominates it is impossible for a ground-based radiometer to distinguish emission from different pressure levels. The combination of Doppler and collisional broadening can be expressed using a Voigt function, in which the purely collisionally broadened lineshape is integrated over all of the possible Doppler shifts. Figure 5.3 illustrates the pressure broadened lineshape for a range of altitudes.

Due to the exponential decrease of atmospheric pressure with altitude and due to the pressure broadening of the line, the measured signal $T_b(\nu, s_0)$ contains information about the vertical distribution of the emitting molecule. Therefore, middle atmospheric water vapour profiles up to approximately 80 km altitude can be determined from the measured spectra. The lower limit of the range is in principle given by the bandwidth and resolution of the spectrometer, but is in practice limited by instrumental artefacts in the atmospheric spectra and by the sharp contrast between the relatively wet troposphere and the dryer stratosphere.

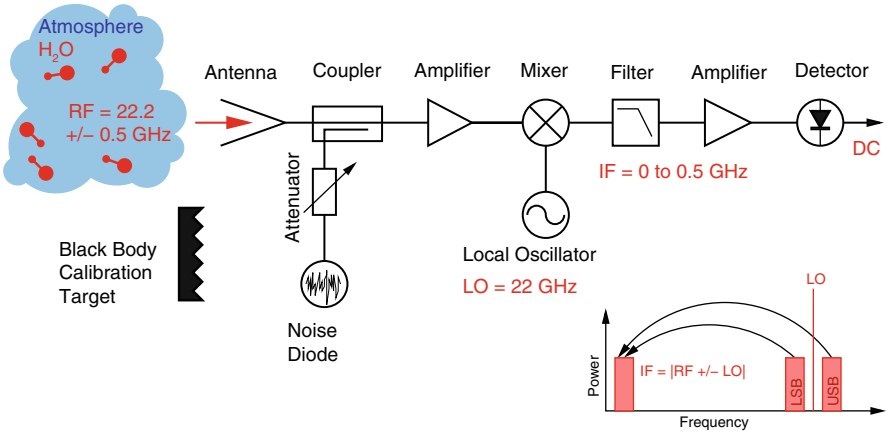

Fig. 5.4 Block-diagram[3] of a microwave radiometer at 22 GHz (What is indicated as detector can in fact be any kind of spectrometer as described in Sect. 5.3.3)

The middle atmospheric signal is attenuated by water vapour in the troposphere, and in fact water vapour in the troposphere dominates the total power in the measurement. The spectrum of water vapour in the troposphere is relatively flat, as compared to that of the middle atmosphere, hence the retrieval of tropospheric attenuation (and hence the troposphere column) does not make use of the spectral shape. In order to calculate the tropospheric attenuation component, the instrument periodically performs total power measurements at a range of angles. This is called a tipping curve measurement (see Sect. 5.3.4).

5.3 Technical Aspects

5.3.1 Receivers

A typical microwave radiometer operates as a heterodyne receiver where the incoming signal from the atmosphere or from calibration standards at microwave frequencies is down converted to an intermediate frequency where the signal can be amplified accordingly before spectral detection takes place. The detecting devices are designed in such a way as to produce outputs proportional to input power. A block-diagram of such a receiver is given in Fig. 5.4.

Generally a single sideband filter is placed in front of the mixer, since otherwise signals which are located symmetrically around the electronically stabilized local oscillator frequency will be mapped onto each other. For instruments operating at 22 GHz this side band suppression is achieved by a wave guide filter, whereas at higher frequencies quasi optical components can be used.

[3] Graphics by A. Murk, IAP

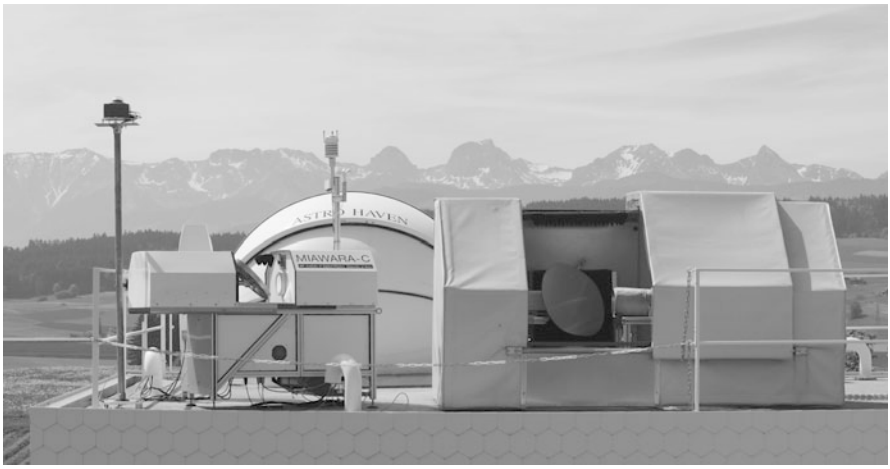

Fig. 5.5 Two water vapour radiometers side by side. Clearly visible is the rotatable mirror that guides radiation from the sky and from calibration loads towards the circular opening of the horn antennas located to the right of the mirror. (Photo courtesy of M.Canavero, IAP)

Some instruments are cooled to cryogenic temperatures to obtain higher sensitivity whereas others are operated at room temperature. The latter are less sensitive, but the reduced maintenance demands can be of importance for monitoring purposes, particularly from remote sites.

An uncooled radiometer is shown in Fig. 5.5. The instrument receives radiation from the atmosphere or from calibration targets via a rotatable mirror and the receiving horn antenna. Normally radiation from the atmosphere is detected at an elevation angle of approx. 20–30°. Thus a measurement near the stratopause is actually measuring an air volume displaced horizontally by 100–150 km from the instrument. In most cases middle atmospheric water vapour does not vary significantly over such distances except near the polar vortex.

5.3.2 Optics

The primary optical part of a microwave radiometer is the antenna which guides the incoming radiation into a waveguide which feeds the incoming signal to the electronic part of the receiver. Some radiometers use small horn antennas that have a wide antenna pattern which then is brought down to a narrow beam by a focusing mirror. While this approach may make a system more compact it also may introduce problems by generating cross polarization and higher side-lobes. Sidelobes could pick up unwanted signals from directions that differ from the actual observing direction. In general it is desirable that the antenna pattern be as narrow as possible. The difference in detected brightness temperature between an ideal pencil beam and a Gaussian beam with finite beamwidth increases in a non-linear way for lower

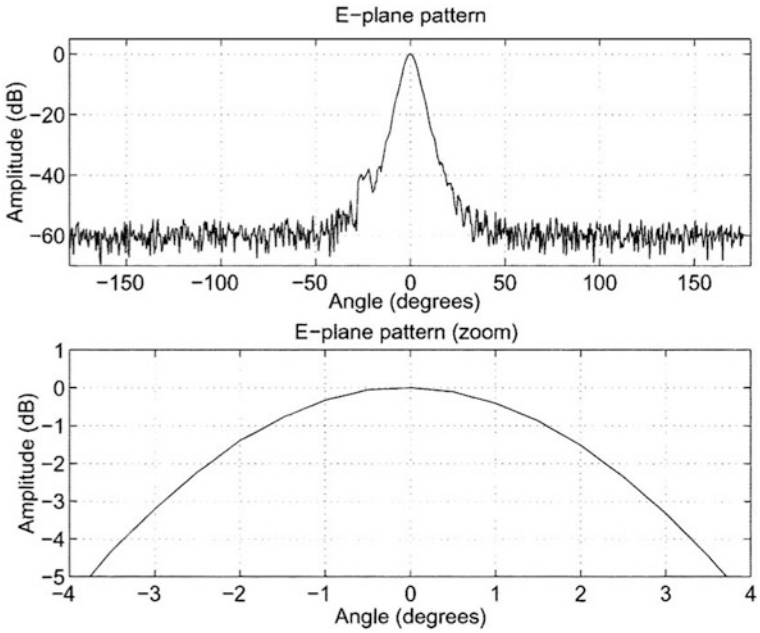

Fig. 5.6 Antenna pattern of a water vapour radiometer

observation elevation angles. It turns out that a half-power beam width of approx. 6° is acceptable in most cases provided that sidelobe levels are kept low. If the antenna pattern is significantly wider the upper and the lower part of the beam see very different parts of the atmosphere.

Antenna patterns have to be measured in detail and they have to be taken into account in the radiative transfer modeling used in the retrieval process of water vapour profiles from the measured spectra. An example of a typical radiation pattern is given in Fig. 5.6.

A limiting instrumental factor of every microwave radiometer are the multiple reflections of microwave radiation within the system and with external structures due to non-ideal matching conditions. Every interface in the optics and within the transmission lines inside the instrument may cause reflections due to a dielectric mismatch. Such reflections can produce a wavy periodic structure that is superimposed on the atmospheric spectrum. This non-atmospheric spectrum is called instrumental baseline and is a characteristic of every instrument. Under severe conditions this effect can corrupt the whole measurement and make it useless. Utmost care must be taken to minimize such baseline effects.

Standing waves from such reflections can be cancelled to some extent by a periodic change of the optical pathlength. For this purpose, the distance between the mirror and the feedhorn of microwave radiometers is varied (e.g. by an axial movement of the mirror), either by a continuous sinusoidal or linear modulation, or averaging together cycles taken in positions separated by 1/4 of the observing wavelength.

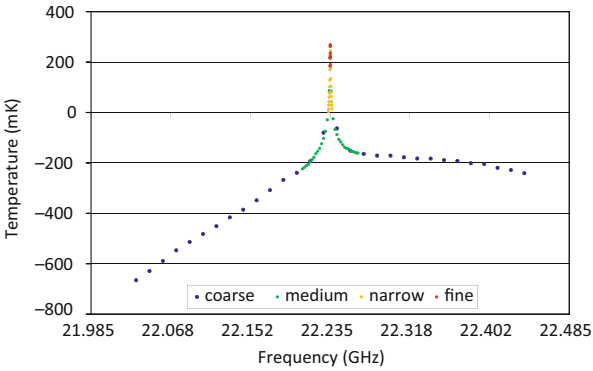

Fig. 5.7 Measured water vapour spectrum at 22.235 GHz obtained with a classical filterbank (Each *dot* represents the measurement at some specific filter center frequency)

5.3.3 Spectrometers

The radio signal with a bandwidth of typically from tens to a few hundred MHz must be spectrally analyzed in order to get the spectral line information. Spectral analysis is performed with a spectrometer. Different types of spectrometers exist for analyzing the signal and are described in more detail below. The main parameters that characterize the spectrometer are overall bandwidth and spectral resolution, linearity in frequency and intensity, and temperature stability. The spectral resolution defines the upper altitude range to which a water vapour profile may be retrieved whereas the overall bandwidth is a measure of the lower boundary in the atmosphere to which information about the distribution can be obtained.

5.3.3.1 Filterbanks with Discrete Elements

In conventional filterbanks the incoming signal is split up in a number of channels with filters of individual bandwidths. Filters covering the central part of the spectrum are generally narrower, typically a few tens of kHz, whereas the ones at the spectral line wing are broader, a few MHz. Such filterbanks are very reliable but are limited to only a few hundred (and usually far fewer) individual filters for practical reasons. Baseline structures are often difficult to fit because of the coarse resolution of the filters in the line wings. An example of a water vapour spectrum as measured with a classical filterbank is shown in Fig. 5.7.

5.3.3.2 Acousto Optical Spectrometers, AOS

In an acousto optical spectrometer the radio frequency signal is guided through a Bragg cell where it generates a phonon pattern that deviates a laser beam to a diode array. The optical pattern is a measure of the spectral power of the incoming microwave signal. A typical spectrum of water vapour as measured with a AOS is

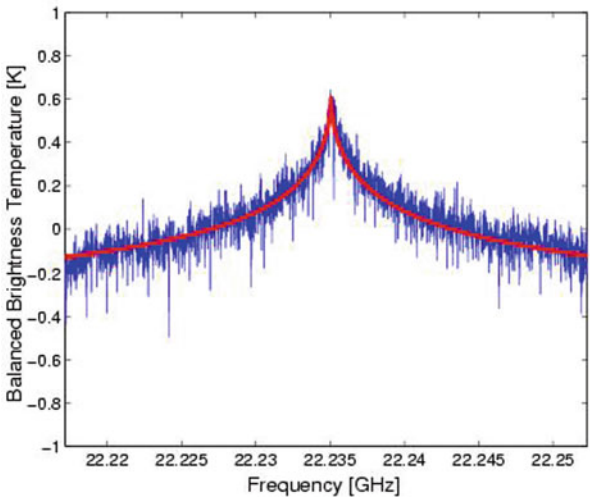

Fig. 5.8 Measured water vapour difference spectrum at 22.235 GHz with an AOS with a fitted line superposed

shown in Fig. 5.8. The measurement provides a bandwidth of typically 1,000 MHz with a frequency resolution of approx. 1 MHz.

5.3.3.3 Chirp Transform Spectrometers, CTS

A powerful way of applying a chirp filter to spectrum analysis is suggested by analogy with the use of chirp waveforms in pulse-compression radar. A chirp waveform is mixed with (i.e. multiplied by) the signal so that each Fourier component is converted into a chirp of the same frequency/time slope but with a starting frequency fixed by that of the original component. The mixed output is processed in a chirp filter of matched slope which correlates, or pulse-compresses, the constituent chirps. The linear correspondence between frequency and time in this system means that frequency differences between the original Fourier components translate to time displacements between their eventual time-compressed outputs, (Hartogh and Hartmann 1990). Such spectrometers have been successfully used for mesospheric investigations.

5.3.3.4 Digital FFT Spectrometers

An FFT spectrometer consists of two parts. First an analog to digital converter samples the electric field of the incoming signal at the input (down converted microwave signal) and then the samples are directly processed by a Field Programmable Gate Array (FPGA), a large collection of logical gates which calculates the FFT in real time. The bandwidth of the spectrometer is given by one half of the sampling frequency according to Nyquist's theorem. The frequency resolution is determined by

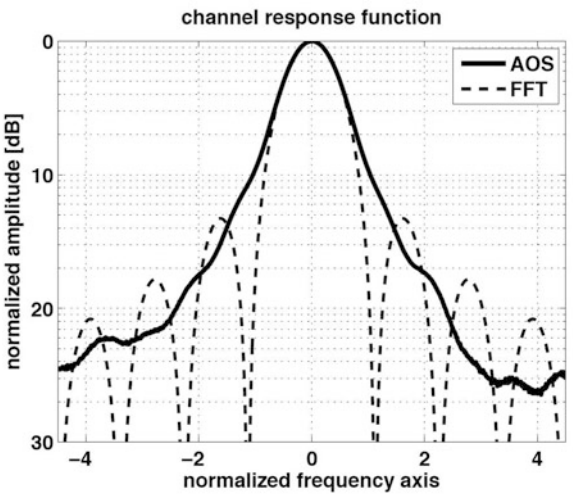

Fig. 5.9 Channel characteristics of an AOS and FFT spectrometer. (The frequency axis is normailzed to the FWHM. The filter characteristics is identical down to about 7 dB, where the AOS channel becomes much broader)

the number of samples taken for one calculation. The 16,000 channels on commercially available FFT spectrometers can be set up to provide spectra as wide as 1 GHz or spectral resolutions as fine as 10 kHz. The channel response function of the FFT spectrometers is the Fast Fourier Transformation of a rectangular window thus equal to the function $(\sin x/x)^2$. A comparison of the channel characteristics of an AOS and an FFT is given in Fig. 5.9. In contrast to acousto-optical spectrometers digital FFT spectrometers offer some advantages. The temperature stability which is critical for AOS is not a concern for FFTs, the costs are significantly lower, and since the FFT does not require a laser the limited life time of a laser is not a concern. Stability seems to be superior for an FFT allowing longer time intervals without calibration. An intercomparison of digital FFT spectrometers and AOS for microwave radiometry of the atmosphere is given in (Müller et al. 2009).

5.3.4 Calibration

5.3.4.1 Total Power Measurements

The purpose of a calibration process is to convert the measurement of the atmospheric radiation from instrument specific units (voltages or counts) into physical units, in this case brightness temperatures. A radiometer is pointed to the atmosphere with an unknown brightness temperature T_b. The corresponding power as generated in the receiver due to the signal entering the antenna is $P_a = kT_aB$. Here k is the Boltzmann constant and B the bandwidth of the receiving element and T_a the antenna temperature.[4] In addition to the signal entering the antenna, the receiver will generate

[4] For an extended object the two temperatures T_a and T_b are the same

noise that is characterized by a noise power $P_r = kT_r B$. Here T_r is the overall noise of the receiver. The output voltage of the radiometer is therefore

$$V_a = Gk(T_a + T_r)B \tag{5.4}$$

where G is the overall gain of the radiometer and that is assumed to be constant within a certain time interval.

By calibrating the system, i.e. by pointing it at two well defined noise sources or calibration standards at temperatures T_H (hot load) and T_C (cold load), we can eliminate the dependence on unknown system parameters (T_r and G), and determine the brightness temperature of an unknown object with a temperature T_a that generates the voltage V in the instrument.

This is usually accomplished by using two microwave absorbers, one held at a monitored temperature close to ambient and the other one immersed in liquid nitrogen.

With the calibrated instrument it is possible to determine the brightness temperature of the unknown object, in our case the atmosphere, according to the so called radiometer equation

$$T_a = \frac{T_H - T_C}{V_H - V_C}(V_a - V_C) + T_C \tag{5.5}$$

or what is equivalent

$$T_a = \frac{T_H - T_C}{V_H - V_C}(V_a - V_H) + T_H. \tag{5.6}$$

The temperature of a liquid nitrogen load, $T_{LN_2} = T_C$, depends on two effects: the dependence of the boiling point of liquid nitrogen on pressure, and the reflectivity due to the interface of air-liquid nitrogen. The dependence of the boiling point temperature on pressure is given by the Clausius Clapeyron equation. Taking care of the relevant thermodynamic parameters and values this results in[5]

$$T_{LN_2} = \left(\frac{1}{77.4} - \frac{8.314}{5586}\ln\frac{p}{1013}\right)^{-1} \tag{5.7}$$

where the temperature is in degree Kelvin and pressure in hPa.

Reflectivity on the interface depends on the dielectric constant of liquid nitrogen, ε_{LN_2} and air. From the literature we find values of ε_{LN_2} in the range of 1.44 and 1.54 for the frequency range of approx. 10–20 GHz. This corresponds to a value of the refractive index of $n_{LN_2} = 1.22$. Contributions due to reflectivity only are an issue in case the antenna beam will pick up any reflected radiation from the ambient.

Very often it is not practical to use a liquid nitrogen load as a calibration target for a routine operation. It is also possible to use the sky itself as a cold calibration load (see Sect. 5.3.4.3).

[5] There are some empirical equations that are easier to handle, e.g. $T_{LN_2} = 68.21 + 0.009037 \cdot p(\text{hPa})$

Another approach is to inject noise from a noise diode. This signal is injected right after the antenna (see Fig. 5.4). In this case the antenna temperature is obtained by combining measurements targeting at a reference load, V_{ref} (what actually can be the sky itself, see next section), the reference with adding a signal from the noise diode, $V_{ref_{on}}$, and the antenna, i.e the sky in our case, V_a. This leads to

$$T_a = T_{ref} + T_{ND} \frac{V_a - V_{ref}}{V_{ref_{on}} - V_{ref}} \tag{5.8}$$

where T_{ND} is the effective noise temperature of the noise diode that has to be calibrated occasionally by external means such as with an external liquid nitrogen calibration. However noise diodes are generally stable for years. This makes them especially useful for sites where external calibrations are performed infrequently. In some cases, where long-term stability is especially important, systems employ two noise diodes so that these can be checked against each other for drift.

5.3.4.2 Balancing Measurements

The water vapour line at 22.235 GHz has an amplitude of only a fraction of 1 K. To detect such a weak line it is necessary to minimize receiver gain non linearities that depend on frequency and input power. This can be achieved through a so called balancing calibration.

In this concept the atmospheric signal, V_{line}, (in units of spectrometer output, e.g. volts or ADC counts) containing the information from water vapour is balanced to a reference signal, V_{ref}. This reference signal should have the same intensity as V_{line} to achieve an ideally balanced signal ΔT_b. Making use of Eq. (5.6) we arrive at:

$$\Delta T_b = T b_{line} - T b_{ref} = \frac{T_{\text{hot}} - T_{\text{cold}}}{V_{\text{hot}} - V_{\text{cold}}} (V_{\text{line}} - V_{\text{ref}}). \tag{5.9}$$

In the case where a noise diode is used, we obtain with Eq. 5.8:

$$\Delta T_b = T b_{line} - T b_{ref} = T_{ND} \frac{V_{line} - V_{ref}}{V_{ref_{on}} - V_{ref}}. \tag{5.10}$$

If the reference spectrum was frequency independent, then this spectrum would retain all of the spectral signal from the water vapour line.

The reference signal intensity must be adjustable to account for variations in the atmospheric signal intensity, mostly due to changes in the tropospheric humidity. There are different possibilities to provide an adjustable reference signal to the receiver. The most simple reference is the sky in zenith direction. The line signal, V_{line}, is observed at a low elevation angle ($\approx$15–30°) which leads to a higher intensity than the zenith signal due to a longer pathlength through the atmosphere. In order to balance the zenith signal an additional noise signal needs to be added. This can be achieved by inserting a piece of absorbing material in the reference beam (at 22 GHz 5–10 % of intensity fill factor of the antenna beam) (Thacker et al. 1995); (Forkman

et al. 2003); (Deuber et al. 2004). An alternative method is to let pass the beam through a thin sheet of plexiglass. Plexiglass acts as a grey-body and will add some noise to the sky brightness temperature (Parrish et al.1988).

Most research groups (Forkman et al. 2003); (Thacker et al. 1995) currently use as absorbing material a piece of egg-shaped, ECCOSORB open cell absorber type CV3. This kind of absorber can cause reflections between the receiver antenna and itself (Forkman et al. 2003) and as a consequence standing waves, so-called baselines, may occur. Since the beam is only partially covered by the absorber, it is also most important that the antenna pattern is the same over the whole frequency range over which the instrument is operating. If this is not the case severe distortions can result in the spectrum (De Wachter et al. 2009).

It has to be kept in mind that when using the sky in zenith direction as a reference load then the contribution of the water vapour signal to the reference signal in this set up has to be accounted for in the retrieval process.

5.3.4.3 Sky as Cold Calibration Target

As mentioned above, in order to relate the measured signal to an actual brightness temperature according to Eq. (5.6) resp. Eq. (5.9) two calibration targets are needed, so called hot and cold loads. Instead of using a calibration load immersed in liquid nitrogen it is also possible to use the sky itself as a cold calibration target. This makes a system independent of the availability of liquid nitrogen which is a major advantage for instruments used on a campaign or at a remote place.

When using the sky itself as calibration load, observation of the brightness temperature at an elevation angle of typically 60° is performed. In order to be able to use this signal as a cold calibration load its brightness temperature, $Tb_{cold-sky}$ must be known.

The brightness temperature that is measured by a ground based instrument observing under the elevation angle ϕ can be related to the zenith opacity, τ, of the atmosphere and an effective mean temperature, T_{eff}, according to:

$$T_b(\phi) = T_0 e^{-\tau A_\phi} + T_{eff}(1 - e^{-\tau A_\phi}). \tag{5.11}$$

$T_0 = 2.7\ K$ is the cosmic background, T_{eff} the effective temperature of the troposphere estimated from the surface temperature T_{amb}, ($T_{eff} = 0.69 \cdot (T_{amb} - 273) + 266.3$), (Han and Westwater 2000) and A_ϕ is the so called air mass factor.

The assumption of an isothermal atmosphere is warranted as atmospheric density falls off exponentially with height so that most of the tropospheric absorption and thus emission occurs near the station.

For small zenith angles the air mass factor can be approximated by

$$A_\phi \approx \frac{1}{\sin(\phi)}. \tag{5.12}$$

In operational use a more accurate relation for the airmass factor should be used that better takes into account atmospheric geometry and curvature (see Section about tropospheric correction below).

If the zenith opacity is known then $Tb_{cold-sky}$ can be estimated according to Eq. (5.11). The opacity τ is determined from a tipping curve measurement, as described below, which gives the name to this calibration method.

5.3.4.4 Determination of the Opacity from Tipping Curve Measurements

The atmospheric opacity under a specific elevation angle ϕ could in principle be determined by just one measurement, provided an additional independent hot and cold load is available to determine $T_b(\phi)$. The opacity would be obtained by solving Eq. (5.11) for τ leading to

$$A_\phi \tau = \tau_\phi = \ln\left(\frac{T_{eff} - T_0}{T_{eff} - T_b(\phi)}\right). \tag{5.13}$$

However in the case where the sky itself shall be used as a cold load this is not possible and another approach, called tipping curve has to be used. A tipping curve measurement is a set of at least two measurements $\{V_i\}$ of the sky at different elevation angles $\{20 \leq \phi_i \leq 90\}$.

Two measurements of the sky at different angles, V_1 and V_2, allow to solve for τ by using Eq. (5.6) and a linearized form of Eq. (5.11) leading to

$$\tau = \frac{(T_{hot} - T_0)(V_2 - V_1)}{(T_{eff} - T_0)(U_{hot}(A_{\phi_2} - A_{\phi_1}) + V_2 A_{\phi_1} - V_1 A_{\phi_2})}. \tag{5.14}$$

A more accurate approach as described in (Han and Westwater 2000) uses an iterative method to find τ. Again a set of at least two sky measurements is needed plus a cold load measurement V_{cold} that is also a sky measurement at its own elevation angle, ϕ_{cold}. An initial value for the opacity has to be chosen, τ_0, (e.g. $\tau_0 = 0.3$). From here the brightness temperature of the sky $Tb(\phi_{cold})$ at elevation angle ϕ_{cold} is calculated according to (5.11) with this value for τ_0. With this value of $Tb(\phi_{cold})$ the tipping curve signals $\{V_i\}$ can be calibrated

$$T_{b_i} = (V_i - V_{hot})\frac{T_{hot} - Tb(\phi_{cold})}{V_{hot} - V_{cold}} + T_{hot}. \tag{5.15}$$

The brightness temperatures Tb_i can be mapped to slant opacities solving (5.11) for $A_\phi \tau$:

$$A_{\phi_i} \tau = \tau_{\phi_i} = \ln\left(\frac{T_{eff} - T_0}{T_{eff} - Tb_i}\right) \tag{5.16}$$

It is apparent that the airmass-opacity pairs $\{A_{\phi_i}, \tau_{\phi_i}\}$ should lie on a straight line that crosses the origin. The slope of this line is the zenith opacity, τ. Therefore a linear fit of the $\{A_{\phi_i}, \tau_{\phi_i}\}$ data gives a new value for τ. The initially chosen value for τ is replaced by the new value and the process is repeated until the y-axis-offset of the fit is satisfyingly small. An y-axis-offset of less than $5 \cdot 10^{-3}$ is mostly achieved after two iterations.

5.3.4.5 Tropospheric Correction

The measured difference signal according Eq. (5.9) is not yet the sought-after information from which the middle atmospheric water vapour can be retrieved. It needs to be corrected for the different pathlengths in the atmosphere and the effects of the troposphere and the bar with absorber. After this correction the middle atmospheric signal in the zenith direction T_z^m at tropopause height is obtained.

In order to obtain this value, we first decompose the line signal Tb_{line} into the signal generated in the middle atmosphere, which is attenuated by the troposphere, plus the contribution from the troposphere (Parrish et al. 1988):

$$Tb_{line} = T_z^m \cdot A_{line}^m \cdot e^{-A_{line}^{tr} \cdot \tau_z} + [T_{eff} \cdot (1 - e^{-A_{line}^{tr} \cdot \tau_z})] \tag{5.17}$$

where A_{line}^m and A_{line}^{tr} is the airmass of the line signal for the middle atmospheric and tropospheric layer respectively. They account for the pathlength at the observation angle. The term in brackets is the tropospheric contribution.

Under the same assumption, we can decompose the reference signal Tb_{ref} into T_z^m, corrected for its pathlength in the middle atmosphere by the airmass A_{ref}^m, attenuated by the troposphere and by the bar with absorber, plus the contribution from the troposphere and from the bar with absorber:

$$Tb_{ref} = T_z^m \cdot A_{ref}^m \cdot e^{-A_{ref}^{tr} \cdot \tau_z} \cdot t_d + [T_{eff} \cdot (1 - e^{-A_{line}^{tr} \cdot \tau_z}) \cdot t_d + T_{ref} \cdot (1 - t_d)] \tag{5.18}$$

where A_{ref}^{tr} is the airmass of the tropospheric layer for the reference signal and t_d is the equivalent transmission of the bar with absorber.

If the two signals are in balance, we can assume that the terms in brackets, the tropospheric emission from the line direction, and the tropospheric emission from the reference direction with the absorber contribution, cancel out, leaving us with

$$\Delta T_b = T_{line} - T_{ref} = T_z^m \cdot A_{line}^m \cdot e^{-A_{line}^{tr} \cdot \tau_z} - T_z^m \cdot A_{ref}^m \cdot e^{-A_{ref}^{tr} \cdot \tau_z} \cdot t_d \tag{5.19}$$

Re-arrangement of the terms gives us the sought-for middle atmospheric signal at zenith that will be used in the retrieval process:

$$T_z^m = f_c \cdot (Tb_{line} - Tb_{ref}) = f_c \cdot \Delta T_b \tag{5.20}$$

where

$$f_c = \frac{1}{A_{line}^m \cdot e^{-\tau_z \cdot A_{line}^{tr}} - A_{ref}^m \cdot e^{-\tau_z \cdot A_{ref}^{tr}} \cdot t_d}. \tag{5.21}$$

We define f_c from Eq. (5.21) as the tropospheric correction factor.

The airmass factors for the troposphere A_ϕ^{tr} and the middle atmosphere A_ϕ^m taking into account the sphericity of the Earth are given by

$$A_\phi^{tr} = \frac{\sqrt{(R+h)^2 - R^2 \cos^2 \phi} - R \sin \phi}{h} \tag{5.22}$$

where $R = 6370$ km is the radius of the Earth and h is the thickness of the troposphere, i.e. ≈10 km, resp.

$$A_{\phi}^{m} = \frac{\sqrt{(R+h+H)^2 - R^2\cos^2\phi} - R\sin\phi}{H} - \frac{\sqrt{(R+h)^2 - R^2\cos^2\phi} - R\sin\phi}{H} \tag{5.23}$$

where $H \approx 90$ km.

The equivalent transmission t_d of the absorber is calculated through:

$$t_d = \frac{T_{ref} - Tb_{ref}}{T_{ref} - Tb(\phi_{ref})} \tag{5.24}$$

Tb_{ref} is the calibrated signal at the reference position i.e. at the zenith angle ϕ_{ref}, $Tb(\phi_{ref})$ the atmospheric signal at this angle calculated from Eq. (5.11), and T_{ref} the physical temperature of the microwave absorber.

5.3.4.6 Instrument Pointing

As shown in previous sections measurement are performed under different elevation angles. An accurate knowledge of elevation angle is thus mandatory in order to prevent any systematic errors from a pointing misalignment. There exist different methods that proofed to be successful for the determination of the absolute pointing of the instrument. One is by scanning the sky with the instrument from approximately 60°–120° and finding the minimum brightness temperature corresponding to zenith direction. The other techniques uses the Sun as an external source. The ephemerides of the Sun are well known and therefore it can be used to accurately determine elevation and azimuth of the instrument pointing by scanning a certain range around the elevation of the Sun passing through the antenna beam. These techniques allow to determine the pointing accuracy to better than 0.05°. For details we refer to (Straub et al. 2010). It is also possible to use a laser shining through the feedhorn and checking the reflected signal from a reference mirror.

5.4 Existing Microwave Radiometers for Water Vapour

An overview of existing microwave radiometers for middle atmospheric water vapour that are run on a regular basis is given in Table 5.2. Some of them are operated within NDACC (Network for the Detection of Atmospheric Composition Change), namely: MIAWARA, WVMS-1, WVMS-3 and the instrument at Onsala. Data from these instrument are available from www.NDACC.org.

Table 5.2 Inventory of existing ground-based microwave instruments for the observation of middle-atmospheric water vapour. The spectral resolution, Δf in kHz, refers to the highest resolution at line center and can be larger at the wings. The bandwidth, B in MHz, refers to the measured total bandwidth. For the retrievals a smaller bandwidth might be used

Instrument name	Site	Spectrometer	Δf (kHz)	B (MHz)	T_{rec} (K)	Preamp	Calibration
–	Onsala	Autocorr.	25	20	170	Amb	Hot-cold
MIAWARA	Bern	Digital FFT	61	1000	135	Amb	Hot-cold
MIAWARA–C	Mobile	Digital crosscorr	30	500	–	Amb	Hot-cold
SWARA	Seoul	Digital FFT	61	1000	140	Amb	Hot-cold
WVMS-1	Lauder	Filter bank	200	40	100	Cooled	Noise diode
WVMS-2	Table Mount.	digital FFT	30	500		Amb	Noise diode
WVMS-3	Mauna Loa	Filter bank	50	60	170	Cooled	Noise diode
cWASPAM1	Andoya	CTS	40	10	30	Cooled	Hot-cold
cWASPAM3	Zugspitze	CTS	40	10	30	Cooled	Hot-cold
MIRA5	Zugspitze	FFT	61	800	145	Amb	Hot-cold

5.5 Retrievals

Most currently operating water vapour microwave measurement groups now use a retrieval based upon the Rodgers optimal estimation method, (Rodgers 1976). In simplest terms, the optimal estimation method provides the optimal solution, $\hat{x}$, given an initial estimate of a physical parameter, x_a, an estimate of the error (variance) of this initial estimate, σ_a, a measurement, x_{meas} of the same physical parameter, and an estimate of the error in this measurement, σ_{meas}. For the case of uncorrelated errors, the equation for the optimal solution can be written as:

$$\hat{x} = (x_a/\sigma_a^2 + x_{meas}/\sigma_{meas}^2)/(1/\sigma_a^2 + 1/\sigma_{meas}^2) \tag{5.25}$$

Thus, in regions where the measurement uncertainty is small relative to the a priori uncertainty the retrieval is drawn close to the measured value, while in regions where the measurement uncertainty is large relative to the a priori uncertainty it is drawn to the a priori value.

In the case of microwave remote sensing there is no direct measurement of the physical parameter of interest, namely the H_2O profile. However, the measurement of the spectrum, $\mathbf{y}$, is linked to the H_2O profile $\mathbf{x}$ by the forward model $\mathbf{y} = \mathbf{K} \cdot \mathbf{x}$. Following the notation of (Rodgers 2000) the value of x_{meas} is related to the measured (vector-)parameter $\mathbf{y}$ so that the equation which needs to be solved becomes:

$$\hat{\mathbf{x}} = \mathbf{x_a} + \mathbf{S_a}\mathbf{K}^{\mathrm{T}}(\mathbf{K}\mathbf{S_a}\mathbf{K}^{\mathbf{T}} + \mathbf{S_y})^{-1}(\mathbf{y} - \mathbf{K}\mathbf{x_a}) \quad \text{[Rodgers 1976, Eq. (21)]} \tag{5.26}$$

where $\mathbf{S_a}$ values are now matrices including the uncertainties in $\mathbf{x_a}$ and the correlations between levels and $\mathbf{S_y}$ for the measurement uncertainties correspondingly. One of the most important features of this method is that, given estimates of uncertainties in the a priori and in the measurement it provides estimates of the uncertainty in the retrieval and of the sensitivity of the retrieval to the measurement and to the a priori.

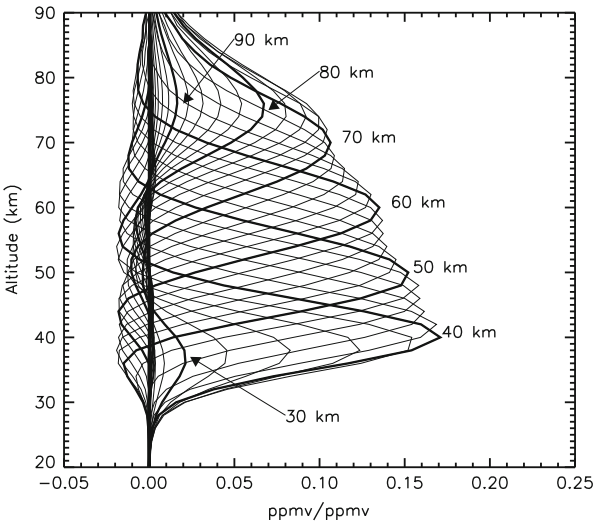

Fig. 5.10 Typical averaging kernels. Each line represents the sensitivity of the retrieval at a given altitude to perturbations over a range of 2 km altitude bins. Lines in bold indicate the sensitivity of the retrieval at the labeled altitude levels

We can now calculate the sensitivity of the retrieved state to the measurement

$$\frac{\partial \hat{\mathbf{x}}}{\partial \mathbf{y}} = \mathbf{D_y} = (\mathbf{S_a^{-1}} + \mathbf{K^T S_y^{-1} K})^{-1} \mathbf{K^T S_y^{-1}} \tag{5.27}$$

and finally the averaging kernel, $\mathbf{A}$, that describes the sensitivity of the retrieved state to changes in the true state

$$\frac{\partial \hat{\mathbf{x}}}{\partial \mathbf{x}} = \frac{\partial \hat{\mathbf{x}}}{\partial \mathbf{y}} \frac{\partial \mathbf{y}}{\partial \mathbf{x}} = \mathbf{D_y K} = \mathbf{A}. \tag{5.28}$$

The averaging kernel is a key quantity for the characterization of the retrieved profile. It describes how the retrieval smoothes the true state and how sensitive it is to the a priori profile.

Figure 5.10 shows the averaging kernels based on a 1-week integration for the WVMS instrument at Mauna Loa, Hawaii. It accounts for the limited vertical resolution and, at least as important, for the sensitivity of the retrieval that decreases towards higher and lower altitudes. It depends amongst others on the measurement covariance matrix, $\mathbf{S_y}$. To account for potential variations in the signal to noise ratio that is given by $\mathbf{S_y}$ the averaging kernels are calculated for each retrieved profile.

To derive the profile as it would be measured by the radiometer system, $\hat{\mathbf{x}}_{\mathbf{ref}}$, from a correlative reference profile, $\mathbf{x_{ref}}$, the averaging kernels are considered as follows:

$$\hat{\mathbf{x}}_{\mathrm{ref}} = \mathbf{x_a} + \mathbf{A}(\mathbf{x_{ref}} - \mathbf{x_a}). \tag{5.29}$$

This equation should be used whenever comparing ground-based microwave measurements to another set of retrievals $\mathbf{x_{ref}}$ with much better vertical resolution. Note that because this method ignores the limitations in vertical resolution in satellites instruments it can result in over-smoothing of these measurements. (Rodgers

and Connor 2003) provide a methodology for assessing uncertainties in satellite measurements.

While the WVMS instrument for which the averaging kernels are shown in Fig. 5.10 has a spectral bandwidth of 30 MHz, and thus could in principle measure at altitudes below 40 km, error terms which represent uncertainties in the baseline error have been included to reduce the sensitivity of the retrievals below this altitude.

Measurements have been possible down to lower altitudes using AOS systems which provide a much larger number of measurement channels, but these systems have historically not been used on long-term deployments due to the difficulty of maintaining stability of an AOS. Recent technological improvements in digital FFT spectrometers have made it possible to field affordable instruments with long-term stability that may make it possible to retrieve water vapour into the lower stratosphere over monthly and longer timescales, but at this point this capability has yet to be proved.

Retrievals in the lower stratosphere are difficult not only because of the need to determine very accurately instrumental baseline artifacts, but because of the very large and highly variable water vapour mixing ratios in the troposphere relative to those in the stratosphere. Because of the much higher amount of water vapour in the troposphere relative to the stratosphere, combined with the 10–15 km FWHM vertical resolution of a water vapour radiometer retrieval, a small fractional error in water vapour in the upper troposphere can cause a significant error in the retrieved water vapour well into the lower stratosphere. In the absence of another source of data to constrain upper tropospheric water vapour values, the retrievals may provide more information about water vapour in the upper troposphere than in the lower stratosphere. The exact altitude where the retrieved water vapour becomes insensitive to variations in the upper troposphere is dependent upon the details of the tropospheric water vapour, but some dependence on the tropospheric profile may be present up to 40 km.

Because the signal being measured is a function not only of the number of water vapour molecules but also of the atmospheric temperature, the retrievals require an estimate of the temperature. Temperatures profiles have been taken from both climatological sources (e.g. MSISE, WACCM) and global forecast models (e.g. ECMWF, NCEP). In many cases combinations of such sources are used, with forecast models being used for stratospheric temperatures and climatological models being used in the mesosphere. Global forecast models are now being extended into the mesosphere, so it may soon be possible to use these models to provide temperature information for microwave radiometer retrievals. Alternatively, since August 2004 the Aura-MLS (MLS = Microwave Limb Sounder) satellite instrument has provided daily global temperature measurements which can be used to provide background temperatures for ground-based microwave retrievals. Replacing the MSISE climatology in the upper stratosphere and mesosphere with temperatures measured by Aura-MLS reduced the variance of the difference between Aura-MLS and the water vapour retrievals from ground based radiometers. Another option is to use a climatology based on the Aura-MLS measurements. This is the approach taken in (Haefele et al. 2009).

The optimal estimation technique allows to investigate in detail different error contributions to the overall error in the retrieved (estimated) profile. Figure 5.11

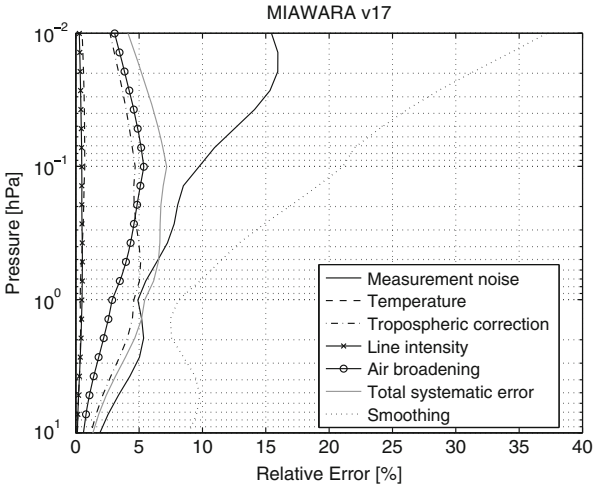

Fig. 5.11 Errors in the retrieved profile resulting from the measurement noise and uncertainties in the temperature profile, the troposphere correction factor, the line intensity and the air broadening parameter. The total systematic error includes all sources except for the measurement noise and the smoothing error (Haefele 2009)

gives an illustration of the error contributions as a function of altitude for the specific retrieval of one of the water vapour radiometers.

5.6 Validation

Microwave radiometry provides the only means of measuring water vapour in the upper stratosphere and mesosphere from the ground. Thus, validation of these measurements must necessarily come from other microwave instruments or from satellite instruments. There have been only a very limited number of direct microwave instrument intercomparisons. (Nedoluha et al. 1999) intercompared two microwave radiometers at Table Mountain, California, in 1995 over a several month period. The instruments showed a systematic bias of 5 %, and tracked variations in water vapour quite consistently with a standard deviation of 5 % between the instruments for weekly measurements.

Direct intercomparison campaigns of middle-atmospheric microwave instruments are of somewhat limited value. They are generally conducted over limited time periods, and thus give no indication of the long-term stability of an instrument. Because water vapour in the middle atmosphere changes only slowly, it is difficult to validate the ability of an instrument to track significant changes without a validation period that extends over several months.

Since upper stratospheric and mesospheric water vapour generally changes relatively slowly both spatially and temporally, validation against satellite sensors does not require extremely close coincidences and has proved to be very successful. Studies during the NASA Atmospheric Laboratory for Application and Science (ATLAS) missions from 1992 to 1994 allowed for comparison between ground-based WVMS instruments and as many as four satellite instruments making water vapour measurements, and even relatively sparse solar occultation measurements from the

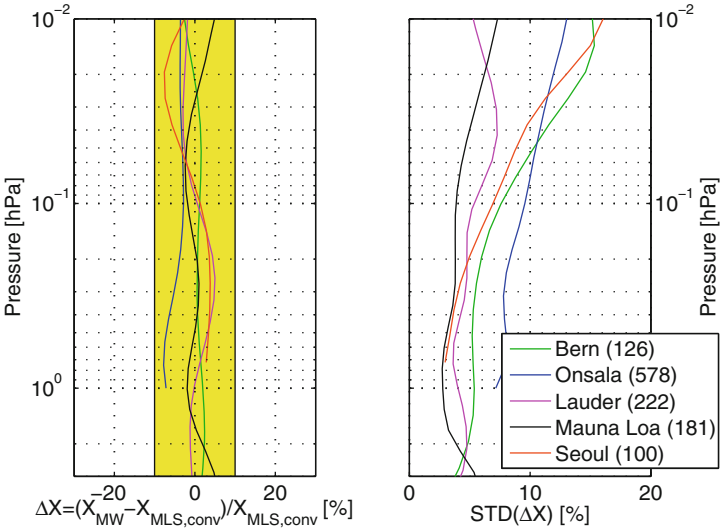

Fig. 5.12 Mean value (*left panel*) and standard deviation (*right panel*) of the relative differences between the volume mixing ratios, X, as retrieved by the ground based radiometers and the reference data (Aura-MLS). The numbers in brackets in the legend indicate the number of available profile pairs at each site

ATMOS-ATLAS instrument provided sufficient coincidences to allow for cross-validation. These comparisons, shown in detail in (Nedoluha et al. 1997) found that retrieved water vapour values from all instruments agreed to better than 1 ppmv for most altitudes from 40–80 km.

Since 2004 the Aura-MLS (Microwave Limb Sounder) instrument has provided water vapour profiles which are sufficiently spatially coincident to usefully compare with a ground-based microwave system on a nearly daily basis. (Nedoluha et al. 2007) compared instruments at Mauna Loa, Hawaii and Lauder, New Zealand to these Aura-MLS measurements and found that the standard deviation of the difference between the weekly WVMS retrievals and coincident MLS retrievals is 0.2 ppmv at Mauna Loa and 0.3–0.4 ppmv at Lauder. The Aura-MLS and WVMS profiles at Mauna Loa show particularly good interannual agreement, including a clear QBO signature.

A study by (Haefele et al. 2009) compares four instruments from the Network for the Detection of Atmospheric Composition Change (NDACC) with measurements from Aura-MLS. The study includes the WVMS instruments at Mauna Loa and Lauder, as well as the MIAWARA instrument in Bern, and an instrument at Onsala, Sweden, that is operated by the Chalmers University of Technology. The retrievals all used the same spectral parameters, and a climatological set of temperature profiles calculated from the Aura-MLS temperature measurements. The values of the retrieved water vapour volume mixing ratios, X, were found to be within 10 % of the Aura-MLS values at all altitudes as illustrated in Fig. 5.12. The ground based instruments do not differ significantly from each other and, in this sense, the five ground based instruments build a consistent network.

The study found good correlation between Aura-MLS and ground-based microwave measurements of seasonal variations in the mesosphere. Most of the instruments performed well at 1 hPa, but instruments in regions with lower tropospheric optical depths clearly performed better than those for which the tropospheric opacity was large. Only the instrument at Mauna Loa (the site with the lowest tropospheric opacity) showed a seasonal variation similar to the Aura-MLS retrievals at 3 hPa (40 km).

5.7 Conclusion

One of the most important current contributions of ground-based microwave measurements is for the validation of long-term change in water vapour as inferred from satellite measurements. From 1991–2005 the HALOE satellite experiment provided global water vapour measurements. These HALOE measurements showed a significant increase in water vapour from 1991–1996, an increase which was confirmed by comparisons with WVMS instruments at Lauder, New Zealand, and Table Mountain, California (Nedoluha et al. 1999). The WVMS instruments at Lauder and at Mauna Loa, Hawaii subsequently confirmed the absence of any significant trend in water vapour in the upper stratosphere and mesosphere from 1996–2002 (Nedoluha et al. 2003). This stability in water vapour since the mid-1990s continues through 2008, and the good interannual agreement between Aura-MLS and WVMS measurements since 2004 hopefully indicates that any future changes in water vapour will be correctly detected. Another strength of ground based water vapour radiometry is the high sensitivity in the upper stratosphere and the mesosphere allowing investigations of atmospheric processes at these altitudes.

References

S.A. Buehler, P. Eriksson, T. Kuhn, A. von Engeln, C. Verdes, Arts, the atmospheric radiative transfer simulator. J. Quant. Spectrosc. Radiat. Transfer **91**, 65–93 (2005)

E. De Wachter, A. Murk, C. Straub., A. Ka, S. Haefele, J.J. Oh, N. Kaempfer, Effects of resonances in corrugated horn antennas for a 22 GHz balancing radiometer. IEEE Geosci. Remote. Sens. Lett. **6**, 3–7 (2009). doi:10.1109/LGRS.2008.2005851

B. Deuber, N. Kämpfer, D. Feist, A new 22 GHz Radiometer for middle atmospheric water vapour profile measurements. IEEE Trans. Geosci. Remote Sens. **42**, 974–984 (2004)

P.C. Eriksson, C. Jimenez, S.A. Buehler, Qpack, a general tool for instrument simulation and retrieval work. J. Quant. Spectrosc. Radiat. Transfer. **91**, 47–64 (2005)

P. Forkman, P. Eriksson, A. Winnberg, The 22 GHz radio-aeronomy reciver at Onsala Space Observatory. J. Quant. Spectrosc. Radiat. Transfer. **77**, 23–42 (2003). doi:10.1016/S0022-4073(02)00073-0

A. Haefele, Measurements of tropospheric, stratospheric and mesospheric water vapor by ground based microwave spectro-radiometry, Ph.D. thesis, Philosophisch-Naturwissenschaftliche Fakultät, Universität Bern, Bern, Switzerland, 2009

A. Haefele, E.D. Wachter, K. Hocke, N. Kämpfer, G.E. Nedoluha, R.M. Gomez, P. Eriksson, P. Forkman, A. Lambert, M.J. Schwartz, Validation of ground based microwave radiometers at 22 GHz for stratospheric and mesospheric water vapor. J. of Geophys. Res. **114**(D23) 305 (2009). doi:10.1029/2009JD011997

Y. Han, E.R. Westwater, Analysis and improvement of tipping calibration for ground-based microwave radiometers. IEEE Trans. Geosci. Remote Sens. **38**, 1260–1276 (2000)

P. Hartogh, G. Hartmann, A high-resolution chirp transform spectrometer for microwave measurements. Meas. Sci. Technol. **1**, 592–595 (1990)

M.A. Janssen, (ed.), *Atmospheric remote sensing by microwave radiometry*, (Wiley Series in Remote Sensing, John Wiley & Sons, Inc., NY, ISBN 0-471-62891-3, 1993)

H. Liebe, MPM—An atmospheric millimeter-wave propagation model. Int. J. Infrared Millime. Waves. **10**, 631–650 (1989)

C. Müller, A. Murk, C. Monstein, N. Kämpfer 2009, Intercomparison of digital fast fourier transform and accousto optical spectrometers for microwave radiometry of the atmosphere. IEEE Trans. Geosci. Remote Sens. **47**, 2233–2239 (2009). doi:10.1109/TGRS.2009.2013695

G.E. Nedoluha, R.M. Bevilacqua, R.M. Gomez, W.B. Waltman, B.C. Hicks, D.L. Thacker, J. Russell III, M. Abrams, H.C. Pumphrey, B.J. Connor, A comparative study of mesospheric 73 water vapor measurements from the ground-based water vapor millimeter-wave spectrometer and space-based instruments. J. Geophys. Res. **102**, 16647–16661 (1997)

G.E. Nedoluha, R.M. Bevilacqua, R.M. Gomez, D.E. Siskind, B.C. Hicks, J. Russell III, B.J. Connor, Increases in middle atmospheric water vapor as observed by the halogen occultation experiment and the ground-based water vapor millimeter-wave spectrometer from 1991 to 1997. J. Geophys. Res. **103**, 3531–3543 (1998)

G.E. Nedoluha, R.M. Bevilacqua, R.M. Gomez, B.C. Hicks, J.M. Russell III, Measurements of middle atmospheric water vapor from low and midlatitude in the Northern Hemisphere, 1995–1998. J. Geophys. Res. 104, (1999)

G.E. Nedoluha, R.M. Bevilacqua, R.M. Gomez, B.C. Hicks, J.M. Russell III, B.J. Connor, An evaluation of trends in middle atmospheric water vapor as measured by HALOE, WVMS, and POAM. J. Geophys. Res. **108**, 4391 (2003). doi:10.1029/2002JD003332

G.E. Nedoluha, R.M. Gomez, B.C. Hicks, R.M. Bevilacqua, J.M. Russell III, B.J. Connor, A. Lambert, A comparison of middle atmospheric water vapor as measured by WVMS, EOS-MLS, and HALOE. J. Geophys. Res. **112**(D24S39) (2007). doi:10.1029/2007JD008757

A. Parrish, R.L. deZafra, R.M. Solomon, J. Barret, A ground-based technique for millimeter wave spectrosopic observations of stratospheric trace consistuents. Radio Sci. **23**, 106–118 (1988)

H. Pickett, R.L. Poynter, E.A. Cohen, M.L. Delitsky, J.C. Pearson, H.S.P. Müller, Submillimeter, millimeter and microwave spectral line catalog. J. Quant. Spectrosc. Radiat. Transfer. **60**, 883–890 (1998)

C. Rodgers, Retrieval of atmospheric temperature and composition from remote measurements of thermal radiation. Rev. Geophys. Space Phys. **14**, 609–624 (1976)

C. Rodgers, B.J. Connor, Intercomparison of remote sounding instruments. J. Geophys. Res. **108**, 4116 (2003). doi:10.1029/2002JD002299

C.D. Rodgers, *Inverse methods for atmospheric sounding: Theory and practice*, vol. 2, (Series on atmospheric, oceanic and planetary physics, World scientific, 2000)

C. Straub, A. Murk, N. Kämpfer, MIAWARA-C, a new ground based water vapor radiometer for measurement campaigns. Atmos. Meas. Tech. Discuss. **3**, 2389–2432 (2010). doi:10.5194/amtd-3-2389-2010

D.L. Thacker, R.M. Bevilacqua, W.B. Waltman, T.A. Pauls, R.M. Gomez, G.E. Nedoluha, R.R. Schwartz, Ground-based sensing of water vapor in the stratosphere and mesosphere. IEEE Trans. Instrum Meas. **44**, 355–359 (1995)

Chapter 6
Fourier Transform Infrared Spectrometry

Matthias Schneider, Philippe Demoulin, Ralf Sussmann and Justus Notholt

6.1 The Measurement

Most atmospheric molecules interact with electromagnetic radiation in the infrared spectral region, which makes infrared remote sensing an important tool for atmospheric research. Figure 6.1 shows the two main components of a ground-based FTIR experiment: a precise solar tracker (left photograph) that captures the direct solar light beam and couples it into a high resolution Fourier Transform Spectrometer (FTS; right photograph). An FTS is based on a Michelson interferometer (see scheme of Fig. 6.2), consisting of a beamsplitter that divides the incoming radiance into 2 beams. One of them is reflected by a fixed mirror or retroreflector while the other one is sent to a moving mirror, causing a variable optical path difference. At the beamsplitter again, they recombine and interfere according to their wavelength and optical path difference. A detector measures the intensity of the interfering beam in dependence on the optical path difference. The optical path difference is measured with a monochromatic laser. The observed intensity fluctuations are an interferogram which is converted by a Fourier Transformation into a spectrum. A very detailed description of Fourier transform spectrometry can be found in the textbook of Davis, Abrams and Brault (Davis et al. 2001).

For operational measurements the ground-based FTIR spectra are measured with a typical resolution of about 0.005 cm^{-1} (i.e. maximum optical path difference, OPD, of 180 cm), which corresponds to a resolution $\lambda/\Delta\lambda$ at 1000 cm^{-1} of approx. 2×10^5.

M. Schneider (✉)
Karlsruhe Institute of Technology (KIT), IMK-ASF Hermann-von-Helmholtz Platz 1, 76344 Leopoldshafen, Germany
e-mail: matthias.schneider@kit.edu

P. Demoulin
Institut d'Astrophysique et de Géophysique Liège, Belgium

R. Sussmann
Karlsruhe Institute of Technology (KIT), IMK-IFU, Garmisch, Germany

J. Notholt
Institut für Umweltphysik, University of Bremen, Bremen, Germany

N. Kämpfer (ed.), *Monitoring Atmospheric Water Vapour,*
ISSI Scientific Report Series 10,
DOI 10.1007/978-1-4614-3909-7_6, © Springer Science+Business Media, LLC 2013

Fig. 6.1 The ground-based FTIR experiment at the Izaña Atmospheric Research Centre. The solar tracker (*left* photograph) is situated at the top of the experimental housing. It collects the direct solar beam and reflects it into the housing of the FTIR spectrometer (*right* photograph). Then the solar beam is coupled into the spectrometer (circular light spot on the *right* part of the photograph)

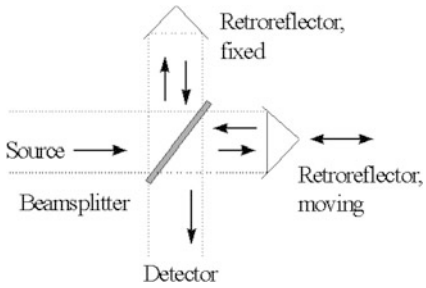

Fig. 6.2 Scheme of an FTIR interferometer

Recording of one spectrum requires between one to a few tens of minutes, depending on the quality required. A constant solar input is also needed to obtain a correct spectrum, so observations can only be performed for clear sky conditions. Infrared solar absorption spectra contain information of more than 25 atmospheric constituents that are important for climate, ozone layer, and tropospheric oxidation processes. They all can be detected simultaneously making the FTIR technique a very powerful tool of atmospheric research. The upper panel of Fig. 6.3 shows a mid-infrared spectra at $700\,cm^{-1}$–$1350\,cm^{-1}$ (7.4–14.3 µm). The bottom panel gives an impression of the huge amount of information present in these high resolution spectra. It shows two spectral microwindows cut out of the whole spectrum with the wavenumber scale being stretched by a factor of 200. Individual rotational-vibrational lines of different absorbers (O_3, H_2O, HDO, CH_4, etc.) are discernable. It is important to mention that all these individual rotational-vibrational lines of these small molecules are spectrally resolved: the shape of the measured absorption lines is dominated by pressure broadening with typical broadening coefficients of 0.02–$0.10\,cm^{-1}atm^{-1}$ (i.e. a typical HWHM of 0.02–$0.10\,cm^{-1}$ at surface level). We observe, for example, that the H_2O and HDO signatures are broader than the N_2O and CH_4 signatures which in turn are broader than the O_3 signatures. Most H_2O and HDO molecules are in the lower troposphere at a pressure above 700 hPa so their lines are rather broad. N_2O and CH_4

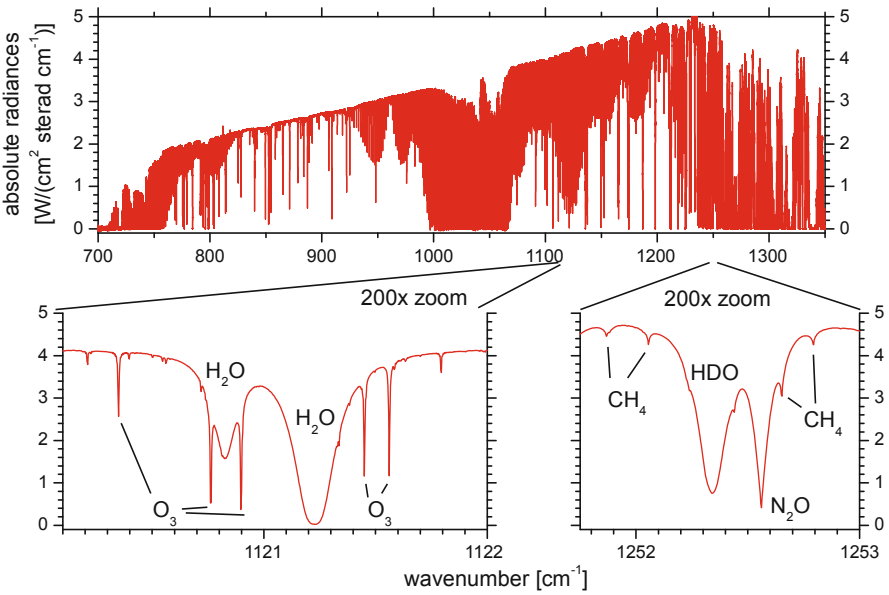

Fig. 6.3 *Upper* panel Spectrum measured by the Fourier Transform Spectrometer with the 700–1350 cm^{-1} filter setting. *Bottom* panels Zoomed spectral microwindows containing H_2O and HDO signatures

mixing ratios are almost constant throughout the troposphere and their signatures are narrower. The O_3 molecules are predominantly in the stratosphere at a pressure below 100 hPa, and their signatures are quite narrow if compared to N_2O, CH_4, and water vapour signatures. Obviously, the high resolution FTIR spectra disclose not only the total column amount of the absorber but also contain some information about its vertical distribution.

Figure 6.3 shows absolute radiances, which are achieved by an absolute calibration of the experiment applying a cavity blackbody. Such an absolute calibration is necessary for detecting atmospheric constituents with broadband signatures (e.g. polar stratospheric clouds), when applying broad spectral microwindows, for measuring lunar absorption spectra or atmospheric emissions. For standard trace gas retrievals (which apply relatively narrow spectral windows and use solar absorption spectra) an absolute calibration is dispensable, since high resolution solar absorption spectra are self-calibrating in the sense that the absorption signature is referenced to the surrounding continuum. This is an important advantage of a ground-based FTIR experiment. The FTS's instrumental line shape is determined on a regular basis by low pressure gas cell measurements (Hase et al. 1999), which assures high quality measurements.

Table 6.1 lists the sites with the ground-based FTIR experiments of the NDACC (Network for Detection of Atmospheric Composition Change) and the TCCON (Total Carbon Column Observing Network). There are around 25 globally distributed high-quality NDACC FTIR experiments. The NDACC measurements cover the spectral range between 700 and 4,500 cm^{-1} (corresponding to 2.2–14.3 µm), whereby the

Table 6.1 Table of ground-based FTIR sites. The intention of this list is to give the reader an overview of existing ground-based FTIR instruments operated within NDACC and TCCON. We do not claim that it considers all ground-based FTIR instruments. Furthermore, it does not collect the sites for which ground-based FTIR water vapour data are already available, but for all these sites water vapour profiles can in principle be generated. For a list of the PI of the different experiments please visit the NDACC IRWG and TCCON webpages (http://www.acd.ucar.edu/irwg/, http://www.tccon.caltech.edu/)

Site	Latitude	Longitude	Altitude	FTS model	First spectra
Eureka, Canada	80.05° N	86.42° W	610 m	125HR	1993
Ny Ålesund, Spitsbergen	78.92° N	11.93° E	15 m	120HR	1992
Thule, Greenland	76.53° N	68.74° W	225 m	120M	1999
Kiruna, Sweden	67.84° N	20.41° E	419 m	125HR	1996
Sodankyla, Finland	67.37° N	26.63° E	179 m	125HR	2009
Poker Flat, Alaska, USA	65.11° N	147.42° W	610 m	120HR	1999
Harestua, Norway	60.21° N	10.75° E	596 m	125M	1994
Bremen, Germany	53.10° N	8.85° E	27 m	125HR	2001
Bialystok, Poland	53.20° N	22.75° E	150 m	125HR	2009
Orleans, France	47.97° N	2.10° E	130 m	125HR	2009
Garmisch, Germany	47.48° N	11.06° E	734 m	125HR	2004
Zugspitze, Germany	47.42° N	10.98° E	2,964 m	125HR	1995
Jungfraujoch, Switzerland	46.55° N	7.98° E	3,580 m	Custom and 120HR	1984
Park Falls, WI, USA	45.95° N	90.27° W	442 m	125HR	2004
Moshiri, Japan	44.4° N	142.3° E	200 m	120HR	1996
Toronto, Canada	43.66° N	79.40° W	174 m	DA8	2001
Rikubetsu, Japan	43.5° N	143.8° E	370 m	120M	1995
Mt. Barcroft, CA, USA	37.58° N	118.24° W	3,800 m	Custom	1998
Lamont, OK, USA	36.61° N	97.49° W	320 m	125HR	2008
Tsukuba, Japan	36.05° N	140.13° E	31 m	120HR	1998
Kitt Peak, AZ, USA	31.96° N	111.59° W	2,120 m	Custom	1978
Izaña, Tenerife, Spain	28.30° N	16.48° W	2367 m	125HR	1999
Mauna Loa, Hawaii	19.54° N	155.58° W	3,459 m	120HR	1991
Addis Abeba, Ethiopia	9.04° N	38.77° E	2,324 m	125M	2009
Ascension Island, United Kingdom	7.92° S	14.42° W	54 m	125HR	2010
Darwin, Australia	12.42° S	130.89° E	30 m	125HR	2005
Reunion Island, France	20.8° S	55.5° E	10 m	120M	2002
Wollongong, Australia	34.45° S	150.88° E	30 m	125HR	1994
Lauder, New Zealand	45.04° S	169.68° E	370 m	120HR	1990
Syowa Base, Antarctica	69.01° S	39.59° E	21 m	120M	2007
Arrival Heights, Antarctica	77.82° S	166.65° E	250 m	120M	1996

spectra are recorded in 6 different filter regions (the top panel of Fig. 6.3 shows one of them). The TCCON is currently constituting. It consist of ground-based FTIR spectrometers, recording direct solar spectra in the near-infrared spectral region (4,000 and 10,000 cm^{-1}, corresponding to 2.5–1 µm) with a typical resolution of 0.02 cm^{-1}. Although, the TCCON focuses on the observation of accurate and precise column-averaged abundances of CO_2, CH_4, N_2O, HF, CO, H_2O (the objective is a precision of a few permil), the spectral resolution of the TCCON measurements is sufficient for retrieving some profile information for tropospheric trace gases including water vapour. The TCCON increases the number of sites with the potential to retrieve water vapour profiles (Schneider et al. 2010b).

6.2 The Inversion Algorithm

The basic equation for analysing solar absorption spectra is Lambert Beer's law:

$$I(\lambda) = I_{\text{sun}}(\lambda) \exp\left(-\int_{\text{TOA}}^{\text{Obs.}} \sigma_x(\lambda, s(T, p))x(s)ds\right) \tag{6.1}$$

Here $I(\lambda)$ is the measured intensity at wavelength λ, I_{sun} the solar intensity, $\sigma_x(\lambda, s)$ is the absorption cross section and $x(s)$ the concentration of an absorber x at location s. The integration is performed along the path of the direct sunlight (from the top of the atmosphere (TOA) to the observer). The cross section σ_x depends on temperature and pressure. At high wavenumbers (above 1000 cm^{-1}) atmospheric emission can be neglected as compared to the direct solar radiances. However, at lower wavenumbers it should be considered, by adding an atmospheric emission correction term to Eq. 6.1. The FTIR retrieval algorithms (SFIT2 and PROFFIT; Pougatchev et al. 1996; Hase et al. 2004) apply precise line-by-line radiative transfer models to simulate the measured spectra. To simulate how the solar light passes through the different layers the radiative transfer models include ray tracing modules (e.g. Hase and Höpfner 1999). For the purpose of numerical handling it is necessary to discretise the atmosphere (discretised into different altitude levels between the Earth surface and the top of the atmosphere). The optical depth for a layer between two adjacent altitude levels is calculated by performing the integration of $\int \sigma_x(\lambda, s(T, p))x(s)ds$ between the two altitude levels. Summing up the optical depths of all layers yields the spectrum as simulated at the observer's site.

By means of the discretisation we can describe the vertical distribution of the absorber in the form of a vector $\vec{x}(z)$ (concentration of absorber x at level z). If we also describe the simulated spectrum, $I(\lambda)$, in the form of a vector $\vec{y}$ containing the radiances in the different spectral bins, we can define a straight forward relation, F, that relates the solar absorption spectrum ($\vec{y}$) to the vertical distribution of the absorber ($\vec{x}$), to parameters describing the atmospheric state ($\vec{p}_{\text{atmos}}$), and to parameters describing the measurement system ($\vec{p}_{\text{exp}}$):

$$\vec{y} = \vec{F}(\vec{x}, \vec{p}_{\text{atmos}}, \vec{p}_{\text{exp}}) \tag{6.2}$$

Here $\vec{F}$ is a vector valued function which simulates the atmospheric radiative transfer and the characteristics of the measurement system (spectral resolution, instrumental line shape, etc.).

The derivatives $\partial y/\partial x$ determine the changes in the spectral fluxes $\vec{y}$ for changes in the vertical distribution of the absorber $\vec{x}$. These derivatives are described in a Jacobian matrix $\mathbf{K}$:

$$\partial\vec{y} = \mathbf{K}\partial\vec{x} \tag{6.3}$$

Inverting $\mathbf{K}$ of Eq. 6.3 would allow an iterative calculation of the sought variables $\vec{x}$, but generally the problem is under-determined, i.e. the columns of $\mathbf{K}$ are not

linearly independent and there are many solutions that are in acceptable agreement with the measurement. However, the measurement introduces new information and consequently reduces the a-priori possible solutions. An optimal estimation (OE) approach combines the measurement information with the a-priori assumption about the vertical distribution of the absorber to produce the most probable distribution of the absorber for the given measurement. The solution is the maximum value of a conditional probability density function (pdf), which is the product of two pdfs: a first, describing the measurement noise (measurement noise covariance $\mathbf{S}_\epsilon$), and a second, describing the a-priori known probabilities of the absorbers' distribution (typical distribution $\vec{x}_a$ and covariance $\mathbf{S_a}$ of the distribution). The maximum value of the conditional pdf is reached at the minimum of its negative logarithm:

$$[\vec{y} - \vec{F}(\vec{x})]^T \mathbf{S}_\epsilon{}^{-1} [\vec{y} - \vec{F}(\vec{x})] + [\vec{x} - \vec{x}_a]^T \mathbf{S_a}^{-1} [\vec{x} - \vec{x}_a] \tag{6.4}$$

Often a detailed climatology of the target absorber is not available, and the a-priori covariances are implemented semi-empirically, e.g. assumption of a variability of the a-priori profile for each level and a correlation length which is defined as an exponentially decaying intercorrelation between the levels. Another approach is to replace the inverse of the a-priori covariance matrix ($\mathbf{S_a}^{-1}$) by an ad-hoc constraint matrix (Tikhonov-Phillips formalism), which allows a constraint of the variability and the first, second, etc. derivatives of the profile with respect to height of each level.

Atmospheric radiative transport is in general a non-linear problem (only for very weak absorbers it is quasi linear), and the Gauss-Newton method is applied to minimise Eq. 6.4 iteratively. The solution for the $(i + 1)th$ iteration is Rodgers (2000):

$$\vec{x}_{i+1} = \vec{x}_a + \mathbf{S_a K_i}^T (\mathbf{K_i S_a K_i}^T + \mathbf{S}_\epsilon)^{-1} [\vec{y} - \vec{F}(\vec{x}_i) + \mathbf{K_i}(\vec{x}_i - \vec{x}_a)] \tag{6.5}$$

When evaluating Eq. 6.4 one assumes Gaussian statistics for the measurement noise and the a-priori covariance. While Gaussian statistics is a reasonable assumption for the measurement noise it is not necessarily valid for the distribution of the absorber. In case of a log-normal distribution of the absorber we still can apply the formalism of Eqs. 6.4 and 6.5 in a strictly correct sense by transforming the absorber's amounts to a logarithmic scale: if $\vec{x}$ is log-normally distributed, ln $(\vec{x})$ is normally distributed and Eqs. 6.4 and 6.5 remain valid.

As aforementioned the measurement alone does not allow for the determination of a unique solution, but it introduces information into the system. This measurement information updates the a-priori covariance $\mathbf{S_a}$ of the absorbers' distribution to $(\mathbf{K}^T \mathbf{S}_\epsilon{}^{-1} \mathbf{K} + \mathbf{S_a}^{-1})^{-1}$ (the a-posteriori covariance of the absorbers' distribution). An important component of the retrieved solution is the averaging kernel matrix $\mathbf{A}$:

$$\mathbf{A} = (\mathbf{K}^T \mathbf{S}_\epsilon{}^{-1} \mathbf{K} + \mathbf{S_a}^{-1})^{-1} \mathbf{K}^T \mathbf{S}_\epsilon{}^{-1} \mathbf{K} \tag{6.6}$$

The averaging kernel matrix $\mathbf{A}$ describes the smoothing of the real vertical distribution of the absorber by the FTIR measurement process. It relates the real variability

$(\vec{x} - \vec{x_a})$ to the measured variability $(\vec{\hat{x}} - \vec{x_a})$:

$$(\vec{\hat{x}} - \vec{x_a}) = \hat{\mathbf{A}}(\vec{x} - \vec{x_a}) \tag{6.7}$$

In addition, the trace of **A** quantifies the amount of information introduced by the measurement. It can be interpreted in terms of degrees of freedom of the measurement.

6.3 Current State of Water Vapour Retrievals

At some NDACC stations ground-based FTIR experiments have been operated for more than 20 years. These measurements allow a unique investigation of long-term trends of different atmospheric trace gases (e.g. HNO_3, HCl, $ClONO_2$, O_3, which were essential for studying stratospheric ozone chemistry (e.g. Rinsland et al. 2003). Recently the FTIR community has increased its efforts of observing the troposphere and the tropopause region. At these altitudes water vapour is a dominating trace gas for radiative forcing. However, the retrieval of atmospheric water vapour profiles from ground-based FTIR measurements is a difficult task due to its large vertical gradient and large temporal variability, and standard retrieval methods are often not suited. The development of water vapour retrievals has recently made substantial progress, but still no common water vapour retrieval method is applied at all NDACC sites. First water vapour profiles measured by a ground-based FTIR experiment were reported by the IMK-ASF FTIR group (Hase et al. 2004) (IMK-ASF: Institute for Meteorology and Climate Research – Trace Constituents in the Stratosphere and Tropopause Region, Karlsruhe). At IMK-ASF the water vapour algorithm has been continuously improved since 2005 (for a review see Schneider 2009b). These efforts made it possible to monitor tropospheric H_2O profiles (including upper tropospheric amounts) and HDO/H_2O ratio profiles by ground-based FTIR experiments. The IMK-ASF FTIR data are validated continuously by extensive intercomparisons to coinciding experiments (e.g. comparison with several hundred coincident RS80/RS92 radiosonde measurements; Schneider et al. 2006a and Schneider et al. 2010a).

The ground-based FTIR group of IUP Bremen (Institute of Environmental Physics of the University of Bremen) applies a retrieval method similar to Schneider et al. (2006a), but uses the water vapour signatures at 3268.6–3273.0 cm^{-1} and 3299.6–3305.0 cm^{-1}, corresponding to 3.02–3.05 µm. In Palm et al. (2010) they show comparisons between total water vapour column amounts measured by ground-based FTIR, ground-based microwave radiometer, and by the satellite sensors SCIAMACHY and AMSU-B. Furthermore, they present the first nighttime FTIR water vapour total column amount measurements (determined from lunar absorption measurements).

At IMK-IFU (Institute for Meteorology and Climate Research – Atmospheric Environmental Research, Garmisch) a retrieval method for integrated water vapour has been developed. It applies absorptions signatures at 11.7–11.9 µm and is based

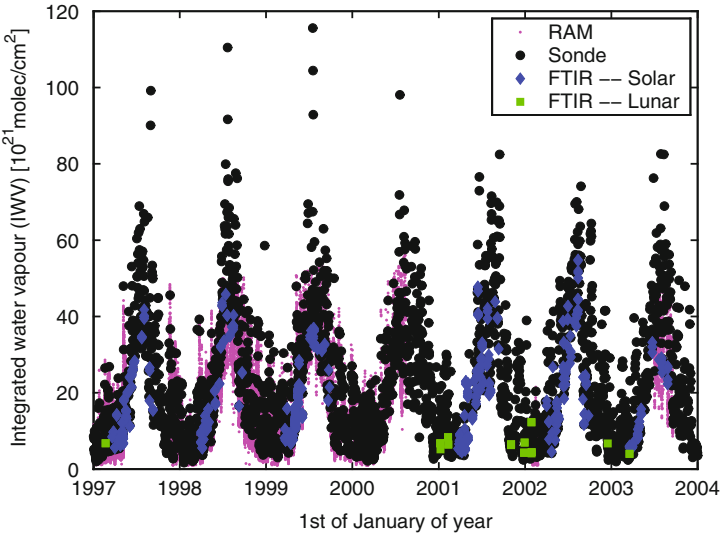

Fig. 6.4 Measurements of the total water vapour column by a ground-based FTIR experiment in Ny Ålesund, Spitsbergen. For comparison water vapour columns derived from sonde measurements and microwave radiometry (RAM) are plotted

on a Tikhonov approach set in a way that the resulting FTIR-sonde correlation shows a slope that equals 1.00. The retrieval has been applied to harmonized Zugspitze, Jungfaujoch and Garmisch time series and trend analysis (Sussmann et al. 2009).

6.4 Water Vapour Total Column Amounts

Although the focus of this book is on water vapour profiles we briefly present results of FTIR water vapour column amount measurements, since the FTIR technique provides this data with very good precision (Schneider et al. 2006a; Palm et al. 2010; Sussmann et al. 2009; Schneider et al. 2010a). A time series of columnar water vapour measurements performed at the AWIPEV station in Ny Ålesund on the Spitsbergen archipelago (79°N) is plotted in Fig. 6.4. The columnar measurements have been compared to several other remote sensing instruments and radio-sondes (Palm et al. 2010), showing the high quality of H_2O measurements. At Ny Ålesund measurements are performed since 1990. From 1990 to 1995 a spectrometer Bruker 120 M was used. In 1995 a Bruker 125 HR replaced the old 120 M spectrometer. Measurements are performed from about mid of March until the end of September each year in solar absorption geometry. This is about the time, the sun is sufficiently high to allow measurements of good quality at the high arctic station of Ny Ålesund. During polar night, measurements in lunar absorption geometry are performed when weather conditions permit (Notholt et al. 1995). Measurements in lunar absorption geometry have a much lower SNR due to the low intensity of the moon compared to

Table 6.2 Results of intercomparison of FTIR, Cimel, and RS92: Number of coincidences (N), mean difference and standard deviation of difference in %

	FTIR (%)	Cimel (%)
Cimel	$N = 677$ (-25.4 ± 12.7)	
RS92	$N = 195$ (-3.33 ± 15.5)	$N = 747$ $(+22.6 \pm 22.7)$

the sun. The information content is lower, and the random noise on the results amounts up to 20 %. All retrievals of the spectra measured by the FTIR instruments were performed using the SFIT2 retrieval code (Pougatchev et al. 1996; Hase et al. 2004) which has been extended using a log-normal state vector for the retrieval (Schneider et al. 2006a). The spectra using moon absorption spectroscopy are corrected for the atmospheric emission by a full radiative calculation.

Table 6.2 resumes some of the results of the continuously performed intercomparisons at the Izaña observatory (Schneider et al. 2010a). It gives mean and standard deviation for the differences between FTIR, Cimel (sunphotometer), and radiosonde Vaisala RS92. The values are given in percent and allow the conclusion that the FTIR provides very precise total column amounts (most of the scatter between FTIR and Cimel and FTIR and radiosonde RS92 is caused by the noise in the Cimel and RS92 data).

Figure 6.5 shows a scatter plot for the 25 FTIR-sonde coincidences that have been obtained during the (19 Aug 2002–17 Nov 2002) AIRS validation campaign with FTIR measurements at the Zugspitze and 180 radiosondes launched at nearby Garmisch. The 25 IWV data from the Garmisch (Vaisala RS80) radiosondes (x-axis in Fig. 6.5) were each obtained from integration of one "Tobin-sonde" VMR profile above the Zugspitze altitude. This profile was derived from a pair of soundings according to the "best-estimate of the state of the atmosphere" principle (Tobin et al. 2006). That is, a first sonde was launched 1 h before t_{op} and a second sonde 5 min before t_{op}. The best estimated humidity profile for the overpass time $VMR_{Tobin(z,t_{op})}$ was then constructed via inter- /extrapolation of the two soundings according to the relation

$$VMR_{Tobin}(z, t_{op}) = VMR_{Sonde}(z, t_0) + (dVMR(z)/dt)(t_{op} - t_0), \tag{6.8}$$

where for t_0 one uses the time of either of the two sondes at a level z as a starting point. For more details about this intercomparison study and the applied FTIR retrieval please refer to Sussmann et al. (2009).

Two FTIR instruments are operated side-by-side at the Jungfraujoch, which allows for studying the variability of atmospheric water vapour. Different criteria for the temporal coincidence between the two FTIR measurements were applied. Figure 6.6 shows how the scatter between the two FTIR instruments depends on the applied coincidence criteria (interval (Δt)): starting at $\Delta t = 3.75$ min, a widening of Δt leads to a secular increase of the scatter, i.e., atmospheric variability dominates the scatter and indicates the high variability of atmospheric water vapour fields even on time scales as small as several minutes.

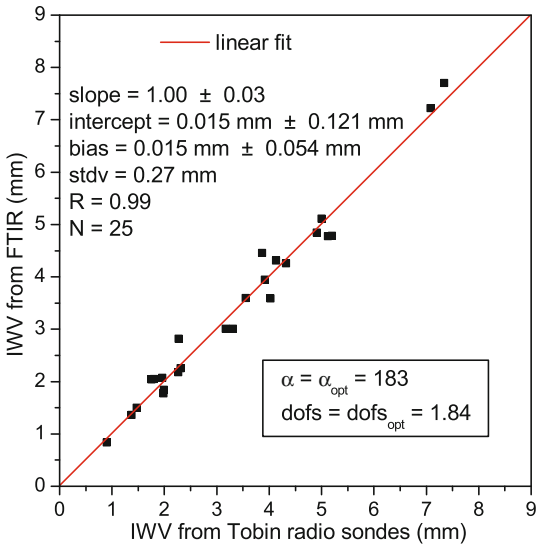

Fig. 6.5 FTIR-sonde scatter plot for columnar water vapour as measured at Zugspitze (Sussmann et al. 2009)

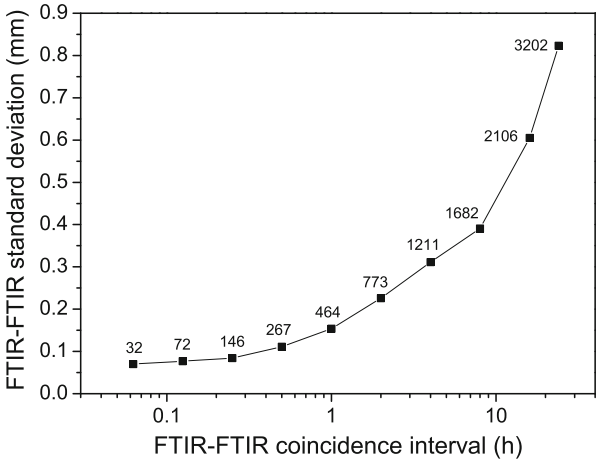

Fig. 6.6 Standard deviation of the IWV differences deduced from coincident measurements with two FTIR systems at the Jungfraujoch between 1995–2001 as a function of the temporal coincidence criterion (numbers give the amount of coincidences, adopted from Sussmann et al. 2009)

6.5 Profiles from Lower to Upper Troposphere

In addition to precise total column amounts the IMK-ASF algorithm (PROFFIT, Hase et al. 2004) allows for a retrieval of vertical profiles with a resolution of 2 km in the lower troposphere, 4 km in the middle troposphere, and 6 km in the upper troposphere. Furthermore, it produces profiles of HDO/H_2O ratio. For details about the analysis method please refer to Schneider and Hase (2009b). In the following we document the quality of the FTIR water vapour profile data as produced by the IMK-ASF algorithm. We do this taking the measurements performed at the Izaña

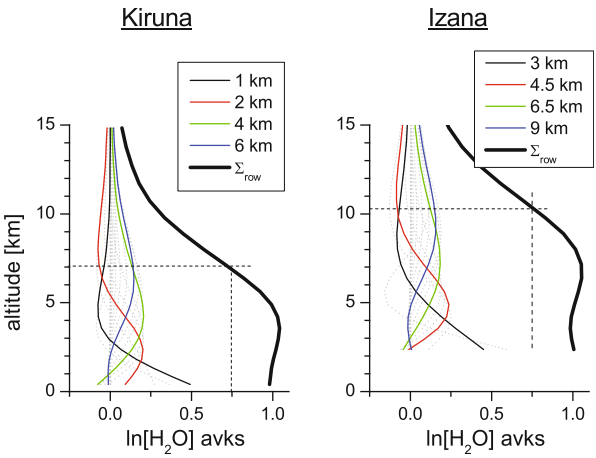

Fig. 6.7 Typical averaging kernels for ground-based FTIR remote sensing of water vapour. *Left* panel for Kiruna (Sweden, 420 m a.s.l.) and *right* panel for Izaña (Tenerife, 2,370 m a.s.l.). Kernels for selected altitudes are highlighted by different colors (see legend). The total sensitivity ($\sum_{\text{row}}$) is depicted as thick black line

Atmospheric Research Centre (Spanish acronym: CIAI) as an example. At CIAI the FTIR water vapour total column amounts and profiles are continuously validated by radiosonde measurements (Schneider et al. 2006a, 2010a). When comparing remotely-sensed vertical distribution profiles with in-situ measured profiles it is important to account for the inherent vertical resolution of the remotely-sensed data. The FTIR system only detects coarse structures of the vertical water vapour distributions (vertical resolution of 3 km in the lower and 8–10 km in the upper troposphere, given as FWHM of the kernels). This is illustrated in Fig. 6.7, which shows typical averaging kernels for ground-based FTIR remote sensing of water vapour for two very distinct sites. The right panel shows the averaging kernels for Izaña (a subtropical high altitude side) and the left panel for Kiruna (a high latitude low altitude site). The red, green, and blue curves highlight the kernels for the altitudes representing the lower, middle, and upper troposphere. The thick black line represents the sum along the rows of the averaging kernel matrix. It yields the total sensitivity of the FTIR technique. We observe a satisfactory sensitivity up to the upper troposphere ($\sum_{\text{row}}$ above 0.75).

According to Eq. 6.7 we can simulate how the radiosonde would measure these coarse structures. Therefore we smooth the vertically highly-resolved radiosonde data with the FTIR averaging kernels $\mathbf{A}$:

$$\hat{x}_{\text{RS92}} = \hat{\mathbf{A}}(x_{\text{RS92}} - x_a) + x_a \tag{6.9}$$

The result is a radiosonde profile ($\hat{x}_{\text{RS92}}$) with the same vertical resolution as the FTIR profile. We compare Izaña FTIR and Vaisala RS92 measurements, correcting the temperature and radiation dependence of the RS92 sensor as suggested by Vömel et al. (2007). Then their precision is estimated to be better than 20 % for altitudes below 15 km.

Figure 6.8 presents comparisons for almost 100 coincidences between June 2005 and February 2007 applying three different FTIR retrieval set ups. It well documents the difficulties encountered when inverting water vapour profiles from ground-based

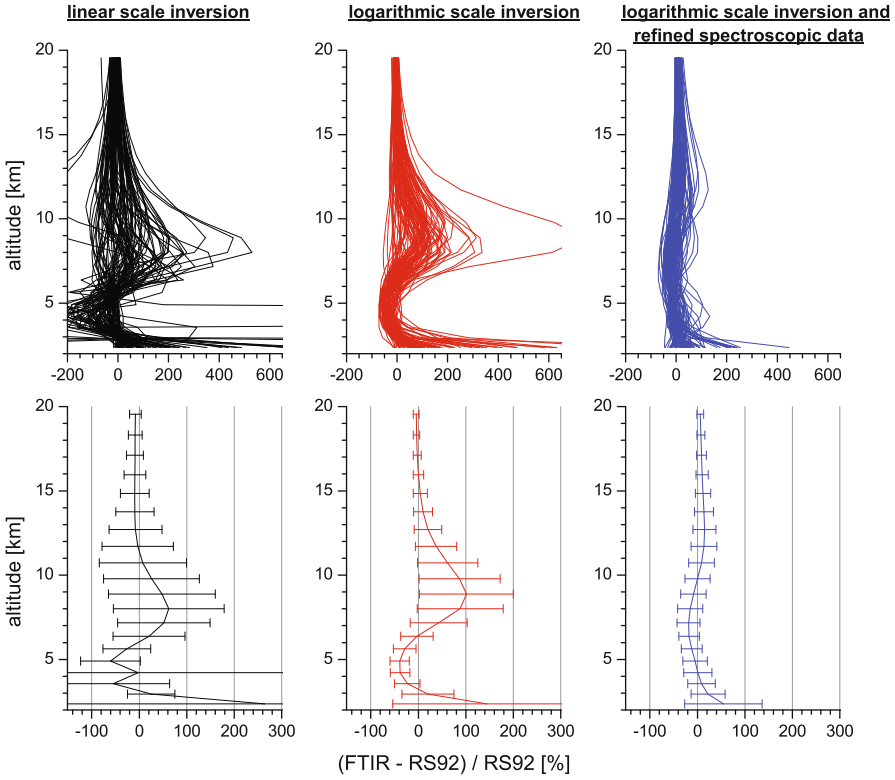

Fig. 6.8 Difference between smoothed Vaisala RS92 profiles and FTIR profiles retrieved by a linear scale inversion algorithm (*black* curves, *left* panels), by a logarithmic scale inversion algorithm (*red* curves, *central* panels), and by a logarithmic scale inversion algorithm and the application of the refined spectroscopic data of Schneider and Hase (2009a)(*blue* curves, *right* panels). *Upper* panels: Individual differences for 93 coincidences (between June 2005 and February 2007); *Bottom* panels: statistics of the differences (mean and standard deviation)

FTIR measurements as well as the progress made in recent years. For all three algorithms we apply the same set of H_2O and HDO lines of different strength. The left panels (black curves) shows a validation of the FTIR profiles inverted on a linear scale. We observe large differences between the RS92 and FTIR profiles. Occasionally, the FTIR algorithm produces negative mixing ratios, i.e. (FTIR − RS92)/RS92 $<$ −100 %. Water vapour is highly variable and a normal distribution is not a proper assumption. Under these conditions Eq. 6.4 does not represent the negative logarithm of a conditional probability density function and its minimum is not the statistically optimal solution (Schneider et al. 2006a; Worden et al. 2006). If we transform the water vapour mixing ratios on a logarithmic scale Eq. 6.4 remains valid, since on a logarithmic scale water vapour is almost normally distributed. Then minimising Eq. 6.4 produces a statistically optimal solution. Inversions performed on a logarithmic scale lead to a significantly reduced scatter between the FTIR and RS92 profiles (see central panels, red curves).

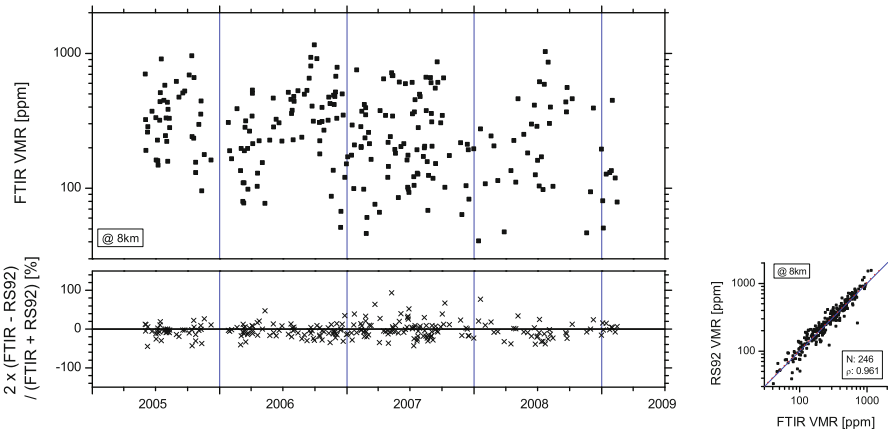

Fig. 6.9 Comparison of CIAI's RS92 and FTIR upper tropospheric (altitude of 8 km) water vapour mixing ratios, whereby the RS92 mixing ratios have been smoothed according to Eq. (6.9). There are 246 coincidences between 2005 and 2009. Left panels: time series for FTIR/RS92 coincidences, *top* panel FTIR mixing ratios given in parts per million, *bottom* panel: difference between FTIR and RS92 ($\frac{2\times(\text{FTIR}-\text{RS92})}{(\text{FTIR}+\text{RS92})}$); *Right* panel correlation plot for all coincident measurements between 2005 and 2009

The logarithmic scale inversion is important progress, but we still observe differences between FTIR and RS92 profiles which are far beyond the expected uncertainties of both experiments. One problem are inconsistencies when simulating the spectral signatures of a large number of different lines with different parameters (different strength, different pressure broadening coefficients, etc.). Applying lines with different strength and pressure broadening coefficients theoretically increases the degrees of freedom of the measurement, but in practise there is no realistic water vapour profile that brings measured and simulated signatures of all the different lines to a reasonable agreement. Schneider and Hase (2009a) analyses this problem in great detail. They empirically adjusted the spectroscopic parameters and applied a non-Voigt line shape model instead of a Voigt line shape. This refinement of the spectroscopic data produces a much better agreement between the simulated and measured spectra and at the same time improves the quality of the inverted water vapour profiles. This is documented in the right panels of Fig. 6.8 (blue curves), which show a comparison of RS92 with FTIR profiles obtained by applying the spectroscopic parameterisation of Schneider and Hase (2009a).

Figure 6.9 compares the upper tropospheric water vapour as measured by the FTIR and Vaisala RS92 radiosondes at CIAI between 2005 and 2008. It depicts data for which FTIR and RS92 measurements were made within 1 h (about 250 data points). The upper panel shows the water vapour mixing ratios as measured by the FTIR and the bottom panel the relative differences between FTIR and RS92. The mixing ratios vary between almost two orders of magnitude (0.004 and 0.12 %), nevertheless, the agreement between both techniques is very satisfactorily: the mean difference and scatter is (-1.8 ± 20.6) %. Vömel et al. (2007) estimated a precision of 10–20 % for

Table 6.3 Summary of vertical resolution (given as FWHM of the kernels) and random uncertainty

	Vertical resolution	Random uncertainty [%]
Lower troposphere	3 km	10–20
Middle troposphere	5 km	10–20
Upper troposphere	8–10 km	10–20

the RS92 mixing ratios, which suggests that a large part of the 20 % scatter between FTIR and RS92 is due to RS92 uncertainties. We conclude that the FTIR technique allows a precise measurement of upper tropospheric water vapour amounts. For more details about CIAI's water vapour profile intercomparison studies please refer to Schneider et al. (2010a). Table 6.3 shows a summary of the characteristics of the water vapour profiles that can be measured by ground-based FTIR systems.

6.6 Tropospheric HDO/H_2O Ratio Profiles

In the middle and upper troposphere water vapour is particularly effective as greenhouse gas (e.g. Held and Soden 2000). It is worrisome that the current understanding of upper tropospheric water vapour transport pathways is incomplete. A continuous observation of the isotopic composition of tropospheric water vapour can help to constrain the atmospheric water vapour transport pathways. In this context the ground-based FTIR technique offers unique possibilities, since it can distinguish different water vapour isotopologues. However, given the small variability of the isotopologue ratios only very precise data are useful. The observation of tropospheric isotopologue ratio profiles by remote sensing techniques is only possible when sophisticated inversion algorithms are applied (it requires additional constraints between the HDO and H_2O sections of the atmospheric state vector, Schneider et al. (2006b; Worden 2006).

The vertical resolution of the FTIR δD profiles is indicated by the averaging kernels shown in Fig. 6.10 for typical Kiruna and Izaña measurements. The δD value is the relative difference of the actual HDO/H_2O ratio to the standard HDO/H_2O ratio called SMOW (Standard Mean Ocean Water) in permil ($\delta D = 1000 \times (\frac{[HDO]/[H_2O]}{SMOW} - 1)$). The vertical resolution of the δD profiles is coarser if compared to the vertical resolution of the H_2O profiles (Fig. 6.7): about 3 km in the lower troposphere and 10 km in the middle/upper troposphere (given as FWHM of the kernels). Figure 6.10 also depicts the sum of all averaging kernels (thick solid black line), which indicates the total sensitivity of the FTIR system with respect to δD. Schneider et al. (2010c) shows that the long-term FTIR tropospheric δD profile measurements are well suited to investigate how water is transported through the atmosphere.

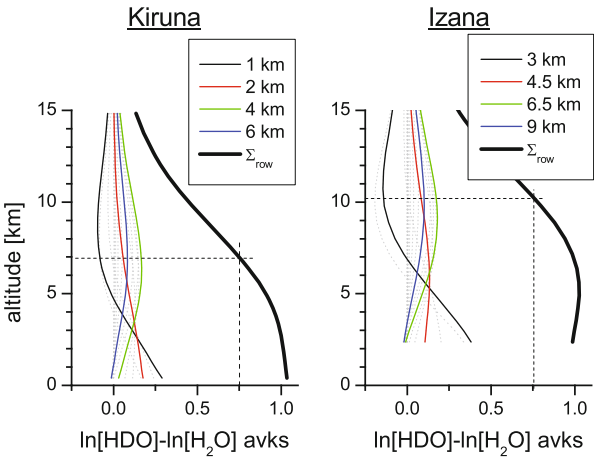

Fig. 6.10 Typical FTIR Averaging kernels for δD (expressed as $\ln[\mathrm{HDO}] - \ln[\mathrm{H_2O}]$). *Left* panels for Kiruna and *right* panels for Izaña. Kernels for selected altitudes are highlighted by different colors (see legend). The total sensitivity ($\sum_{\mathrm{row}}$) is depicted as *thick black line*

6.7 Potential

Water vapour total column amounts and profiles can be calculated for all the FTIR stations as listed in Table 6.1. Moreover, for the stations where mid-infrared spectra are recorded, δD profiles can be produced. As can be seen for some sites high quality measurements date back to the early 90s. Reprocessing the historic FTIR measurements applying the new retrieval developments would provide a consistent long-term time series with a wide geographical coverage. Since the raw data (solar absorption spectra) are stored improved products can be generated in the future whenever the analysis methods improve. Currently, uncertainties in the spectroscopic line parameterisation is one of the most important uncertainties concerning the remote sensing of atmospheric water vapour. We expect that this situation, and consequently the quality of the remote sensed water vapour products, will improve during the next years.

The FTIR technique offers a unique possibility to monitor tropospheric δD profiles. Determining δD profiles time series at different FTIR NDACC stations will allow an investigation of the transport of water vapour into the middle/upper troposphere, a key issue of current climate research.

Acknowledgments The authors wish to thank Tobias Borsdorf, Frank Hase, and Mathias Palm for fruitful discussions and contributions to this manuscript.

References

S.P. Davis, M.C. Abrams, J.W. Brault, *Fourier transform spectrometry*. Academic Press (2001). ISBN 0-12-042510-6

F. Hase, M. Höpfner, Atmospheric ray path modeling for radiative transfer algorithms. Appl. Opt. **38**, 3129–3133 (1999). doi:10.1364/AO.38.003129

F. Hase, T. Blumenstock, C. Paton-Walsh, Analysis of the instrumental line shape of high-resolution fourier transform ir spectrometers with gas cell measurements and new retrieval software. Appl. Opt. **38**, 3417–3422 (1999). doi:10.1364/AO.38.003417

F. Hase, J.W. Hannigan, M.T. Coffey, A. Goldman, M. Hopfner, N.B. Jones, C.P. Rinsland, S.W. Wood, Intercomparison of retrieval codes used for the analysis of high-resolution, groundbased FTIR measurements. J. Quant. Spectrosc. Ra. **87**, 25–52 (2004). doi:10.1016/j.jqsrt.2003.12.008

I.M. Held, B.J. Soden, Water vapour feedback and global warming. Annu. Rev. Energy Envirion. **25**, 441–475 (2000)

J. Notholt, von der P. Gathen, S. Peil, Heterogeneous conversion of HCl and $ClONO_2$ during the Arctic winter 1992/1993 initiating ozone depletion. J. Geophys. Res. **100**, 11269–11274 (1995). doi:10.1029/95JD00850

M. Palm, C. Melsheimer, S. Noël, S. Heise, J. Notholt, J. Burrows, O. Schrems, Integrated water vapor above Ny Ålesund, Spitsbergen: A multisensor intercomparison. Atmos. Chem. Phys. **10**, 1215–1226 (2010). doi:10.5194/acp-10-1215-2010

N.S. Pougatchev, B.J. Connor, N.B. Jones, C.P. Rinsland, Validation of ozone profile retrievals from infrared ground-based solar spectra. Geophys. Res. Lett. **23**, 1637–1640 (1996) doi:10.1029/96GL01501

C.P. Rinsland, E. Mahieu, R. Zander, N.B. Jones, M.P. Chipperfield, A. Goldman, J. Anderson, J.M. Russell, P. Demoulin, J. Notholt, G.C. Toon, J.-F. Blavier, B. Sen, R. Sussmann, S.W. Wood, A. Meier, D.W.T. Griffith, L.S. Chiou, F.J. Murcray, T.M. Stephen, F. Hase, S. Mikuteit, A. Schulz, T. Blumenstock, Long-term trends of inorganic chlorine from ground-based infrared solar spectra: Past increases and evidence for stabilization. J. Geophys. Res. **108**, 4252 (2003). doi:10.1029/2002JD003001

C.D. Rodgers, *Inverse methods for atmospheric sounding: Theory and praxis*, World Scientific Publishing Co., Singapore (2000). ISBN 981-02-2740-X

M. Schneider, F. Hase, Improving spectroscopic line parameterisation by means of atmospheric spectra: Theory and example for water vapour and solar absorption spectra. J. Quant. Spectrosc. Radiat. Transfer. **110**, 1825–1839 (2009a). doi:10.1016/j.jqsrt.2009.04.011

M. Schneider, F. Hase, Ground-based FTIR water vapour profile analyses. Atmos. Meas. Tech. **2**, 609–619 (2009b)

M. Schneider, F. Hase, T. Blumenstock, Water vapour profiles by ground-based FTIR spectroscopy: Study for an optimised retrieval and its validation. Atmos. Chem. Phys. **6**, 811–830 (2006a)

M. Schneider, F. Hase, T. Blumenstock, Ground-based remote sensing of HDO/H_2O ratio profiles: Introduction and validation of an innovative retrieval approach. Atmos. Chem. Phys. **6**, 4705–4722 (2006b)

M. Schneider, P.M. Romero, F. Hase, T. Blumenstock, E. Cuevas, R. Ramos, Continous quality assessment of atmospheric water vapour measurement techniques: FTIR, Cimel, MFRSR, GPS, and Vaisala RS92 Atmos. Meas. Tech., **3** 323–338 (2010a). doi:10.5194/amt-3-323-2010

M. Schneider, E. Sepulveda, O. Garcia, F. Hase, T. Blumenstock, Remote sensing of water vapour profiles in the framework of the total carbon column observing network(tccon). Atmos. Meas. Tech. **3**, 1785–1795 (2010b)

M. Schneider, K. Yoshimura, F. Hase, T. Blumenstock, The ground-based ftir network's potential for investigating the atmospheric water cycle. Atmos. Chem. Phys. **10**, 3427–3442 (2010c). doi:10.5194/acp-10-3427-2010

R. Sussmann, T. Borsdorff, M. Rettinger, C. Camy-Peyret, P. Demoulin, P. Duchatelet, E. Mahieu, C. Servais, Technical note: Harmonized retrieval of column-integrated atmospheric water vapor from the FTIR network—first examples for long-term records and station trends. Atmos. Chem. Phys. **9**, 8987–8999 (2009)

D.C. Tobin, H.E. Revercomb, R.O. Knuteson, B.M. Lesht, L.L. Strow, S.E. Hannon, W.F. Feltz, L.A. Moy, E.J. Fetzer, T.S. Cress, Atmospheric radiation measurement site atmospheric state best estimates for Atmospheric Infrared Sounder temperature and water vapor retrieval validation. J. Geophys. Res. **111**, D09S14 (2006). doi:10.1029/2005JD006103

H. Vömel, H. Selkirk, L. Miloshevich, J. Valverde-Canossa, J. Valéds, E. Kyrö, R. Kivi, W. Stolz, G. Peng, J.A. Diaz, Radiation dry bias of the vaisala RS92 humidity sensor. J. Atmos. Oceanic. Tech. **24**, 953–963 (2007). doi:10.1175/JTECH2019.1

J. Worden, K. Bowman, D. Noone, R. Beer, S. Clough, A. Eldering, B. Fisher, A. Goldman, M. Gunson, R. Herman, S.S. Kulawik, M. Lampel, M. Luo, G. Osterman, C. Rinsland, C. Rodgers, S. Sander, M. Shephard, H. Worden, Tropospheric emission spectrometer observations of the tropospheric HDO/H_2O ratio: Estimation approach and characterization. J. Geophys. Res. **111**, D16 309 (2006). doi:10.1029/2005JD006606

Chapter 7
Lidar

Thierry Leblanc, Thomas Trickl and Hannes Vogelmann

7.1 Introduction

Lidar (for "light detection and ranging") is a remote sensing measurement technique using the scattering and propagation properties of light by gases, liquids, and solids to infer some of their physical properties. This technique has many applications from the ground, aircraft or space such as atmospheric sensing, oceanography, and topography. The earliest records of using the lidar technique for atmospheric remote sensing date back to the 1930s when searchlight projectors were used to determine atmospheric density (Hulburt 1937; Elterman 1951). Following the emergence of lasers in the 1960s, lidar instruments typically in use today for atmospheric remote sensing are based on the emission of essentially monochromatic light by one or several laser sources. The best-known properties of the atmosphere that can be measured by lidar are air density, wind speed and direction, air temperature, the concentrations of ozone, carbon dioxide, and water vapour, and the density, basic shape and size of aerosols, ice crystals, and water droplets. Comprehensive reviews of the various existing lidar techniques for atmospheric remote sensing can be found, for example, in (Measures 1992) and (Weitkamp 2005).

In this chapter we focus on the characterization of lidar methods for the measurement of water vapour reaching the Upper Troposphere and Lower Stratosphere (UT/LS), a region of the Earth's atmosphere that is particularly relevant to climate

This work was carried out at the Jet Propulsion Laboratory, California Institute of Technology, under a contract with the National Aeronautics and Space Administration.

T. Leblanc (✉)
JPL-Table Mountain Facility, 24490 Table Mountain Road,
Wrightwood, CA 92397-0367, USA
e-mail: leblanc@tmf.jpl.nasa.gov

T. Trickl · H. Vogelmann
Karlsruher Institut für Technologie, Institut für Meteorologie
und Klimaforschung, Atmosphärische Umweltforschung (IMK-IFU),
Kreuzeckbahnstr. 19, 82467 Garmisch-Partenkirchen Germany
e-mail: thomas.trickl@kit.edu

N. Kämpfer (ed.), *Monitoring Atmospheric Water Vapour,*
ISSI Scientific Report Series 10,
DOI 10.1007/978-1-4614-3909-7_7, © Springer Science+Business Media, LLC 2013

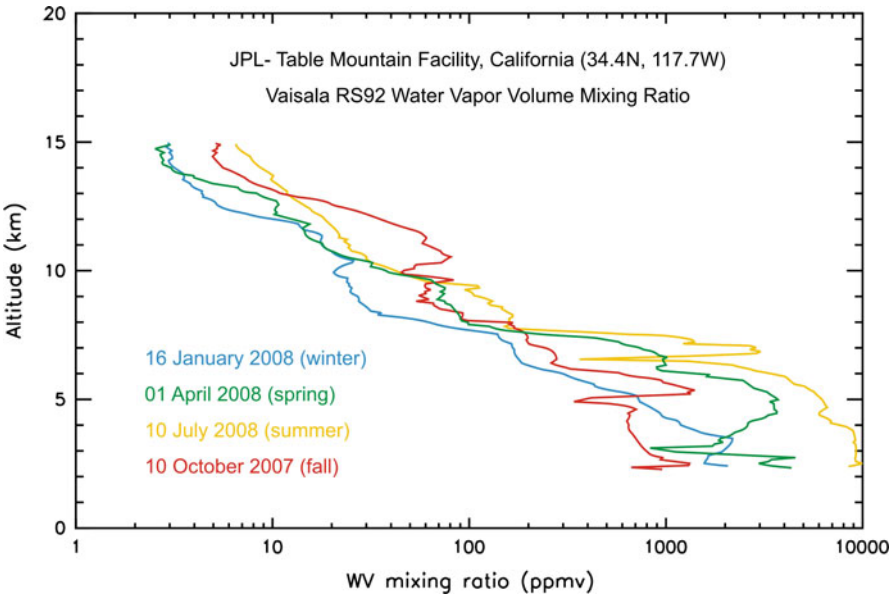

Fig. 7.1 Typical water vapour profiles measured at the JPL Table Mountain Facility, California (34.4° N 117.7° W). The mixing ratio decreases by a factor of 1,000 between the boundary layer and the tropopause

change (Oltmans and Hofmann 1995; de F. Forster and Shine 1999). Today, ground-based lidar sounding of water vapour up to the middle troposphere (i.e., 8 km altitude) is rather mature (Grant 1991; Whiteman et al. 1992; Ferrare et al. 1995; Sherlock et al. 1999a; Turner et al. 2002; Vogelmann and Trickl 2008). However, extending operation to the tropopause and beyond (typically above 12 km) is impeded by the drop, by more than four orders of magnitude, in the water vapour mixing ratio from the ground to the lower stratosphere (see Fig. 7.1). At the same time the backscatter signal strongly diminishes as a function of distance. Hence, particularly powerful laser systems and large telescopes for receiving the backscattered radiation are needed for lidar measurements of water vapour extending to the UT/LS. The implementation of lidar systems that can measure water vapour up into this region is, therefore, a significant and contemporary challenge (Leblanc et al. 2012). The two existing lidar techniques dedicated to the measurement of atmospheric water vapour are Differential Absorption Lidar (DIAL), using the wavelength dependence of light absorption by water vapour (Wulfmeyer and Bösenberg 1998b), and the Raman method, using inelastic backscattering of light by water vapour with respect to a reference well-mixed gas (Hinkley 1976). Both these techniques have advantages and drawbacks. For example, because of the high abundance of water vapour in the lower tropospheric layers, routine measurements in the stratosphere by a water vapour DIAL can only be achieved from an aircraft or spacecraft (Browell et al. 1998; Ehret et al. 1999), which is practically prohibited for routine monitoring by their high operating cost. For this reason and because of a less demanding laser technology, the Raman lidar technique is usually preferred. However, the vibrational

Raman scattering process is several orders of magnitude weaker than the elastic light scattering involved in the DIAL technique (Hinkley 1976).

In the next section we briefly describe the general lidar principle and we present the lidar equation describing the lidar signals. As for many other lidar applications, this equation is the starting point for the retrieval of water vapour using both the DIAL and the Raman lidar techniques. Each technique is described in detail in Sects. 7.3 and 7.4.

7.2 Lidar Principle and Equation

A schematic of the lidar principle is presented in Fig. 7.2. A laser pulse at wavelength λ_E is emitted into the atmosphere. The light is scattered by the atmospheric molecules and particles, and a fraction is collected back on the ground with a telescope of area A_L. Knowing the speed of light, the distance r to scattering molecules or particles is deduced from the travel time of the photons on their way upward and then back to the lidar. Since the lidar includes the light source itself, the lidar technique is known as an active remote sensing technique, in contrast to other remote sensing instruments such as radiometers and spectrometers which are passive. The precise timing of the lidar-measured samples and the high-speed electronics available today yield a high vertical resolution (from a few meters to a few hundred meters) compared with most passive instruments which are sensitive to light reaching the instrument with no spatio-temporal information of its origin. The light collected by the lidar telescope is geometrically and spectrally separated (e.g., with optical filters and beam splitters) and detected with photosensitive devices (e.g., photomultipliers (PMT) and avalanche photo-diodes (APD)) where it is converted to electronic signals ("lidar signals"). The signals are sampled in time (i.e., distance), and after various corrections they are proportional to the product of the number of photons emitted by the laser and the number of backscattering molecules.

For a vertically pointing lidar sytem, one of the simplest and most general forms of the Lidar Equation expressing the number of photons backscattered at distance r from the lidar by a volume element of thickness δr, and collected at the detection wavelength λ_D can be written:

$$P_D(r,\lambda_D) = P_E(r,\lambda_E)\,\kappa_L(\lambda_D)\,\frac{O_L(r)\,A_L\delta r}{r^2}\,\beta(r,\lambda_E \rightarrow \lambda_D)\,t_{\uparrow}(r,\lambda_E)\,t_{\downarrow}(r,\lambda_D). \tag{7.1}$$

The subscripts "E","D","L" stand for "emitted", "detected", and "lidar" respectively.

P_E is the number of photons emitted, per laser shot, at emission wavelength λ_E,
P_D is the number of photons detected, per laser shot, at detection wavelength λ_D,
κ_L is the overall optical transmittance and quantum efficiency of the receiver channel,
O_L is the telescope field-of-view and laser beam overlap factor (between 0 and 1),
A_L is the area of the receiving telescope,
β is the total backscatter coefficient for the type of scattering considered,
$t_{\uparrow}$ and $t_{\downarrow}$ are the total atmospheric transmittances (between 0 and 1) along the beam path from the lidar to the scattering layer (arrow "up") and back (arrow "down"), respectively.

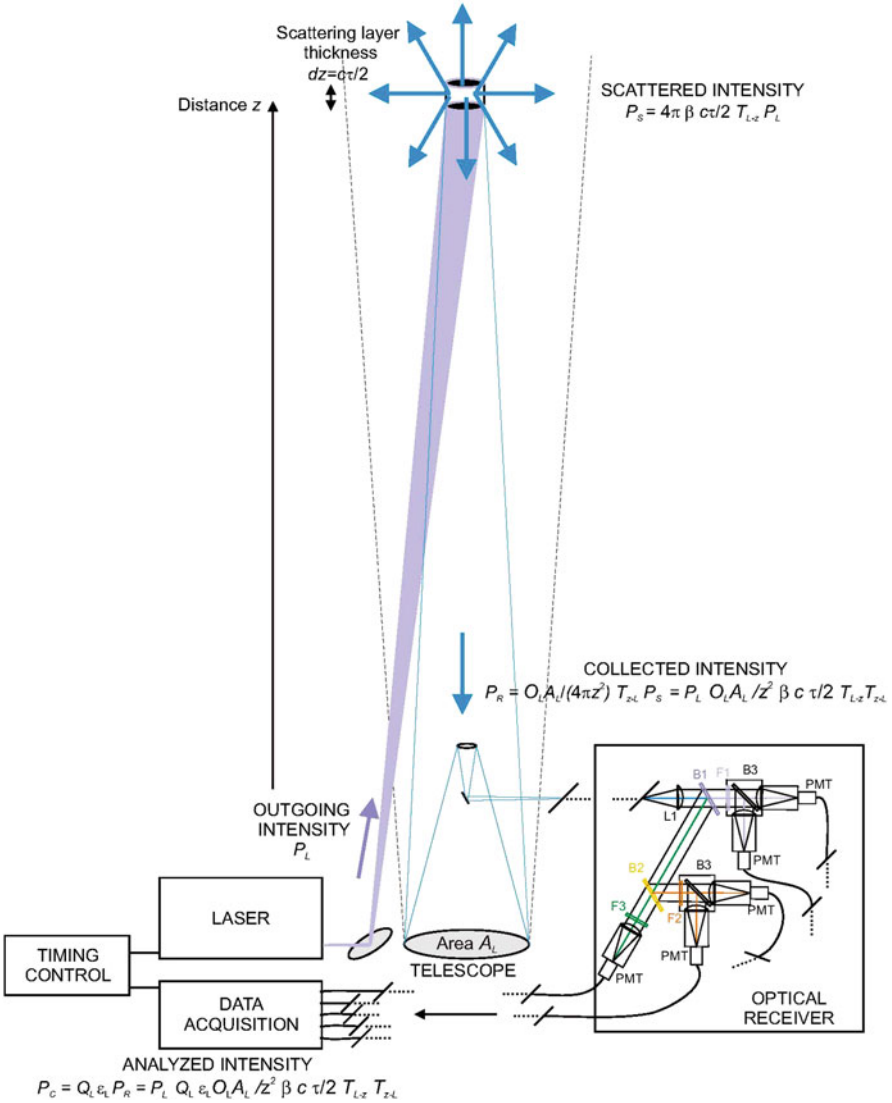

Fig. 7.2 Schematic of a typical lidar setup. The relative sizes of the emitter, receiver and atmospheric parts are not to scale. The various intensities reported and the number of receiving channels are only indicative (see text for details)

These two terms can be expressed as a function of the extinction coefficient α resulting from light scattering and absorption along the laser beam path:

$$t_{\uparrow}(r,\lambda_E)\,t_{\downarrow}(r,\lambda_D) = \exp\left[-\int_0^r \alpha\left(r',\lambda_E\right)dr'\right]\exp\left[-\int_0^r \alpha\left(r',\lambda_D\right)dr'\right] \quad (7.2)$$

Equations 7.1 and 7.2 are valid for all detection wavelengths, all types of atmospheric scatterer, and all types of scattering process. The appropriate choice of the emission and detection wavelengths allows further development and/or simplification of these equations, which commonly refers to using a specific "lidar technique", for example, DIAL or Raman.

In the case of the Differential Absorption Lidar (DIAL) technique, the emission and detection wavelengths can be chosen so that the transmittance terms expanded in Eq. 7.2 become essential. They can be further expanded by separating the total extinction along the laser beam path into molecular extinction and particulate extinction terms ($\alpha = \alpha_M + \alpha_P$), then by separating molecular extinction into molecular (Rayleigh) scattering and molecular absorption terms ($\alpha_M = \alpha_R + \alpha_A$), and finally by separating the molecular absorption term into individual contributions of each absorber. Each of these contributions can be expressed as the product of the number density N_i of the absorber by its absorption cross-section σ_i. For a detection wavelength identical to the emission wavelength ($\lambda_D = \lambda_E = \lambda$), the total extinction along the laser beam path on the way up ($t_\uparrow$) is equal to that on its way back ($t_\downarrow$), and Eqs. 7.1 and 7.2 combined together become:

$$P_D(r,\lambda) = P_E(r,\lambda)\,\kappa_L(\lambda)\,\frac{O_L(r)\,A_L\delta r}{r^2}\beta(r,\lambda) \times \exp\left[-2\int_0^r \alpha_R\left(r',\lambda\right) + \alpha_P\left(r',\lambda\right) + \sum_i \sigma_i(\lambda)\,N_i\left(r'\right)dr'\right]. \quad (7.3)$$

The DIAL technique is used to retrieve the number density N_i of atmospheric species such as ozone, carbon dioxide, nitrous oxide, and water vapour, by inverting Eq. 7.3 with respect to $\sigma_i N_i$.

In the case of the Raman and Rayleigh backscatter techniques, the emission and detection wavelengths are chosen so that the essential information lies in the total backscatter coefficient β of Eq. 7.1 and not in the terms expanded in Eq. 7.2 (DIAL case). To first order, β characterizes the type of scattering involved at the detection wavelength. If the detection wavelength is identical to the emission wavelength, the collected signal is the result of all backscattering processes regardless of the type of molecules or particles involved. This backscattered signal typically consists of elastic scattering from both molecules and particles ("Rayleigh backscatter lidar" or "Rayleigh-Mie backscatter lidar") and inelastic scattering due to rotational Raman transition in molecules ("Rotational- Raman lidar"). This technique does not allow the selection of specific atmospheric species, but can be used for the detection of aerosols and clouds (typically below 30 km), or for the determination of atmospheric density and temperature (typically above 30 km). If the detection wavelength is different from the emission wavelength (inelastic scattering) and spectrally well selected, the collected signal is the result of backscattering processes from a specific type of molecule. In this case the backscatter coefficient β can be expressed as the product of the molecule's Raman backscatter cross-section σ_M and its number density N_M:

$$\beta(r,\lambda_E \rightarrow \lambda_D) = \sigma_M(T(r),\lambda_L,\lambda_D)\,N_M(r) \quad (7.4)$$

σ_M is a function of wavelength and temperature (see next section). Atmospheric temperature being a function of altitude, the cross-section can therefore be expressed as a function of wavelength and range. Introducing Eqs. 7.2 and 7.4 into 7.1 yields:

$$P_D\left(r,\lambda_D\right) = P_E\left(r,\lambda_E\right)\kappa_L\left(\lambda_D\right)\frac{O_L\left(r\right)A_L\delta r}{r^2}\sigma_M\left(r,\lambda_L \rightarrow \lambda_D\right)N_M\left(r\right) \times \exp\left[-\int_0^r \alpha\left(r',\lambda_E\right)+\alpha\left(r',\lambda_D\right)dr'\right]. \tag{7.5}$$

The Raman backscatter technique is used to retrieve water vapour mixing ratio and various properties of clouds and aerosols by inverting Eq. 7.5 with respect to $\sigma_M N_M$. Starting from Eq. 7.5, Sect. 7.3 further details the retrieval of water vapour mixing ratio q_{H_2O} using the Raman technique, while starting from Eq. 7.3, Sect. 7.4 further details the DIAL technique for the retrieval of water vapour number density N_{H_2O}.

7.3 Water Vapour Raman Lidar

7.3.1 Raman Scattering

Light scattering in the atmosphere includes a large variety of elastic and inelastic processes. Raman scattering was named after C. V. Raman who first made the parallel between Compton's interaction between X-Rays and electrons, and inelastic scattering of light by molecules (Raman and Krishnan 1928). In this case the wavelength of the scattered light is shifted by an amount that depends on the energy difference between its vibrational and/or rotational states. Quantum physics, in principle, allows all scattering processes occurring within a given molecule to be solved theoretically, the more complex the molecule is, the more complex its Raman spectrum (Weber 1979). Quantitatively, the intensity of the backscattered light at a given wavelength is equal to the product of the intensity of the incident light and the Differential Raman Scattering Cross-Section of the molecule, a complex and anisotropic function of wavelength, temperature, polarizabiltiy, and amplitude of the various vibrational and rotational modes of the molecule. A full description of Raman scattering for atmospheric remote sensing applications can be found in (Hinkley 1976) and (Weitkamp 2005).

A significant advantage of using Raman backscatter over Rayleigh backscatter is that for well chosen wavelength shifts the light collected at the shifted wavelength is backscattered by only one type of molecule. In other words, one can select appropriate wavelengths in order to have no contribution from other molecules and more importantly, particles. However the fraction of the total energy scattered at that wavelength (i.e., the Raman cross-section) is typically three orders of magnitude smaller than for elastic scattering, which allows its practical application to remote sensing of only the most abundant molecules in the atmosphere. To illustrate this

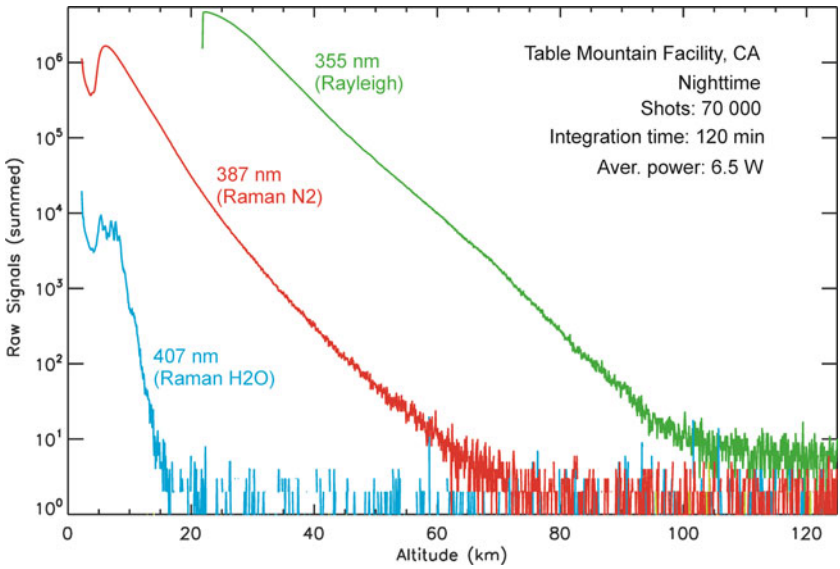

Fig. 7.3 Typical high-intensity Rayleigh and Raman lidar signals (here collected by the JPL Table Mountain Facility water vapour Raman lidar). Note the factor of 10^5 at 15 km in the magnitude of the nitrogen and water vapour Raman returns, and the factor of about 10^3 between the nitrogen Raman and the Rayleigh returns

difference in scattering magnitude, Fig. 7.3. shows typical lidar signals acquired by the JPL-Table Mountain Facility water vapour Raman lidar, and Table 7.1 summarizes the power-aperture requirement of water vapour Raman lidar systems compared with that of other lidar techniques.

Table 7.1 Typical power-aperture products[a] (Wm^2) required to achieve measurements with an uncertainty on the target species of 15 % or less for a 1 h integration time[b]

	Boundary layer	Free troposphere	Lower stratosphere	Upper stratosphere	Upper mesosphere
Rayleigh aerosols	0.0005	0.005	0.01	0.05	–
Raman aerosols	0.05	0.5	1	5	–
Rayleigh DIAL ozone	0.01	0.1	1	10	–
Raman DIAL ozone	0.1	1	10	100	–
Rayleigh temperature	–	–	0.01	0.1	5
Vib. Raman temperature	–	0.1	1	5	–
Rot. Raman temperature	0.01	0.1	1	5	–
Raman water vapour	0.1	2–5	5–50	–	–

[a] Power-aperture product is defined as the product of the laser output power at the emitted wavelength by the area of the receiving telescope.
[b] Nighttime estimations based on actual lidar systems with receiver overall efficiencies comprised between 0.05 and 0.2; estimations may vary based on total noise level resulting from electronics, sky background light and field-of-view.

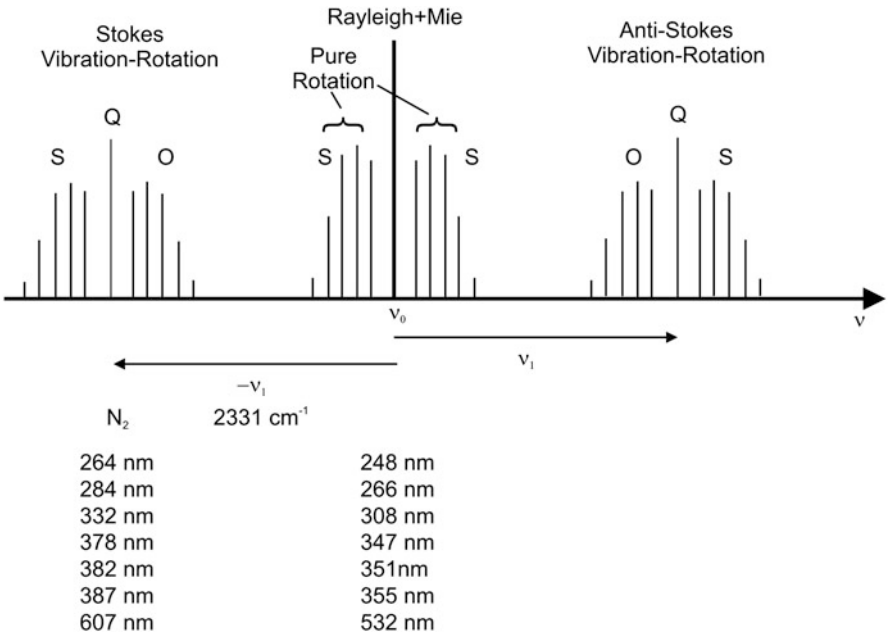

Fig. 7.4 Simplified Raman spectrum of the nitrogen molecule, and corresponding approximate wavelength shifts for commonly used lasers

7.3.2 Water Vapour Raman Lidar Retrieval

For implementing a Raman water vapour lidar, a minimum of two channels is required, one receiving the lidar signals at a wavelength Raman-shifted by water vapour ($M = H_2O$, $\lambda_D = \lambda_{H_2O}$), and one at a wavelength Raman-shifted by a reference molecule having a well known mixing ratio throughout the altitude range considered. For altitudes below 80 km, the two natural candidates are the well-mixed gases nitrogen and oxygen. In the rest of this chapter we will use nitrogen ($M = N_2$, $\lambda_D = \lambda_{N_2}$), the most abundant, and practically, easiest and most commonly used reference molecule for Raman lidar applications. Any upcoming discussion on the use of nitrogen similarly applies to oxygen unless otherwise stated.

Under normal atmospheric conditions, a limited number of transition lines will account for most of the molecule total Raman cross-section, and the Raman spectrum of simple molecules such as nitrogen can be reduced to a few vibration-rotation and pure rotational bands, as shown in Fig. 7.4. The strongest Stokes Q-branch (which is itself made of a large number of very closely spaced rotational lines not shown on the figure) occurs at a frequency shift of $\nu_1 \sim 2,330\,\mathrm{cm}^{-1}$ (Trickl et al. 1995) corresponding to the transition from the ground-state to the first vibrational state of N_2. For this reason, most, if not all, existing water vapour Raman lidars use this region

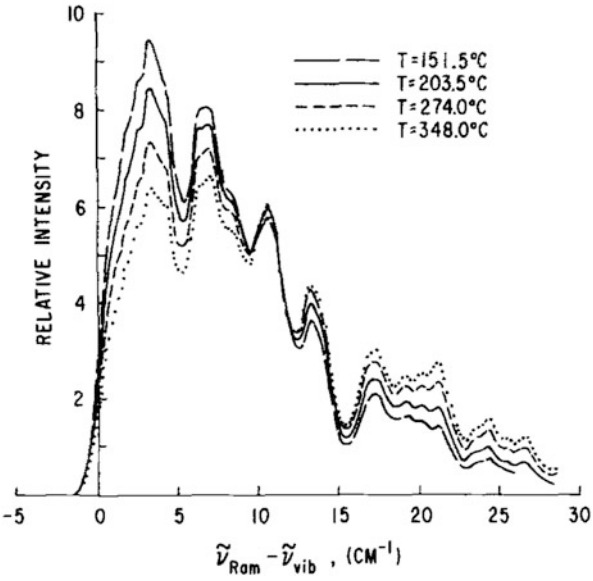

Fig. 7.5 Theoretical calculations of the Raman ν_1-band contour for water vapour at four temperatures. (From Bribes et al. 1976)

of the nitrogen Raman spectrum to collect signal backscattered by the reference molecule.

Water vapour is an asymmetric top molecule and its Raman spectrum is more complex than that of nitrogen. In particular, one of its strongest component, the Stokes Q-branch occurring in the OH-stretching band near the frequency shift of 3,654 cm^{-1} (Bribes et al. 1976) contains many rotational lines which underlie significant anisotropy and a complex dependence on temperature, as shown in Fig. 7.5. For measurements encompassing the entire troposphere, this temperature dependence cannot be ignored when designing the lidar receiver (see hereafter the discussion on the water vapour filter spectral width). Nevertheless, most, if not all, existing water vapour Raman lidars use this OH-stretching band for the collection of the water vapour signal.

Figure 7.6 is a color-coded schematic of a typical water vapour Raman lidar receiver when using a tripled-frequency Nd:YAG laser (i.e., emitting at 355 nm), and the Raman shifts of 2,330 cm^{-1} (387 nm) for Nitrogen, and 3,654 cm^{-1} (407 nm) for water vapour. The components in black represent the necessary parts of the receiver, which includes one water vapour channel and one nitrogen channel. The components in blue and green colors represent system upgrades the purpose of which will be discussed later. Eq. 7.5 applied to the water vapour and nitrogen channels can be written:

$$P_{\mathrm{H_2O}}(r) = P_E \kappa_{H_2O} \frac{O_{H_2O}(r)\, A_{H_2O} \delta r}{r^2} \sigma_{H_2O}(r)\, N_{H_2O}(r) \times \exp\left[-\int_0^r \left(\alpha_E(r') + \alpha_{H_2O}(r') \right) \mathrm{d}r' \right], \tag{7.6a}$$

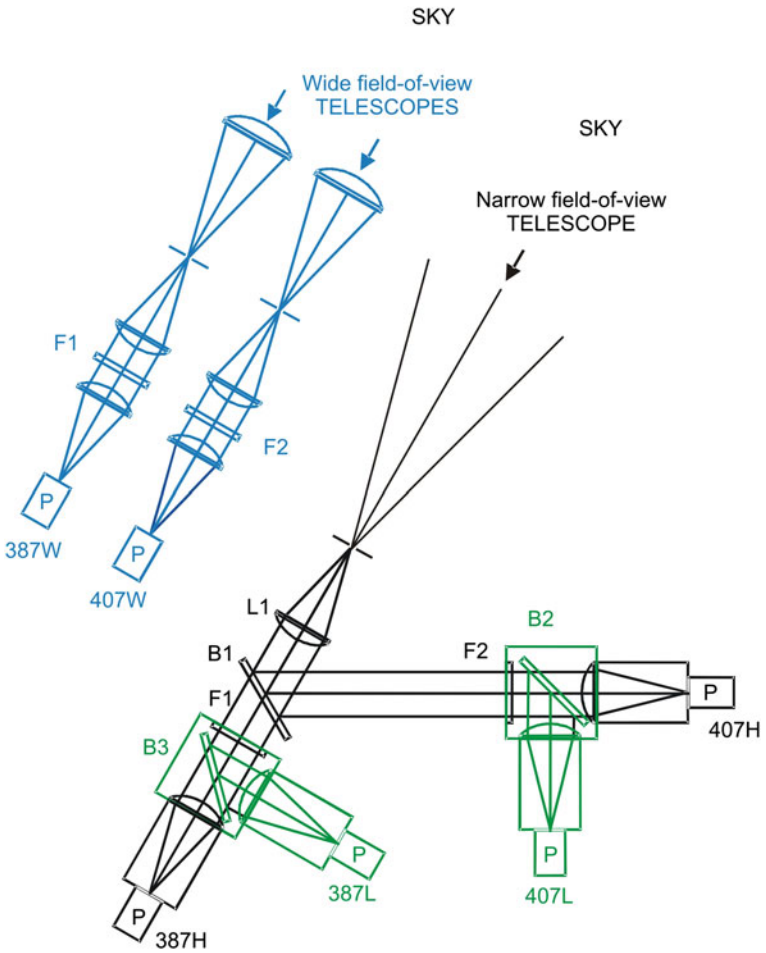

Fig. 7.6 Typical water vapour Raman lidar receiver (The minimum configuration is represented in *black*. The *green* parts represent an upgrade for saturation correction. Components in *blue* represent an upgrade for the calculation of the overlap functions (see text for details).“*H*” and “*L*” stand for “high” and “low” intensity signals, “*W*” stands for “wide field-of-view”, “*B*” for “beam-splitter”, “*F*” for “filter”, “*L*” for “lens”, and “*P*” for “photomultiplier tube”.)

$$P_{N_2}(r) = P_E \kappa_{N_2} \frac{O_{N_2}(r)\, A_{N_2} \delta r}{r^2} \sigma_{N_2}(r)\, N_{N_2}(r) \times \exp\left[-\int_0^r \left(\alpha_E(r') + \alpha_{N_2}(r') \right) \mathrm{d}r' \right]. \tag{7.6b}$$

For brevity we omitted all dependencies that do not affect the discussion, and included subscripts instead. The above equations describe the collected signals for ideal noise-free lidar instrumentation. In reality, the total acquired signal is a combination of

the collected light backscattered in the atmosphere and noise originating from both residual sky background light and from the instrumentation. In addition, the signals are usually subject to a non-linear photon-counting efficiency (especially true at very high-count rates). This commonly called "saturation" or "pile-up" effect can be empirically corrected (Donovan et al. 1993) and (Whiteman et al. 1992), or can be greatly reduced by using an analog channel instead of photon counting (Newsom et al. 2009). An experimental correction method consists of evaluating the saturation parameters by fitting the ratio of a saturated signal to a non-saturated one, which can be achieved by splitting the collected signal into high- ($> 90\,\%$) and low- ($< 10\,\%$) intensity channels. The system upgrade consisting of adding low-intensity channels is represented in green in Fig. 7.6. After noise extraction and saturation correction, the ratio of the corrected signals $\overline{P}$ collected in the water vapour and nitrogen channels can be written:

$$R\left(r\right) = \frac{\overline{P}_{H_2O}\left(r\right)}{\overline{P}_{N_2}\left(r\right)} = \frac{\kappa_{H_2O}}{\kappa_{N_2}} \frac{O_{H_2O}\left(r\right) A_{H_2O}}{O_{N_2}\left(r\right) A_{N_2}} \frac{\sigma_{H_2O}\left(r\right)}{\sigma_{N_2}\left(r\right)} \frac{N_{H_2O}\left(r\right)}{N_{N_2}\left(r\right)} \times \exp\left[-\int_0^r \left(\alpha_{H_2O}\left(r'\right) - \alpha_{N_2}\left(r'\right)\right) \mathrm{d}r'\right]. \tag{7.7}$$

As discussed in Sect. 7.2, the extinction terms can be separated into molecular and particulate extinction $\alpha = \alpha_M + \alpha_P$. Molecular extinction α_M can be calculated for each channel prior to computing the ratio $R(r)$ using climatological, modeled, or measured profiles of the air number density, and the density of the atmospheric absorbers, leaving only the particulate extinction contribution inside the exponential term of Eq. 7.7.

Water vapour mixing ratio can be expressed as a function of number density:

$$q\left(r\right) = 0.781 \frac{N_{H_2O}\left(r\right)}{N_{N_2}\left(r\right)}$$

Equation 7.7 can then be reformulated in a more compact way:

$$R\left(r\right) = \kappa_{eff} \kappa_O\left(r\right) \kappa_\sigma\left(r\right) \kappa_\alpha\left(r\right) q\left(r\right) \tag{7.8}$$

$\kappa_{eff} = \frac{\kappa_{H_2O}}{\kappa_{N_2}} \frac{A_{H_2O}}{A_{N_2}} \frac{1}{0.781}$ is a constant expressing the ratio of all the optical and quantum efficiencies of the receiver as well as other constant terms. If an oxygen channel is used instead of nitrogen, the constant 0.781 representing the well-mixed fraction of nitrogen in dry air, is replaced by 0.209.

$\kappa_O\left(r\right) = \frac{O_{H_2O}(r)}{O_{N_2}(r)}$ is the ratio of the overlap functions of the water vapour and nitrogen channels

$\kappa_\sigma\left(r\right) = \frac{\sigma_{H_2O}(r)}{\sigma_{N_2}(r)}$ is the ratio of the water vapour and nitrogen Raman cross-sections

$\kappa_\alpha\left(r\right) = \exp\left[-\int_0^r \left(\alpha_{H_2O}\left(r'\right) - \alpha_{N_2}\left(r'\right)\right) \mathrm{d}r'\right]$ is the ratio of the particulate extinction along the return path of the beam at the water vapour and nitrogen wavelengths (called "extinction differential")

Depending on the lidar instrument setup, the four multiplicative terms in front of the term $q(r)$ in Eq. 7.8 have a varying degree of dependence in range and wavelength and can be estimated with a varying degree of accuracy. Their estimation is known as the "lidar calibration".

7.3.3 Calibration

There are two well-known calibration approaches. An "internal" (or "independent") calibration can be done by experimentally calculating each term preceding $q(r)$ in Eq. 7.8. That includes the determination of all constant terms, as well as the precise characterization of all range- and wavelength-dependencies. The other approach is commonly called "external" calibration, which consists of two steps: first minimizing (or estimating) the range and wavelength dependencies, then calculating the remaining proportionality factor between $R(r)$ and $q(r)$. This second step can be achieved by normalizing the signal ratio to an external measurement of water vapour (e.g., radiosonde). Both internal and external calibration approaches are now reviewed.

7.3.3.1 Internal Calibration

In order to perform a complete internal calibration, it is necessary to fully characterize the four multiplicative terms in front of the term $q(r)$ in Eq. 7.8, i.e., necessary to:

1. Estimate the transmittance of all the optics (telescope mirrors, beam splitters, collimators, etc.) either by using the manufacturers' specifications, or experimentally by using identical filters, removing the beam splitter immediately preceding the detectors, and collecting light from a daytime environment (diffused spectrum) (Vaughan et al. 1988).
2. Estimate the product $\kappa_{eff}\kappa_{\sigma}$ in Eq. 7.8 by calculating the convolution of the transmission of the water vapour/nitrogen filter by the water vapour/nitrogen Raman cross-section in the spectral region of interest (Sherlock et al. 1999b; Whiteman 2003a, 2003b). For spectrally narrow water vapour filters, an altitude-dependent correction is necessary to account for the temperature dependence of the Raman cross-section. The effect of this dependence is illustrated in Fig. 7.7 (from (Whiteman 2003a)) representing the variation of the ratio of the detected intensities at 2 different temperatures (200 K and 300 K) as a function of the filter width.
3. Estimate the altitude dependence of the ratio of the overlap functions κ_O by assuming that the photomultipliers efficiencies are known (or already calculated) and by replacing the water vapour filter by a filter identical to that used in the nitrogen channel, then calculating the ratio of the signals obtained in both channels (Vaughan et al. 1988; Whiteman et al. 1992). To estimate routinely the altitude dependence of this overlap function, a pair of wide field-of-view channels can complement the original pair of (assumed narrow field-of-view) channels. By calculating the ratio of the narrow field-of-view channel intensity to the

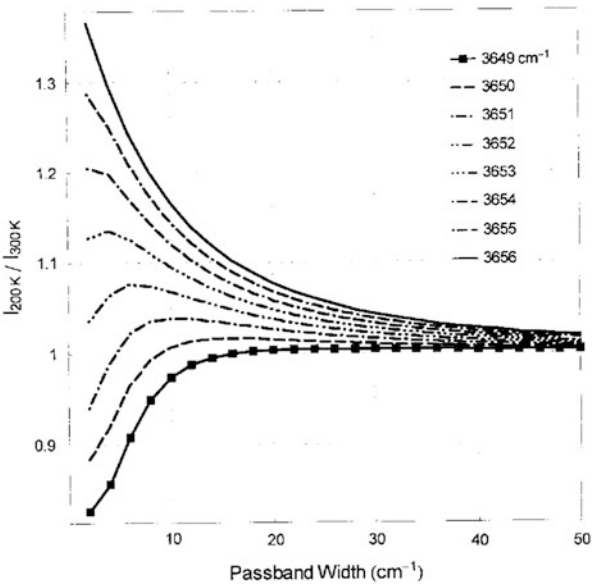

Fig. 7.7 Effect of the convolution of the temperature-dependent water vapour cross-section and the filter passband width (from Whiteman 2003a). The ratio of the intensities at two different temperatures (200 K and 300 K) is as a function of the water vapour filter spectral width. See text for details or reference therein

corresponding wide field-of-view channel intensity, an estimate of the overlap factor can be obtained. The addition of a pair of narrow field-of-view channels is schematized in blue in Fig. 7.6.

4. Estimate the ratio of the detector efficiencies, either experimentally and assuming full overlap (Vaughan et al. 1988) or by simply using the manufacturers' specifications.
5. Ensure that the extinction differential $\kappa_\alpha(r)$ is nearly 1.0 in the altitude range considered ($\Delta t_{P\downarrow} = 1$), or estimate it by using climatological, modeled, or observed profiles of atmospheric aerosols, and assuming that their microphysical properties (including their wavelength dependence) are well-known.

The resulting uncertainties for each procedure range from 2 to 15 %. Overall, the accuracy of the internal calibration of water vapour Raman lidars can easily reach 12–15 %. Table 7.2 summarizes the uncertainties associated with the procedures described above.

Some of these procedures can be combined into one single step by using a laboratory-calibrated lamp with well-known irradiances at the water vapour and nitrogen wavelengths (Sherlock et al. 1999b). For NIST-traceable lamps, the absolute irradiances are usually known to within 1–2 %. They must be convolved to the spectral width of the water vapour and nitrogen filters. The lamp must be placed in a position that allows the detectors to collect the light in a configuration that resembles as much as possible that of normal atmospheric data acquisition. Practically, it is almost impossible to reproduce, and the different geometry between the detector illumination from the lamp and from the sky can lead to significant uncertainty in the estimation of the absolute calibration constant.

Table 7.2 Measurement error budget summary

	Error source	Error (bottom)[a] %	Error (center) %	Error (top) %	Error (0–5 km) %	Error (5–10 km) %	Error (indiff.) %
Precision	Photon counting	<0.3	1–10	>30	–	–	–
Retrieval[b]	Noise correction	–	0–1	1–20	–	–	–
	Saturation correction	0–10	0–1	–	–	–	–
	Overlap function	1–30	0–1	–	–	–	–
	Fluorescence	–	–	–	0–1	0–10	–
	Absorption by constituents	–	–	–	0.1–0.5	0.1–2	–
	Molecular extinction	–	–	–	0.2–5	0.1–0.5	–
	Particular extinction	–	–	–	0.5–10	0.1–2	–
Internal	Lamp	–	–	–	–	–	5–10
Calibration	Diffuse sunlight	–	–	–	–	–	5–30
	Receiver transmission	–	–	–	–	–	2–5
	Raman cross-sections	–	–	–	–	–	5–12
External	Balloon borne sensor	–	–	–	3–7	3–50	–
Calibration	Balloon position/statistics[c]	–	–	–	3–30	3–30	–
	Ground based microwave	–	–	–	–	–	3–5
	Ground based GPS	–	–	–	–	–	5–7
	Column scaling	–	–	–	–	–	3–15
	Satellite (overall)[c]	–	–	–	–	–	15–50
Hybrid	Lamp (transfer)	–	–	–	–	–	0.5–2
Calibration	External source	–	–	–	3–15	–	–
	Coincident position/statistics[c]	–	–	–	1–10	–	–

[a]"Bottom" means bottom part of nominal range, "center" means center part of nominal range, "top" means top part of nominal range, "indiff." means neither a function of signal strength or altitude.
[b]Retrieval errors range from minimum value when correction is successful, to maximum value when correction is unsuccessful or absent.
[c]Coincidence errors range from minimum value when spatio-temporal coincidence is good and/or number of samples is high, to maximum value when spatio-temporal coincidence is poor and/or number of samples is low.

Some of the procedures listed above can also be combined if daytime sky background data are acquired, and by assuming that the solar spectrum transmitted through the atmosphere is well-known (Sherlock et al. 1999b). In principle, this method is similar to that using a calibrated lamp except that diffused sunlight is used as the light source. It has the advantage of using the same geometry as used for the actual measurement of atmospheric water vapour. However, the fraction of the solar spectrum transmitted through the atmosphere at each of the water vapour and nitrogen wavelengths and collected by the telescope must be known accurately. It therefore requires a thorough knowledge of atmospheric aerosol composition, which is usually not accessible.

7.3.3.2 External Calibration

Given an appropriate lidar experimental configuration and assuming clean skies, the range and/or wavelength dependence of the terms κ_O,κ_σ and κ_α in Eq. 7.8 can be minimized or estimated. The ratio $R(r)$ is then directly proportional to water vapour mixing ratio $q(r)$, and a simple normalization of this ratio to an externally measured

reference value is only needed. In this case the accuracy of the lidar measurements will not only depend on the experimental set up, but also on the accuracy of the external measurement, and on the accuracy of the normalization procedure. In theory the simplest procedure is to use a high quality in-situ hygrometer measurement on the ground next to the lidar and normalize the lidar profile to this ground value. In practice this cannot be achieved because the lidar is blind in the first one to a few hundreds of meters above the site. Additionally, the signal collected from the lowest layers is likely to be affected by incomplete beam-telescope fov overlap and/or saturation effect. Most currently existing external calibration procedures use either a water vapour measurement well above the lidar site, or a ground-based measurement of column integrated water vapour. These are briefly reviewed now.

1. *Calibration using balloon-borne measurements*:
   Since they are widely accessible, and relatively inexpensive, meteorological operational radiosondes provided the first external measurement source to calibrate early water vapour Raman lidar systems (Cooney 1972; Melfi 1972). Today, despite a growing awareness of several limitations in their use, they still remain the preferred choice of most lidar researchers. The accuracy of the best radiosonde measurements over the past two decades ranges from 3 % to 10 %, and is highly dependent on the type of sensor, on altitude, and on atmospheric conditions. For some manufacturers, sensor type and/or instrument setup has changed several times in the past decades, each new version bearing its own systematic biases (Miloshevich et al. 2006). Hence, these changes have caused discontinuities in various long-term water vapour records (Wang and Zhang 2008). These discontinuities logically propagate to the lidar profiles that use them for calibration.
   Another large source of error in the determination of the lidar calibration constant using radiosonde is sampling. The lidar samples a single column of the atmosphere and the measurement is integrated over time, while the radiosonde measurement is instantaneous on board a balloon drifting away from its launch site. The naturally high temporal and spatial variability of atmospheric water vapour combined with the non-simultaneity and non-collocation of the lidar and radiosonde measurements can lead to calibration errors reaching 15–20 % for a radiosonde launched from the lidar site (Leblanc and McDermid 2008a). Using the measurement of a radiosonde launched more than 30 km away from the lidar site is not recommended. Using a single launch to determine the lidar calibration constant is also not recommended. Finally, some radiosonde measurements have altitude-dependent biases (Miloshevich et al. 2004, 2009). If the altitude at which the lidar profiles are normalized changes from profile to profile, then an additional calibration error is introduced in the lidar profiles.
   Some of the measurement biases found with operational radiosondes do not exist for research-grade hygrometers such as the Cryogenic Frost-Point Hygrometer (CFH) (Voemel et al. 2007), the NOAA Frost-Point Hygrometer (Oltmans 1985), and the FLASH-B Lyman-α instruments (Yushkov et al. 1998) (see Chaps. 2 and 3 of this book). They are preferred instruments for measurements in the upper

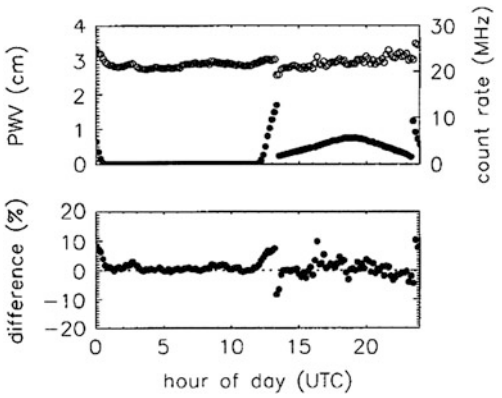

Fig. 7.8 Precipitable Water Vapour (PWV) computed from the CART Raman lidar profiles and difference with co-located microwave (from Turner and Goldsmith 1999). The discontinuity at 13:00 UT corresponds to the automatic system setup change between nighttime (0:00–13:00) and daytime (13:00–24:00) (no longer present since 2005 (Newsom et al. 2009)

troposphere and lower stratosphere (Miloshevich et al. 2009). However, their cost is prohibitive to be used routinely and they are usually launched on a research campaign basis only. The uncertainties associated with sampling are identical to those mentioned for the meteorological radiosondes. Consequently there is little advantage in preferring them to the radiosondes for the only purpose of lidar calibration.

2. *Calibration using ground-based column-integrated water vapour measurements*: Over the past decade, several techniques have emerged to retrieve atmospheric integrated water content from the ground. The first mention of the use of such a technique for systematic water vapour Raman lidar calibration is by (Turner and Goldsmith 1999). The water vapour content of the uncalibrated lidar profile is integrated and scaled against the column water vapour measurement of a co-located microwave radiometer (Han et al. 1994). An example of the calibration variability throughout a 24 h continuous measurement series is given in Fig. 7.8. The top plot shows the lidar-calibrated precipitable water vapour (PWV, open circles), the bottom plot shows the difference with the microwave-measured PWV. The filled circles on the top plot characterize the sky background (increased during daytime from 12 UT to 24 UT). The total water vapour column can be retrieved by microwave with an uncertainty of about 3–7 % (Westwater et al. 1989). Total precipitable water can also be retrieved by GPS (Bevis et al. 1992). The accuracy of the GPS water product is reported to be around 5–10 %.

In both the GPS and microwave cases, the lidar calibration accuracy is limited by that of the external measurements, but also by the lack of lidar measurement in the lowermost layers causing the lidar integrated column to be only partial. Though the altitude fraction of the missing information is small, the water content fraction can be large because the lowest layers are also the moistest and contribute most to the total column. Finally, the GPS or microwave instruments do not necessarily look at the zenith like a typical lidar and any measurement off-zenith will introduce an error due to non-co-location similar to that mentioned for radiosonde, though not as large because more weight is being applied to the lower layers which are closer in distance to the lidar site than the upper layers. Overall, the lidar calibration using integrated

water vapour measurements does not yield a better accuracy than that obtained when using simultaneous and co-located radiosondes.

7.3.3.3 Hybrid Calibration for Routine Measurements and Long-Term Stability

Neither the independent nor external calibration methods reviewed above is well adapted if taken alone to the combined need for accuracy and long-term stability (which is required for applications such as the routine and long-term monitoring of atmospheric water vapour). The internal calibration is time consuming, requires significant experimental efforts, and can disturb considerably the experimentation setup. It is, therefore, not achievable on a routine basis. Calibration values calculated from single radiosonde launches can be subject to large errors due to the non-simultaneity and non co-location of the lidar and radiosonde measurements. Multiple radiosonde launches are necessary to increase the statistics and reduce these errors, which can become expensive if performed on a daily basis. Finally, calibration using ground-based microwave or GPS measurements of vertically integrated water vapour can be considered only if the lowermost layers are well covered by the lidar, which rarely happens in practice.

A proper combination of internal and external calibration can address the need for both accuracy and long-term stability. This hybrid method combines the daily use of one (or two overlapping) laboratory calibrated lamp(s) permanently mounted over the lidar receiver, and the occasional deployment of campaigns for external calibration (typically once a year). The lamp is used daily for a partial calibration of the lidar receiver that is "transferred" into absolute calibration during the campaigns (Leblanc and McDermid 2008a). The partial calibration requires only a few minutes illumination of the receiver by the lamp with the laser blocked or turned off and the roof hatch closed, just before and after each routine water vapour measurement. The ratio of the signals collected by the water vapour and nitrogen channels is monitored daily between the absolute calibration campaigns, then converted ("transferred") to absolute calibration during the campaigns. It is assumed that the fraction of the optical system monitored by the lamp reflects changes in the entire optical system. The method is valid only if the ratio of the lamp irradiance at the water vapour and nitrogen channels wavelength remains constant or drifts only slowly with time between two campaigns, and if the transfer of the partial calibration to the campaign-averaged absolute calibration is performed throughout undisturbed experimental conditions. The 10 - month monitoring of the partial calibration constant shown in Fig. 7.9 (from (Leblanc and McDermid 2008a)) reveals a drift not exceeding 0.11 % between times of planned instrumental change, which corresponds to a decadal drift of 1 %.

The hybrid method has the double advantage of routinely identifying any fine variations in the lidar receiver transmission ratio (partial calibration), and optimizing the absolute calibration (multiple balloon launches reduce the sample error). Furthermore, the transfer of the partial calibration ensures that the absolute calibration is not constrained by additional theoretical and/or technical difficulties already mentioned,

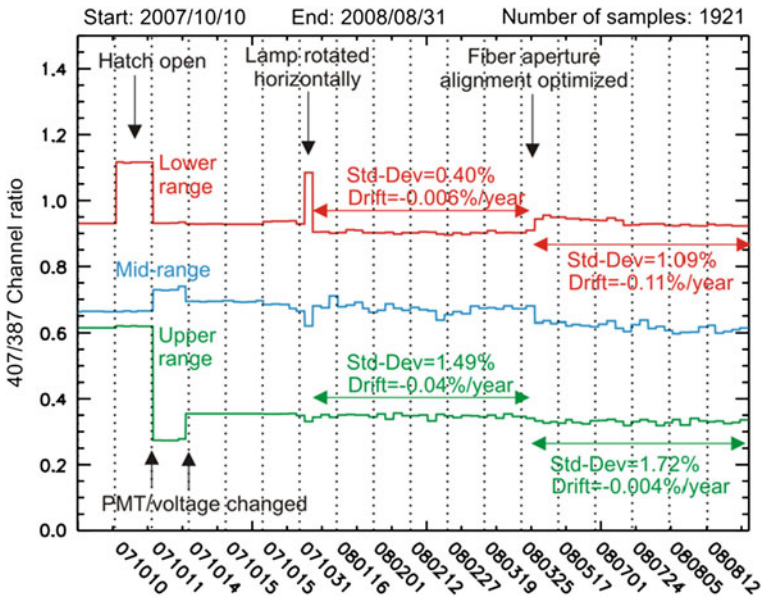

Fig. 7.9 Time evolution of the JPL Table Mountain water vapour Raman lidar receiver partial calibration constants obtained during the so-called lamp runs (from (Leblanc and McDermid 2008a)) (see text for details). The system includes three pairs of channels (high-intensity in *green*, low-intensity and narrow fov in blue, and low-intensity and wide fov in *red*). The bottom axis is not a linear function of time

such as the accurate determination of the absolute transmission and efficiencies of the lidar receiver, the accurate knowledge of illumination geometry.

7.3.4 Precision

Precision is defined here as the total error limiting the repeatability of the measurement given a frozen atmosphere, i.e., typically the standard deviation that would be obtained if a lidar system was repeatedly sensing the same atmosphere over and over. As mentioned in Sect. 7.3.2, the collected signal is a combination of signal from backscattered light and noise from electronics and sky background, which can be expressed:

$$S_{H_2O} = P_{H_2O} + n_{H_2O} \qquad \text{and} \qquad S_{N_2} = P_{N_2} + n_{N_2}$$

The precision is mainly deduced from the random noise associated with the photon counting process. The counting process follows the statistics of the well-known Poisson distribution, and the absolute precision for each detection channel can be

expressed by:

$$\Delta S_{H_2O} = \sqrt{S_{H_2O}} \qquad \text{and} \qquad \Delta S_{N_2} = \sqrt{S_{N_2}}.$$

The relative precision of the measurement for each channel can be deduced from Eqs. 7.6a and 7.6b with the assumption that there is no random error associated with the saturation and atmospheric extinction corrections:

$$\frac{\Delta P_{H_2O}}{P_{H_2O}} = \frac{\Delta S_{H_2O}}{P_{H_2O}} = \frac{\sqrt{S_{H_2O}}}{S_{H_2O} - n_{H_2O}} \qquad \text{and} \qquad \frac{\Delta P_{N_2}}{P_{N_2}} = \frac{\Delta S_{N_2}}{P_{N_2}} = \frac{\sqrt{S_{N_2}}}{S_{N_2} - n_{N_2}}.$$

Following Eq. 7.8 and the laws of error propagation, the resulting relative precision on water vapour mixing ratio can be written:

$$\frac{\Delta q}{q} = \sqrt{\frac{S_{H_2O}}{\left(S_{H_2O} - n_{H_2O}\right)^2} + \frac{S_{N_2}}{\left(S_{N_2} - n_{N_2}\right)^2}}.$$

At very high count rates (lower part of the atmosphere), the relative error due to photon counting is negligible, and in normal operating conditions, precision at these altitudes always remains within 0.5 %.

7.3.5 Accuracy

The accuracy of the water vapour Raman lidar measurements strongly depends on the method of calibration. For an independent absolute calibration, the accuracy results from many uncertainties: instrumentation manufacturing specifications, determination of the overlap functions, signal absolute transmission through the receiver, and accuracy of the water vapour and nitrogen Raman cross-sections. As discussed earlier, the total error in the water vapour measurements using independent calibration can easily reach 12–15 %. It can be reduced to about 5–7 % by using accurate external measurements and an adequate method for the normalization of the lidar signal to the external measurements (large enough statistics). The various error sources associated with the measurement of water vapour by Raman lidar and their magnitude are compiled in Table 7.2.

After calibration (including the determination of the overlap function), the next largest systematic errors are caused by fluorescence of the Rayleigh-backscattered signal in the lidar receiver, by inadequate (or no) atmospheric extinction correction, inadequate background noise extraction, and inadequate saturation correction. Because Raman scattering is more than three orders of magnitude smaller than Rayleigh scattering, and because water vapour mixing ratio falls down to a few parts-per-million in the upper troposphere, residual fluorescence of any of the receiver optics will critically impact the signal received in the water vapour channel. For measurements in the upper troposphere, this fluorescence must be suppressed as early as

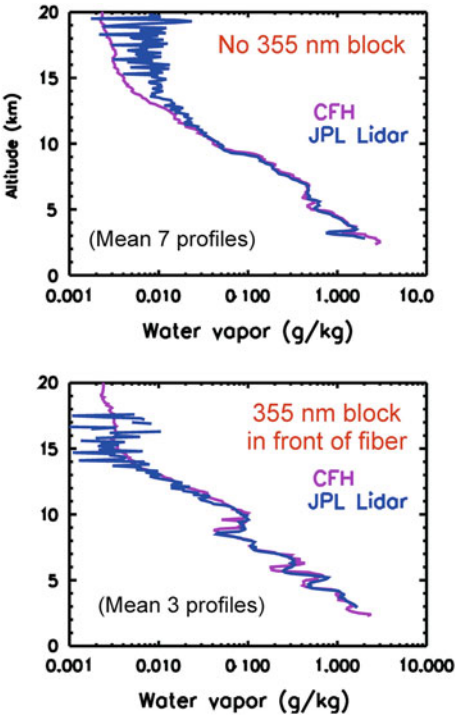

Fig. 7.10 Effect of signal contamination by fluorescence (adapted from Leblanc et al. 2008b). *Top* Average of seven profiles measured with no anti-fluorescence optics in the receiver. *Bottom* Average of three profiles measured with a temporary 355 nm blocking filter at the entrance of the lidar receiver. The Cryogenic Frost-Point Hygrometer (CFH) sondes were launched from the lidar site and constitute the reference

possible in the receiver entrance, and the overall rejection factor must reach 10^{12} to avoid contamination caused by strong Rayleigh return above 10 km. The excess signal due to contamination by fluorescence causes a significant wet bias in the lidar profile. For a conventional Raman lidar (i.e., not including specifically dedicated anti-fluorescent optics), water vapour mixing ratio can easily be overestimated by 10 % at 10 km, increasing upward (Leblanc et al. 2008b). Figure 7.10 illustrates the effect of contamination by fluorescence in the case of the JPL system at Table Mountain in October 2007. The top plot shows an average of seven water vapour profiles obtained with no anti-fluorescence optics in its receiver. The bottom plot shows an average of three profiles obtained with a 355 nm blocking filter placed at the entrance of the receiver, which prevents strong Rayleigh returns causing fluorescence downstream. The profiles are compared against simultaneous CFH measurements, considered here as the reference.

For noise extraction, the error can reach 20–50 % at the top of the profile if signal-induced noise is interfering with the atmospheric signal. For saturation correction, it can reach 15 % at the bottom of the profile if highly saturated signals are used and not well corrected. An appropriate lidar experimental configuration must be chosen to reduce these errors as much as possible (typically down to 1 %)

Table 7.3 Historical[a] overview of water vapour Raman lidar

Year	Bibliographical reference	Laser used	Featuring	σ_H/σ_N ratio[b]	Calibration method
1928	Raman, Nature		Raman Scattering		
1960	Maiman, Nature		First laser (Ruby)		
1967	Leonard, Nature	N_2 (337 nm)	N_2 up to 1 km		
1968	Cooney, APL	Ruby (694 nm)	N_2 up to 3 km		
1969	Melfi, APL	Ruby × 2 (347 nm)	H_2O up to 2 km		Not reported
1970	Cooney, JAM	Ruby × 2 (347 nm)	H_2O up to 2.5 km		Not reported
1971	Cooney, JAM	Ruby × 2 (347 nm)	H_2O up to 2 km	5.1 (75 %)	Sonde (10 %)
1972	Melfi, AO	Ruby × 2 (347 nm)	H_2O up to 2 km	3.8 (25 %)	Sonde
1976	Bribes, APL	Raman $H_2O(T)$ ν_1 band	F(T)		
	Penney, JOSA	Raman $H_2O(T)$ ν_1 band	2.5 (10%)		
1979	Pourny, AO	Ruby × 2 (347 nm)	H_2O up to 1.8 km		Independent
1980	Renaut, OL	Nd:YAG × 4 (266 nm)	H_2O daytime up to 1 km		Independent
1985	Cooney, AO	KrF × 3 (248 nm)	H_2O daytime up to 1 km		Not reported
	Melfi, BAMS	Nd:YAG × 3 (355 nm)	H_2O up to 5 km		Sonde
1988	Vaughan, QJRMS	Nd:YAG × 3 (355 nm)	H_2O up to 8 km		Independent
1989	Melfi, JAM	Nd:YAG × 3 (355 nm)	H_2O up to 7 km		Sonde
1992	Ansmann, AP-B	XeCl (308 nm)	H_2O daytime up to 2 km		Not reported
	Whiteman, AO	Nd:YAG × 3 (355 nm)	H_2O up to 7 km		Sonde
1993	Whiteman, OL			F(T)	
1994	Goldsmith, BAMS	XeF/KrF (351/248 nm)	H_2O daytime up to 1 km		Sonde
	Bisson, OSA Tech	XeCl (308 nm)	H_2O daytime up to 4 km		Not reported
	Digest Rajan, GRL	Nd:YAG (355/532 nm)	H_2O up to 5 km		Sonde
1995	Ferrare, JAOT	XeF (351 nm)	H_2O daytime up to 10 km with detailed error assessment		Sonde × 2
1996	Heaps, AO	XeF (351 nm)	Airborne system		Not reported
1998	Goldsmith, AO	Nd:YAG × 3 (355 nm)	H_2O up to 10 km		Sonde(IOP)
1999	Turner, JAOT	Nd:YAG × 3 (355 nm)	H_2O up to 10 km		Microwave (3 %)
	Bisson, AO	XeCl (308 nm)	H_2O up to 4 km		Sonde
	Sherlock, AO-a and b	Nd:YAG × 2 (532 nm)	H_2O up to 10 km		Independent
2000	Ansmann, JAOT	Multi-laser	Multi-Raman		Sonde
2001	Whiteman, AO		Model aircraft, Ram vs. DIAL		
2002	Turner, JAOT	Nd:YAG × 3 (355 nm)	Automated 24 h H_2O		Microwave
2003	Whiteman, AO-a and b	Nd:YAG × 3 (355 nm)	Review	F(T)	Sonde
	Pappalardo, SPIE		Satellite validation, networking		Sonde
2004	Avila, JMS			F(T)	
2008	Leblanc, JAOT	Nd:YAG × 3 (355 nm)	H_2O up to 15 km		Sonde
	Leblanc, AO		Calibration		Hybrid

[a] Non-exhaustive list which reflects successive advances made in the field, such as new lasers, improved performance, new calibration method, new applications, etc.

[b] The "σ_H/σ_N ratio" column refers to progress made in the determination of the Raman cross-sections

7.3.6 *Historical, Platforms, Geometry, Cost, and Transportability*

Table 7.3 contains a non-exhaustive chronological summary of the main advances made in connection with the measurement of water vapour by Raman lidar. Among these table entries, some are noteworthy: the determination of the water vapour and nitrogen cross-section ratio by (Penney and Lapp 1976) remains one of the most accurate to date, (Melfi and Whitemann 1985) demonstrated the usefulness of the

technique for meteorological applications. Today the largest fraction of existing water vapour Raman lidars is dedicated to measurement in the lower troposphere, and in conjunction with aerosol measurements (De Tomasi and Perrone 2003). These instruments are ground-based systems with only one pair of channels specifically dedicated to the measurement of water vapour. The required laser power for these systems is moderate and the collecting area typically consists of a telescope with a diameter smaller than 60 cm, and a wide enough aperture/field-of-view to collect signals backscattered in the lowest 500 m of the atmosphere. Most of these systems were not designed to be transportable. However, the instrumentation involved allows them to be built in a compact enough way to fit in a truck trailer. Most systems' line of sight is zenith. A few lidars operate at angles ranging from zenith to less than 30 degrees elevation, but, again the measurements in these cases are dedicated to the study of the boundary layer, not the UT/LS. There are less than ten Raman lidar systems worldwide currently dedicated to the measurement of water vapour in the free troposphere or the UT/LS. All these systems are zenith pointing and all include large telescope areas and high power lasers.

Almost all water vapour Raman lidars are currently ground-based. The design and deployment of such systems onboard aircraft is extremely rare (Heaps and Burris 1996; Whiteman et al. 2010). No space-borne Raman water vapour lidars is currently operated or projected.

Compared to other research grade instruments, and especially compared to airborne and space borne instruments, a Raman lidar is relatively inexpensive. The two major upfront costs are for the laser and a large-size high-quality telescope. The normal operating cost and the annual maintenance/repair cost are low (limited manpower required, especially if the system is semi- or fully automatic). Airborne systems are not much more expensive, but the high end-to-end cost of an airborne system lies principally in the aircraft operation.

7.3.7 Temporal and Vertical Resolution and Range, and weather dependence

The temporal and vertical resolutions of current water vapour Raman lidars vary widely depending on the instrument, atmospheric conditions, and type of application. They range from integration over a few minutes and/or vertical resolution of a few meters for studies of the boundary layer, to measurement times of several hours and/or a vertical resolution of several kilometers for climatological studies and long-term monitoring in the UT/LS. Table 7.4 summarizes various past and present configurations of the technique and their corresponding applications.

Like most lidar techniques the Raman technique works best during nighttime under clear-weather and clean-sky conditions. Measurements are possible in the presence of thin aerosols, and in the presence of thin clouds. The presence of thicker aerosols (major volcanic eruption, or thick fire or pollution plumes) requires a careful extinction correction. Measurements are still possible in clouds optically thin enough

Table 7.4 Typical characteristics of past and present water vapour Raman lidar systems

Laser	λ_{out} (nm)	λ_{H_2O} (nm)	λ_{N_2} (nm)	PAP (Wm[a])	Bibliographical reference	Vertical resolution (m)	Integration time (min)	Range (km)	Application
KrF	248	264	273	0.67[a]	Cooney, AO, 1985	< 10	< 5	1(day)	BL
				0.18[a]	De Tomasi, NCC, 2000	15	30	1.2(day)	BL
4 × Nd:YAG	266	284	295	0.22[a]	Renaut, JAOT, 1988	30	~8	2.5(day)	BL
XeCl	308	332	347	34[a]	Ansmann, AP-B, 1992	60	< 2	9(night)	BL to LT
						200	10–15	2(day)	BL 24 h
				23[a]	Bisson, AO, 1999	75	5	10(night)	LT
						75	10	4(day)	BL 24 h
				8[a]	Goldsmith, BAMS, 1994	75	10	6	BL to LT
2×Ruby	347	378	399	0.0005[a]	Pourny, AO, 1979	30	20	2	BL
XeF	351	382	403	1.8[a]	De Tomasi, JGR, 2003	15	45	5	BL to LT
				8[a]	Goldsmith, BAMS, 1994	75	10	7	BL to LT
3 × Nd:YAG	355	387	407	5.5[a]	Whiteman, AO, 2008	15	30	15	BL to LS
				4.2	Leblanc, JAOT, 2008	75	120	15	LT to LS
				3.3[a]	Pappalardo, SPIE, 2003	60	10	10	BL to UT
				3.1[a]	Turner, JAOT, 2002	78	10	8 (night)	BL to UT
								3.5(day)	BL 24 h
2 × Nd:YAG	532	607	660	4.3	Barnes, Person. Comm.	300	120	14	LT to UT
				7.5[a]	Sherlock, AO, 1999	75	>60	10	LT to UT

BL Boundary layer, *LT* Free Troposphere (lower), *UT* Upper troposphere, *LS* Lower stratosphere.
[a] As reported in referenced publication.

to allow laser beam transmission through them. Daytime measurements in the lower troposphere are possible if the lidar operates in the ultraviolet and uses spectrally narrow filters (Renaut et al. 1980; Cooney et al. 1985; Ansmann et al. 1992b; Goldsmith et al. 1994; Turner et al. 2002). The signal-to-noise ratios achieved with existing lidar power-aperture products do not currently allow daytime measurements of water vapour in the UT/LS.

7.3.8 Caveats and bottlenecks

As mentioned previously, the most powerful water vapour Raman lidar systems currently in use reach their detection limit in the UT/LS. The best existing systems have a detection threshold of 2–4 ppmv for one-hour integration. This corresponds to 50 % error under moist upper troposphere conditions (midlatitudes), and 100 % error in drier conditions (tropical tropopause layer). However this limitation is expected to wane in the next decade as higher commercial laser power becomes available, increased efficiency of the optical and electronic components is expected, and as future lidar systems' optimization increases signal-to-noise ratio. Another limitation is the calibration error. Besides a foreseeable progress in the accurate determination of water vapour cross-sections, there is no significant progress to be expected in the determination of the lidar calibration constant using an internal approach. The accuracy of the measurement is, therefore, subjugated to that of the external calibration methods, and, in particular, to that of the external source of measurement used.

7.3.9 Future Potential

Three key components ultimately determine the performance of a lidar: The power aperture product (PAP) which is the product of the laser power at the emitted wavelength by the effective area of the receiving telescope (expressed in Wm^2), the receiver overall efficiency which ranges from 10^{-3} to 0.15 depending on the instrument, and the noise level, which depends on wavelength, the telescope aperture, and the purity of the electronics (sky light and atmospheric conditions are not considered here).

Within the next ten years, significantly more powerful lasers are expected to be used at several stations, and more efficient receiver components will be available. Major design efforts can also be made to reduce the sources of signal loss and contaminating noise. If a factor of ten can be gained in the signal-to-noise ratio, this would allow a detection limit better than 0.2 ppmv, and an altitude range increased by 5–10 km for typical UT/LS water vapour mixing ratio and sky background noise values. Table 7.5 summarizes the performance of a few examples of current and future Raman lidars dedicated to water vapour measurement in the UT/LS, as simulated using their instrumental characteristics, and assuming climatological winter (dry) and summer (wet) water vapour profiles. "MLO" refers to the NOAA lidar at Mauna

Table 7.5 Key instrumental parameters of selected existing and projected lidar systems

	Elev. (m)	λ_{OUT} (nm)	Pulse energy (mJ)	Rep. rate (Hz)	Telesc. Diam. (m)	PAP (Wm^2)	Receiv. eff.
MLO	3400	532	330	30	0.74	4.3	0.01
TMW	2285	355	620	10	0.91	4.0	0.05
REU[d]	2100	532	800	30	1.20	27	0.16
Predicted 2020[e]	2000	355	1000	50	1.20	30	0.43

	Integr. time (min)	Vert. res. (m)	NFDL[a] (ppmv)	Detection range[b] (km)	z(10 %)[b] DRY (km)	z(10 %)[c] WET (km)
MLO	60	300	2.3	15	10.0	10.6
TMW	60	75	1.8	18	10.7	11.4
REU[d]	60	75	< 1.5	> 22	12.5	13.4
Predicted 2020[e]	120	75	< 1.5	> 27	17	18.0

[a] *NFDL* Noise-free Detection Limit, H_2O mixing ratio required to provide 1 photon count per bin for the given integration time assuming noise-free signals
[b] Detection Range, Altitude at which detection limit is reached
[c] z (10 %), Altitude at which precision drops below 10 % (as computed with sky background level typical of new moon)
[d] REU, Projected instrumental parameters (system to start operation in 2012)
[e] Predicted 2020, Based on current rate of technological progress (lasers, optics, telescopes)

Loa Observatory, Hawaii (Barnes et al. 2008). "TMW" refers to the JPL Raman lidar at Table Mountain Facility, California (Leblanc et al. 2012). "REU" refers to the future Rayleigh/Raman lidar to be deployed at the high-altitude observatory of Maïdo (French overseas territory of Reunion Island, Indian Ocean) (Hauchecorne, Personal Communication, 2008). "Predicted 2020" refers to a projected high performance lidar equipped with the best available commercial technology in 2020. The Noise-free Detection Limit (NFDL) reported in Tab. 7.5 is the lowest mixing ratio that would cause the lidar to detect an average of 1 photon per altitude bin during the reported integration period.

Because of the emerging potential of this technique, the international Network for the Detection of Stratospheric Composition Change (NDACC, formerly NDSC) has recently included Raman lidar among its suite of instruments for the long-term monitoring of water vapour in the UT/LS. Based on today's systems capability, the number of available systems, and future progress in their technology, the first estimates of water vapour interannual variability in the UT/LS using Raman lidar are not expected to occur until at least 2015. However, from that point on, Raman lidar will constitute one of the most reliable sources of long-term water vapour measurement in the UT/LS, with an expected significance comparable to that of the renowned DIAL ozone and temperature lidar measurements made in the framework of NDACC over the past two decades.

7.4 Water-Vapour Sounding with Differential-Absorption Lidar Systems

The development of differential-absorption lidar (DIAL) systems to measure the vertical distribution of water vapour has a history of more than three decades (Schotland 1966; Murray et al. 1976; Browell et al. 1979, 1981; Cahen et al. 1982; Zuev 1983; Grant et al. 1987; Bösenberg et al. 1991; Ehret et al. 1993; Higdon et al. 1994; Senff et al. 1994; Sachse et al. 1995; Moore et al. 1996; Browell et al. 1996; Wulfmeyer et al. 1998a; Ehret et al. 1999; Bruneau et al. 2001a; Bruneau et al. 2001b; Little et al. 2001; Nagasawa et al. 2001; Browell et al. 2001; Poberaj et al. 2002; Ertel et al. 2004; Machol et al. 2004; Flentje et al. 2005; Ertel et al. 2005; Linné et al. 2006; Kiemle et al. 2008; Wirth et al. 2009). Because of the strong light absorption in moist layers, ground-based DIAL measurements have been limited more or less to the lower troposphere, whereas DIAL sounding in the very dry upper troposphere and lower stratosphere has been the privilege of air-borne lidar systems operated on significantly stronger absorption lines of H_2O. Apart from the strong light absorption in the moist boundary layer the principal range limitation of ground-based systems has been due to low laser power, until the early 1990s determined by the use of dye lasers and small receivers. Wulfmeyer and Bösenberg (1998b) emphasize that making the laser and receiver specifications of a DIAL comparable to those of a Raman lidar would result in a similar performance, but with the great advantage of a much better daytime operating range.

The only ground-based DIAL system so far fulfilling the important goal of reaching the upper troposphere was recently described by (Vogelmann and Trickl 2008). This system, operated at the NDACC site of Garmisch-Partenkirchen/Zugspitze in the German Alps, currently combines a laser pulse energy of up to 250 mJ with a receiving telescope of 0.65 m diameter. Similarly important, the lidar laboratory is located at an altitude of 2,675 m at the Schneefernerhaus high-altitude station on the south-western slope of the Zugspitze. This offers the advantage of avoiding major light losses caused by absorption in the moist boundary layer. In this section we use the results for the Zugspitze DIAL system in order to characterize the potential of the DIAL method for ground-based measurements throughout the free troposphere.

7.4.1 The DIAL Method

Due to a spectrum with well-resolved absorption lines the H_2O molecule is particularly well suited for DIAL measurements, the only disadvantage being the moderate atmospheric backscatter coefficients in the near infrared (IR). As an example Fig. 7.11 shows the section of the absorption spectrum of H_2O around 817.2 nm, within the preferred absorption band in several DIAL systems. One laser wavelength is set to a specific line centre leading to light absorption in the atmosphere ($\lambda_{E1} = \lambda_{D1} = \lambda_{on}$). A second wavelength (reference wavelength) is chosen in a nearby region with minimum absorption, as indicated in Fig. 7.11 ($\lambda_{E2} = \lambda_{D2} = \lambda_{off}$). The approach is highly

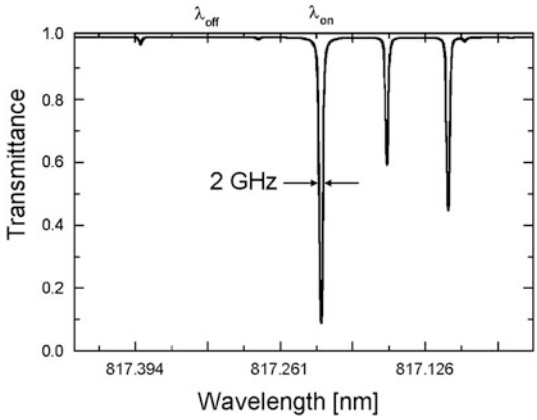

Fig. 7.11 Spectrum of H_2O near 817 nm calculated for 0.1 bar air at 230 K, a H_2O volume mixing ratio of 1 % and a path length of 1 km using HITRAN (Rothman et al. 2003, 2005); the "on" and "off" wavelength positions are indicated

substance-specific since other trace constituents with sharp spectral signatures are easily separated by an appropriate line selection.

Keeping the notations used in Sect. 7.2, the Rayleigh lidar equation, Eq. 7.3, can now be written for each wavelength:

$$P_i(r) = P_{E1}(\lambda_i)\,\kappa_L(\lambda_i)\,\frac{O_i(r)\,A_L\delta r}{r^2}\beta(r,\lambda_i)\,t_\uparrow(r,\lambda_i)\,t_\downarrow(r,\lambda_i), \qquad i = on, off. \tag{7.9}$$

For an appropriate optical design O_{on}/O_{off} is independent of altitude for rather short distances, and using the notations and definitions of Sect. 7.2 a simple transformation and combination of these two equations yields:

$$\frac{\mathrm{d}}{\mathrm{d}r}\left[\ln\left(\frac{P_{on}(r)}{P_{off}(r)}\right)\right] = \frac{\mathrm{d}}{\mathrm{d}r}\left[\ln\left(\frac{\beta(r,\lambda_{on})}{\beta\left(r,\lambda_{off}\right)}\right)\right] - \left[\alpha_\uparrow(r,\lambda_{on}) + \alpha_\downarrow(r,\lambda_{on}) - \alpha_\uparrow\left(r,\lambda_{off}\right) - \alpha_\downarrow\left(r,\lambda_{off}\right)\right]. \tag{7.10}$$

The total backscatter coefficient β can be expressed as the sum of particulate and molecular (Rayleigh) backscatter $\beta = \beta_R + \beta_P$, and the total extinction α along the beam path can be expressed as the sum of particulate extinction, molecular scattering, and molecular absorption $\alpha = \alpha_R + \alpha_P + \alpha_a$. For a water-vapour DIAL the wavelengths may be selected closely spaced so that the absorption differential between the *on* and *off* wavelengths is reduced to that of water vapour only ($\alpha_a = \alpha_{H_2O,\uparrow} + \alpha_{H_2O,\downarrow} = \sigma_\uparrow N_{H_2O} + \sigma_\downarrow N_{H_2O}$), where σ is the absorption cross-section of water vapour, and N_{H_2O} its number density. σ is altitude dependent due to the changing line broadening as a function of pressure and temperature. This dependence was neglected in the general form of the lidar equation described in Sect. 7.2. In Eq. 7.10 the influence of broad-band processes, such as light backscattering by aerosols, is mostly avoided by taking the ratio of the two backscatter signals.

Additionally, the Rayleigh and particle backscatter and extinction coefficients for both wavelengths are essentialy equal, and Eq. 7.10 may therefore be simplified to

$$\frac{\mathrm{d}}{\mathrm{d}r}\left[\ln\left(\frac{P_{on}(r)}{P_{off}(r)}\right)\right] = -\left(\sigma_{\uparrow}(r,\lambda_{on}) + \sigma_{\downarrow}(r,\lambda_{on}) - \sigma_{\uparrow}\left(r,\lambda_{off}\right) - \sigma_{\downarrow}\left(r,\lambda_{off}\right)\right) N_{H_2O}(r).$$

Rearranging this equation yields the so-called DIAL equation for the number density of water-vapour:

$$N_{H_2O}(r) = -\frac{1}{\Delta\sigma_{\uparrow}(r) + \Delta\sigma_{\downarrow}(r)} \frac{\mathrm{d}}{\mathrm{d}r}\left[\ln\left(\frac{P_{on}(r)}{P_{off}(r)}\right)\right] \tag{7.11}$$

where $\Delta\sigma_{\uparrow}(r) = \sigma_{\uparrow}(r,\lambda_{on}) - \sigma_{\uparrow}\left(r,\lambda_{off}\right)$ and $\Delta\sigma_{\downarrow}(r) = \sigma_{\downarrow}(r,\lambda_{on}) - \sigma_{\downarrow}\left(r,\lambda_{off}\right)$.

The differences in the upward and downward coefficients are caused by the Rayleigh-Brillouin broadening of the backscattered narrow-band laser light (Fiocco and Wolf 1968; Fiocco et al. 1971). The bandwidth becomes comparable with the atmospheric absorption line width of H_2O. As a consequence the light absorption is slightly modified on the downward path, leading to different absorption cross sections $\sigma_{\uparrow}$ and $\sigma_{\downarrow}$ for the upward and downward propagation of the light (Ansmann and Bösenberg 1987). This effect is rather small in the case of pure Rayleigh scattering or even negligible for cases dominated by light scattering by aerosols. In the mixed case density errors of more than 20 % may be reached in vertical sections with significant aerosol gradients.

In order to understand this the line-shape functions must be included in the lidar equation. As a consequence both the lidar and DIAL equations become much more complex. Folded integration over different line shapes and the extinction terms, both varying as a function of altitude, is needed.

The aerosol contribution re-enters the expression due to the line-broadening effects (see Fig. 7.12) (Ansmann and Bösenberg 1987; Bösenberg 1998). The Doppler broadening of the laser light by the aerosols is much smaller than that for Rayleigh light backscattering by the atmospheric N_2 and O_2 molecules. To a good approximation, the line shape of the backscattered light is given by:

$$h(r,\nu) = L_{\uparrow}(\nu)\frac{\beta_P(r,\nu)}{\beta(r,\nu)} + L_{\downarrow}(r,\nu)\frac{\beta_R(r,\nu)}{\beta(r,\nu)} \tag{7.12}$$

$L_{\uparrow}$ is the frequency distribution of the laser light assumed to be narrower than one tenth of the absorption line width, $L_{\downarrow}$ the Rayleigh-Brillouin line shape at altitude r, both distributions being normalized to one. The distributions are both centred around the laser frequency ν_L. h is part of the extinction term of the lidar equation and, thus, enters the calculation for the returning light.

The method is described in detail in Bösenberg (1998) and one example of the correction of a free-tropospheric measurement with slightly elevated aerosol is given by Vogelmann and Trickl (2008). The modified DIAL Eq. 7.11 may be written as:

$$N_{H_2O}(r) = \frac{1}{\left(\Delta\sigma_{\uparrow}(r,\lambda_{on}) + \Delta\sigma_{\downarrow}\left(r,\lambda_{off}\right)\right)}\left(G(r,\lambda_{on}) - \frac{\mathrm{d}}{\mathrm{d}r}\left[\ln\left(\frac{P_{on}(r)}{P_{off}(r)}\right)\right]\right) \tag{7.13}$$

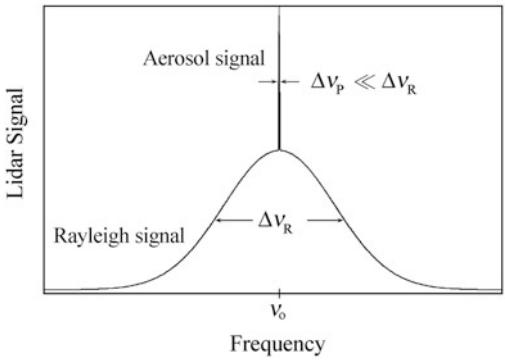

Fig. 7.12 Spectrum of narrow-band laser light backscattered from the atmosphere

with

$$G\left(r,\lambda_{on}\right)=g_1\left(r,\lambda_{on}\right)\frac{\mathrm{d}}{\mathrm{dr}}Q_\beta\left(r,\lambda_{on}\right)+g_2\left(r,\lambda_{on}\right)Q_\beta\left(r,\lambda_{on}\right)$$

The terms g_1 and g_2 are sensitivity factors,

$$g_1=\frac{\int_0^\infty t_\downarrow L_\downarrow \mathrm{d}\nu-\int_0^\infty \mathrm{t}_\uparrow \mathrm{L}_\uparrow \mathrm{d}\nu}{Q_\beta\int_0^\infty t_\downarrow L_\downarrow \mathrm{d}\nu-\left(1-\mathrm{Q}_\beta\right)\int_0^\infty \mathrm{t}_\uparrow \mathrm{L}_\uparrow \mathrm{d}\nu},$$

$$g_2=\frac{\mathrm{d}}{\mathrm{dr}}\left(t_\downarrow L_\downarrow\right)\mathrm{d}\nu,$$

and Q_β is the reciprocal scattering ratio:

$$Q_\beta=\frac{\beta_R}{\beta_R+\beta_P}$$

The main assumptions (Bösenberg 1998) are:

1. The laser bandwidth is almost negligible.
2. The correction factor G for λ_{off} is negligible due to an appropriate wavelength choice in a range with minimum absorption.

The corrections are important only in the presence of significant aerosol, in particular in the region of pronounced concentration gradients. For a water-vapour DIAL operated in the free troposphere the influence of aerosols is mostly rather small.

In practice, the derivative in the DIAL equation is, e.g., calculated by linear least-squares fits centred at the data point of interest. We calculate

$$\frac{\mathrm{d}}{\mathrm{dr}}\ln\left(\frac{P_{on}\left(r\right)}{P_{off}\left(r\right)}\right)=\frac{\frac{\mathrm{d}}{\mathrm{dr}}\left(\frac{P_{on}(r)}{P_{off}(r)}\right)}{\left(\frac{P_{on}(r)}{P_{off}(r)}\right)} \tag{7.14}$$

in order to avoid the density bias caused by the assymetric noise distribution for the logarithm. For equidistant data points the result of the fits may be expressed in a

rather simple formula, resulting in the following solution of the DIAL equation for the i^{th} data point (Vogelmann and Trickl 2008):

$$N_{H_2O,i} = \frac{1}{\Delta\sigma_{\uparrow i} + \Delta\sigma_{\downarrow i}} \left(G_i - \frac{1}{q_i \delta} \frac{\sum_{j=i-k}^{i+k} (j-i)\, q_j}{\sum_{j=i-k}^{i+k} (j-i)^2} \right) \tag{7.15}$$

with $q_i = \frac{P_{on}(r_i)}{P_{off}(r_i)}$, 2k+1 being the number of data points symetrically arranged around r_i included in a single fit, and δr being the size of the altitude bin of the transient digitizer. The denominator may be further simplified by considering that

$$\sum_{j=i-k}^{i+k} (j-i)^2 = \frac{k\,(k+1)\,(2k+1)}{3} \tag{7.16}$$

Using Eqs. 7.15 and 7.16 results in a rather fast computation of the densities. It is advisable to limit the interval size, 2 k, to a moderate value since a least-squares fit is not a perfect numerical filter. *A-posteriori* filtering of the retrieved densities with an optimized, range dependent numerical filter adjusted to the local noise level is the better choice for smoothing.

The calibration of the system is based on absorption cross sections and line parameters for water vapour from the literature. For the Zugspitze system values for the band system around 815 nm accurately determined by (Ponsardin and Browell 1997) are taken. These authors list detailed formulae and parameters for Doppler and pressure broadening, as well as values for the pressure shift. As an example, Fig. 7.13 shows the strong 12,236.56 cm^{-1} line of H_2O for air pressures corresponding to the altitude of the lidar laboratory and the upper troposphere around 10 km. This demonstrates the strong variation of the absorption lines within the troposphere. Although Ponsardin and Browell calculated the correct Galatry line shapes they determined effective Voigt parameters for a more convenient calculation of the spectral lines. Comments on the accuracy of these spectroscopic data may be found further below.

7.4.2 Requirements for Wide-range Tropospheric DIAL Sounding of Water Vapour

DIAL measurements of water vapour are usually performed in the near-IR spectral range where band systems of H_2O are sufficiently weak for avoiding complete absorption on the first kilometre exist at around 720 nm and 815 nm. The next band system at around 935 nm is too strong for ground-based applications, but has been successfully applied even to detecting stratospheric water vapour in an airborne lidar (Ehret et al. 1999; Poberaj et al. 2002; Flentje et al. 2005; Kiemle et al. 2008). For shorter wavelengths, where Rayleigh backscattering strongly increases, no suitable

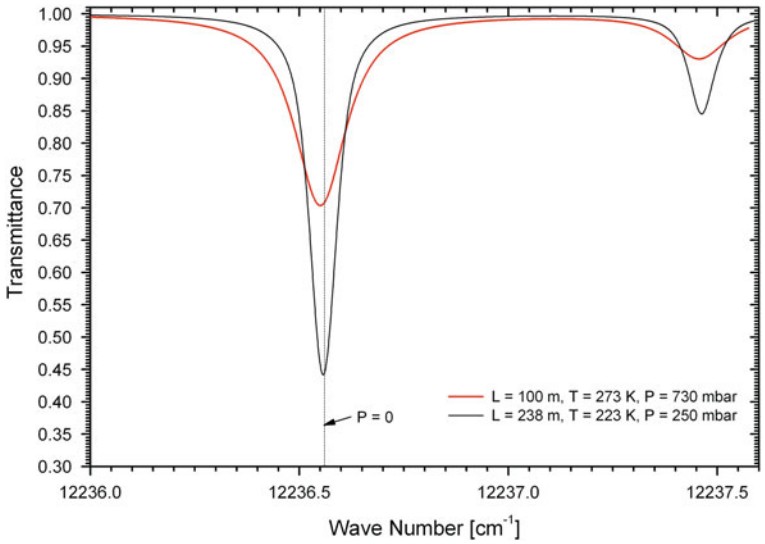

Fig. 7.13 Atmospheric transmittances in water vapour in the vicinity of 817 nm calculated with HITRAN data for conditions typical of the Schneefernerhaus research station (lidar: 2,675 m a.s.l.) and roughly 10 km and approximately equivalent absorption paths L. The pressure shifts were taken from (Ponsardin and Browell 1997)

band systems of H_2O are available. The atmospheric line widths of water vapour in the wavelength range around 800 nm are about 2–4 GHz. As a consequence, a tunable pulsed laser system with a bandwidth not exceeding 0.2 GHz (i.e., 5×10^{-7} of the laser frequency), and an even higher frequency stability is required. Most importantly, a spectral purity of the laser emission of at least 99.8 % is needed for avoiding significant light transmission outside the spectral line used for the measurement.

Dye lasers have been the most important sources of narrow-band tunable radiation. However, due to the lack of suitable pump lasers exiting the dye fluorescence, the near-IR single-pulse light energies of dye lasers do not exceed 100 mJ although energies of up to 220 mJ have been obtained at shorter wavelengths (Eikema et al. 1997). Furthermore, considerable efforts are needed to achieve high spectral purity due to the strong amplification of broad-band spontaneous emission (ASE).

With the advent of flashlamp-pumped Ti:sapphire lasers a significant increase in near-IR output was achieved (Esterowitz et al. 1985; Lacovara et al. 1985; Brown and Fisher et al. 1993; Hoffstädt 1997). Pulsed Ti:sapphire lasers are tunable from less than 700 nm to more than 950 nm, with the gain maximum being located at 780 nm. By flashlamp pumping, the output may reach levels previously only available in the fixed-frequency pump lasers. Pulse energies of almost 1 J look feasible, which (considering pulse repetition rates between 10 and 50 Hz) means a considerable gain in average power approaching that typically used in Raman lidar systems.

The optimum performance of a ground-based DIAL system is estimated by simulation in the shot-noise-limit. Here, we briefly present the results for the Zugspitze

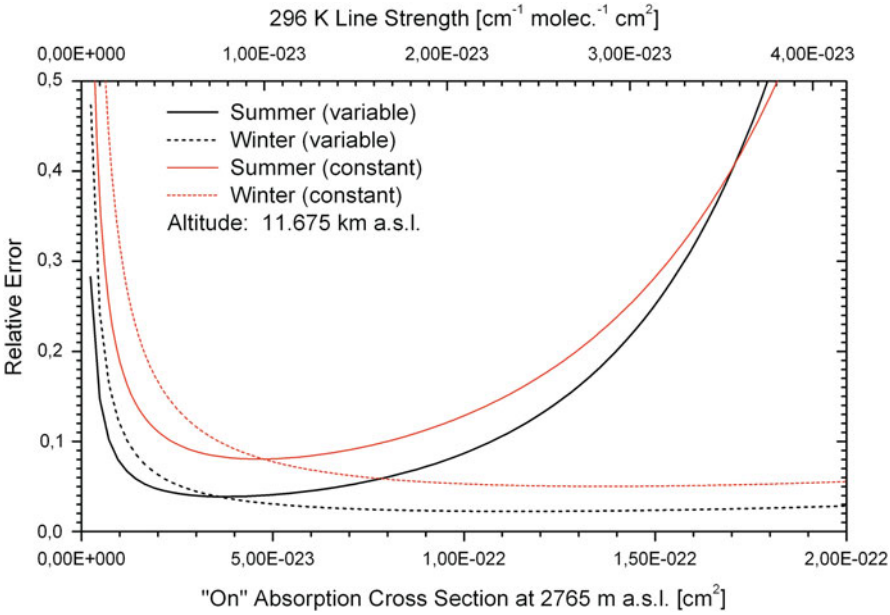

Fig. 7.14 Relative error of the water-vapour density at 817 nm as a function of the absorption cross section at an altitude of 11.675 m a.s.l. (i.e, 9 km above the lidar laboratory) for the LOWTRAN 7 seasonal models "midlatitude summer" and "midlatitude winter" [LOWTRAN 7]; the results are shown for line widths variable and constant as a function of altitude. Top scale: 296 K line strength. The strongest line ($4.98 \times 10^{-23}\,\mathrm{cm}^{-1}\mathrm{molecule}^{-1}\mathrm{cm}^2$ (Ponsardin and Browell 1997) above) is highly suitable under dry conditions

system (Vogelmann and Trickl 2008). The calculations were carried out for a pulse energy at 817 nm of 0.5 J, signal averaging over 10^4 laser shots, a 0.65 m-diameter telescope, comparable in size to receivers used in Raman lidar systems, vertical averaging intervals of 250 m and light detection losses of 70 %. The simulations were based on average seasonal profiles and, therefore, do not cover complex situations with high humidity at low altitudes and a sudden drop to very dry conditions above. In such cases the advantage of a high-altitude lidar site mostly outside the moist boundary layer becomes particularly important, as will be demonstrated further below.

As an example of the simulations we give in Fig. 7.14 the shot-noise-limited error at an altitude of 11.675 km a.s.l. (i.e., 9 km above the lidar) as a function of the absorption cross section for the LOWTRAN 7 seasonal models "mid-latitude summer" and "mid-latitude winter" [LOWTRAN-7 model]. The error calculations were carried out for both a constant and the true (pressure- and temperature-dependent) absorption cross section growing with increasing altitude (Ponsardin and Browell 1997). Due to the lower cross section (broader lines) in the lower free troposphere the light losses by absorption in the altitude range with the highest humidity is reduced and, due to the growing cross section, the upper-tropospheric errors are reduced by a factor

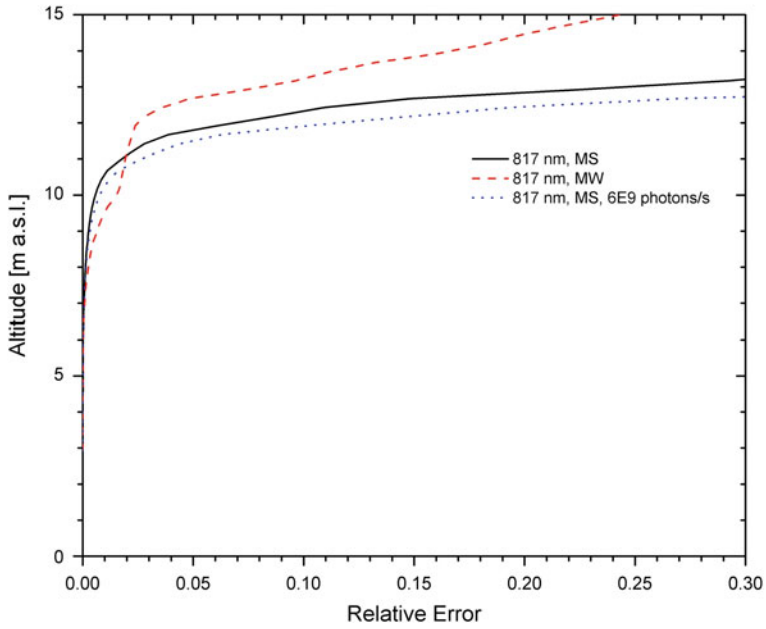

Fig. 7.15 Relative error of the water-vapour density at 817 nm as a function of altitude for the optimum absorption cross sections shown in Fig. 7.14; the range reduction during daytime is rather small (Vogelmann and Trickl 2008). MS and MW refer to the LOWTRAN 7 seasonal models "midlatitude summer" and "midlatitude winter" respectively. For the *dotted line*, a typical daylight photon flux reaching the detector was estimated

of two (see Fig. 7.14). The errors as a function of altitude for the optimum cross sections are given in Fig. 7.15. For both seasonal models a range up to 12 km a.s.l. is obtained.

In practice the backscatter profiles are not shot-noise limited. Limitations are mostly given by the overall detection noise, electromagnetic interference (mostly by the laser) and the solar background. By spectral filtering the backscattered light with 0.5 nm-bandwidth interference filters the solar background is substantially diminished and the vertical range is reduced by just a few hundred meters with respect to night-time conditions (see Fig. 7.15). The specifications so far achieved with the Zugspitze DIAL are discussed further below, in comparison with the results of the simulations that represent the ideal situation.

7.4.3 Laser Systems

Due to a particularly wide tuning range in the near IR, covering the three band systems of H_2O mentioned in the preceding subsection, its high output power and its reasonable thermal performance the Ti:sapphire laser has become the preferred laser

source for DIAL sounding of water vapour (Moore et al. 1996; Browell et al. 1996; Nagasawa et al. 2001; Ertel 2004; Ertel et al. 2005; Vogelmann and Trickl 2008) although also alexandrite lasers and optical parametric oscillators (OPOs) have been used (Wulfmeyer 1998a; Wulfmeyer and Bösenberg 1998b; Bruneau et al. 2001a; Poberaj et al. 2002; Vogelmann and Trickl 2008). Most systems use laser-pumping of Ti:sapphire (e.g., Moore et al. 1996; Ertel et al. 2005). As a consequence the output pulse energies are moderate, and only the air-borne LASE system emits more than 100 mJ (up to 150 mJ) per pulse (Moore et al. 1996; Wulfmeyer and Bösenberg 1998b). In contrast to the other systems the Zugspitze DIAL (Vogelmann and Trickl 2008) uses a flashlamp-pumped Ti:sapphire laser. For this well characterized laser, built by (Hoffstädt 1997), very high pulse energies of more than 0.7 J could be expected in single narrow-band pulses.

In order to avoid line shape corrections the laser bandwidth must be reduced to about one tenth of the absorption line width (≥ 2 GHz) or less. This requires single-longitudinal mode (SLM) operation of the laser. Different approaches for achieving single-mode operation of these systems have been reported. In most systems continuous-wave diode lasers directly seed the Ti:sapphire crystals. This, although limiting the wavelength tuning range, is particularly important in mobile or air-borne systems where an efficient active feedback control of the laser frequencies is needed. The master oscillators of the Zugspitze DIAL are two pulsed single-longitudinal mode (SLM) Optical Parametric Oscillators (OPOs) in Littman cavity configuration (Continuum, model Mirage (Bösenberg and Guyer 1993), pumped by a frequency doubled Nd:YAG laser (Continuum, model Powerlite 8020). This approach combines the advantages of very wide tunability and of reducing the number of expensive seed lasers, in particular laser-pumped continuous Ti:sapphire lasers that could also provide a large tuning range. On the other hand the use of sensitive pulsed oscillators requires higher passive (mechanical and thermal) stability. The OPOs were modified for a more stable single-mode operation (Vogelmann and Trickl 2008). Pulses next to the Fourier-transform limit were obtained, e.g., for near-Gaussian pulses 4.0 ns long 130 ± 15 MHz (Fourier limit: 110 MHz). Active frequency locking to a precise interferometer system (Cluster LM007) is used to keep the laser frequency at the H_2O line centre.

The layout of the complete laser system, including the OPOs and the Ti:sapphire laser, is shown in Fig. 7.16 (see Table 7.6 for specifications). The Ti:sapphire laser is set up in ring configuration with a ring circumference of 4.8 m. Radiation is coupled into or out from the ring by high-speed polarization switching. The flashlamp-pumped Ti:sapphire ring laser currently emits up to 250 mJ per pulse and fires at a repetition rate of 20 Hz. This limitation is caused by arcing problems at the high-altitude laboratory, where the full flashlamp load voltage of 30 kV could not be applied. A spectral purity of at least 99.9 % was determined for the laser system, sufficient for quantitative DIAL measurements.

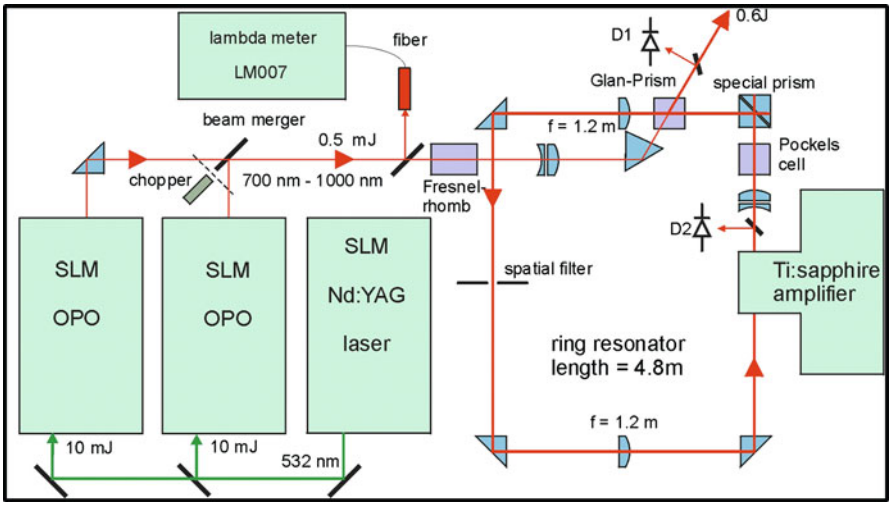

Fig. 7.16 Layout of the laser system of the Zugspitze DIAL (*D1, D2* fast photodiodes (Vogelmann and Trickl 2008).)

7.4.4 Receiver

Similar to a Raman lidar system as much of the backscattered light as possible must be collected, necessitating a large telescope in the lidar receiver. Therefore, for the Zugspitze system the principal component of the receiver (Fig. 7.17; specifications: Table 7.6) is a Newtonian telescope with an 0.65 m-diameter parabolic mirror (f = 2 m), more or less limited by the dimensions of the slit of the costly astronomical dome above the laboratory. The light entering the telescope is collimated and fed through a 5 nm interference filter, separated into near- and far-field channels with a 1- % beam splitter, and finally detected with avalanche photodiodes (APDs). In the far-field channel an additional 0.5 nm-bandwidth inference filter is installed during daytime in order to reduce further the solar background.

The laser beam is sent into the atmosphere at a distance of not more than 0.7 m from the telescope axis, which ensures a full beam overlap (beginning of the operating range) at a distance of 300 m. This makes possible comparisons with the FTIR and the *in-situ* measurements at the Zugspitze summit (2,962 m a.s.l.) Vogelmann et al. 2011. The telescope axis, the laser beam, and the optical axis of the ocular are aligned in a common plane. The near-field contribution in the far-field channel is cut off by an adjustable-slit aperture. This aperture also rejects a major part of the solar background, outside the useful rectangular field of view. The signals for the "on" and "off" wavelengths are separated by sequential detection. Optionally, a second far-field channel can be added (as indicated in the figure) if the detection spectral bandwidth must be further reduced with at least one Fabry-Perot etalon in the future.

Table 7.6 The most important specifications of the Zugspitze DIAL

Laser System	
Laser oscillators	2 KTP Littman OPOs, pumped at 532 nm
Number of wavelengths	2, both next to 817 nm
Pulse repetition rate	20 s^{-1} (10 s^{-1} for each wavelength)
Pulse length	2–4 ns
Pulse energy	0.25 J around 800 nm
Tuning range	700–950 nm
Single-shot bandwidth	130–250 MHz
Frequency noise	±35 MHz
Spectral purity	>99.9 %
Beam pointing stability	≈30 μrad
Beam diameter	7 mm
Beam divergence	≈0.25 mrad
Receiver	
Main-mirror diameter	0.65 m
Focal length	2 m
Number of channel	2 (optionally 3)
Far-field field of view	1.25 mrad × 3 mrad
Near-field field of view	2.5 mrad × 8 mrad
Detectors	Si APD (3 mm diameter)
APD detection efficiency	77 %
APD noise (after amplification)	200 μV (peak to peak, 10^4 shots averaged)
Typical peak signal	300 μV
Spectral filtering near field	5 nm
Spectral filtering far field	0.5 nm
Sample rate of transient digitizer	20 MHz
Digital resolution	12 bit
Number of shots	10^4
Vertical resolution for H_2O	varied from 50 to 260 m (VDI 1999)

The pre-amplified signal from each APD is recorded by a 12 bit transient digitizer with 16,384 registers and a sample rate of 20 MHz, which provides a spatial resolution of 7.5 m.

7.4.5 System Performance

In this and the following subsection we discuss the performance so far achieved for the wide-range Zugspitze DIAL. The system has been thoroughly tested since the summer of 2004. In 2007 routine operation was started, with typically two measurement days per week, if the weather conditions are favourable. A number of examples of measurements, obtained under different conditions, are shown in (Vogelmann and Trickl 2008). Here, we just take three of them are presented to illustrate the present capabilities of this lidar.

A particularly demanding measurement made under extremely dry conditions (minimum relative humidity of the order of 1 % between 4.3 and 4.8 km) and at around noon, is given in Fig. 7.18. The strong absorption line at 817.223 nm was

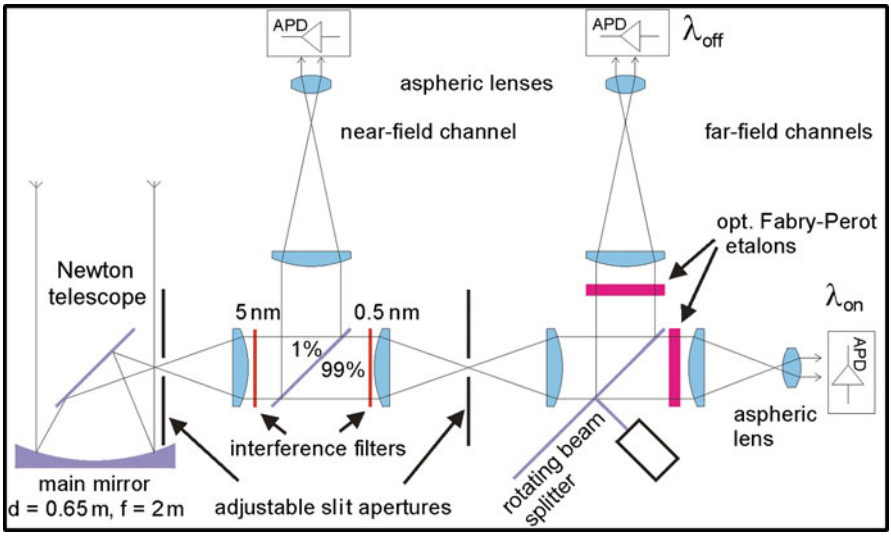

Fig. 7.17 Layout of the receiver of the Zugspitze DIAL (The λ_{off} far-field channel is optional and not yet installed. *APD* avalanche photodiode (Vogelmann and Trickl 2008))

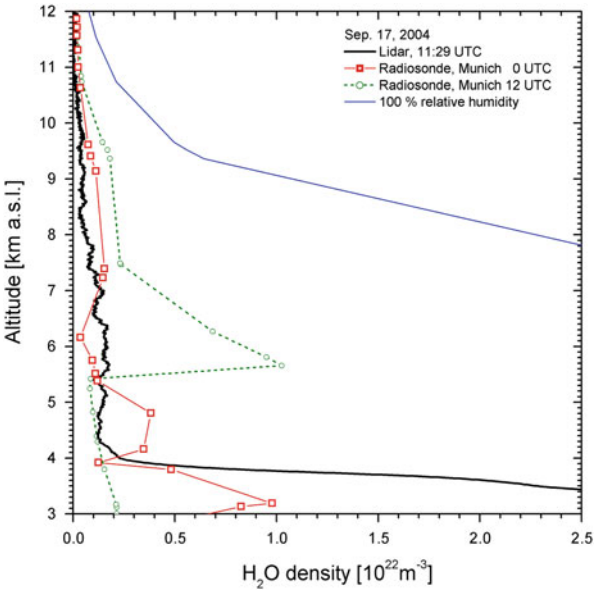

Fig. 7.18 DIAL measurement on 17 September 2004 at 11:29 UTC (12:29 Central European Time, i.e., local time) together with the H_2O densities derived from the Munich radiosonde data from the same day; the sonde 100 % relative humidity is also given. The artificially looking peak at 5.7 km in the dashed green curve is due to a change in temperature. It is seen also in the water vapour densities for Stuttgart and Payerne, but not in that for Prague where the air mass came from

used for this measurement. Despite the strong solar background water vapour may be distinguished from the noise up to about 11 km. The very low humidity arose from a vertically rather extended stratospheric air intrusion below 6 km arriving from the north east. This situation was qualitatively confirmed by a number of surrounding radiosounding stations. In Fig. 7.18 we show for comparison the results of the station

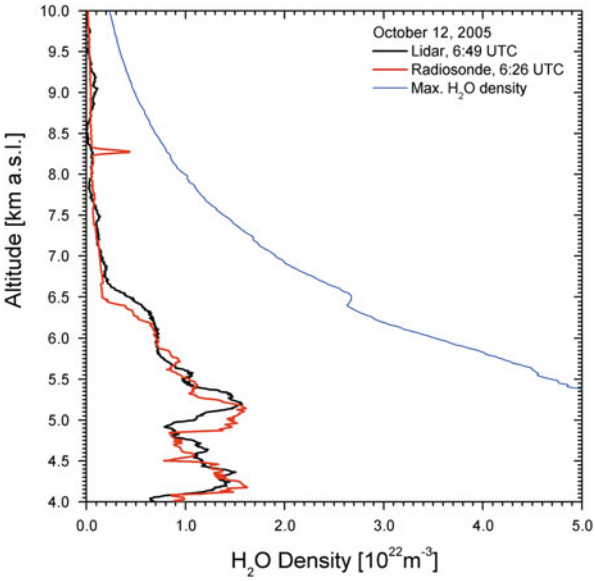

Fig. 7.19 Comparison of an almost simultaneous measurement of the Zugspitze DIAL and with a RS80 radiosonde lauched at Garmisch-Partenkirchen on 12 October 2005, the maximum possible water-vapour density (100 % relative humidity) is derived from the sonde temperature profile (Vogelmann and Trickl 2008)

in Oberschleißheim next to Munich, 100 km roughly north of the lidar. Due to the considerable time difference and distance between both measurements there are residual discrepancies. A comparison of the two sonde measurements shows the subsidence of the dry layer, which reached the Zugspitze summit after 18:00 UTC.

For better comparison, several RS80 radiosondes were launched in Garmisch-Partenkirchen by the Meteorological Institute of the University of Munich in autumn 2005. Although the distance of the launch site to the lidar is just 10 km the influence of the differences in time and space was mostly not negligible. In Fig. 7.19 the results of a successful comparison are shown. Apart from some vertical displacement, rather likely caused by the sonde drifting outside the Alps, the agreement is very good up to 8 km.

The lidar results have also been compared with the dew-point-mirror instrument operated at the Zugspitze summit, i.e., 300 m above the lidar laboratory (Vogelmann and Trickl 2008). The agreement is frequently satisfactory. It is interesting to note that all clear discrepancies between the station and the lidar measurements are positive. An analysis for 2007 data shows that, with one exception, the positive excursions of the station humidity occurred during periods with potential convection possibly uplifting moist air from lower elevations along the slopes. At 3,000 m a. s. l. the laser beam is likely to be outside this surface layer.

Figure 7.20 shows an example of a narrow stratospheric air intrusion at 3.2 km a. s. l. This narrow layer arrived approximately from the east. Thus, the Munich radiosonde, which ascended almost at the time of the lidar measurement, probed roughly the same phase of the air mass. The agreement of the two measurements is quite astonishing, both showing as little as 1 % relative humidity. This indicates the absence of significant mixing with the air surrounding this thin dry tongue in

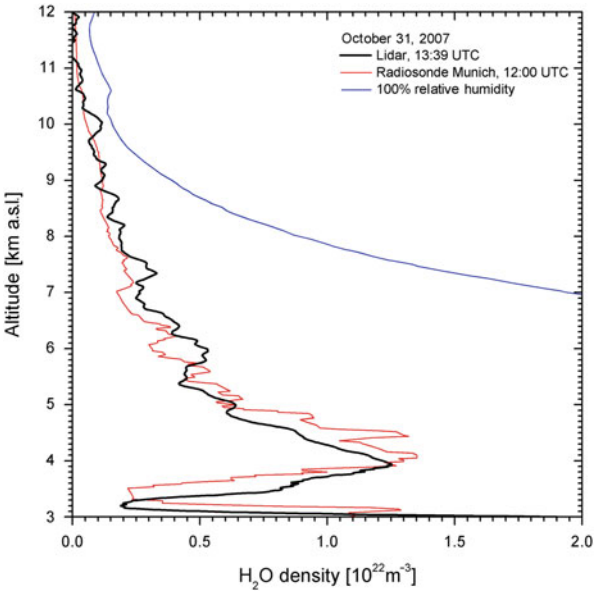

Fig. 7.20 Measurements of Zugspitze DIAL and Munich radiosonde during a stratospheric intrusion event on 31 October, 2007; the density for 100 % relative humidity is derived from the sonde temperature profile. The lidar data were re-evaluated with higher vertical resolution than in Fig. 15 of (Vogelmann and Trickl 2008) in order to show the true system performance within the stratospheric air layer at 3.2 km

the middle and lower troposphere during the long travel from Greenland to the Alps. When the intrusion had descended to the Zugspitze summit (2,962 m a. s. l.) three hours later the relative humidity had grown to 13 %, which is about three times the error specified for the *in-situ* measurement.

The routine measurements have revealed a considerable variability of the free-tropospheric water-vapour densities over one year by roughly a factor of 30. By using different wavelength pairs there is rarely a problem in reaching more than 10 km.

7.4.6 Error Considerations

The error discussion presented here focuses on the most important contributions. More complete error analyses have, e.g., been given by (Wulfmeyer and Walther 2001a, b). The preliminary error analysis for the Zugspitze DIAL shows that, for a correct operation of the highly linear detection electronics, most of the uncertainty in the upper-tropospheric measurements is caused by the high noise emitted by the preamplifiers of the APDs. There is also a minor signal contribution from electromagnetic interference by the stray fields of the powerful Ti:sapphire laser. However, any further error contribution cannot be evaluated until the noise level is significantly reduced.

The current sensitivity limit of the lidar in the upper troposphere is chosen as the amplitude of the density noise, which is roughly 1.5×10^{20} m^{-3} (and sometimes even better), corresponding to about 18 ppm of H_2O for an altitude of 10 km. Anticipating a substantial increase in laser pulse energy and an order-of-magnitude reduction in

signal-processing noise the sensitivity limit of the Zugspitze DIAL could be improved to about 2.5 ppm, i.e. below the stratospheric H_2O mixing ratio of typically 4–5 ppm.

In the presence of sufficient humidity (i.e., mostly below 8 km) the results of radiosondes have been reproduced to within a few per cent, apart from differences explainable by probing different volumes. This also confirms our appropriate choice of line strengths. It is important to note that there is a substantial difference between the H_2O line strengths in (Ponsardin and Browell 1997) and in other listings, in particular older versions of HITRAN (Rothman et al. 2003, 2005). A comparison of the 296 K line strengths published by Ponsardin and Browell, with those given by (Toth 1994) and (Mérienne et al. 2003) revealed ratios of 0.8969 ± 0.015 (standard deviation) and 0.8997 ± 0.011, respectively. A much better agreement (+3 % deviation from Ponsardin and Browell) is found for the work by (Schermaul et al. 2001a, b). Because of the very detailed, convincing descriptions by Ponsardin and Browell and because of the successful validation of LASE (Browell et al. 1996) the line parameters of Ponsardin and Browell were adopted.

The data of (Schermaul et al. 2001a, b) were very recently carefully re-evaluated by (Tolchenov and Tennyson 2008) with emphasis on line-overlap issues and are the basis in the near infrared of the latest HITRAN version (Rothman et al. 2009). The deviation of 817 nm HITRAN line strengths with respect those by Ponsardin and Browell is now just 1 %, with some exceptions. The line parameters by Ponsardin and Browell performed better in a recent intercomparison of integrated water vapour of the Zugspitze DIAL and the Zugspitze Fourier-transform mid-infrared solar spectrometer (Vogelmann et al. 2011).

7.5 Conclusions

Due to their good temporal and spatial resolution DIAL measurements are ideal for detailed studies of tropospheric trace gases. The DIAL technique is also highly suitable for routine measurements due to its stable calibration. The first ground-based DIAL system covering almost the entire free troposphere is the new high-power lidar at the Schneefernerhaus research station in the Northern Alps. Excellent daytime performance has been demonstrated. Although a measurement error corresponding to 5 % of the average seasonal humidity, as demanded by the climate-research community (e.g. Harries 1997) and suggested by the performance simulations, is not obtained above 9 km, the results indicate, that the final performance of the system could be close to that predicted in the simulations based on ideal conditions. Cases in which upper-tropospheric measurements are not possible due to complete light absorption at lower altitudes are rare. This demonstrates the advantage of the high-altitude lidar laboratory.

The daytime capability of an optimized ground based DIAL and measurement times of potentially just a few minutes are clear advantages with respect to Raman lidar systems. These properties are particularly important for an investigation of the impact of the tropospheric dynamics on the water-vapour distribution, resulting in

changes on time scales of much less than one hour. However, the operation of a ground-based DIAL is limited to the troposphere because the stronger 935 nm band system of H_2O cannot be applied due to quantitative light absorption at low altitudes. By contrast, air-borne DIAL systems operated at 935 nm have successfully achieved lower stratospheric measurements of water vapour up to more than 16 km (Kiemle et al. 2008). The benefit of air-borne systems is the capability of three-dimensional mapping of the water-vapour density over an entire region. Unfortunately, routine measurements are prohibited by the high cost of the missions.

References

Ansmann, J. Bösenberg, Correction scheme for spectral broadening by Rayleigh scattering in differential absorption lidar measurements of water vapor in the troposphere. Appl. Opt. **26**, 3026–3032 (1987)

A. Ansmann, M. Riebesell, U. Wandinger, C. Weitkamp, E. Voss, W. Lahmann, W. Michaelis, Combined Raman elastic-backscatter LIDAR for vertical profiling of moisture, aerosol extinction, backscatter, and LIDAR ratio. Appl. Phys. B. **55**, 18–28 (1992b)

J.E. Barnes, T. Kaplan, H. Vömel, W.G. Read, NASA/Aura/Microwave limb sounder water vapor validation at Mauna Loa Observatory by Raman lidar. J. Geophys. Res. **113**, (2008). doi:10.1029/2007JD008842

M. Bevis, S. Businger, T.A. Herring, C. Rocken, R.A. Anthese, R.H. Ware, GPS meteorology: Remote sensing of atmospheric water vapor. J. Geophys. Res. **97**, 15787–15801 (1992)

J. Bösenberg, *A differential absorption lidar system for high resolution water vapor measurements in the troposphere* (Tech. Rep. Report 71, Max-Planck-Institut für Meteorologie, Hamburg, Germany, 1991)

J. Bösenberg, Ground-based differential absorption lidar for water-vapor and temperature profiling: Methodology. Appl. Opt. **37**, 3845–3860 (1998)

W.R. Bosenberg, D.R. Guyer, Broadly tunable, single-frequency optical parametric frequency-conversion system. J. Opt. Soc. Am. B. **10**, 1716–1722 (1993). http://josab.osa.org/abstract.cfm?URI=josab-10-9-1716

J. Bribes, R. Gaufrès, M. Monan, M. Lapp, C.M. Penney, Raman band contours for water vapor as a function of temperature. Appl. Phys. Lett. **28**, 336–337 (1976)

E.V. Browell, T.D. Wilkerson, T.J. McIlrath, Water vapor differential absorption lidar development and evaluation. Appl. Opt. **18**, 3474–3483 (1979)

E.V. Browell, A.F. Carter, T.D. Wilkerson, Airborne differential absorption lidar system for water vapor investigations. Opt. Eng. **20**, 84–90 (1981)

E.V. Browell, S. Ismail, W.M. Hall, A.S. Moore, S.A. Kooi, V.G. Brackett, M.B. Clayton, J.D. Barrick, F.J. Schmidlin, N.S. Higdon, S.H. Melfi, D.N. Whiteman, *Advances in atmospheric remote sensing with lidar,* chap. LASE validation experiment (Springer, 1996) pp. 289–295

E.V. Browell, S. Ismail, W.B. Grant, Differential absorption lidar (DIAL) measurements from air and space. Appl. Phys. B. **67**, 399–410 (1998)

E.V. Browell, M.A. Fenn, C.F. Butler, W.B. Grant, S. Ismail, R.A. Ferrare, S.A. Kooi, V.G. Brackett, M.B. Clayton, M.A. Avery, J.D.W. Barrick, H.E. Fuelberg, J.C. Maloney, R.E. Newell, Y. Zhu, M.J. Mahoney, B.E. Anderson, D.R. Blake, W.H. Brune, B.G. Heikes, G.W. Sachse, H.B. Singh, R.W. Talbot, Large-scale air mass characteristics observed over the remote tropical Pacific Ocean during March–April 1999: Results from PEM-Tropics B field experiment. J. Geophys. Res. 1**06**, 32481–32501 (2001)

A. Brown, C. Fisher, A 6.5-J ashlamp-pumped Ti:Al2O3 laser. IEEE J. Quantum Electro. **29**, 2513–2518 (1993). ISSN 0018-9197, doi:10.1109/3.247709

D. Bruneau, P. Quaglia, C. Flamant, M. Meissonnier, J. Pelon, Airborne lidar LEANDRE II for water-vapor profiling in the troposphere. I. System description. Appl. Opt. **40**, 3450–3460 (2001a). doi:10.1364/AO.40.003450

D. Bruneau, P. Quaglia, C. Flamant, J. Pelon, Airborne lidar LEANDRE II for water-vapor profiling in the troposphere. II. First results. Appl. Opt. **42**, 3462–3475 (2001b). doi:10.1364/AO.40.003462

C. Cahen, G. Mègie, P. Flamant, Lidar monitoring of the water vapor cycle in the troposphere. J. Appl. Meteor. **21**, 1506–1515 (1982)

J. Cooney, Measurement of atmospheric temperature profiles by Raman backscatter. J. Appl. Meteorol. **11**, 108–112 (1972)

J. Cooney, K. Petri, A. Salik, Measurements of high resolution atmospheric water-vapor profiles by use of a solar blind Raman lidar. Appl. Opt. **24**, 104–108 (1985). http://ao.osa.org/abstract.cfm?URI=ao-24-1-104

P. M. de F. Forster, K.P. Shine, Stratospheric water vapour changes as a possible contributor to observed stratospheric cooling. Geophys. Res. Lett. **26**, 3309–3312 (1999)

F. De Tomasi, M.R. Perrone, Lidar measurement of tropospheric water vapor and aerosols pro_les over southern Italy. J. Geophys. Res. **108**, 4286–4297 (2003)

D.P. Donovan, J.A. Whiteway, A.I. Carswell, Correction for nonlinear photon-counting effects in lidar systems. Appl. Opt. **32**, 6742–6753 (1993). http://ao.osa.org/abstract.cfm?URI=ao-32-33-6742

G. Ehret, C. Kiemle, W. Renger, G. Simmet, Airborne remote sensing of tropospheric water vapor with a near-infrared di_erential absorption lidar system. Appl. Opt. **32**, 4534–4551 (1993)

G. Ehret, K.P. Hoinka, J. Stein, A. Fix, C. Kiemle, G. Poberaj, Low stratospheric water vapor measured by an airborne DIAL. J. Geophys. Res. **104**, 31351–31359 (1999)

K.S.E. Eikema, W. Ubachs, W. Vassen, W. Hogervorst, Lamb shift measurements in the 1 1S ground state of helium. Phys. Rev. A. **55**, 1866–1884 (1997)

L. Elterman, The mesurement of stratospheric density distribution with the searchlight technique. J. Geophys. Res. **58**, 509–520 (1951)

K. Ertel, Application and Development of water vapor DIAL systems, Ph.D. thesis, Max- Planck-Institut für Meteorologie, Universität Hamburg, Hamburg, Germany, 2004

K. Ertel, H. Linné, J. Bösenberg, Injection-seeded pulsed Ti:sapphire laser with novel stabilization scheme and capability of dual-wavelength operation. Appl. Opt. **44**, 5120–5126 (2005)

L. Esterowitz, R. Allen, C.P. Khattak, *Tunable Solid State Lasers*, vol. 47, (Springer Series in Optical Sciences, Springer, 1985), pp. 73–75

R.A. Ferrare, S.H. Melfi, D.N. Whiteman, K.D. Evans, F.J. Schmidlin, D.O. Starr, A comparison of water vapor measurements made by Raman lidar and radiosondes. J. Atmos. Ocean. Tech. **12**, 1177–1195 (1995)

G. Fiocco, J.B.D. Wolf, Frequency spectrum of laser echoes from atmospheric constituents and determination of the aerosol content of air. J. Atmos. Sci. **25**, 488–496 (1968)

G. Fiocco, G. Benedetti-Michelangeli, K. Maischberger, E. Madonna, Measurement of the temperature and aerosol to molecule ratio in the troposphere by optical radar. Nature. **229**, 78–79 (1971)

H. Flentje, A. Dörnbrack, G. Ehret, A. Fix, C. Kiemle, G. Poberaj, M. Wirth, Water vapor heterogeneity related to tropopause folds over the North Atlantic revealed by airborne water vapor differential absorption lidar. J. Geophys. Res. **110** (2005). doi:10.1029/2004JD004957

J.E.M. Goldsmith, S.E. Bisson, R.A. Ferrare, K.D. Evans, D.N. Whiteman, S.H. Melfi, Raman lidar profiling of atmospheric water vapor: Simultaneous measurements with two collocated systems. Bull. Amer. Meteorol. Soc. **75**, 975–982 (1994)

W.B. Grant, Differential absorption and Raman lidar for water vapor profile measurements: A review. Opt. Eng. **30**, 40–48 (1991)

W.B. Grant, J.S. Margolis, A.M. Brothers, D.M. Tratt, CO2 DIAL measurements of water vapor. Appl. Opt. **26**, 3033–3042 (1987). http://ao.osa.org/abstract.cfm?URI=ao-26-15-3033

Y. Han, J.B. Snider, E. R. Westwater, R.A. Ferrare, Observations of water vapor by ground-based microwave radiometers and Raman lidar. J. Geophys. Res. **99**, 18695–18702 (1994)

J.E. Harries, Atmospheric radiation and atmospheric humidity. Q. J. R. Meteorol. Soc. **123**, 2173–2186 (1997)

A. Hauchecorne, M.L. Chanin, Density and temperature profiles obtained by lidar between 35 and 70 km. Geophys. Res. Lett. **7**, 565–568 (1980)

W.S. Heaps, J. Burris, Airborne Raman lidar. Appl. Opt. **35**, 7128–7135 (1996). http://ao.osa.org/abstract.cfm?URI=ao-35-36-7128

N.S. Higdon, E.V. Browell, P. Ponsardin, B.E. Grossmann, C.F. Butler, T.H. Chyba, M.N. Mayo, R.J. Allen, A.W. Heuser, W.B. Grant, S. Ismail, S.D. Mayor, A.F. Carter, Airborne differential absorption lidar system for measurements of atmospheric water vapor and aerosols. Appl. Opt. **33**, 6422–6438 (1994)

E. Hinkley, *Topics in Applied Physics*, vol. 14, chap. Laser monitoring of the atmosphere, (Springer, New York, 1976) p. 380

A. Hoffstädt, Design and performance of a high-average-power ashlamp-pumped Ti:sapphire laser and amplifier. IEEE J. Quantum Electr. **33**, 1850–1863 (1997). ISSN 0018-9197, doi: 10.1109/3.631292

E.O. Hulburt, Observations of a searchlight beam to an altitude of 28 kilometers. J. Opt. Soc. Am. **27**, 377–382 (1937)

C. Kiemle, M. Wirth, A. Fix, G. Ehret, U. Schumann, T. Gardiner, C. Schiller, N. Sitnikov, G. Stiller, First airborne water vapor lidar measurements in the tropical upper troposphere and mid-latitudes lower stratosphere: accuracy evaluation and intercomparisons with other instruments. Atmos. Chem. Phys. **8**, 5245–5261 (2008)

P. Lacovara, L. Esterowitz, R. Allen, Flash-lamp-pumped Ti:Al2O3 laser using fluorescent conversion. Opt. Lett. 10, 273{275 (1985). http://ol.osa.org/abstract.cfm?URI=ol-10-6-273

T. Leblanc, I.S. McDermid, Accuracy of Raman lidar water vapor calibration and its applicability to long-term measurements. Appl. Opt. **47**, 5592–5603 (2008a). URL http://ao.osa.org/abstract cfm?URI=ao-47-30-5592

T. Leblanc, I.S. McDermid, T.G. McGee, L. Twigg, G. Sumnicht, D.N. Whiteman, K. Rush, M. Cadirola, D. Venable, R. Connell, B. Demoz, H. Vömel, L. Miloshevich, Measurements of humidity in the atmosphere and validation experiments (MOHAVE, MOHAVE II): Results overview, in reviewed and revised papers of the 24th international laser radar conference, boulder, CO, 23–27 June 2008, pp. 1013–1016 (2008b)

T. Leblanc, I.S. McDermid, T.D. Walsh, Ground-based water vapor Raman lidar measurements up to the upper troposphere and lower stratosphere for long-term monitoring, Atmos. Meas. Tech., **5**, (2012). doi:10.5194/amt-5-17-2012

H. Linné, B. Hennemuth, J. Bösenberg, K. Ertel, Water vapour flux profiles in the convective boundary layer. Theor. Appl. Climatol. **87**, 201–211 (2006)

L.M. Little, G.C. Papen, Fiber-based lidar for atmospheric water-vapor measurements. Appl. Opt. **40**, 3417–3427 (2001)

LOWTRAN 7,—, LOWTRAN 7 model, ONTAR Corporation, 9 Village Way, North Andover, MA 01845-2000 USA, URL http://www.ontar.com

J.L. Machol, T. Ayers, K.T. Schwenz, K.W. Koenig, R.M. Hardesty, C.J. Senff, M.A. Krainak, J.B. Abshire, H.E. Bravo, S.P. Sandberg, Preliminary measurements with an automated compact differential absorption lidar for the profiling of water vapor. Appl. Opt. **43**, 3110–3121 (2004)

R.M. Measures, *Laser remote sensing: Fundamentals and applications* (Krieger Pub. Co., Malabar, FL 1992)

S.H. Melfi, Remote measurements of the atmosphere using Raman scattering. Appl. Opt. **11**, 1605–1610 (1972). http://ao.osa.org/abstract.cfm?URI=ao-11-7-1605

S.H. Melfi, D. Whiteman, Observation of lower-atmospheric moisture structure and its evolution using a Raman lidar. Bull. of the Am. Met. Soc. **66**, 1288–1292 (1985)

M.-F. Mérienne, A. Jenouvrier, C. Hermans, A.C. Vandaele, M., Carleer, C. Clerbaux, P.-F. Coheur, R. Colin, S. Fally, M. Bach, Water vapor line parameters in the 13,000–9,250 cm^{-1} region. J. Quant. Spectrosc. Radiat. Transfer. **82**, 99–117 (2003)

L.M. Miloshevich, H. Paukkunen, H. Vömel, S.J. Oltmans, Development and validation of a time lag correction for Vaisala radiosonde, 1757 humidity measurements. J. Atmos. Ocean. Tech. **21**, 1305–1327 (2004)

L.M. Miloshevich, H. Vömel, D.N. Whiteman, B.M. Lesht, F.J. Schmidlin, F. Russo, Absolute accuracy of water vapor measurements from six operational radiosonde types launched during AWEX-G and implications for AIRS validation. J. Geophys. Res. **111**(D09S10) (2006). doi:10.1029/2005JD006083

L.M. Miloshevich, H. Vömel, D. Whiteman, T. Leblanc, Accuracy assessment and correction of Vaisala RS92 radiosonde water vapor measurements. J. Geophys. Res. 114 (2009). doi: 10.1029/2008JD011565

A.S. Moore, K.E. Brown, W.M. Hall, J.C. Barnes, W.C. Edwards, L.B. Petway, A.D. Little, W.S. Luck, I.W. Jones, C.W. Antill, E.V. Browell, S. Ismail, *Advances in Atmospheric Remote Sensing with Lidar*, chap. Development of the lidar atmospheric sensing experiment (LASE)-an advanced airborne DIAL instrument, (Springer, 1996) pp. 281–288

E.R. Murray, R.D. Hake Jr., J.E. van der Laan, J.G. Hawley, Atmospheric water vapor measurements with an infrared (10 μm) differential-absorption lidar system. Appl. Phys. Lett. **28**, 542–543 (1976)

C. Nagasawa, T. Nagai, M. Abo, Y. Shibata, O. Uchino, *Development of airborne DIAL for water vapor measurement*, ed. by U.N. Singh, T. Itabe, N. Sugimoto in Lidar Remote Sensing for Industry and Environment Monitoring, Proceedings of SPIE, vol. 4153 (The International Society for Optical Engineering, 2001) pp. 599–606

R.K. Newsom, D.D. Turner, B. Mielke, M. Clayton, R. Ferrare, C. Sivaraman, Simultaneous analog and photon counting detection for Raman lidar. Appl. Opt. **48**, 3903–3914 (2009)

S.J. Oltmans, *Measurements of water vapor in the stratosphere with a frost point hygrometer*, in Measurement and Control in Science and Industry, Proceeding 1985 International Symposium on Moisture and Humidity, (Instrument Society of America Washington, DC, 1985) pp. 251–258

S.J. Oltmans, D.J. Hofmann, Increase in lower-stratospheric water vapour at a mid-latitude Northern Hemisphere site from 1981 to 1994. Nature. **374**, 146–149 (1995). doi:10.1038/374146a0.

C.M. Penney, M. Lapp, Raman-scattering cross sections for water vapor. J. Opt. Soc. Am. **66**, 422–425 (1976)

G. Poberaj, A. Fix, A. Assion, M. Wirth, C. Kiemle, G. Ehret, Airborne all-solid-state DIAL for water vapour measurements in the tropopause region: system description and assessment of accuracy. Appl. Phys. B. **75**, 165–172 (2002). doi:10.1007/s00340-002-0965-x

P.L. Ponsardin, E.V. Browell, Measurements of H_2 ^{16}O linestrengths and air-induced broadenings and shifts in the 815 nm spectral region. J. Mol. Spectrosc. **185**, 58–70 (1997)

C.V. Raman, K.S. Krishnan, A new type of secondary radiation. Nature. **121**, 501–502 (1928)

D. Renaut, J.C. Pourny, R. Capitini, Daytime Raman-lidar measurements of water vapor. Opt. Lett. **5**, 233–235 (1980). http://ol.osa.org/abstract.cfm?URI=ol-5-6-233.

L. Rothman, A. Barbe, D.C. Benner, L.R. Brown, C. Camy-Peyret, M.R.Carleer, K. Chance, C. Clerbauxf, V. Dana, V. Devi, A. Fayth, J.-M. Flaud, R.R. Gamache, A. Goldman, D. Jacquemart, K.W. Jucks, W.J. Lafferty, J.-Y. Mandin, S.T. Massie, V. Nemtchinov, D.A. Newnham, A. Perrin, C.P. Rinsland, J. Schroeder, K.M. Smith, M.A.H. Smith, K. Tang, R.A. Toth, J.V. Auwera, P. Varanasi, K. Yoshino, The HITRAN molecular spectroscopic database: Edition of 2000 including updates through 2001. J. Quant. Spectrosc. Radiat. Transfer. **82**, 5–44 (2003)

L.S. Rothman, D. Jacquemart, A. Barbe, D.C. Benner, M. Birk, L.R. Brown, M.R. Carleer Jr., C.C.K. Chance, L.H. Coudert, V. Dana, V.M. Devi, J-M. Flaud, R.R. Gamache, A. Goldman, J-M. Hartmannh, K.W. Jucks, A.G. Maki, J-Y. Mandin, S.T. Massie, J. Orphal, A. Perrin, C.P. Rinsland, M.A.H. Smith, J. Tennyson, R.N. Tolchenov, R.A. Toth, J.V. Auwera, P. Varanasi, G. Wagner, The HITRAN 2004 molecular spectroscopic database. J. Quant. Spectrosc. Radiat. Transfer. **96**, 139–204 (2005)

L.S. Rothman, I.E. Gordon, A., Barbe, D.C. Benner, P.F. Bernath, M. Birk, V. Boudon, L.R. Brown, A. Campargue, C-P. Champion, K. Chance, L.H. Coudert, V. Dana, V.M. Devi, S. Fally, J-M. Flaud, R.R. Gamache, A. Goldman, D. Jacquemart, I. Kleiner, N. Lacome, W.J. Lafferty, J-Y.

Mandin, S.T. Massie, S.N. Mikhailenko, C.E. Miller, N. Moazzen-Ahmadi, O.V. Naumenko, A.V. Nikitin, J. Orphal, V.I. Perevalov, A. Perrin, A. Predoi-Cross, C.P. Rinsland, M. Rotger, M. Simečková, M. Smith, K. Sung, S.A. Tashkun, J. Tennyson, R.A. Toth, A.C. Vandaele, J. Vander Auwera, The HITRAN 2008 molecular spectroscopic database. J. Quant. Spectros. Rad. Trans. **110**, 533–57 (2009)

G. Sachse, L. Wang, C. Antill, S. Ismail, E.V. Browell, *Optical Remote Sensing of the Atmosphere*, chap. Line-center/side-line diode laser seeding for DIAL measurements of the atmosphere, (Optical Society of America, 1995) pp. 289–295

R. Schermaul, R.C.M. Learner, D.A. Newnham, R.G. Williams, J. Ballard, N.F. Zobov, D. Belmiloud, J. Tennyson, The water vapor spectrum in the region 8,600–15,000 cm^{-1}: Experimental and theoretical studies for a new spectral line database I. Laboratory measurements. J. Mol. Spectrosc. **208**, 32–42 (2001a)

R. Schermaul, R.C.M. Learner, D.A. Newnham, J. Ballard, N.F. Zobov, D. Belmiloud J. Tennyson, The water vapor spectrum in the region 8,600–15,000 cm^{-1}: Experimental and theoretical studies for a new spectral line database II. Linelist construction. J. Mol. Spectrosc. **208**, 43–50 (2001b)

R.M. Schotland, Some observations of the vertical profile of water vapor by a laser optical radar, in *Proceedings of the 4th Symposium on Remote Sensing of the Environment*, University of Michigan, 1966, pp. 273–283

C. Senff, J. Bösenberg, G. Peters, Measurement of water vapor flux profiles in the convective boundary layer with lidar and Radar-RASS. J. Atmos. Ocean. Tech. **11**, 85–93 (1994)

V. Sherlock, A. Garnier, A. Hauchecorne, P. Keckhut, Implementation and validation of a Raman lidar measurement of middle and upper tropospheric water vapor. Appl. Opt. 38, 5838–5850 (1999a). doi:10.1364/AO.38.005838

V. Sherlock, A. Hauchecorne, J. Lenoble, Methodology for the independent calibration of Raman backscatter water-vapor lidar systems. Appl. Opt. **38**, 5816–5837 (,1999b). http://ao.osa.org/abstract.cfm?URI=ao-38-27-5816

R. Tolchenov, J. Tennyson, Water line parameters from the refitted spectra constrained by empirical upper state levels: Study of the 9,500–14,500 cm^{-1} region. J. Quant. Spectros. Rad. Trans. **109**, 559–568 (2008)

R.A. Toth, Measurements of H_2 ^{16}O line positions and strengths: 11,610 to 12,861 cm^{-1}. J. Mol. Spectrosc. **166**, 176–183 (1994)

T. Trickl, D. Proch, K.L. Kompa, The Lyman-Birge-Hopfield system of nitrogen: Revised calculation of the energy levels. J. Mol. Spectros. **171**, 374–384 (1995)

D.D. Turner, J.E.M. Goldsmith, Twenty-four-hour Raman lidar water vapor measurements during the atmospheric radiation measurement program's 1996 and 1997 water vapor intensive observation periods. J. Atmos. Ocean. Tech. **16**, 1062–1076 (1999)

D.D. Turner, R. A. Ferrare, L.A.H. Brasseur, W.F. Feltz, T.P., Tooman, Automated retrievals of water vapor and aerosol profiles from an operational Raman lidar. J. Atmos. Ocean. Tech. **19**, 37–50 (2002). doi:10.1175/1520-0426(2002)019h0037:AROWVAi2.0.CO;2

G. Vaughan, D.P. Wareing, L. Thomas, V. Mitev, Humidity measurements in the free troposphere using Raman backscatter, Q. J. Roy. Meteorol. Soc. **114**, 1471–1484 (1988). doi:10.1002/qj.49711448406, http://dx.doi.org/10.1002/qj.49711448406

VDI, VDI (Verein Deutscher Ingenieure) Guide Line 4210, *Remote sensing, Atmospheric measurements with LIDAR*, Measuring gaseous air pollution with the DAS LIDAR (1999)

H. Vogelmann, T. Trickl, Wide-range sounding of free-tropospheric water vapor with a differential-absorption lidar (DIAL) at a high-altitude station. Appl. Opt. **47**, 2116–2132 (2008). doi: 10.1364/AO.47.002116

H. Vogelmann, R. Sussmann, T. Trickl, T. Borsdorff, Intercomparison of atmospheric water vapor soundings from the differential absorption lidar (DIAL) and the solar FTIR system on Mt. Zugspitze. Atmos. Meas. Technol. **4**, 835–841 (2011)

H. Vömel, D.E. David, K. Smith, Accuracy of tropospheric and stratospheric water vapor measurements by the cryogenic frost point hygrometer: Instrumental details and observations. J. Geophys. Res. 112, (2007). doi:10.1029/2006JD007224

J. Wang, L. Zhang, Systematic errors in global radiosonde precipitable water data from comparisons with ground-based GPS measurements. J. Clim., **21**, 2218–2238 (2008). doi:10.1175/2007JCLI1944.1

A. Weber, *Topics in Current Physics*, vol. 11, chap. Raman Spectroscopy of Gases and Liquids, (Springer, Berlin, Germany, 1979) p. 290

C. Weitkamp, Lidar, *Range-Resolved Optical Remote Sensing of the Atmosphere* (Springer, Berlin, Germany, 2005)

E.R. Westwater, M. Falls, I.A. Popa Fotino, Ground-based microwave radiometric observations of precipitable water vapor: A comparison with ground truth from two radiosonde observing systems. J. Atmos. Ocean. Tech. **6**, 724–730 (1989)

N.D. Whiteman, S.H. Melfi, R.A. Ferrare, Raman lidar system for the measurement of water vapor and aerosols in the Earth's atmosphere, Appl. Opt. **31**, 3068–3082 (1992)

D.N. Whiteman, Examination of the traditional Raman lidar technique. I. evaluating the temperature-dependent lidar equations. Appl. Opt. **42**, 2571–2592 (2003a). http://ao.osa.org/abstract.cfm?URI=ao-42-15-2571

D.N.Whiteman, Examination of the traditional Raman lidar technique. II. evaluating the ratios for water vapor and aerosols. Appl. Opt. 42, 2593–2608 (2003b). http://ao.osa.org/abstract.cfm?URI=ao-42-15-2593

D.N. Whiteman, K. Rush, S. Rabenhorst, W. Welch, M. Cadirola, G. McIntire, F. Russo, M. Adam, D. Venable, R. Connell, I. Veselovskii, R. Forno, B. Mielke, B. Stein, T. Leblanc, S. McDermid, H. Vömel, Airborne and ground-based measurements using a high-performance Raman lidar. J. Atmos. Ocean. Technol. **27**, 1781–1801 (2010). doi:10.1175/2010JTECHA1391.1

M. Wirth, A. Fix, P. Mahnke, H. Schwarzer, F. Schrandt, G. Ehret, The airborne multi-wavelength water vapour differential absorption lidar WALES: system design and performance, Appl. Phys. B 96 (2009), 201–213

V. Wulfmeyer, Ground-based differential absorption lidar for water-vapor and temperature profiling: Development and specifications of a high-performance laser transmitter. Appl. Opt. **37**, 3804–3824 (1998a)

V. Wulfmeyer, J. Bösenberg, Ground-based differential absorption lidar for water-vapor profiling: Assessment of accuracy, resolution, and meteorological applications. Appl. Opt. **37**, 3825–3844 (1998b). doi:10.1364/AO.37.003825

V. Wulfmeyer, C. Walther, Future performance of ground-based and airborne water-vapor differential absorption lidar. I. Overview and theory. Appl. Opt. **40**, 5304–5320 (2001a)

V. Wulfmeyer, C. Walther, Future performance of ground-based and airborne water-vapor differential absorption lidar. II. Simulations of the precision of a near-infrared, high-power system. Appl. Opt. **40**, 5321–5336 (2001b)

V. Yushkov, S. Merkulov, V.A., *Optical balloon hygrometer for upper stratosphere and stratosphere water vapour measurements*, ed. by J. Wang, B. Wu, T. Ogawa, Z.-H. Guan, Optical remote sensing of the atmosphere and clouds, vol. 3501 of Proceeding of SPIE, (SPIE International Society for Optical Engine, 1998) pp. 439–445

V.V. Zuev, V.E. Zuev, Y.S. Makushkin, V. N. Marichev, A.A. Mitsel, Laser sounding of atmospheric humidity: experiment. Appl. Opt. **22**, 3742–3746 (1983)

Part III
Networks and Global Monitoring

Chapter 8
Role of Ground-based Networks and Long-term Programmes for Global Monitoring

Geir O. Braathen

Water vapour is the most abundant greenhouse gas in the atmosphere. Water vapour is also the most important gaseous source of infrared opacity in the atmosphere, accounting for about 60 % of the natural greenhouse effect for clear skies (Kiehl and Trenberth 1997). However, changes in its concentration are considered to be a result of climate feedbacks related to the warming of the atmosphere rather than a direct result of industrialization. The feedback loop in which water is involved is critically important to projecting future climate change, but as yet is still fairly poorly measured and understood. A discussion of the role of water vapour in the climate system can be found in Chap. 4 of The Working Group I contribution to the IPCC's Fourth Assessment Report (AR4) (Trenberth et al. 2007). An account of the hydrological cycle, clouds, precipitation and interactions between precipitation and aerosols can be found in (Barrie et al. 2009).

In 2000, the SPARC Programme published its Assessment of Upper Tropospheric and Stratospheric (UTS) Water Vapour (Kley et al. 2000). The key topic addressed in this report was the analysis and the assessment of the long-term changes of UTS water vapour, with an emphasis on the observed increase of water in the stratosphere. The report had a strong focus describing and comparing relevant data sets using in situ hygrometers and remote sensing instruments from laboratories all over the world in order to create a suitable data set, including historical data back to the 1940s. Data presented in the report are available at the SPARC data centre (see link at the end of this chapter). The distribution and variability of UTS water vapour and the impact of the increased water vapour on radiation, dynamics and chemistry were discussed.

Following the recommendations of this report, climatological measurement programmes have continued, new campaigns to investigate UTS water vapour have been carried out, new satellite observation programmes have been launched, and many model and laboratory studies have been made to explain the observations. Emerging from the new observations, an additional "puzzling" question became apparent in that unexpectedly high relative humidities were observed, largely in the cold tropopause

G. O. Braathen (✉)
WMO, 7 bis, Avenue de la Paix CH-1211 Geneva 2, Switzerland
e-mail: GBraathen@wmo.int

N. Kämpfer (ed.), *Monitoring Atmospheric Water Vapour,*
ISSI Scientific Report Series 10,
DOI 10.1007/978-1-4614-3909-7_8, © Springer Science+Business Media, LLC 2013

region both inside and outside of clouds (Peter et al. 2008). Data quality, in particular knowing the absolute accuracy and not simply the relative discrepancies between different sensors, has become a crucial issue if we are to assess these observations. These accuracy issues have lead to the need of cross validation of established and recently developed hygrometers, both in the field and in the laboratory.

In light of these developments, it seems timely to update the SPARC water vapour assessment of 2000. In particular, there is a need to summarise the relevant results over the past decade from various field experiments, laboratories and models in a comprehensive report or review publication. The major goal of such an exercise is to assess the value and the accuracy of recent measurements and to give new recommendations and guidelines for future research on water vapour in the upper troposphere and the stratosphere. Therefore, the SPARC Scientific Steering Group proposed during its annual meeting in September 2007 to initiate a new water vapour initiative coordinated by Cornelius Schiller, Thomas Peter and Karen Rosenlof. In particular, there is a need to summarise the relevant results over the past decade from various field experiments, laboratories and models in a comprehensive report or review publication. The major goal of such an exercise is to assess the value and the accuracy of recent measurements and to give new recommendations and guidelines for future research on upper troposphere and stratosphere water vapour. A major outcome of the activity is expected to be an updated Water Vapour Assessment (WAVAS) report that summarises findings and recommends future directions.

IGACO (**Integrated Global Atmospheric Chemistry Observations**) is a theme in the former International Global Observing Strategy (IGOS) and now belongs under the GEO (Group on Earth Observations) umbrella.

IGACO activities are based on the IGACO Theme Report that was prepared by an expert international group convened by the World Meteorological Organization (WMO) and the European Space Agency (ESA) (Barrie and Langen 2004) and reviewed independently by eminent scientists including two Nobel Prize winners. IGACO (International Global Atmospheric Chemistry Observations) is a strategy for bringing together ground-based, aircraft and satellite observations of thirteen chemical species in the atmosphere. The implementation of IGACO will be organised through the Global Atmospheric Watch (GAW) programme of WMO. For IGACO, four focus areas have been selected: Ozone, Aerosols, Greenhouse gases and Air Quality/Long-range transport. Activities in each focus area will be linked to corresponding GAW Science Advisory Groups (SAGs).

In addition to the four focus areas, cross-cutting activities (i.e., activities common to all focus areas) will be coordinated through the IGACO Implementation Team, co-chaired by WMO Commission for Atmospheric Sciences (CAS) and Committee on Earth Observation Satellites (CEOS), represented by ESA.

The implementation of IGACO will take place in phases, with the first phase lasting 2006–2010, and the second phase from 2010 onwards. Long-term activities have been included as tasks in the GAW Strategic Implementation Plan for 2008–2015 (WMO 2008a). In each phase, activities will be defined taking into account scientific priorities and feasibility aspects.

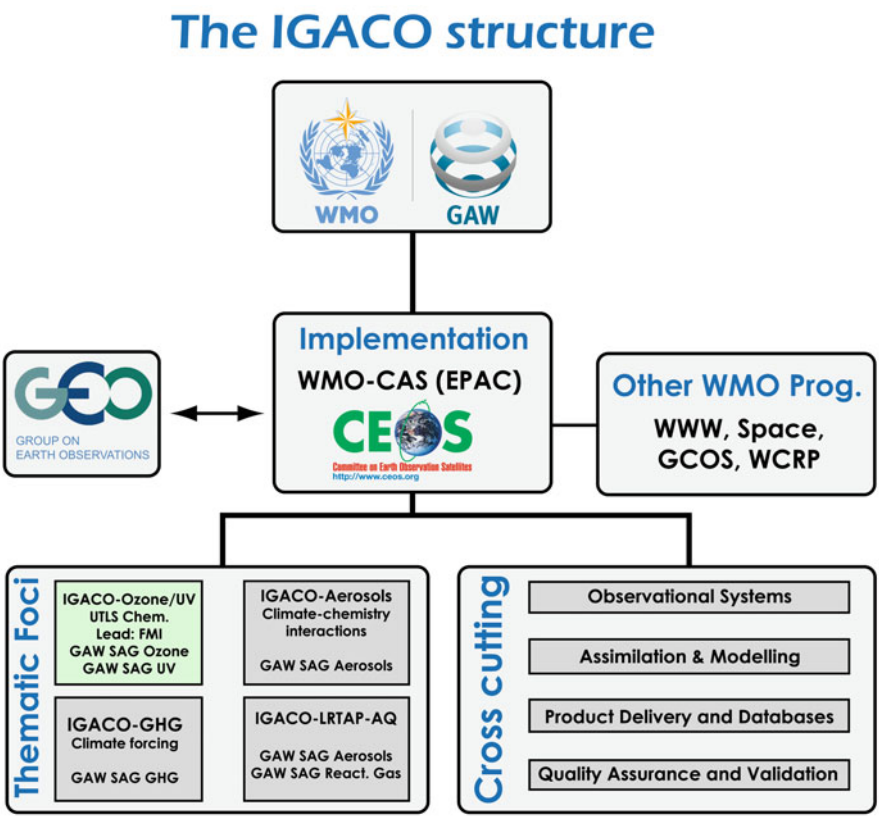

Fig. 8.1 The IGACO Structure

Everyday work is coordinated by WMO jointly with a secretariat hosted by a research institution in the field. The IGACO-Ozone secretariat is hosted by the Finnish Meteorological Institute. Figure 8.1 shows the structure of IGACO.

Water vapour (tropospheric and stratospheric) is one of the constituents selected by the IGACO report, and its importance for air quality, for the oxidative capacity of the atmosphere, for climate and for stratospheric ozone depletion is discussed in the report. Water vapour will be measured from in-service passenger aircraft (Airbus) through the European project IAGOS-ERI (discussed later in this chapter). The IAGOS-ERI project contributes to WMO's Global Atmosphere Watch Programme within the framework of the IGACO strategy.

Two major ground-based networks deal with measurements of water vapour in the free troposphere and above:

The **Network for the Detection of Atmospheric Composition Change** (NDACC) consists of more than 70 remote-sensing research stations for observing and understanding the physical and chemical state of the stratosphere and upper troposphere and for assessing the impact of stratosphere changes on the underlying

troposphere and on global climate. NDACC has strict data quality requirements. The goals of NDACC are to:

- Detecting trends in overall atmospheric composition and understanding their impacts on the stratosphere and troposphere,
- Studying atmospheric composition variability at interannual and longer timescales,
- Establishing links and feedbacks between climate change and atmospheric composition,
- Calibrating and validating space-based measurements of the atmosphere,
- Supporting process-focused scientific field campaigns, and
- Testing and improving theoretical models of the atmosphere

Figure 8.2 shows a map of the NDACC stations.

Incepted initially as the Network for the Detection of Stratospheric Change (NDSC) (Kurylo and Solomon 1990), NDACC began network operations officially in January 1991, although some stations offer data records back to the 1980s. Nowadays, while NDACC remains committed to monitoring changes in the stratosphere with an emphasis on the long-term evolution of the ozone layer, its priorities have broadened considerably to encompass issues such as the detection of trends in overall atmospheric composition and understanding their impacts on the stratosphere and troposphere, and establishing links between climate change and atmospheric composition. NDACC recognises water vapour as one of the key compounds to observe in order to understand the links between atmospheric chemistry and climate. Complementary information on the total column, vertical distribution and temporal changes of atmospheric water vapour is measured within NDACC with several observational techniques: Microwave radiometers have been used since the inception of NDSC/NDACC for water vapour measurements in the stratosphere and mesosphere. There are five stations in NDACC that measure water vapour with the microwave technique (Onsala, Sweden; Bern, Switzerland; Table Mountain, Wrightwood, California; Mauna Loa, Hawaii; Lauder, New Zealand).

Recently the Raman Lidar has been designated as NDACC-approved for profile measurements of water vapour in the troposphere and across the tropopause. Several Raman lidar stations (London, Ontario, Canada; Rom Tor-Vergata, Italy; Table Mountain, Wrightwood, California; Observatoire de Haute Provence, France; Mauna Loa, Hawaii) have been accepted in 2010 as NDACC water vapour instruments. A travelling system for mobile intercomparisons has also been accepted. Water vapour sondes (cryogenic frost point hygrometers and Lyman-α hygrometers) have been approved for profile measurements in the troposphere and stratosphere. Fourier Transform infrared spectrometers are also able to measure water vapour. Nearly twenty NDACC stations are equipped with FTIR instruments. All these measurement techniques are described in detail in the other chapters of this book.

Figure 8.3 shows the measurement capabilities of the various instrument types deployed in the NDACC network in terms of species measured and altitude range.

The diagram on Fig. 8.4 shows how NDACC is organised.

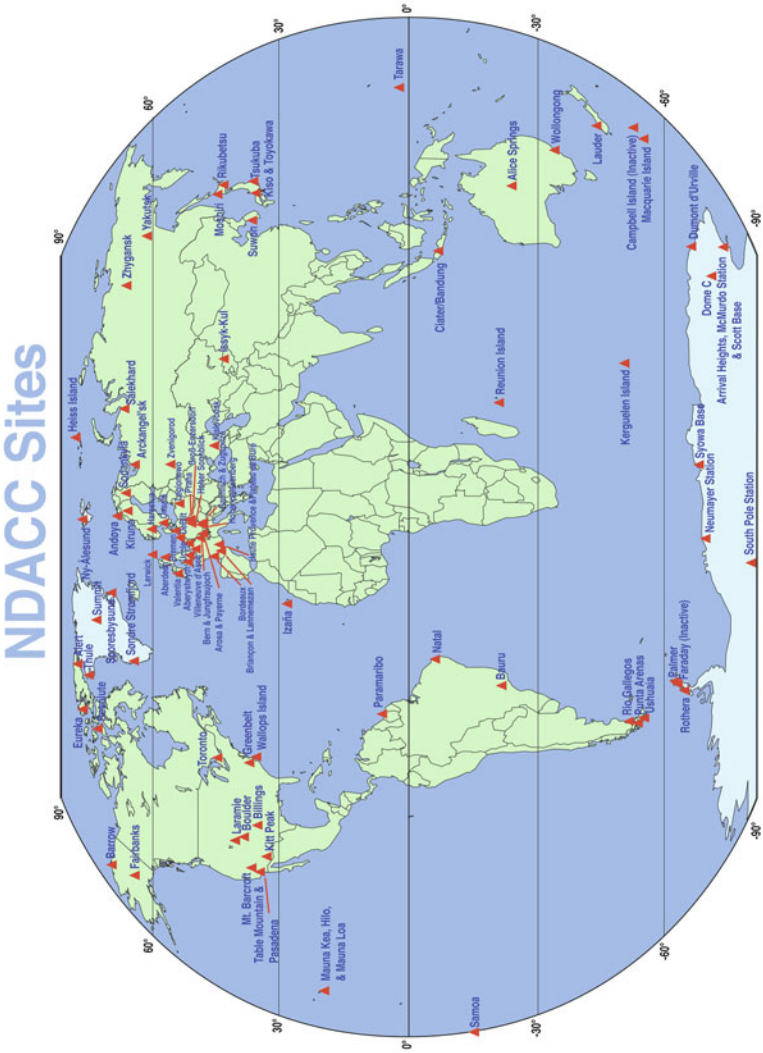

Fig. 8.2 The NDACC network consists of approx. 70 stations covering the two polar regions, middle latitudes in both hemispheres, and the tropical region

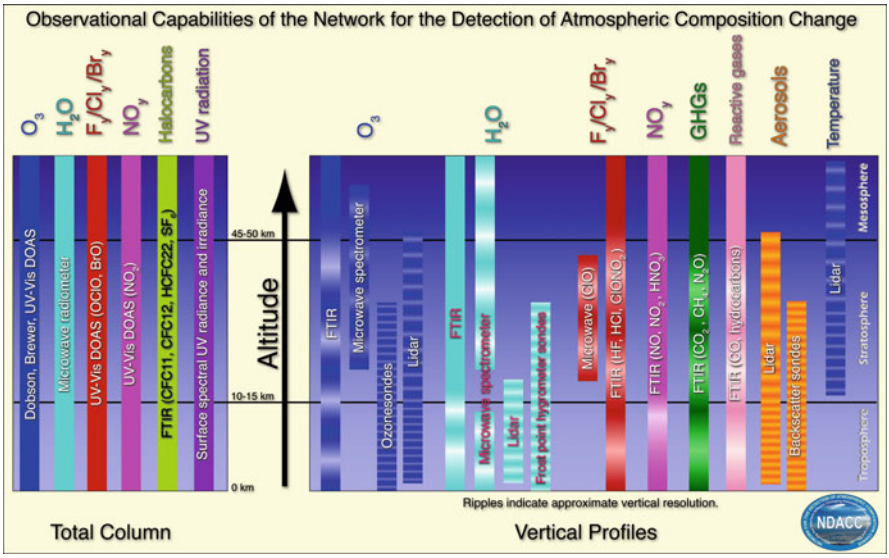

Fig. 8.3 The NDACC network is capable of measuring a large number of atmospheric species. In this chart the different species have been lumped together in ten different categories. For each category of species it is indicated which types of instruments that are capable of measuring one or more species. Bars of uniform colour represent total column measurements and bars with ripples indicate vertically resolved measurements, where the extent of the bar roughly indicates the vertical range and the density of the ripples indicate the vertical resolution of the measurements

The **Global Climate Observing System** (GCOS) is a joint undertaking of the World Meteorological Organization (WMO), the Intergovernmental Oceanographic Commission (IOC) of the United Nations Educational Scientific and Cultural Organization (UNESCO), the United Nations Environment Programme (UNEP) and the International Council for Science (ICSU). Its goal is to provide comprehensive information on the total climate system, involving a multidisciplinary range of physical, chemical and biological properties, and atmospheric, oceanic, hydrological, cryospheric and terrestrial processes. It includes both in situ and remote sensing components, with its space based components coordinated by the Committee on Earth Observation Satellites (CEOS) and the Coordination Group for Meteorological Satellites (CGMS). GCOS is intended to meet the full range of national and international requirements for climate and climate-related observations. As a system of climate-relevant observing systems, it constitutes, in aggregate, the climate observing component of the Global Earth Observation System of Systems (GEOSS). Water vapour is defined as an Essential Climate Variable (ECV) by GCOS.

The **GCOS Reference Upper Air Network** (GRUAN) is an international reference observational network, designed to meet climate requirements and to fill a major void in the current global observing system (Seidel et al. 2009). The GRUAN Implementation Meeting took place in Lindenberg, Germany on 26–28 February 2008 (WMO 2008b). The expression "upper air" is usually used for the region of the atmosphere which is above the lower troposphere. Although no distinct lower

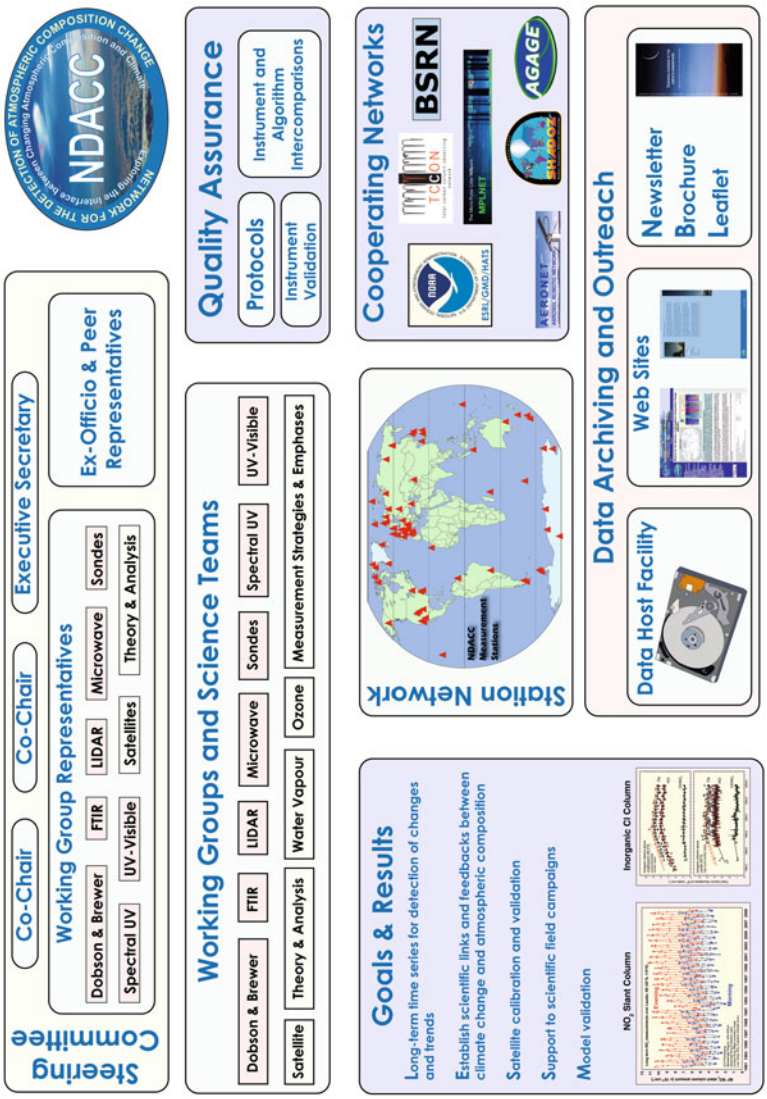

Fig. 8.4 The structure of the Network for the Detection of Atmospheric Composition Change (NDACC)

limit is set, the term is generally applied to levels above that at which the pressure is 850 hPa.

Upper air observations within the GRUAN network will provide long-term high-quality climate records, will be used to calibrate and validate data from space based remote sensors, to test their long-term stability, to ensure multi-mission consistency in case of gaps between satellite missions, and will provide accurate data for the study of atmospheric processes. GRUAN has been identified by the climate community as being required to generate long-term high quality climate records, to constrain and calibrate data from more spatially-comprehensive global observing systems (inc. satellites and current radiosonde networks), and to fully characterize the properties of the atmospheric column. GRUAN is building on existing observational networks, such as NDACC, the Atmospheric Radiation Measurement (ARM) Programme, GCOS Upper Air Network (GUAN), Global Atmosphere Watch (GAW), Baseline Surface Radiation Network (BSRN) and the GCOS Surface Network (GSN). For measurements of water vapour, GRUAN will focus on high-quality radiosondes and frost point hygrometers of various kinds for vertically resolved measurements of water vapour in the troposphere, the tropopause region and the lower stratosphere. GRUAN is still under establishment, so there are no water vapour results yet from that network. A link to the GRUAN web page is given below in the section on useful links.

In addition to measurements from balloons and ground based instruments of NDACC and GRUAN water vapour is also measured from in-service aircraft:

The programme entitled **Measurements of OZone, water vapour, carbon monoxide and nitrogen oxides by in-service AIrbus airCraft** (MOZAIC) was initiated in 1993 by European scientists, aircraft manufacturers and airlines to better understand the natural variability of the chemical composition of the atmosphere and how it is changing under the influence of human activity, with particular interest in the effects of aircraft (Marenco et al. 1998). MOZAIC consists of automatic and regular measurements of reactive gases by five long range passenger airliners. A large database of measurements (about 30,000 flights since 1994) allows studies of chemical and physical processes in the atmosphere, validations of global chemistry transport models and satellite retrievals. MOZAIC data provide detailed climatologies of trace gases at 9–12 km where subsonic aircraft emit most of their exhaust and which is a very critical domain (e.g. radiatively and with respect to Stratosphere-Troposphere exchanges) still imperfectly described in existing models. MOZAIC data also provide frequent vertical profiles over a large number of airports (Frankfurt, Paris, Vienna, New-York, Atlanta, Tokyo, Beijing, Sao Paulo, Johannesburg etc.). The instrumentation used to measure water vapour in the MOZAIC project is described in Chap. 2. The data in the MOZAIC data base has been used, and is still being used by many scientists around the world. By mid-2010 approx. 150 scientific publications have made use of MOZAIC data.

The research project MOZAIC has evolved towards the European Research Infrastructure IAGOS (In-service Aircraft for a Global Observing System) that is ensured through two projects:

Integration of routine Aircraft measurements into a Global Observing System—Design Study (IAGOS-DS) is a Design Study for New Infrastructures funded through the European Commission's 6th Framework Programme for the 2005–2009 time period. It pursues the preparation of the distributed infrastructure IAGOS-ERI for observations of atmospheric composition, aerosols, clouds and contrails on the global scale from commercial in-service aircraft. For this purpose, new instrument packages are developed based on the former MOZAIC instrumentation for O_3, H_2O, CO and NO_y/NO_x. A link to the project web page is given below in the section on useful links.

In-service Aircraft for a Global Observing System—European Research Infrastructure (IAGOS-ERI) will establish and operate a distributed infrastructure for long term observations of atmospheric composition, aerosol and cloud particles on a global scale from a fleet of initially 10–20 long range in-service aircraft of internationally operating airlines. A link to the project web page is given below in the section on useful links.

Civil Aircraft for Regular Investigation of the atmosphere Based on an Instrument Container (CARIBIC) is an innovative scientific project to study and monitor important chemical and physical processes in the Earth's atmosphere (Brenninkmeijer et al. 2007). Detailed and extensive measurements are made during long distance flights. An airfreight container with automated scientific apparatus which are connected to an air and particle (aerosol) inlet underneath the aircraft is deployed on an Airbus A340–600 from Lufthansa since December 2004. The water vapour analyzer operates with two different measuring principles: a cryocooled chilled mirror condensation type hygrometer (Buck Research Instruments, Boulder, USA) and a laser based dual channel photoacoustic water vapour detector (WaSulTM- Hygro, Hilase Ltd., Szeged, Hungary). The instrument is supervised by Institute for Meteorology and Climate Research (IMK), Forschungszentrum Karlsruhe, Germany. On the average one flight is carried out per week.

IAGOS and CARIBIC are complementary projects in the sense that IAGOS gives frequent measurements of a limited number of parameters, whereas CARIBIC gives data on a large number of parameters with less frequency.

The Global Atmosphere Watch (GAW) programme of WMO is a partnership involving 80 countries, which provides reliable scientific data and information on the chemical composition of the atmosphere, its natural and anthropogenic change, and helps to improve the understanding of interactions between the atmosphere, the oceans and the biosphere. The rationale for the Global Atmosphere Watch is the need to understand and control the increasing influence of human activity on the global atmosphere. Among the grand challenges are:

- Stratospheric ozone depletion and the increase of ultraviolet (UV) radiation;
- Changes in the weather and climate related to human influence on atmospheric composition, particularly, greenhouse gases, ozone and aerosols;
- Risk reduction of air pollution on human health and issues involving long-range transport and deposition of air pollution

GAW focuses on global networks for GHGs, ozone, UV, aerosols, selected reactive gases, and precipitation chemistry. The mission of GAW, taking into account the Integrated Global Atmospheric Chemistry Observations (IGACO) strategy, is to:

- Reduce environmental risks to society and meet the requirements of environmental conventions,
- Strengthen capabilities to predict climate, weather and air quality,
- Contribute to scientific assessments in support of environmental policy,

through

- Maintaining and applying global, long-term observations of the chemical composition and selected physical characteristics of the atmosphere,
- Emphasising quality assurance and quality control,
- Delivering integrated products and services of relevance to users, GAW is considered the atmospheric chemistry component of the Global Climate Observing System (GCOS).

Details on the GAW programme can be found in the GAW strategic plan (WMO 2008a). Figure 8.5 shows the structure of GAW.

The **WMO Information System** (WIS) is the pillar of the WMO strategy for managing and moving weather, water and climate information in the Twenty-first century. WIS provides an integrated approach suitable for all WMO Programmes to meet the requirements for routine collection and automated dissemination of observed data and products, as well as data discovery, access and retrieval services for all weather, climate, water and related data produced by centres and Member countries in the framework of any WMO Programme.

WIS is being designed to dramatically extend WMO Members' ability to collect and disseminate data and products. It will be the core information system utilized by WMO Members, providing linkages for all WMO and supported programmes associated with weather, climate, water, and related natural disasters. It is being built upon the Global Telecommunication System of WMO's World Weather Watch, using standard elements and at a pace feasible for all Members. More information can be found in the project and implementation plan for WIS (WMO 2009).

Figure 8.6 shows a diagram of the WMO Information System.

The networks and programmes mentioned in this chapter are important contributions to the Global Earth Observing System of Systems (GEOSS). They are particularly relevant to its climate, weather and water cycle Societal Benefit Areas (SBAs).

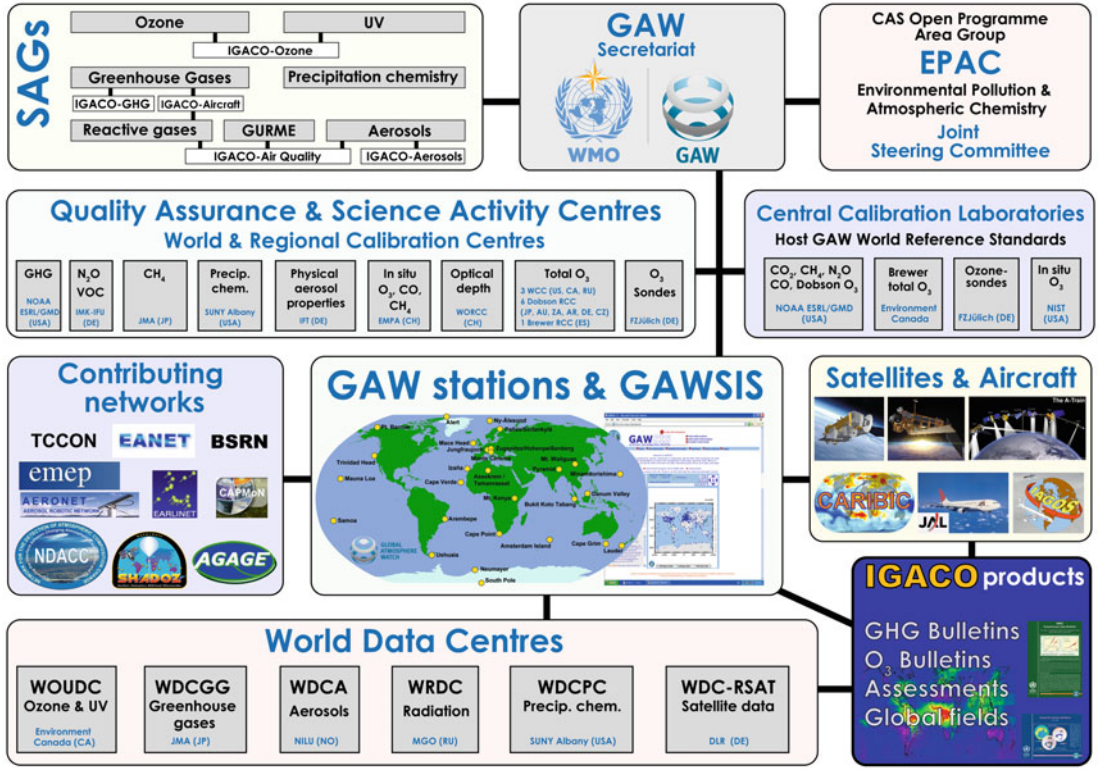

Fig. 8.5 The Global Atmosphere Watch System (GAW). The system is governed by the EPAC Joint Steering Committee and the seven Science Advisory Groups (SAGs). On the left is a box showing networks that contribute to or collaborate with GAW

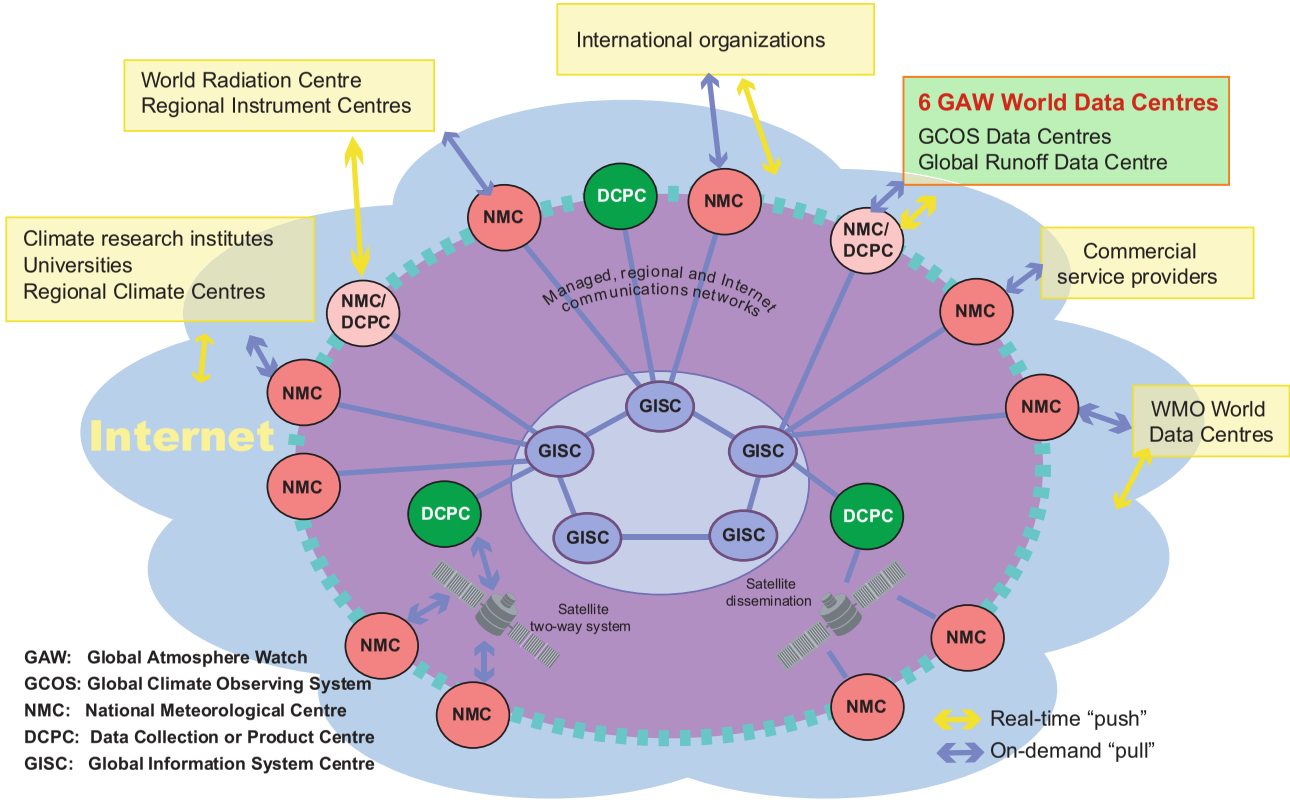

Fig. 8.6 The WMO Information System (WIS). WIS encompasses three types of centres. For regional and global connectivity, Global Information System Centres (GISCs) will collect and distribute the information meant for routine global dissemination, while serving as collection and distribution centres in their areas of responsibilities; they provide entry points, through unified portals and comprehensive metadata catalogues, for any request for data held within the WIS. Connected to the GISCs, the Data Collection or Production Centres (DCPCs) will be responsible for the collection or generation of sets of data, forecast products, processed or value-added information, and/or for providing archiving services. National Centres (NCs) will collect and distribute data on a national basis and will coordinate or authorize the use of the WIS by national users, normally under a policy established by the respective permanent representative with WMO

Useful links

More information on networks and programmes can be found by consulting the following links:

CARIBIC: http://www.caribic-atmospheric.com/
GAW: http://www.wmo.int/pages/prog/arep/gaw/gaw_home_en.html
GCOS: http://www.wmo.int/pages/prog/gcos/
GEO/GEOSS: http://earthobservations.org
GRUAN: http://www.gruan.org
IAGOS-DS: http://www.iagos.org/Related_Projects
IAGOS-ERI: http://www.iagos.org/
IGACO-Ozone/UV: http://www.igaco-o3.fi/en/index.html
MOZAIC: http://mozaic.aero.obs-mip.fr/web/
NDACC: http://www.ndacc.org
SPARC data centre: http://www.sparc.sunysb.edu/
WIS: http://www.wmo.int/pages/prog/www/WIS/

References

L. Barrie, J. Langen, The changing atmosphere: An integrated global atmospheric chemistry observation theme for the IGOS partnership, 2004, Tech. Rep. WMO GAW Report no. 159, European Space Agency, ESA SP-1282 and world meteorological organization, WMO TD No. 1235, (2004), ftp://ftp.wmo.int/Documents/PublicWeb/arep/gaw/gaw159.pdf

L. Barrie, U. Lohmann, S. Yuter, 2009, *Z. Levin, W.R. Cotton*: *Aerosol Pollution Impact on Precipitation*, Chap. 1, Introduction, Springer Science + Business Media B.V. (2009). ISBN: 978-1-4020-8689-2

C.A.M. Brenninkmeijer, P. Crutzen, F. Boumard, T. Dauer, B. Dix, R. Ebinghaus, D. Filippi, H. Fischer, H. Franke, U. Frieß, J. Heintzenberg, F. Helleis, M. Hermann, H.H. Kock, C. Koeppel, J. Lelieveld, M. Leuenberger, B.G. Martinsson, S. Miemczyk, H.P. Moret, H.N. Nguyen, P. Nyfeler, D. Oram, D. O'Sullivan, S. Penkett, U. Platt, M. Pupek, M. Ramonet, B. Randa, M. Reichelt, T.S. Rhee, J. Rohwer, K. Rosenfeld, D. Scharffe, H. Schlager, U. Schumann, F. Šlemr, D. Sprung, P. Stock, R. Thaler, F. Valentino, P. van Velthoven, A. Waibel, A. Wandel, K. Waschitschek, A. Wiedensohler, I. Xueref-Remy, A. Zahn, U. Zech, H. Ziereis, Civil aircraft for the regular investigation of the atmosphere based on an instrumented container: The new CARIBIC system. Atmos. Chem. Phys. **7**, 4953–4976 (2007)

J.T. Kiehl, K.E Trenberth, Earth's annual global mean energy budget, Bull. Am. Met. Soc. **78**, 197–208 (1997)

D. Kley, J.M. Russell III, C. Phillips, SPARC assessment of upper tropospheric and stratospheric water vapour, Tech. Rep. SPARC Report No. 2, WCRP-113, WMO/TD No. 1043, world meteorological organization, (2000), http://www.atmosp.physics.utoronto.ca/SPARC/WAVASFINAL_000206/WWW_wavas/Cover.html

M.J. Kurylo, S. Solomon, Network for the detection of stratospheric change, Tech. Rep. NASA Report, Code EEU, NASA (1990)

A. Marenco, V. Thouret, P. Nédélec, H. Smit, M. Helten, D. Kley, F. Karcher, P. Simon, K. Law, J. Pyle, G. Poschmann, R.V. Wrede, C. Hume, T. Cook, Measurement of ozone and water vapor

by Airbus in-service aircraft: The MOZAIC airborne program, An overview. J. Geophys. Res. **103**, 25631–25642 (1998)

S.J. Oltmans, D.J. Hofmann, Increase in lower-stratospheric water vapour at a mid-latitude Northern Hemisphere site from 1981 to 1994. Nature, **374**, 146–149, (1995). doi:10.1038/374146a0

S.J. Oltmans, H. Vömel, D.J. Hofmann, K.H. Rosenlof, D. Kley, The Increase in stratospheric water vapor from Balloonborne, Frostpoint Hygrometer Measurements at Washington, D.C., and Boulder, Colorado. Geophys. Res. Lett. **27**, 3453–3456 (2000)

T. Peter, M. Krämer, O. Möhler, Upper tropospheric humidity: A report on an international workshop, 12–15 June 2007, Karlsruhe, Germany, SPARC Newsletter no. 30 (2008), http://www.atmosp.physics.utoronto.ca/SPARC/Newsletter30Web/53294-1%20SPRAC%20Newsletter-LR.pdf

M. Scherer, H. Vömel, S. Fueglistaler, S.J. Oltmans, J. Staehelin, Trends and variability of midlatitude stratospheric water vapour deduced from the re-evaluated Boulder balloon series and HALOE, Atmos. Chem. Phys. **8**, 1391–1402 (2008)

D. Seidel, F. Berger, H. Diamond, J. Dykema, D. Goodrich, F. Immler, W. Murray, T. Peterson, D. Sisterson, M. Sommer, P. Thorne, H. Vömel, J. Wang, Reference Upper-Air Observations for Climate: Rationale, Progress, and Plans. Bull. Amer. Meteorol. Soc. **90**, 361–369 (2009). doi:10.1175/2008BAMS2540.1

K. Trenberth, P. Jones, P. Ambenje, R. Bojariu, D. Easterling, A. Klein Tank, D. Parker, F. Rahimzadeh, J. Renwick, M. Rusticucci, B. Soden, P. Zhai, *Climate Change 2007: The Physical Science Basis. Contribution of Working Group I to the Fourth Assessment Report of the Intergovernmental Panel on Climate Change*, eds. by S. Solomon, D. Qin, M. Manning, Z. Chen, M. Marquis, K.B. Averyt, M. Tignor, H.L. Miller chap. Observations: Surface and Atmospheric Climate Change (Cambridge University Press, Cambridge, 2007)

WMO, WMO/GAW Strategic Plan: 2008–2015—A Contribution to the Implementation of the 141 WMO Strategic Plan: 2008–2011, Tech. Rep. WMO TD No. 1384, world meteorological organization (2008a), ftp://ftp.wmo.int/Documents/PublicWeb/arep/gaw/gaw172-26sept07.pdf

WMO, World meteorological organization, intergovernmental oceanographic commission, united nations environment programme, international council for science, GCOS reference upper air network (GRUAN). Report of the GRUAN implementation meeting Lindenberg, Germany, Tech. rep., world meteorological organization (2008b), http://www.wmo.int/pages/prog/gcos/Publications/gcos-121.pdf. Accessed 26–28 Feb 2008

WMO, Project And Implementation Plan, WMO Information System, "Managing and Moving Weather, Water and Climate Information in the 21st Century", World Weather Watch Information Systems and Services, Tech. rep., World Meteorological Organization (2009), http://www.wmo.int/ pages/prog/www/WIS/documents/WIS-ProjectPlan-v1-1.doc.

Chapter 9
Satellite Sensors Measuring Atmospheric Water Vapour

Joachim Urban

9.1 Introduction

Because of its importance in the atmosphere (for surface weather, energy balance of the climate system, and atmospheric chemistry), water vapour has been measured from space since the early days of satellite Earth observation by a variety of sensors and different techniques covering the altitude range from the surface up to the lower thermosphere region around 100 km. Information on the water content of the troposphere, where the bulk of atmospheric water resides, is available from nadir sounding (down-looking) instruments, widely used since the 1960s in the operational meteorological observation systems. Measurements of the small water vapour amounts of only a few water molecules per million air molecules in the upper troposphere and throughout the entire middle atmosphere require use of the limb sounding observation geometry, in emission or (solar, stellar, satellite-to-satellite) occultation, providing high sensitivity owing to the long emission or absorption path along the line-of-sight.

Generally, limb scanning techniques allow to obtain vertically well resolved profile measurements of water vapour throughout the middle atmosphere with resolution of typically only a few kilometres, since altitude information is obtained from the relative pointing information of the scanning satellite sensors. Water, cloud, or aerosol absorption are often limiting factors of limb observations in the troposphere and lowermost stratosphere, depending on wavelength. The vertical resolution of a nadir measurement is determined by the frequency dependence of the water absorption in the observed set of spectral channels, and retrievals provide the (Jacobian weighted) average humidity over wider layers of typically several kilometres thickness. The penetration depth of a nadir sounder into the troposphere depends on the absorption in the observed spectral band(s), which is often dominated by cloud absorption but also depends on the amount of water vapour itself as a dryer atmosphere allows deeper penetration.

J. Urban (✉)
Department of Earth and Space Sciences, Chalmers University of Technology,
41296 Göteborg, Sweden
e-mail: joaurb@chalmers.se

N. Kämpfer (ed.), *Monitoring Atmospheric Water Vapour,*
ISSI Scientific Report Series 10,
DOI 10.1007/978-1-4614-3909-7_9, © Springer Science+Business Media, LLC 2013

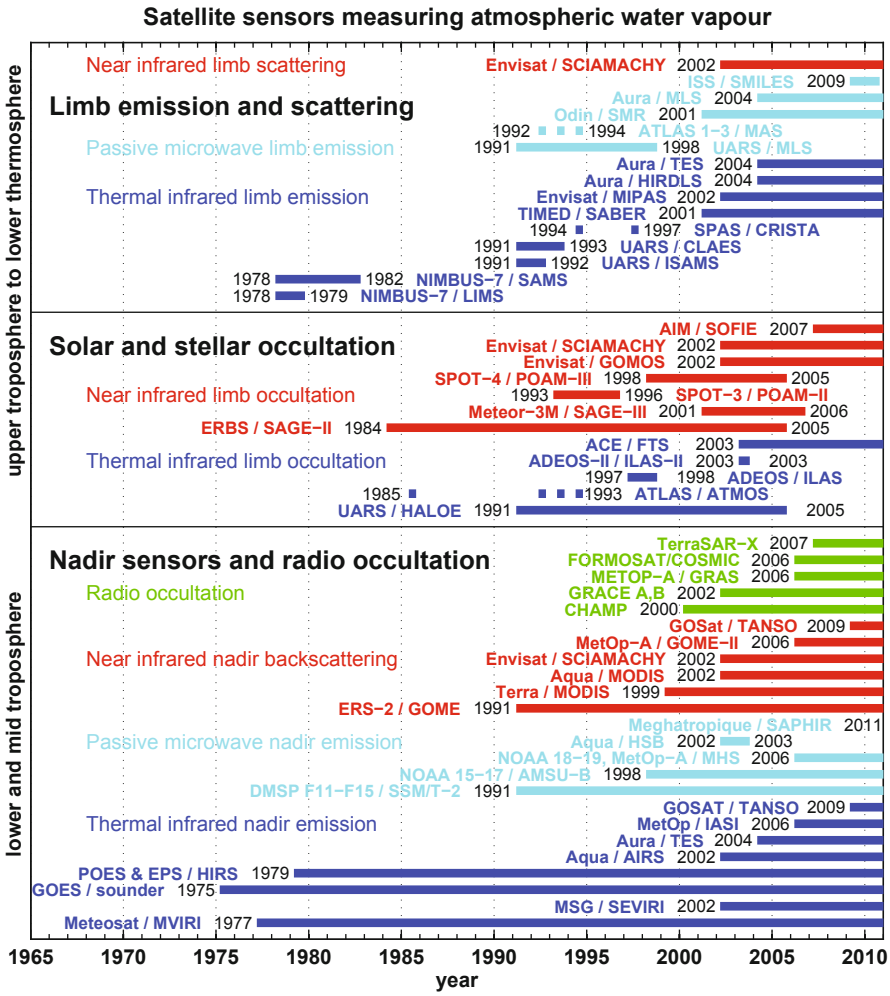

Fig. 9.1 Overview of satellite instruments measuring atmospheric water vapour, sorted with respect to observation technique and roughly divided in altitude regions

Nadir sounding techniques find their application on satellites in geo-stationary Earth orbits (GEO) at about 36,000 km, fixed to a selected longitude, and in low Earth orbits (LEO) below 1,000 km. Limb sounders providing vertical profiles of water vapour are mainly used from low Earth orbits. Sun-synchronous polar low Earth orbits are characterised by fixed local equator crossing times and near global coverage, obtained during 14–15 orbits per day, and are for example used by operational meteorological satellites at altitudes of 800–850 km. Orbits with larger inclination and limited latitudinal coverage, drifting with respect to the local solar

time, are used by many research satellites, the Space Shuttle, and the International Space Station.

This chapter gives an overview of the numerous techniques and sensors to measure atmospheric water vapour from space. A list of satellite sensors is given in Fig. 9.1. Spectral signatures of water vapour can be observed in the visible, near infrared, thermal infrared and microwave regions of the electromagnetic spectrum. The relevant spectral regions are illustrated in Figs. 9.2, 9.3 and 9.4, for the nadir and limb sounding geometries. Section 9.2 describes sensors for measurements of vertically resolved water vapour profiles in the mid and upper troposphere. Techniques for sounding of total precipitable water, determined by the water abundance in the lower troposphere, are summarised in Sect. 9.3. Section 9.4 focuses on limb sounding techniques providing vertical profile information in the altitude range from the upper troposphere up to the thermosphere.

9.2 Techniques and Sensors for Measurements of Tropospheric Water Vapour Profiles

The aim of this survey is to give a description of sensors providing vertically resolved information on water vapour in the mid troposphere and higher, i.e. above the boundary layer. The longest continuous records of mid and upper tropospheric water measurements from space are provided by operational meteorological satellites employing nadir looking sensors in two distinct frequency regions, namely in the thermal infrared spectral region around the 6.3 µm vibrational water absorption band and in the microwave region targeting the 183.3 GHz rotational water line.

9.2.1 Thermal Infrared Nadir Emission Sounding

9.2.1.1 HIRS

Historically, the first satellites providing measurements of infrared emission of water vapour in the 6.0–6.5 µm band utilising scanning radiometers were part of NASA's "Television and InfraRed Observation Satellite" (TIROS) series of low Earth orbit (LEO) satellites, flown in the early 1960s. The TIROS observations were followed by the NIMBUS satellite series, launched between 1966 and 1978, carrying different medium resolution instruments sensitive in the 6.4–7.2 µm range. Nimbus-6 included an instrument called "High Resolution Infrared Radiation Sounder" (HIRS). Advanced versions of this instrument, HIRS/2 and successors, based on multiple water vapour channels within the 6.5–8.2 micron range, have since then been flown on every satellite of the "TIROS-N/Advanced-TIROS-N" (1978–1998) and the succeeding "Polar Operational Environmental Satellites" series (POES, 1998–2009), also known as the "US National Oceanic and Atmospheric Administration" (NOAA) polar orbiter series. In total sixteen satellites have been launched from TIROS-N in

1978 to NOAA-19 in February 2009. HIRS/2 and successors are discrete stepping scan instruments using a single telescope and a rotating filter wheel containing twenty individual spectral filters, providing spectral measurements from one visible channel (0.69 μm), seven short wave channels (3.7–4.6 μm) and twelve long wave channels (6.7–15 μm). An elliptical scan mirror provides cross-track scanning of 56 steps in increments of 1.8 degrees (corresponding to a total swath[1] width of ∼2200 km). The pixel resolution is approximately 20 km at nadir and has been improved to 10 km for HIRS/4. The various HIRS instruments provide a continuous satellite record of mid to upper tropospheric humidity dating back to 1979.

Advanced versions of HIRS will be included in a new generation of US environmental satellites which will become operational after 2010, called the "National Polar-orbiting Operational Environmental Satellite System" (NPOESS), an interagency program merging the parallel military and civilian operational meteorological satellite systems into a single program, replacing both the "Polar-orbiting Operational Environmental Satellite system" (POES) and the "Defence Meteorological Satellite Program" (DMSP) series. Moreover, the US meteorological systems are nowadays coordinated, in the framework of the "Initial Joint Polar-orbiting Satellite System" (IJPS), with the European "Eumetsat Polar System", consisting itself of a series of three Meteorological Operational (MetOp) satellites to be flown successively over more than 14 years from 2006, with MetOp-A, launched in October 2006, being the first.

Information and data: http://www.ncdc.noaa.gov/oa/pod-guide/ncdc

9.2.1.2 Aqua/AIRS

Infrared sounders covering a wide spectral range with high spectral resolution have become operational during the last decade.

Launched into a low Earth orbit in May 2002, the "Atmospheric Infrared Sounder" (AIRS) is one of six instruments on board the Aqua research satellite, part of NASA's "Earth Observing System" (EOS) (Aumann et al. 2003; Chahine et al. 2006). AIRS is a high-resolution infrared sounder measuring up-welling radiances in 2378 spectral channels covering the infrared spectral band from 3.74–15.4 μm. A set of four channels in the visible and near infrared range observes wavelengths from 0.4–1.0 μm to provide cloud cover and spatial-variability characterisation. The instrument is an array grating infrared spectrometer with a spectral resolution of 1200 ($\lambda/d\lambda$). AIRS operates in a cross-track scanning mode with a field of view within $\pm 49.5°$ from nadir, corresponding to a swath of 1650 km. The instantaneous field of view is 1.1° (circular) which translates to a horizontal resolution at nadir of ∼13.5 km. Moisture profiles can be obtained from AIRS with an accuracy of better than 20 % from the surface to nearly 200 hPa (Susskind et al. 2003), with a vertical resolution of 3–4 km (Maddy and Barnet 2008). On the EOS-Aqua satellite AIRS was operated

[1] Swath width refers to the strip of the Earth's surface from which data are collected by a satellite.

in combination with the (cloud-insensitive) "Advanced Microwave Sounder Unit-A" (AMSU-A) and the "Humidity Sounder for Brazil" (HSB) for improving the all weather capability of the payload. The HSB instrument ceased operation due to a technical failure in February 2003.

Links: http://airs.jpl.nasa.gov
http://aqua.nasa.gov

9.2.1.3 Aura/TES

The "Thermal Emission Spectrometer" (TES) is a high-resolution infrared imaging Fourier-transform spectrometer on board NASA's "Earth Observation System" Aura satellite, launched in July 2004, offering nadir and additional limb viewing capabilities in the 0–34 km altitude range. The instrument covers the spectral range from 3.2–15.4 µm (or 650–3050 cm^{-1}) at a spectral resolution of 0.1 cm^{-1} (low resolution) or 0.025 cm^{-1} (high resolution), driven by optical path differences of 8.45 cm (nadir) or ± 33.8 cm (limb). Four single-line detector arrays optimised for different spectral regions, are used to obtain continuous spectral coverage over a wide range. The instrument scans conically at a 45° cone about nadir. The observed radiances are imaged onto an array of 16 detectors that have a combined horizontal footprint of 5.3 km by 8.4 km with spatial resolution of 0.5 × 5 km. The corresponding field-of-view at the atmospheric limb is 37 × 23 km with a resolution of 2.3 × 23 km. The high spectral and spatial resolution along with the flexible nadir and limb sounding capabilities allow the instrument to measure vertical profiles on a global scale of a large number of infrared-active species, from Earth's surface up to the lower stratosphere, including water and its isotopes (e.g. Worden et al. 2006, 2007). In the nadir view, TES provides vertical information of the more abundant tropospheric species such as H_2O, HDO, O_3, CO, and CH_4. Tropospheric water profile information (below ∼15 km) can be obtained with a resolution of about 4 km (Worden et al. 2004).

Links: http://tes.jpl.nasa.gov
http://aura.gsfc.nasa.gov

9.2.1.4 MetOp/IASI

Besides HIRS/4, the payload of the Eumetsat MetOp series of operational polar sun-synchronous satellites (operated at ∼820 km altitude with an inclination of 98.7° to the equator and a 9:30 am local equator crossing time for the descending node) includes also the "Infrared Atmospheric Sounding Interferometer" (IASI) which measures tropospheric water vapour among many other target species in the thermal infrared range. IASI is a "Fourier Transform Spectrometer" (FTS) using several detectors to fully cover the wide spectral range from 3.62–15.5 µm (645–2760 cm^{-1}), thus including the strong water vapour $\nu 2$ vibrational absorption band in the 5.5–7.5 µm (1300–1800 cm^{-1}) region, the strong CO_2 absorption band around 15 µm (∼650 cm^{-1}) for temperature retrieval, the ozone 9.6 µm (1040 cm^{-1}) band, as well

as some lines of the CH_4 $\nu 3$ absorption band around 3.7 µm (2700 cm^{-1}) near the band limit. The spectral resolution of IASI is 0.3–0.5 cm^{-1} (0.5 cm^{-1} apodized), determined by the FTS optical path difference of 2 cm. To achieve global coverage, the instrument performs horizontal scans every 50 km with a full swath width of ~2200 km (± 48.3°) corresponding to 2 × 15 mirror positions. The instantaneous field-of-view is 3.3° × 3.3° or 50 × 50 km at nadir, with each of the single steps being composed of 2 × 2 circular pixels, each corresponding to a 12 km diameter footprint on the ground at nadir (Clerbaux et al. 2009). Water information can be retrieved mainly below the tropopause with an altitude resolution of 3–3.5 km (Herbin et al. 2009). A typical spectrum measured by the nadir looking IASI instrument is shown in Fig. 9.3.

Links: http://www.eumetsat.int

9.2.1.5 GOSAT/TANSO

The Japanese "Greenhouse gases Observing Satellite" (GOSAT), also called "IBUKI", is dedicated to the measurement of the major greenhouse gases carbon dioxide and methane from space. GOSAT was launched in January 2009 into a sun-synchronous orbit at 667 km and carries the "Thermal And Near-infrared Sensor for carbon Observation" (TANSO). TANSO is composed of the "Fourier Transform Spectrometer" (FTS) and the "Cloud and Aerosol Imager" (CAI). The FTS observes sunlight reflected from the Earth's surface and light emitted from the atmosphere and the surface in four spectral bands at 758–775 nm (for O_2), 1.56–1.72 µm (for CO_2 and CH_4), 1.92–2.08 µm (for CO_2 and H_2O), and 5.56–14.3 µm (for CO_2 and CH_4) with a spectral resolution of 0.2 cm^{-1}. Two polarisations are measured in bands 1–3. CAI images, taken during daytime using ultraviolet, visible, and near-infrared channels, are used for flagging and correction of cloud effects in the FTS's field of view. The FTS takes fifty-six thousand measurements with a field of view corresponding to 10.5 km over a three day period, covering the entire globe. The retrieval of tropospheric H_2O profiles is not a primary objective of the mission, but the water signal is contained in the spectral measurements. GOSAT/TANSO is here listed for the sake of completeness.

Links: http://www.gosat.nies.go.jp

9.2.1.6 Meteosat/MVIRI and MSG/SEVIRI

Infrared radiation from the water absorption bands is also routinely measured by instruments on geo-stationary Earth orbits (GEO's). The first satellite with water vapour imaging capability was the European Meteosat-1, launched in 1977, carrying an imaging radiometer with a 5.7–7.1 µm water vapour channel. Since then, infrared water vapour radiometers (scanning or imaging) have been used in all major geo-stationary meteorological satellites, such as for example the European Meteosat and US GOES series.

"Meteosat First Generation" (MFG) refers to a series of geo-stationary satellites that have provided images of the full Earth disc. Data for weather forecasts have been continuously acquired for a quarter of a century. The first Meteosat, Meteosat-1, was launched in 1977, and the last of the first generation, Meteosat-7, in 1997 (in 2009 still in operation over the Indian ocean). The main instrument, the "Meteosat Visible and InfraRed Imager" (MVIRI) provides data 24 h a day from three spectral channels in the visible (0.45–1.0 μm, imaging during daylight), thermal infrared (transparent, for imaging during day and night, of cloud tops and over oceans), and water vapour regions (5.7–7.1 μm, for middle to upper tropospheric water vapour) of the electromagnetic spectrum. The radiation is gathered by a reflecting telescope with a primary mirror diameter of 400 mm which acquires radiance data from the full Earth disc during a 25-min period, providing images all 30 min.

The MFG system is being replaced by "Meteosat Second Generation" (MSG), with two of four satellites already having been launched in August 2002 and December 2005, providing (as did before MFG) services in a 2-satellite geostationary configuration placed at 0° longitude with one satellite as a backup. The main instrument on MSG is the "Spinning Enhanced Visible and InfraRed Imager" (SEVIRI), which scans the Earth's surface sufficiently fast to permit a repeat cycle of 15 min for 12 spectral channels in the visible, and infrared region (compared to three on the previous system), including water, ozone and carbon dioxide absorption bands, with improved horizontal resolution of 1 km for the high-resolution visible channel, and 2.5 km for the others. Tropospheric humidity is provided in two layers in the upper-middle troposphere at ∼300–600 hPa and in the middle troposphere at ∼600–800 hPa. The horizontal resolution of the tropospheric humidity products is of the order of 100 km.

Links: http://www.eumetsat.int

9.2.1.7 GOES Imager and Sounder

After pioneering Earth observation from geo-stationary orbits in the 1960s with the "Applications Technology Satellite" (ATS) series, a set of six spacecraft launched from December 1966 to May 1974, NASA launched the first "Geostationary Operational Environmental Satellite" (GOES) in 1975. The latest, GOES-14, was launched in June 2009. NOAA operates usually two meteorological satellites in geo-stationary orbit over the equator at 75° and 135° W, one monitoring thus North and South America and most of the Atlantic Ocean and the other North America and the Pacific Ocean basin, covering together roughly the range from 20° to 190° W longitude. The satellites carry two primary instruments, an imager and a sounder. The sounder provides data to determine the vertical temperature and moisture profile of the atmosphere, surface and cloud top temperatures, and ozone distribution. Channels at 7.43, 7.02, and 6.51 μm are used for observing moisture at three levels (low, mid, upper-level). The GOES I-M imager is a five channel (one visible, four infrared) imaging radiometer designed to sense radiant and solar reflected energy from sampled areas of the Earth. It includes a 6.50–7.00 μm channel for moisture. The full

Earth disc is imaged within 26 min with a horizontal resolution at nadir of 8 km for the moisture channel (1 km for the visible channel).

Links: http://www.oso.noaa.gov/goes

It should be noted that geo-stationary weather satellites are also operated by various other space agencies and countries (e.g. Russia, Japan, India, China).

e.g. http://www.jma.go.jp/jma/jma-eng/satellite

Measuring technique	Thermal infrared nadir emission sounding		
Observation geometry	Nadir		
Platform	Operational meteorological LEO and GEO satellites, LEO research satellites		
	Meteosat/MVIRI	GEO	1977
	MSG/SEVIRI	GEO	2002
	GOES imager/sounder	GEO	1975
	NOAA/HIRS	LEO	1979
	Aqua/AIRS	LEO	2002
	Aura/TES	LEO	2004
	MetOp/IASI	LEO	2007
Spectral range	Thermal infrared (between 3 and 16 µm)		
Vertical resolution	Several kilometres		
Horizontal resolution	Depending on orbit, typically 10–20 km for LEO		
Vertical range	Troposphere below 10 km (300 hPa)		
Horizontal range	Depending on orbit		
Daytime/nighttime	Both (thermal emission)		
Bottlenecks, limitations	Strong sensitivity to clouds, cloud screening leads to dry bias		
Additional products	Various trace gases, temperature, cloud heights		

9.2.2 Passive Microwave Nadir Emission Sounding

A disadvantage of measuring water vapour using infrared radiation is that measurements in cloudy regions can in general not be used, and cloud affected pixels have to be avoided and filtered out. For example, the humidity record created from HIRS measurements has a clear sky or dry bias, since cloudy regions associated with high humidity are omitted (e.g. Buehler et al. 2008). Measurements at longer wavelengths are considerably less sensitive to clouds and instruments measuring microwave radiation have therefore continuously been used on board operational low Earth orbiting meteorological satellites since the early 1990s.

9.2.2.1 SSM/T-2, AMSU-B, MHS

Recent instruments are the "Special Sensor Microwave" (SSM/T-2) water vapour profiler on board the "Defence Meteorological Satellite Program" (DMSP) satellites

F-11 to F-15 (launched 1991, August 1994, March 1995, April 1997, December 1999), the "Advanced Microwave Sounding Unit-B" (AMSU-B) on board NOAA-15, 16, and 17 (launched in May 1998, September 2000, June 2002), and the "Microwave Humidity Sounder" (MHS) on board NOAA-18, MetOp-A, and NOAA-19 (launched in May 2005, October 2006, and February 2009). These very similar instruments measure radiation originating from a number of different tropospheric layers. The instruments are five channel cross-track step-scanning microwave total power radiometers utilising three (double sideband) channels spanning the highly opaque 183 GHz water vapour line (183.31 ± 1.00 GHz, 183.31 ± 3.00 GHz, and 183.31 ± 7.00 GHz), as well as two window channels close to 90 GHz and around 150 or 157 GHz, allowing deeper penetration into the troposphere.

To give an example, the total swath width for the SSM/T-2 is approximately 1500 km with each observation having a spatial resolution of the order of 50 km. This instrument was flown on the DMSP Block 5D-2 satellites (F11-F15) starting with F11 launched in 1991. The sensor was recently succeeded by the "Special Sensor Microwave Imager/Sounder" (SSMIS) package, a passive conically scanning microwave radiometer that combines and extends the imaging and sounding capabilities of three previously separate DMSP microwave sensors (the SSM/T-1 temperature sounder, the SSMI/T-2 moisture sounder, and the SSMI). SSMIS measures microwave energy at 24 discrete frequencies from 19 to 183 GHz with a swath width of 1700 km and a horizontal resolution of $\sim$35 km. The first SSMIS sensor was launched on board the DMSP F-16 platform in October 2003 and became operational in November 2005. For comparison, the MHS instrument on NOAA-18/19 and MetOp-A employs (nearly) the same five channels in the 89–183 GHz range, but with a swath width of about 2150 km and a 3 dB field-of-view of 1.1° translating to a resolution of 15 km at nadir.

Other similar nadir looking humidity sensors were employed or are planned to be employed by other agencies (e.g. Japan, Brazil, India) on low Earth orbit operational meteorological or research satellites. Examples are the AMSU-B like "Humidity Sounder for Brazil" (HSB) on the Aqua satellite (operating from May 2002 to February 2003), or the SAPHIR sensor on the French-Indian "Meghatropique" mission which is planned to be launched in 2011 in a 20° inclined tropical orbit. SAPHIR is a passive sounding instrument with six double sideband channels within $\pm$ 13 GHz of the 183.31 GHz absorption line of water vapour, allowing retrieval of water vapour profiles from the surface up to about 10 km. The scanning is cross-track, up to an incidence angle of 50° corresponding to a swath width of $\sim$2300 km and the resolution at nadir is of the order of 10 km.

Links: http://www.oso.noaa.gov
http://www.ncdc.noaa.gov/oa
http://projects.osd.noaa.gov/IJPS
http://smsc.cnes.fr/MEGHAT
http://mirs.nesdis.noaa.gov
http://www.eumetsat.int

Measuring technique	Microwave nadir emission sounding		
Observation geometry	Nadir		
Platform	Mainly on operational meteorological LEO satellites		
	DMSP F11-F15	SSM/T-2	1991
	NOAA 15-17	AMSU-B	1998
	NOAA 18-19, MetOp-A	MHS	2006
	Aqua	HSB	2002–2003
	Megatropique	SAPHIR	2011
Spectral range	89–190 GHz (channels around 183 GHz line, window channels)		

Channel characteristics of microwave humidity sounder

AMSU-B and SSM/T-2			MHS		SSMIS	
channel	ν_0 [GHz]	width [GHz]	channel	ν_0 [GHz]	channel	ν_0 [GHz]
16	89.00 ± 0.9	1.0	H1	89.000	17,18	91.655
17	150.00 ± 0.9	1.0	H2	157.000	8	150.000
18	183.31 ± 1.0	0.5	H3	183.311 ± 1.0	9	183.310 ± 1.0
19	183.31 ± 3.0	1.0	H4	183.311 ± 3.0	10	183.310 ± 3.0
20	183.31 ± 7.0	2.0	H5	190.311	11	183.310 ± 6.6

Vertical resolution	Several kilometres
Horizontal resolution	10–15 km at nadir (MHS)
Vertical range	Troposphere (below 10 km)
Horizontal range	Near global (mostly on polar orbits)
Daytime/nighttime	Both (thermal emission)
Bottlenecks, limitations	Limited altitude information from pressure broadening, only sensitive to region with largest water abundance (troposphere),sensitivity to tropospheric clouds (large ice particles or water drops)

9.2.3 Radio Occultation Instruments

The radio occultation technique makes use of the microwave signal emitted by "Global Positioning System" (GPS) satellites. A radio occultation instrument receives radio signals from GPS navigation satellites through the Earth atmospheric limb. The GPS constellation of satellites consists nominally of 24 satellites distributed in six orbital planes around the globe at an altitude of 20200 km (circular orbits with inclination of 55° and a period of 12 h). An occultation occurs whenever a GPS satellite rises or sets on the Earth limbs as seen from the radio occultation instrument which itself is on a low Earth orbit (LEO) satellite. The GPS signal is refracted and slowed by the Earth's atmosphere. Comparison of the measured delayed phase path with the phase path that would be expected in the absence of an atmosphere allows to derive bending angles and thus refraction. In the stratosphere and upper troposphere, where water vapour density is low, refraction is dominated by the vertical air density gradients, and accurate vertical profiles of air density, pressure and temperature can be retrieved from roughly 5–30 km. In the lower and mid troposphere, water vapour effects can be dominant and vertically very well resolved water vapour profiles ($\sim$100 m) are retrievable up to about 12 km (or $\sim$200 hPa) using auxiliary temperature profiles, for example from a weather prediction model.

9.2.3.1 MetOp/GRAS

The "GNSS (Global Navigation Satellite System) Receiver for Atmospheric Sounding" (GRAS) is a GPS receiver that is operated on the MetOp series of the Eumetsat Polar System (MetOp-A was launched in 2006). The GRAS receiver can track up to eight GPS satellites for navigation purposes, two additional satellites for rise and two others for set occultation measurements. GRAS provides roughly 600 atmospheric temperature and humidity profiles per day derived from GPS radio occultations.

Links: http://www.eumetsat.int
http://garf.grassaf.org

9.2.3.2 FORMOSAT-3/COSMIC

The "Constellation Observing System for Meteorology, Ionosphere and Climate" (COSMIC), launched in April 2006, is the first mission to employ a constellation of six small micro-satellites in low Earth orbits (at 700–800 km, with inclination angle of 72°) using limb occultation of radio signals received from 24 US GPS satellites to collect atmospheric sounding data. The "FORMOSAT-3 Program" is an international research collaboration between Taiwan's "National Space Organization" (NSPO) and the "University Corporation for Atmospheric Research" (UCAR) in the United States. Over 2000 satellite-to-satellite occultations per day provide temperature and tropospheric humidity data uniformly distributed over the Earth's atmosphere (Anthes et al. 2008; Chou et al. 2009).

Links: http://tacc.cwb.gov.tw
http://www.cosmic.ucar.edu

Besides the missions FORMOSAT/COSMIC and Metop/GRAS, GPS radio occultation receivers have also been employed on other satellites such as the "CHAllenging Minisatellite Payload" (CHAMP), launched in 2001 (e.g. Heise et al. 2006), the "GRavity And Climate Experiment" (GRACE), launched in 2002 (e.g. Wickert et al. 2006), and TerraSAR-X, launched in 2007, providing an operational multi-satellite constellation for GPS based tropospheric humidity soundings. Various radio occultation systems are already planned for the time frame after 2010 and the increase of global positioning system satellites will moreover provide an even denser coverage of water measurements. Future missions may be based on ∼28 operational (US) GPS satellites, ∼24 operational (Russian) GLONASS satellites, and ∼30 operational (European) GALILEO satellites.

Links: http://isdc.gfz-potsdam.de

Measuring technique	Radio occultation sounding	
Observation geometry	Satellite to satellite limb occultation	
Platform	Various satellites, e.g.	
	CHAMP	2000
	GRACE A,B	2002
	METOP-A/GRAS	2006
	FORMOSAT/COSMIC	2006
	TerraSAR-X	2007

Spectral Range	GPS: 1.57542 GHz (L1) and 1.2276 GHz (L2)
Vertical resolution	∼100 m
Horizontal resolution	500–1000 km
Vertical range	Troposphere
Horizontal range	Global
Bottlenecks, limitations	Temperature dependence of water retrieval
Additional products	Temperature
Future potential	Possibly large number of operational soundings using signals from 28 GPS, 24 GLONASS, and 30 GALILEO satellites

9.3 Nadir Techniques for Measurements of Total Water Vapour

Moisture in the lower troposphere makes up the bulk of the atmospheric water vapour column. On meteorological satellites, the total precipitable water vapour is sounded using visible, near infrared, thermal infrared, passive microwave, and radio-occultation techniques.

9.3.1 Thermal Infrared Nadir Emission Sounding

Thermal infrared techniques exploit frequency bands away from the 6.3 µm water vapour absorption maximum, e.g. around 8 or even 11 µm, which are sensitive to the water vapour absorption in the lower troposphere. The total water vapour can be obtained by integrating the vertical water profile. Instruments are for example the aforementioned infrared nadir sounders HIRS, AIRS, and IASI. See Sect. 9.2.1 for a description of the instruments.

9.3.2 Passive Microwave Nadir Emission Sounding

Passive nadir sensors using channels at 23.8 and 31.4 GHz, i.e. operating at microwave frequencies around the weak 22.235 GHz water line, are sensitive to surface and water emissions from altitudes close to the ground. Retrieval algorithms also exploit information from channels around the strong 183 GHz water line and at 90 and 150 GHz, for better sensitivity. Over land and sea ice, the large variability of the surface emissivity make retrievals generally more difficult than over the ocean where the emissivity is well known. The operational products retrieved from the microwave nadir sensors provide therefore data only over the oceans (e.g. Dyras and Serafin-Rek 2002; Ferraro et al. 2005), whilst retrieval over land require more sophisticated techniques to be applied (e.g. Liu and Weng 2005; Melsheimer et al. 2007; Melsheimer and Heygster 2008). Relevant instruments are for example the NOAA "Advanced Microwave Sounding Unit-A" (AMSU-A) and the US DMSP "Special Sensor Microwave Imager" (SSM/I). Instruments targeting similar spectral channels have been employed by various other programs and space agencies.

9.3.2.1 AMSU-A

The "Advanced Microwave Sounding Unit-A" (AMSU-A) is a multi-channel microwave nadir sounder that measures global atmospheric temperature profiles and provides information on atmospheric water in all of it's forms (vapour, liquid, ice). The AMSU-A instrument consists of two independent modules (AMSU-A1 and AMSU-A2). Whilst AMSU-A1 provides twelve channels in the 50–60 GHz oxygen band for retrieving the atmospheric temperature profile up to ∼2 hPa, AMSU-A2 has two channels at 23.8 and 31.4 GHz to identify precipitation and correct for surface emissivity, atmospheric liquid water, and water vapour effects. These window channels are also used to derive rain rate, sea ice concentration, and snow cover, for example. AMSU-A is a cross-track step-scanning total power microwave radiometer with instantaneous field-of-view providing a spatial resolution at nadir of 48 km. The antenna provides a cross-track scan within ± 48.3° from nadir with a total of 30 steps per (8 s) scan. The instrument is a descendant of the NOAA "Microwave Sounding Unit" (MSU), providing improved sampling and sensitivity. The first AMSU-A instrument was launched as part of the NOAA "Advanced TIROS Operational Vertical Sounder" (ATOVS) system on NOAA-15 in May 1998 and was employed on nearly all operational meteorological LEO missions of the NOAA polar orbiter series since then.

Links: http://www.oso.noaa.gov
http://projects.osd.noaa.gov/IJPS

9.3.3 Near Infrared Nadir Techniques

Techniques based on nadir observations in the visible and near infrared part of the electromagnetic spectrum can also be used to derive total column precipitable water vapour in the atmosphere from back-scattered and emitted radiation. These measurements are very sensitive to boundary layer water vapour since information is derived from attenuation of reflected solar light from the surface. Since data in the near infrared spectral range are analysed, measurements are restricted to daytime and to (almost) cloud-free ground scenes.

9.3.3.1 ERS-2/GOME, Envisat/SCIAMACHY, and MetOp/GOME-II

The "Global Ozone Monitoring Experiment" (GOME) on ERS-2 and the "Scanning Imaging Absorption spectroMeter for Atmospheric CHartographY" (SCIAMACHY) on Envisat measure back-scattered and emitted light in the ultraviolet, visible and near infrared parts of the electro-magnetic spectrum at nadir. Total water vapour column amounts are retrieved from the spectral measurements in the visible wavelength region around 700 nm using an "Air Mass Corrected Differential Optical

Absorption Spectroscopy" (AMC-DOAS) method, providing a global record of total water vapour data since the GOME launch in 1991. The ground pixel size of GOME is 40 km × 320 km compared to 30 km × 60 km for SCIAMACHY (Noël et al. 1999, 2005). An updated version of the "Global Ozone Monitoring Experiment" (GOME-2) is also part of the operational MetOp satellite payload (ground pixel 80 × 40 km), assuring long-term continuity of this data record (Noël et al. 2008).

Links: http://www.iup.uni-bremen.de/amcdoas/

9.3.3.2 Terra/MODIS and Aqua/MODIS

The two "Moderate Resolution Imaging Spectroradiometer" (MODIS) instruments were launched on 18 December 1999 on board the Terra platform and on 4 May 2002 on board Aqua. The two satellites are on sun-synchronous, near-polar, circular orbits at 705 km altitude with complementary local equator crossing times at 10:30 am/pm (Terra) and 1:30 am/pm (Aqua). The viewing swath width of MODIS is 2,330 km (cross track), allowing near daily global coverage. MODIS measures in 36 spectral bands between 0.405 and 14.385 µm. During daytime, total column (precipitable) water vapour data are retrieved applying a near infrared algorithm over clear land areas and above clouds over both land and ocean. Additionally, channels in the thermal infrared provide atmospheric profile information during both day and night. MODIS measures total water at high 1 km horizontal resolution based on near infrared channels during the day, and at 5 km resolution both during day and night using cloud free thermal infrared channels. MODIS was the first space instrument to use near infrared bands together with the traditional thermal infrared bands to retrieve total precipitable water.

Links: http://modis.gsfc.nasa.gov
http://terra.nasa.gov
http://aqua.nasa.gov

Measuring technique	Near infrared nadir solar back-scatter technique	
Observation geometry	Nadir sounding	
Platform	ERS-2/GOME	1991
	Terra/MODIS	1999
	Aqua/MODIS	2002
	Envisat/SCIAMACHY	2002
	MetOp-A/GOME-II	2006
Units	Total precipitable water vapour	
Spectral range	UV-VIS to near-infrared	
Vertical resolution	Total column (precipitable) water	
Horizontal resolution	Between 1 × 1 km (MODIS) and 40 × 320 km (GOME)	
Vertical range	Troposphere, mainly boundary layer	

Horizontal range	Depending on orbit
Daytime/nighttime	Daytime only (solar back-scattering)
Bottlenecks, limitations	Strong sensitivity to clouds, only cloud free pixels.
Additional products	Various trace gases
Future potential	Sounding of chemical minor species with improved horizontal resolution using sensitive array detectors, also from GEO orbits

9.4 Limb Sounding of Water Vapour From the Upper Troposphere to the Lower Thermosphere

The abundance of water vapour decreases with altitude throughout the troposphere. Transport through the cold tropical tropopause layer, which acts as a cold trap, leads to very low water vapour concentrations of less than ~8 ppmv in the stratosphere and above. The low water vapour concentrations require sensitive limb sounding techniques to be employed for altitude resolved measurements in the upper troposphere and throughout the middle atmosphere.

9.4.1 Near Infrared Limb Occultation Sounding

Solar occultation sounding is a sensitive technique providing information on a large number of species including water vapour. The technique is based on the measurement of the wavelength dependent extinction of solar radiation passing through the limb of the atmosphere during sunrises and sunsets seen from the satellite. Calibration is done by measuring the solar spectrum outside the atmosphere before or after each occultation event. This protects in principle from long term instrumental drifts, an important technical feature for long term monitoring of atmospheric gases. Solar occultation instruments are operated in the UV/VIS, near infrared and thermal infrared spectral ranges. A disadvantage of the technique is that the spatial-temporal sampling is limited by the relatively few sunsets and sunrises which can be observed from a given orbit per day. This disadvantage can partly be overcome using the stellar occultation technique.

9.4.1.1 SAGE-II and SAGE-III

The "Stratospheric Aerosol and Gas Experiment II" (SAGE-II) was launched into a non sun-synchronous, circular 57° inclination orbit at 650 km on board the "Earth Radiation Budget Satellite" (ERBS) in October 1984 and operated over 21 years until it was powered-off in August 2005. The instrument used the solar occultation technique to measure the limb transmittances of solar radiation passing through the Earth's limb in seven channels centred at wavelengths ranging from 0.385–1.02 µm. The instrument provided 1 km vertical resolution profiles of aerosol extinction (at 0.385, 0.453, 0.525, and 1.02 µm), H_2O, O_3, and NO_2 essentially in the upper troposphere, lower and middle stratosphere. SAGE-II was preceded by the sister instruments SAM-II ("Stratospheric Aerosol Measurement II") on NIMBUS-7, which

has been measuring 1.0 µm aerosol extinction in the polar regions from 1978–1993, and SAGE-I (on the "Applications Explorer Mission-B" satellite), which performed near global measurements of aerosol extinction (at 0.45 and 1.0 µm), O_3, and NO_2 from 1979–1981. The data sets provided by these instruments are among the longest with respect to stratospheric ozone, aerosol, and water vapour. The SAGE-II instrument was a seven-channel Sun photo-meter that used a Cassegrainian-configured telescope, holographic grating and seven silicon photo-diodes to define the seven spectral channel band-passes centred at wavelengths of 1020, 940, 600, 525, 453, 448, and 385 nm. Water vapour was measured at 940 nm. The strong sensitivity to aerosol loading limited unfortunately the usefulness of SAGE-II water vapour data for trend analyses, despite the outstanding long data set (Thomason et al. 2004; Taha et al. 2004).

The SAGE mission was supplemented by the "Stratospheric Aerosol and Gas Experiment III" (SAGE-III) which also obtained profile measurements of aerosol extinction, H_2O, O_3, NO_2, NO_3, OClO, clouds, temperature and pressure in the mesosphere, stratosphere, and upper troposphere with a vertical resolution of 0.5–1 km. This instrument was flown on board the Russian Meteor-3M platform which launched in December 2001 and ceased operation in March 2006. SAGE-III measured profiles of water vapour from the surface to an altitude of 50 km.

Links: http://www-sage2.larc.nasa.gov
http://www-sage3.larc.nasa.gov

9.4.1.2 POAM-II and POAM-III

The "Polar Ozone and Aerosol Measurement II" (POAM-II) experiment was a visible and near infrared solar occultation instrument which measured the vertical distribution of atmospheric H_2O, O_3, NO_2, aerosol extinction, and temperature by observing solar extinction (during ∼14 sunsets and sunrises per day) in the atmosphere in nine narrow-band channels, covering the spectral range from approximately 350–1060 nm. POAM-II was launched aboard the French SPOT-3 ("Satellite Pour l'Observation de la Terre 3") satellite in September 1993 into a sun-synchronous polar orbit. The mission focused on high latitudes. Sunrise measurements were made in a latitude band from 55–71° north whilst sunsets occurred between 63–88° south. Highest latitudes were sounded close to the equinoxes. The POAM-II mission was ended with the failure of the SPOT-3 satellite in November 1996. A follow-on instrument, POAM-III, was launched on the SPOT-4 satellite in March 1998 in a similar orbit. POAM-III included several improvements relative to POAM-II in terms of sensitivity, wavelengths and bandwidths, interference filter technology, and number of sun sensors, thus simplifying initial acquisition of the Sun at the beginning of sunrise and sunset events. Water vapour was measured by two channels: channel-7 at 922.4 nm with width of 2.6 nm (off peak) and channel-8 at 935.9 nm with width of 2.9 nm (on peak). Water vapour profiles were retrieved above 5 km from the cloud tops to about 50 km with a vertical resolution of 1 km below 30 km (quickly degrading above). Details about the POAM-II instrument can be found in (Glaccum et al.

1996). The retrieval process is described by Lumpe et al. (1997), and information on validation is provided by Lumpe et al. (2006).

Links: http://wvms.nrl.navy.mil/POAM

9.4.1.3 Envisat/GOMOS

GOMOS is a medium resolution spectrometer measuring in the ultraviolet, visible and near infrared spectral regions using the stellar occultation technique. The instrument consists of four spectrometers covering the 248–371 nm, 387–693 nm, 750–776 nm and 915–956 nm spectral ranges with resolutions of 1.2 nm (ultraviolet, visible) and 0.2 nm (near infrared), allowing for measurements of O_3, NO_2, NO_3, atmospheric density (from Rayleigh extinction) and aerosols (ultraviolet and visible measurements), as well as O_2 and H_2O (near infrared measurements at 760 nm and 936 nm, respectively), from the upper troposphere to the mesosphere. Additionally, two fast photometers sampling at a frequency of 1 kHz (compared to a nominal integration of time 0.5 s) in the ranges 644–705 nm and 466–528 nm are used to correct for perturbations from scintillation effects and to determine vertical profiles of temperature with high vertical resolution (200 m). Detectors with high quantum efficiency and very low noise and a large telescope (30×20 cm aperture) are used to collect sufficient signal to use even very faint stars for the occultation measurements. Nine stars are sufficiently bright to provide useful spectra for stratospheric H_2O. The altitude coverage of vertical profiles retrieved from GOMOS measurements is generally between an altitude level in the upper troposphere and 120 km, depending on the star characteristics and on the illumination conditions. During an occultation, GOMOS measures the stellar light in 0.5 s integration time intervals corresponding to an interval of 1.7 km of altitude projected at the limb (e.g. Bertaux et al. 2004; Kyröla et al. 2004). However, the data analysis has been difficult due to a pixel-to-pixel non-uniformity of the CCD detector, coupled with motion of the star on the CCD caused by scintillation. Water vapour profiles from GOMOS have therefore not yet been publicly available at the time of writing (September 2010).

Links: http://envisat.esa.int/instruments/gomos
http://earth.esa.int

9.4.1.4 AIM/SOFIE

The "Aeronomy of Ice in the Mesosphere" (AIM) satellite was launched in April 2007 in a circular polar sun-synchronous (12 am/pm) orbit at 600 km with the objective to investigate polar mesospheric clouds (PMC's) and the environment in which they form. The "Solar Occultation For Ice Experiment" (SOFIE) on board AIM is an infrared solar occultation differential absorption radiometer performing every day 15 sunset measurements in narrow latitude bands between 65° S and 85° S and 15 sunrise measurements at 65° N to 85° N. The latitude coverage depends on the day of the year with highest latitudes sounded close to the equinoxes. The instrument is a

broadband radiometer using 16 spectral bands at wavelengths from 0.33–5.006 µm for observing vertical profiles of temperature, pressure, H_2O, O_3, CO_2, CH_4, NO and PMC particle extinction. Water vapour is measured in two channels centred at 2.462 µm (band-5) and 2.618 µm (band-6). Retrievals from band-6 provide vertical profiles between 15 and 105 km with a vertical resolution of the order of 1.5–2 km (Russell-III et al. 2009; Gordley et al. 2009).

Links: http://aim.hamptonu.edu
http://www.nasa.gov/mission_pages/aim

Measuring technique	Near infrared limb occultation sounding	
Observation geometry	Limb sounding in solar, lunar or stellar occultation configuration	
Platform	ERBS/SAGE-II	1984–2005
	SPOT-3/POAM-II	1993–1996
	SPOT-4/POAM-III	1998–2005
	Meteor/SAGE-III	2001–2006
	Envisat/GOMOS	2002
	Envisat/SCIAMACHY	2002
	AIM/SOFIE	2007
Spectral range	Near-infrared	
Vertical resolution	0.5–2 km	
Horizontal resolution	500–1000 km	
Vertical range	Between 5 and 100 km (depending on sensitivity and clouds)	
Horizontal range	Solar occultation: 15 sunrise and 15 sunset occultations per day sampled at similar latitudes in both hemispheres. Stellar occultation: near global coverage, depending on orbit.	
Daytime/nighttime	Sunrise, sunset (solar occultation), night-time for stellar or lunar occultation	
Bottlenecks, limitations	Limited geographical sampling by solar occultations, observed latitudes vary slowly with time and near global coverage can only be obtained after a longer period (orbit dependent); Fixed local solar time (sunset, sunrise); Sensitivity to cirrus clouds limits sampling in troposphere (cloud screening required)	
Additional products	Various trace gases, temperature, aerosol and cloud information	

9.4.2 Near Infrared Limb Scattering Technique

Satellite instruments that measure the spectrum of limb scattered sunlight at ultraviolet, visible and near infrared wavelengths allow for the retrieval of trace gas and aerosol profiles at a vertical resolution comparable to that of solar occultation measurements, but with significantly better global coverage.

9.4.2.1 Envisat/SCIAMACHY

SCIAMACHY ("Scanning Imaging Absorption spectroMeter for Atmospheric CHartographY") on Envisat, launched in February 2002, is a spectrometer performing global measurements of many different trace gases in troposphere and stratosphere by

observing solar transmitted, reflected, and scattered radiation and terrestrial emitted radiation in several regions between 240 and 2380 nm (240–314 nm, 309–340.5 nm, 394–620 nm, 604–805 nm, 785–1,050 nm, 1,000–1,750 nm, 1,940–2,040 nm and 2,265–2,380 nm) with a moderate spectral resolution of between 0.2 nm and 1.5 nm. The instrument makes use of three viewing geometries, namely limb sounding, nadir sounding and solar/lunar occultation. With its wavelength coverage and spectral resolution, SCIAMACHY measurements provide global information on many species and parameters including O_3, BrO, OClO, ClO, SO_2, H_2CO, NO_2, CO, CO_2, CH_4, H_2O, N_2O, pressure, temperature, aerosol, radiation, cloud cover and cloud top height (Bovensmann et al. 1999). During daytime, profiles of water vapour can be retrieved from limb measurements around 1,375–1,390 nm (1.5 nm resolution) in the altitude range ∼10–25 km with a vertical resolution at the limb of roughly 2.5 km (Rozanov et al. 2009). Solar occultation observations provide information on water vapour from 15–50 km with vertical resolution of ∼2.5 km, retrieved from the 928–968 nm band (at 0.5 nm spectral resolution) (Noël et al. 2010). Whilst limb scatter measurements provide a daily global coverage from the sun-lit side of the polar sun-synchronous (10 am/pm) orbit, solar occultation measurements are limited to the 49° N–68° N latitude range (Weber 2009). SCIAMACHY performs lunar occultation measurements at southern latitudes between 40° S and 90° S. Water vapour profiles can be retrieved in the 17–50 km range from an absorption window at 1,350–1,420 nm. Additionally, nadir observations around 700 nm provide information on the total tropospheric water column (see Sect. 8.3.3). SCIAMACHY nadir and limb spectra are shown in Fig. 9.2 for illustration of the water signal observable in the visible and near infrared spectral region.

Links: http://www.sciamachy.de

Measuring technique	Near infrared limb scattering
Observation geometry	Limb
Platform	Envisat/SCIAMACHY 2002
Spectral range	UV/VIS and near-infrared (from 240–2380 nm)
Vertical resolution	2.5 km
Horizontal resolution	500–1000 km
Vertical range	10–25 km
Horizontal range	Near global (depending on orbit)
Daytime/nighttime	Requires sun light, daytime only
Bottlenecks, limitations	Strong sensitivity to cirrus clouds and aerosols in the line-of-sight limits global sampling.
Corrections needed?	Cloud screening
Additional products	Various trace gases, temperature, aerosol, cloud information
Future potential	Sounding of troposphere and stratosphere with improved vertical and horizontal sampling and resolution through use of imaging techniques and sensitive array detectors

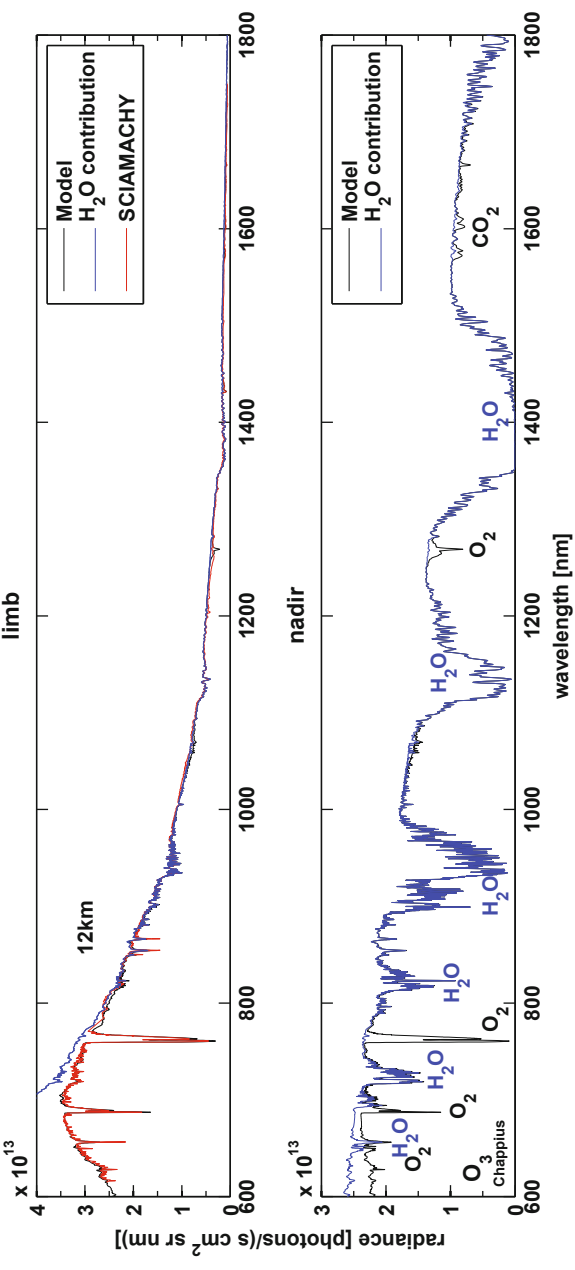

Fig. 9.2 Overview of spectral ranges for sounding of water vapour from space. I Visible and near infrared wavelength range. *Top* Limb measurement of SCIAMACHY and model calculation for a tangent altitude of 12 km. *Bottom* model calculation for the nadir geometry. Simulations by Alexei Rozanov, University of Bremen, using the SCIATRAN-3.0 radiative transfer model

9.4.3 Thermal Infrared Limb Occultation Sounding

Solar occultation sounding in the thermal infrared spectral region is a sensitive technique for measuring vertically well resolved profiles of middle atmospheric water vapour.

9.4.3.1 UARS/HALOE

The "Halogen Occultation Experiment" (HALOE) on board NASA's "Upper Atmosphere Research Satellite" (UARS) measured vertical profiles of middle atmospheric constituents and temperature from September 1991 until November 2005 during about 15 sunsets and 15 sunrises per day. HALOE used the solar occultation technique in the infrared region at wavelengths between 2.45 and 10 µm and employed gas filter correlation radiometry for the measurement of the vertical distributions of HCl, HF, CH_4, and NO and broadband filter radiometry for observing H_2O, NO_2, O_3, and temperature derived from CO_2 absorption. Water vapour was retrieved from a channel at 6.54–6.67 µm (1,500–1,528 cm^{-1}) in the altitude range between roughly 10 and 80 km with a vertical resolution of 2–3 km. Due to the occultation viewing geometry and the 57° inclined UARS orbit (at 585 km), the latitudinal coverage is from 80° S to 80° N over the course of one year (e.g. Russell-III et al. 1993; Harries et al. 1996).

Links: http://haloe.gats-inc.com

9.4.3.2 ATMOS on Spacelab and Space Shuttle

The "Atmospheric Trace Molecule Spectroscopy Experiment" (ATMOS) was a solar occultation infrared sounder which observed the extinction of solar radiation when passing through the stratosphere during three missions on board the Space Shuttle in March 1992, April 1993, and November 1994 ("Atmospheric Laboratory for Applications and Science", ATLAS-1,2,3) (Gunson et al. 1996). The experiment was based on a high resolution continuous-scanning Fourier spectrometer which measured the atmospheric absorption of solar radiation over the wavelength range 2–16 µm at a resolution of 0.01 cm^{-1}. The ATMOS instrument was previously flown on Spacelab-3 (STS-51B) in 1985. Vertical profiles were retrieved between about 20 and 80 km at 3–6 km vertical resolution, with limited instantaneous latitudinal coverage typical for a solar occultation experiment. The water vapour retrieval uses information in various windows within the instrument's spectral range. See Irion et al. (2002) and Michelsen et al. (2002) for a description of the data.

Links: http://asd-www.larc.nasa.gov/spectroscopy/ASDatmos.html
http://nssdc.gsfc.nasa.gov/nmc/

9.4.3.3 ADEOS/ILAS and ADEOS-II/ILAS-II

The "Improved Limb Atmospheric Spectrometer" (ILAS) on board the Japanese "Advanced Earth Observing Satellite" (ADEOS, later renamed to "Midori"), launched in August 1996, made vertical profile measurements of stratospheric water vapour from November 1996 through June 1997. Its successor ILAS-II was launched on board JAXA's "Advanced Earth Observing Satellite-II" (ADEOS-II or "Midori-II") in December 2002. ILAS-II routine operation was started from April 2003 and ended in October 2003. ILAS and ILAS-II focused on measurements of vertical profiles of atmospheric trace species including water vapour, aerosol, temperature and pressure in the stratosphere at high latitudes of both hemispheres. Due to the sun-synchronous polar orbit (at 800 km with equator crossing time at 10:30 hours), sunset and sunrise seen from the satellite occurred at middle and high latitudes in both hemispheres in very narrow latitude bands. There were about 14 observation points per day in each hemisphere and the latitude of observation gradually shifted with the seasons within the ranges 54–71° N and 64–88° S. The ILAS instrument was a solar occultation sensor based on two grating spectrometers covering 6.21–11.77 µm and 0.753–0.784 µm with array detectors. The absorption around 6.5 µm was used for water vapour retrievals, providing information in the 10–70 km altitude range with a vertical resolution ranging from 2–3.5 km (Sasano et al. 1999; Kanzawa et al. 2002). The ILAS-II instrument used four observation channels (two more channels than ILAS), three channels for observations in the infrared band, and one channel in the visible part of the spectrum. Vertical water vapour profile information was retrieved from the ILAS-II infrared channel (6.21–11.77 µm or 850–1610 cm^{-1}) in the altitude range from 15–55 km with a vertical resolution of 1.3–2.9 km (Nakajima et al. 2006).

Links: http://db.cger.nies.go.jp/ilas/
http://db.cger.nies.go.jp/ilas2/

9.4.3.4 ACE/FTS

The "Atmospheric Chemistry Experiment Fourier Transform Spectrometer" (ACE/FTS) is a high-resolution Fourier transform spectrometer on the Canadian ACE (or SCISAT) satellite, launched in August 2003 in an orbit at 650 km with 74° inclination (Bernath et al. 2005). The mission concept is based on the ATMOS (*Atmospheric Trace MOlecule Spectroscopy*) instrument that flew several times (1992, 1993, and 1994) on the Space Shuttle. The ACE-FTS instrument has been considerably improved and miniaturised compared to ATMOS. Due to the ACE orbit, solar occultation observations are performed mainly at high and middle latitudes, and only during even-numbered months in the tropics. Multiple micro-windows, mainly in the 5–7.3 µm (1,362–2,004 cm^{-1}) range, are used to retrieve water vapour profiles between 5 and 90 km with a vertical resolution of 3–4 km. Additionally, HDO is retrieved from 7–38 km using spectral windows in the 6.7–7.1µm (1,402–1,498 cm^{-1}) and 3.7–3.8 µm (2,612–2,724 cm^{-1}) ranges (Boone et al. 2005; Nassar et al. 2005, 2007).

Links: http://www.ace.uwaterloo.ca

Measuring technique	Thermal infrared limb occultation sounding	
Observation geometry	Limb sounding in solar occultation configuration	
Platform	UARS/HALOE	1991–2005
	ATLAS/ATMOS	1985, 1992, 1993, 1994 (Space Shuttle)
	ADEOS/ILAS	1997–1998
	ADEOS-II/ILAS-II	2003
	ACE/FTS	2003
Spectral range	Thermal infrared (from 2 to 16 µm)	
Vertical resolution	2–4 km	
Horizontal resolution	500–1000 km	
Vertical range	5–90 km	
Horizontal range	Solar occultation: 15 sunrise and 15 sunset occultations per day, sampled at similar latitudes on a given day	
Daytime/nighttime	Sunrise, sunset (solar occultation)	
Bottlenecks, limitations	Limited geographical sampling by solar occultations, observed latitudes vary slowly with time and near global coverage can only be obtained after a longer period (orbit dependent); Fixed local solar time (sunset, sunrise); Sensitivity to clouds limits sampling in troposphere (cloud screening required)	
Additional products	Various trace gases, temperature, aerosol and cloud information	

9.4.4 Thermal Infrared Limb Emission Sounding

Sounding of thermal emission at the Earth's limb provides the possibility for continuous global observations during day and night. The first limb viewing thermal infrared emission instrument was the "Limb Radiance Inversion Radiometer" (LRIR) on Nimbus-6, launched in 1975, which employed wide band radiometry with the goal to determine global profiles of atmospheric temperature and pressure (from CO_2 emission), as well as stratospheric water vapour and ozone. However, due to high noise levels and spurious signals from internal reflections the water vapour channel data were not useful (Bracken 2000). After this there have been several improved limb sounding instruments measuring thermal emission in the mid infrared region: LIMS and SAMS were launched on Nimbus-7 in 1978, ISAMS and CLAES on UARS in 1991, SABER on TIMED in 2001, MIPAS on Envisat in 2002, as well as HIRDLS and TES on Aura in 2004. These instruments provide(d) vertically resolved information on middle atmospheric water vapour during day and night with good, often near global, coverage.

9.4.4.1 NIMBUS-7/LIMS

The "Limb Infrared Monitor of the Stratosphere" (LIMS) was launched on Nimbus-7 in 1978 and acquired infrared radiance profiles with high vertical resolution over

a 7 months period. The instrument was turned off due to depletion of cryogen in June 1979. LIMS, a follow-on to LRIR, had six spectral channels providing data on the constituents NO_2 at 6.1 µm , H_2O at 6.2 µm, O_3 at 9.6 µm, HNO_3 at 11.3 µm, as well as two channels centred at the 15 µm band of CO_2 for retrieval of the temperature profile. Nimbus-7 was placed in a sun-synchronous, nearly circular orbit, with a noon equator crossing time on the ascending node. The LIMS optical axis was placed such that scanning was done out of the orbital plane, preventing direct sunlight from entering the telescope but limiting the geographical data coverage to 84° N to 64° S. LIMS provided the first global scale simultaneous observations of H_2O, HNO_3 and NO_2. Concentrations of water vapour were determined with an instantaneous vertical field of view at the horizon of 4 km between about 100 hPa and 1 hPa (∼15–50 km) (Gille and Russell III 1984; Russell III et al. 1984; Jones et al. 1986; Bracken et al. 2000).

Links: http://nssdc.gsfc.nasa.gov/nmc/

9.4.4.2 NIMBUS-7/SAMS

The "Stratospheric and Mesospheric Sounder" (SAMS), a pressure-broadening spectral radiometer, was also part of the Nimbus-7 payload, launched in 1978. The instrument observed thermal limb emission and solar radiance fluorescence from the atmosphere for nearly five years. The SAMS instrument employed the pressure modulation radiometry technique in conjunction with multi-layer dielectric interference filters to isolate the desired spectral regions. It measured CO_2 at 4.3 µm and 15 µm (for temperature), H_2O at 2.7 µm and 20–100 µm, CO at 4.7 µm, NO at 7.7 µm, N_2O at 5.3 µm, and CH_4 at 7.7 µm using six detectors and seven pressure modulation cells. Compared to earlier missions, SAMS extended the pressure modulation technique to gases other than CO_2, to measure emission from the upper atmosphere for which conventional wide band spectral filtering techniques did not provide adequate performance (Taylor et al. 1981, 1987). Albeit the retrieval of the SAMS water vapour channel data appeared to be problematic, information on the latitudinal and seasonal variation of water vapour in the middle atmosphere has been obtained for the period 1979–1981, from 45° S–65° N between 0.1–10 hPa (∼30–65 km) with a vertical resolution of approximately 8 km (Munro and Rodgers 1994; Bracken 2000).

Links: http://nssdc.gsfc.nasa.gov/nmc/

9.4.4.3 UARS/ISAMS

The "Improved Stratospheric and Mesospheric Sounder" (ISAMS), an infrared radiometer derived from SAMS on Nimbus-7, observed thermal emission from the Earth's limb using the technique of pressure modulator radiometry to derive vertical profiles of temperature and mixing ratios of CO, H_2O, CH_4, O_3, HNO_3, N_2O_5, NO_2,

N_2O and aerosol extinction. The spectral range covered by the 8 pressure-modulated channels was 2.7–100 µm and included a channel for water vapour at 6.9 µm . ISAMS was one of the instruments on the "Upper Atmosphere Research Satellite" (UARS) and operated from September 1991 to July 1992. The ISAMS data coverage extends from 80° S–80° N, but due to the UARS yaw manoeuvres the coverage is restricted to either 34° S–80° N or 34° N–80° S. Vertical profiles of temperature and composition were made with a vertical resolution better than 3 km (Taylor et al. 1993, Zaragoza et al. 1998).

Links: http://nssdc.gsfc.nasa.gov/nmc/
http://badc.nerc.ac.uk/data/isams

9.4.4.4 UARS/CLAES

The "Cryogenic Limb Array Etalon Spectrometer" (CLAES) was another infrared emission sounder on the UARS satellite launched in 1991. It remotely measured stratospheric composition (H_2O, N_2O, NO, NO_2, N_2O_5, HNO_3, CFC-l2, CFC-l1, HCl, $ClONO_2$, O_3, and CH_4) and temperature in the 10 to 60 km altitude range. The CLAES instrument consisted of four cryogenically cooled solid-etalon Fabry-Perot spectrometers (bandwidth 0.25 cm^{-1}), coupled with a reflective telescope and a solid-state linear detector array. The high-resolution multi-channel CLAES measurements allowed for the retrieval of both target and contaminant species. The target gas retrieval is thus less sensitive to the presence of contaminants than broadband radiometry where non-target species need to be modelled in the retrieval process. The stratospheric composition and temperature were determined from measurements of limb emission spectra in the 3.5–12 µm wavelength range. A linear detector array of 20 discrete detectors simultaneously covered the ∼15–60 km altitude range with 2.8 km vertical resolution. CLAES had a design lifetime of only 18 months determined by the Ne/CO_2 cryogen (Roche et al. 1993). Water vapour profiles (V7) are available from January 1992 to May 1993. The best quality was obtained for night-time profiles and pressure levels higher than 10 hPa and lower than 1 hPa.

Links: http://www.spasci.com/CLAES

9.4.4.5 CRISTA on the Space Shuttle

CRISTA "CRyogenic Infrared Spectrometers and Telescopes for the Atmosphere" is a limb scanning satellite experiment measuring middle and far infrared (4–71 µm) emissions of the Earth's atmosphere from the upper troposphere to the lower thermosphere, including water vapour. To reach good sensitivity the optics were cryogenically cooled using liquid helium (3 K). Three telescopes and four grating spectrometers of medium spectral resolution (∼400) allowed to observe three viewing directions simultaneously and to achieve a horizontal resolution of 300–400 km and a good vertical resolution of ∼2 km, within the 10–150 km target altitude region. CRISTA was mounted on the free-flying CRISTA-SPAS satellite which was

launched with the Space Shuttle during two short missions from 3–12 November 1994 and 7–19 August 1997. In orbit it was released from the cargo bay and retrieved at the end of the shuttle mission. Water vapour around the tropopause was for example retrieved from a line at 784 cm^{-1} (12.8 µm). (See e.g. Grossmann et al. 2002; Offermann et al. 2002; Schaeler et al. 2005, 2009).

Links: http://www.crista.uni-wuppertal.de

9.4.4.6 TIMED/SABER

The "Sounding of the Atmosphere using Broadband Emission Radiometry" (SABER) is one of four instruments on board the "Thermosphere, Ionosphere, Mesosphere Energetics and Dynamics" (TIMED) spacecraft, launched in December 2001 into a 74.1° inclined orbit at 625 km. SABER measures profiles of kinetic temperature, pressure and density, profiles of emission rates of NO, OH, O_2, and mixing ratios of O, H, O_3, H_2O, and CO_2. Mission goal is to explore the mesosphere and lower thermosphere globally in order to investigate fundamental processes governing the energetics, chemistry, dynamics, and transport of the atmospheric region extending from 60 km to 180 km. The instrument is a 10 channel multi-spectral broadband radiometer receiving thermal emission from the atmospheric limb in the near to mid infrared over the range 1.27 µm to 17 µm (7,865–650 cm^{-1}). Thermal emissions from the atmospheric limb are scanned from approximately 180 km down to the Earth's surface, providing vertical distributions of constituents and temperature profiles. The latitudinal coverage is determined by a 60-day yaw cycle. Observations of latitudes from 83° S to 52° N are performed in the South viewing phase and latitudes from 53° S – 82° N are covered in the North viewing phase. Water profiles between 15–80 km are retrieved from measurements in the 6.6 µm thermal infrared channel. Since non-LTE is an issue at infrared wavelength in the upper stratosphere, mesosphere and thermosphere, all inversions above the mid-stratosphere are done using a full non-LTE code (e.g. Russell-III et al. 1999; Feofilov et al. 2009).

Links: http://saber.gats-inc.com/
http://www.timed.jhuapl.edu

9.4.4.7 Envisat/MIPAS

The "Michelson Interferometer for Passive Atmospheric Sounding" (MIPAS) was launched on board the Envisat satellite in February 2002 in a near polar sun-synchronous orbit (inclination: 98.55° at 800 km, equator crossing 10am/pm) (Carli et al. 2004; Fischer et al. 2008). The instrument observes a wide spectral interval throughout the mid infrared from 4.15–14.6 µm (685–2,410 cm^{-1}) with a high spectral resolution of 0.035 cm^{-1}. Operation in full resolution based on an optical path difference of 20 cm ended however in March 2004, when a problem with the interferometer was encountered. Operation was resumed in January 2005 with

reduced pathlength of 8.2 cm and corresponding spectral resolution of 0.121 cm^{-1} (apodized). MIPAS spectrally resolves a large number of emission features of atmospheric minor constituents. The water vapour measurement provides information from 6 to 68 km with a vertical resolution of about 3.5–4.5 km between 6 – 42 km (coarser above) (Milz et al. 2005, 2009). In reduced resolution mode, the improved spatio-temporal sampling leads to a better vertical resolution of 2–4 km below 30 km (von Clarmann et al. 2009; Chauhan et al. 2009). An average of 400 MIPAS limb spectra is shown in Fig. 9.3 along with a model calculation high-lighting the water vapour contribution in the thermal infrared region.

Links: http://envisat.esa.int/instruments/mipas
http://earth.esa.int/
http://www-imk.fzk.de/asf/ame/envisat-data

9.4.4.8 Aura/TES

The "Thermal Emission Spectrometer (TES)" on board Aura, launched in July 2004, is a high-resolution Fourier transform spectrometer operating over the wavelength range 2.3–16.7 µm using an external two-axis pointing mirror which allows either an off-nadir or limb view. The instruments has been described in Sect. 9.2.1. TES may be instructed to image the limb providing spectral measurements from the ground up to 34 km with a vertical resolution of 2.3 km. The instrument is cooled using Stirling-cycle mechanical coolers and employs four detector arrays, each of 32 elements, which operate simultaneously (e.g. Worden et al. 2006, 2007).

Links: http://tes.jpl.nasa.gov

9.4.4.9 Aura/HIRDLS

The "High Resolution Dynamics Limb Sounder" (HIRDLS) instrument on Aura, launched in 2004, was designed to provide global measurements of temperature, trace constituents and aerosols from the middle troposphere to the mesosphere at high vertical and high horizontal resolution, to be achieved by making vertical scans at several azimuth angles across the satellite orbit track. HIRDLS measures thermal emissions from the atmospheric limb at multiple spectral channels in the range 6–17 µm. Each element of the array of twenty-one detectors, cooled to 65 K by a Stirling-cycle mechanical cooler, corresponds to an atmospheric field of 10 km horizontal by 1 km vertical. The telescope views the atmosphere via a two-axis tilting mirror which provides altitude and azimuth scanning. Shortly after launch it was discovered that 80 % of the optical path was blocked (most likely by a piece of

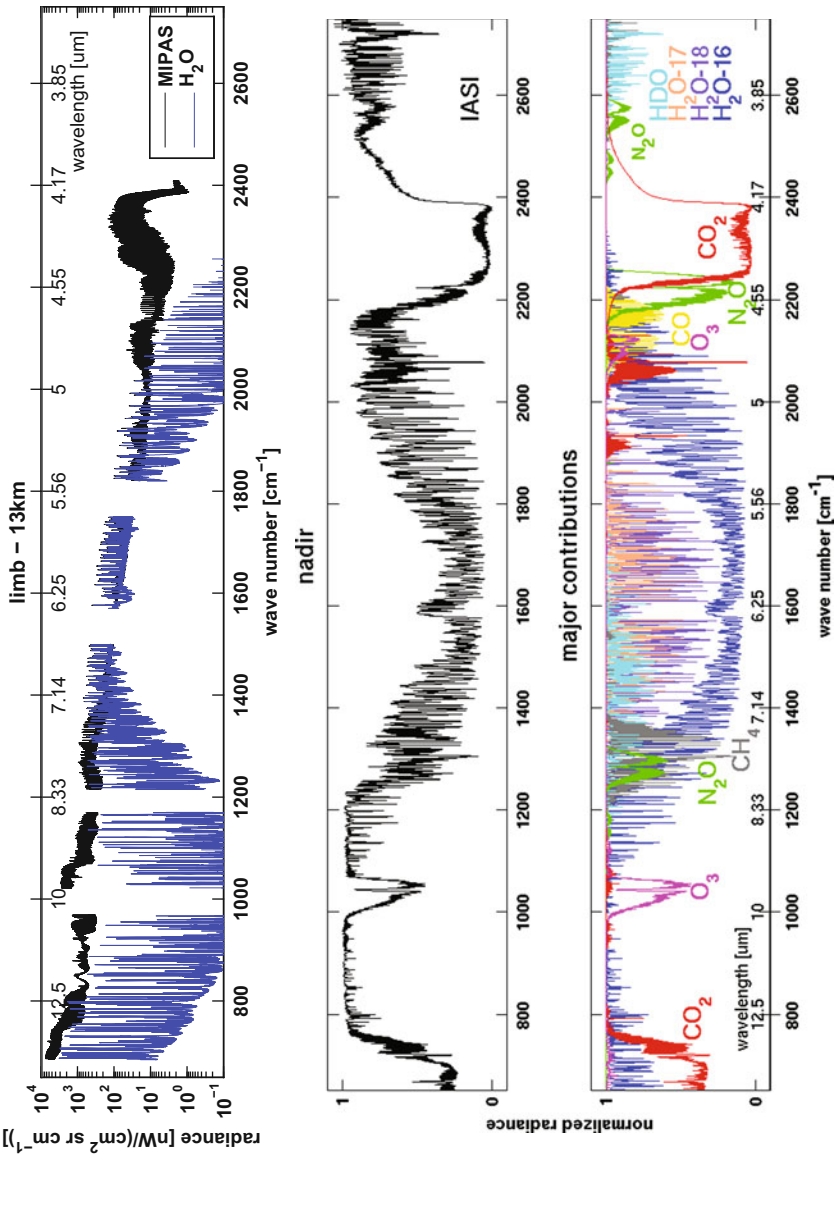

Fig. 9.3 Overview of spectral ranges for sounding of water vapour from space. II Thermal infrared. *Top* Wide band spectrum obtained from the MIPAS limb sounder on Envisat. Shown is an average spectrum at 13 km tangent height, built from about 400 individual spectra measured in September 2003 at Northern mid-latitudes. The "H_2O contribution" is the calculated radiance contribution of the average of the 400 individually retrieved H_2O profiles. *Middle* Measurement of the IASI nadir sounder on MetOp over Western Australia on 20 December 2006. The normalised radiances were obtained by dividing by the local Earth blackbody function. *Bottom* Corresponding model calculations (in normalised units) for the main infrared absorbing gases (nadir case). The MIPAS spectrum and limb calculations were kindly provided by Johannes Plieninger and Gabi Stiller (Research Center Karlsruhe). The IASI spectrum and nadir calculations were obtained by courtesy of P. Coheur (University Libre de Bruxelles), adapted from Fig. 3 in (Clerbaux et al. 2009)

thermal blanketing material) and measurements at high vertical resolution could be made only at one across-track scan angle. Due to this severe limitation, data reduction has been delayed and water vapour data have not yet been made available at the time of writing (September 2010).

Links: http://www.eos.ucar.edu/hirdls

Measuring technique	Thermal infrared limb emission sounding	
Observation geometry	Limb	
Platform	NIMBUS-7/LIMS	1978–1979
	NIMBUS-7/SAMS	1978–1982
	UARS/ISAMS	1991–1992
	UARS/CLAES	1991–1993
	CRISTA/SPAS	1994, 1997 (Space Shuttle)
	TIMED/SABER	2001
	Envisat/MIPAS	2002
	Aura/TES	2004
	Aura/HIRDLS	2004
Spectral range	Thermal infrared (from 2–17 μm), far infrared	
Vertical resolution	From 2–8 km, depending on instrument sensitivity and vertical sampling	
Horizontal resolution	500–1000 km	
Vertical range	~5–80 km or higher	
Horizontal range	Near global (depending on orbit)	
Daytime/nighttime	Both (thermal emission)	
Bottlenecks, limitations	Strong sensitivity to cirrus clouds and aerosols in the line-of-sight limits global sampling, non-LTE affects accuracy at high altitudes.	
Corrections needed?	Non-LTE in upper stratosphere and above, cloud screening.	
Future potential	Sounding of troposphere and stratosphere with improved vertical and horizontal sampling and resolution through use of imaging techniques and sensitive array detectors.	

9.4.5 Microwave Limb Emission Sounding

Observation of thermal emission of strong water vapour lines residing in the microwave range are relatively insensitive to clouds and non-LTE effects and allow information to be obtained during day and night. A good spatial and temporal sampling can potentially be achieved with limb observations in this spectral region, depending on the individual sensors sensitivity and field-of-view.

9.4.5.1 UARS/MLS and MAS/ATLAS

Millimetre wave limb sounding instruments dedicated to middle atmospheric research were successfully employed in the early nineties. The first instrument of this type, the "Microwave Limb Sounder" (MLS), was launched on board the "Upper Atmosphere Research Satellite" (UARS) in September 1991 (Barath et al. 1993; Waters 1993), whilst the "Millimeter-wave Atmospheric Sounder" (MAS), targeting similar frequency bands, was flown on board the "Atmospheric Laboratory for Applications and Science" (ATLAS) platform in the Space Shuttle's cargo bay during three short missions in March 1992, April 1993, and November 1994 (Croskey et al. 1992. Both instruments were equipped with double sideband heterodyne radiometers based on Schottky-diode detectors operating around 60 GHz (O_2 for temperature) and in the 183–205 GHz range as well as with filter-bank spectrometers. The observations of the emissions of the water line at 183 GHz provided information in the 15–80 km altitude range (Aellig et al. 1993; Hartmann et al. 1996; Aellig et al. 1996; Read et al. 2004). After the early failure of the UARS/MLS 183 GHz radiometer in April 1993, water vapour information was still retrieved between 464 and 146 hPa (∼6–14 km) from the water continuum emissions observed in the 204 GHz (ClO) channel (Read et al. 2001), providing an upper tropospheric humidity time series from 1991–1998. UARS is in a 57° inclination orbit and MLS observed the atmospheric limb perpendicular to the orbit track. Regular UARS yaw manoeuvres allowed either the high southern latitudes 34° N – 81° S or northern latitudes 81° N – 34° S to be observed.

Links: http://mls.jpl.nasa.gov
http://www.mps.mpg.de/en/projekte/mas

9.4.5.2 Odin/SMR

First limb observations in the sub-millimetre wavelength range from space were conducted by the Sub-Millimetre Radiometer (SMR) on board the Odin satellite, launched in February 2001 into a polar sun-synchronous orbit (Murtagh et al. 2002; Frisk et al. 2003). The SMR instrument consists of four mechanically cooled single sideband Schottky-diode receivers in the 486–581 GHz range and one millimetre receiver at 119 GHz (for O_2). Measurements of several different water lines, spectrally resolved by auto-correlation spectrometers with 1 MHz resolution, were time-shared with astronomical and other atmospheric observation modes. Measurements of the 488.5 GHz and 556.9 GHz lines, on a basis of one observation day per week, provide information in the altitude range from about 20 to 75 km and 50 to 110 km, respectively, with a vertical resolution of ∼3 km (Urban et al. 2007). Additionally, water vapour in the upper troposphere and lowermost stratosphere is retrieved from water emissions measured near 501 and 544 GHz arising from continuum and far-wing emissions of the strong 556.9 GHz water line (Ekström et al. 2007, 2008; Urban et al. 2008). Moreover, Odin/SMR was the first instrument to globally measure profiles of the four main water vapour isotopes (H_2O-18, H_2O-17, HDO) from space, using

bands around 490 and 551 GHz (Urban et al. 2007). Typical Odin water line measurements are shown in Fig. 9.4, along with model calculations for the 0–1000 GHz spectral region.

Links: http://odin.rss.chalmers.se

9.4.5.3 Aura/MLS

The Microwave Limb Sounder (MLS) on Aura was launched in July 2004, equipped with Schottky-diode double sideband radiometers operating in the millimetre, submillimetre, and far infrared spectral ranges (Waters et al. 2006). Measurements of the 183 GHz water vapour line, the same line which was observed by the UARS/MLS instrument, are resolved by a filter-bank and a digital autocorrelation spectrometer and provide information in the pressure range from 316–0.01 hPa (∼10–80 km) with a vertical resolution of 3–4 km in the stratosphere (Froidevaux et al. 2006; Read et al. 2007; Lambert et al. 2007). An example of the Aura/MLS 183 GHz measurement is given in Fig. 9.4. Profile measurements are performed continuously during day and night with good spatio-temporal sampling. Note that both Aura/MLS and Odin/SMR are operated on sun-synchronous platforms allowing near global coverage to be obtained on a daily basis.

Links: http://mls.jpl.nasa.gov

9.4.5.4 JEM/SMILES

Whilst the aforementioned heterodyne limb sounders are based on Schottky-diode heterodyne detectors, other instruments have been developed such as the Japanese Sub-Millimeter Limb Emission Sounder (SMILES). This instrument employed for the first time sensitive SIS-detector technology in space (SMILES 2002; Kasai et al. 2006), providing roughly a ten-fold improvement of the receiver noise temperature compared to conventional Schottky-diode receivers. Water vapour continuum emissions were measured in two bands around 625 and 650 GHz, allowing vertical profile information to be retrieved in the upper troposphere and lower stratosphere with an estimated vertical resolution of 2–3 km. SMILES was launched in September 2009 and is installed on the Japanese Experiment Module (JEM) of the "International Space Station" (ISS). The instrument provided data from October 2009 to April 2010.

Links: http://smiles.tksc.jaxa.jp
http://smiles.nict.go.jp

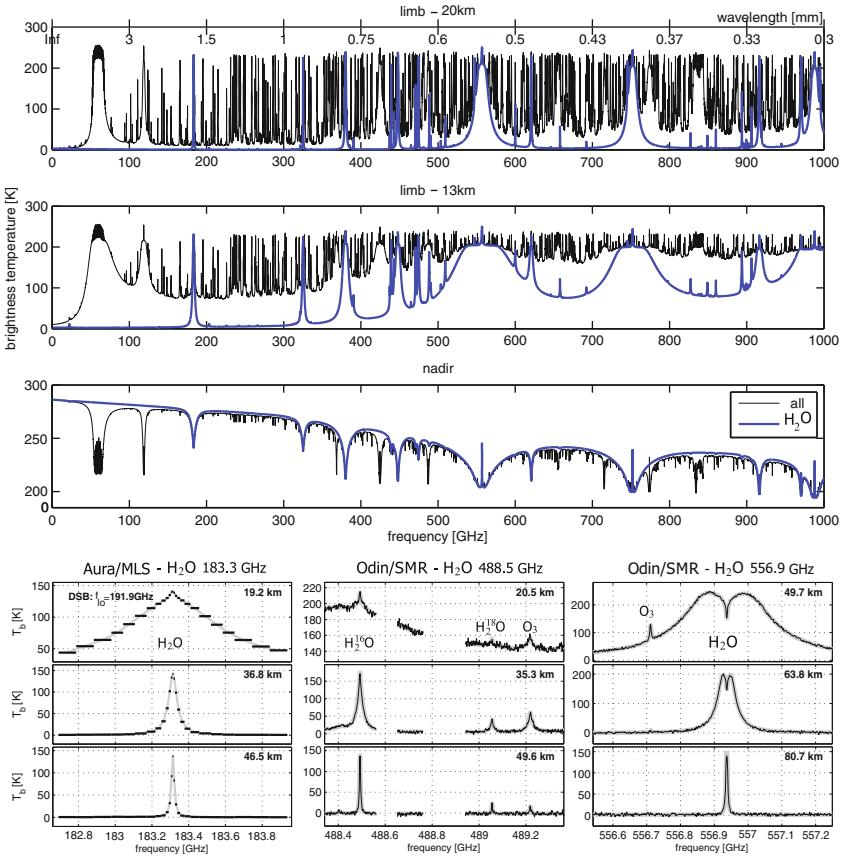

Fig. 9.4 Overview of spectral ranges for sounding of water vapour from space. III Model calculations for the millimetre and sub-millimetre wavelength range. *Top rows* limb observation geometry, tangent heights 20 km and 13 km. *Middle row* nadir geometry. Based on simulations with the MOLIERE-5 forward model (Urban et al. 2004). *Bottom* Typical water line measurements of the Aura Microwave Limb Sounder (Aura/MLS) at 183.3 GHz (left), and of the Odin Sub-Millimetre Radiometer (Odin/SMR) at 488.5 GHz (middle) and at 556.9 GHz (right). MLS data were kindly provided by Bill Read (JPL)

Measuring technique	Microwave limb emission sounding	
Observation geometry	limb	
Platform	UARS/MLS	1991–1998
	ATLAS/MAS	1992, 1993, 1994 (3 missions on) (Space Shuttle)
	Odin/SMR	2001
	Aura/MLS	2004

	JEM/SMILES	2009–2010 (on International) (Space Station)
Spectral range	Currently from 183 GHz to 2.532 THz	
Vertical resolution	2–5 km, depending on frequency, antenna and sensitivity	
Horizontal resolution	500–1000 km	
Vertical range	Between 5 and 120 km	
Horizontal range	Near global (depending on orbit)	
Daytime/nighttime	Both (thermal emission)	
Bottlenecks, limitations	Signal absorption by tropospheric water vapour and thick tropospheric clouds (large ice particles or water drops) determines lower altitude limit (absorption increases with frequency).	
Additional products	Various trace gases, temperature, cloud information	
Future potential	UT/LS sounding with improved vertical and horizontal sampling and resolution through use of imaging techniques and more sensitive detectors (improved Schottky mixers, use of SIS detector technology)	

Table 9.1 Links to selected satellite data centres

NOAA National Environmental Satellite, Data, and Information Service (NESDIS): http://www.nesdis.noaa.gov/
NOAA Office of Satellite Data Processing and Distribution (OSDPD): http://www.osdpd.noaa.gov
NOAA National Climatic Data Center (NCDC): http://www.ncdc.noaa.gov
NOAA National Geophysical Data Center (NGDC): http://www.ngdc.noaa.gov
NOAA Comprehensive Large Array-data Stewardship System (CLASS): http://www.nsof.class.noaa.gov
NASA Goddard Earth Sciences (GES) Data and Information Services Center (DISC), Distributed Active Archive Center (DAAC): http://daac.gsfc.nasa.gov
British Atmospheric Data Centre (BADC): http://badc.nerc.ac.uk Centre for Atmospheric Chemistry Products and Services (ETHER): http://ether.ipsl.jussieu.fr
European Organisation for the Exploitation of Meteorological Satellites (EUMETSAT): http://www.eumetsat.int
European Space Agency (ESA), Earth Observation Principal Investigator portal (EOPI): http://eopi.esa.int

9.5 Satellite Data Centres

Information on how data can be obtained is usually indicated on the individual satellite mission and instrument home pages (see links in each subsection). Depending on mission and instrument, data can often be obtained from larger satellite data centres which also provide useful information on the satellite sensors, algorithms and data products. For the convenience of the reader, Table 9.1 provides links to some major data centres.

Acknowledgments The author is very grateful for the many valuable comments received, notably from M. Milz, M. Weber, K. Hocke, J.C. Lambert, Th. Flury, E. De Wachter, N. Livesey, and J. Russel-III. Model calculations and spectral data for the illustrations were kindly provided by A. Rozanov, G. Stiller, J. Plieninger, C. Clerbaux, P. Coheur, and B. Read.

References

C.P. Aellig, N. Kämpfer, R.M. Bevilacqua, , Error analysis of ClO, O3, and H2O abundance profiles retrieved from millimeter wave limb sounding measurements. J. Geophys. Res. **98**, 2975–2983 (1993). doi:10.1029/92JD02131

C.P. Aellig, N. Kämpfer, C. Rudin, R.M. Bevilacqua, W. Degenhardt, P. Hartogh, C. Jarchow, K. Künzi, J.J. Olivero, C. Croskey, J.W. Waters, H.A. Michelsen, Latitudinal distribution of upper stratospheric ClO as derived from space borne microwave spectroscopy. Geophys. Res. Lett. **23**, 2321–2324, (1996). doi:10.1029/96GL01215

R. Anthes, P. Bernhardt, Y. Chen, L. Cucurull, K. Dymond, D. Ector, S. Healy, S.P. Ho, D. Hunt, Y.H. Kuo, H. Liu, K. Manning, C. McCormick, T. Meehan, W. Randel, C. Rocken, W. Schreiner, S. Sokolovskiy, S. Syndergaard, D. Thompson, K. Trenberth, T.K. Wee, N.Yen, Z. Zeng, The COSMIC/FORMOSAT-3 mission: early results. Bull. Am. Meteorol. Soc. **89**, 313–333 (2008)

H. Aumann, M. Chahine, C. Gautier, M. Goldberg, E. Kalnay, L. McMillin, H. Revercomb, P. Rosenkranz, W. Smith, D. Staelin, L. Strow, J. Susskind, AIRS/AMSU/HSB on the Aqua mission: design, science objectives, data products, and processing systems. IEEE Trans. Geosci. Remote Sens. **41**, 253–264,2003 doi:10.1109/TGRS.2002.808356

F. Barath, M. Chavez, R. Cofield, D. Flower, M. Frerking, M. Gram ,W. Harris, J. Holden, R. Jarnot, W. Kloezeman, G. Klose, G. Lau, M. Loo, B. Maddison, R. Mattauch, R. McKinney, G. Peckham, H. Pickett, G. Siebes, F. Soltis, R. Suttie, J. Tarsala, J. Waters, W. Wilson, The upper atmosphere research satellite microwave limb sounder experiment. J. Geophys. Res. **98**, 10,751–10,762 (1993)

P.F. Bernath, C.T. McElroy, M.C. Abrams, C.D. Boone, M. Butler, C. Camy-Peyret, M. Carleer, C. Clerbaux, P.F. Coheur, R. Colin, P. DeCola, M. DeMaziôère, J.R. Drummond, D. Dufour, W.F.J. Evans, H. Fast, D. Fussen, K. Gilbert, D.E. Jennings, E.J. Llewellyn, R.P. Lowe, E. Mahieu, J.C. McConnell, M. McHugh, S.D. McLeod, R. Michaud, C. Midwinter, R. Nassar, F. Nichitiu, C. Nowlan, C.P. Rinsland, Y.J. Rochon, N. Rowlands, K. Semeniuk, P. Simon, R. Skelton, J.J. Sloan, M.A. Soucy, K. Strong, P. Tremblay, D. Turnbull, K.A. Walker, I. Walkty,D.A. Wardle, V. Wehrle, R. Zander, J. Zou, Atmospheric chemistry experiment (ACE): Mission overview. Geophys. Res. Lett. **32**, L15S01 (2005). doi:10.1029/2005GL022386

J. Bertaux, A. Hauchecorne, F. Dalaudier, C. Cot, E. Kyrölä, D. Fussen, J. Tamminen, G. Leppelmeier, V. Sofieva, S. Hassinen, O. d Andon, G. Barrot, A. Mangin, B. Théodore, M. Guirlet, O. Korablev, P. Snoeij, R. Koopman, R. Fraisse, First results on GOMOS/Envisat. Adv.Space Res. **33**, 1029–1035(2004)

C.D. Boone, R. Nassar, K.A. Walker, Y. Rochon, S.D. McLeod, C.P. Rinsland, P.F. Bernath, Retrievals for the atmospheric chemistry experiment Fourier-transform spectrometer. App. Optics. **44**, 7218–7231 (2005). doi:10.1364/AO.44.007218

H. Bovensmann, J. Burrows, M. Buchwitz, J. Frerick, S. Noel, V. Rozanov, K. Chance, A. Goede, SCIAMACHY: Mission objective and measurement modes. J. Atmos. Sci. **56**, 127–150 (1999)

J. Bracken, *Development of Limb Sounders "The Spectral Side"; Science, Spectral Selection and Technology* (Atmospheric, Oceanic and Planetary Physics, University of Oxford, 2000). http://www.atm.ox.ac.uk/user/bracken/limb.html

S. Buehler, M. Kuvatov, V. John, M. Milz, B. Soden, D. Jackson, J. Notholt, An uppertropospheric humidity data set from operational satellite microwave data. J. Geophys. Res. **113**, (2008). doi:10.1029/2007JD009314

B. Carli, D. Alpaslan, M. Carlotti, E. Castelli, S. Ceccherini, B.M. Dinelli, A. Dudhia, J.M. Flaud, M. Hoepfner, V. Jay, L. Magnani, H. Oelhaf, V. Payne, C. Piccolo, M. Prosperi, P. Raspollini, J. Remedios, M. Ridolfi, R. Spang, First results of MIPAS/ENVISAT with operational Level 2 code. Adv. Space Res. **33**, 1012–1019 (2004). doi:10.1016/S0273–1177(03)00584–2

M. Chahine, T. Pagano, H. Aumann, R. Atlas, C. Barnet, J. Blaisdell, L. Chen, M. Divakarla, E. Fetzer, MGoldberg, C. Gautier, S. Granger, S. Hannon, F. Irion, R. Kakar, E. Kalnay, B. Lambrigtsen, S.Y. Lee, J. Le Marshall, W. McMillan, L. McMillin, E. Olsen, H. Revercomb, P. Rosenkranz, W. Smith, D. Staelin, L. Strow, J. Susskind, D. Tobin, W. Wolf, L. Zhou, AIRS: Improving weather forecasting and providing new data on greenhouse gases. Bull. Am. Meteorol. Soc. **87**, 911–926 (2006)

S. Chauhan, M. Höpfner, G.P. Stiller, T. von Clarmann, B. Funke, N. Glatthor, U. Grabowski, A. Linden, S. Kellmann, M. Milz, T. Steck, H. Fischer, L. Froidevaux, A. Lambert, M.L. Santee, M. Schwartz, W.G. Read, N.J. Livesey, , MIPAS reduced spectral resolution UTLS-1 mode measurements of temperature, O3, HNO3, N2O, H2O and relative humidity over ice: retrievals and comparison to MLS. Atmos. Measure. Tech. **2**, 337–353 (2009). ISSN 1867–1381, http://www.atmos-meas-tech.net/2/337/2009/

M.D. Chou, C.H. Weng, P.H. Lin, FORMOSAT-3/COSMIC humidity retrievals and comparisons with AIRS retrievals and NCEP/NCAR reanalyses. J. Geophys. Res. **114**, (2009). doi:10.1029/2008JD010227

C. Clerbaux, A. Boynard, L. Clarisse, M. George, J. Hadji-Lazaro, H. Herbin, D. Hurtmans, M. Pommier, A. Razavi, S. Turquety, C. Wespes, P.F. Coheur, Monitoring of atmospheric composition using the thermal infrared IASI/MetOp sounder. Atmos. Chem. Phys. **9**, 6041–6054 (2009). ISSN 1680–7316, http://www.atmos-chem-phys.net/9/6041/2009/

C. Croskey, N. Kämpfer, R. Bevilacqua, G. Hartmann, K. Künzi, P. Schwartz, J. Olivero, S. Puliafito, C. Aellig, G. Umlauft, W. Waltman, W. Degenhardt, The millimeter wave atmospheric sounder (MAS): A shuttle-based remote sensing instrument. IEEE Trans. Geosci. Remote Sens. **40**, 1090–1100 (1992)

I. Dyras, D. Serafin-Rek, The use of AMSU data from NOAA-15 satellite for meteorological products generation. Adv. Space Res. **30,** 2461–2466, (2002) ISSN 0273–1177, doi:10.1016/S0273–1177(02)80306–4

M. Ekström, P. Eriksson, B. Rydberg, D. Murtagh, First Odin sub-mm retrievals in the tropical upper troposphere: humidity and cloud ice signals. Atmos. Chem. Phys. **7**, 459–469 (2007)

M. Ekström, P. Eriksson, W. Read, M. Milz, D. Murtagh, Comparison of satellite limbsounding humidity climatologies of the uppermost tropical troposphere. Atmos. Chem. Phys **8**, 309–320 (2008). ISSN 1680–7316, http://www.atmos-chem-phys.net/8/309/2008/

A.G. Feofilov, A.A. Kutepov, W.D. Pesnell. R.A. Goldberg, B.T. Marshall, L.L. Gordley, M. García-Comas, M. López-Puertas, R.O. Manuilova, V.A. Yankovsky, S.V. Petelina, J.M. Russell III, Daytime SABER/TIMED observations of water vapor in the mesosphere: retrieval approach and first results. Atmos. Chem. Phys. **9**, 8139–8158, (2009). doi:10.5194 acp-9–8139-2009, http://www.atmos-chem-phys.net/9/8139/2009/

R. Ferraro, F. Weng, N. Grody, L. Zhao, H. Meng, C. Kongoli, P. Pellegrino, S. Qiu, C. Dean, NOAA operational hydrological products derived from the advanced microwave sounding unit. IEEE Trans. Geosci. Remote Sens. **43**, 1036–1049 (2005). ISSN 0196–2892, doi: 10.1109/TGRS.2004.843249

H. Fischer, M. Birk, C. Blom, B. Carli, M. Carlotti, T. von Clarmann, L. Delbouille, A. Dudhia, D. Ehhalt, M. Endemann, J.M. Flaud, R. Gessner, A. Kleinert, R. Koopman, J. Langen, M. Löpez-Puertas, P. Mosner, H. Nett, H. Oelhaf, G. Perron, J. Remedios, M. Ridolfi, G. Stiller, R. Zander, MIPAS: an instrument for atmospheric and climate research. Atmos. Chem. Phys. **8**, 2151–2188, (2008). ISSN 1680–7316, http://www.atmos-chem-phys.net/8/ 2151/2008/

U. Frisk, M. Hagström, J. Ala-Laurinaho, S. Andersson, J.C. Berges, J.P. Chabaud, M. Dahlgren, A. Emrich, H.G. Florén, G. Florin, M. Fredrixon, T. Gaier, R. Haas, T. Hirvonen, Å. Hjalmarsson, B. Jakobsson, P. Jukkala, P. Kildal, E. Kollberg, J. Lassing, A. Lecacheux, P. Lehikoinen, A. Lehto, J. Mallat, C. Marty, D. Michet, J. Narbonne, M. Nexon, M. Olberg, O. Olofsson, G.

Olofsson, A. Origné, M. Petersson, P. Piironen, R. Pons, D. Pouliquen, I. Ristocelli, C. Rosolen, G. Rouaix, A. Räisänen, G. Serra, F. Sjöberg, L. Stenmark, S. Torchinsky, J. Tuovinen, C. Ullberg, E. Vinterhav, N. Wadefalk, H. Zirath, P. Zimmermann, R. Zimmermann, The Odin satellite: I. Radiometer design and test. Astro. Astrophys. **402**, L27–34 (2003)

L. Froidevaux, N.J. Livesey, W.G. Read, Y.B. Jiang, C. Jimenez, M.J. Filipiak, M.J. Schwartz, M.L. Santee, H.C. Pumphrey, J.H. Jiang, D.L. Wu, G.L. Manney, B.J. Drouin, J.W. Waters, E.J. Fetzer, P.F. Bernath, C.D. Boone, K.A. Walker, K.W. Jucks, G.C. Toon, J.J. Margitan, B. Sen, C.R. Webster, L.E. Christensen, J.W. Elkins, E. Atlas, R.A. Lueb, R. Hendershot, Early validation analyses of atmospheric profiles from EOS MLS on the Aura Satellite. IEEE Trans. Geosci. Remote Sens. **44**, 1106–1121 (2006). doi:10.1109/TGRS.2006.864366

J.C. Gille, J.M. Russell III, The limb infrared monitor of the stratosphere:Experiment description, performance, and results. J. Geophys. Res. **89**, 5125{5140 (1984). doi:10.1029/JD089iD04p05125

W. Glaccum, R.L., Lucke, R.M. Bevilacqua, E.P. Shettle, J.S. Hornstein, D.T. Chen, J.D. Lumpe, S.S. Krigman, D.J. Debrestian, M.D., Fromm, F. Dalaudier, E. Chassefière, C. Deniel, C.E. Randall, D.W. Rusch, J.J. Olivero, C. Brogniez, J. Lenoble, R. Kremer, The polar ozone and aerosol measurement instrument. J. Geophys. Res. **101**, 14479–14488 (1996). doi:10.1029/96JD00576

L. Gordley, M. Hervig, C. Fish, J. Russell-III, S. Bailey, J. Cook, S. Hansen, A. Shumway, G. Paxton, L. Deaver, T. Marshall, J. Burton, B. Magill, C. Brown, E. Thompson, J. Kemp, The solar occultation for ice experiment, J. Atmos. Solar-Terr. Phys. **71**, 300–315 (2009). ISSN 1364-6826, doi:10.1016/j.jastp.2008.07.012

K. Grossmann, D. Offermann, O. Gusev, J. Oberheide, M. Riese, R. Spang, The CRISTA-2 mission. J. Geophys. Res., **107**, 8173 (2002). doi:10.1029/2001JD000667

M. Gunson, M. Abbas, M. Abrams, M. Allen, L. Brown, T.L. Brown, A. Chang, A. Goldman, F. Irion, L. Lowes, E. Mahieu, G. Manney, H. Michelsen, M. Newchurch, C. Rinsland, R. Salawitch, G. Stiller, G. Toon, Y. Yung, R. Zander, The atmospheric trace molecule spectroscopy (ATMOS) experiment: Deployment on the ATLAS space shuttle missions. Geophys. Res. Lett. **23**, 2333–2336 (1996)

J.E. Harries, J.M. Russell, A.F. Tuck, L.L. Gordley, P. Purcell, K. Stone, R.M. Bevilacqua, M. Gunson, G. Nedoluha, W.A. Traub, Validation of measurements of water vapor from the halogen occultation experiment (HALOE). J. Geophys. Res. **101**, 10205–10216 (1996). doi:10.1029/95JD02933

G.K. Hartmann, R.M. Bevilacqua, P.R. Schwartz, N. Kämpfer, K.F. Künzi, C.P.Aellig, A. Berg, W. Boogaerts, B.J. Connor, C.L. Croskey, M. Daehler, W. Degenhardt, H.D. Dicken, D. Goldizen, D. Kriebel, J. Langen, A. Loidl, J.J. Olivero, T.A. Pauls, S.E. Puliafito, M.L. Richards, C. Rudin, J.J. Tsou, W.B. Waltman, G. Umlauft, R. Zwick, Measurements of O_3, H_2O and ClO in the middle atmosphere using the millimeter-wave atmospheric sounder (MAS). Geophys. Res. Lett. **23**, 2313–2316 (1996). doi:10.1029/96GL01475

S. Heise, J. Wickert, G. Beyerle, T. Schmidt, C. Reigber, Global monitoring of tropospheric water vapor with GPS radio occultation aboard CHAMP. Adv. Space Res. **37**, 2222–2227 (2006)

H. Herbin, D. Hurtmans, C. Clerbaux, L. Clarisse, P.-F. Coheur, H_2^{16} O and HDO measurements with IASI/MetOp. Atmos. Chem. Phys. Dis. **9**, 9267–9290 (2009)

F.W. Irion, M.R. Gunson, G.C. Toon, A.Y. Chang, A. Eldering, E. Mahieu, G.L. Manney, H.A. Michelsen, E.J. Moyer, M.J. Newchurch, G.B. Osterman, C.P. Rinsland, R.J. Salawitch, B. Sen, Y.L. Yung, R. Zander, Atmospheric trace molecule spectroscopy (ATMOS) experiment version 3 data retrievals. Appl. Optics. **41**, 6968–6979 (2002). doi:10.1364/AO.41.006968

R.L. Jones, J.A. Pyle, J.E. Harries, A.M. Zavody, J.M. Russell III, J.C. Gille, The water vapour budget of the stratosphere studied using LIMS and SAMS satellite data. Quarterly J. Royal Meteorol. Soc. **112**, 1127–1143 (1986). doi:10.1256/smsqj.47411

H. Kanzawa, C. Schiller, J. Ovarlez, C. Camy-Peyret, S. Payan, P. Jeseck, H. Oelhaf, M. Stowasser, W.A. Traub, K.W. Jucks, D.G. Johnson, G.C. Toon, B. Sen, J.-F. Blavier, J.H. Park, G.E. Bodeker, L.L. Pan, T. Sugita, H. Nakajima, T. Yokota, M. Suzuki, M. Shiotani, Y. Sasano, Validation and data characteristics of water vapor profiles observed by the Improved Limb

Atmospheric Spectrometer (ILAS) and processed with the version 5.20 algorithm. J. Geophys. Res. **107**, 8217 (2002). doi:10.1029/2001JD000881

Y. Kasai, C. Takahashi, J. Urban, S. Hoshino, K. Takahashi, J. Inatani, M. Shiotani, H.Masuko, Stratospheric ozone isotope enrichment studied by sub-millimeter wave heterodyne radiometry: The observation capabilities of SMILES. IEEE Transactions on Geoscience and Remote Sensing, 44, 676–693 (2006). doi:10.1109/TGRS.2005.861754

E. Kyröla, J. Tamminen, G. Leppelmeier, V. Sofieva, S. Hassinen, J. Bertaux, A. Hauchecorne, F. Dalaudier, C. Cot, O. Korablev, O.F. d'Andon, G. Barrot, A. Mangin, B. Theodore, M. Guirlet, F. Etanchaud, P. Snoeij, R. Koopman, L. Saavedra, R. Fraisse, D. Fussen, F. Vanhellemont, GOMOS on Envisat: An overview, Adv. Space Res. **33**, 1020–1028 (2004)

A. Lambert, W. Read, N. Livesey, M. Santee, G. Manney, L. Froidevaux, D. Wu, M. Schwartz, H. Pumphrey, C. Jimenez, G. Nedoluha, R. Coeld, D. Cuddy, W. Daffer, B. Drouin, R. Fuller, R. Jarnot, B. Knosp, H. Pickett, V. Perun, W. Snyder, P. Stek, R. Thurstans, P. Wagner, J. Waters, K. Jucks, G. Toon, R. Stachnik, P. Bernath, C. Boone, K. Walker, J. Urban, D. Murtagh, J. Elkins, E. Atlas, Validation of the aura microwave limb sounder middle atmosphere water vapor and nitrous oxide measurements. J. Geophys. Res. **112** (2007). doi:10.1029/2007JD008724

Q. Liu, F. Weng, One-dimensional variational retrieval algorithm of temperature, water vapor, and cloud water profiles from advanced microwave sounding unit (AMSU). IEEE Trans. Geosci. Remote Sens. 43, 1087{1095 (2005). ISSN 0196-2892, doi:10.1109/TGRS.2004.843211

J. Lumpe, R. Bevilacqua, C. Randall, G. Nedoluha, K. Hoppel, J. Russell, V.L. Harvey, C. Schiller, B. Sen, G. Taha, G. Toon, H. Vömel, Validation of polar ozone and aerosol measurement (POAM) III version 4 stratospheric water vapor. J. Geophys. Res. **111**(11) 301 (2006). doi: 10.1029/2005JD006763

J.D. Lumpe, R.M. Bevilacqua, K.W. Hoppel, S.S., Krigman, D.L. Kriebel, D.J. Debrestian, C.E. Randall, D.W. Rusch, C. Brogniez, R. Ramananahérisoa, E.P. Shettle, J.J. Olivero, J. Lenoble, P. Pruvost, POAM II retrieval algorithm and error analysis. J. Geophys. Res. **102**, 23593–23614 (1997). doi:10.1029/97JD00906

E. Maddy, C. Barnet, Vertical resolution estimates in version 5 of AIRS operational retrievals, IEEE Trans. Geosci. Remote Sens. **46**, 2375–2384 (2008)

C. Melsheimer, G. Heygster, Improved retrieval of total water vapor over polar regions from AMSU-B microwave radiometer data. IEEE Trans. Geosci. Remote Sens. **46**, 2307–2322 (2008), ISSN 0196-2892, doi:10.1109/TGRS.2008.918013

C. Melsheimer, S. Mieruch, S. Noel, G. Heygster, Comparison of total water vapor columns retrieved from satellite measurements: microwave radiances from AMSU-B and visible spectra from GOME/SCIAMACHY, in Geoscience and Remote Sensing Symposium, 2007. IGARSS 2007. IEEE Int. 1701–1704 (2007). doi:10.1109/IGARSS.2007.4423145

H.A. Michelsen, G.L. Manney, F.W. Irion, G.C. Toon, M.R. Gunson, C.P. Rinsland, R. Zander, E. Mahieu, M.J. Newchurch, P.N. Purcell, E.E. Remsberg, J.M. Russell, H.C. Pumphrey, J.W. Waters, R.M. Bevilacqua, K.K. Kelly, E.J. Hintsa, E.M. Weinstock, E.-W. Chiou, W.P. Chu, M.P. McCormick, C.R. Webster, ATMOS version 3 water vapor measurements: Comparisons with observations from two ER-2 Lyman-α hygrometers, MkIV, HALOE, SAGE II, MAS, and MLS. J. Geophys. Res. **107**, 4027 (2002). doi:10.1029/2001JD000587

M. Milz, T. von Clarmann, H. Fischer, N., Glatthor, U. Grabowski, M. Höpfner, S. Kellmann, M. Kiefer, A. Linden, G. Mengistu Tsidu, T. Steck, G.P. Stiller, B. Funke, M. López-Puertas, M.E. Koukouli, Water vapor distributions measured with the Michelson interferometer for passive atmospheric sounding on board Envisat (MIPAS/Envisat). J. Geophys. Res. **110**, 24307 (2005). doi:10.1029/2005JD005973

M. Milz, T.v. Clarmann, P. Bernath, C. Boone, S.A. Buehler, S. Chauhan, B. Deuber, D.G. Feist, B. Funke, N. Glatthor, U. Grabowski, A. Griesfeller, A. Haefele, M. Höpfner, N. Kämpfer, S. Kellmann, A. Linden, S. Müller, H. Nakajima, H., Oelhaf, E., Remsberg, S., Rohs, J. M., Russell III, C. Schiller, G.P. Stiller, T. Sugita, T. Tanaka, H. Vömel, K. Walker, G. Wetzel, T. Yokota, V. Yushkov, G. Zhang, Validation of water vapour profiles (version 13) retrieved by the

IMK/IAA scientific retrieval processor based on full resolution spectra measured by MIPAS on board Envisat. Atmos. Meas. Tech. Dis. **2**, 489–559 (2009)

R. Munro, C. Rodgers, Latitudinal and season variations of water vapour in the middle 173 atmosphere. Geophys. Res. Lett. 21, 661–664 (1994)

D. Murtagh, U. Frisk, F. Merino, M. Ridal, A. Jonsson, J. Stegman, G. Witt, P. Eriksson, C. Jiménez, G. M_egie, J. de La Noë, P. Ricaud, P. Baron, J. Pardo, A. Hauchecorne, E. Llewellyn, D. Degenstein, R. Gattinger, N. Lloyd, W. Evans, I. McDade, C. Haley, C. Sioris, von, C. Savigny, B. Solheim, J. McConnell, K. Strong, E. Richardson, G. Leppelmeier, E., Kyrölä, H., Auvinen, L., Oikarinen, An overview of the Odin atmospheric mission. Can. J. Phys. **80**, 309–319 (2002)

H. Nakajima, T. Sugita, T. Yokota, T. Ishigaki, Y. Mogi, N. Araki, K. Waragai, N. Kimura, T. Iwazawa, A. Kuze, J. Tanii, H. Kawasaki, M. Horikawa, T. Togami, N. Uemura, H. Kobayashi, Y. Sasano, Characteristics and performance of the Improved Limb Atmospheric Spectrometer-II (ILAS-II) on board the ADEOS-II satellite. J. Geophys. Res. **111**, 11 (2006). doi: 10.1029/2005JD006334

R. Nassar, P.F. Bernath, C.D. Boone, G.L. Manney, S.D. McLeod, C.P. Rinsland, R. Skelton, K.A. Walker, Stratospheric abundances of water and methane based on ACE-FTS measurements. Geophys. Res. Lett. **32**(L15S04) (2005). doi:10.1029/2005GL022383

R. Nassar, P.F. Bernath, C.D. Boone, A. Gettelman S.D. McLeod, C.P. Rinsland, Variability in HDO/H_2O abundance ratios in the tropical tropopause layer. J. Geophys. Res. **11**, 221305 (2007). doi:10.1029/2007JD008417

S. Noël, M. Buchwitz, H. Bovensmann, R. Hoogen, J. P. Burrows, Atmospheric water vapor amounts retrieved from GOME satellite data. Geophys. Res. Lett. **26**, 1841–1844 (1999). doi:10.1029/1999GL900437

S. Noël, M. Buchwitz, H. Bovensmann, J. Burrows, Validation of SCIAMACHY AMCDOAS water vapour columns. Atmos. Chem. Phys. **5**, 1835–1841 (2005)ISSN 1680-7316, http://www.atmos-chem-phys.net/5/1835/2005/

S. Noël, S. Mieruch, H. Bovensmann, J.P. Burrows, Preliminary results of GOME-2 water vapour retrievals and first applications in polar regions. Atmos. Chem. Phys. **8**, 1519–1529 (2008)

S. Noël, K. Bramstedt, A. Rozanov, H. Bovensmann, J. Burrows, Water vapour profiles from SCIAMACHY solar occultation measurements derived with an onion peeling approach. Atmos. Meas. Tech. 3, 523–535 (2010). doi:10.5194/amt-3-523-2010, http://www.atmos-meas-tech.net/3/523/2010/

D. Offermann, B. Schaeler, M. Riese, M. Langfermann, M. Jarisch, G. Eidmann, C. Schiller, H. Smit, W. Read, Water vapor at the tropopause during the CRISTA 2 mission. J. Geophys. Res. **107**, 8173 (2002). doi:10.1029/2001JD000700

W. Read, J. Waters, D. Wu, E. Stone, Z. Shippony, A. Smedley, C. Smallcomb, S. Oltmans, D. Kley, H. Smit, J. Mergenthaler, M. Karki, UARS microwave limb sounder upper tropospheric humidity measurement: Method and validation. J. Geophys. Res. 106, 32207–32258 (2001)

W. Read, D. Wu, J. Waters, H. Pumphrey, A new 147–56 hPa water vapor product from the UARS microwave limb sounder. J. Geophys. Res. 109 (2004). doi:10.1029/2003JD004366

W.G. Read, A. Lambert, J. Bacmeister, R.E. Cofield, L.E. Christensen, D.T. Cuddy, W.H. Daffer, B.J. Drouin, E. Fetzer, L. Froidevaux, R. Fuller, R. Herman, R.F. Jarnot, J.H. Jiang, Y.B. Jiang, K. Kelly, B.W. Knosp, L.J. Kovalenko, N.J. Livesey, H.-C. Liu, G.L. Manney, H.M. Pickett, H.C. Pumphrey, K.H. Rosenlof, X. Sabounchi, M.L. Santee, M.J. Schwartz, W.V. Snyder, P.C. Stek, H. Su, L.L. Takacs, R.P. Thurstans, H. Vömel, P.A. Wagner, J.W. Waters, C.R. Webster, E.M. Weinstock, D.L. Wu, Aura microwave limb sounder upper tropospheric and lower stratospheric H2O and relative humidity with respect to ice validation. J. Geophys. Res. **112**, 24 (2007). doi:10.1029/2007JD008752

A. Roche, J. Kumer, J. Mergenthaler, G. Ely, W. Uplinger, J. Potter, T. James, L. Sterritt, The cryogenic limb array etalon spectrometer (CLAES) on UARS: Experiment description and performance. J. Geophys. Res. **98**, 10763–10775 (1993)

A. Rozanov, S. Dhomse, V. Rozanov, H. Bovensmann, M. Weber, J. Burrows, First Retrievals of stratospheric water vapor content from SCIAMACHY limb measurements, manuscript in preparation (2009)

J. Russell-III, J. Gille, E. Remsberg, L. Gordley, P. Bailey, H. Fischer, A. Girard, S. Drayson, W. Evans, J. Harries, Validation of water vapor results measured by the limb infrared monitor of the stratosphere experiment on NIMBUS 7. J. Geophys. Res. **89**, 5115–5124 (1984)

J. Russell-III, L. Gordley, J. Park, S. Drayson, D. Hesketh, R. Cicerone, A. Tuck, J. Frederick, J. Harries, P. Crutzen, The halogen occultation experiment. J. Geophys. Res. 98, 10777–10797 (1993). doi:10.1029/93JD00799

J. Russell-III, M. Mlynczak, L. Gordley, J. Tansock, R. Esplin, *An overview of the SABER experiment and preliminary calibration results* (SPIE, 1999) pp. 277–288

J. Russell-III, S. Bailey, L. Gordley, D. Rusch, M. Horányi, M. Hervig, G. Thomas, C. Randall, D. Siskind, M. Stevens, M. Summers, M. Taylor, C. Englert, P. Espy, W. McClintock, A. Merkel, The aeronomy of ice in the mesosphere (AIM) mission: Overview and early science results. J. Atmos. Solar-Terr. Phys. **71**, 289–299 (2009). ISSN 1364-6826, doi:10.1016/j.jastp.2008.08.011, global Perspectives on the Aeronomy of the Summer Mesopause Region, 8th International Workshop on Layered Phenomena in the Mesopause Region

Y. Sasano, M. Suzuki, T. Yokota, H. Kanzawa, improved limb atmospheric spectrometer (ILAS) for stratospheric ozone layer measurements by solar occulation technique. Geophys. Res. Lett. **26**, 197–200 (1999). doi:10.1029/1998GL900276

B. Schaeler, D. Offermann, V. Kuell, M. Jarisch, H. Feldmann, A. Ebel, Regional and global trace gas distributions and inferred transports in the upper troposphere and lower stratosphere. J. Geophys. Res., 110 (2005). doi:10.1029/2004JD004994

B. Schaeler, D. Offermann, V. Kuell, M. Jarisch, Global water vapour distribution in the upper troposphere and lower stratosphere during CRISTA-2. Adv. Space Res. **43**, 65–73 (2009). doi: doi:10.1016/j.asr.2008.06.019

SMILES, *JEM/SMILES mission plan* (Tech. Rep., NASDA / CRL, version 2.1., 2002)

J. Susskind, C. Barnet, J. Blaisdell, Retrieval of atmospheric and surface parameters from AIRS/AMSU/HSB data in the presence of clouds. IEEE Trans. Geosci. Remote Sens. **41**, 390–409 (2003). doi:10.1109/TGRS.2002.808236

G. Taha, L. W. Thomason and Burton, S. P., 2004, Comparison of Stratospheric Aerosol and Gas Experiment (SAGE) II version 6.2 water vapor with balloon-borne and space-based instruments, J. Geophys. Res., 109, 18 313{+, doi:10.1029/2004JD004859.

F. Taylor, C. Rodgers, J. Whitney, S. Werret, J. Barnett, G. Peskett, P. Venters, J. Ballard, C. Palmer, R. Knight, P. Morris, Remote sensing of atmospheric structure and composition by pressure modulator radiometry from space: The ISAMS experiment on UARS. J. Geophys. Res. **98**, 10799–10814 (1993)

F. W., Taylor, 1987, Infrared remote sensing of the middle atmosphere from satellites: the Stratospheric and Mesospheric Sounder experiment 1978 - 1983, Surveys in Geophysics, 9, 123{148, doi:10.1007/BF01904119.

F.W. Taylor, J.J. Barnett, I. Colbeck, R.L. Jones, C.D. Rodgers, M.J. Wale, E.J. Williamson, Performance and early results from the stratospheric and mesospheric sounder (SAMS) on Nimbus 7. Adv. Space Re. 1, 261–265 (1981). ISSN 0273-1177, doi:DOI:10.1016/0273-1177(81) 90068-5

L.W. Thomason, S.P. Burton, N. Iyer, J.M. Zawodny, J. Anderson, A revised water vapor product for the stratospheric aerosol and gas experiment (SAGE) II version 6.2 data set. J. Geophys. Res. **109**, 6312 (2004). doi:10.1029/2003JD004465

J. Urban, Tropical ascent of lower stratospheric air analysed using measurements of the Odin Sub-Millimetre Radiometer, in Proceeding Reunion Island Int. Symp. Tropical Stratosphere—Upper Troposphere, 5–9 November 2007, St. Gilles, Reunion Island, France, ed. by H. Bencherif, Universitéde la Réunion (2008) pp. 29–34

J. Urban, P. Baron, N. Lautié, K. Dassas, N. Schneider, P. Ricaud, J. de La Noë, MOLIERE (v5): A versatile forward-and inversion model for the millimeter and sub-millimeter wavelength range. J. Quant. Spectrosc. Radiat. Transfer. **83**, 529–554 (2004)

J. Urban, N. Lautié, D. Murtagh, P. Eriksson, Y. Kasai, S. Loßow, E. Dupuy, J. de La Noë, U. Frisk, M. Olberg, E. Le Flochmoën, P. Ricaud, Global observations of middle atmosphericwater vapour by the Odin satellite: An overview, Planetary and Space Science, 55, 1093–1102 (2007). doi:10.1016/j.pss.2006.11.021, special issue 2nd General Assembly of Asia Oceania Geophysical Society (2005): Highlights in Planetary Science

T. von Clarmann, M. Höpfner, S. Kellmann, A. Linden, S. Chauhan, B. Funke, U. Grabowski, N. Glatthor, M. Kiefer, T. Schieferdecker, G.P. Stiller, S. Versick, Retrieval of temperature, H_2O, O_3, HNO_3, CH_4, N_2O, $ClONO_2$ and ClO from MIPAS reduced resolution nominal mode limb emission measurements. Atmos. Measure. Tech. **2**, 159–175 (2009). ISSN 1867-1381, http://www.atmos-meas-tech.net/2/159/2009/

J. Waters, *Microwave limb sounding*, chap. 8, Wiley Series in Remote Sensing, ed. M.A. Janssen, Atmospheric remote sensing by microwave radiometry (New York, 1993) ISBN 0–471-62891–3

J. Waters, L. Froidevaux, R. Harwood, R. Jarnot, H. Pickett, W. Read, P. Siegel, R. Cofield, M. Filipiak, D. Flower, J. Holden, G. Lau, N. Livesey, G. Manney, H. Pumphrey, M. Santee, D. Wu, D. Cuddy, R. Lay, M. Loo, V. Perun, M. Schwartz, P. Stek, R. Thurstans, M. Boyles, K. Chandra, M. Chavez, G.S. Chen, B. Chudasama, R. Dodge, R. Fuller, M. Girard, J. Jiang, Y. Jiang, B. Knosp, R. LaBelle, J. Lam, K. Lee, D. Miller, J. Oswald, N. Patel, D. Pukala, O. Quintero, D. Scaff, W. Van Snyder, M. Tope, P. Wagner, M. Walch, The earth observing system microwave limb sounder (EOS MLS) on the aura satellite, IEEE Trans. Geosci. Remote Sens. **44**, 1075 (2006)

M. Weber, SCIAMACHY H2O measurement capabilities, personal communication.(2009)

J. Wickert, T. Schmidt, G. Beyerle, G. Michalak, R. König, S. Heise, C. Reigber, , *GPS Radio Occultation with CHAMP and GRACE: Recent Results*, in Atmosphere and Climate, ed. by U. Foelsche, G. Kirchengast, A. Steiner, (Springer, Berlin, Heidelberg, 2006) pp. 3–16 ISBN 978–3-540- 34121–5, doi:10.1007/3–540-34121–8 1, URL http://dx.doi.org/10.1007/3–540-34121–8_1

J. Worden, S.S. Kulawik, M.W. Shephard, S.A. Clough, H. Worden, K. Bowman, A. Goldman, Predicted errors of tropospheric emission spectrometer nadir retrievals from spectral window selection. J. Geophys. Res. **109**, 9308 (2004). doi:10.1029/2004JD004522

J. Worden, K. Bowman, D. Noone, R. Beer, S. Clough, A. Eldering, B. Fisher, A. Goldman, M. Gunson, R. Herman, S.S. Kulawik, M. Lampel, M. Luo, G. Osterman, C. Rinsland, C. Rodgers, S. Sander, M. Shephard, H. Worden, , Tropospheric Emission Spectrometer observations of the tropospheric HDO/H2O ratio: Estimation approach and characterization. J. Geophys. Res. **111**, 16309 (2006). doi:10.1029/2005JD006606

J. Worden, D. Noone, K. Bowman, R. Beer, A. Eldering, B. Fisher, M. Gunson, A. Goldman, R. Herman, S.S. Kulawik, M. Lampel, G. Osterman, C. Rinsland, C. Rodgers, S. Sander, M. Shephard, C.R. Webster, H. Worden, Importance of rain evaporation and continental convection in the tropical water cycle. Nature. **445**, 528–532 (2007). doi:10.1038/nature05508

G.L. Zaragoza, M. López-Puertas, A. Lambert, J.J. Remedios, F.W. Taylor, Evidences of non-LTE emission in the ISAMS water vapour channels, Adv. Space Res. **22**, 1513–1516 (1998). doi:10.1016/S0273–1177(99)00016–2

Chapter 10
Combining and Merging Water Vapour Observations: A Multi-dimensional Perspective on Smoothing and Sampling Issues

Jean-Christopher Lambert, Coralie de Clercq and Thomas von Clarmann

10.1 Introduction

As detailed in previous chapters of this book, the atmospheric abundance of water vapour (H_2O) is monitored from the ground, balloons, aircrafts and satellites with a variety of measurement techniques, from *in situ* thin film capacitive sensing (Chap. 2) and frost point hygrometry (Chap. 3), through Lyman-α fluorescence hygrometry (Chap. 4), to emission and absorption remote sensing from the ground (Chaps. 5–7) and from satellites (Chap. 9) in the millimetric, infrared and visible spectral ranges. The comparison of satellite data against correlative measurements from the ground, aircrafts, balloons and other satellites, is a common practice of satellite validation (e.g. Russell III et al. 1984; Rind et al. 1993; Goss-Custard et al. 1996; Harries et al. 1996; Lahoz et al. 1996; Schwab et al. 1996; Wagner et al. 2003; Noël et al. 2005; Lumpe et al. 2006; Vömel et al. 2007; Carleer et al. 2008; Thomason et al. 2009; Milz et al. 2009 and many other references given in Chap. 11). The intercomparison of H_2O observations—from similar instruments as well as from different observational techniques—acquired during field measurement campaigns like ATMIS (England et al. 1992), TARFOX (Ferrare et al. 2000), LAPBIAT (Deuber et al. 2005), AWEX-G (Miloshevich et al. 2006) and MOHAVE (Leblanc et al. 2008), is also a well established method to reach a better understanding of atmospheric H_2O, of the real observational capabilities offered by each measurement technique, and of the respective error bars. Observations are also compared to modelling results for model evaluation purposes (e.g. Lahoz et al. 1993) and in data assimilation systems (Thornton et al. 2009, and references therein).

J.-C. Lambert (✉)
Belgian Institute for Space Aeronomy (IASB-BIRA),
Avenue Circulaire 3, B-1180 Brussels, Belgium
e-mail: j-c.lambert@aeronomy.be

C. de Clercq
IASB-BIRA, Belgian Institute for Space Aeronomy, Brussels, Belgium

T. von Clarmann
Karlsruhe Institute of Technology, IMK/KIT, Karlsruhe, Germany

N. Kämpfer (ed.), *Monitoring Atmospheric Water Vapour,*
ISSI Scientific Report Series 10,
DOI 10.1007/978-1-4614-3909-7_10, © Springer Science+Business Media, LLC 2013

Nevertheless, every measurement technique, every platform, every operation mode has its own perception of the atmospheric water vapour field in terms of sampling and averaging. Every technique also has its own error bars, uncertainties, and range of sensitivity. Relevant characteristics are summarised in the instrument fact sheets compiled in Appendix A of the same book. Where the water vapour field exhibits notable spatial patterns and temporal variability, differences in perception of these patterns and variability can impact significantly the comparison of two data sets. The fact is that water vapour is one of the atmospheric species with the most variable distribution in time and space. Various physical processes like evaporation and condensation, transport phenomena, chemical reactions and couplings make the water vapour concentration vary with altitude at scales from metres to tens of kilometres, horizontally at scales from metres up to hundreds of kilometres, and temporally at scales from minutes to decades.

Scales and ranges of atmospheric water vapour abundance to be addressed depend on the targeted scientific studies. They may require observations of the integrated vertical column, of partial columns, or of the vertical distribution of concentration from the ground up to the mesopause or over a specific altitude range like the Upper Troposphere/Lower Stratosphere (UT/LS) region. There may be requirements on the vertical, horizontal and temporal resolution and sampling. Studies may need individual profiles of excellent accuracy or rather zonal means with statistical significance, or regional averages of more complex structures linked to circulation patterns like, e.g., the polar vortex and the extra-tropical barriers. Targeted temporal signals to be measured may be long-term trends, special events, and temporal cycles on seasonal, day-to-day, diurnal and even hourly scales. But there is no single measurement technique or platform capable of addressing all atmospheric water vapour signals at all temporal and spatial scales of interest.

Fortunately, in several cases the individual capabilities of complementary measurement systems—covering, e.g., distinct altitude ranges, geographical areas or time periods—can be usefully enhanced by merging their data sets appropriately into a hybrid data set—covering, e.g., the union of the two distinct altitude ranges, geographical areas or time periods. In practice, depending on the final usage of the hybrid data set, data merging can be based on an optimisation with respect to the statistical representativeness of the data records, to their respective random errors, to their respective information content, to the smoothness of the derivative of the hybrid data product, on the minimisation of a cost function etc. The development of a global climatology of water vapour from global radiosonde network data by (Peixoto and Oort 1996) is an illustration of data merging of complementary measurements acquired by a network of similar but not identical measurement systems. The integrated use of network data enhances the monitoring capabilities of single stations, but the study by Peixoto and Oort points to issues of undersampling of large geographical areas, in addition to the classical data inhomogeneity issues inherent to ground networks. The ingestion of observations by a numerical weather prediction system and by a chemical data assimilation system (e.g. Swinbank and O'Neill 1994; Fisher and Lary 1995; Errera and Fonteyn 2001; Chipperfield et al. 2002;

Thornton et al. 2009) is a data merging technique extending the individual capabilities of measurement systems and of models. Modelling results are constrained by the assimilated observations, which improve global analyses and forecasts produced by the model. In return, the model fills in the gaps between satellite data acquired asynoptically along the orbit, to produce global synoptic fields. But a prerequisite for proper data assimilation is that the modelling results and the observations offer a mutually consistent perception of spatial patterns and temporal variability. A further family of applications assuming similar perception of the atmospheric field is the use of water vapour observations in conjunction with simultaneous observations of other species, e.g. methane and ozone, in order to study the hydrogen budget and its trends (e.g. Evans et al. 1998), changes in vertical transport and in troposphere-stratosphere exchanges, and the compacity of tracer-tracer correlations (e.g. Plumb and Ko 1992). Significant sampling and smoothing differences between water vapour data and other species might have a direct impact on the targeted correlations.

Positioned at the interface between retrieval specialists and data users interested in atmospheric water vapour measurements, this chapter intends to increase awareness to important data comparison and merging issues that should not be neglected for a species exhibiting so rapid changes and so intense gradients. Considering the wide spectrum of possible data comparison and merging studies, this chapter cannot be meant to provide a once-and-for-all solution to all smoothing and sampling problems, with unique mathematical formulation. The chapter starts with some generalities on the main uncertainties affecting atmospheric data retrievals and their combination. It goes on with illustrations based on Michelson Interferometer for Passive Atmospheric Sounding (MIPAS), a limb infrared emission profiler operating onboard ESA's Envisat satellite (Fischer et al. 2008). The material presented consists in an adaptation of results published in the existing literature as well as further developments.

10.2 Smoothing and Sampling Issues of Data Comparison

In his assessment of the error budget of temperature profile sounding by infrared spectroscopy, (Rodgers 1990) introduces to three independent error components: a random error due to measurement noise, an error term due to uncertainties on model parameters and inverse model, and the smoothing error term (formerly called null space error) which characterises the *a priori* content and finite resolution of the measurement. Rodgers describes the error terms as covariance matrices, rather than simple error variances. The first component, S_N, refers to the classical noise of metrology: any signal produced by a remote sensing instrument contains noise components associated with dark current, controller instabilities, thermic and acoustic constraints, electronic noise due to solar particles and magnetic fields in the space environment etc. The second term, S_M, associates uncertainties on forward model parameters (including radiative transfer modelling, field-of-view of the instrument, attitude of the satellite and related pointing errors, absorption cross-sections...) and

on inverse model parameters (e.g. the way intermediate quantities—representing the effects, when relevant, of clouds, of topography, of rotational Raman scattering, or of multiple scattering—are assembled to obtain the final H_2O data product). The smoothing error covariance, S_S, refers to the sensitivity of the retrieval to any *a priori* information or numerical constraint. This error, which accounts both for a possible bias between the retrieved and the true atmospheric state variables caused by the constraint used in the retrieval, and for the fact that the retrieval represents a smoothed picture of the true atmospheric state, is usually large at altitudes where the measurement is not sensitive to the true atmospheric state and the retrieval thus driven by any kind of *a priori* information. More details are given in (Rodgers 2000) and elsewhere in this book, e.g. in Sect. 5.5 of Chap. 5 on microwave measurements.

Within linear theory, the covariance matrix associated with smoothing error can be written as:

$$\mathbf{S}_S = \mathbf{A}\mathbf{S}_A\mathbf{A}^T \tag{10.1}$$

where $\mathbf{A}$ is the averaging kernel matrix and $\mathbf{S}_A$ the covariance matrix representing atmospheric variability. The averaging kernel matrix is defined as the product of two Jacobian matrices: the weighting function matrix $\mathbf{K}$ (Jacobian of the forward model), which represents the sensitivity of the measurement to the real atmospheric profile, is multiplied by the gain matrix $\mathbf{G}$ (Jacobian of the inverse model), which represents the sensitivity of the retrieval to the radiance measurement. The smoothing error depends, according to this definition, on both measurement and retrieval properties and, according to Eq. 10.1 also on atmospheric variability. These three contributions should be considered together for a proper interpretation of individual atmospheric water vapour observations, for a sound combination of complementary data, and for an accurate assessment of error bars.

The concepts and formalism adopted by (Rodgers 1990) for the characterisation of vertical profile retrieval from infrared measurements were adapted later for the quantitative comparison of two infrared remote sensors (Rodgers and Connor 2003). Virtually, these error concepts and mathematical formalism can be further extended to the comparison of not only any remotely sensed data, but also *in situ* measurements, and even modelling results. While the concept of averaging kernels and smoothing errors hold in any dimension, e.g. in the horizontal and temporal domains, it is usually applied only to the vertical domain. To be complete, the error budget of a data comparison or merging must also include uncertainties due to the non-perfect co-location of the measurements to be combined (Rodgers' studies assume perfect temporal and geographical coincidence of the measurements). (von Clarmann 2006) has established the formal equivalence of errors due to less than perfect coincidence and the smoothing error, and a formalism has been proposed to tackle both within one unified formalism.

Tentatively, we can list the following generic contributions to the error budget of a data comparison:

1. errors due to measurement noise of the individual measurement systems: $\mathbf{S}_{1N}$ and $\mathbf{S}_{2N}$

2. uncertainties associated with the forward and inverse models and parameters: $\mathbf{S}_{1M}$ and $\mathbf{S}_{2M}$
3. comparison errors due to differences in smoothing of atmospheric variability:
   - vertical smoothing:

$$\mathbf{S}_{SV} = (\mathbf{A}_{1V} - \mathbf{A}_{2V})\mathbf{S}_V(\mathbf{A}_{1V} - \mathbf{A}_{2V})^T \tag{10.2}$$

   - horizontal smoothing:

$$\mathbf{S}_{SH} = (\mathbf{A}_{1H} - \mathbf{A}_{2H})\mathbf{S}_H(\mathbf{A}_{1H} - \mathbf{A}_{2H})^T \tag{10.3}$$

   - temporal smoothing:

$$\mathbf{S}_{St} = (\mathbf{A}_{1t} - \mathbf{A}_{2t})\mathbf{S}_t(\mathbf{A}_{1t} - \mathbf{A}_{2t})^T \tag{10.4}$$

4. comparison errors due to differences in sampling of atmospheric structures, often called errors due to vertical/horizontal/temporal mismatch:
   - vertical sampling: $\mathbf{S}_{dH_2O/dz}$
   - horizontal sampling: $\mathbf{S}_{dH_2O/dH}$
   - temporal sampling: $\mathbf{S}_{dH_2O/dt}$

where:

$\mathbf{A}_{ij}$ = vertical (j = V), horizontal (j = H) and temporal (j = t) averaging kernels of system i; while the vertical and horizontal components of the $\mathbf{A}$ are evaluated together in one step, we present them here separately for reasons of clarity;
$\mathbf{S}_V$, $\mathbf{S}_H$ and $\mathbf{S}_t$ = vertical, horizontal and temporal covariance of atmospheric variability;
$\mathbf{S}_{dH_2O/dz}$, $\mathbf{S}_{dH_2O/dH}$ and $\mathbf{S}_{dH_2O/dt}$ = errors due to differences in sampling of the structured and variable water vapour field, i.e. vertical, geographical and temporal mismatches, assuming that the four coordinates are independent. If these errors are dependent another statistical formulation is needed.

The discussion of measurement errors and retrieval errors associated with each individual measurement system is out of scope of this general chapter. Detailed quality information for each measurement technique addressed in this book is described in Chaps. 1–6, and estimates of bias, precision, stability and other data quality indicators are summarised in the corresponding technique and instrument fact sheets provided in Appendix A. The correct way to calculate the total error from the various contributions depends on the data manipulations performed to compare the data or to obtain the merged data set, and on the possible existence of correlations between the data sets. E.g., if the two measurement systems have common error sources, associated covariances may not be just summed up, but should be combined e.g. according to Eq. 14 in (von Clarmann 2006). This section introduces to error concepts which relate to differences in smoothing and sampling of atmospheric variability and gradients, in the general context of data comparison and data merging. In support, smoothing and sampling properties inherent to each measurement technique are also

provided in the corresponding technique and instrument fact sheets of Appendix A. For clarity, smoothing errors are discussed here separately for each dimension. Consideration of, e.g., vertical and horizontal smoothing in one step on the basis of 2-dimensional averaging kernels (c.f. von Clarmann et al. 2009a) allows to include their mutual influence.

10.2.1 Smoothing Issues

10.2.1.1 Differences in Vertical Smoothing

Three error contributions relate to uncertainties arising from differences in smoothing of the atmospheric structures and variability. During the early developments of remote sensing in the 1960s, weighting functions, gain matrices and averaging kernels had already been used in geological remote sensing (Backus and Gilbert 1967, 1968, 1970) and in atmospheric remote sensing (e.g. Conrath 1969; Twomey 1974; Rodgers 1976; Aruga and Igarashi 1976) to characterise vertical information content and discuss vertical resolution issues. Several decades later, vertical averaging kernels associated with a profile or column retrieval are widely used as diagnostics of information content aspects, like measurement sensitivity as a function of altitude, the number of independent pieces (partial columns) of information, and vertical resolution. (Rodgers 2000) shows how the algebraic analyse of averaging kernels can help determining such quantities.

What is more rarely done—or more rarely published—is the quantitative assessment of the vertical smoothing error associated with the retrieval. For Optimal Estimation retrievals, this error can be inferred considering the approximation given in (Rodgers 1990, 2000) on the relation between the retrieved quantity $\mathbf{X}'$, the true profile $\mathbf{X}$, the averaging kernel matrix $\mathbf{A}_V$, the *a priori* profile $\mathbf{X}_A$ used in the retrieval, and the sum of the measurement and retrieval errors ϵ_x:

$$\mathbf{X}' = \mathbf{X}_A + \mathbf{A}_V(\mathbf{X} - \mathbf{X}_A) + \epsilon_x \tag{10.5}$$

In an ideal case with noise-free measurements, the vertical smoothing error can be calculated as the difference between the result of this equation ($\mathbf{X}'$) and the true profile ($\mathbf{X}$), thus:

$$\epsilon_{smoothing} = \mathbf{X}_A - \mathbf{X} + \mathbf{A}_V(\mathbf{X} - \mathbf{X}_A) \tag{10.6}$$

and the associated covariance matrix can be written as (Rodgers 2000):

$$\mathbf{S}_S = (\mathbf{I} - \mathbf{A}_V)^T \mathbf{S}_V (\mathbf{I} - \mathbf{A}_V) \tag{10.7}$$

The covariance matrix associated with the smoothing error can be calculated on the basis of $\mathbf{A}_V$ and $\mathbf{S}_V$, two quantities associated with the retrieval. Using Eq. 10.6 the smoothing error can be evaluated also on the basis of independent water vapour

profile measurements. In practice, $\mathbf{X}$ is unknown, but the vertical smoothing error can be estimated by substituting in Eq. 10.6 a correlative profile $\mathbf{X}_{CORR}$ that has been measured at much higher resolution, so that its own vertical smoothing error can be neglected. For water vapour retrievals with moderate and large vertical smoothing (from satellites and from ground-based FTIR spectrometers and microwave radiometers), appropriate X_{CORR} candidates are correlative profile data measured by balloon- and air-borne in situ instruments and by lidar. An alternative is to use water vapour profile data produced by chemical-transport models or data assimilation systems. This possibility will be illustrated later in the example section on MIPAS.

An obvious prerequisite for this estimation of the vertical smoothing error via Eq. 10.5 and 10.6 is the availability of the averaging kernels and of the *a priori* associated with the retrieval. This availability becomes the rule for ground-based microwave and FTIR instruments associated with networks like the Network for the Detection of Atmospheric Composition Change (NDACC), but there is currently no standard for satellite data. Full retrieval information is provided routinely in the best cases only, mainly with current satellites. In the worst cases, including most historical satellites, no averaging kernels were evaluated at the time of the retrieval and it is likely that they will never be available. In other cases, partial information can be available. E.g., with the MIPAS scientific data processors operated at IMK, proxies such as the altitude resolution vector or the diagonal elements of the averaging kernels are routinely provided, while averaging kernels associated with individual profile retrievals are occasionally made available on request (von Clarmann et al. 2009b). It also happens that a set of generic averaging kernels calculated independently from operational retrievals are available to users. That was the case for MIPAS H_2O profile retrievals with the near-real-time processor, for which averaging kernels calculated for four seasons (January, April, July and October) and six latitude zones (90–65°, 65–20° and 20–0° in both hemispheres) are available to the data users via a technical note (Ceccherini and Ridolfi 2002).

To compare and merge profile data meaningfully, errors associated with differences in vertical smoothing of the atmospheric profile have to be estimated and, if needed, taken into account. A method for reducing such errors in profile data comparisons was proposed by (Rodgers and Connor 2003). Full application of this method requires access to the averaging kernels and error covariances, not always available as explained above, and the use of forward and retrieval models to simulate the retrieval of one instrument using the retrieval of the other. Although successful, this rigorous method is not always applicable in its entirety and approximations and other practices are commonly used instead. Technical difficulties may also arise when the two data sets to be compared are not provided on a common altitude or pressure grid, which is the general case. Appropriate re-gridding of data characterised by large smoothing properties has been proposed by (Calisesi et al. 2005).

According to Eq. 10.2, two data sets which smooth differently a highly structured and variable atmospheric profile — thus a large difference $(\mathbf{A}_{1V} - \mathbf{A}_{2V})$, cannot be compared as they are, otherwise the profile-to-profile difference will be dominated by a large term $(\mathbf{A}_{1V} - \mathbf{A}_{2V})\mathbf{S}_V(\mathbf{A}_{1V} - \mathbf{A}_{2V})^T$. To minimize this term as much as possible, one common practice consists in smoothing the high resolution data set

$\mathbf{X}_2$, down to the low resolution of data set $\mathbf{X}_1$. This can be achieved by modification of Eq. 10.5:

$$\mathbf{X}_2\_degraded = \mathbf{X}_A + \mathbf{A}_{V1}(\mathbf{X}_2 - \mathbf{X}_A) \tag{10.8}$$

For retrievals of $\mathbf{X}_1$ not involving any explicit a priori profile $\mathbf{X}_A$, this equation simplifies to a convolution of the high resolution profile $\mathbf{X}_2$ with the averaging kernel matrix of the low resolution profile $\mathbf{X}_1$. The result of this operation is the measurement of the high resolution instrument as the low resolution instrument would have seen it. Subsequently, $(\mathbf{A}_{1V} - \mathbf{A}_{2V})$ in Eq. 10.2 becomes null and differences in vertical smoothing do not contribute anymore to the profile-to-profile difference.

Another option to remove from the artificial components of the profile-to-profile difference caused by *a priori* information, is to resample both profiles on a common altitude grid coarse enough to allow complete removal of the formal *a priori* information even from the coarser resolved retrieval, as proposed by (von Clarmann and Grabowski 2007). Since resampling on the coarse grid alone does not remove the *a priori* information, resampling and re-regularisation have to be performed in one step, where the new regularisation has to provide a profile which can be resampled on the coarse grid without any loss of information.

When averaging kernels of the highly smoothed retrieval $\mathbf{X}_1$ are not available, a compromise often used consists in smoothing the high resolution data $\mathbf{X}_2$ with a generic function offering a similar bandwidth, e.g. a Gaussian or sine shape with same Full Width Half Maximum (FWHM) or same Backus-Gilbert spread. Smoothing with a boxcar function is sometimes used for the comparison of partial columns, e.g. to validate the tropospheric column of water vapour retrieved from nadir satellite measurements by means of radiosonde profile data. If well calibrated on the characteristics of the two measurement systems, this kind of generic smoothing can reduce the term $(\mathbf{A}_{1V} - \mathbf{A}_{2V})\mathbf{S}_V(\mathbf{A}_{1V} - \mathbf{A}_{2V})^T$ adequately. This option is also used as a test by users who fear that degrading the high resolution profile $\mathbf{X}_2$ with the averaging kernel matrix $\mathbf{A}_{1V}$ and *a priori* profile $\mathbf{X}_A$ might corrupt the independency of $\mathbf{X}_2$ and introduce additional errors, arguing that $\mathbf{A}_{1V}$ is not a measured quantity but it is evaluated on the basis of forward and inverse models of $\mathbf{X}_1$. To avoid misinterpretation of the comparison results after such an operation, it must be kept in mind that the rationale of degrading the high resolution data set $\mathbf{X}_2$ is to remove comparison errors due to differences in smoothing. The agreement between $\mathbf{X}_1$ and $\mathbf{X}_2$ may have improved thanks to the prior degradation of $\mathbf{X}_2$, but the vertical smoothing error of $\mathbf{X}_1$ has obviously not disappeared from the data product that will be provided to users. This error must be evaluated and documented appropriately. In addition to reading this documentation, the user is always advised to verify the fitness of the data for his purposes. E.g., if he intends to use as it is a tropospheric column data product characterised by wide and asymmetric averaging kernels, he might wish to compare this data product with accurate tropospheric column measurements directly, without using averaging kernels, and see if the intended use of the data is hampered as a consequence of the wide and asymmetric smoothing, in which case another kind of use should be envisaged.

10.2.1.2 Differences in Horizontal Smoothing

The literature offers several examples of studies caring for the problem of horizontal resolution and smoothing of the retrieved information. For example, (Roscoe and Pyle 1987) discuss the consequences of photochemical changes of NO, NO_2, OH and ClO concentration along the optical path of a solar occultation measurement; (Swartz et al. 2006) study line-of-sight ozone column density measured by an airborne spectrometer and the effects of horizontal inhomogeneity; (von Clarmann et al. 2009a) calculate 2D averaging kernels for the MIPAS satellite limb sounder in order to discuss its horizontal resolution and potential horizontal undersampling effects; they apply this method to constrained profile retrievals and find the horizontal resolution depending also on the constraint applied in the vertical domain; the validation of ozone (Cortesi et al. 2007) and temperature (Ridolfi et al. 2007) profile data from MIPAS with ozonesonde and lidar data proposes an assessment of the comparison uncertainties due to differences in horizontal smoothing of atmospheric patterns. The finite horizontal resolution inherent to limb remote sounding constitutes the background for two-dimensional tomographic retrievals, e.g. of temperature from EOS MLS, MIPAS and PREMIER emission measurements (Livesey and Read 2000; Steck et al. 2005; Ungermann et al. 2009). Nevertheless, consideration of horizontal smearing remains atypical and has not been given yet the same attention as that given to vertical smoothing issues. As in the vertical direction, any smoothing of horizontal variability can generate the horizontal smoothing error. Its expression can be formalised as in Eq. 10.3. Unfortunately this is only in exceptional cases that horizontal averaging kernels associated with are known. The horizontal smoothing error depends on the existence of atmospheric inhomogeneities and gradients with finer structures than the ones resolved by the instrument. In consequence the largest errors on water vapour data might be expected in the troposphere. This error is also inherent to both the measurement system and the retrieval scheme and cannot be dissociated from their combination. It is worth noting that horizontal smoothing can be inherent to the observation geometry (e.g. limb measurements integrate atmospheric information along optical paths of several hundred kilometres), but also to a combination of the observation sequence and atmospheric effects (e.g. the integration of individual observations over hours with a view to increase signal-to-noise ratio, interacts with atmospheric transport to produce horizontal smoothing along air trajectories).

As in the vertical direction, the comparison of two data sets can be hampered if they offer significantly different resolutions and horizontal smoothing. In the case of atmospheres horizontally homogeneous at the scale of the air mass probed by the instruments, neglecting the actual difference in resolution leads to sub-optimal collocation criteria for validation and under-constraining observation operators for data assimilation. Where inhomogeneities of the atmosphere occur at scales comparable with the horizontal resolution of at least one of the two instruments, neglecting the difference in horizontal smoothing of atmospheric homogeneities adds, to the individual measurement and retrieval errors characterising each data set, discrepancies due to the differences in horizontal smoothing. In cases of large atmospheric inhomogeneities, the comparison error due to smoothing differences can even exceed the individual error bars of each data set and make meaningless the bias and scatter derived from the comparison.

10.2.1.3 Differences in Temporal Smoothing

There is to our knowledge no study focusing on temporal smoothing issues, but rather *ad hoc* consideration of possible effects. The attention given to temporal smoothing differences depends greatly on the species and the common practices in application in the community. For ozone in the troposphere and stratosphere, the literature often neglects differences in temporal smoothing: e.g., satellite measurements acquired within a few seconds of integration are commonly compared with daily means of the ozone measurements acquired several times a day by ground-based instruments. The result is not always as noisy and biased as we would have suspected: provided that the winds transport ozone approximately throughout the air mass actually probed by the satellite, the integration of ground-based ozone values along the day, thus across the satellite air mass, compensates for the difference in horizontal smoothing between the satellite and the ground-based instrument. The efficiency of this compensation will depend drastically on the respective patterns of winds and of the actual air mass probed by the satellite. For example, if we assume that stratospheric ozone is controlled at first order by zonal transport, air masses probed by solar occultation in the east-west direction will enable better compensation than limb sounding along the north-south trajectory of polar orbiting satellites. Such considerations might also apply to water vapour in the middle and high stratosphere—sufficiently far away from the polar vortex border—where its distribution reflects at first order the distribution of CH_4, its main source, that is, an altitude-latitude structure with zonal symmetry with H_2O increasing upwards and polewards from its tropical minimum near 40 hPa (Rind et al. 1993; Chiou et al. 1993; Mote et al. 1993; Carr et al. 1995; Elson et al. 1996).

For species exhibiting faster and larger changes than ozone, like water vapour, data analysis usually starts with the definition of stringent co-location criteria in time which, at the same time they reduce temporal mismatches, reduce differences in temporal sampling. This approach is the one usually adopted for comparisons of atmospheric water vapour data in the troposphere and the lower stratosphere, where transport, chemistry and other phenomena make the distribution and variability of this species more complex than in the upper stratosphere.

Sometimes temporal smoothing effects can be hidden, for example, in the aforementioned study of solar occultation measurements by (Roscoe and Pyle 1987): solar local time changes along the long optical path of the measurement, producing photochemical changes of the concentration of several species (NO, NO_2, OH and ClO), and in that case horizontal smoothing may be considered as equivalent to temporal smoothing of diurnal cycle effects. For atmospheric water vapour, there is no diurnal cycle of photochemical origin to date. This example of hidden temporal smoothing might apply only in the mesosphere, where atmospheric tides introduces a diurnal cycle resulting in horizontal variations of the H_2O concentration, but the amplitude of this effect has not been estimated yet. At lower altitudes there are many other sources of temporal variability, occurring or not at diurnal frequencies, like evaporation and condensation, transport phenomena, and chemical reactions.

10.2.2 Sampling Issues

As opposed to smoothing issues, which rely on specialised concepts such as information content and averaging kernels, sampling issues should be easier to identify and address by the widest community since they rely more on common sense. The principle is quite simple: atmospheric structures and cycles should be sampled at least at Nyquist rate (Nyquist 1928). The Nyquist rate is the minimum sampling rate required to avoid aliasing, equal to twice the highest frequency contained within the signal. This principle applies to temporal, geographical and vertical signals without any distinction. In practice, we will see hereafter that one has only limited action on the temporal, geographical and vertical sampling rates. Owing to the extremely wide range of frequencies contained in water vapour signals below the hygropause, low-pass filtering is often used to limit the Nyquist rate to the signal targeted by the intended study, e.g. at daily, monthly or decadal scales. It has to be noted that the smoothing characteristics of a measurements system acts as an inherent low-pass filter with certain anti-aliasing characteristics. E.g., the horizontal smearing of MIPAS of several hundreds of kilometres prevents aliasing of phenomena of smaller scale.

10.2.2.1 Sampling Characteristics of Water Vapour Observations

Sampling characteristics of a measurement system for atmospheric water vapour are determined by the measurement method (response time of the Cryogenic Frost point Hygrometer (CFH), limb scanning sequence optimised for signal-to-noise ratio . . .) and the properties of the platform (type of orbit, standard balloon launch time, network configuration . . .) Every measurement system offers well defined sampling capabilities out of which aliasing and other sampling errors will affect its data. Figure 10.1 shows the geographical coverage of the global radiosonde network stations which delivered humidity measurements to the Integrated Global Radiosonde Data Archive in 2003 (graph courtesy NOAA/NESDIS). The activity of a station varies from year to another and the actual geographical sampling offered by the network is in constant evolution. Despite this evolution, the geographical sampling is always biased towards Northern Hemisphere and towards lands and coasts. The undersampling of high-frequency tropospheric features over oceans and in the Southern Hemisphere is evident. It is likely that the network misses a list of atmospheric states and that zonal averages might be biased. Undersampling of the troposphere by networks of CFH sonde stations and ground-based lidars and FTIRs is even worse. Regarding temporal sampling, most of stations launch radiosondes twice daily at times close to 00 and 12 UT. Some stations provide observations more frequently, others only once per day. The actual sampling of the global water vapour field by the radiosonde network and the corresponding sampling errors can have implications for numerical weather prediction (Garand et al. 1992) and for climate studies (Elliott and McGaffen 1991) relying on network data. Such considerations add to issues of station-to-station inhomogeneity that should be taken into account when making integrated use of network data (e.g. Lait 2002b; Thompson et al. 2007).

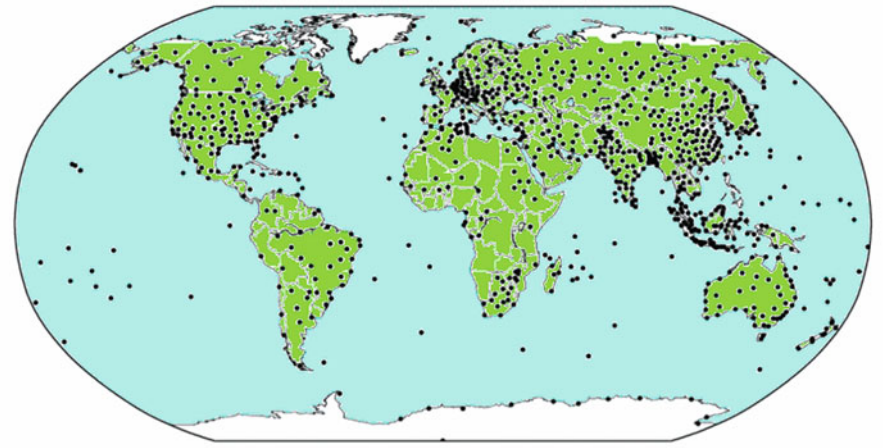

Fig. 10.1 Geographical sampling of WMO's global radiosonde network (courtesy NOAA/NESDIS)

Ground-based remote sensing (lidar, FTIR, microwave radiometer) can operate at higher temporal frequencies, of the order of several measurements a hour. Actual sampling rate reported in data archives is nevertheless lower and with periods of interruption, due to the presence of clouds (FTIR and lidar operation requires clear skies) and instrumental issues.

Satellites are often proposed as the solution for global sampling of the atmosphere within short time periods. Global sampling every 6 h can indeed be reached through coordinated satellite constellations like the Joint Polar-orbiting Operational Satellite System, which currently consists of the MetOp morning satellite operated by the EUMETSAT and the afternoon satellite operated by NOAA. Twice daily sampling can be achieved with single flying nadir-viewing and limb-scanning satellites measuring emissions of water vapour. With nadir-viewing satellites measuring backscatter sunlight in the visible spectral range, and with instruments measuring visible stellar occultation, sampling is already limited to sunlit part of the globe and to its night-time part, respectively. The poorest latitude/time sampling characterises solar occultation instruments, as illustrated in Fig. 10.2.

This figure presents the latitude/time sampling, as achieved by three solar occultation satellites having measured water vapour in the stratosphere until 2005. The occurrence of solar occultation events along the satellite trajectory, and in particular the latitude range over which solar occultation will occur, is determined directly by the inclination of the orbit. SAGE-II and HALOE operated aboard the ERBS (launched in 1984) and UARS (launched in 1991) platforms, respectively, both on a 57° inclination orbit. POAM-III operated aboard SPOT-4 (launched in 1998), on a quasi-polar sun-synchronous orbit (98.8° inclination). Other parameters influencing the precession of the satellite and its attitude (e.g., an in-flight yaw manoeuvre changed the attitude of UARS every 36 days to enable sounding of both hemispheres

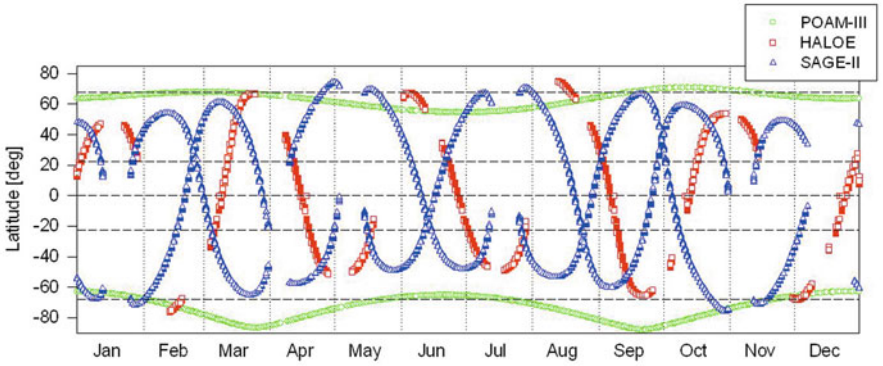

Fig. 10.2 Latitude-time sampling of the stratosphere by three solar occultation instruments: POAM-III (polar orbit), HALOE (57° inclination orbit) and SAGE-II (57° inclination orbit)

and also to avoid sunlight striking some of the instruments) superimpose their effects to produce the actual latitude/time coverage. They explain the difference between the SAGE-II and HALOE sampling despite the fact that ERBS and UARS orbits have the same inclination.

As already remarked for the radiosonde network, depending on the temporal and geographical frequencies of interest, sampling errors might affect or not the use of individual solar occultation data sets. For example, we have already mentioned the potential bias of zonal averages constructed on data sets with undersampled frequencies and with unrepresented atmospheric states. Different techniques have been developed to fill in geographical gaps and to reconstruct global fields from asynoptic observations acquired in the stratosphere by satellites, aircrafts, balloons and ground-based sensors. Among them, we may cite quasi-conservative coordinate (Schoeberl et al. 1989; Lait et al. 2002a) trajectory-mapping (Morris et al. 2000), trajectory-hunting (Danilin et al. 2002a, b), Lagrangian mapping MATCH (Rex et al. 1999), and statistical techniques (Sparling 2000; Neu et al. 2003). Together with recent studies (e.g. Henne et al. 2010) exploring the concepts of point-to-area representativeness (Nappo et al. 1982) and of catching area (Larssen et al. 1999) in the framework of air pollution monitoring and assessments, they offer interesting perspectives in evaluating the representativeness and completeness of a data set, in comparing the representativeness of two data sets, and in identifying methods to reduce combination errors due to differences in sampling and smoothing.

10.2.2.2 Effects of the Differences in Sampling

The global combination of two data sets obtained at different sampling rates can be subject to errors due to the difference in sampling of atmospheric structures and variability. For example, Fig. 10.2 recommends some caution when combining solar occultation data from different satellites, and comparing Fig. 10.1 and 10.2

recommends some caution when combining network data with solar occultation data. A serious but not uncommon situation is when sampling errors from one and the other system compensate each other.

Looking at the more regional scale in the framework of a data comparison, differences in spatial and temporal sampling lead to the classical temporal and spatial co-location mismatches which, in presence of variability and gradient, can enhance the total error of the data comparison. Usually the co-location error term is a function of the total differential of the water vapour field between the two measurements being compared:

$$\epsilon_{co-location} = f\left[\frac{\partial H_2O}{\partial z}dz + \frac{\partial H_2O}{\partial H}dH + \frac{\partial H_2O}{\partial t}dt\right] \tag{10.9}$$

Assuming that there are no differences in smoothing between the two measurement systems, data sets are usually selected on the basis of more or less stringent co-location criteria expected to limit co-location errors under the error bars of the individual measurements. In practice, co-location criteria can not be as stringent as desirable if we want to obtain a statistically significant amount of comparison pairs. The reason for this compromise often comes from sampling differences. We had already mentioned the difference in temporal smoothing and sampling in the previous section, a difference that can only rarely be controlled since directly linked to the measurement techniques. Geographical sampling issues are illustrated in Fig. 10.3, which shows the actual sampling of the stratospheric water vapour field at the 121 hPa pressure level, achieved in one month by MIPAS (January 2003) in a radius of 500 km around the NDACC station of Reunion Island in the Indian Ocean. It appears clearly that MIPAS data are acquired on predefined latitude circles, with the consequence that the distance in latitude between MIPAS and the station can not go under a minimum value. The latter ranges from zero for stations located on MIPAS latitude circles, through about 50 km at Reunion Island, to 250 km for stations just half way between two latitude circles of MIPAS measurements. In the absence of large and permanent gradients, the sampling difference generates in the comparisons some noise that can be reduced statistically by comparing numerous pairs of data. In cases of large, permanent gradients, like in the example given in Fig. 10.3 for a station at the border of the inter-tropical convergence zone, this distance generates a bias between the two systems, which can not be eliminated by performing comparisons on a large amount of data, and which might well be attributed erroneously to one of the two measurement systems if the sampling difference is ignored.

Sampling issues can also affect the vertical dimension. The simplest and most common issue relates to the difference in altitude/pressure grids on which data are provided. Regridding is usually required prior to any data manipulation, from simple data comparisons in the original VMR/pressure space, to more sophisticated comparisons involving the simulation of the retrieval of one instrument using the retrieval of the other (Rodgers and Connor 2003). But regridding of data exhibiting large smoothing properties can impact on the comparison results if differences in vertical smoothing are not taken into account properly (Calisesi et al. 2005).

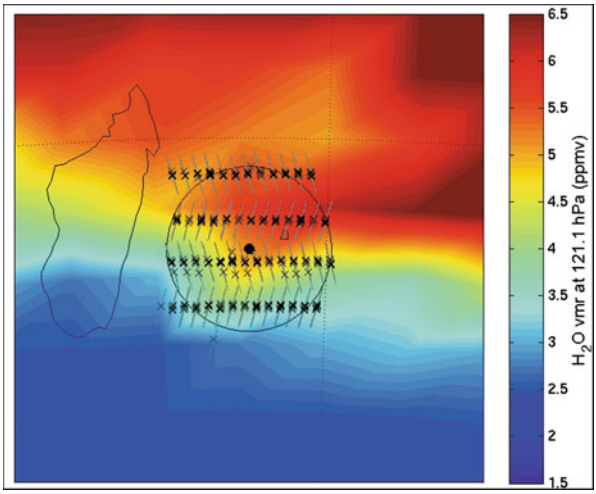

Fig. 10.3 Sampling by MIPAS of the stratospheric water vapour field at the 121 hPa level, in a radius of 500 km around the NDACC station of La Réunion (Indian Ocean, 21° S, 55° E), achieved after one month of measurements in January 2003. The large island on the left is Madagascar. Crosses and tilted lines represent, respectively, the tangent points at 121 hPa and the corresponding 95 % spread of the retrieved information. *Grey lines* rising to the *left* and to the *right* represent late evening and early morning overpasses, respectively. (Assimilated H_2O field: Q. Errera and the BASCOE team at BIRA-IASB)

Among other vertical sampling issues we may cite vertical co-location errors due to limb/occultation pointing uncertainties and tangent height registration errors. Depending on the measurement system, altitude assignment errors may appear in comparisons in the form of discrepancy varying monotonically with altitude. In such cases, they can be identified by cross-correlation of the satellite and the correlative profile (De Clercq et al. 2004). But uncertainties in the tangent altitude and/or tangent pressure can also propagate on the retrieved water vapour mixing ratios. In cases when the tangent pressure is retrieved but not the absolute tangent altitude, as with MIPAS (Ridolfi et al. 2000), it is advisable to use pressure coordinates instead of geometric coordinates as to minimise related mismatch.

Vertical co-location errors arise also from the bias between the altitude of the retrieval and the centroid (or barycentre) of the true information content (Backus and Gilbert 1967, 1970). The latter error affects mainly nadir remote sensing data with poor resolution and largely asymmetric averaging kernels. It reflects the large spread of the retrieved data and ideally it is already accounted for when the comparison uses somehow the averaging kernels to reduce vertical smoothing errors.

Again, one may cite different studies using statistical and transport modelling tools (Nappo et al. 1982; Schoeberl et al. 1989; Larssen et al. 1999; Morris et al. 2000; Danilin et al. 2002b, Sparling 2000; Neu et al. 2003; Henne et al. 2010), building on the concepts of point-to-area representativeness and of catching area, which offer interesting perspectives in evaluating combination errors due to differences in sampling.

10.3 Illustrations with MIPAS H_2O Profile Data

In this section we propose practical illustrations of the above considerations, based on the MIPAS limb infrared emission satellite profiler (Fischer and Oelhaf 1996; Fischer et al. 2008), onboard Envisat since 2002:

- Description of horizontal smoothing properties of MIPAS water vapour profile data retrieved operationally by ESA's off-line Instrument Processing Facility (IPF) version 4.61.
- Potential effects of the MIPAS smoothing properties on aeronomic use of water vapour data.
- Comparative study of the errors contributing potentially to the discrepancy between MIPAS water vapour data and correlative profile observations acquired at higher horizontal resolution (by sondes, airborne *in situ* sensors and lidars).
- Comparative study of the errors contributing potentially to the discrepancy between MIPAS water vapour data and correlative partial column observations acquired at higher horizontal resolution (by FTIR spectrometers and microwave radiometers).

10.3.1 Smoothing Properties of MIPAS H_2O Profile Data

Smoothing properties of a remote sensing system can be described by the actual location of the centroid (or barycentre) of the retrieved information and the spread of this retrieved information around this centroid (Backus and Gilbert 1970). Practically, the horizontal resolution and the space/time sampling achievable by MIPAS are determined jointly by properties of the scanning sequence, of the instrument (e.g., the field of view), of the orbit, and by a combination of radiative processes, including competing emissions and absorptions, which occur along optical paths of several hundred kilometres. It might happen that the centroid (or barycentre) of the retrieved information differ from the tangent point by hundreds of kilometres, and that the retrieved information spreads significantly around the centroid, moreover in preferred directions determined by the limb scanning sequence and by instrumental and orbital properties. We will explore this possibility hereafter.

The MIPAS instrument is a high resolution Fourier Transform Spectrometer designed to measure limb emission spectra in the middle and upper atmosphere. Four spectral channels cover the middle infrared spectral range from 650 to 2400 cm^{-1} at about 0.025 cm^{-1} spectral resolution in its original full resolution mode operational by 2004, allowing the detection of a bouquet of atmospheric species including water vapour (Milz et al. 2009), ozone (O_3), nitrogen oxides (NO, NO_2, N_2O_5), source gases (CH_4, N_2O, CO), nitrogen and chlorine reservoirs ($ClONO_2$, PAN, HNO_3...), and CFCs. The instrument operates aboard Envisat, a polar platform (orbit inclination of 98.6°) flying at a mean altitude of 800 km with sun-synchronous precession. Every 100 min, Envisat crosses the descending node at the mean solar time of 10:00 am.

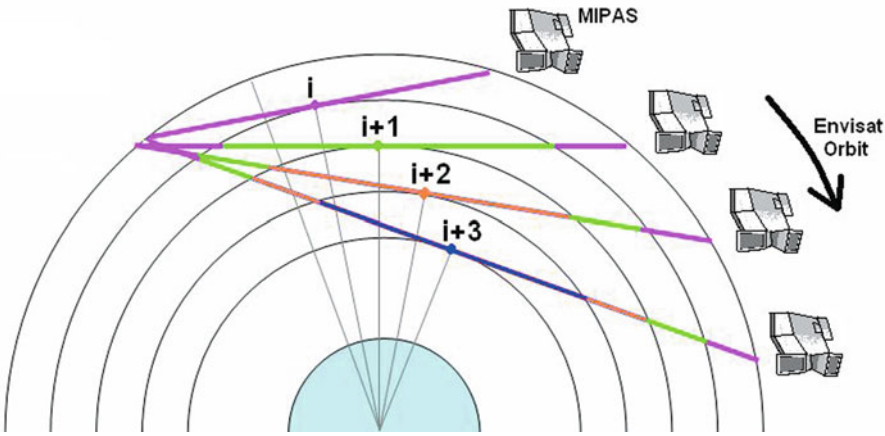

Fig. 10.4 Geometrical scheme of the MIPAS sounding during four successive measurements of a limb scanning sequence (tangent altitudes i down to i+3) in the nominal backward viewing mode. Successive tangent points follow the orbital progression of Envisat. The atmospheric layer between tangent points i and i+1 is intersected by all individual scans from tangent altitude i+1 down to the lowest tangent altitude. (Reproduced from DeClercq and Lambert 2006)

The nominal observation mode of MIPAS is backward viewing along track. The field of view of the instrument is 3 km in the vertical and 30 km in the horizontal at the tangent point.

Schematised in Fig. 10.4, the MIPAS limb-scanning sequence spans vertically the atmosphere from 68 km down to 6 km in tangent altitude, with a vertical spacing between successive measurements of 3 km in the troposphere and stratosphere and a coarser spacing above. Two geometrical effects compete to make the geolocation of the tangent points varying with the tangent altitude. Downward scanning produces a retrograde motion of tangent points with respect to the satellite, of about 1.1° between the upper and lowest tangent points of the sequence. The Envisat satellite itself orbits in the opposite direction at a speed of about 7.45 km/s. At the end of a complete sequence (72 s), the satellite has progressed of 4.28° along its orbit. The net effect is an angular spacing of about 3.18° in the orbit plane between the upper and lowest tangent points of the sequence.

Geometrical considerations of the orbit, limb scanning mode and instrumental field-of-view already suggest that MIPAS sounds the atmospheric field of water vapour anisotropically, with some spread along track (close to the North-South direction) and across track (30 km determined by the field of view). Further study of radiative transfer and retrieval aspects are needed to determine quantitatively the along-track spread of the retrieved information and the possible displacement of its centroid with respect to the tangent point. (von Clarmann et al. 2009a) report such a study and propose two-dimensional averaging kernels for the one-dimensional H_2O profile retrievals.

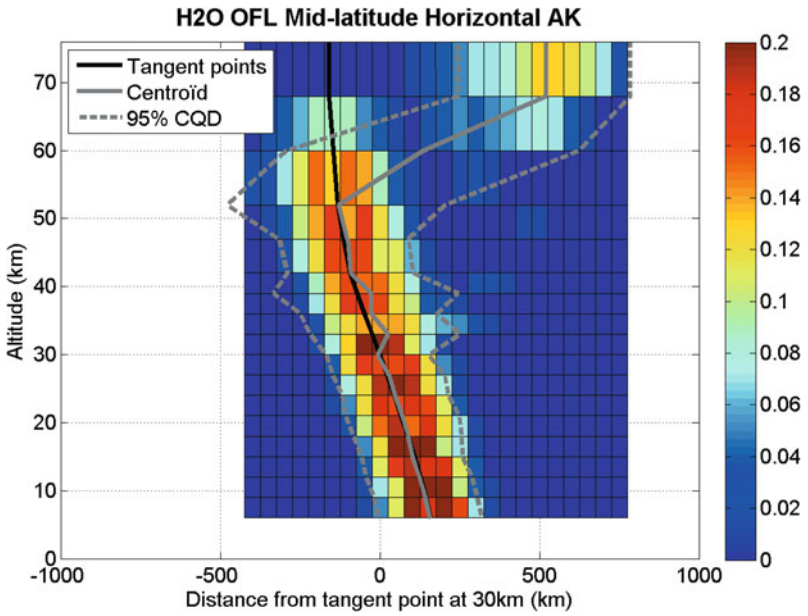

Fig. 10.5 Horizontal averaging kernels for the MIPAS retrieval of H_2O vertical profiles, calculated for a middle latitude standard atmosphere and plotted as a function of altitude and of along-track distance from the tangent point at tangent altitude of 30 km. (Reproduced from von Clarmann et al. 2009a)

Figure 10.5 reproduces their results for the vertical profile retrieval of water vapour at middle latitudes in summer. The represented averaging kernels indicate, as a function of altitude, the along-track region where the retrieved profile information originates from and they describe the horizontal smoothing of the retrieval. The black line shows the geometrical displacement of the successive tangent points and the grey line the centroid of the retrieved information. Tangent points and centroids do not differ by more than a few 10 km, except at the uppermost altitude of 68 km where the peak of information is displaced by up to about 510 km towards the satellite due to saturation effects. The information spread is reported in Fig. 10.5 as the 95 % centered quantile distance (CQD). It increases with altitude and ranges from 262 km in the UT/LS, to 315 km at 52 km tangent altitude, and to 683 km at 68 km tangent altitude. The corresponding FWHM of the horizontal averaging kernel ranges from 210 km at 6 km tangent altitude to 330 km at 68 km tangent altitude. Compared to the MIPAS along-track sampling, which is about 510 km, the horizontal smearing in terms of FWHM often is a factor of about 2 smaller. That means that the atmosphere is horizontally undersampled not only in the across-track direction, because across-track distance between measured air volumes is larger than the horizontal extension of the field of view, but also in the along-track direction, although lines of sight overlap.

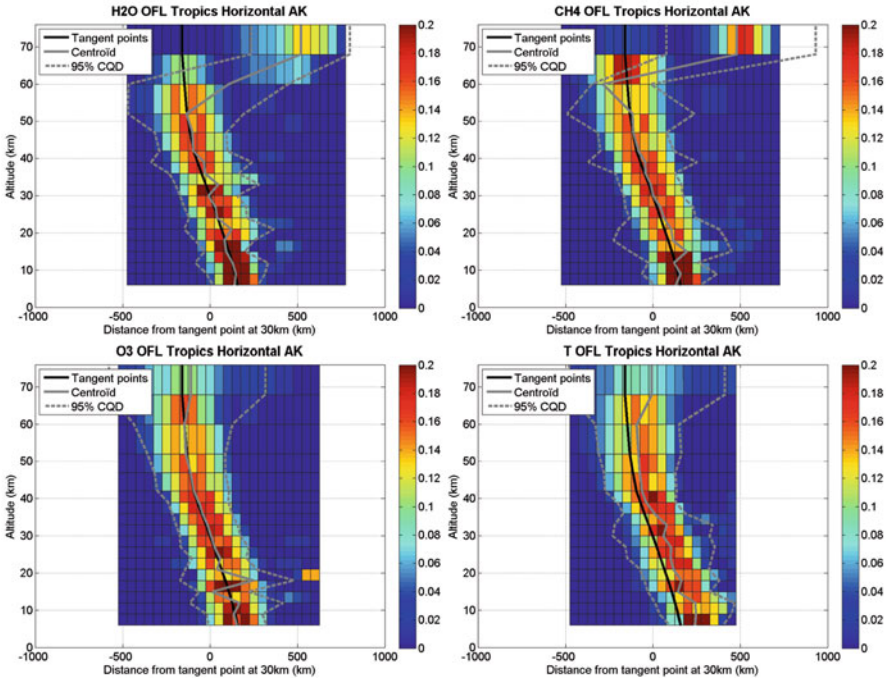

Fig. 10.6 Horizontal averaging kernels for the MIPAS off-line retrieval of water vapour, methane, ozone and temperature vertical profiles, calculated for a tropical standard atmosphere. The colour scale is the same as in Fig. 10.5

10.3.2 Tracer-tracer Correlations and Hydrogen Budget Using MIPAS

The use of water vapour observations in conjunction with observations of methane, improves studies of the hydrogen budget and its trends and of changes in vertical transport and troposphere-stratosphere exchanges (e.g. Evans et al. 1998; Nedoluha et al. 2003). Indeed, upper stratospheric H_2O is dependent upon the amount of CH_4 that has been oxidized—and is therefore sensitive to changes in stratospheric transport—while $H_2O + 2CH_4$ is nearly insensitive to the amount of CH_4 oxidation. Measurements of the budget $H_2O + 2CH_4$ in the upper stratosphere are thus a better indicator of the amount of water vapour entering the stratosphere than the measurement of H_2O alone. Simultaneous measurements of temperature can also help identifying the troposphere-stratosphere exchanges responsible for the extreme dryness of the stratosphere (Lelieveld et al. 2007). Tracer-tracer correlations and their compacity are also used as indicators of stratospheric transport, vertical transport and troposphere-stratosphere exchanges, and in studies of stratosphere-climate coupling (Plumb and Ko 1992; Boering et al. 1994; Waugh et al. 1997), and they are used now in data assimilation systems to improve or constraint dynamics.

A prerequisite to such studies is that MIPAS smoothing properties do not vary from one species to another. To verify this assumption, we present in Fig. 10.6

horizontal averaging kernels for methane and ozone and for temperature calculated with the same method and tools as in (von Clarmann et al. 2009a), but now for a tropical standard atmosphere. In the UT/LS and the whole stratosphere, the centroid displacement with respect to the tangent point and the spread of the retrieved information on water vapour, methane and ozone, is very similar and in favour of combined use.

At the 60 km tangent altitude, the centroid displacement varies dramatically with the species: from zero displacement for ozone, it reaches 125 km in the opposite direction to the satellite for methane, and 220 km in the direction towards the satellite for water vapour. At such altitudes, any gradient will thus alter significantly the combined use of simultaneous MIPAS retrievals of multiple species. At the uppermost altitude of 68 km, information on water vapour and methane has a similar displacement of about 720 km towards the satellite, while the displacement for ozone remains within 70 km towards the satellite. The case of the temperature profile data is somewhat different: while the spread of the information resembles that of the retrieved species, the entire profile is displaced by about 35 to 70 km in the stratosphere and 120 km in the mesosphere. This might be problematic in the vicinity of dynamical barriers like the polar vortex and the extra-tropical barrier, where temperature and all species experiences significant gradients in the meridian direction.

10.3.3 Error Budget for the Validation of MIPAS H_2O Profile Data

As explicated in the second section of this chapter, the error budget of a data combination includes different contributions reflecting the differences in smoothing and sampling of atmospheric structures and variability. Hereafter we illustrate the quantitative importance that such comparison errors can have on the comparison of MIPAS water vapour profile data with correlative observations acquired at much better horizontal resolution, for example from radiosondes, CFH sondes and FTIR spectrometers.

We assume the following random error components:

- MIPAS total random error is the one reported by (Dudhia 2000). It includes measurement errors, retrieval errors and errors associated with uncertainties on the retrieval parameters.
- Comparison error due to horizontal co-location mismatch is calculated as the difference between H_2O values at the centroid of the MIPAS air mass and H_2O values above the station, the H_2O values being calculated from H_2O fields assimilated by BASCOE (references below).
- Comparison error due to differences in horizontal smoothing is calculated by mapping the two-dimensional averaging kernels reported in (von Clarmann et al. 2009a) into H_2O fields assimilated by BASCOE.

Vertical smoothing errors have been omitted intentionally in this section, for three reasons. First, comparison errors associated with vertical smoothing differences have

been studied in details by several authors (e.g. Rodgers and Connor 2003; Calisesi et al. 2005). Second, for the ESA data product version 4.61 no other MIPAS vertical averaging kernels are available than the set of generic kernels calculated prior to launch (Ceccherini and Ridolfi 2002). Third, similar error assessments for MIPAS ozone and temperature profile data have shown that the contribution of vertical smoothing errors to the comparison error budget remains small (Cortesi et al. 2007; Ridolfi et al. 2007). Note that this latter argument might be incorrect in case of severe gradients like at hygropause.

The water vapour values and gradients are estimated from four-dimensional fields generated by the Belgian Assimilation System of Chemical Observations from Envisat (BASCOE, Errera and Fonteyn 2001; Errera et al. 2008; Thornton et al. 2009). BASCOE is a data assimilation system of stratospheric chemistry using the four-dimensional variational (4D-VAR) method. In the course of a run, BASCOE can ingest satellite observations. The resulting "assimilated field" is an estimate of the chemical composition of the stratosphere based both on the set of observations and on the physical laws describing the evolution of the system synthesized into the model. They are defined at 37 hybrid pressure levels from 0.1 hPa down to the surface. The horizontal resolution of BASCOE standard outputs available publicly is 3.75° in latitude by 5° in longitude. A version with improved resolution is under evaluation. For our study we have used off-line version v3d24 of BASCOE fields.

Figure 10.7 compares the different random error components estimated at four stations characterised with different dynamics and chemistry: Sodankylä in the Arctic, Payerne in the Swiss Alps, Mauna Loa in the Hawaiian archipelago, and Dumont d'Urville in French Antarctica. All these stations launch regularly balloon-borne radiosondes measuring humidity during ascent. They are also affiliated with NDACC and are equipped with other water vapour measurement systems. According to Fig. 10.7, the MIPAS random error dominates all individual error components in large parts of the vertical profile. This is still the case near 2–3 hPa, but the sum of the (horizontal) smoothing and (horizontal) sampling components exceeds the MIPAS random error. There are a few exceptions where the co-location error becomes the dominating component: in the tropics below 100 hPa, where sharp gradients are sustained by the extra-tropical barrier and a the border of the inter-tropical convergence zone; and in Antarctica near 20–50 hPa where the wintertime polar vortex separates over short distances inner dehydrated air masses from outer humid air masses.

Over the entire stratosphere, the smallest component remains the error due to horizontal smoothing differences. Figure 10.7 suggests that in the tropics this component becomes more important in the UT/LS and upper troposphere. The tools used here do not enable us to estimate comparison errors at lower altitudes in the troposphere, but intuitively we can expect smoothing and sampling errors becoming rapidly more important, and even exceeding by far MIPAS errors, as atmospheric variability increases by one order of magnitude at these altitudes.

Figure 10.8 illustrates the annual variation (over 2003) of the comparison errors estimated at the 121 hPa level at two different stations of the Southern Hemisphere. It confirms the close link between comparison errors and the MIPAS perception of natural variability. At Reunion Island, on the Tropic of Capricorn, meridian gradients

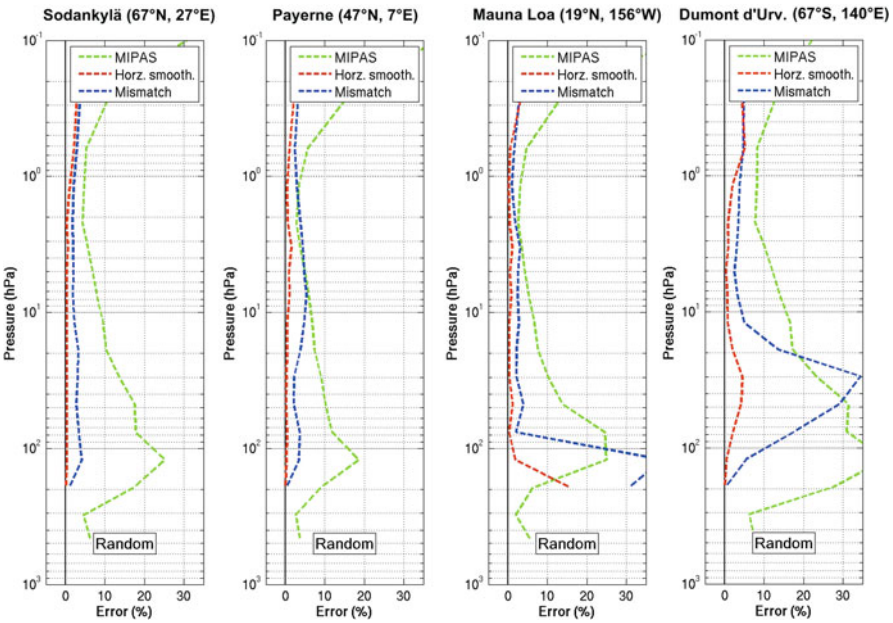

Fig. 10.7 Vertical profile of the total random error estimate for MIPAS water vapour retrievals (in *green*), and estimates of the random component of comparison errors (e.g. between MIPAS and sondes) due to differences in horizontal smoothing (in *red*) and to horizontal co-location mismatch (in *blue*). From *left* to *right*: Sodankylä year-round (Finland, 67° N, 11° E), Payerne (Swiss Alps, 48° N, 7° E) in October–December, Mauna Loa (Hawaii, 19° N, 155° W) in April–June, and Dumont d'Urville (Antarctica, 67° S, 140° E) in July–September 2003

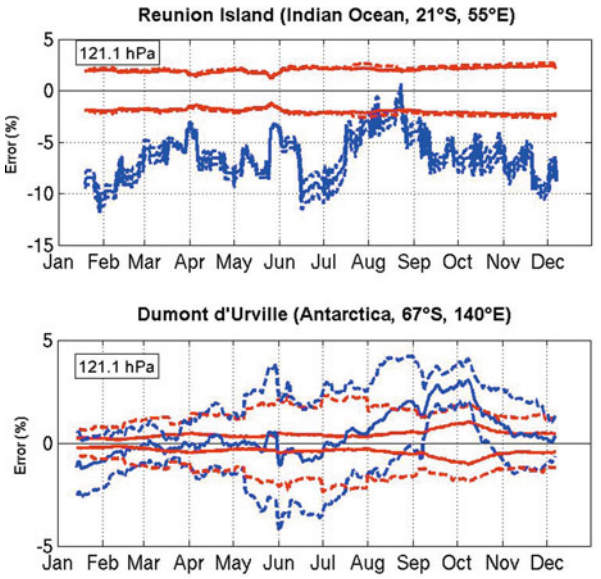

Fig. 10.8 Annual variation (over 2003) of the comparison errors due to horizontal smoothing differences and spatial mismatch between MIPAS and ground-based stations at the 121.1 hPa pressure level, estimated at the NDACC stations of Reunion Island (Indian Ocean, 21° S) and Dumont d'Urville (Antarctica, 67° S). Dashed lines represent the random component which adds to the systematic errors represented as solid lines. MIPAS errors have been omitted for clarity

between MIPAS tangent points and the station produce a permanent negative bias ranging from −10 % in summer to −2 % in winter, and a random noise within the 1 % level. MIPAS horizontal smoothing errors vary slightly over the year, fluctuating in the 1–3 % range for the systematic component and less than 1 % for the random component. At Dumont d'Urville, on the Antarctic Polar Circle, comparison errors remain within the 1–2 % level until the formation of the polar vortex in June. In spring, meridian gradients associated with the polar vortex produce a permanent positive bias reaching +4 % during the ozone hole period. This bias disappears as soon as the vortex dissipates in November.

10.4 Conclusion

In this chapter we have discussed several of the potentially important issues that can impact on the comparison and merging of complementary atmospheric water vapour data. In the second section, the error budget of a data comparison has led us to consider smoothing and sampling errors of the individual measurement systems—errors which depend on the presence of natural structures and variability—and the associated comparison errors when smoothing and sampling properties of the two systems differ significantly. The discussion has included a few cases where the separation between temporal and horizontal smoothing issues is not clear. In the last section, illustrations building on the experience gained with MIPAS validation have provided quantitative evidence of the importance of horizontal smoothing and sampling issues where and when atmospheric gradients and variability are significant. These results have direct implications for the interpretation of MIPAS data, for their ingestion in chemical data assimilation systems, and for their validation and integrated use with observations from *in situ* sensors (CFH, radiosonde, airborne sensors) and remote sensing instruments (FTIR spectrometer, lidar, microwave radiometer) acquired at higher horizontal resolution.

A conclusion of the discussion of the error budget is that smoothing and sampling problems posed by the comparison and merging of water vapour measurements can have very different causes and can vary significantly from one case to another. An appropriate solution must consider the measurement (instrument + retrieval) characteristics of every individual observation, and the way they interact with natural variability and gradients. There exists no single solution or interpretation applicable to all cases. In some cases the impact of smoothing and sampling issues can be reduced, e.g., by appropriate selection of the data sets to be compared or merged, or by adaptation of their smoothing properties. Recent studies (e.g. Henne et al. 2010) exploring the concepts of point-to-area representativeness (Nappo et al. 1982) and of catching area (Larssen et al. 1999), offer interesting perspectives in reducing comparison errors due to differences in horizontal and temporal smoothing. In other cases the differences in sampling of atmospheric structures introduces biases and noise that can not be reduced. Estimates of sampling and smoothing errors are required for the proper interpretation of the data and of their combination. In

particular, when such errors exceed the errors bars of the individual measurement systems, data comparison and merging becomes meaningless and there is nothing to gain from the complementarity of the two systems. Finally, there are fortunately many cases without any significant smoothing or sampling problem, for which straightforward treatment of the data will provide sound scientific results.

Acknowledgments The authors wish to thank Slimane Bekki (CNRS), Klemens Hocke (U. Bern), Jörg Langen (ESA) and Jo Urban (Chalmers University) for reviewing this chapter and for constructive suggestions. They are grateful to Quentin Errera and the BASCOE team at BIRA-IASB for the provision of assimilated water vapour fields and for informative discussions. ISSI and University of Bern are acknowledged for initiating and hosting activities of the ISSI WG on Atmospheric Water Vapour. Parts of this work were supported by BELSPO and ESA via ProDEx project SECPEA (Activity 4), by the ESA-funded validation project Multi-TASTE, and by the EC FP6 project GEOmon (WP 4.2).

References

T. Aruga, T. Igarashi, Vertical distribution of ozone: a new method of determination using satellite measurements. Appl. Opt. **15**, 261–272 (1976)

G.E. Backus, F. Gilbert, Numerical applications of a formalism for geophysical inverse problems. Geophys. J. R. Astr. Soc. **13**, 247–276 (1967)

G.E. Backus, F. Gilbert, The resolving power of gross Earth data. Geophys. J. R. Astr. Soc. **16**, 169–205 (1968)

G.E. Backus, F. Gilbert, Uniqueness in the inversion of inaccurate gross earth data. Philos. T. Roy. Soc. Ser. A **266**, 123–192 (1970)

K.A. Boering, B.C. Daube Jr., S.C. Wofsy, M. Loewenstein, J.R. Podolske, E.R. Keim, Tracer-tracer relationships and lower stratospheric dynamics: CO_2 and N_2O correlations during SPADE. Geophys. Res. Lett. **21**, 2567–2570 (1994)

Y. Calisesi, V.T. Soebijanta, R. Oss, Regridding of remote soundings: Formulation and application to ozone profile comparison. J. Geophys. Res. **110**, (2005) doi:10.1029/2005JD006122

M.R. Carleer, C.D. Boone, K.A. Walker, P.F. Bernath, K. Strong, R.J. Sica, C.E. Randall, H. Vömel, J. Kar, M. Höpfner, M. Milz, T. von Clarmann, R. Kivi, J. Valverde-Canossa, C.E. Sioris, M.R.M. Izawa, E. Dupuy, C.T. McElroy, J.R. Drummond, C.R. Nowlan, J. Zou, F. Nichitiu, S. Lossow, J. Urban, D. Murtagh, D.G. Dufour, Validation of water vapour profiles from the Atmospheric Chemistry Experiment (ACE) Atmos. Chem. Phys. Discuss. **8**, 4499–4559 (2008)

E.S. Carr, R.S. Harwood, P.W. Mote, G.E. Peckham, R.A. Suttie, W.A. Lahoz, A. O'Neill, L. Froidevaux, R.F. Jarnot, W.G. Read, J.W. Waters, R. Swinbank, Tropical stratospheric water vapor measured by the Microwave Limb Sounder (MLS). Geophys. Res. Let. **22**, 691–694 (1995)

S. Ceccherini, M. Ridolfi, Averaging Kernels for MIPAS near real time level 2 retrievals, Tech. rep., IFAC-OST0201, Issue 1, revision 0, 13pp, 14 June 2002

E.W. Chiou, M.P. McCormick, L.R. McMaster, W.P. Chu, J.C. Larsen, D. Rind, S. Oltmans, Intercomparison of stratospheric water vapor observed by satellite experiments: stratospheric aerosol and gas experiment ii versus limb infrared monitor of the stratosphere and atmospheric trace molecule spectroscopy. J. Geophys. Res. **98**, 4875–4887

M.P. Chipperfield, B.V. Khattatov, D.J. Lary, Sequential assimilation of stratospheric chemical observations in a three-dimensional model. J. Geophys. Res. **107**, 4585 (2002). doi:10.1029/2002JD002110

B.J. Conrath, On the estimation of relative humidity profiles from medium-resolution infrared spectra obtained from a satellite. J. Geophys. Res. **74**, 3347–3361 (1969)

U. Cortesi, J.C. Lambert, C.D. Clercq, G. Bianchini, T. Blumenstock, A. Bracher, E. Castelli, V. Catoire, K.V. Chance, M.D. Mazière, P. Demoulin, S. Godin-Beekmann, N. Jones, K. Jucks, C. Keim, T. Kerzenmacher, H. Kuellmann, J. Kuttippurath, M. Iarlori, G.Y. Liu, Y. Liu, I.S. McDermid, Y.J. Meijer, F. Mencaraglia, S. Mikuteit, H. Oelhaf, C. Piccolo, M. Pirre, P. Raspollini, F. Ravegnani, W.J. Reburn, G. Redaelli, J.J. Remedios, H. Sembhi, D. Smale, T. Steck, A. Taddei, C. Varotsos, C. Vigouroux, A. Waterfall, G. Wetzel, S. Wood, Geophysical validation of MIPAS-ENVISAT operational ozone data. Atmos. Chem. Phys. **7**, 4807–4867 (2007)

M.Y. Danilin, M.K.W. Ko, R.M. Bevilacqua, L.V. Lyjak, L. Froidevaux, M.L. Santee, J.M. Zawodny, K.W. Hoppel, E.C. Richard, J.R. Spackman, E.M. Weinstock, R.L. Herman, K.A. McKinney, O. Wennberg, F.L. Eisele, R.M. Stimpe, C.J. Scott, J.W. Elkins, T.V.Bui, Comparison of ER-2 aircraft and POAM III, MLS, and SAGE II satellite measurements during SOLVE using traditional correlative analysis and trajectory hunting technique. J. Geophys. Res. **107**, 8315 (2002a). doi:10.1029/2001JD000781

M.Y. Danilin, M.K.W. Ko, L. Froidevaux, M.L. Santee, L.V. Lyjak, R.M. Bevilacqua, J.M.Y. Zawodny, H. Sasano, Irie, Y. Kondo, J.M. Russell III, C.J. Scott, W.G. Read, Trajectory hunting as an effective technique to validate multiplatform measurements: Analysis of the MLS, HALOE, SAGE-II, ILAS, and POAM-II data in October-November 1996. J. Geophys. Res. **107**, 4420 (2002b). doi:10.1029/2001JD002012

C. De Clercq, J.-C. Lambert, A forward model of limb infrared emission spectra in a twodimensional atmosphere, in ESA Atmospheric Science Conference, Frascati, Italy, 8–12 May 2006, ESA Special Publication SP-628, p. 6pp (2006)

C. De Clercq, J.-C. Lambert, Y. Calisesi, H. Claude, R. Stubi, C. von Savigny, et al., Integrated characterisation of envisat ozone profile data using ground-based network data, in Envisat & ERS Symposium, Salzburg, Austria, 6–10 September 2004, ESA Special Publication SP-572, p. 10 pp) (2004)

B. Deuber , A. Haefele, D.G. Feist, L. Martin, N. Kämpfer, G.E. Nedoluha, V. Yushkov, S. Khaykin, R. Kivi, H. Vömel, Middle Atmospheric Water Vapour Radiometer—MIAWARA: Validation and first results of the LAUTLOS/ WAVVAP campaign. J. Geophys. Res. **110** (2000). doi: 10.1029/2004JD005543

A. Dudhia, MIPAS ultimate retrieval accuracy final report, Tech. rep., PO-TN-OXF-GS-0014, ESA Contract CCN5 11886/96NL/GS, Task 4.3 Final Report, 15 pp., 19 June 2000

W.P. Elliott, D.J. McGaffen, On the Utility of Radiosonde Humidity Archives for Climate Studies. Bull. Am. Meteorol. Soc. **72**, 1507–1520 (1991)

L.S. Elson, W.G. Read, J.W. Waters, P.W. Mote, J.S. Kinnersley, R.S Harwood, Space-time variations in water vapor as observed by the UARS Microwave Limb Sounder. J. Geophys. Res. **101**, 9001–9015 (1996)

M.N. England, R.A. Ferrare, S.H. Melfi, D.N. Whiteman, T.A. Clark, Atmospheric water vapor measurements: Comparison of microwave radiometry and lidar. J. Geophys. Res. **97**, 899 (1992)

Q. Errera, D. Fonteyn, Four-dimensional variational chemical assimilation of CRISTA stratospheric measurements. J. Geophys. Res. **106**, 12 253–12 265 (2001)

Q. Errera, F. Daerden, S. Chabrillat, J.C. Lambert, W.A. Lahoz, S. Viscardy, S. Bonjean, D. Fonteyn, D-var Assimilation of MIPAS chemical observations: ozone and nitrogen dioxide analyses. Atmos. Chem. Phys. **8**, 6169–6187 (2008)

S.J. Evans, R. Toumi, J.E. Harries, M.R. Chipperfield, J.M. Russell III, Trends in stratospheric humidity and the sensitivity of ozone to these trends. J. Geophys. Res. **103**, 8715–8725 (1998)

R. Ferrare, S. Ismail, E. Browell, V. Brackett, M. Clayton, S. Kooi, S.H. Melfi, D. Whiteman, G. Schwemmer, K. Evans, P. Russell, J. Livingston, B. Schmid, B. Holben, L. Remer, A. Smimov, P.V. Hobbs, Comparison of aerosol optical properties and water vapor among ground and airborne lidars and Sun photometers during TARFOX. J. Geophys. Res. **105**, 9917–9933 (2000)

H. Fischer, H. Oelhaf, Remote sensing of vertical profiles of atmospheric trace constituents with MIPAS limb-emission spectrometer. Appl. Opt. **35**, 2787–2796 (1996). ISSN 1680-7316

H. Fischer, M. Birk, C. Blom, B. Carli, M. Carlotti, T. von Clarmann, L. Delbouille, A. Dudhia, D. Ehhalt, M. Endemann, J.M. Flaud, R. Gessner, A. Kleinert, R. Koopman, J. Langen, M. Lopez-Puertas, P. Mosner, H. Nett, H. Oelhaf, G. Perron, J. Remedios, M. Ridolfi, G. Stiller, R. Zander, MIPAS: an instrument for atmospheric and climate research. Atmos. Chem. Phys. **8**, 2151–2188, ISSN 1680-7316 (2008). URL http://www.atmos-chem-phys.net/8/102151/2008/

M. Fisher, D. Lary, Lagrangian 4-dimensional variational data assimilation of chemical species. Quant. J. Roy. Met. Soc. **121**, 1681–1704 (1995)

L. Garand, C. Grassotti, J. Hall, G.L. Klein, On differences in radiosonde humidityreporting practices and their implications for numerical weather prediction and remote sensing. Bull. Am. Met. Soc. **73**, 1417–1423 (1992)

M. Goss-Custard, J.J. Remedios, A. Lambert ,F.W. Taylor, C.D. Rodgers, M. Lopez-Puertas, G. Zaragoza, M.R. Gunson, M.R. Suttie, J.E. Harries, J.M. Russell III, Measurements of water vapor distributions by the improved stratospheric and mesospheric sounder: Retrieval and validation. J. Geophys. Res. **101**, 9907–9928 (1996)

J.E. Harries, J.M. Russell III, A.F. Tuck, L.L. Gordley, P. Purcell, K. Stone, R.M. Bevilacqua, M. Gunson, G. Nedoluha, W.A. Traub, Validation of measurements of water vapor from the Halogen Occultation Experiment (HALOE). J. Geophys. Res. **101**, 10 205–10 216 (1996)

S.A.B. Henne, D. Folini, S. Solberg, J. Klausen, B. Buchmann, Assessment of parameters describing representativeness of air quality in-situ measurement sites. Atmos. Chem. Phys. **10**, 3561–3581 (2010)

W.A. Lahoz, E.S. Carr, L. Froidevaux, R.S. Harwood, J.B. Kumer, J.L. Mergenthaler, G.E. Peckham, W.G. Read, P.D. Ricaud, A.E. Roche, J.W. Waters, Northern hemisphere mid-stratosphere vortex processes diagnosed from H_2O, N_2O and potential vorticity. Geophys. Res. Let. **20**, 2671–2674 (1993)

W.A. Lahoz, M.R. Suttie, L. Froidevaux, R.S. Harwood, C.L. Lau, T.A. Lungu, G.E. Peckham, H.C. Pumphrey, W.G. Read, Z. Shippony, R.A. Suttie, J.W. Waters, G.E. Nedoluha, S.J. Oltmans, J.M. Russell III, W.A. Traub, Validation of UARS Microwave Limb Sounder 183 GHz H_2O measurements. J. Geophys. Res. **101**, 10 129–10 149 (1996)

L.R. Lait, Systematic differences between radiosonde instruments, Geophys. Res. Lett. **29** (2002b). doi:10.1029/2001GL014337

L.R. Lait, M.R. Schoeberl, P.A. Newman et al. Ozone loss from quasi-conservative coordinate mapping during the 1999–2000 SOLVE/THESEO 2000 campaigns. J. Geophys. Res. **107**, 8274 (2002a). doi:10.1029/2001JD000998

S. Larssen, R. Sluyter, C. Helmis, Criteria for EUROAIRNET—The EEA Air Quality Monitoring and Information Network. Tech. rep., European Environment Agency (1999)

T. Leblanc, I.S. McDermid, T.G. McGee, L. Twigg, G. Sumnicht, D.N. Whiteman, K. Rush, M. Cadirola, D Venable, R. Connell, B. Demoz, H. Vömel, L. Miloshevich, Measurements of humidity in the atmosphere and validation experiments (MOHAVE, MOHAVE II): Results overview, in Reviewed and Revised Papers of The 24th International Laser Radar Conference, Boulder, CO, 23–27 June 2008, pp. 1013–1016

J. Lelieveld, C. Brühl, P. Jöckel, B. Steil., Crutzen, P, H. Fischer, M.A. Giorgetta, P. Hoor, M.G. Lawrence, R. Sausen, H. Tost, Stratospheric dryness: model simulations and satellite observations. Atmos. Chem. Phys. **7**, 1313–1332 (2007). doi:10.5194/acp-7-1313-2007

N.J. Livesey, W.G. Read, Direct Retrieval of Line-of-Sight Atmospheric Structure from Limb Sounding Observations. Geophys. Res. Lett. **27**, 891–894 (2000)

J. Lumpe, R. Bevilacqua, C. Randall, G. Nedoluha, K. Hoppel, J. Russell, V.L. Harvey, C. Schiller, B. Sen, G. Taha, G. Toon, H. Vömel, 2006, Validation of Polar Ozone and Aerosol Measurement (POAM) III version 4 stratospheric water vapor. J. Geophys. Res. **111**, D11 301, doi: 10.1029/2005JD006763 (2000)

L.M. Miloshevich, H. Vömel, D.N. Whiteman, B.M. Lesht, F.J. Schmidlin, F. Russo, Absolute accuracy of water vapor measurements from six operational radiosonde types launched during AWEX-G and implications for AIRS validation. J. Geophys. Res. **111**, D09S10 (2006). doi:10.1029/2005JD006083

M. Milz, T. von Clarmann, P. Bernath, C. Boone, S.A. Buehler, S. Chauhan, B. Deuber, D.G. Feist, B. Funke, N. Glatthor, U. Grabowski, A. Griesfeller, A. Haefele, M. Höpfner, N. Kämpfer, S. Kellmann, A. Linden, S. Müller, H. Nakajima, H. Oelhaf, E. Remsberg, S. III J.M.R. Rohs, C. Schiller, G.P. Stiller, T. Sugita, T. Tanaka, H. Vömel, K. Walker, G. Wetzel, T. Yokota, V. Yushkov, G. Zhang, Validation of water vapour profiles (version 13) retrieved by the IMK/IAA scientific retrieval processor based on full resolution spectra measured by MIPAS on board Envisat. Atmos. Meas. Tech. **2**, 379–399 (2009)

G.A. Morris, J.F. Gleason, J. Ziemke, M.R. Schoeberl, Trajectory mapping: A tool for validation of trace gas observations. J. Geophys. Res. **105**, 17875–17894 (2000). doi:10.1029/1999JD901118

P.W. Mote, J.R. Holton, J.M. Russell III, B.A. Boville, A comparison of observed (Haloe) and modeled (CCM2) methane and stratospheric water vapor Geophys. Res. Let. **20**, 1419–1422 (1993)

C.J. Nappo, J.Y. Caneill, R.W. Furman, F.A. Gifford, J.C. Kaimal, M.L. Kramer, T.J. Lockhart, M.M. Pendergast, R.A. Pielke, D. Randerson, J.H. Shreffer, J.C. Wyngaard, The Workshop on the Representativeness of Meteorological-Observations, June 1981, boulder, CO, Bull. Am. Met. Soc. **63**, 761–764 (1982)

G.E. Nedoluha, R.M. Bevilacqua, R.M. Gomez, B.C. Hicks, J.M. Russell III, B.J. Connor, An evaluation of trends in middle atmospheric water vapor as measured by HALOE, WVMS, and POAM. J. Geophys. Res. **108** (2003). doi:10.1029/2002JD003332

J.L. Neu, L.C. Sparling, R.A. Plumb, Variability of the subtropical "edges" in the stratosphere. J. Geophys. Res. p. 4482 (2003). doi:10.1029/2002JD002706

S. Noël, M. Buchwitz, H. Bovensmann, J.P. Burrows, Validation of SCIAMACHY AMCDOAS water vapour columns. Atmos. Chem. Phys. **5**, 1835–1841 (2005)

H.T. Nyquist, 1928 Certain topics in telegraph transmission theory, reprinted in Proc. of the IEEE, **90**(2), Feb. 2002

J.P. Peixoto, A.H. Oort, The climatology of relative humidity in the atmosphere. J. Clim. **9**, 3443–3463 (1996)

R.A. Plumb, M.K.W. Ko, Interrelationships between mixing ratios of long-lived stratospheric constituents. J. Geophys. Res. **97**, 10145–10156

M. Rex, P. Von der Gathen, G.O. Braathen, N.P.L. Harris, E. Reimer, A. Beck, R. Alfier, R. Kruger-Carstensen, M.P. Chipperfield, H. DeBacker, F. O'Connor, H. Dier, V Dorokhov, H. Fast, A. Gamma, M. Gil, E. Kyro, Z. Litynska, I.S. Mikkelsen, M. Molyneux, G. Murphy, S.J. Reid, M. Rummukainen, C. Zerefos, Chemical ozone loss in the arctic winter 1994/95 as determined by the Match technique. J. Atmos. Chem. **32**, 35–59 (1999)

M. Ridolfi, B. Carli, M. Carlotti, T. von Clarmann, B. Dinelli, A. Dudhia, J.-M. Flaud, M. Höpfner, P.E. Morris, P. Raspollini, G. Stiller, R.J. Wells, Optimized forward and retrieval scheme for MIPAS near-real time data processing. Appl. Optics **39**, 1323–1340 (2000)

M. Ridolfi, U. Blum, B. Carli, V. Catoire, S. Ceccherini, H. Claude, C. De Clercq, K.H. Fricke, F. Friedl-Vallon, M. Iarlori, P. Keckhut, B. Kerridge, J.-C. Lambert, Y.J. Meijer, L. Mona, H. Oelhaf, G. Pappalardo, M. Pirre, V. Rizi, C. Robert, D. Swart, T. von Clarmann, A. Waterfall, G. Wetzel, Geophysical validation of temperature retrieved by the ESA processor from MIPAS/ENVISAT atmospheric limb-emission measurements. Atmos. Chem. Phys. **7**, 4459–4487 (2007)

D. Rind, E.-W. Chiou, W. Chu, S. Oltmans, J. Lerner, J. Larsen, M.P. McCormick, L. McMaster, Overview of the Stratospheric Aerosol and Gas Experiment II Water Vapor Observations: Method, Validation, and Data Characteristics. J. Geophys. Res. **98**, 4835–4874 (1993)

C. Rodgers, 2000, Inverse methods for atmospheric sounding: Theory and Practice, vol. 2 of Series on Atmospheric, Oceanic and Planetary Physics, World Scientific Publishing Co

C. Rodgers, B.J. Connor, Intercomparison of remote sounding instruments. J. Geophys. Res. **108**, 4116 (2003). doi:10.1029/2002JD002299

C.D. Rodgers, The vertical resolution of remotely sounded temperature profiles with a priori statistics. J. Atm. Sci. **33**, 707–709 (1976)

C.D. Rodgers, Characterization and error analysis of profiles retrieved from remote sounding measurements. J. Geophys. Res. **95**, 5587–5595 (1990)

H.K. Roscoe, J.A. Pyle, Measurements of solar occultation—The error in a naive retrieval if the constituent's concentration changes. J. Atmos. Chem. **5**, 323–341 (1987). ISSN 0167-7764

J.M. Russell III, J.C. Gille, E.E. Remsberg, L.L. Gordley, P.L. Bailey, H. Fischer, A. Girard, S.R. Drayson, W.F.J. Evans, J.E. Harries, Validation of Water Vapor Results Measured by the Limb Infrared Monitor of the Stratosphere Experiment on NIMBUS 7. J. Geophys. Res. **89**, 5115–5124 (1984)

M. Schoeberl, L.R. Lait, P.A. Newman, R.L. Martin, M.H. Profitt, D.L. Hartmann, M. Loewenstein, J. Podolske, S.E. Strahan, J. Anderson, K.R. Chan, B. Gary, Reconstruction of the constituent distribution and trends in the antarctic polar vortex from ER-2 ight observations. J. Geophys. Res. **94**, 16815–16845 (1989)

J.J. Schwab, R.-J. Pan, J. Zhang, What constitutes a valid intercomparison of satellite and in situ stratospheric H_2O measurements. J. Geophys. Res. **101**, 1517–1528 (1996)

L.C. Sparling, Statistical perspectives on stratospheric transport. Rev. Geophys. **38**, 417–436 (2000)

T. Steck, M. Höpfner, T. von Clarmann, U. Grabowski, Tomographic retrieval of atmospheric parameters from infrared limb emission observations. Appl. Opt. **44**, 3291–3301 (2005). doi: 10.1364/AO.44.003291

W. Swartz, J.-H. Yee, C. Randall, R. Shetter, E.V. Browell, J.F. Burris, T.J. McGee, M.A. Avery, Comparison of high-latitude line-of-sight ozone column density with derived ozone fields and the effects of horizontal inhomogeneity. Atmos. Chem. Phys. **6**, 1843–1852 (2006)

R. Swinbank, A. O'Neill, A stratosphere- troposphere data assimilation system. Mon. Weather Rev. **122**, 686–702 (1994)

L.W. Thomason, J.R. Moore, M.C. Pitts, J.M. Zawodny, E.-W. Chiou, An evaluation of the SAGE III Version 4 aerosol extinction coefficient and water vapor data products. Atmos. Chem. Phys. Discuss. **9**, 22177–22222 (2009)

A.M. Thompson, J.C. Witte, H.G.J. Smit, S.J. Oltmans, B.J. Johnson, V.W.J.H. Kirchhoff, F.J. Schmidlin, Southern Hemisphere Additional Ozonesondes (SHADOZ) 1998–2004 tropical ozone climatology: 3. instrumentation, station-to-station variability, and evaluation with simulatedight profiles. J. Geophys. Res. **112**, D03 304 (2007). doi:10.1029/2005JD007042

H.E. Thornton, D.R. Jackson, S. Bekki, N. Bormann, Q. Errera, A.J. Geer, W.A. Lahoz, S. Rharmili, The ASSET intercomparison of stratosphere and lower mesosphere humidity analyses. Atmos. Chem. Phys. **9**, 995–1016 (2009)

S. Twomey, Information content in remote sensing. Appl. Opt. **13**, 942–945 (1974)

J. Ungermann, L. Hoffmann, P. Preusse, M. Kaufmann, M. Riese, Tomographic retrieval approach for mesoscale gravity wave observations by the PREMIER Infrared Limb-Sounder. Atmos. Meas. Tech. Discuss. **2**, 2809–2850 (2009)

H. Vömel, J.E. Barnes, R.N. Forno, M. Fujiwara, F. Hasebe, S. Iwasaki, R. Kivi, N. Komala, E. Kyrö, T. Leblanc, B. Morel, S.-Y. Ogino, W. Read, S. Ryan, S. Saraspriya, H. Selkirk, M. Shiotani, J.V. Canossa, D. Whiteman, Validation of Aura Microwave Limb Sounder water vapor by balloon-borne Cryogenic Frost point Hygrometer measurements. J. Geophys. Res. **112**, D24S37 (2007). doi:10.1029/2007JD008698

T. von Clarmann, Validation of remotely sensed profiles of atmospheric state variables: strategies and terminology. Atmos. Chem. Phys. **6**, 4311–4320 (2006)

T. von Clarmann, U. Grabowski, Elimination of hidden a priori information from remotely sensed profile data. Atmos. Chem. Phys. **7**, 397–408

T. von Clarmann, C. De Clercq, M. Ridolfi, M. Höpfner, J.-C. Lambert, The horizontal resolution of MIPAS. Atmos. Meas. Tech. **2**, 47–54 (2009a)

T. von Clarmann, G. Stiller, U. Grabowski, J. Orphal, Technical note: Trend estimation from irregularly sampled, correlated data. Atmos. Chem. Phys. Discuss. **9**, 27 675–27 692 (2009b)

T. Wagner, J. Heland, M. Zöger, U. Platt, A fast H_2O total column density product from GOME—validation with in-situ aircraft measurements. Atmos. Chem. Phys. **3**, 651–663 (2003)

D. Waugh, R.A. Plumb, J.W. Elkins, D.W. Fahey, G.S. Dutton, M. Loewenstein, J.R. Podolske, E.R. Keim, K.A. Boering, S.C. Wofsy, M.H. Proffitt, K.K. Kelly, C.R. Webster, R.D. May, K.R. Chan, P.A. Newman, L.R. Lait, Mixing of polar vortex air into middle latitudes as revealed by tracer-tracer scatter plots. J. Geophys. Res. **102**, 13 119–13 134 (1997)

Chapter 11
Survey of Intercomparisons of Water Vapour Measurements

Klemens Hocke, Lorenz Martin and Niklaus Kämpfer

The survey begins with a discussion of the necessity of intercomparisons. Then the history of intercomparisons is surveyed over the time interval from 1773 to 1976. Past scientific works on water vapour intercomparisons are often forgotten. However it can be motivating and helpful if we know more about the roots of intercomparisons and hygrometers.

The number of intercomparisons of water vapour measurements strongly increased in the period 1977 to 2010. It is impossible to give details about the recent achievements within the present chapter. On the other hand it is not fair to pick out a few articles for a detailed discussion. This is the reason why we give an overview of intercomparisons since 1977 by means of tables of literature references. Hopefully the reference tables can introduce intercomparison studies to you which you otherwise would have overlooked or forgotten.

We send our regrets to all authors which we forgot to mention in this survey chapter. You may inform us since your articles could be referenced in an update of the survey chapter in a few years. The survey is strongly supported by the new interactive Water Vapour Literature Database which is a practical work tool of the water vapour community: http://www.watervapour.org.

11.1 Motivation for Intercomparisons

In spite of major technical advances, a comprehensive climate observing system does not exist (Trenberth et al. 2006). Benchmark observations of high-accuracy measurement techniques and a much-needed step forward in the quality of water vapour observations are required to anchor and harmonize a global climate observing system consisting of various measurement networks as described in Chap. 8.

The health of the climate monitoring system must be tracked by regular intercomparisons to benchmark observations revealing instrumental drifts and other failures of

K. Hocke (✉) · L. Martin · N. Kämpfer
Institute of Applied Physics, University of Bern, Sidlerstr. 5 CH-3012 Bern, Switzerland
e-mail: klemens.hocke@iap.unibe.ch

N. Kämpfer (ed.), *Monitoring Atmospheric Water Vapour,*
ISSI Scientific Report Series 10,
DOI 10.1007/978-1-4614-3909-7_11, © Springer Science+Business Media, LLC 2013

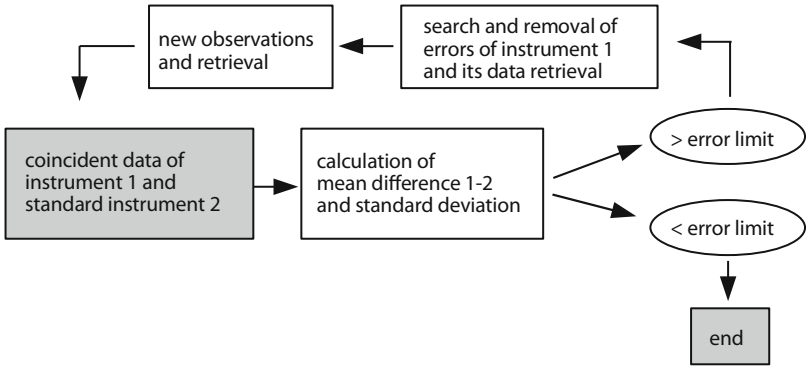

Fig. 11.1 Simplified scheme of intercomparison of instrument 1 and standard instrument 2. Errors of technique and retrieval of instrument 1 are assumed to be removable

system components. Trenberth et al. (2006) and Oltmans et al. (2000) recommended frost point hygrometry as benchmark, and the Global Reference Upper-Air Network (GRUAN, Chap. 8) regulary launches balloons with frost point hygrometers. Sonntag (1994) classified frost point hygrometry as a secondary standard for humidity measurement while gravimetric hygrometry and precision humidity generators in national laboratories are primary standards.

A great variety of in situ and remote sensing techniques exists for measurement of atmospheric water vapour in all regions from the moist lower troposphere to the extreme dry stratosphere and mesosphere. Each time a new measurement technique arises, the new technique must be compared with the other techniques. Ideally, measurements of the new instrument are compared with coincident measurements of a standard or a reference instrument with a known uncertainty (e.g., frost point hygrometer, Lyman-α hygrometer). In practise, the intercomparison is handicaped by different resolution of sounding volumes and imperfect coincidence/collocation of measurement pairs, as described in Chap. 10.

Assessment of the systematic error of the new technique with respect to a standard instrument is essential for recognition of unknown technical errors of the new instrument and for discovery of methodology errors, false assumptions, and bugs in the retrieval algorithms. In the best case, the error sources of the new instrument and retrieval technique can be removed, so that the new instrument will provide accurate data. The scheme of the optimization process is shown in Fig. 11.1.

If the error sources of the new instrument are unremovable (e.g., limits of method and technique), the data of the new instrument might be adjusted to the data of the standard instrument as shown in Fig. 11.2. This adjustment process (or correction) must be controlled by further intercomparisons of recalibrated data of instrument 1 with those of the standard instrument. More advanced methods such as nonlinear regression or neural network technique might be chosen for the calibration (instead of scatter plots which are utilized later as a simple example for calibration of historical hygrometer data). The applied correction should be valid for measurements in various atmospheric regions and conditions. Miloshevich et al. (2001)

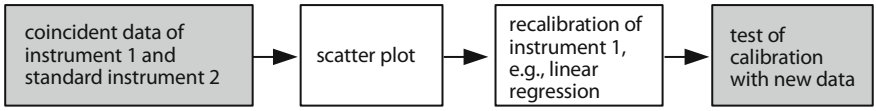

Fig. 11.2 Simplified scheme of intercomparison and recalibration of instrument 1 with respect to the standard instrument 2. This scheme is for the case of unremovable errors and limitations of instrument 1

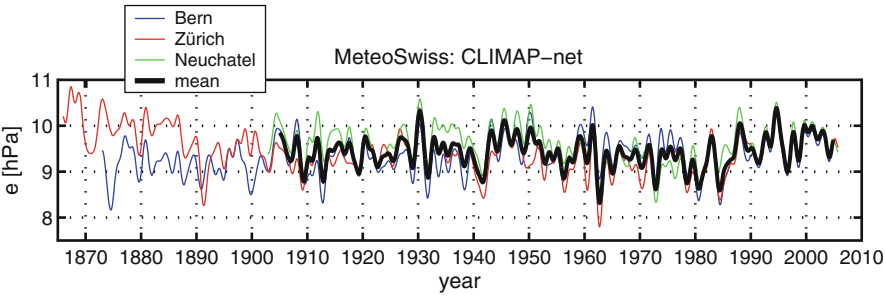

Fig. 11.3 Long-term series of water vapour pressure e in Switzerland (2 m above surface). A low pass filter (periods $>$ 1.5 years) has been applied. Water vapour pressure is almost constant since 1905: The linear trend of the black line is 0.08 % per decade. Only recently, since 1980, a positive linear trend of 3.2 % per decade is present. The time series of water vapour pressure may contain systematic errors due to instrumental changes

describe several corrections for the Vaisala RS80-A sensor. These corrections reduce the temperature-dependence error, the time-lag error, the radiation error, and some other errors occurring during the radiosonde measurement. Häberli (2006) applied the dry bias correction to the RS80 humidity data of the network of Alpine radiosondes (SRS-400, VIZ, RS80, RS90). Routine intercomparisons and harmonization of measurements of worldwide networks of ground stations, radiosondes, airplanes, and satellites are required for an optimal data assimilation into chemistry general circulation models of climate and weather (Harries 1976).

Another aspect is the reconstruction of long-term series of humidity over the last 50 to 150 years. These series are a patchwork of measurements by different kinds of hair hygrometers and psychrometers. Long-term series of water vapour pressure at three sites in Switzerland are shown in Fig. 11.3. The observational data can inform about long-term trends and variability of humidity. Contrary to historical series of temperature and precipitation, long-term series of water vapour pressure and relative humidity are almost not available for research.

One open question is the assumed tendency of the Earth's atmosphere to conserve the average relative humidity during warming and cooling phases. This characteristic has been simulated by atmosphere models and can be qualitatively explained by the Clausius-Clapeyron equation. Observational evidence for the conservation of relative humidity does not exist yet and might be derived from homogenized long-term series of relative humidity. Paltridge et al. (2009) reported about negative trends (about -1 % per decade) in NCEP reanalysis data of relative humidity of the


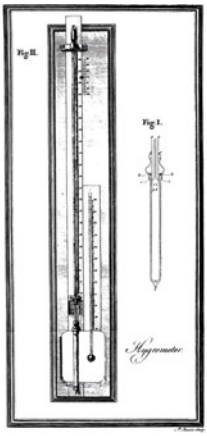

Fig. 11.4 *Left* Paper-disk-hygrometer invented by J. Coventry and manufactured by G. Adams (London, 1750–1800). Courtesy of Museo Galileo (Florence). *Middle* Construction plan of De Luc's first hygrometer ("thermometer" with ivory bulb and mercury). Courtesy of Phil. Trans. Roy. Soc. (De Luc 1773). *Right* De Luc's whalebone hygrometer (ca. 1780, whalebone strip included). Photograph copyright and courtesy of http://www.freunde-alter-wetterinstrumente.de

middle and upper troposphere. NCEP reanalysis data are mainly based on radiosonde observations and need much more homogenization efforts, particularly the data before 1970. Paltridge et al. (2009) concluded that we should try to retrieve as much informations as possible from the past radiosonde humidity measurements in order to learn about the tropospheric water vapour feedback.

11.2 History of Intercomparisons of Water Vapour Measurements

The eighteenth century brought improvements of hygrometers and new water vapour measurement techniques. De Luc (1787) compared measurements of various hygrometers as described in the first chapter of the first volume of *Neue Ideen über die Meteorologie*. In the second volume, De Luc (1788) compared his first hygrometer (mercury in an ivory vessel) with his new whalebone hygrometer. These hygrometers are shown in the middle and right panel of Fig. 11.4 respectively. He noted that the expansions of the ivory vessel and the whalebone strip had different, nonlinear dependencies on relative humidity. De Luc (1791) analysed coincident measurements of the expansion of various hygroscopic substances (whalebone, quill, deal) while changing from extreme moist to extreme dry air. He favoured whalebone as a sensitive material for the use in hygrometers with long-term stability. Alexander von Humboldt recommended the robust whalebone hygrometer of De Luc for the use in humid, tropical regions and favoured Saussure's hair hygrometer in dry highlands since the response time of the hair hygrometer is superior (Daniell 1823).

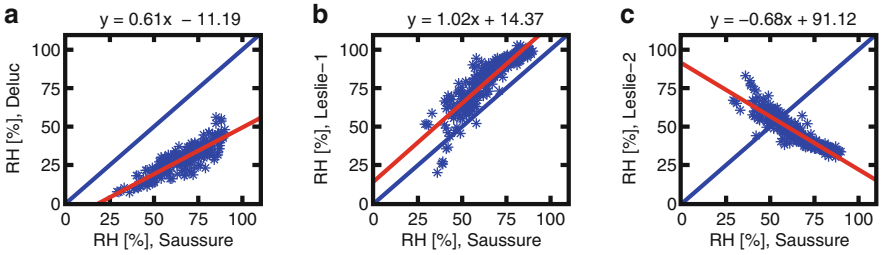

Fig. 11.5 Intercomparisons of coincident measurements of three hygrometers with respect to Saussure's hair hygrometer using data of Böckmann (1803). At that time, relative humidity was measured in arbitrary degrees on different scales. **a** Scatter plot of De Luc versus Saussure, **b** Leslie's hygrometer version 1 versus Saussure, **c** Leslie's hygrometer version 2 versus Saussure. The linear regression line is depicted by the red line, and the formula of the red line is given in the title

The wet and dry bulb thermometer (psychrometer) is based on a different measurement principle and measures the cooling by evaporation of water. It was first developed by Hutton in 1792 who missed to publish his invention. He recognized that the temperature difference of the dry and the wet bulb increased with dryness of air. Leslie (1800) invented a differential psychrometer with two thermometers in conjunction. Lüdicke (1802) and Daniell (1823) explained that Leslie's hygrometer introduced new errors and recommended the removal of the conjunction between the wet and dry bulb thermometer.

Lüdicke (1802) performed a qualitative intercomparison of the hair hygrometer (De Saussure 1783), a psychrometer, and a stone hygrometer (gravimetric adsorption measurement). Later Böckmann (1803) noted that publications of intercomparisons of hygrometers were still rare and emphasized the necessity of detailed description and comparison of instruments and methods – otherwise the measurements have no value. He compared relative humidity measurements of two Leslie hygrometers with coincident measurements of the hair hygrometer (De Saussure 1783) and the whale-bone hygrometer (De Luc 1787). Leslie's hygrometers are two slightly different versions of a wet and dry bulb thermometer in conjunction and with a gold-beater skin around the wet bulb. Böckmann (1803) presented eight tables listing the coincident relative humidity measurements of the four hygrometers as well as pressure, temperature, and wind data. He concluded that he is not satisfied with the measurements of Leslie's hygrometers and that he has no time for further data analysis and instrumental corrections of Leslie's hygrometers.

Böckmann's data consist of about 221–287 coincident humidity measurements recorded from end of May to begin of November (year and location are not mentioned in the article, possibly before 1803 and at Karlsruhe in Germany). Now – after more than 200 years – we revisit the experimental data of C. W. Böckmann and retrieve scatter diagrams and systematic biases of Leslie's and De Luc's hygrometers with respect to Saussure's hygrometer which are shown in Fig. 11.5. At that time, relative humidity was measured in degrees on various scales (e.g., from 0 to 40 degrees, from 0 to 80 degrees, from 0 to 100 degrees).

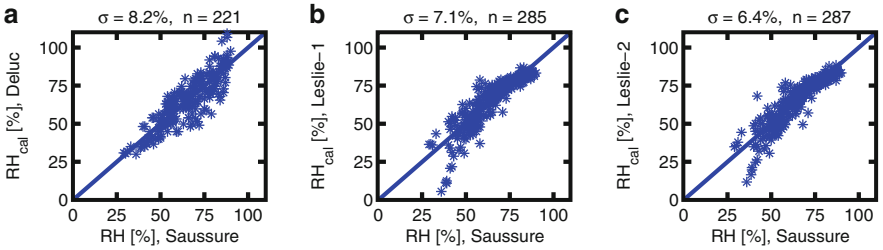

Fig. 11.6 Scatter plots of the recalibrated data of De Luc's and Leslie's hygrometers versus the data of Saussure's hygrometer observed by Böckmann (1803). The recalibration is perfomed by means of the linear relationships found in Fig. 11.5. Standard deviation σ of the hygrometer pair is given in the title

Linear relationships roughly exist for all hygrometer pairs in Fig. 11.5. The anticorrelation of the hygrometer data sets in Fig. 11.5c is possibly due to a reversed scale of Leslie's hygrometer 2. Using linear models (as given by the formulas of Fig. 11.5), we can recalibrate the measurement series of De Luc's and Leslie's hygrometers, so that these measurement harmonize with the measurements of Saussure's hygrometer. The recalibrated data are again compared with the data of Saussure's hygrometer in Fig. 11.6. The data are now harmonized and have no systematic biases. The standard deviations range between 6 and 8 % relative humidity as given in the titles of Fig. 11.6. We have performed an almost complete cross-validation. Of course it is possible to search for more sophisticated models of recalibration, to remove outliers of the data, and to perform statistical tests with samples. However this example impressively demonstrates that data of various hygrometers can be put together if data of intercomparison campaigns are available.

There are only a few journal articles about intercomparisons of hygrometers during the time interval from 1800 to 1950. Possibly intercomparisons have been performed during this period but the results were hidden in technical and annual reports which are difficult to access now (or the results were not documented at all). Today one wishes that more intercomparisons would have been published in past times since the intercomparisons permit the harmonization of long-term series of humidity.

Daniell (1820) invented the dew point hygrometer with cooling by evaporation of ether. The instrument is explained in the middle and right-hand-side graph of Fig. 11.7. Ether evaporates within the bulb A and condensates inside the bulb D which is cooled from outside by liquid ether. In the moment of the appearance of a dew ring around the bulb A, the thermometer of bulb A gives the dew point temperature. Daniell (1820) presented coincident measurements of the dew point hygrometer and De Luc's hygrometer. A quantification of the differences of both hygrometers might be possible by means of Daniell's measurement tables. Daniell (1823) reported that a passage in Pliny the Elder's Naturalis Historia gave him in 1812 the idea to invent the dew point hygrometer which is still one of the most accurate instruments for humidity measurement.

Trowbridge (1896) compared the hair hygrometer to the wet- and dry-bulb thermometer. Differences of about 1–3 % were obtainded in the relative humidity range

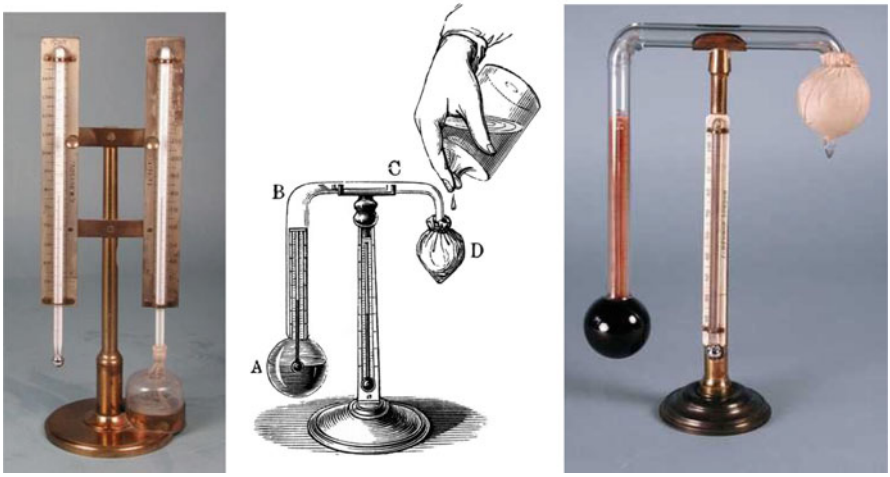

Fig. 11.7 *Left* Wet and dry bulb hygrometer sold by J. M. Bryson (Edinburgh) around 1870. *Middle* Scheme of Daniell's dew point hygrometer (courtesy of Wikipedia). *Right* Daniell's dew point hygrometer by J. Newman (London) around 1830. Photograph copyright and courtesy of http://www.freunde-alter-wetterinstrumente.de

from 20 to 85 %. Day (1908) reported about health implications of dry air indoors during wintertime and compared measurements of Regnault's hygrometer, sling psychrometer, stationary psychrometer, and chemical hygrometer. He found a close agreement between the chemical hygrometer and the sling psychrometer at the lower humidities (ca. 1 % difference for relative humidities at 20–30 %).

A chemical hygrometer measures the air volume difference when water vapour is extracted from air by means of a chemical absorbent (e.g., sulfuric acid). Carpenter (1935) described this measurement technique in detail and utilized the chemical hygrometer for calibration of psychrometers. Intercomparisons of coincident measurements of the same air currents by several chemical hygrometers gave a random error of about 0.02 % for relative humidities between 0.3 and 2.2 %. The reader is referred to the textbook of Sonntag (1966) which describes history and optimization processes of all kind of hygrometers during the past 250 years.

Passive microwave remote sensing from ground and aircraft was pioneered by Dicke et al. (1946). They introduced theory, measurement technique, and data analysis of a microwave radiometer operated close to the 22 GHz line of water vapour. However, ground-based profiling of water vapour in the middle atmosphere had to wait about 30 years longer (Radford et al. 1977). Staelin (1969) gave a review of the earlier days of passive microwave remote sensing and presented intercomparisons of 22 GHz line profiles from ground-based microwave radiometers and those derived from radiosonde humidity observations by means of radiative transfer calculation.

Brewer et al. (1948) extended the temperature range of the dew point hygrometer by cooling the mirror with liquid air. They measured frost point temperatures down to −100 °C during an aircraft flight. Thus the frost point hygrometer of Brewer et al. (1948) was capable to measure the absolute humidity of the extreme dry air of the

upper troposphere and lower stratosphere. Brewer et al. (1948) speculated that only a solar radiation absorption method could be an alternative at upper altitudes. Barrett et al. (1949) launched a photoelectric frost point hygrometer on a balloon radiosonde and measured water vapour up to 30 km altitude. They also observed a saturated layer just below the tropopause. Brewer (2009) provided a vivid retrospective of the discovery of stratospheric dryiness.

Fowle (1912) explored the 1.13μ and 1.47μ infrared absorption bands of atmospheric water vapour in the solar spectrum and determined water vapour columns. Infra-red solar spectroscopy in a high-altitude aircraft was firstly employed by Yarnell and Goody (1952) who observed the $6.3\,\mu$ absorption band of atmospheric water vapour at about 11 km altitude. Houghton and Seeley (2006) compared infrared solar spectroscopic observations with coincident measurements of a frost point hygrometer. They obtained a close agreement of both techniques yielding a typical error of about $2-3\,^{\circ}$C for frost point temperature at the tropopause.

Murcray et al. (1962) presented an intercomparison of infrared sun seeking spectrometers, frost point hygrometers, and cooled vapour trap observations. The vertical profiles of the H_2O mass mixing ratio from the surface to the mid-stratosphere are shown in Fig. 11.8. The quality of this intercomparison study is astonishing – almost comparable with present day field campaigns. However it seems that stratospheric water vapour was overestimated by a factor of 8 since the measurement point of the cooled vapour trap at $h = 27\,$km in Fig. 11.8 corresponds with a H_2O volume mixing ratio of about 60 ppmV. The cooled-vapour trap measurement was adopted from Barclay et al. (1960). Gutnick (1961) was possibly a driving force for the intercomparison study of Murcray et al. (1962) since Gutnick emphasized the differences between humidity profiles obtained by English and US-American scientists.

The state-of-the-art of stratospheric humidity observations at the begin of the 1960s was further summarized by Grantham et al. (1964). At that time it was unclear if the systematic biases of the observations were due to atmospheric variability or to fundamental errors of measurement techniques and data analysis. Particularly there was no agreement if the H_2O volume mixing ratio starts to increase beyond the tropopause or if the mixing ratio remains constant (as preferred by the English scientists). Murcray et al. (1966) presented infrared spectrometer data showing an increase of stratospheric H_2O VMR with altitude and even more important, stratospheric H_2O VMR was now in the reasonable range between 3 and 10 ppmV.

Observations by balloon-borne frost point hygrometers were continued from the 1960s to the 1970s at Washington. Mastenbrook (1968) found that earlier balloon-borne measurements of stratospheric water vapour were contaminated by water vapour from the balloon and the instrument package. Frost point temperatures measured during descent were lower than during ascent of the balloon. The descending sondes of Mastenbrook (1968) were free of contaminations and measured values of about 6 ppmV for H_2O VMR at 28 km altitude. Mastenbrook (1974) reported about a temporal increase of stratospheric H_2O VMR from 3 to 5 ppmV at 28 km altitude over Washington D.C. Further a significant annual cycle of lower stratospheric water vapour was found in the time series. Farmer (1974) presented stratospheric

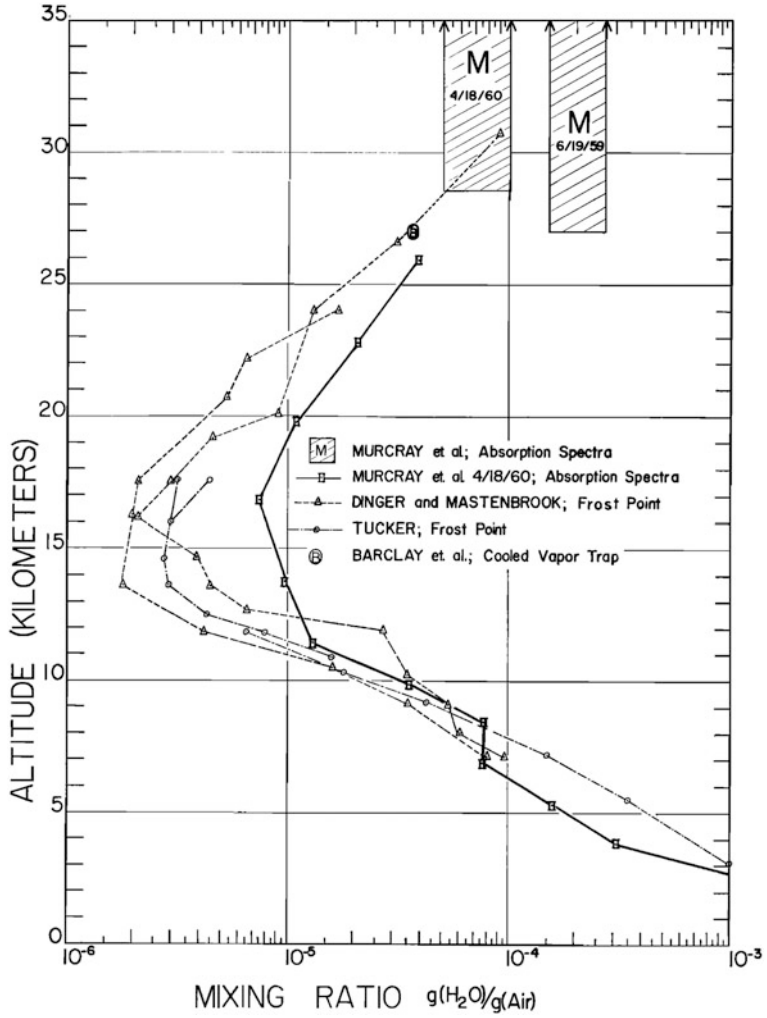

Fig. 11.8 Possibly the first high-quality intercomparison of profiles of H_2O mass mixing ratio observed by three different measurement techniques. Courtesy of Murcray et al. (1962)

water vapour measurements of airborne infrared spectrometers giving volume mixing ratios between 2 and 3 ppmV at 16 km altitude and at various latitudes.

Melfi et al. (1969) introduced a new remote sensing technique: Raman scattering by water vapour in the lower and middle troposphere. Comparisons of water vapour profiles observed by Raman lidar and radiosonde were presented by Melfi (1972).

The review article of Harries (1976) about stratospheric water vapour is a good closure of the historical part of our survey. Harries summarized the situation of stratospheric water vapour observations. At that time, stratospheric water vapour below 40 km altitude was generally found to lie in the range from 0.8 to 8 ppmV,

a maximum of stratospheric water vapour was observed over the equator, and an annual cycle was known.

Harries assumed that a part of the divergence in the water vapour observations was of instrumental origin. He concluded that more international collaborations are needed for finding of systematic errors, harmonization of the observations, optimal retrieval of a water vapour climatology, and integration of observational data into atmospheric models ("*It therefore seems imperative that workers, either by personal initiative or under an international program, should combine to compare their instrumental sensitivities and errors so that some standardization of results may be achieved.*"). This advice has been followed in the next three decades as shown by the rapid increase of intercomparison studies since 1977.

11.3 Recent Intercomparisons

We give a brief overview of intercomparisons of water vapour measurements since 1977. New measurement techniques and the growth of observational networks of satellites, ground stations, and airborne platforms led to a fast increase of intercomparisons.

The SPARC Assessment of Water Vapour comprises many of the measurement techniques and intercomparison activities until the year 2000 (Kley et al. 2000). The SPARC report summarized that a significant increase in the number and quality of stratospheric water vapour measurements occurred from 1975 to 2000, particularly with the advent of satellite observations. Stated accuracy of most in situ and remote instruments as well as direct or indirect comparisons of coincident field measurements cluster within a $\pm 10\,\%$ range. The SPARC report emphasized the task of long-term monitoring of water vapour in the upper troposphere and stratosphere. Rosenlof et al. (2001) analyzed ten data sets of stratospheric water vapour measurements covering the period 1954 to 2000. They found a positive trend of 10 %/decade and assumed a long-term change of transport of water vapour into the stratosphere as most probable cause. At the moment a new SPARC Assessment of Water Vapour is in work.

The present survey cannot be so detailed like the SPARC report, and it is impossible to describe all the intercomparisons of water vapour measurements since 1977. We just recall that microwave radiometry grew up in the 1980s (Chap. 5) while GPS remote sensing and ground-based FTIR (Chap. 6) in the 1990s. Terahertz remote sensing of water vapour has been successfully performed by the Odin/SMR satellite experiment since 2001 and is designated for other missions such as JEM/SMILES and PREMIER (Chap. 9). Inversion methods, intercomparison techniques, consideration of averaging kernels and multi-resolution for accurate intercomparisons enlarged since 1980 (Chap. 10).

An outstanding validation effort is the AquaVIT formal intercomparison of atmospheric water measurements (Saathoff et al. 2009). The AquaVIT measurement campaign performed a blind intercomparison of 22 in situ measurement instruments

of water vapour within the AIDA chamber. The AIDA chamber is calibrated by national standards and can set up levels of pressure, temperature, and water vapour volume mixing ratio which are typical for the middle/upper troposphere and the lower stratosphere up to about 20 km altitude. The in situ instruments achieved systematic errors less than 10 % for H_2O VMR $>$ 10 ppm. Only 2–3 measurement techniques achieved small systematic errors for H_2O VMR $<$ 10 ppm. The cryogenic frost point hygrometer (CFH) showed systematic errors less than 2 % and might be regarded as the winner. Though the results of the AquaVIT intercomparison are invaluable, additional errors of the in situ instruments may occur under flight conditions in the real atmosphere.

Another extraordinary intercomparison has been performed by McCormack et al. (2008) who validated predictions of mesospheric water vapour as deduced from the high-altitude NWP model NOGAPS-Alpha forecast by means of data assimilation of Aura/MLS data. The agreement between the predicted and observed water vapour distribution show the progress which has been achieved in modeling and observation of the middle atmosphere. Engelbart et al. (2006) give a detailed summary of the state of the art of integrating lidar, radar, radiometer, radiosonde, and other techniques for combined profiling of temperature, wind, water vapour, liquid water, and clouds.

11.3.1 Water Vapour Literature Database

The selection of the articles has been carried out by experts of the ISSI and COST working groups on atmospheric water vapour. All articles of the survey can be accessed via the new interactive Water Vapour Literature Database (http://www.watervapour.org).

The experts of the individual instrument groups inserted the references and the pdf-files of the relevant validation studies into the Water Vapour Literature Database. We apologize to all authors of validation studies which we missed to mention in the survey. All authors are invited to insert their studies into the Water Vapour Literature Database, since the present survey and our literature database are updated from time to time. The updated survey is available as a clickable pdf-file in the Water Vapour Literature Database.

The diversity of the "jungle" of water vapour measurements increases from year to year so that a loss of orientation could occur. The main work of the survey is to sort the validation studies of the Water Vapour Literature Database by means of tables which give a rough orientation about what has been achieved and which tasks are waiting. The survey and the literature database save time since each expert group or newcomer can take advantage of the knowledge and the articles of the other expert groups.

11.3.2 Classification of Measurement Techniques

It is useful to recall the measurement principles which exist for water vapour measurements. Various classifications of measurement techniques have been suggested.

Sonntag (1966) identified 16 different measurement techniques while the World Meteorological Organization (WMO 2008) suggested 5 major groups of measurement techniques of humidity. Considering their recommendations, we suggest a slightly modified classification into:

1. Sorption methods (change of properties of hygroscopic materials, e.g., electrical capacitance, hair length, weight, . . .)
2. Evaporation of water (psychrometer: temperature difference of wet and dry bulb)
3. Condensation of water vapour (measurement of dewpoint or frostpoint temperature with a chilled mirror)
4. Interaction of electromagnetic radiation and water vapour:
   a. absorption
   b. emission
   c. backscattering
   d. refraction
5. Other methods (e.g., ultrasonic wave speed, diffusion of water vapour, . . .) (Sonntag 1966)

The WMO classification group of gravimetric methods is now shifted into the group of sorption methods, and we introduce a rest group of "other methods". In addition, emission (e.g., microwave radiometry of thermal emission of water vapour), backscattering (e.g., lidar), and refraction (e.g., GPS signal path delay) of electromagnetic radiation are new subgroups which were not considered in the WMO guide (WMO 2008).

11.3.3 Tables of Intercomparison Studies

Kley et al. (2000) gave detailed descriptions of many of the instruments in the SPARC Assessment of Water Vapour which is a fundament of the present survey. The abbreviations of the instruments and satellite missions are explained by Table 11.1. It is evident that about 80 % of the experiments in Table 11.1 are from the group 4 (interaction of electromagnetic radiation and water vapour). Nevertheless the frost point hygrometers (group 3) and the capacitive humidity sensors (group 1) are crucial for in-situ measurements of atmospheric water vapour and for validation of remote sensing techniques of group 4.

Fluorescence hygrometers (e.g., FISH, FLASH) perform in-situ measurements of water vapour but actually it is a remote sensing technique. The instrument firstly dissociates water vapour molecules by transmission of Lyman-α radiation and secondly measures the fluorescence light of OH radicals. Thus the backscattering group 4c seems to be appropriate for fluorescence hygrometers.

Table 11.1 Explanation of abbreviation

Abbreviation	Explanation	cl.[a]
ACE/FTS	Atmospheric Chemistry Experiment, Fourier Transform Spectrometer	4a
AIRS	Atmospheric Infrared Sounder (Aqua satellite)	4a
ALIAS	Aircraft Laser Infrared Absorption Spectrometer	4c
AMIP	Atmospheric Model Intercomparison Project (14 GCMs)	–
AMSU	Advanced Microwave Sounding Unit (NOAA satellite)	4a
AMSOS	Airborne Microwave Stratospheric Observing System (lear jet)	4b
ATMOS	Infrared Fourier transform spectrometer (Spacelab 3)	4a
ATOVS	Advanced TIROS Operational Vertical Sounder	4a
Aura/MLS	Microwave Limb Sounder (Aura satellite)	4b
Aura/TES	Tropospheric Emission Sounder (Aura satellite)	4b
CAM	Community Atmosphere Model (NCAR)	–
CCGCM	Coupled Chemistry General Circulation Model	–
CFH	Cryogenic Frostpoint Hygrometer (Univ. of Colorado)	3
COSMO-EU	Consortium for Small-scale Modeling, European Union	–
CRISTA	Cryogenic Infrared Spectrometers and Telescopes for the Atmosphere	4a
DIAL	Differential Absorption Lidar	4c
ECMWF-Re	European Center for Medium-range Weather Forecast, Reanalysis	–
FISH	Fast In situ Stratospheric Hygrometer (Lyman-α fluorescence)	4c
FLASH-B	Fluorescent Advanced Stratospheric Hygrometer, Balloon	4c
FLASH-R	Fluorescent Advanced Stratospheric Hygrometer, Rocket	4c
FPH	Frost Point Hygrometer	3
FTIR	Fourier Transform Infrared Spectrometer (ground-based)	4a
FTV	Fourier Transform Visible Spectrometer (ground-based)	4a
GCMs	Set of General Circulation Models	–
GFDL	Geophys. Fluid Dyn. Lab. General Circulation model	–
GOES	Geostationary Operational Environmental Satellite	4a
GOME	Global Ozone Monitoring Experiment (ERS, Metop)	4a
GPS-Col	ground-based GPS receiver (water vapour column)	4d
GPS-RO	GPS Radio Occultation (water vapour profile)	4d
HALOE	Halogen Occultation Experiment (UARS satellite)	4a
Hammonia	Hamburg Model of the neutral and ionized atmosphere	–
Harv. Ly-α	Harvard Lyman-α fluorescence hygrometer	4c
HIRS	downlooking High-Resolution Infrared Radiation Sounder	4a
IASI	Infrared Atmosphering Sounding Interferometer	4a
ILAS-II	Improved Limb Atmosphere Spectrometer	4a
IMG/ADEOS	Interferometric Monitor for Greenhouse Gases (ADEOS satellite)	4a
Lagrange	Lagrangian advection-condensation model	–
LIMS	Limb Infrared Monitor of the Stratosphere (Nimbus-7 satellite)	4b
MAS	Millimeter-Wave Atmospheric Sounder (Space Shuttle)	4b
Meisei	Radiosonde RS2-91 Meisei Electric	1
METEOSAT	meteorological geostationary satellite	4a
MIPAS	Michelson Interferometer for Passive Atmospheric Sounding (ENVISAT)	4b
MM5	Mesoscale weather prediction model	–
MOZAIC	Measurement of OZone and water vapour by Airbus In-service airCraft)	1
MWR-S	Microwave radiometer, stratospheric profile	4b
MWR-T	Microwave radiometer, tropospheric profile and column	4b
NCEP-Re	National Centers for Environmental Prediction, Reanalysis (NCEP/NCAR)	–
Odin/SMR	Odin Sub-Millimetre Receiver (satellite experiment)	4b
POAM	Polar Ozone and Aerosol Measurement (sun occultation, satellite)	4a
Raman	Raman Lidar	4c
REMO	Regional Model (MPI for Meteorology)	–

Table 11.1 (continued)

Abbreviation	Explanation	cl.[a]
RS80	Vaisala Radiosonde RS80	1
RS92	Vaisala Radiosonde RS92	1
SAGE-II	Stratospheric Aerosol and Gas Experiment II (ERBS satellite)	4a
SAW	Surface Acoustic Wave Dew Point Hygrometer	3
SCIAMACHY	Scanning Imaging Absorption Spectrometer (ENVISAT)	4a
SEVIRI	Spinning Enhanced Visible and InfraRed Imager (Meteosat satellite)	4a
SnowWhite	Meteolabor chilled-mirror hygrometer	3
SPM	Sun photometer	4a
SPURT	Spurenstoff (trace gas) transport in the tropopause region (aircraft)	1
Sippican	Sippican (VIZ) resistive hygristor	1
SSM/I	Special Sensor Microwave Imager	4a
TDL	tunable diode laser hygrometer	4c
tmt	trajectory mapping technique	–
TRMM/TMI	Tropical Rainfall Meas. Mission / Tropical Microwave Imager	4a
UARS/MLS	Microwave Limb Sounder (UARS satellite)	4b
UM	Unified Model (MetOffice and Hadley Centre)	–
WACCM	Whole Atmosphere Community Climate Model	–
WALES	Water Vapour Lidar Experiment in Space	4c

[a] According to the classification scheme at begin of 11.3.2

Six tables are presented containing intercomparisons of instruments with respect to in situ techniques, ground-based, airborne, and spaceborne remote sensing. The fields of the tables contain numbers which are linked to reference tables in Sect. 11.4. The reference tables are further linked to the bibliography and to pdf-files of the Water Vapour Literature Database (the most actual and clickable pdf-file of the survey is available in the literature database or can be directly requested by the authors). Some compromise has been made since there was not enough space to list each type of hygrometer sensor on radiosondes. Some intercomparison studies do not provide any information about the hygrometer sensor on the radiosonde. Table 11.4 is a bit mixed since it includes DIAL airborne-airborne and airborne-groundbased intercomparisons. However we hope that the readers can use the tables to get a quick overview on the intercomparison studies of various measurement techniques since 1977.

If all hyperlinks of the survey pdf-file do not work, then it could depend on browser settings of your computer. Further it is useful to know about back and forward buttons of the pdf-viewer, so that you can switch from the table field to the reference and back again. In some applications you can find the buttons in the menue panel, otherwise you may try combinations on your keyboard, e.g., alt and cursor arrow or apple and cursor arrow.

Table 11.2 Intercomparisons of H_2O measurements with respect to *in situ* techniques (field number 1.2(3) stands for 3 publications in row 1 and column 2)

	RS80	RS90	RS92	Sippican	FPH	CFH	SnowWhite
RS80	1.1(2)	1.2(3)	1.3(1)	1.4(1)	1.5(2)	1.6(2)	1.7(4)
RS90	2.1(2)	[]	2.3(1)	2.4(2)	[]	2.6(2)	2.7(2)
RS92	[]	[]	[]	3.4(1)	[]	3.6(3)	3.7(2)
Sippican	4.1(1)	4.2(2)	4.3(1)	[]	[]	4.6(1)	4.7(3)
FPH	5.1(3)	[]	[]	[]	[]	5.6(1)	5.7(2)
CFH	6.1(1)	[]	6.3(3)	[]	6.5(1)	6.6(1)	6.7(4)
SnowWhite	7.1(5)	7.2(4)	7.3(3)	7.4(3)	7.5(1)	7.6(3)	7.7(1)
Harv.Ly-α	[]	[]	[]	[]	8.5(1)	8.6(1)	[]
FLASH-B	[]	[]	[]	[]	9.5(1)	9.6(1)	[]
Absorption[d]	[]	[]	[]	[]	10.5(1)	[]	[]
Raman	11.1(4)	11.2(1)	11.3(2)	[]	11.5(1)	11.6(2)	11.7(2)
DIAL	12.1(7)	[]	12.3(1)	[]	12.5(2)	[]	[]
FTIR	13.1(1)	[]	[]	[]	[]	[]	[]
FTV	[]	14.2(1)	[]	[]	[]	[]	[]
MWR-T	15.1(2)	15.1(1)	15.3(2)	15.4(4)	[]	[]	[]
SPM	16.1(1)	[]	[]	16.4(1)	[]	[]	[]
GPS-Col	17.1(2)	17.2(3)	17.3(1)	17.4(1)	[]	[]	[]
GPS-RO	18.1(1)[b]	[]	18.3(1)	[]	[]	[]	[]
Aura/MLS	[]	19.2(1)	19.3(1)	[]	[]	19.6(3)	[]
UARS/MLS	20.1(1)	[]	[]	[]	20.5(4)	[]	[]
LIMS	[]	[]	[]	[]	21.5(1)	[]	[]
Aura/TES	[]	22.2(1)	22.3(1)	[]	[]	22.6(1)	[]
HALOE	[]	[]	[]	[]	23.5(3)	[]	[]
SAGE-II	24.1(2)	[]	[]	24.4(1)	[]	24.6(1)	[]
ACE/FTS	[]	[]	[]	[]	25.5(1)	25.6(1)	[]
MIPAS	[]	[]	[]	[]	26.5(1)	[]	[]
Odin/SMR	[]	[]	[]	[]	[]	[]	[]
POAM	[]	[]	[]	[]	28.5(2)	[]	[]
AMSU	29.1(1)[a]	[]	[]	[]	[]	[]	[]
AIRS	30.1(1)	30.2(1)	30.3(1)	30.4(1)	[]	30.6(1)	30.7(1)
GOES	31.1(1)	2.31(1)	[]	[]	[]	[]	[]
SEVIRI	32.1(1)[c]	[]	[]	[]	[]	[]	[]
MOZAIC	33.1(1)	[]	[]	[]	33.5(2)	[]	[]
AMSOS	[]	[]	[]	[]	[]	[]	[]
ECMWF-Re	35.1(1)	[]	[]	35.4(1)	35.5(1)	[]	35.7(1)
Dropsonde	36.1(2)	36.2(1)	[]	[]	[]	[]	36.7(1)
ATOVS	37.1(1)	[]	[]	[]	[]	[]	[]
TRMM/TMI	38.1(1)	38.2(1)	38.3(1)	[]	[]	[]	[]
IMG/ADEOS	39.1(1)	[]	[]	[]	[]	[]	[]
TDL	[]	[]	[]	[]	40.5(1)	40.6(1)	[]
METEOSAT	41.1(1)	[]	[]	[]	[]	[]	[]
CCGCM	42.1(1)	[]	[]	[]	42.5(1)	[]	[]
SAW	43.1(1)	[]	[]	[]	43.5(2)	[]	[]

[a] Upper tropospheric humidity (UTH)
[b] Various radiosondes from worldwide network
[c] IWV of various radiosondes

Table 11.3 Intercomparisons of H_2O measurements with respect to *in situ* techniques (field number 6.1(2) stands for 2 publications in row 6 and column 1)

	Harv.Ly-α	FLASH-B	FISH	NOAA Ly-α	TDL
RS80	[]	1.2(1)	[]	[]	[]
RS90	[]	2.2(2)	[]	[]	[]
RS92	[]	3.2(2)	[]	[]	[]
Sippican	[]	[]	[]	[]	[]
FPH	[]	[]	5.3(2)	5.4(1)	[]
CFH	6.1(2)	6.2(4)	[]	[]	[]
SnowWhite	[]	7.2(1)	[]	[]	[]
Harv.Ly-α	[]	[]	[]	[]	8.5(3)
FLASH-B	[]	[]	9.3(1)	[]	[]
TDL	10.1(3)	[]	[]	[]	[]
Raman	[]	[]	[]	[]	[]
DIAL	[]	[]	[]	[]	[]
FTIR	[]	[]	[]	[]	[]
MWR-T	[]	[]	[]	[]	[]
SPM	15.1(1)	[]	[]	[]	[]
GPS-Col	[]	[]	[]	[]	[]
GPS-RO	[]	[]	[]	[]	[]
Aura/MLS	18.1(1)	[]	[]	[]	[]
UARS/MLS	19.1(1)	[]	[]	[]	[]
LIMS	[]	[]	[]	20.4(1)	[]
Aura/TES	[]	[]	[]	[]	[]
ATMOS	22.1(1)	[]	[]	22.4(1)	[]
HALOE	23.1(1)	[]	23.3(1)	[]	[]
SAGE-II	[]	[]	[]	24.4(1)	[]
ACE/FTS	[]	[]	[]	[]	[]
CRISTA	[]	[]	26.3(1)	[]	[]
MIPAS	[]	27.2(1)	27.3(1)	[]	[]
Odin/SMR	[]	[]	[]	[]	[]
POAM	29.1(2)	[]	29.3(1)	[]	29.5(1)
AMSU	[]	[]	[]	[]	[]
AIRS	31.1(1)	[]	[]	[]	[]
SEVIRI	[]	[]	[]	[]	[]
MOZAIC	[]	[]	33.3(2)	33.4(1)	[]
AMSOS	[]	34.2(1)	34.3(2)	[]	[]
ECMWF-Re	[]	35.2(1)	[]	[]	[]
FLASH-R	[]	36.2(1)	[]	[]	[]
GOME	[]	[]	37.3(1)	[]	[]
SAW	[]	[]	[]	[]	38.5(1)

Table 11.4 Intercomparisons of H_2O measurements with respect to ground and airborne remote sensing

	Raman	DIAL	FTIR	MWR-T	MWR-S	limb occult.[a]	limb emiss.[a]	emission[a]
RS80	1.1(9)	1.2(5)	1.3(5)	1.4(3)	[]	[]	1.7(1)	[]
RS90	2.1(1)	2.2(1)	2.3(1)	[]	[]	[]	[]	[]
RS92	3.1(3)	3.2(2)	3.3(4)	3.4(2)	[]	[]	[]	[]
Sippican	4.1(1)	4.2(1)	[]	4.4(8)	[]	[]	[]	[]
FPH	5.1(1)	5.2(3)	[]	[]	5.5(1)	[]	5.7(1)	[]
CFH	6.1(2)	[]	[]	[]	6.5(1)	[]	[]	[]
SnowWhite	7.1(2)	7.2(1)	[]	[]	[]	[]	[]	[]
Harv.Ly-α	[]	[]	[]	[]	[]	[]	[]	[]
FLASH-B	[]	9.2(1)	[]	[]	9.5(1)	[]	[]	[]
FISH	[]	10.2(1)	[]	[]	[]	[]	[]	[]
Dropsonde	[]	11.2(1)	[]	[]	[]	[]	[]	[]
Raman	12.1(3)	12.2(4)	12.3(1)	12.4(2)	[]	[]	[]	[]
DIAL	13.1(1)	13.2(2)	[]	13.4(2)	[]	[]	[]	[]
FTIR	14.1(1)	[]	14.3(1)	14.4(2)	[]	[]	[]	[]
MWR-T	15.1(3)	15.2(1)	15.3(1)	15.4(2)	15.5(1)	[]	[]	[]
SPM	[]	16.2(2)	16.3(4)	16.4(3)	[]	[]	[]	[]
GPS-Col	17.1(2)	[]	17.3(1)	17.4(7)	[]	[]	[]	[]
GPS-RO	[]	[]	[]	[]	[]	[]	[]	[]
Aura/MLS	19.1(1)	[]	19.3(1)	[]	19.5(4)	[]	[]	[]
UARS/MLS	[]	[]	[]	[]	20.5(3)	[]	20.7(1)	[]
Aura/TES	[]	[]	[]	[]	[]	[]	[]	[]
ATMOS	[]	[]	[]	[]	22.5(1)	22.6(1)	[]	[]
LIMS	[]	[]	[]	[]	[]	23.6(1)	23.7(1)	23.8(2)
HALOE	[]	[]	[]	[]	24.5(8)	[]	[]	24.8(1)
SAGE-II	[]	[]	[]	[]	[]	[]	[]	[]
ACE/FTS	26.1(1)	[]	[]	[]	26.5(1)	[]	[]	[]
MIPAS	[]	27.2(1)	[]	[]	27.5(2)	[]	27.7(1)	[]
Odin/SMR	[]	[]	[]	[]	[]	[]	[]	[]
POAM	[]	[]	[]	[]	29.5(2)	[]	[]	[]
AMSU	[]	[]	30.3(1)	[]	[]	[]	[]	[]
AIRS	31.1(1)	[]	[]	31.4(1)	[]	[]	[]	[]
GOES	32.1(1)	[]	[]	[]	[]	[]	[]	[]
SEVIRI	[]	[]	[]	[]	[]	[]	[]	[]
MOZAIC	[]	[]	[]	[]	[]	[]	[]	[]
AMSOS	[]	35.2(1)	[]	[]	35.5(1)	[]	[]	[]
ECMWF-Re	[]	36.2(2)	[]	36.4(1)	[]	[]	[]	[]
REMO	[]	37.2(1)	[]	[]	[]	[]	[]	[]
limb emiss.[a]	[]	[]	[]	[]	[]	38.6(1)	38.7(1)	38.8(1)
emission[a]	[]	[]	[]	[]	[]	39.6(1)	39.7(1)	39.8(1)
absorption[a]	[]	[]	[]	[]	[]	40.6(1)	40.7(1)	40.8(1)
MWR-S	[]	[]	[]	[]	41.5(3)	[]	[]	[]
SCIAMACHY	[]	[]	42.3(1)	[]	[]	[]	[]	[]
MM5	[]	43.2(1)	[]	[]	[]	[]	[]	[]

[a] Balloon-borne

Table 11.5 Intercomparisons of H_2O measurements with respect to airborne and spaceborne instruments

	MOZAIC	AMSOS	GPS-RO	GPS-Col	Aura/MLS	UARS/MLS	IASI	MAS	GOME	SCIAMACHY
MOZAIC	[]	[]	[]	[]	1.5(1)	1.6(2)	[]	[]	[]	[]
SPURT	2.1(1)	[]	[]	[]	[]	[]	[]	[]	[]	[]
AMSOS	[]	[]	[]	[]	3.5(1)	[]	[]	[]	[]	[]
GPS-RO	[]	[]	[]	[]	[]	[]	[]	[]	[]	[]
GPS-Col	[]	[]	[]	5.4(1)	[]	[]	[]	[]	[]	[]
MWR-T	[]	[]	[]	[]	[]	6.6(2)	[]	[]	[]	[]
Aura/MLS	[]	[]	[]	[]	7.5(1)	[]	[]	[]	[]	[]
Aura/TES	[]	[]	[]	[]	[]	[]	[]	[]	[]	[]
HALOE	9.1(1)	9.2(1)	[]	[]	9.5(2)	9.6(2)	[]	[]	[]	[]
SAGE-II	[]	[]	[]	[]	10.5(1)	10.6(1)	[]	[]	[]	[]
ACE/FTS	[]	[]	[]	[]	11.5(1)	[]	[]	[]	[]	[]
CRISTA	[]	[]	[]	[]	[]	12.6(1)	[]	[]	[]	[]
MIPAS	13.1(1)	13.2(2)	[]	[]	13.5(4)	[]	[]	[]	[]	[]
Odin/SMR	14.1(2)	14.2(1)	[]	[]	14.5(2)	[]	[]	[]	[]	[]
POAM	[]	15.2(1)	[]	[]	15.5(1)	[]	[]	[]	[]	[]
AIRS	[]	[]	16.3(1)	16.4(2)	16.5(3)	[]	[]	[]	[]	[]
HIRS	[]	[]	[]	[]	[]	[]	[]	[]	[]	[]
LIMS	[]	[]	[]	[]	[]	[]	[]	[]	[]	[]
ATMOS	[]	[]	[]	[]	[]	19.6(2)	[]	19.8(1)	[]	[]
ECMWF-Re	20.1(2)	20.2(2)	20.3(1)	20.4(1)	20.5(1)	20.6(1)	[]	[]	20.9(2)	20.10(3)
NCEP-Re	[]	[]	21.3(1)	21.4(1)	[]	[]	[]	[]	[]	[]
COSMO-EU	[]	[]	[]	[]	[]	22.6(1)	[]	[]	[]	[]
Meisei	[]	[]	[]	23.4(1)	[]	[]	[]	[]	[]	[]
tmt	[]	[]	[]	[]	[]	24.6(1)	[]	[]	[]	[]
GOME	[]	[]	[]	[]	[]	[]	[]	[]	[]	25.10(1)
ALIAS	[]	[]	[]	[]	26.5(1)	[]	[]	[]	[]	[]
WALES	[]	[]	[]	[]	[]	[]	27.7(1)	[]	[]	[]
SPM	[]	[]	[]	28.4(1)	[]	[]	[]	[]	[]	[]
SSM/I	[]	[]	[]	[]	[]	[]	[]	[]	29.9(1)	29.10(2)

Table 11.6 Intercomparisons of H_2O measurements with respect to airborne and spaceborne instruments

	HALOE	SAGE-II	ACE/FTS	MIPAS	Odin/SMR	POAM
MOZAIC	6-1.1(1)	[]	[]	6-1.4(1)	6-1.5(2)	[]
SPURT	[]	[]	6-2.3(1)	[]	[]	[]
AMSOS	6-3.1(1)	[]	[]	6-3.4(2)	6-3.5(1)	6-3.6(1)
GPS-RO	[]	[]	[]	[]	[]	[]
GPS-Col	[]	[]	[]	[]	[]	[]
Aura/MLS	6-6.1(2)	6-6.2(1)	6-6.3(1)	6-6.4(4)	6-6.5(2)	6-6.6(1)
UARS/MLS	6-7.1(3)	6-7.2(1)	[]	[]	6-7.5(1)	[]
Aura/TES	[]	[]	[]	[]	[]	[]
HALOE	[]	6-9.2(1)	6-9.3(2)	6-9.4(1)	6-9.5(2)	6-9.6(3)
SAGE-II	6-10.1(1)	[]	6-10.3(1)	[]	6-10.5(1)	6-10.6(1)
ACE/FTS	6-11.1(2)	6-11.2(1)	[]	6-11.4(2)	6-11.5(3)	6-11.6(1)
MIPAS	6-12.1(1)	[]	6-12.3(1)	[]	6-12.5(1)	[]
Odin/SMR	6-13.1(1)	[]	6-13.3(2)	[]	[]	[]
POAM	6-14.1(4)	6-14.2(1)	6-14.3(1)	6-14.4(1)	[]	[]
AIRS	[]	[]	[]	[]	[]	[]
HIRS	[]	[]	[]	[]	[]	[]
LIMS	[]	6-17.2(2)	[]	[]	[]	[]
ATMOS	6-18.1(2)	6-18.2(2)	[]	[]	[]	[]
ECMWF-Re	6-19.1(1)	6-19.2(1)	[]	[]	[]	[]
NCEP-Re	[]	[]	[]	[]	[]	[]
ILAS-II	[]	[]	[]	6-21.4(2)	[]	[]
Hammonia	[]	[]	[]	[]	6-22.5(1)	[]
WACCM	[]	[]	[]	[]	6-23.5(1)	[]
CAM	[]	[]	[]	[]	[]	[]
GCMs	[]	[]	[]	[]	[]	[]
Lagrange	[]	[]	[]	[]	[]	[]
GFDL	[]	[]	[]	[]	[]	[]
UM	6-28.1(1)	[]	[]	[]	[]	[]
1-D model	[]	6-29.2(1)	[]	[]	[]	[]

Table 11.7 Intercomparisons of H_2O measurements with respect to airborne and spaceborne instruments

	AIRS	AMSU	SSM/I	METEOSAT	LIMS
MOZAIC	[]	[]	[]	[]	[]
SPURT	[]	[]	[]	[]	[]
AMSOS	[]	[]	[]	[]	[]
GPS-RO	[]	[]	[]	[]	[]
GPS-Col	7-5.1(1)	7-5.2(1)	[]	[]	[]
Aura/MLS	7-6.1(3)	[]	[]	[]	[]
UARS/MLS	[]	[]	[]	[]	[]
Aura/TES	[]	[]	[]	[]	[]
HALOE	[]	[]	[]	[]	[]
SAGE-II	[]	[]	[]	[]	[]
ACE/FTS	[]	[]	[]	[]	[]
MIPAS	[]	[]	[]	[]	[]
Odin/SMR	[]	[]	[]	[]	[]
POAM	[]	[]	[]	[]	[]
AIRS	[]	7-15.2(2)	[]	[]	[]
HIRS	[]	7-16.2(1)	7-16.3(1)	7-16.4(1)	[]
LIMS	[]	[]	[]	[]	[]
ATMOS	[]	[]	[]	[]	7-18.5(1)
ECMWF-Re	7-19.1(2)	7-19.2(1)	[]	[]	[]
NCEP-Re	[]	7-20.2(1)	[]	[]	[]
ILAS-II	[]	[]	[]	[]	[]
Hammonia	[]	[]	[]	[]	[]
WACCM	[]	[]	[]	[]	[]
CAM	7-24.1(2)	[]	[]	[]	[]
GCMs	[]	7-25.2(1)	[]	[]	[]
Lagrange	[]	7-26.2(1)	[]	[]	[]
GFDL	[]	[]	7-27.3(1)	[]	[]
AMIP	[]	[]	[]	7-28.4(1)	[]

11.4 Reference Tables

Now the columns of the tables 11.2 to 11.6 are listed, and literature references are given for each table field. The field is indexed by (table number – row.column), e.g., (2-18.6) refers to the field at row 18 and column 6 of Table 11.2.

RS80

Field	Versus	Article	Field	Versus	Article
2-1.1	RS80	Wang et al. (2002)	2-1.1	RS80	Elliott and Gaffen (1993)
2-2.1	RS90	Miloshevich et al. (2006)	2-2.1	RS90	Vance et al. (2004)
2-2.1	RS90	Sapucci et al. (2005)	2-4.1	Sippican	Sapucci et al. (2005)
2-5.1	FPH	Vömel et al. (2003)	2-5.1	FPH	Miloshevich et al. (2004)
2-5.1	FPH	Kley et al. (1997)	2-6.1	CFH	Whiteman et al. (2006)
2-7.1	SnowWhite	Miloshevich et al. (2006)	2-7.1	SnowWhite	Fujiwara et al. (2003)
2-7.1	SnowWhite	Whiteman et al. (2006)	2-7.1	SnowWhite	Wang et al. (2003)
2-7.1	SnowWhite	Sapucci et al. (2005)	2-11.1	Raman	Ferrare et al. (1995)
2-11.1	Raman	Ferrare et al. (2000a)	2-11.1	Raman	Turner et al. (2000)
2-11.1	Raman	Sherlock et al. (1999)	2-11.1	Raman	Whiteman et al. (2006)
2-12.1	DIAL	Ferrare et al. (2000b)	2-12.1	DIAL	Vogelmann et al. (2006)
2-12.1	DIAL	Browell et al. (1979)	2-12.1	DIAL	Machol et al. (2004)
2-12.1	DIAL	Vogelmann and Trickl (2008)	2-12.1	DIAL	Steinhagen et al. (1998)
2-12.1	DIAL	Wulfmeyer and Bösenberg (1998)	2-12.1	DIAL	Browell et al. (1998)
2-13.1	FTIR	Turner et al. (2000)	2-15.1	MWR-T	Turner et al. (2000)
2-15.1	MWR-T	Solheim and Godwin (1998)	2-16.1	SPM	Steinhagen et al. (1998)
2-17.1	GPS-Col	Wang and Zhang (2008)	2-17.1	GPS-Col	Wang and Zhang (2008)
2-18.1	GPS-RO	Heise et al. (2006)	2-20.1	UARS/MLS	Read et al. (2001)
2-24.1	SAGE-II	Larsen et al. (1993)	2-24.1	SAGE-II	Rind et al. (1993)
2-29.1	AMSU	Buehler et al. (2008)	2-30.1	AIRS	Miloshevich et al. (2006)
2-31.1	GOES	Soden et al. (2004)	2-32.1	SEVIRI	Schroedter-Homscheidt et al. (2008)
2-33.1	MOZAIC	Vaughan et al. (2005)	2-35.1	ECMWF-Re	Spichtinger et al. (2005)
2-36.1	Dropsonde	Vance et al. (2004)	2-36.1	Dropsonde	Kley et al. (1997)
2-37.1	ATOVS	Schulz et al. (2009)	2-38.1	TRMM/TMI	Holloway and Neelin (2009)
2-39.1	IMG/ADEOS	Herbin et al. (2007)	2-41.1	METEOSAT	Brogniez et al. (2006)
2-42.1	CCGCM	Sun and Held (1996)	2-43.1	SAW	Cardell et al. (2001)

RS90

Field	Versus	Article	Field	Versus	Article
2-1.2	RS80	Suortti et al. (2008)	2-1.2	RS80	Vance et al. (2004)
2-1.2	RS80	Sapucci et al. (2005)	2-4.2	Sippican	Sapucci et al. (2005)
2-4.2	Sippican	Mattioli et al. (2007)	2-7.2	SnowWhite	Miloshevich et al. (2006)
2-7.2	SnowWhite	Vance et al. (2004)	2-7.2	SnowWhite	Mattioli et al. (2007)
2-7.2	SnowWhite	Sapucci et al. (2005)	2-11.2	Raman	Soden et al. (2004)
2-14.2	FTV	Coheur et al. (2003)	2-15.2	MWR-T	Mattioli et al. (2007)
2-17.2	GPS-Col	Wang et al. (2007)	2-17.2	GPS-Col	Wang and Zhang (2008)
2-17.2	GPS-Col	Mattioli et al. (2007)	2-19.2	Aura/MLS	Read et al. (2007)
2-22.2	Aura/TES	Shephard et al. (2008)	2-30.2	AIRS	Miloshevich et al. (2006)
2-31.2	GOES	Soden et al. (2004)	2-36.2	Dropsonde	Vance et al. (2004)
2-38.2	TRMM/TMI	Holloway and Neelin (2009)			

RS92

Field	Versus	Article	Field	Versus	Article
2-1.3	RS80	Suortti et al. (2008)	2-2.3	RS90	Suortti et al. (2008)
2-4.3	Sippican	Nash et al. (2006)	2-6.3	CFH	Vömel et al. (2007c)
2-6.3	CFH	Miloshevich et al. (2009)	2-6.3	CFH	Whiteman et al. (2006)
2-7.3	SnowWhite	Miloshevich et al. (2006)	2-7.3	SnowWhite	Whiteman et al. (2006)
2-7.3	SnowWhite	Nash et al. (2006)	2-11.3	Raman	Leblanc et al. (2008)
2-11.3	Raman	Whiteman et al. (2006)	2-12.3	DIAL	Vogelmann and Trickl (2008)
2-15.3	MWR-T	Fiorucci et al. (2008)	2-15.3	MWR-T	Miloshevich et al. (2009)
2-17.3	GPS-Col	Wang and Zhang (2008)	2-18.3	GPS-RO	Chou et al. (2009)
2-19.3	Aura/MLS	Read et al. (2007)	2-22.3	Aura/TES	Shephard et al. (2008)
2-30.3	AIRS	Miloshevich et al. (2006)	2-38.3	TRMM/TMI	Holloway and Neelin (2009)

Sippican

Field	Versus	Article	Field	Versus	Article
2-1.4	RS80	Sapucci et al. (2005)	2-2.4	RS90	Suortti et al. (2008)
2-2.4	RS90	Sapucci et al. (2005)	2-3.4	RS92	Miloshevich et al. (2006)
2-7.4	SnowWhite	Nash et al. (2006)	2-7.4	SnowWhite	Miloshevich et al. (2006)
2-7.4	SnowWhite	Sapucci et al. (2005)	2-15.4	MWR-T	Morland et al. (2009)
2-15.4	MWR-T	Martin et al. (2006a)	2-15.4	MWR-T	Cimini et al. (2006)
2-15.4	MWR-T	Ingold et al. (1998)	2-16.4	SPM	Morland et al. (2009)
2-17.4	GPS-Col	Guerova et al. (2006)	2-24.4	SAGE-II	Larsen et al. (1993)
2-30.4	AIRS	Miloshevich et al. (2006)	2-35.4	ECMWF-Re	Morland et al. (2009)

FPH

Field	Versus	Article	Field	Versus	Article
2-1.5	RS80	Miloshevich et al. (2004)	2-1.5	RS80	Kley et al. (1997)
2-6.5	CFH	Vömel et al. (2007a)	2-7.5	SnowWhite	Vömel et al. (2003)
2-8.5	Harv. Ly-α	Vömel et al. (2007b)	2-9.5	FLASH-B	Vömel et al. (2007b)
2-10.5	absorption	Ellsaesser et al. (1980)	2-11.5	Raman	Ferrare et al. (1995)
2-12.5	DIAL	Ferrare et al. (2000b)	2-12.5	DIAL	Ehret et al. (1993)
2-20.5	UARS/MLS	Lahoz et al. (1996)	2-20.5	UARS/MLS	Pumphrey (1999)
2-20.5	UARS/MLS	Pumphrey (1999)	2-20.5	UARS/MLS	Read et al. (2001)
2-21.5	LIMS	Remsberg et al. (1984)	2-23.5	HALOE	Harries et al. (1996)
2-23.5	HALOE	Scherer et al. (2008)	2-23.5	HALOE	Randel et al. (2006)
2-25.5	ACE/FTS	Carleer et al. (2008)	2-26.5	MIPAS	Milz et al. (2009b)
2-28.5	POAM	Lumpe et al. (2006)	2-28.5	POAM	Randel et al. (2006)
2-33.5	MOZAIC	Helten et al. (1998)	2-33.5	MOZAIC	Helten et al. (1999)
2-35.5	ECMWF-Re	Ovarlez van Velthoven (1997)	2-40.5	TDL	Read et al. (2007)
2-42.5	CCGCM	Stenke and Grewe (2005)	2-43.5	SAW	Cardell et al. (2001)

CFH

Field	Versus	Article	Field	Versus	Article
2-1.6	RS80	Suortti et al. (2008)	2-1.6	RS80	Miloshevich et al. (2001)
2-1.6	RS80	Whiteman et al. (2006)	2-2.6	RS90	Haefele (2005)
2-2.6	RS90	Suortti et al. (2008)	2-3.6	RS92	Haefele (2005)
2-3.6	RS92	Suortti et al. (2008)	2-3.6	RS92	Whiteman et al. (2006)
2-3.6	RS92	Miloshevich et al. (2009)	2-4.6	Sippican	Miloshevich et al. (2006)
2-5.6	FPH	Vömel et al. (2007a)	2-6.6	CFH	Vömel et al. (2007a)
2-7.6	SnowWhite	Miloshevich et al. (2006)	2-7.6	SnowWhite	Hasebe et al. (2007)
2-8.6	Harv. Ly-a	Read et al. (2007)	2-9.6	FLASH-B	Vömel et al. (2007b)
2-11.6	Raman	Ferrare et al. (1995)	2-19.6	Aura/MLS	Vömel et al. (2007a)
2-19.6	Aura/MLS	Vömel et al. (2007d)	2-22.6	Aura/TES	Shephard et al. (2008)
2-24.6	SAGE-II	Pruvost et al. (1993)	2-25.6	ACE/FTS	Carleer et al. (2008)
2-30.6	AIRS	Miloshevich et al. (2006)	2-40.6	TDL	Read et al. (2007)

SnowWhite

Field	Versus	Article	Field	Versus	Article
2-1.7	RS80	Vaughan et al. (2005)	2-1.7	RS80	Suortti et al. (2008)
2-1.7	RS80	Wang et al. (2003)	2-1.7	RS80	Sapucci et al. (2005)
2-2.7	RS90	Suortti et al. (2008)	2-2.7	RS90	Sapucci et al. (2005)
2-3.7	RS92	Suortti et al. (2008)	2-3.7	RS92	Nash et al. (2006)
2-4.7	Sippican	Wang et al. (2003)	2-3.7	Sippican	Nash et al. (2006)
2-3.7	Sippican	Sapucci et al. (2005)	2-5.7	FPH	Suortti et al. (2008)
2-5.7	FPH	Vömel et al. (2003)	2-6.7	CFH	Suortti et al. (2008)
2-6.7	CFH	Vömel et al. (2007a)	2-6.7	CFH	Whiteman et al. (2006)
2-6.7	CFH	Hasebe et al. (2007)	2-7.7	SnowWhite	Miloshevich et al. (2006)
2-11.7	Raman	Behrendt et al. (2007a)	2-11.7	Raman	Whiteman et al. (2006)
2-30.7	AIRS	Miloshevich et al. (2006)	2-35.7	ECMWF-Re	Fortuin et al. (2007)
2-36.7	Dropsonde	Vance et al. (2004)			

Harv. Ly-α:

Field	Versus	Article	Field	Versus	Article
3-6.1	CFH	Vömel et al. (2007a)	3-6.1	CFH	Read et al. (2007)
3-10.1	TDL	Hintsa et al. (1999)	3-10.1	TDL	Danilin et al. (2002)
3-10.1	TDL	Herman et al. (2002)	3-15.1	SPM	Halthore et al. (1997)
3-18.1	Aura/MLS	Read et al. (2007)	3-19.1	UARS/MLS	Fueglistaler et al. (2009)
3-22.1	ATMOS	Michelsen et al. (2002)	3-23.1	HALOE	Fueglistaler et al. (2009)
3-29.1	POAM	Lumpe et al. (2006)	3-29.1	POAM	Danilin et al. (2002)
3-31.1	AIRS	Gettelman et al. (2004)			

FLASH-B

Field	Versus	Article	Field	Versus	Article
3-1.2	RS80	Suortti et al. (2008)	3-2.2	RS90	Suortti et al. (2008)
3-2.2	RS90	Haefele (2005)	3-3.2	RS92	Suortti et al. (2008)
3-3.2	RS92	Haefele (2005)	3-6.2	CFH	Haefele (2005)
3-6.2	CFH	Suortti et al. (2008)	3-6.2	CFH	Vömel et al. (2007a)
3-6.2	CFH	Vömel et al. (2007b)	3-7.2	SnowWhite	Suortti et al. (2008)
3-27.2	MIPAS	Milz et al. (2009b)	3-34.2	AMSOS	Müller et al. (2008)
3-35.2	ECMWF-Re	Maturilli et al. (2006)	3-36.2	FLASH-R	Lossow et al. (2008a)

FISH

Field	Versus	Article	Field	Versus	Article
3-5.3	FPH	Zöger et al. (1999b)	3-5.3	FPH	Busen et al. (1995)
3-9.3	FLASH-B	Sitnikov et al. (2007)	3-23.3	HALOE	Zöger et al. (1999a)
3-26.3	CRISTA	Offermann et al. (2002)	3-27.3	MIPAS	Milz et al. (2009b)
3-29.3	POAM	Lumpe et al. (2006)	3-33.3	MOZAIC	Helten et al. (1998)
3-33.3	MOZAIC	Kunz et al. (2008)	3-34.3	AMSOS	Müller et al. (2008)
3-37.3	ECMWF-Re	Wagner et al. (2003)			

NOAA Ly-α

Field	Versus	Article	Field	Versus	Article
3-5.4	FPH	Friehe et al. (1986)	3-20.4	LIMS	Russell III et al. (1984)
3-22.4	ATMOS	Michelsen et al. (2002)	3-24.4	SAGE-II	Schwab et al. (1996)
3-33.4	MOZAIC	Helten et al. (1998)			

TDL

Field	Versus	Article	Field	Versus	Article
3-8.5	Harv. Ly-α	Hintsa et al. (1999)	3-8.5	Harv. Ly-α	Danilin et al. (2002)
3-8.5	Harv. Ly-α	Herman et al. (2002)	3-29.5	POAM	Danilin et al. (2002)
3-38.5	SAW	Cardell et al. (2001)			

Raman

Field	Versus	Article	Field	Versus	Article
4-1.1	RS80	Turner et al. (2000)	4-1.1	RS80	Whiteman et al. (1992)
4-1.1	RS80	Whiteman (2003)	4-1.1	RS80	Turner et al. (1999)
4-1.1	RS80	Han et al. (1994)	4-1.1	RS80	Vaughan et al. (1988)
4-1.1	RS80	Goldsmith et al. (1994)	4-1.1	RS80	Behrendt et al. (2008)
4-2.1	RS90	Whiteman et al. (2006)	4-3.1	RS92	Leblanc et al. (2008)
4-3.1	RS92	Leblanc et al. (2008)	4-3.1	RS92	Whiteman et al. (2006)
4-4.1	Sippican	Gerber et al. (2004)	4-5.1	FPH	Turner et al. (1999)
4-6.1	CFH	Whiteman et al. (2006)	4-6.1	CFH	Leblanc T. et al. (2008)
4-7.1	SnowWhite	Behrendt et al. (2007a)	4-7.1	SnowWhite	Whiteman et al. (2006)
4-12.1	Raman	Turner et al. (2002)	4-12.1	Raman	Leblanc et al. (2008)
4-12.1	Raman	Goldsmith et al. (1994)	4-13.1	DIAL	Ferrare et al. (2004)
4-14.1	FTIR	Turner et al. (2000)	4-15.1	MWR-T	Turner et al. (2000)
4-15.1	MWR-T	Turner et al. (1999)	4-17.1	GPS-Col	Barnes et al. (2008)
4-17.1	GPS-Col	Whiteman et al. (2006)	4-19.1	Aura/MLS	Barnes et al. (2008)
4-26.1	ACE/FTS	Carleer et al. (2008)	4-31.1	AIRS	Whiteman et al. (2006)
4-32.1	GOES	Soden et al. (2004)			

DIAL

Field	Versus	Article	Field	Versus	Article
4-1.2	RS80	Ehret et al. (1993)	4-1.2	RS80	Wulfmeyer and Bösenberg (1998)
4-1.2	RS80	Machol et al. (2004)	4-1.2	RS80	Ferrare et al. (2004)
4-1.2	RS80	Browell et al. (1998)	4-1.2	RS80	Higdon et al. (1994)
4-1.2	RS80	Cahen et al. (1982)	4-2.2	RS90	Vogelmann and Trickl (2008)
4-3.2	RS92	Vogelmann and Trickl (2008)	4-4.2	Sippican	Ferrare et al. (2004)
4-5.2	FPH	Ferrare et al. (2004)	4-5.2	FPH	Bruneau et al. (2001)
4-5.2	FPH	Higdon et al. (1994)	4-7.2	SnowWhite	Ferrare et al. (2004)
4-9.2	FLASH-B	Kiemle et al. (2008)	4-10.2	FISH	Kiemle et al. (2008)
4-11.2	Dropsonde	Poberaj et al. (2002)	4-12.2	Raman	Behrendt et al. (2007a)
4-12.2	Raman	Behrendt et al. (2007a)	4-12.2	Raman	Ferrare et al. (2004)
4-13.2	DIAL	Behrendt et al. (2007a)	4-13.2	DIAL	Behrendt et al. (2007b)
4-15.2	MWR-T	Ferrare et al. (2004)	4-16.2	SPM	Ferrare et al. (2000b)
4-16.2	SPM	Ferrare et al. (2000a)	4-27.2	MIPAS	Kiemle et al. (2008)
4-35.2	AMSOS	Müller et al. (2008)	4-36.2	ECMWF-Re	Flentje et al. (2007)
4-36.2	ECMWF-Re	Ehret et al. (1999)	4-36.2	REMO	Hennemuth et al. (2008)
4-43.2	MM5	Flentje et al. (2005)			

FTIR

Field	Versus	Article	Field	Versus	Article
4-1.3	RS80	Schneider et al. (2006a)	4-1.3	RS80	Schneider et al. (2006b)
4-1.3	RS80	Sussmann et al. (2009)	4-1.3	RS80	Palm et al. (2008)
4-2.3	RS90	Palm et al. (2008)	4-3.3	RS92	Palm et al. (2008)
4-3.3	RS92	Schneider and Hase (2009a)	4-3.3	RS92	Schneider et al. (2009b)
4-3.3	RS92	Schneider et al. (2009)	4-12.3	Raman	Turner et al. (2000)
4-14.3	FTIR	Sussmann et al. (2009)	4-15.3	MWR-T	Turner et al. (2000)
4-16.3	SPM	Schmid et al. (1996)	4-16.3	SPM	Ingold et al. (2000)
4-16.3	SPM	Schneider et al. (2009)	4-16.3	SPM	Demoulin et al. (1996)
4-17.3	GPS-Col	Schneider et al. (2009)	4-19.3	Aura/MLS	Lambert et al. (2007)
4-30.3	AMSU	Palm et al. (2008)	4-42.3	SCIAMACHY	Palm et al. (2008)

MWR-T

Field	Versus	Article	Field	Versus	Article
4-1.4	RS80	Solheim and Godwin (1998)	4-1.4	RS80	Han et al. (1994)
4-1.4	RS80	Westwater et al. (1989)	4-3.4	RS92	Fiorucci et al. (2008)
4-3.4	RS92	Miloshevich et al. (2009)	4-4.4	Sippican	Martin et al. (2006a)
4-4.4	Sippican	Mätzler and Morland (2008)	4-4.4	Sippican	Morland et al. (2009)
4-4.4	Sippican	Martin et al. (2006a)	4-4.4	Sippican	Martin et al. (2006b)
4-4.4	Sippican	Cimini et al. (2006)	4-4.4	Sippican	Ingold et al. (1998)
4-4.4	Sippican	Westwater et al. (1989)	4-12.4	Raman	Fiorucci et al. (2008)
4-12.4	Raman	Whiteman et al. (2006)	4-13.4	DIAL	Steinhagen et al. (1998)
4-13.4	DIAL	Wang et al. (2002)	4-14.4	FTIR	Fiorucci et al. (2008)
4-14.4	FTIR	Turner et al. (2000)	4-15.4	MWR-T	Cimini et al. (2006)
4-15.4	MWR-T	Deuber et al. (2005a)	4-16.4	SPM	Halthore et al. (1997)
4-16.4	SPM	Morland et al. (2009)	4-16.4	SPM	Mätzler et al. (2002)
4-17.4	GPS-Col	Martin et al. (2006a)	4-17.4	GPS-Col	Mätzler et al. (2002)
4-17.4	GPS-Col	Wang et al. (2007)	4-17.4	GPS-Col	Whiteman et al. (2006)
4-17.4	GPS-Col	Duan et al. (1996)	4-17.4	GPS-Col	Bevis et al. (1992)
4-17.4	GPS-Col	Deuber et al. (2005a)	4-31.4	AIRS	Whiteman et al. (2006)
4-36.4	ECMWF-Re	Morland et al. (2009)			

MWR-S

Field	Versus	Article	Field	Versus	Article
4-5.5	FPH	Deuber et al. (2005b)	4-6.5	CFH	Deuber et al. (2005b)
4-9.5	FLASH-B	Deuber et al. (2005b)	4-15.5	MWR-T	Deuber et al. (2005b)
4-19.5	Aura/MLS	Nedoluha et al. (2007)	4-19.5	Aura/MLS	Lambert et al. (2007)
4-19.5	Aura/MLS	Hocke et al. (2006)	4-19.5	Aura/MLS	Haefele et al. (2009)
4-20.5	UARS/MLS	Lahoz et al. (1996)	4-20.5	UARS/MLS	Nedoluha et al. (1997)
4-20.5	UARS/MLS	Pumphrey (1999)	4-22.5	ATMOS	Nedoluha et al. (1997)
4-24.5	HALOE	Nedoluha et al. (1997)	4-24.5	HALOE	Nedoluha et al. (2007)
4-24.5	HALOE	Deuber et al. (2005b)	4-24.5	HALOE	Harries et al. (1996)
4-24.5	HALOE	Deuber et al. (2004)	4-24.5	HALOE	Nedoluha et al. (2003)
4-24.5	HALOE	Nedoluha et al. (1999)	4-24.5	HALOE	Nedoluha et al. (1998)
4-26.5	ACE/FTS	Hocke et al. (2006)	4-27.5	MIPAS	Hocke et al. (2006)
4-27.5	MIPAS	Milz et al. (2009b)	4-29.5	POAM	Deuber et al. (2005b)
4-29.5	POAM	Nedoluha et al. (2003)	4-35.5	AMSOS	Müller et al. (2008)
4-41.5	MWR-S	Haefele et al. (2009)	4-41.5	MWR-S	Nedoluha et al. (1999)
4-41.5	MWR-S	Nedoluha et al. (1995)			

Balloon limb occultation

Field	Versus	Article	Field	Versus	Article
4-22.6	ATMOS	Michelsen et al. (2002)	4-23.6	LIMS	Russell III et al. (1984)
4-38.6	limb emiss.	Murcray et al. (1990)	4-39.6	emission	Ellsaesser et al. (1980)
4-40.6	absorption	Ellsaesser et al. (1980)			

Balloon limb emission

Field	Versus	Article	Field	Versus	Article
4-1.7	RS80	Wetzel et al. (1995)	4-5.7	FPH	Wetzel et al. (1995)
4-20.7	UARS/MLS	Lahoz et al. (1996)	4-23.7	LIMS	Russell III et al. (1984)
4-27.7	MIPAS	Milz et al. (2009b)	4-38.7	limb emiss.	Murcray et al. (1990)
4-39.7	emission	Murcray et al. (1990)	4-40.7	absorption	Murcray et al. (1990)

Balloon-borne emission

Field	Versus	Article	Field	Versus	Article
4-23.8	LIMS	Russell III et al. (1984)	4-23.8	LIMS	Remsberg et al. (1984)
4-24.8	HALOE	Harries et al. (1996)	4-38.8	limb emission	Murcray et al. (1990)
4-39.8	emission	Murcray et al. (1990)	4-40.8	absorption	Murcray et al. (1990)

MOZAIC

Field	Versus	Article	Field	Versus	Article
5-2.1	SPURT	Kunz et al. (2008)	5-9.1	HALOE	Oikonomou and O'Neill (2006)
5-13.1	MIPAS	Ekström et al. (2008)	5-14.1	Odin/SMR	Ekström et al. (2007)
5-14.1	Odin/SMR	Ekström et al. (2008)	5-20.1	ECMWF-Re	Luo et al. (2008)
5-20.1	ECMWF-Re	Oikonomou and O'Neill (2006)			

AMSOS

Field	Versus	Article	Field	Versus	Article
5-9.2	HALOE	Oikonomou and O'Neill (2006)	5-13.2	MIPAS	Müller et al. (2008)
5-13.2	MIPAS	Milz et al. (2009b)	5-14.2	Odin/SMR	Müller et al. (2008)
5-15.2	POAM	Müller et al. (2008)	5-20.2	ECMWF-Re	Feist et al. (2007)
5-20.2	ECMWF-Re	Müller et al. (2008)			

GPS-RO

Field	Versus	Article	Field	Versus	Article
5-16.3	AIRS	Chou et al. (2009)	5-20.3	ECMWF-Re	Heise et al. (2006)
5-21.3	NCEP-Re	Chou et al. (2009)			

GPS-Col

Field	Versus	Article	Field	Versus	Article
5-5.4	GPS-Col	Vey et al. (2009)	5-6.4	MWR-T	Deuber et al. (2005a)
5-16.4	AIRS	Rama Varma Raja et al. (2008)	5-16.4	AIRS	Whiteman et al. (2006)
5-20.4	ECMWF-Re	Morland et al. (2006)	5-21.4	NCEP-Re	Vey et al. (2009)
5-23.4	Meisei	Shoji (2009)	5-28.4	SPM	Nyeki et al. (2005)

Aura/MLS

Field	Versus	Article	Field	Versus	Article
5-1.5	MOZAIC	Ekström et al. (2008)	5-3.5	AMSOS	Müller et al. (2008)
5-7.5	Aura/MLS	Fetzer et al. (2008)	5-9.5	HALOE	Lambert et al. (2007)
5-9.5	HALOE	Nedoluha et al. (1997)	5-10.5	SAGE-II	Lambert et al. (2007)
5-11.5	ACE/FTS	Lambert et al. (2007)	5-13.5	MIPAS	Hocke et al. (2006)
5-13.5	MIPAS	Chauhan et al. (2009)	5-13.5	MIPAS	Ekström et al. (2008)
5-13.5	MIPAS	Lambert et al. (2007)	5-14.5	Odin/SMR	Ekström et al. (2008)
5-14.5	Odin/SMR	Lambert et al. (2007)	5-15.5	POAM	Lambert et al. (2007)
5-16.5	AIRS	Fetzer et al. (2008)	5-16.5	AIRS	Ray and Rosenlof (2007)
5-16.5	AIRS	Read et al. (2007)	5-20.5	ECMWF-Re	James et al. (2008)
5-26.5	ALIAS	Read et al. (2007)			

UARS/MLS

Field	Versus	Article	Field	Versus	Article
5-1.6	MOZAIC	Spichtinger et al. (2002)	5-1.6	MOZAIC	Read et al. (2001)
5-6.6	MWR-T	Bender et al. (2008)	5-9.6	HALOE	Pumphrey (1999)
5-9.6	HALOE	Read et al. (2004)	5-10.6	SAGE-II	Read et al. (2001)
5-12.6	CRISTA	Offermann et al. (2002)	5-19.6	ATMOS	Pumphrey (1999)
5-19.6	ATMOS	Michelsen et al. (2002)	5-20.6	ECMWF-Re	Oikonomou and O'Neill (2006)
5-22.6	COSMO-EU	Bender et al. (2008)	5-24.6	tmt	Morris et al. (2000)

IASI

Field	Versus	Article
5-27.7	WALES	Wulfmeyer et al. (2005)

MAS

Field	Versus	Article
5-19.8	ATMOS	Michelsen et al. (2002)

GOME

Field	Versus	Article	Field	Versus	Article
5-20.9	ECMWF-Re	Noel et al. (2008)	5-20.9	ECMWF-Re	Wagner et al. (2003)
5-29.9	SSM/I	Wagner et al. (2005)			

SCIAMACHY

Field	Versus	Article	Field	Versus	Article
5-20.10	ECMWF-Re	Noel et al. (2008)	5-20.10	ECMWF-Re	Noel et al. (2005)
5-20.10	ECMWF-Re	Noel et al. (2004)	5-25.10	GOME	Noel et al. (2008)
5-29.10	SSM/I	Noel et al. (2005)	5-29.10	SSM/I	Noel et al. (2004)

HALOE

Field	Versus	Article	Field	Versus	Article
6-1.1	MOZAIC	Oikonomou and O'Neill (2006)	6-3.1	AMSOS	Müller et al. (2008)
6-6.1	Aura/MLS	Lambert et al. (2007)	6-6.1	Aura/MLS	Nedoluha et al. (1997)
6-7.1	UARS/MLS	Lahoz et al. (1996)	6-7.1	UARS/MLS	Fueglistaler et al. (2009)
6-10.1	SAGE-II	Thomason et al. (2004)	6-10.1	SAGE-II	Read et al. (2004)
6-11.1	ACE/FTS	McHugh et al. (2005)	6-11.1	ACE/FTS	Carleer et al. (2008)
6-12.1	MIPAS	Milz et al. (2005)	6-13.1	Odin/SMR	Lossow et al. (2008b)
6-14.1	POAM	Lumpe et al. (2006)	6-14.1	POAM	Lucke et al. (2008)
6-14.1	POAM	Randel et al. (2006)	6-18.1	ATMOS	Harries et al. (1996)
6-18.1	ATMOS	Michelsen et al. (2002)	6-19.1	ECMWF-Re	Thornton et al. (2009)
6-28.1	UM	Harries (1997)			

SAGE-II

Field	Versus	Article	Field	Versus	Article
6-6.2	Aura/MLS	Lambert et al. (2007)	6-7.2	UARS/MLS	Read et al. (2001)
6-9.2	HALOE	Thomason et al. (2004)	6-11.2	ACE/FTS	Carleer et al. (2008)
6-14.2	POAM	Lumpe et al. (2006)	6-17.2	LIMS	Chiou et al. (1993)
6-17.2	LIMS	Rind et al. (1993)	6-18.2	ATMOS	Chiou et al. (1993)
6-18.2	ATMOS	Michelsen et al. (2002)	6-19.2	ECMWF-Re	Thornton et al. (2009)
6-29.2	1-D model	Boering et al. (1995)			

ACE/FTS

Field	Versus	Article	Field	Versus	Article
6-2.3	SPURT	Hegglin et al. (2008)	6-6.3	Aura/MLS	Lambert et al. (2007)
6-9.3	HALOE	Carleer et al. (2008)	6-9.3	HALOE	McHugh et al. (2005)
6-10.3	SAGE-II	Carleer et al. (2008)	6-12.3	MIPAS	Carleer et al. (2008)
6-13.3	Odin	Carleer et al. (2008)	6-13.3	Odin/SMR	Lossow et al. (2008b)
6-14.3	POAM	Carleer et al. (2008)			

MIPAS

Field	Versus	Article	Field	Versus	Article
6-1.4	MOZAIC	Ekström et al. (2008)	6-3.4	AMSOS	Müller et al. (2008)
6-3.4	AMSOS	Milz et al. (2009b)	6-6.4	Aura/MLS	Hocke et al. (2006)
6-6.4	Aura/MLS	Ekström et al. (2008)	6-6.4	Aura/MLS	Lambert et al. (2007)
6-6.4	Aura/MLS	Chauhan et al. (2009)	6-9.4	HALOE	Milz et al. (2009b)
6-11.4	ACE/FTS	Carleer et al. (2008)	6-11.4	ACE/FTS	Milz et al. (2009b)
6-14.4	POAM	Milz et al. (2009b)	6-21.4	ILAS-II	Milz et al. (2009b)
6-21.4	ILAS-II	Griesfeller et al. (2008)			

Odin/SMR

Field	Versus	Article	Field	Versus	Article
6-1.5	MOZAIC	Ekström et al. (2008)	6-1.5	MOZAIC	Ekström et al. (2008)
6-3.5	AMSOS	Müller et al. (2008)	6-6.5	Aura/MLS	Ekström et al. (2008)
6-6.5	Aura/MLS	Jones et al. (2009)	6-7.5	UARS/MLS	Ekström et al. (2008)
6-9.5	HALOE	Lossow et al. (2008b)	6-9.5	HALOE	Jones et al. (2009)
6-10.5	SAGE-II	Jones et al. (2009)	6-11.5	ACE/FTS	Carleer et al. (2008)
6-11.5	ACE/FTS	Lossow et al. (2008b)	6-11.5	ACE/FTS	Lossow et al. (2007)
6-12.5	MIPAS	Ekström et al. (2008)	6-22.5	Hammonia	Lossow et al. (2009)
6-23.5	WACCM	Lossow et al. (2009)			

POAM

Field	Versus	Article	Field	Versus	Article
6-3.6	AMSOS	Müller et al. (2008)	6-6.6	Aura/MLS	Lambert et al. (2007)
6-9.6	HALOE	Lumpe et al. (2006)	6-9.6	HALOE	Lucke et al. (2008)
6-9.6	HALOE	Randel et al. (2006)	6-10.6	SAGE-II	Lumpe et al. (2006)
6-11.6	ACE/FTS	Carleer et al. (2008)			

AIRS

Field	Versus	Article	Field	Versus	Article
7-5.1	GPS-Col	Rama Varma Raja et al. (2008)	7-6.1	Aura/MLS	Fetzer et al. (2008)
7-6.1	Aura/MLS	Ray and Rosenlof (2007)	7-6.1	Aura/MLS	Read et al. (2007)
7-19.1	ECMWF-Re	Hocke et al. (2007)	7-19.1	ECMWF-Re	Lamquin et al. (2009)
7-24.1	CAM	Gettelman and Fu (2008)	7-24.1	CAM	Gettelman et al. (2006)

AMSU

Field	Versus	Article	Field	Versus	Article
7-5.2	GPS-Col	Johnsen et al. (2004)	7-15.2	AIRS	Milz et al. (2009a)
7-15.2	AIRS	Fetzer et al. (2003)	7-16.2	HIRS	Buehler et al. (2008)
7-19.2	ECMWF-Re	Brogniez and Pierrehumbert (2007)	7-20.2	NCEP-Re	Brogniez and Pierrehumbert (2007)
7-25.2	GCMs	Brogniez and Pierrehumbert (2007)	7-26.2	Lagrange	Brogniez and Pierrehumbert (2006)

SSM/I

Field	Versus	Article	Field	Versus	Article
7-16.3	HIRS	Soden et al. (2005)	7-27.3	GFDL	Soden et al. (2005)

METEOSAT

Field	Versus	Article	Field	Versus	Article
7-28.4	AMIP	Brogniez et al. (2005)	7-17.4	HIRS	Brogniez (2004)

LIMS

Field	Versus	Article
7-18.5	ATMOS	Gunson et al. (1990)

11.5 What Do We Learn from the Tables?

Sometimes it is good to go one step back from the object of interest. The tables provide an impression about what is going on in the field of water vapour intercomparisons. They give orientation about available intercomparisons between various measurement techniques and platforms. Usually a lidar scientist is not well informed about intercomparisons performed by a radiometer scientist and vice versa. The tables further help to identify lacks of the intercomparison strategies. It is important that each individual instrument is somehow validated by a standard or a reference instrument.

Tables 11.2 and 11.3 show a tendency that there exist many intercomparisons between balloon-borne hygrometers but not so much intercomparisons between satellite missions and balloon-borne hygrometers. For example, data from FLASH-B and SnowWhite are quite rarely used in satellite validation studies. A reason could be that access of radiosonde data is usually difficult. This may lead to a preference of satellite-to-satellite and satellite-to-model intercomparisons (Tables 11.5 and 11.6). Aura/MLS and HALOE serve as a reference for many other satellites and ground stations.

Ground-based remote sensing is well established in intercomparisons as shown by Table 11.4. FTIR has a slight deficit of intercomparisons since the application of ground-based FTIR to remote sensing of water vapour is quite new. Intercomparisons of model and reanalysis data with observations are partly included in the tables. Further work on this topic is needed and more cooperations between modelers and observers would be useful.

These thoughts are very preliminary since further inputs of other experts can change the picture of the tables.

11.6 Surface Humidity and Technological Progress

Measurement of surface humidity can be of interest for atmospheric scientists who measure the vertical profile of water vapour by means of remote sensing techniques and air-borne hygrometers. Since hygrometers are developed in laboratories and are firstly tested at the surface, technological progress often appear at first in articles about surface humidity. Here we introduce various articles of the last decades showing the wide spectrum from sensor development for industrial purposes to atmospheric sciences. Many of the articles were published in journals which are usually overlooked by atmospheric scientists.

Bell et al. (2008) analysed the social and economic drivers of development in humidity measurement and standardization and identified two key triggers: (1) Actions against global warming (energy efficiency and climate research) will require increasingly accurate humidity measurements and their interpretation; (2) Ever-increasing consumer demand and global market forces will require better humidity control in manufacturing processes and increased global technical interoperability.

High-purity manufacturing increasingly requires gases pure to parts per billion or even parts per trillion. Existing standards only underpin measurements to slightly below 1 part per million. A notable example is the research and improvement of hydrogen fuel cells, especially cell lifetime, which critically depends on humidity. This calls for advanced extremely miniaturized relative humidity and gas temperature sensors, which are robust against extreme conditions (Bell et al. 2008). Chen and Lu (2005) gave a detailed review of materials and mechanisms of humidity sensors. Tsai et al. (2010) described the fabrication of humidity sensors by multi-walled carbon nanotubes. It is expected that nanotechnology leads to advanced relative humidity sensors (Bell et al. 2008).

Makkonen and Laakso (2005) explained that conventional humidity probes are disturbed by icing of the sensor head and, in the case of an aspirated psychrometer, icing of the dry-bulb thermometer. These problems have seriously hampered all meteorological studies in cold and humid environments, in which humidity data based on aspirated psychrometers, hair hygrometers, dew cells, mirror dew-point probes and capacitance hygrometers have been used. The Vaisala HMP243 probe utilizes a heated capacitance sensor for a correct determination of the frost point. The results of Makkonen and Laakso (2005) confirmed that the relative humidity is frequently well above the frost point, both due to radiative cooling and to the advection of moist air, and that the conventional humidity measurements were unable to detect these events.

Heinonen (2006) presented a tutorial on uncertainty in humidity measurements and calibrations. He addressed the uncertainty budget for a dew-point generator as well as the operation of secondary and primary standards. Details were given for the uncertainties of chilled-mirror dew-point hygrometers, impedance RH hygrometers, and psychrometers.

Kwon et al. (2008) investigated quartz crystal microbalance (QCM) dew-point sensors which are based on frequency measurement. Theses sensors have fast response time, high sensitivity, high accuracy and can distinguish between supercooled dew and frost from a single scan through the resonant frequency of the quartz resonator as a function of the temperature. Hansford et al. (2006) described a surface-acoustic-wave (SAW) sensor which is utilized as lightweight dew-/frost-point hygrometer for balloon-borne water vapour profiling. Intercomparisons were obtained for SAW with respect to coincident measurements of SnowWhite and A-Humicap. Hudoklin et al. (2010) thoroughly tested the automation of supercooled water elimination by cooling for a chilled-mirror hygrometer.

Tunable diode laser absorption spectroscopy was used for measurement of transpiration rates of plant leaves Hunsmann et al. (2008) as well as for balloon-borne profiling of atmospheric water vapour up to about 25 km altitude Gurlit et al. (2005). The latter experiment was performed with the lightweight diode laser spectrometer CHILD (Compact High-altitude In-situ Laser Diode) for balloon-borne measurements of water vapour and methane. The CHILD instrument consists of a new dual-species open-path multipass Herriott cell. Simultaneous measurements of humidity fluctuations over a crop made with a specially modified Lyman-alpha hygrometer and a fine-wire thermocouple psychrometer were compared by Redford et al. (1980). On the other hand, a balloon-borne Lyman-alpha hygrometer (optical

fluorescent hygrometer FLASH-B) was utilized by Khaykin et al. (2010) for measurement of water vapour in the upper troposphere and stratosphere. The Harvard Lyman-alpha hygrometer was further tested and validated by Weinstock et al. (2009).

Okamura (2000) reviewed sensors for moisture content measurements by microwave technology, especially from the aspect of subsurface sensing. Delahaye et al. (2001) reported about humidity fluctuation measurements of a shipborne microwave refractometer with a time resolution of 0.02 s. A great advantage of the refractometer is that the contamination by salt, as is typical for other devices at sea, has been found to be negligible for the conditions encountered. Microwave refractometers can be designed for measurement on meteorological balloons. Chan and Cole (1978) described an expendable lightweight microwave radio refractometer.

Liu (1986) derived the statistical relation between surface humidity and integrated water vapour using data of radiosondes and spaceborne microwave radiometers above oceans. Haan (2008) analysed data of radiosondes and GPS ground stations in the Netherlands. He found that the change over time of IWV is closely related to the change in specific humidity at 2 km. A multisensor microwave retrieval of near-surface 10 m specific humidity (Qa) using satellite observations from the advanced microwave sounding unit-A (AMSU-A), the Special Sensor Microwave Temperature Sounder-2, and the Special Sensor Microwave Imager was developed by Jackson et al. (2009). The surface humidity above oceans measured by spaceborne microwave radiometers was then compared with the International Comprehensive Ocean-Atmosphere Data Set (ICOADS).

11.7 Towards a Value-added Interactive Survey

The role of intercomparisons of water vapour measurements for a comprehensive climate observing system will further increase. The scientists should ease their lifes by creating research infrastructures such as the Water Vapour Literature Database. Discussions within the water vapour community and first practical experiences with the literature database indicate that scientists are eager to cooperate. We are grateful to our colleagues who already contributed to the present survey. The survey will be updated from time to time and will survive in a fresh state as a clickable pdf file with direct links to articles of the literature database. A *value-added interactive survey project* rises, and you are kindly invited to participate.

References

F.R. Barclay, M.J.W. Elliott, P. Goldsmith, J.V. Jelley, A direct measurement of the humidity in the stratosphere using a cooled-vapour trap. Quart. J. Roy. Meteorol. Soc. **86**, 259–264 (1960)

J. Barnes, T. Kaplan, H. Vömel, W.G. Read. NASA/Aura/Microwave limb sounder water vapor validation at Mauna Loa observatory by Raman lidar. J. Geophys. Res. **113**, D15SO3 (2008) doi: 10.1029/2007JD008842

E. Barrett, L. Herndon, H., Carter, A preliminary note on the measurement of water-vapor content in the middle stratosphere. J Meteorol. **6**, 367–368 (1949)

A. Behrendt, V. Wulfmeyer, P. Girolamo, C. Kiemle, H.-S. Bauer, T. Schaberl, D. Summa, D. Whiteman, B. Demoz, E. Browell, S. Ismail, R. Ferrare, S. Kooi, G. Ehret, J. Wang, Intercomparison of water vapor data measured with Lidar during IHOP-2002. Part I: Airborne to ground-based Lidar systems and comparisons with chilled-mirror hygrometer radiosondes. J. Atmos. Oceanic Technol. **24**, 3–21 (2007a) doi: 10.1175/JTECH1924.1

A. Behrendt, V. Wulfmeyer, C. Kiemle, G. Ehret, C. Flamant, T. Schaberl, H.-S. Bauer, S. Kooi, S. Ismail, R. Ferrare, E.V. Browell, D.N. Whiteman, Intercomparison of water vapor data measured with Lidar during IHOP-2002. Part II: Airborne-to-Airborne systems. J. Atmos. Ocean. Tech. **24**, 22–39 (2007b) doi: 10.1175/JTECH1925.1

A. Behrendt, V. Wulfmeyer, A. Wieser, S. Pal, A. Riede, M. Schiller, M. Radlach, K. Träumner, G. Wagner, A. Fix, Synergetic measurements with three collocated scanning lidars: Water vapor dial, rotational raman lidar, and doppler lidar. Reviewed and revised papers presented at the 24th international laser radar conference (ILRC). 1025–1028 (2008)

S. Bell, R. Benyon, N. Böse, M. Heinonen, A Roadmap for humidity and moisture measurement. Int. J. Thermophys. **29**, 1537–1543 (2008)

M. Bender, G. Dick, J. Wickert, T. Schmidt, S. Song, G. Gendt, M. Ge, M. Rothacher, Validation of GPS slant delays using water vapour radiometers and weather models. Meteorol. Z. **17**, 807–812 (2008)

M. Bevis, S. Businger, T. Herring, C. Rocken, R. Anthes, R. Ware, GPS meteorology: Remote sensing of atmospheric water vapor. J. Geophys. Res. **97**(D14), 15787–15801 (1992)

C. Böckmann, Gleichzeitige beobachtungen der hygrometer von Leslie, saussure und De Luc. Annalen der Physik. **15**, 355–376 (1803)

K.A. Boering, E.J. Hintsa, S.C. Wofsy, J.G. Anderson, Jr. B. C.D., A.E. Dessler, M. Loewenstein, M.P. McCormick, J.R. Podolske, E.M. Weinstock, G.K. Yue, Measurements of stratospheric carbon dioxide and water vapor at northern midlatitudes: Implications for troposphere to stratosphere transport. Geophys. Res. Lett. **22**(20), 2737–2740 (1995)

A. Brewer, B. Cwilong, G. Dobson, Measurement of absolute humidity in extremely dry air. Proc. Phys. Soc. **60**, 52–70 (1948)

A.W. Brewer, The discovery of stratospheric dryiness. SPARC newsletter on Brewer-Dobson Workshop (Oxford, 1999), *reprinted by The Eggs—Newsletter and information service of the EGU (Vol. 27)* (2009)

H. Brogniez, African Free Tropospheric Humidity: Elaboration of a METEOSAT archive, Climatic analysis and Evaluation of models. *Laboratoire de Meteorologie Dynamique*, (Unversite Pierre et Marie Curie, France, 2004)

H. Brogniez, R. Pierrehumbert, Using microwave observations to assess large-scale control of the free tropospheric water vapor in the mid-latitudes. Geophys. Res. Lett. **33**, L14801 (2006) doi:10.1029/2006GL026240

H. Brogniez, R. Pierrehumbert, Intercomparison of tropical tropospheric humidity in GCMs with AMSU-B water vapor data. Geophys. Res. Lett. **34**, L17812 (2007) doi:10.1029/2006GL029118

H. Brogniez, R. Roca, L. Picon, Evaluation of the tropical free tropospheric Humidity in AMIP-2 simulations using METEOSAT Water Vapor channel data. Geophys. Res. Lett. **32**, (2005) doi:10.1029/2005GL024341

H. Brogniez, R. Roca, L. Picon, A clear sky radiances archive from METEOSAT. J. Geophys. Res. **111**, (2006) doi:10.1029/2006JD007238

E.V. Browell, T.D. Wilkerson, T.J. McIlrath, Water vapor differential absorption lidar development and evaluation. Appl. Opt. **18**, 3474–3483 (1979)

E.V. Browell, S. Ismail, W.B. Grant, Differential absorption lidar (DIAL) measurements from air and space. Appl. Phys. B **67**, 399–410 (1998)

D. Bruneau, P. Quaglia, C. Flamant, J. Pelon, Airborne Lidar LEANDRE II for water-vapor profiling in the troposphere. II. first results. Appl. Opt. **42**, 3462–3475 (2001) doi:10.1364/AO.40.003462

S.A. Buehler, M. Kuvatov, V.O. John, M. Milz, B.J. Soden, J. Notholt, An upper tropospheric humidity data set from operational satellite microwave data. J. Geophys. Res. **113**, D14110 (2008) doi:10.1029/2007JD009314

R. Busen, A. Buck, A high-performance hygrometer for aircraft use: Description, installation, and ight data. J. Atmos. Ocean. Tech. **12**, 73–84 (1995)

C. Cahen, G. Mégie, P. Flamant, Lidar monitoring of the water vapor cycle in the troposphere. J. Appl. Meteor. **21**, 1506–1515 (1982)

G. Cardell, F. Noca, K. Watson, M. Hoenk, Micro weather station for In Situ atmospheric measurements in the troposphere. JPL Technical Report Server (JPL/Caltech, USA, 2001)

M.R. Carleer, C.D. Boone, K.A. Walker, P.F. Bernath, K. Strong, R.J. Sica, C.E. Randall, H. Vömel, J. Kar, M. Höpfner, M. Milz, T. von Clarmann, R. Kivi, J. Valverde-Canossa, C.E. Sioris, M.R.M. Izawa, E. Dupuy, C.T. McElroy, J.R. Drummond, C.R. Nowlan, J. Zou, F. Nichitiu, S. Lossow, J. Urban, D. Murtagh, D.G., Dufour, Validation of water vapour profiles from the atmospheric chemistry experiment (ACE). Atmos. Chem. Phys. Discuss. **8**, 4499–4559 (2008)

T. Carpenter, A chemical hygrometer. J. Biol. Chem. **112**, 123–133 (1935)

C. Chan, R. Cole, An expendable lightweight microwave radio refractometer. J. Phys. E: Sci. Instrum. **11**, 1104–1108 (1978)

S. Chauhan, M. Höpfner, G.P. Stiller, T. von Clarmann, B. Funke, N. Glatthor, U. Grabowski, A. Linden, S. Kellmann, M. Milz, T. Steck, H. Fischer, L. Froidevaux, A. Lambert, M.L. Santee, M. Schwartz, W.G. Read, N.J. Livesey, MIPAS reduced spectral resolution UTLS-1 mode measurements of temperature, O_3, HNO_3, N_2O, H_2O and relative humidity over ice: retrievals and comparison to MLS. Atmos. Meas. Tech. Discuss. **2**, 439–487 (2009)

Z. Chen, C. Lu, Humidity Sensors: A review of materials and mechanisms. Sensor Letters, **3**, 274–295 (2005)

E. Chiou, M. McCormick, L. McMaster, W. Chu, J. Larsen, D. Rind, S. Oltmans, Intercomparison of stratospheric water vapor observed by satellite experiments: Stratospheric aerosol and gas experiment II versus limb Infrared monitor of the stratosphere and atmospheric trace molecule spectroscopy. J. Geophys. Res. **98**(D3), 4875–4887 (1993)

M. Chou, C. Weng, P. Lin, Analyses of FORMOSAT-3/COSMIC humidity retrievals and comparisons with AIRS retrievals and NCEP/NCAR reanalyses. J. Geophys. Res. **114**, D00G03 (2009) doi:10.1029/2008JD010227

D. Cimini, T.J. Hewison, L. Martin, J. Güldner, C. Gaffard, F.S. Marzano, Temperature and humidity profile retrievals from ground-based microwave radiometers during TUC. Meteorol. Z. **15**, 45–56 (2006)

P.-F. Coheur, C. Clerbaux, M. Carleer, S. Fally, D. Hurtmans, R. Colin, C. Hermans, A.C. Vandaele, B. Barret, M.D. Mazière, H.D. Backer, Retrieval of atmospheric water vapor columns from FT visible solar absorption spectra and evaluation of spectroscopic databases. J. Quant. Spectrosc. Radiat. Transfer. **82**, 133–150 (2003)

J. Daniell, Eine neues hygrometer, welches die Kraft und des gewicht des wasserdampfs in der atmosphäre, und den entsprechenden grad der verdünstung misst. Annalen der Physik. **65**, 169–205 (1820)

J. Daniell, Meteorological essays and observations, chapter An essay upon the construction and uses of a new hygrometer, p 140–205. T. and G. Underwood (pp. 479), London, (1823)

M.Y. Danilin, M.K.W. Ko, R.M. Bevilacqua, L.V. Lyjak, L. Froidevaux, M.L. Santee, J.M. Zawodny, K.W. Hoppel, E.C. Richard, J.R. Spackman, E.M. Weinstock, R.L. Herman, K.A. McKinney, P.O. Wennberg, F.L. Eisele, R.M. Stimpe, C.J. Scott, J.W. Elkins, T.V. Bui, Comparison of ER-2 aircraft and POAM III, MLS, and SAGE II satellite measurements during SOLVE using traditional correlative analysis and trajectory hunting technique. J. Geophys. Res. **107**(D5), 8315 (2002) doi:10.1029/2001JD000781

F.H. Day, Deficient Humidity Indoors. Mon. Weather Rev. **36**, 404–406 (1908)

S. de Haan, Meteorological applications of a surface network of Global Positioning System receivers. Master's thesis (University of Wageningen, Wageningen, The Netherlands, 2008)

J. De Luc, Account of a new hygrometer. Phil. Trans. Roy. Soc. **63**, 404–460 (1773)

J. De Luc, A Second paper on hygrometry. Phil. Trans. Roy. Soc. **81**, 1–42. (1791)
J.A. De Luc, Neue Ideen über die Meteorologie, Erster Teil. F. Nicolai, Berlin und Stettin, p 459 (1787)
J.A. De Luc, Neue Ideen über die Meteorologie, Zweiter Teil. F. Nicolai, Berlin und Stettin, p. 366 (1788)
H.-B. De Saussure, Essais sur l'hygrométrie. S. Fauche Père et Fils, Neuchatel, Switzerland, 367 (1783)
J.-Y. Delahaye, C. Guerin, J.P. Vinson, H. Dupuis, A. Weill, H. Branger, L. Eymard, J. Lavergnat, G. Lachaud, A new shipborne microwave refractometer for estimating the evaporation flux at the sea surface. J. Atmos. Ocean. Tech. **18**, 459–475 (2001)
P. Demoulin, B. Schmid, G. Roland, C. Servais, Vertical column abundance and profile retrievals of water vapor above the Jungfraujoch. Proceedings of Atmospheric Spectroscopy Applications 1996 meeting, Reims, 4–6 September 1996, p 131–134 (1996)
B. Deuber, N. Kämpfer, D.G. Feist, A New 22-GHz radiometer for middle atmospheric water vapor profile measurements. IEEE Trans. Geosci. Remote Sens. **42**, 974–984 (2004)
B. Deuber, J. Morland, L. Martin, N. Kämpfer, Deriving the tropospheric integrated water vapor from tipping curve derived opacity near 22 GHz. Radio Sci. **40**, RS5011 (2005a) doi:10.1029/2004RS003233
B. Deuber, A. Haefele, D.G. Feist, L. Martin, N. Kämpfer, G.E. Nedoluha, V. Yushkov, S. Khaykin, R. Kivi, H. Vömel, Middle Atmospheric Water Vapour Radiometer—MIAWARA: Validation and first results of the LAUTLOS / WAVVAP campaign. J. Geophys. Res. **110**, D13306 (2005b) doi:10.1029/2004JD005543
R. Dicke, R. Beringer, R. Kyhl, A. Vane, atmospheric absorption measurements with a microwave radiometer. Phys. Rev. **70**, 340–348 (1946)
J. Duan, M. Bevis, P. Fang, Y. Bock, S. Chiswell, S. Businger, C. Rocken, F. Solheim, T.V. Hove, R. Ware, S. McClusky, T.A. Herring, R.W. King, GPS meteorology: Direct estimation of the absolute value of precipitable water. J. Appl. Meteorol. **35**, 830–838 (1996)
G. Ehret, C. Kiemle, W. Renger, G. Simmet, Airborne remote sensing of tropospheric water vapor with a near-infrared differential absorption lidar system. Appl. Opt. **32**, 4534–4551 (1993)
G. Ehret, K.P. Hoinka, J. Stein, A. Fix, C. Kiemle, G. Poberaj, Low stratospheric water vapor measured by an airborne DIAL. J. Geophys. Res. **104**, 31351–31359 (1999)
M. Ekström, P. Eriksson, B. Rydberg, D.P. Murtagh, First Odin sub-mm retrievals in the tropical upper troposphere: humidity and cloud ice signals. Atmos. Chem. Phys. **7**, 459–469 (2007)
M. Ekström, P. Eriksson, W.G. Read, M. Milz, D.P. Murtagh, Comparison of satellite limb-sounding humidity climatologies of the uppermost tropical troposphere. Atmos. Chem. Phys. **8**, 309–320 (2008)
W. Elliott D. Gaffen, Effects of conversion algorithms on reported upper-air dewpoint depressions. Bullet. Amer. Meteorol. Soc. 74, 1323–1325 (1993)
H. Ellsaesser, J. Harries, D. Kley, R. Penndorf, Stratospheric H_2O. Planet. Space Sci. **28**, 827–835 (1980)
D. Engelbart, W. Monna, J. Nash, C. Mätzler, Integrated ground-based remote sensing stations for atmospheric profiling. Office for Official Publication of the European Communities,COST Action 720—Final Report, (720) (2006)
C. Farmer, Infrared Measurements of Stratospheric Composition. Can. J. Chem. **52**, 1544–1559 (1974)
D.G. Feist, A.J. Geer, S. Müller, N. Kämpfer, Middle atmosphere water vapour and dynamical features in aircraft measurements and ECMWF analyses. Atmos Chem Phys. **7**, 5291–5307 (2007)
R. Ferrare, S. Ismail, E. Browell, V. Brackett, M. Clayton, S. Kooi, S.H. Melfi, D. Whiteman, G. Schwemmer, K. Evans, P. Russell, J. Livingston, B. Schmid, B. Holben, L. Remer, A. Smimov, P.V. Hobbs, Comparison of aerosol optical properties and water vapor among ground and airborne lidars and Sun photometers during TARFOX. J. Geophys. Res. **105**, 9917–9933 (2000a)

R. Ferrare, S. Ismail, E. Browell, V. Brackett, S. Kooi, M. Clayton, P.V. Hobbs, S. Hartley, J.P. Veefkind, P. Russell, J. Livingston, D. Tanré, P. Hignet, Comparisons of LASE, aircraft, and satellite measurements of aerosol optical properties and water vapor during TARFOX. J. Geophys. Res. **105**, 9935–9947 (2000b)

R.A. Ferrare, S.H. Melfi, D.N. Whiteman, K.D. Evans, F.J. Schmidlin, D.O. Starr, A Comparison of Water Vapor Measurements Made by Raman Lidar and Radiosondes. J. Atmos. Ocean. Tech. **12**, 1177–1195 (1995)

R.A. Ferrare, E.V. Browell, S. Ismail, J.D.W. Barrick, G.S. Diskin, G.W. Sachse, S.A. Kooi, L.H. Brasseur, V.G. Brackett, M.B. Clayton, J.E.M. Goldsmith, B.M. Lesht, J.R. Podolske, F.J. Schmidlin, D.D. Turner, D.N. Whiteman, B.B. Demoz, D. Tobin, H.E. Revercomb, L.M. Miloshevich, P.D. Girolamo, Characterization of Upper-Troposphere Water Vapor Measurements during AFWEX Using LASE. J. Atmos. Ocean. Tech. **21**(12), 1790–1808 (2004) doi:10.1175/JTECH–1652.1

E. Fetzer, L. McMillin, D. Tobin, H. Aumann, M. Gunson, W. McMillan, D. Hagan, M. Hofstadter, J. Yoe, D. Whiteman, J. Barnes, R. Bennartz, H. Vömel, V. Walden, M. Newchurch, P. Minnett, R. Atlas, F. Schmidlin, E. Olsen, M. Goldberg, Z. Sisong, D. HanJung, W. Smith, H. Revercomb, AIRS/AMSU/HSB validation. IEEE Trans. Geosci. Remote Sens. **41**, 418–431 (2003). doi: 10.1109/TGRS.2002.808293

E. Fetzer, W.G. Read, D. Waliser, B.H. Kahn, B. Tian, H. Vömel, F.W. Irion, H. Su, A. Eldering, de la M. Torre Juarez, J. Jiang, V. Dang, Comparison of upper tropospheric water vapor observations from the Microwave Limb Sounder and Atmospheric Infrared Sounder. J. Geophys. Res. **113**, D22110 (2008). doi: 10.1029/2008JD010000

I. Fiorucci, G. Muscari, C. Bianchi, P.D. Girolamo, F. Esposito, G. Grieco, D. Summa, G. Bianchini, L. Palchetti, M. Cacciani, T.D. Iorio, G. Pavese, D. Cimini, de R.L. Zafra, Measurements of low amounts of precipitable water vapor by millimeter wave spectroscopy: An intercomparison with radiosonde, Raman lidar, and Fourier transform infrared data. J. Geophys. Res. **113**, D14314, (2008). doi: 10.1029/2008JD009831

H. Flentje, A. Dörnbrack, G. Ehret, A. Fix, C. Kiemle, G. Poberaj, M. Wirth, Water vapor heterogeneity related to tropopause folds over the North Atlantic revealed by airborne water vapor differential absorption lidar. J. Geophys. Res. **110**, D03115 (2005). doi:10.1029/2004JD004957

H. Flentje, A. Dörnbrack, A. Fix, G. Ehret, E. Hólm, Evaluation of ECMWF water vapour fields by airborne differential absorption lidar measurements: a case study between Brazil and Europe. Atmos. Chem. Phys. **7**, 5033–5042 (2007)

J.P.F. Fortuin, C.R. Becker, M. Fujiwara, F. Immler, H.M. Kelder, M.P. Scheele, O. Schrems, G.H.L. Verver, Origin and transport of tropical cirrus clouds observed over Paramaribo, Suriname (5.8N, 55.2W). J. Geophys. Res. **112**, D09107 (2007). doi:10.1029/2005JD006420

F. Fowle, The spectroscopic determination of aqueous vapor. Astrophys. J. **35**, 149–162 (1912)

C. Friehe, R. Grossman, Y. Pann, Calibration of an airborne lyman-alpha hygrometer and measurement of water vapor flux using a thermoelectric hygrometer. J. Atmos. Ocean. Tech. **3**, 299–304 (1986)

S. Fueglistaler, A.E. Dessler, T. Dunkerton, I. Q. Folkins, Fu, P. Mote, Tropical tropopause layer. Rev. Geophys. **47**, RG1004 (2009). doi: 10.1029/2008RG000267

M. Fujiwara, M. Shiotani, F. Hasebe, H. Vömel, S.J. Oltmans, P.W. Ruppert, T. Horinouchi, T. Tsuda, Performance of the Meteolabor Snow White Chilled-Mirror Hygrometer in the Tropical Troposphere: Comparisons with the Vaisala RS80 A/H-Humicap Sensors. J. Atmos. Ocean. Tech. **20**, 1534–1542 (2003)

D. Gerber, I. Balin, D.G. Feist, N. Kämpfer, V. Simeonov, B. Calpini, van den H. Bergh, Ground-based water vapour soundings by microwave radiometry and Raman lidar on Jungfraujoch (Swiss Alps). Atmos. Chem. Phys. **4**, 2171–2179 (2004)

A. Gettelman, Q. Fu, Observed and simulated upper-tropospheric water vapor feedback. J. Clim. **21**, 3282–3289 (2008) doi:10.1175/2007JCLI2142.1

A. Gettelman, E.M. Weinstock, E.J. Fetzer, F.W. Irion, A. Eldering, E.C. Richard, K.H. Rosenlof, T.L. Thompson, J.V. Pittman, C.R. Webster, R.L. Herman, Validation of aqua satellite data in

the upper troposphere and lower stratosphere with in situ aircraft instruments. Geophys. Res. Lett. **31**, L22107 (2004). doi:10.1029/2004GL020730.
A. Gettelman, W.D. Collins, E.J. Fetzer, A. Eldering, F.W. Irion, P.B. Duffy, G. Bala, Climatology of upper-tropospheric relative humidity from the atmospheric infrared sounder and implications for climate. J. Clim. **19**, 6104–6121 (2006). doi:10.1175/JCLI3956.1
J. Goldsmith, S.E. Bisson, R.A. Ferrare, K.D. Evans, N.D. Whiteman, S.H. Melfi, Raman lidar profiling of atmospheric water vapor: Simulaneous measurements with two collocated systems. Bul. Amer. Meteorol. Soc. **75**(6), 975–982 (1994)
D. Grantham, N. Sissenwine, H. Salmela, AFCRL Stratospheric Humidity Program. Technical Report BT-1035.22, (Air Force Cambridge Research Labs., USA, 1964)
A. Griesfeller, von T. Clarmann, J. Griesfeller, M. Höpfner, M. Milz, H. Nakajima, T. Steck, T. Sugita, T. Tanaka, T. Yokota, Intercomparison of ILAS-II version 1.4 and version 2 target parameters with MIPAS-Envisat measurements. Atmos. Chem. Phys. **8**, 825–843 (2008)
G. Guerova, J.-M. Bettems, E. Brockmann, C. Mätzler, Assimilation of COST-716 near real time GPS data in the nonhydrostatic limited area model used at MeteoSwiss. Meteorol. Atmos. Phys. **91**, 149–164 (2006)
M.R. Gunson, C.B. Farmer, R.H. Norton, R. Zander, C.P. Rinsland, J.H. Shaw, B.-C. Gao, Mesurements of CH_4, N_2O, CO, H_2O, and O_3 in the middle atmosphere by the Atmospheric Trace Molecule Spectroscopy experiment on Spacelab 3. J. Geophys. Res. **95**, 13867–13882 (1990)
W. Gurlit, R. Zimmermann, C. Giesemann, T. Fernholz, V. Ebert, J. Wolfrum, U. Platt, J. Burrows, Lightweight diode laser spectrometer CHILD (Compact High-altitude In-situ Laser Diode) for balloonborne measurements of water vapor and methane. Appl. Opt., **44**, 91–102 (2005)
M. Gutnick, How Dry Is the Sky? J. Geophys. Res. **66**, 2867–2871 (1961)
C. Häberli, Assessment, correction and impact of the dry bias in radiosonde humidity data during the MAP SOP. Q. J. R. Meteorol. Soc. **132**, 2827–2852 (2006)
A. Haefele, Atmosphärische Wasserdampfprofile von 0–60 km aus optimierter Kombination von Mikrowellendaten und Ballonsondierungen. Diploma thesis, Chap 7, Institute of Applied Physics, (University of Bern, Switzerland, 2005)
A. Haefele, E. De Wachter, K. Hocke, N. Kämpfer, G. E. Nedoluha, R. M. Gomez, P. Eriksson, P. Forkman, A. Lambert, M. J. Schwartz, Validation of ground-based microwave radiometers at 22 GHz for stratospheric and mesospheric water vapor. J. Geophys. Res. **114**, D23305 (2009). doi:10.1029/2009JD011997
R. Halthore, T. Eck, B. Holben, B. Markham, Sun photometric measurements of atmospheric water vapor column abundance in the 940-nm band. J. Geophys. Res. **102**(D4), 4343–4352 (1997)
Y. Han, J.B. Snider, E.R. Westwater, R.A. Ferrare, Observations of water vapor by ground-based microwave radiometers and Raman lidar. J. Geophys. Res. **99**(D9), 18695–18702 (1994)
G. Hansford, R. Freshwater, L. Eden, K. Turnbull, D. Hadaway, V. Ostanin, R. Jones, Lightweight dew-/frost-point hygrometer based on a surface-acoustic-wave sensor for balloon-borne atmospheric water vapor profile sounding. Rev. Sci. Instrum. **77**, 014502 (2006)
J. Harries, The Distribution of Water Vapor in the Stratosphere. Rev. Geophys. **14**, 565–575 (1976)
J. Harries, J.M. Russell III, A.F. Tuck, L.L. Gordley, P. Purcell, K. Stone, R.M. Bevilacqua, M. Gunson, G. Nedoluha, W.A. Traub, Validation of measurements of water vapor from the Halogen occultation experiment (HALOE). J. Geophys. Res. **101**(D6), 10205–10216 (1996)
J.E. Harries, Atmospheric radiation and atmospheric humidity. Q. J. R. Meteorol. Soc. **123**, 2173–2186 (1997)
F. Hasebe, M. Fujiwara, N. Nishi, M. Shiotani, H. Vömel, S. Oltmans, H. Takashima, S. Saraspriya, N. Komala, Y. Inai, In situ observations of dehydrated air parcels advected horizontally in the Tropical Tropopause Layer of the western Pacific. Atmos. Chem. Phys. **7**, 807–813 (2007)
M.I. Hegglin, C.D. Boone, G.L. Manney, T.G. Shepherd, K.A. Walker, P.F. Bernath, W.H. Daffer, P. Hoor, C. Schiller, Validation of ACE-FTS satellite data in the upper troposphere/lower stratosphere (UTLS) using non-coincident measurements. Atmos. Chem. Phys. **8**, 1483–1499 (2008)

M. Heinonen, Publication of the EUROMET Workshop P758, chapter Uncertainty in humidity measurements. (2006)
S. Heise, J. Wickert, G. Beyerle, T. Schmidt, C. Reigber, Global monitoring of tropospheric water vapor with GPS radio occultation aboard CHAMP. Adv. Space Res. **37**, 2222–2227 (2006)
M. Helten, H. Smit, W. Straeter, D. Kley, P. Nedelec, M. Zöger, R. Busen, Calibration and performance of automatic compact instrumentation for the measurement of relative humidity from passenger aircraft. J. Geophys. Res. **103**, 25643–25652 (1998)
M. Helten, H. Smit, D. Kley, J. Ovarlez, H. Schlager, R. Baumann, U. Schumann, P. Nedelec, A. Marenco, In-ight comparison of MOZAIC and POLINAT water vapour measurements. J. Geophys. Res. **104**, 26087–26096 (1999)
B. Hennemuth, A. Weiss, J. Bösenberg, D. Jacob, H. Linné, G. Peters, S. Pfeifer, Quality assessment of water cycle parameters in REMO by radar-lidar synergy. Atmos. Chem. Phys. **8**, 287–308 (2008)
H. Herbin, D. Hurtmans, S. Turquety, C. Wespes, B. Barret, J. Hadji-Lazaro, C. Clerbaux, P.-F. Coheur, Global distributions of water vapour isotopologues retrieved from IMG/ADEOS data. Atmos. Chem. Phys. **7**, 3957–3968 (2007)
R.L. Herman, K. Drdla, J.R. Spackman, D.F. Hurst, P.J. Popp, C.R. Webster, P.A. Romashkin, J.W. Elkins, E.M. Weinstock, B.W. Gandrud, G.C. Toon, M.R. Schoeberl, H. Jost, E.L. Atlas, T.P. Bui, Hydration, dehydration, and the total hydrogen budget of the 1999/2000 winter Arctic stratosphere. J. Geophys. Res. **107**(D5), 8320 (2002). doi:10.1029/2001JD001257
N.S. Higdon, E.V. Browell, P. Ponsardin, B.E. Grossmann, C.F. Butler, T.H. Chyba, M.N. Mayo, R.J. Allen, A.W. Heuser, W.B. Grant, S. Ismail, S.D. Mayor, A.F. Carter, Airborne differential absorption lidar system for measurements of atmospheric water vapor and aerosols. Appl. Opt. **33**, 6422–6438 (1994)
E.J. Hintsa, E.M. Weinstock, J.G. Anderson, R.D. May, D.F. Hurst, On the accuracy of in situ water vapor measurements in the troposphere and lower stratosphere with the Harvard Lyman-α hygrometer. J. Geophys. Res. **104**(D7), 8183–8189 (1999)
K. Hocke, A. Haefele, C.L. Drian, N. Kämpfer, D. Ruffieux, von T. Clarmann, M. Milz, T. Steck, L. Froidevaux, H.C. Pumphrey, C. Jimenez, K.A. Walker, P. Bernath, Y.M. Timofeyev, A.V. Polyakov, Cross-validation of recent satellite and ground-based measurements of ozone and water vapor in the middle atmosphere. Atmospheric Science Conference, ESA SP-628 (2006)
K. Hocke, N. Kämpfer, A. Haefele, D. Ruffieux, From the troposphere to the thermosphere: combining atmospheric profiles from satellites, ECMWF, and ground-based microwave radiometry. ENVISAT Symposium 2007, ESA SP-636 (2007)
C.E. Holloway, J.D. Neelin, Moisture vertical structure, column water vapor, and tropical deep convection. J. Atmos. Sci. **66**, 1665–1683 (2009). doi:10.1175/2008JAS2806.1
J.T. Houghton, J.S. Seeley, Spectroscopic observations of the water-vapour content of the stratosphere. Quart. J. Roy. Meteorol. Soc. **86**, 358–370 (1960)
D. Hudoklin, E. Barukcic, J. Drnovsek, Engaging frost formation in a chilled-mirror hygrometer. Int. J. Thermophys. **29**, 1598–1605 (2010)
S. Hunsmann, K. Wunderle, S. Wagner, U. Rascher, U. Schurr, V. Ebert, Absolute, high resolution water transpiration rate measurements on single plant leaves via tunable diode laser absorption spectroscopy (TDLAS) at 1.37 μm. Appl. Phys. B **92**, 393–401 (2008)
T. Ingold, R. Peter, N. Kämpfer, Weighted mean tropospheric temperature and transmittance determination at millimeter-wave frequencies for ground-based applications. Radio Sci. **33**, 905–918 (1998)
T. Ingold, B. Schmid, C. Mätzler, P. Demoulin, N. Kämpfer, Modeled and empirical approaches for retrieving columnar water vapor from solar transmittance measurements in the 0.72, 0.82, and 0.94μm absorption bands. J. Geophys. Res. **105**(D19), 24327–24343 (2000)
D. Jackson, G.A. Wick, F.R. Robertson, Improved multisensor approach to satellite-retrieved near-surface specific humidity observations. J. Geophys. Res. **114**, D16303 (2009). doi:10.1029/2008JD011341

R. James, M. Bonazzola, B. Legras, K. Surbled, S. Fueglistaler, Water vapor transport and dehydration above convective outow during Asian monsoon. Geophys. Res. Lett. **35**, L20810 (2008). doi:10.1029/2008GL035441

K.P. Johnsen, J. Miao, S.Q. Kidder, Comparison of atmospheric water vapor over Antarctica derived from CHAMP/GPS and AMSU-B data. Phys. Chem. Earth. **29**(2–3), 251–255 (2004). doi:10.1016/j.pce.2004.01.005

A. Jones, J. Urban, D.P. Murtagh, P. Eriksson, S. Brohede, C. Haley, D. Degenstein, A. Bourassa, C. von Savigny, T. Sonkaew, A. Rozanov, H. Bovensmann, J. Burrows, Evolution of stratospheric ozone and water vapour time series studied with satellite measurements. Atmos. Chem. Phys. Discuss. **9**, 1157–1209 (2009)

S.M. Khaykin, V.A. Yushkov, L.I. Korshunov, A.N.J. Lukiyanova, Humidity of the tropical lower stratosphere: observations and analysis. Izv. Atmos. Ocean. Phys. **46**, 76–84 (2010)

C. Kiemle, M. Wirth, A. Fix, G. Ehret, U. Schumann, T. Gardiner, C. Schiller, N. Sitnikov, G. Stiller, First airborne water vapor lidar measurements in the tropical upper troposphere and mid-latitudes lower stratosphere: accuracy evaluation and intercomparisons with other instruments. Atmos. Chem. Phys. **8**, 5245–5261 (2008)

D. Kley, H.G.J. Smit, H. Vömel, H. Grassl, V. Ramanathan, P.J. Crutzen, S. Williams, J. Meywerk, S.J. Oltmans, Tropospheric water-vapour and ozone cross-sections in a zonal plane over the central equatorial Pacific Ocean. Quart. J. Roy. Meteorol. Soc. **123**, 2009–2040 (1997)

D. Kley, J.M. Russell III (ed.), C. Phillips, SPARC assessment of upper tropospheric and stratospheric water vapour. SPARC report, SPARC water vapour working group, pages 2. p. 312 (2000)

A. Kunz, C. Schiller, F. Rohrer, H.G.J. Smit, P. Nedelec, N. Spelten, Statistical analysis of water vapour and ozone in the UT/LS observed during SPURT and MOZAIC. Atmos. Chem. Phys. **8**, 6603–6615 (2008)

S.-Y. Kwon, J.-C. Kim, B.-I. Choi, Accurate dew-point measurement over a wide temperature range using a quartz crystal microbalance dew-point sensor. Meas. Sci. Technol. **19**, p. 115206 (2008)

W. Lahoz, M. Suttie, L. Froidevaux, R. Harwood, C. Lau, T. Lungu, G. Peckham, H. Pumphrey, W. Read, Z. Shippony, R. Suttie, J. Waters, G. Nedoluha, S. Oltmans, J. Russell III, W. Traub, Validation of UARS microwave limb sounder 183 GHz H_2O measurements. J. Geophys. Res. **101**(D6), 10129–10149 (1996)

A. Lambert, W. Read, N. Livesey, M. Santee, G. Manney, L. Froidevaux, D. Wu, M. Schwartz, H. Pumphrey, C. Jimenez, G. Nedoluha, R. Cofield, D. Cuddy, W. Daffer, B. Drouin, R. Fuller, R. Jarnot, B. Knosp, H. Pickett, V. Perun, W. Snyder, P. Stek, R. Thurstans, P. Wagner, J. Waters, K. Jucks, G. Toon, R. Stachnik, P. Bernath, C. Boone, K. Walker, J. Urban, D. Murtagh, J. Elkins, E. Atlas, Validation of the aura microwave limb sounder middle atmosphere water vapor and nitrous oxide measurements. J. Geophys. Res. **112**, D24S36 (2007). doi:10.1029/2007JD008724

N. Lamquin, K. Gierens, C.J. Stubenrauch, R. Chatterjee, Evaluation of upper tropospheric humidity forecasts from ECMWF using AIRS and CALIPSO data. Atmos. Chem. Phys. **9**, 1779–1793 (2009)

J. Larsen, E.W. Chiou, W.P. Chu, M.P. McCormick, L.R. McMaster, S. Oltmans, D. Rind, A comparison of the stratospheric aerosol and gas experiment II tropospheric water vapor to radiosonde measurements. J. Geophys. Res. **98**(D3), 4897–4917 (1993)

T. Leblanc, I.S. McDermid, Accuracy of raman lidar water vapor calibration and its applicability to long-term measurements. Appl. Opt. **47**(30), 5592–5603 (2008)

T. Leblanc et al., Measurements of humidity in the atmosphere and validation experiments (MOHAVE, MOHAVE II): results overview. Reviewed and revised papers of the 24th international laser radar conference, 1013–1016 (2008)

J. Leslie, Beschreibung eines Hygrometers, welches auf richtigern Grundsätzen als alle bisherige beruht, und eines neuen Photometers. Ann. Phys. **5**, 235–256 (1800)

W. Liu, Statistical relation between monthly mean precipitable water and surface-level humidity over global oceans. Mon. Wea. Rev. **114**, 1591–1602 (1986)

S. Lossow, J. Urban, P. Eriksson, D. Murtagh, J. Gumbel, Critical parameters for the retrieval of mesospheric water vapour and temperature from Odin/SMR limb measurements at 557 GHz. Adv. Space Res. **40**, 835–845 (2007)

S. Lossow, M. Khaplanov, J. Gumbel, J. Stegman, G. Witt, P. Dalin, S. Kirkwood, J.D. Schmidlin, K.H. Fricke, A. Blum, Middle atmospheric water vapour and dynamics in the vicinity of the polar vortex during the Hygrosonde-2 campaign. Atmos. Chem. Phys. Discuss. **8**, 12227–12252 (2008a)

S. Lossow, J. Urban, J. Gumbel, P. Eriksson, D. Murtagh, Observations of the mesospheric semi-annual oscillation (MSAO) in water vapour by Odin/SMR. Atmos. Chem. Phys. **8**, 6527–6540 (2008b)

S. Lossow, J. Urban, H. Schmidt, D.R. Marsh, J. Gumbel, P. Eriksson, D. Murtagh, Wintertime water vapor in the polar upper mesosphere and lower thermosphere: first satellite observations by Odin submillimeter radiometer. J. Geophys. Res. **114**, D10304 (2009). doi:10.1029/2008JD011462

R.L. Lucke, D.R. Korwan, R.M. Bevilacqua, J.S. Hornstein, E.P. Shettle, D.T. Chen, M. Daehler, J.D. Lumpe, M.D. Fromm, D. Debrestian, B. Neff, M. Squire, G. König-Langlo, J. Davies, The Polar Ozone and Aerosol measurement (POAM) III instrument and early validation results. J. Geophys. Res. **104**(D15), 18785–18799 (2008)

A. Lüdicke, Vergleichung des Leslie'schen Hygrometers mit dem Haar- und Steinhygrometer unter der Dunstglocke, nebst einem Vorschlage zu[r] Verbesserung jenes Thermo-Hygrometers. Ann. Phys. **10**, 110–117 (1802)

J. Lumpe, R. Bevilacqua, C. Randall, G. Nedoluha, K. Hoppel, J. Russell, V.L. Harvey, C. Schiller, B. Sen, G. Taha, G. Toon, H. Vömel, Validation of polar ozone and aerosol measurement (POAM) III version 4 stratospheric water vapor. J. Geophys. Res. **111**, D11301 (2006). doi:10.1029/2005JD006763

Z. Luo, D. Kley, R. Johnson, H. Smit, Ten years of measurements of tropical upper-tropospheric water vapor by MOZAIC. Part II: assessing the ECMWF humidity analysis. J Clim **21**, 1449–1466 (2008)

J.L. Machol, T. Ayers, K.T. Schwenz, K.W. Koenig, R.M. Hardesty, C.J. Senff, M.A. Krainak, J.B. Abshire, H.E. Bravo, S.P. Sandberg, Preliminary measurements with an automated compact differential absorption lidar for the profiling of water vapor. Appl. Opt. **43**, 3110–3121 (2004)

L. Makkonen, T. Laakso, Humidity measurements in cold and humid environments. Layer. Meteorol. **116**, 131–147 (2005)

L. Martin, C. Mätzler, T. Hewison, D. Ruffieux, Intercomparison of integrated water vapour measurements. Meteorol. Z. **15**, 57–64 (2006a)

L. Martin, M. Schneebeli, C. Mätzler, Tropospheric water and temperature retrieval for AS-MUWARA. Meteorol. Z. **15**, 37–44 (2006b)

H.J.Mastenbrook, Water vapor distribution in the stratosphere and high troposphere. J. Atmos. Sci. **25**, 299–311 (1968). doi:10.1175/15200469(1968)025j0299:WVDITS¿2.0.CO;2

H.J. Mastenbrook, Water-vapor measurements in the lower stratosphere. Can. J. Chem. **52**, 1527–1531 (1974)

V. Mattioli, E.R. Westwater, D. Cimini, J.C. Liljegren, B.M. Lesht, S.I. Gutman, F.J. Schmidlin, Analysis of radiosonde and ground-based remotely sensed PWV data from the 2004 North slope of Alaska arctic winter radiometric experiment. J. Atmos. Ocean. Tech. **24**, 415–431 (2007). doi:10.1175/JTECH1982.1

M. Maturilli, F. Fierli, V. Yushkov, A. Lukyanov, S. Khaykin, A. Hauchecorne, Stratospheric water vapour in the vicinity of the Arctic polar vortex. Ann. Geophys. **24**, 1511–1521 (2006)

C. Mätzler, J. Morland, Advances in surface-based radiometry of atmospheric water. IAP research report 2008-02-MW, Institut für angewandte physik, Universität Bern, Bern, Switzerland. (2008)

C. Mätzler, L. Martin, G. Guerova, T. Ingold, http://op.gfz-potsdam.de/D1/COST716, chapter assessment of integrated-water-vapour data at Bern from GPS, sun photometry, microwave radiometry and radiosonde. (2002)

J.P. McCormack, K.W. Hoppel, D.E. Siskind, Parameterization of middle atmospheric water vapor photochemistry for high-altitude NWP and data assimilation. Atmos. Chem. Phys. **8**, 7519–7532 (2008)

M. McHugh, B. Magill, K.A. Walker, C.D. Boone, P.F. Bernath, J.M. Russell III, Comparison of atmospheric retrievals from ACE and HALOE. Geophys. Res. Lett. **32**, L15S10 (2005). doi:10.1029/2005GL022403

S.H. Melfi, Remote measurements of the atmosphere using raman scattering. Appl. Opt. **11**(7), 1605–1610 (1972)

S.H. Melfi, J.D. Lawrence Jr., M.P. McCormick, Observation of raman scattering by water vapor in the atmosphere. Appl. Phys. Lett. **15**(9), 295–297 (1969)

H. Michelsen, G. Manney, F. Irion, G. Toon, M. Gunson, C. Rinsland, R. Zander, E. Mahieu, M. Newchurch, P. Purcell, J. Russell III, H. Pumphrey, J. Waters, R. Bevilacqua, K. Kelly, E. Hintsa, E. Weinstock, E.-W. Chiou, W. Chu, M. McCormick, C. Websterx, ATMOS Version 3 water vapor measurements: comparisons with observations from two ER-2 Lyman-alpha hygrometers, MkIV, HALOE, SAGE II, MAS, and MLS. J. Geophys. Res. **107**(D3), p. 4027 (2002). doi:10.1029/2001JD000587

M.L. Miloshevich, A. Paukkunen, H. Vomel, S.J. Oltmans, Development and validation of a time lag correction for vaisala radiosonde humidity measurements. J. Atmos. Ocean. Technol. **21**, 1305–1327 (2004)

L. Miloshevich, H. Vömel, A. Paukkunen, A. Heymsfield, S.J. Oltmans, Characterization and correction of relative humidity measurements from Vaisala RS80-A radiosondes at cold temperatures. J. Atmos. Ocean. Tech. **18**, 135–156 (2001)

L. Miloshevich, H. Vömel, D.N. Whiteman, T. Leblanc, Accuracy assessment and correction of Vaisala RS92 radiosonde water vapor measurements. J. Geophys. Res. **114**, D11305 (2009). doi:10.1029/2008JD011565

L.M. Miloshevich, H. Vömel, D.N. Whiteman, B.M. Lesht, F.J. Schmidlin, F. Russo, Absolute accuracy of water vapor measurements from six operational radiosonde types launched during AWEX-G and implications for AIRS validation. J. Geophys. Res. **111**, D09S10 (2006). doi:10.1029/2005JD006083

M. Milz, T. von Clarmann, H. Fischer, N. Glatthor, U. Grabowski, M. Höpfner, S. Kellmann, M. Kiefer, A. Linden, G.M. Tsidu, T. Steck, G.P. Stiller, B. Funke, M. López-Puertas, M.E. Koukouli, Water vapor distributions measured with the michelson interferometer for passive atmospheric sounding on board Envisat (MIPAS/Envisat). J. Geophys. Res. **110**, D24307 (2005). doi:10.1029/2005JD005973

M. Milz, S.A. Buehler, V.O. John, Comparison of AIRS and AMSU-B monthly mean estimates of upper tropospheric humidity. Geophys. Res. Lett. **36**, L10804 (2009a). doi:10.1029/2008GL037068

M. Milz, T. v. Clarmann, P. Bernath, C. Boone, S.A. Buehler, S. Chauhan, B. Deuber, D.G. Feist, B. Funke, N. Glatthor, U. Grabowski, A. Griesfeller, A. Haefele, M. Höpfner, N. Kämpfer, S. Kellmann, A. Linden, S. Müller, H. Nakajima, H. Oelhaf, E. Remsberg, S. Rohs, J.M. Russell III, C. Schiller, G.P. Stiller, T. Sugita, T. Tanaka, H. Vömel, K. Walker, G. Wetzel, T. Yokota, V. Yushkov, G. Zhang, Validation of water vapour profiles (version 13) retrieved by the IMK/IAA scientific retrieval processor based on full resolution spectra measured by MIPAS on board Envisat. Atmos. Meas. Tech. Discuss. **2**, 489–559 (2009b)

J. Morland, M.A. Liniger, H. Kunz, I. Balin, S. Nyeki, C. Mätzler, N. Kämpfer, Comparison of GPS and ERA40 IWV in the alpine region, including correction of GPS observations at jungfraujoch (3584 m). J. Geophys. Res. **111**, D04102 (2006). doi:10.1029/2005JD006043

J. Morland, M.C. Coen, K. Hocke, P. Jeannet, C. Mätzler, Tropospheric water vapour above Switzerland over the last 12 years. Atmos. Chem. Phys. **9**, 5975–5988 (2009)

G.A. Morris, J.F. Gleason, J. Ziemke, M.R. Schoeberl, Trajectory mapping: a tool for validation of trace gas observations. **105**(D14), 17,875–17,894 (2000)

S.C. Müller, N. Kämpfer, D.G. Feist, A. Haefele, M. Milz, N. Sitnikov, C. Schiller, C. Kiemle, J. Urban, Validation of stratospheric water vapour measurements from the airborne microwave radiometer AMSOS. Atmos. Chem. Phys. **8**(12), 3169–3183 (2008)

D. Murcray, A. Goldman, J. Kosters, R. Zander, W. Evans, N. Louisnard, C. Alamichel, M. Bangham, S. Pollitt, B. Carli, B. Dinelli, S. Piccioli, A. Volboni, W. Traub, K. Chance, Intercomparison of stratospheric water vapor profiles obtained during the balloon intercomparison campaign. J. Atmos. Chem. **10**, 159–179 (1990)

D. Murcray, F.H. Murcray, W.J. Williams, Distribution of water vapor in the stratosphere as determined from infrared absorption measurements. J. Geophys. Res. **67**, 759–766 (1962)

D.G. Murcray, F.H. Murcray, W.J. Williams, Further data concerning the distribution of water vapour in the stratosphere. Quart. J. Roy. Meteorol. Soc. **92**, 159–161 (1966)

J. Nash, R. Smout, T. Oakley, B. Pathack, S. Kurnosenko WMO intercomparison of high quality radiosonde systems. Vacoas, Mauritius, 2–25 February 2005. Final report. WMO instruments and methods of observation programme, page pp.118 (2006)

G. Nedoluha, R. Bevilacqua, R. Gomez, W. Waltman, B. Hicks, D. Thacker, J. Russell III, M. Abrams, H. Pumphrey, B. Connor A comparative study of mesospheric water vapor measurements from the ground-based water vapor millimeter-wave spectrometer and space-based instruments. J. Geophys. Res. **102**(D14), 16647–16661 (1997)

G.E. Nedoluha, R.M. Bevilacqua, R.M. Gomez, D.L. Thacker, W.B. Waltman, T.A. Pauls, Ground-based measurements of water vapor in the middle atmosphere. J. Geophys. Res. **100**(D2), 2927–2939 (1995)

G.E. Nedoluha, R.M. Bevilacqua, R.M. Gomez, D.E. Siskind, B.C. Hicks, J.M. Russell III, B.J. Connor, Increases in middle atmospheric water vapor as observed by the Halogen Occultation Experiment and the ground-based Water Vapor Millimeter-wave Spectrometer from 1991 to 1997. J. Geophys. Res. **103**(D3), 3531–3543 (1998)

G.E. Nedoluha, R.M. Bevilacqua, R.M. Gomez, B.C. Hicks, J.M. Russell III, Measurements of middle atmospheric water vapor from low and midlatitude in the Northern Hemisphere, 1995–1998. J. Geophys. Res. **104**(D16), 19257–19266 (1999)

G.E. Nedoluha, R.M. Bevilacqua, R.M. Gomez, B.C. Hicks, J.M. Russell III, B.J. Connor, An evaluation of trends in middle atmospheric water vapor as measured by HALOE, WVMS, and POAM. J. Geophys. Res. **108**(D13), 4391 (2003). doi:10.1029/2002JD003332

G.E. Nedoluha, R.M. Gomez, B.C. Hicks, R.M. Bevilacqua, J.M. Russell III, B.J. Connor, A. Lambert, A comparison of middle atmospheric water vapor as measured by WVMS, EOS-MLS, and HALOE. J. Geophys. Res. **112**, D24S39 (2007). doi:10.1029/2007JD008757

S. Noel, M. Buchwitz, J.P. Burrows, First retrieval of global water vapour column amounts from SCIAMACHY measurements. Atmos. Chem. Phys. **4**, 111–125 (2004)

S. Noel, M. Buchwitz, H. Bovensmann, J.P. Burrows Validation of SCIAMACHY AMCDOAS water vapour columns. Atmos. Chem. Phys. **5**, 1835–1841 (2005)

S. Noel, S. Mieruch, H. Bovensmann, J.P. Burrows, Preliminary results of GOME-2 water vapour retrievals and first applications in polar regions. Atmos. Chem. Phys. **8**, 1519–1529

S. Nyeki, L. Vuilleumier, J. Morland, A. Bokoye, P. Viatte, C. Mätzler, N. Kämpfer, A 10-year integrated atmospheric water vapor record using precision filter radiometers at two high-alpine sites. Geophys. Res. Lett. **32**, L23803 (2005). doi:10.1029/2005GL024079

D. Offermann, B. Schaeler, M. Riese, M. Langfermann, M. Jarisch, G. Eidmann, C. Schiller, H.G. Smit, W. Read, Water vapor at the tropopause during the CRISTA 2 mission. J. Geophys. Res. **107**(D23), 8176 (2002). doi:10.1029/2001JD000700

E.K. Oikonomou, A. O'Neill, Evaluation of ozone and water vapor fields from the ECMWF re-analysis ERA-40 during 1991–1999 in comparison with UARS satellite and MOZAIC aircraft observations. J. Geophys. Res. **111**, D14109 (2006). doi:10.1029/2004JD005341

S. Okamura, Microwave Technology for Moisture Measurement. Subsurface Sensing Technologies and Applications. **1**, 205–227 (2000)

S.J. Oltmans, H. Vömel, D.J. Hofmann, K.H. Rosenlof, D. Kley, The Increase in Stratospheric Water Vapor from Balloonborne, Frostpoint Hygrometer Measurements at Washington, D.C., Boulder, Colorado. Geophys. Res. Lett. **27**, 3453–3456 (2000)

J. Ovarlez, P. van Velthoven, Comparison of water vapor measurements with data retrieved from ECMWF analyses during the POLINAT experiment. J. Appl. Meteor. **36**, 1329–1335 (1997)

M. Palm, C. Melsheimer, S. Noel, J. Notholt, J. Burrows, O. Schrems, Integrated water vapor above Ny Alesund, Spitsbergen: a multisensor intercomparison. Atmos. Chem. Phys. Discuss. **8**, 21171–21199 (2008)

G. Paltridge, A. Arking, M. Pook, Trends in middle- and upper-level tropospheric humidity from NCEP reanalysis data. Theor. Appl. Climatol. (2009). doi: 10.1007/s00704-009-0117-x

G. Poberaj, A. Fix, A. Assion, M. Wirth, C. Kiemle, G. Ehret, Airborne all-solid-state DIAL for water vapour measurements in the tropopause region: system description and assessment of accuracy. Appl. Phys. B. **75**, 165–172 (2002)

P. Pruvost, J. Ovarlez, J. Lenoble, W.P. Chu, Comparison of Stratospheric Aerosol and Gas Experiment II and Balloon-Borne Stratospheric Water Vapor Measurements. J. Geophys. Res. **98**(D3), 4889–4896 (1993)

H. Pumphrey, Validation of a new prototype water vapor retrieval for the UARS Microwave Limb Sounder. J. Geophys. Res. **104**(D8), 9399–9412 (1999)

H. Radford, M. Litvak, C. Gottlieb, E. Gottlieb, S. Rosenthal, A. Lilley, Mesospheric Water Vapor Measured From Ground-Based Microwave Observations. J. Geophys. Res. **82**, 472–478 (1977)

M.K. Rama Varma Raja, S.I. Gutman, J.G. Yoe, L.M. McMillian, J. Zhao, The validation of AIRS retrievals of integrated precipitable water vapor using measurements from a network of ground-based GPS receivers over the contiguous United States. J. Atmos. Ocean. Technol. **25**, 416–428 (2008)

W.J. Randel, F. Wu, H. Vömel, G.E. Nedoluha, P. Forster, Decreases in stratospheric water vapor after 2001: Links to changes in the tropical tropopause and the Brewer-Dobson circulation. J. Geophys. Res. **111** (2006). doi:10.1029/2005JD006744

E.A. Ray K.H. Rosenlof, Hydration of the upper troposphere by tropical cyclones. J. Geophys. Res. **112**, D12311 (2007). doi:10.1029/2006JD008009

W.G. Read, J.W. Waters, D.L. Wu, E.M. Stone, Z. Shippony, A.C. Smedley, C.C. Smallcomb, S. Oltmans, D. Kley, H.G.J. Smit, J.L. Mergenthaler, M.K. Karki, UARS Microwave Limb Sounder upper tropospheric humidity measurement: Method and validation. J. Geophys. Res. **106**(D23), 32207–32258 (2001)

W.G. Read, D.L. Wu, J.W. Waters, H.C. Pumphrey, A new 147-56 hPa water vapor product from the UARS Microwave Limb Sounder. J. Geophys. Res. **109**, D06111 (2004). doi:10.1029/2003JD004366

W.G. Read, A. Lambert, J. Bacmeister, R.E. Cofield, L.E. Christensen, D.T. Cuddy, W.H. Daffer, B.J. Drouin, E. Fetzer, L. Froidevaux, R. Fuller, R. Herman, R.F. Jarnot, J.H. Jiang, Y.B. Jiang, K. Kelly, B.W. Knosp, L.J. Kovalenko, N.J. Livesey, H.-C. Liu, G.L. Manney, H.M. Pickett, H.C. Pumphrey, K.H. Rosenlof, X. Sabounchi, M.L. Santee, M.J. Schwartz, W.V. Snyder, P.C. Stek, H. Su, L.L. Takacs, R.P. Thurstans, H. Vömel, P.A. Wagner, J.W. Waters, C.R. Webster, E.M. Weinstock, D.L. Wu, Aura Microwave Limb Sounder upper tropospheric and lower stratospheric H_2O and relative humidity with respect to ice validation. J. Geophys. Res. **112**, D24S35. doi:10.1029/2007JD008752 (2007)

T.G. Redford, S.B. Verma, N.J. Rosenberg, Humidity Fluctuations over a Vegetated Surface Measured with a Lyman-Alpha Hygrometer and a Fine-Wire Thermocouple Psychrometer. J. Appl. Meteor. **19**, 860–867 (1980)

E. Remsberg, J. Russell III, L. Gordley, J. Gille, P. Bailey, Implications of the Stratospheric Water Vapor Distribution as Determined from the Nimbus 7 LIMS Experiment. J. Atmos. Sci. **41**, 2934–2948 (1984)

D. Rind, E.-W. Chiou, W. Chu, S. Oltmans, J. Lerner, J. Larsen, M.P. McCormick, L. McMaster, Overview of the Stratospheric Aerosol and Gas Experiment II Water Vapor Observations: Method, Validation, and Data Characteristics. J. Geophys. Res. **98**(D3), 4835–4856 (1993)

K.H. Rosenlof, S.J. Oltmans, D. Kley, J.M. Russell III, E.-W. Chiou, W.P. Chu, D.G. Johnson, K.K. Kelley, H.A. Michelsen, G.E. Nedoluha, E.E. Remsberg, G.C. Toon, M.P. McCormick, Stratospheric water vapor increases over the past half-century. Geophys. Res. Lett. **28**, 1195–1198 (2001)

J.M. Russell III, J.C. Gille, E.E. Remsberg, L.L. Gordley, P.L. Bailey, H. Fischer, A. Girard, S.R. Drayson, W.F.J. Evans, J.E. Harries, Validation of Water Vapor Results Measured by the Limb Infrared Monitor of the Stratosphere Experiment on NIMBUS 7. J. Geophys. Res. **89**(D4), 5115–5124 (1984)

H. Saathoff, C. Schiller, V. Ebert, D.W. Fahey, R.-S. Gao, O. Möhler, AQUAVIT Team (2009), The AquaVIT formal intercomparison of atmospheric water measurement. Eurochamp-2, http://www.eurochamp.org/

L.F. Sapucci, L.A.T. Machado, R.B. da Silveira, G. Fisch, J.F.G. Monico, Analysis of Relative Humidity Sensors at the WMO Radiosonde Intercomparison Experiment in Brazil. J. Atmos. Ocean. Tech. **22**(6), 664–678 (2005) doi:10.1175/JTECH1754.1

M. Scherer, H. Vömel, S. Fueglistaler, S.J. Oltmans, J. Staehelin, Trends and variability of mid-latitude stratospheric water vapour deduced from the re-evaluated Boulder balloon series and HALOE. Atmos. Chem. Phys. **8**, 1391–1402 (2008)

B. Schmid, K.J.Thome, P. Demoulin, R. Peter, C. Mätzler, J. Sekler, Comparison of modeled and empirical approaches for retrieving columnar water vapor from solar transmittance measurements in the 0.94-μm region. J. Geophys. Res. **101**(D5), 9345–9358 (1996)

M. Schneider, F. Hase, Improving spectroscopic line parameters by means of atmospheric spectra: Theory and example for water vapor and solar absorption spectra. J. Quant. Spectrosc. Radiat. Transfer. (2009a). doi:10.1016/j.jqsrt.2009.04.011

M. Schneider, F. Hase, Reviewing the development of a ground-based FTIR water vapour profile analysis. Atmos. Meas. Tech. Discuss. **2**, 1221–1246 (2009b)

M. Schneider, F. Hase, T. Blumenstock, Ground-based remote sensing of HDO/H_2O ratio profiles: introduction and validation of an innovative retrieval approach. Atmos. Chem. Phys. **6**, 4705–4722 (2006a)

M. Schneider, F. Hase, T. Blumenstock, Water vapour profiles by ground-based FTIR spectroscopy: study for an optimised retrieval and its validation. Atmos. Chem. Phys. **6**, 811–830 (2006b)

M. Schneider, P.M. Romero, F. Hase, T. Blumenstock, E. Cuevas, R. Ramos, Quality assessment of Izanas upper-air water vapour measurement techniques: FTIR, Cimel, MFRSR, GPS, and Vaisala RS92. Atmos. Meas. Tech. Discuss. **2**, 1625–1662 (2009)

M. Schroedter-Homscheidt, A. Drews, S. Heise, Total water vapor column retrieval from MSG-SEVIRI split window measurements exploiting the daily cycle of land surface temperatures. Remote Sens. Environ. **112**, 5115–5124 (2008)

J. Schulz, P. Albert, H.-D. Behr, D. Caprion, H. Deneke, S. Dewitte, B. Dürr, P. Fuchs, A. Gratzki, P. Hechler, R. Hollmann, S. Johnston, K.-G. Karlsson, T. Manninen, R. Müller, M. Reuter, A. Riihelä, R. Roebeling, N. Selbach, A. Tetzlaff, W. Thomas, M. Werscheck, E. Wolters, A. Zelenka, Operational climate monitoring from space: the EUMETSAT Satellite Application Facility on Climate Monitoring (CM-SAF). Atmos. Chem. Phys. **9**, 1687–1709 (2009)

J.J. Schwab, R.-J. Pan, J. Zhang, What constitutes a valid intercomparison of satellite and in situ stratospheric H_2O measurements. J. Geophys. Res. **101**(D1), 1517–1528 (1996)

M. Shephard, R.L. Herman, B.M. Fisher, K.E. Cady-Pereira, S.A. Clough, V.H. Payne, D.N. Whiteman, J.P. Comer, H. Vömel, L.M. Miloshevich, R. Forno, M. Adam, G.B. Osterman, A. Eldering, J.R. Worden, L.R. Brown, H.M. Worden, S.S. Kulawik, D.M. Rider, A. Goldman, R. Beer, K.W. Bowman, C.D. Rodgers, M. Luo, C.P. Rinsland, M. Lampel, M.R. Gunson, Comparison of Tropospheric Emission Spectrometer nadir water vapor retrievals with in situ measurements. J. Geophys. Res. **113**, D15S24 (2008). doi:10.1029/2007JD008822

V. Sherlock, A. Garnier, A. Hauchecorne, P. Keckhut, Implementation and Validation of a Raman Lidar Measurement of Middle and Upper Tropospheric Water Vapor. Appl. Opt. **38**(27), 5816–5837 (1999)

Y. Shoji, A Study of Near Real-time Water Vapor Analysis Using a Nationwide Dense GPS Network of Japan. J. Meteor. Soc. Japan. **87**, 1–18 (2009). doi:10.2151/jmsj.87.1

N.M. Sitnikov, V.A. Yushkov, A.A. Afchine, L.I. Korshunov, V.I. Astakhov, A.E. Ulanovskii, M. Kraemer, A. Mangold, C. Schiller, F. Ravegnani, The FLASH instrument for water vapor measurements on board the high-altitude airplane. Instruments and Experimental Techniques. **50**(1), 113–121 (2007)

B. Soden, D. Jackson, V. Ramaswamy, M. Schwarzkopf, X. Huang, The Radiative Signature of Upper Tropospheric Moistening. Science. **310**, 841–844 (2005). doi:10.1126/science.1115602

B.J. Soden, D.D. Turner, B.M. Lesht, L.M. Miloshevich, An analysis of satellite, radiosonde, and lidar observations of upper tropospheric water vapor from the Atmospheric Radiation Measurement Program. J. Geophys. Res. **109**, D04105 (2004). doi:10.1029/2003JD003828

F. Solheim, J.R. Godwin, Passive ground-based remote sensing of atmospheric temperature, water vapor, and cloud liquid water profiles by a frequency synthesized microwave radiometer. Meteorol. Z. **7**, 370–376 (1998)

D. Sonntag, *Hygrometrie*. (Akademie–Verlag, Berlin, 1966), pp 1086

D. Sonntag, Advancements in the field of hygrometry. Meteorol. Z. **3**, 51–66 (1994)

P. Spichtinger, K. Gierens, W. Read, The statistical distribution law of relative humidity in the global tropopause region. Meteorol. Z. **11**, 83–88 (2002). doi:10.1127/0941–2948/2002/0011–0083

P. Spichtinger, K. Gierens, H. Wernli, A case study on the formation and evolution of ice supersaturation in the vicinity of a warm conveyor belt's outow region. Atmos. Chem. Phys. **5**, 973–987 (2005)

D. Staelin, Passive remote sensing at microwave wavelengths. Proc. IEEE. **57**, 427–439 (1969)

H. Steinhagen, S. Bakan, J. Bösenberg, H. Dier, D. Engelbart, J. Fischer, G. Gendt, U. Görsdorf, J. Güldner, F. Jansen, V. Lehmann, U. Leiterer, J. Neisser, V. Wulfmeyer, Field campaign LINEX 96/1—Possibilities of water vapor observation in the free troposphere. Meteorol. Z. **7**, 377–391 (1998)

A. Stenke, V. Grewe, Simulation of stratospheric water vapor trends: impact on stratospheric ozone chemistry. Atmos. Chem. Phys. **5**, 1257–1272 (2005)

D.-Z. Sun, I.M. Held, A Comparison of Modeled and Observed Relationships between Interannual Variations of Water Vapor and Temperature. J. Clim. **9**, 665–675 (1996)

T.M. Suortti, A. Kats, R. Kivi, N. Kämpfer, U. Leiterer, L.M. Miloshevich, R. Neuber, A. Paukkunen, P. Ruppert, H. Vömel, V. Yushkov, Tropospheric comparisons of Vaisala radiosondes and balloon-borne frost-point and Lyman-α hygrometers during the LAUTLOS-WAVVAP experiment. J. Atmos. Ocean. Technol. **25**, 149–166 (2008)

R. Sussmann, T. Borsdorff, M. Rettinger, C. Camy-Peyret, P. Demoulin, P. Duchatelet, E. Mahieu, C. Servais Technical Note: New trends in column-integrated atmospheric water vapor: Method to harmonize and match long-term records from the FTIR network to radiosonde characteristics. Atmos. Chem. Phys. Discuss. **9**, 13199–13233 (2009)

L.W. Thomason, S.P. Burton, N. Iyer J.M. Zawodny, J. Anderson, A revised water vapor product for the Stratospheric Aerosol and Gas Experiment (SAGE) II version 6.2 data set. J. Geophys. Res. **109**(D6), D06312 (2004). doi:10.1029/2003JD004465

H.E. Thornton, D.R. Jackson, S. Bekki, N. Bormann, Q. Errera, A.J. Geer, W.A. Lahoz, S. Rharmili, The ASSET intercomparison of stratosphere and lower mesosphere humidity analyses. Atmos. Chem. Phys. **9**, 995–1016 (2009)

K. Trenberth, B. Moore, T. Karl, C. Nobre, Monitoring and Prediction of the Earths Climate: A Future Perspective. J. Clim. **19**, 5001–5008 (2006)

C.C. Trowbridge, The Use of the Hair Hygrometer. Science. **4**, 62–65 (1896)

J. Tsai, C.C. Lub, J. Lia, Fabrication of humidity sensors by multi-walled carbon nanotubes. J. Experim. Nanoscience. **5**, 302–309 (2010)

D.T. Turner, J.E.M. Goldsmith, Twenty-Four-Hour Raman Lidar Water Vapor Measurements during the Atmospheric Radiation Measurement Program 1996 and 1997 Water Vapor Intensive Observation Periods. J. Atmos. Ocean. Tech. **16**, 1062–1076 (1999)

D.D. Turner., W.F. Feltz, R.A. Ferrare, Continuous Water Vapor Profiles from Operational Ground-Based Active and Passive Remote Sensors. Bull. Am. Meteorol. Soc. **81**, 1301–1317 (2000)

D.D. Turner, R.A. Ferrare, L.A.H. Brasseur, W.F. Feltz, T.P. Tooman, Automated Retrievals of Water Vapor and Aerosol Profiles from an Operational Raman Lidar. J. Atmos. Ocean. Tech. **19**(1), 37–50 (2002)

A.K. Vance, J.P. Taylor, T.J. Hewison, J. Elms, Comparison of In Situ Humidity Data from Aircraft, Dropsonde, and Radiosonde. J. Atmos. Ocean. Tech. **21**, 921–932 (2004)

G. Vaughan, D.P. Wareing, L. Thomas, V. Mitev, Humidity measurements in the free troposphere using Raman backscatter. Q. J. Roy. Meteorol. Soc. **114**, 1471–1484 (1988)

G. Vaughan, C. Cambridge, L. Dean, A. WPhillips, Water vapour and ozone profiles in the midlatitude upper troposphere. Atmos. Chem. Phys. **5**, 963–71 (2005)

S. Vey, R. Dietrich, M. Fritsche, A. Rülke, P. Steigenberger, and M. Rothacher, On the homogeneity and interpretation of precipitable water time series derived from global GPS observations. J. Geophys. Res. **114**. D10101. doi:10.1029/2008JD010415

H. Vogelmann, Entwicklung und Aufbau eines Hochleistungs-Wasserdampf-LIDAR-Systems auf der Zugspitze. Master's thesis, Universität Augsburg, Augsburg, Germany. (2006)

H. Vogelmann, T. Trickl, Wide-range sounding of free-tropospheric water vapor with a differential-absorption lidar (DIAL) at a high-altitude station. Appl. Opt. **47**(12), 2116–2132 (2008)

H. Vömel, M. Fujiwara, M. Shiotani, F. Hasebe, S.J. Oltmans, J.E. Barnes, The behavior of the snow white chilled-mirror hygrometer in extremely dry conditions. J. Atmos. Ocean. Techn. **20**(11), 1560–1567 (2003)

H. Vömel, D.E. David, K. Smith, Accuracy of tropospheric and stratospheric water vapor measurements by the cryogenic frost point hygrometer: instrumental details and observations. J. Geophys. Res. **112**, D08305 (2007a). doi:10.1029/2006JD007224

H. Vömel, V. Yushkov, S. Khaykin, L. Korshunov, E. Kyrö, R. Kivi, Intercomparisons of stratospheric water vapor sensors: FLASH-B and NOAA/CMDL Frost-point hygrometer. J. Atmos. Oceanic Technol. **24**, 941–952 (2007b)

H. Vömel, H. Selkirk, L. Miloshevich, J. Valverde-Canossa, J. Valdés, E. Kyrö, R. Kivi, W. Stolz, G. Peng, J. A. Diaz, Radiation dry bias of the vaisala RS92 Humidity sensor. J. Atmos. Ocean. Tech. **24**, 953–963 (2007c)

H. Vömel, J.E. Barnes, R.N. Forno, M. Fujiwara, F. Hasebe, S. Iwasaki, R. Kivi, N. Komala, E. Kyrö, T. Leblanc, B. Morel, S.-Y. Ogino, W. Read, S. Ryan, S. Saraspriya, H. Selkirk, M. Shiotani, J.V. Canossa, D. Whiteman, Validation of Aura Microwave Limb Sounder water vapor by balloon-borne Cryogenic Frost point Hygrometer measurements. J. Geophys. Res. **112**, D24S37 (2007d). doi:10.1029/2007JD008698

T. Wagner, J. Heland, M. Zöger, U. Platt, A fast H_2O total column density product from GOME-validation with in-situ aircraft measurements. Atmos. Chem. Phys. **3**, 651–663 (2003)

T. Wagner, S. Beirle, M. Grzegorski, S. Sanghavi, U. Platt, El-Nino induced anomalies in global data sets of water vapour and cloud cover derived from GOME on ERS-2. J. Geophys. Res. **110**, D15104 (2005). doi:10.1029/2005JD005972

J. Wang, L. Zhang, Systematic Errors in Global Radiosonde Precipitable Water Data from Comparisons with Ground-Based GPS Measurements. J. Climate. **21**, 2218–2238 (2008)

J. Wang, D.J. Carlson, D.B. Parsons,T.F. Hock, D. Lauritsen, H.L. Cole, K. Beierle, E. Chamberlain, Performance of operational radiosonde humidity sensors in direct comparison with a chilled mirror dew-point hygrometer and its climate implication. Geophys. Res. Lett. **30**, 1860 (2003). doi:10.1029/2003GL016985

J. Wang, L. Zhang, A. Dai, T. v. Hove, J. v. Baelen, A near-global 2-hourly data set of atmospheric precipitable water from ground-based GPS measurements. J. Geophys. Res. **112**, D11107 (2007). doi:10.1029/2006JD007529

J.R. Wang, P. Racette, M.E. Triesky, E.V. Browell, S. Ismail, L.A. Chang, Profiling of Atmospheric Water Vapor With MIR and LASE. IEEE Trans. Geosci. Remote. Sens. **40**, 1211–1219 (2002)

E. M. Weinstock, J. B. Smith, D.S. Sayres, J.V. Pittman, J.R. Spackman, E.J. Hintsa, T.F. Hanisco, E.J. Moyer, J.M.S. Clair, M.R. Sargent, J.G. Anderson, Validation of the Harvard Lyman-a in situ water vapor instrument: Implications for the mechanisms that control stratospheric water vapor. J. Geophys. Res. **114**, D23301 (2009). doi:10.1029/2009JD012427

R.E. Westwater, M.J. Falls, I.A.P. Fotino, Ground-Based Microwave Radiometric Observations of Precipitable Water Vapor: A comparison with ground truth from two radiosonde observing systems. J. Atmos. Ocean. Tech. **6**(4), 724–730 (1989)

G. Wetzel, T. von Clarmann, H. Oelhaf, H. Fischer, Vertical profiles of N_2O_5 along with CH_4, N_2O, and H_2O in the late Arctic winter retrieved from MIPAS-B infrared limb emission measurements. J. Geophys. Res. **100**(D11), 23173–23181 (1995)

D.N. Whiteman, Examination of the traditional Raman lidar technique. I. Evaluating the temperature-dependent lidar equations. Appl. Opt. **42**(15), 2571–2592 (2003)

D.N. Whiteman, S.H. Melfi, R.A. Ferrare, Raman lidar system for the measurement of water vapor and aerosols in the Earths atmosphere. Appl. Opt. **31**(16), 3068–3082 (1992)

D.N. Whiteman, F. Russo, B. Demoz, L.M. Miloshevich, I. Veselovskii, S. Hannon, Z. Wang, H. Vömel, F. Schmidlin, B. Lesht, P.J. Moore, A.S. Beebe, A. Gambacorta, C. Barnet, Analysis of Raman lidar and radiosonde measurements from the AWEX-G field campaign and its relation to Aqua validation. J. Geophys. Res. **111**, D09S09 (2006) doi:10.1029/2005JD006429

WMO, Guide to meteorological instruments and methods of observation. WMO-No. 8, 7th ed., pp. 681, World Meteorological Organization, Geneva, Switzerland, (2008)

V. Wulfmeyer, J. Bösenberg, Ground-based differential absorption lidar for water-vapor profiling: assessment of accuracy, resolution, and meteorological applications. Appl. Opt. **37**, 3825–3844 (1998)

V. Wulfmeyer, H. Bauer, P.D. Girolamo, C. Serio, Comparison of active and passive water vapor remote sensing from space: an analysis based on the simulated performance of IASI and space borne differential absorption lidar. Remote Sens. Environ. **95**, 211–230 (2005)

J. Yarnell, R. Goody, Infra-red solar spectroscopy in a high-altitude aircraft. J. Sci. Instrum. **29**, 352–357 (1952)

M. Zöger, A. Engel, D.S. McKenna, C. Schiller, U. Schmidt, T. Woyke, Balloon-borne in situ measurements of stratospheric H_2O, CH_4 and H_2 at midlatitudes. J. Geophys. Res. **104**(D1), 1817–1825 (1999a)

M. Zöger, A. Afchine, N. Eicke, M.-T. Gerhards, E. Klein, D.S. McKenna, U. Mörschel, U. Schmidt, V. Tan, F. Tuitjer, T. Woyke, C. Schiller, Fast in situ stratospheric hygrometers: A new family of balloon-borne and airborne Lyman-α photofragment uorescence hygrometers. J. Geophys. Res. **104**(D1), 1807–1816 (1999b)

Appendix A
Fact sheets

A.1 Technique Fact Sheets

A.1.1 Lyman(α) Photofragment Fluorescence

Platform	Balloon
Measuring technique	Photofragment fluorescence
Observation geometry	N/A
Units	Volume mixing ratio, vmr
Vertical resolution	Depending on balloon vertical ascent velocity, typically 20–150 m
Horizontal resolution	N/A
Temporal resolution	>1 sec sampling time
Vertical range	Balloon ceiling height at 30–40 km
Horizontal range	N/A
Stability/drift	<3 %
Precision	3–6 %
Systematic error	5–10 %
Daytime/nighttime	Depending on instrument
Weather conditions	No strong precipitation
Interferences/contamination (payload, spectral)	Water contamination from balloon and payload during balloon ascent higher than 90 hPa
Bottlenecks, limitations	Can be used only at solar zenith angle >98°
Absolute or calibration needed?	Calibration against standard
Corrections needed?	O_2 absorption at Ly(α) wavelenghts
Auxiliary data	N/A
Averaging kernels	N/A
A priori information	Pressure and temperature
Spectroscopic parameters	N/A
Vapour pressure equations used	N/A
Transportability/Suitability for campaign	Yes
System availability	N/A
Data processing time	N/A
Additional products	N/A
Future potential	Regular soundings for accurate fine structure and trends observations
Caveats	N/A

N. Kämpfer (ed.), *Monitoring Atmospheric Water Vapour,*
ISSI Scientific Report Series 10,
DOI 10.1007/978-1-4614-3909-7, © Springer Science+Business Media, LLC 2013

References

S. Khaykin, J. Pommereau, H. Vömel, L. Korshunov, V. Yushkov, J. Nielsen, Water vapour in the tropical UT/LS from balloon observations with FLASH-B hygrometer. Geophy. Res. Abs., **10** (2008)

D. Kley, E. Stone, Measurement of water vapor in the stratosphere by photodissociation with Ly$-\alpha$ (1216 å) light, Rev. Sci. Instrum., **49**, 691–697 (1978)

M. Zöger, A. Afchine, N. Eicke, M. T. Gerhards, E. Klein, D.S. McKenna, U. Mörschel, U. Schmidt, V. Tan, F. Tuitjer, T. Woyke, C. Schiller, Fast in situ stratospheric hygrometers: A new family of balloon-borne and airborne Lyman-α photofragment fluorescence hygrometers. J. Geophys. Res. **104**, 1807–1816 (1999)

A.1.2 Thin Film Polymer Humidity Sensor

Platform	Meteorological balloon, aircraft
Measuring technique	Thin hydrophilic polymer layer on a glass substrate acts as the dielectric of a capacitor
Observation geometry	N/A
Units	% RH_w, range 0–100 % RH_w
Vertical resolution	Dependant on application
Horizontal resolution	In situ point measurements
Temporal resolution	Dependant on sampling temperature
Vertical range	From surface to tropopause
Horizontal range	N/A
Stability/drift	Dependant on stability of long-term calibration reference
Precision	1 % RH_w
Systematic error	Dependant on sensor type: 0.1–1 % RH_W
Daytime/nighttime	Both
Weather conditions	All weather
Interferences/contamination (payload, spectral)	Polymer is sensitive to pollution by aerosols or liquids
Bottlenecks, limitations	No stratospheric humidity data, some users have found it hard to trace sensor/calibration changes
Absolute or calibration needed?	Calibration is needed
Corrections needed?	Temperature dependent bias correction, time lag error correction
Auxiliary data	N/A
Averaging kernels	N/A
A priori information	N/A
Spectroscopic parameters	N/A
Vapour pressure equations used	Typically Wexler (1976) formulation for e_w (liquid), and the Hyland and Wexler (1983) formulation for e_i (ice)
Transportability/Suitability for campaign	Yes
System availability	N/A
Data processing time	Near real time
Additional products	N/A
Future potential	N/A
Caveats	N/A

References

M. Helten, H.G.J. Smit, W. Straeter, D. Kley, P. Nedelec, M. Zöger, R. Busen, Calibration and performance of automatic compact instrumentation for the measurement of relative humidity from passenger aircraft. J. Geophys. Res., **103**, 25643–25652 (1998)

L. Miloshevich, H. Vömel, D.N. Whiteman, T. Leblanc, Accuracy assessment and correction of Vaisala RS92 radiosonde water vapor measurements. J. Geophys. Res. **114**, D11305 (2009). doi:10.1029/2008JD011565

L.M. Miloshevich, H. Vömel, D.N. Whiteman, B.M. Lesht, F.J. Schmidlin, F. Russo, Absolute accuracy of water vapor measurements from six operational radiosonde types launched during AWEX-G and implications for AIRS validation. J. Geophys. Res. **111**, D09S10 (2006). doi: 10.1029/2005JD006083

L. Miloshevich, H. Vömel, A. Paukkunen, A. Heymsfield, S.J. Oltmans, Characterization and correction of relative humidity measurements from vaisala RS80-A radiosondes at cold temperatures. J. Atmos. Ocean. Tech. **18**, 135–156 (2001). doi: 10.1175/1520-0426(2001)018<0135:CACORH>2.0.CO;2

A.1.3 Ground-based FTIR

Platform	Ground-based
Measuring technique	Solar (in some cases lunar) absorption spectrometry
Observation geometry	Solar (in some cases lunar) absorption
Units	Volume mixing ratio (vmr) in ppmv, partial columns/total columns (molec/cm^2)
Vertical resolution	Given as FWHM of the averaging kernels: lower troposphere 3 km; middle troposphere 6 km; upper troposphere/lower stratosphere: 10 km
Horizontal resolution	Horizontal resolution depends on elevation angle of sun or moon (vertical resolution multiplied by tangens of zenith angle)
Temporal resolution	5–10 min
Vertical range	Sensitive to all H_2O between instrument and sun (moon); Vertical profiling possible from surface up to 10–15 km (upper end depends on H_2O slant column amounts)
Horizontal range	Single point measurement
Stability/drift	Total column: degradation of optical elements, detectors, instrumental line shape may cause small drifts; Partial columns/Profiles: instrumental line shape degradation may cause drifts
Precision	Total column: 1–2 %; Partial columns: lower troposphere 10 %, middle troposphere 10 %, upper troposphere 10–100 %
Systematic error	Total column: 1–5 %; Partial columns: 20 %
Daytime/nighttime	Daytime/nighttime (by means of lunar absorption spectra (only total column amounts with reduced precision))
Weather conditions	Stable optical depth in field of view
Interferences/contamination (payload, spectral)	Minor contaminations due to spectroscopic interferences with HNO_3, O_3, CH_4, CO_2
Bottlenecks, limitations	Large instrument, limited transportability
Absolute or calibration needed?	Self calibrating (differential absorption principle); Low pressure cell measurements for quality check of instrumental line shape
Corrections needed?	No a posteriori corrections needed

Auxiliary data	Temperature profiles from radiosondes and/or Reanalysis (NCEP, ECMWF)
Averaging kernels	Important component of the produced data: give information about measurement and a priori content
A priori information	Humidity from radiosondes, models or climatologies
Spectroscopic parameters	From spectroscopic databases (e.g. HITRAN)
Vapour pressure equations used	N/A
Transportability/Suitability for campaign	Limited transportability, there are several mobile ground-based FTIR systems (installed in big shipping containers)
System availability	N/A
Data processing time	N/A
Additional products	Many infrared active atmospheric gases, temperature
Future potential	Measurement of δD (HDO/H_2O) and δ^{18} ($H_2^{18}O/H_2O$) profiles; Long-term upper tropospheric H_2O data
Caveats	Averaging kernels required for proper interpretation

References

S.P. Davis, M.C. Abrams, J.W. Brault, Fourier transform spectrometry, p. 262. (2001)

F. Hase, J.W. Hannigan, M.T. Coffey, A. Goldman, M. Hopfner, N.B. Jones, C.P. Rinsland, S.W. Wood, Intercomparison of retrieval codes used for the analysis of high-resolution, ground-based FTIR measurements. J. Quant. Spectrosc. Ra. **87**, 25–52 (2004). doi: 10.1016/j.jqsrt.2003.12.008

M. Schneider, F. Hase, T. Blumenstock, Water vapour profiles by ground-based FTIR spectroscopy: study for an optimised retrieval and its validation. Atmos. Chem. Phys. **6**, 811–830 (2006)

A.1.4 Differential-absorption Lidar DIAL

Platform	Ground-based
Measuring technique	Absorption of laser light in the atmosphere
Observation geometry	Vertically pointing
Units	Molecular number density (molec m^{-3})
Vertical resolution	50–300 m (altitude dependent)
Horizontal resolution	N/A
Temporal resolution	$<$15 min (instrument and application dependent)
Vertical range	$\sim$300 m to 12 km a.s.l. (system dependent)
Horizontal range	N/A
Stability/drift	No drift
Precision	5 to 20 % (instrument dependent)
Systematic error	5 to 20 % (instrument dependent)
Daytime/nighttime	Both
Weather conditions	Clear sky
Interferences/contamination (payload, spectral)	Aerosol
Bottlenecks, limitations	Absorption in low-lying layers
Absolute or calibration needed?	N/A
Corrections needed?	Occasional aerosol corrections

Auxiliary data	N/A
Averaging kernels	N/A
A priori information	N/A
Spectroscopic parameters	H_2O line strengths for 725, 817, 935 nm
Vapour pressure equations used	N/A
Transportability/ Suitability for campaign	System dependent
System availability	N/A
Data processing time	N/A
Additional products	Optionally aerosol backscatter coeff.
Future potential	UT/LS measurements possible in the future given higher power systems
Caveats	Demanding, but stable adjustments

References

J. Bösenberg, Ground-based differential absorption lidar for water-vapor and temperature profiling: methodology, Appl. Opt. **37**, 3845–3860 (1998)

H. Vogelmann, T. Trickl, Wide-range sounding of free-tropospheric water vapor with a differential-absorption lidar (DIAL) at a high-altitude station. Appl. Opt. **47**, 2116–2132 (2008) doi: 10.1364/AO.47.002116

V. Wulfmeyer, J. Bösenberg, Ground-based differential absorption lidar for water-vapor profiling: Assessment of accuracy, Resolution, and meteorological applications. Appl. Opt. **37**, 3825–3844, (1998b) doi: 10.1364/AO.37.003825

A.1.5 Raman Lidar

Platform	Ground-based
Measuring technique	Raman Backscatter of laser light by atmospheric molecules
Observation geometry	Typically looking at zenith
Units	Volume mixing ratio
Vertical resolution	From a few meters to a few kilometers (altitude and instrument dependent)
Horizontal resolution	N/A
Temporal resolution	From a few minutes to a few hours (instrument and application dependent)
Vertical range	Bottom: from ground to 1 km above site; Top: from 8 to 17 km (instrument dependent)
Horizontal range	N/A
Stability/drift	Unknown (technique is too young for proper assessment)
Precision	From <0.1 % (bottom) to >50 % (top) (altitude, instrument, and time-integration dependent)
Systematic error	5–20 % (instrument dependent)
Daytime/nighttime	Typically nighttime only; A few existing instruments designed for daytime
Weather conditions	Clear sky only (thin cirrus OK)
Interferences/contamination (payload, spectral)	None
Bottlenecks, limitations	Today's technology does not allow proper accuracy/precision in the UT/LS; Calibration

Absolute or calibration needed?	Calibration needed (typically against radiosonde)
Corrections needed?	Yes for raw signals, no for output products
Auxiliary data	N/A
Averaging kernels	N/A
A priori information	Normalization to external measurement
Spectroscopic parameters	N/A
Vapour pressure equations used	N/A
Transportability/ Suitability for campaign	Several existing mobile systems (5–15 m trailers)
System availability	N/A
Data processing time	N/A
Additional products	Temperature in some cases
Future potential	UT/LS measurements possible in the future given higher power systems
Caveats	Careful calibration approach is needed if measurements are to be used for long-term monitoring

References

S.H. Melfi, J.D. Lawrence, M.P. McCormick, Observation of raman scattering by water vapor in the atmosphere. Appl. Phys. Lett. **15**, 295–297 (1969)

V. Sherlock, A. Hauchecorne, J. Lenoble, Methodology for the independent calibration of raman backscatter water-vapor lidar systems. Appl. Opt. **38**, 5816–5837 (1996) http://ao.osa.org/abstract.cfm?URI=ao-38-27-5816

G. Vaughan, D.P. Wareing, L. Thomas, V. Mitev, Humidity measurements in the free troposphere using Raman backscatter. Q. J. Roy. Meteorol. Soc. **114**, 1471–1484 (1988) doi: 10.1002/qj.49711448406. http://dx.doi.org/10.1002/qj.49711448406

A.1.6 Microwave radiometry

Platform	Ground-based
Measuring technique	Passive, pressure broadened emission line
Observation geometry	Uplooking, typically 20–40° elevation
Units	Volume mixing ratio, vmr
Vertical resolution	10–20 km, increasing with altitude
Horizontal resolution	Field of view typically 6°
Temporal resolution	Depending on tropospheric humidity, hours at 50 km, days in the mesosphere
Vertical range	25–80 km
Horizontal range	N/A
Stability/drift	N/A
Precision	5 % @50 km, 10 % @70 km (based on satellite validation)
Systematic error	5–10 %
Daytime/nighttime	Independent of day- or nighttime
Weather conditions	Not critical, unless precipitation
Interferences/contamination (payload, spectral)	Electromagnetic interference from communication signals
Bottlenecks, limitations	High tropospheric humidity
Absolute or calibration needed?	Calibration with liquid nitrogen needed in regular intervals
Corrections needed?	No

Auxiliary data	Temperature profiles from radiosondes and/or Reanalysis
Averaging kernels	Important component of the produced data: give information about measurement and a priori content
A priori information	A priori info for water vapour needed e.g. from climatology
Spectroscopic parameters	From spectroscopic databases (JPL and HITRAN)
Vapour pressure equations used	N/A
Transportability/ Suitability for campaign	Compact systems exists for campaigns
System availability	N/A
Data processing time	N/A
Additional products	Opacity at the used microwave frequency
Future potential	Traveling standard, cheaper technology allowing to build more instruments
Caveats	Averaging kernels required for proper interpretation

References

G.E. Nedoluha, R.M. Bevilacqua, R.M. Gomez, D.L. Thacker, W.B. Waltman, T.A. Pauls, Ground-based measurements of water vapor in the middle atmosphere. J. Geophys. Res. **100**, 2927–2939 (1995)

A. Parrish, R. deZafra, P. Solomon, J. Barrett, A ground-based technique for millimeter wave spectroscopic observations of stratospheric trace constituents. Radio Sci. **23**, 106–118 (1988)

C.D. Rodgers, *Inverse methods for atmospheric sounding : Theory and practice*, Series on atmospheric, oceanic and planetary physics, vol. 2 (World Scientific 2003)

A.1.7 Chilled mirror hygrometry

Platform	Sounding balloons
Measuring technique	Dew/frost-point of chilled mirror
Observation geometry	N/A
Units	K, mPa, vmr, RH_w
Vertical resolution	Depends on heating/cooling method of Hygrometer. Ranges from 10s of meters to many 100s of meters
Horizontal resolution	N/A
Temporal resolution	N/A
Vertical range	Depends on cooling method and feedback controller: 0 to 28 km for CFH, 0 to less than tropopause for Snow White, ∼tropopause to 28 km for NOAA/ESRL
Horizontal range	N/A
Stability/ drift	N/A
Precision	Depending on implementation 4 to >25 %
Systematic error	Depending on implementation 4 to >25 %
Daytime/ nighttime	Depends on implementation
Weather conditions	No rain or 'wet' clouds (may be more restrictive for some)
Interferences/ contamination (payload, spectral)	Balloon contamination limits vertical range Rain may terminate measurement
Bottlenecks, limitations	N/A
Absolute or calibration needed?	Absolute

Corrections needed?	No
Auxiliary data	N/A
Averaging kernels	N/A
A priori information	N/A
Spectroscopic parameters	N/A
Vapour pressure equations used	Uses vapour pressure equation over ice. Differences between different formulations (Goff Gratch 1946, Hyland and Wexler 1983, Buck Research 1996, WMO 2000, Murphy and Koop 2005) at low temperatures less than 1 %.
Transportability/ Suitability for campaign	Yes
System availability	N/A
Data processing time	N/A
Additional products	N/A
Future potential	N/A
Caveats	Frostpoint observations may be hard to interpret in region where mirror condensate freezes. In some instrument this region is hard to identify. Loss of controller stability may be hard to identify

References

M.E. Hoenk, G. Cardell, F. Noca, R.K. Watson, A surface acoustic wave hygrometer for high-resolution measurements of atmospheric humidity. J. Acoust. Soc. Am. **108**, p. 2495 (2000) Acoustical Society of America

H.J. Mastenbrook, J.E. Dinger, Distribution of water vapor in the stratosphere. J. Geophys. Res. **66**, 1437–1444 (1961)

H. Vömel, D.E. David, K. Smith, Accuracy of tropospheric and stratospheric water vapor measurements by the cryogenic frost point hygrometer: Instrumental details and observations. J. Geophys. Res. **112** (2007). doi: 10.1029/2006JD007224

A.2 Instrument Fact Sheets

A.2.1 FLASH-B Radiosonde

Technique	Lyman-alpha photofragement fluorescence
Platform	small balloon radiosonde and interface with few type of radiosonde exists
Observation geometry	Open cell co-axial layout
Observing frequency/ wavelength/ wave number	316 nm
Units	Volume mixing ratio, vmr
Vertical resolution	Depending on balloon vertical speed, typically 20–150 m
Horizontal resolution	N/A
Temporal resolution	4 s
Frequency of operation	0.2 s
Vertical range	7–34 km
Horizontal range	N/A
Stability/ drift	<3 %

Precision	5.5 %
Systematic error	10 %
Daytime/ nighttime	Nighttime
Weather conditions	No strong precipitation
Interferences/contamination (payload, spectral)	Water contamination from balloon and payload during balloon ascent higher than 90 hPa
Bottlenecks, limitations	can be used only at SZA>98°
Absolute or calibration needed?	Calibration against MBW 373 L (dew point hygrometer)
Corrections needed?	Quenching correction for z>28 km
Auxiliary data	p, T
Averaging kernels	N/A
A priori information	N/A
Spectroscopic parameters	N/A
Vapour pressure equations used	N/A
Transportability/ Suitability for campaign	Small size, small weight sonde/ suitable
System availability	Available through central aerological obs., Moscow
Data set availability	On a campaign basis
Data processing time	<1 months
Instrument contributing to networks	N/A
Technical upgrade	N/A
Caveats	N/A
Version number	4.0

References

S. Khaykin, J. Pommereau, H. Vömel, L. Korshunov, V. Yushkov, J. Nielsen, Water vapour in the tropical UT/LS from balloon observations with FLASH-B hygrometer. Geophysical Research Abstracts, **10** (2008)

V. Yushkov, N. Sitnikov, I. Zaitzev, J.P. Pommereau, A. Garnier, Stratospheric water vapor measurements in the winter arctic with optical fluorescence hygrometer on short and long duration balloons, in *Proceedings of the 15th ESA Symposium on European Rocket and Balloon programmes and Related Research*, Biarritz, France, ESA SP-471, 28–31 May 2001, ed. by B. Warmbein, pp. 263–268

A.2.2 "Snow White®" Radio Sonde

Technique	In situ, chilled mirror hygrometer (cooling with a Peltier element) measuring the mirror temperature that corresponds to either the dew or the frost point temperature
Platform	Meteorological radiosonde (interfaces to a few types of radiosondes exist)
Observation geometry	In situ (air sampled on top of the instrument)
Observing frequency/ wavelength/ wave number	N/A
Units	Kelvin or degree Celsius(dew/frost point temperature), or % RH (relative humidity, that needs the corresponding air temperature from the radiosonde)
Vertical resolution	About 5 m (ascent speed of 5 m/s)

Horizontal resolution	In-situ point measurements
Temporal resolution	1 s sampling time
Frequency of operation	Not better than 2 h (time between two radiosonde launches), intensive operation only during field campaigns; yet no radiosonde station with routine operation
Vertical range	Surface to tropopause
Horizontal range	Single location
Stability/ drift	No electronic drift during the sounding (references are traced back by the system); sensor shortly unstable during the transition from dew to ice on the mirror, instantaneous stability also depends on the feed-back circuit of the cooling and ice detection system as well as on the upper cooling power limit of the Peltier element
Precision	± 0.1 K (mirror temperature), better than ± 1 % RH (relative humidity)
Systematic error	± 0.1 K (mirror temperature), ± 0.2 K (air temperature), ± 2 % of the relative humidity value: i.e. ± 2 % RH at saturation ± 1 % RH in dry air above lower RH detection limit. However measurements exhibit a larger uncertainty in special conditions
Daytime/ nighttime	Two instrument types, one for all times and one for night-time only (the night-time version provides more accurate results than the other one)
Weather conditions	No precipitation and no thick clouds (unless special air inlet)
Interferences/ contamination (payload, spectral)	Water on sonde box and balloon: slight possible influence in the troposphere
Bottlenecks, limitations	Errors in the lower troposphere if the proper phase of condensate on the mirror cannot be determined; in clouds contained liquid water or ice crystals evaporate in the sensor as parts of it are heated in such situation and the sensor indicates then RH > 100 %; lower limit of the detectable relative humidity is about 3 %, increasing to about 5 % at -80 °C (cooling efficiency of the Peltier element)
Absolute or calibration needed?	Absolute measuring principle (no individual calibration)
Corrections needed?	Some corrections and quality flagging are needed after the sounding. Most of them can be performed by the ground data acquisition software
Auxiliary data	The linked radiosonde provides temperature, pressure, altitude and wind. Point-mirror reflectivity and Peltier current
Averaging kernels	N/A
A priori information	N/A
Spectroscopic parameters	N/A
Vapour pressure equations used	Vapour pressure equation fixed in the ground data acquisition system (Magnus type), or chosen by data user (e.g. Goff and Gratch)
Transportability/ Suitability for campaign	Easily transportable, light weight sonde (Snow White: 0.5 kg) and light weight ground system; dedicated to campaign applications; needs balloon inflating device
System availability	Meteolabor AG, Switzerland, http://www.meteolabor.ch
Data set availability	On demand (several field campaigns)
Data processing time	1 month

Instrument contributing to networks	Contributing to research campaigns or to validation/calibration purposes within networks.
Technical upgrade	A few upgrades since the first available version in 1997
Caveats	See above
Version number	ASW35 (two types: day usage/night usage)

References

M. Fujiwara, M. Shiotani, F. Hasebe, H. Vömel, S.J. Oltmans, P.W. Ruppert, T. Horinouchi, T. Tsuda, Performance of the Meteolabor Snow White Chilled-Mirror Hygrometer in theTropical Troposphere: Comparisons with the Vaisala RS80 A/H-Humicap Sensors. J. Atmos. Ocean. Tech. **20**, 1534–1542 (2003). doi: 10.1175/1520-0426(2003)020

L.M. Miloshevich, H. Vömel, D.N. Whiteman, B.M. Lesht, F.J. Schmidlin, F. Russo, Absolute accuracy of water vapor measurements from six operational radiosonde types launched during AWEX-G and implications for AIRS validation. J. Geophys. Res., **111**, D09S10 (2006). doi: 10.1029/2005JD006083

H. Vömel, M. Fujiwara, M. Shiotani, F. Hasebe, S.J. Oltmans, J.E. Barnes, The Behavior of the Snow White Chilled-Mirror Hygrometer in Extremely Dry Conditions. J. Atmos. Ocean. Techn. **20**, 1560–1567 (2003). doi: 10.1175/1520-0426(2003)020<1560:TBOTSW>2.0.CO;2

A.2.3 Vaisala Radiosondes with Polymer Humidity Sensor RS80-A, RS80-H, RS90 and RS92

Technique	Thin-film capacitance RH sensors: HUMICAP-A (RS80-A) HUMICAP-H (RS80-H,RS90,RS92)
Platform	Meteorological radiosonde (RS80, RS90, RS92, Vaisala)
Observation geometry	N/A
Observing frequency/ wavelength/ wave number	N/A
Units	% RH_W, range 0–100 % RH_W
Vertical resolution	Dependent on time response: HUMICAP-A: +20 °C: ∼5 m; −20 °C: ∼50 m; −40 °C: ∼100 m; −60 °C: ∼500 m HUMICAP-H: +20 °C: ∼2.5 m; −20 °C: ∼25 m; −40 °C: ∼100 m; −60 °C: ∼300 m
Horizontal resolution	In situ point measurement
Temporal resolution	RH time response is temperature dependent HUMICAP-A: +20 °C: ∼1 s; −20 °C: ∼10 s; −40 °C: ∼20 s; −60 °C: ∼100 s HUMICAP-H: +20 °C: ∼0.5 s; −20 °C: ∼5 s; −40 °C: ∼20 s; −60 °C: ∼60 s
Frequency of operation	Dependent on application, e.g. daily at 12 UT and 00 UT in the operational synoptics
Vertical range	From surface to tropopause
Horizontal range	N/A

Stability/ drift	Depending on stability calibration by manufacturer (Vaisala)
Precision	HUMICAP-A: 1 % RH_W, HUMICAP-H: 0.5 % RH_W
Systematic error	RS80-A (to dry values due to improper calibration at low temperatures by manufacturers Fraction 0.1 (−20 °C), 0.3 (−40 °C), 0.5 (−60 °C) RS80-H, RS90, RS92: Fraction <0.05 at lower temperatures
Daytime/ nighttime	Both
Weather conditions	All weather
Interferences/ contamination (payload, spectral)	Contamination of the polymer by sticky aerosols or liquid clouds. Since RS90/92 this is reduced by the alternately heated dual sensor design
Bottlenecks, limitations	No stratospheric data
Absolute or calibration needed?	Calibration by manufacturer (Vaisala)
Corrections needed?	RS80-A: dry bias after Miloshevich, 2001 Correction factor 1.1 (−20 °C), 1.5 (−40 °C), 2.0 (−60 °C) RS80-H, RS90, RS92: Correction factor <1.05 at lower temperatures
Auxiliary data	N/A
Averaging kernels	N/A
A priori information	N/A
Spectroscopic parameters	N/A
Vapour pressure equations used	Wexler (1976) formulation for e_w (liquid water), and the Hyland and Wexler (1983) formulation for e_i (ice), where e_i is the saturation vapour pressure (SVP) over ice and e_w is the SVP over liquid water
Transportability/ Suitability for campaign	Yes
System availability	N/A
Data set availability	N/A
Delivery time	Near real time
Instrument contributing to networks	WMO-operational network; GRUAN-network
Technical upgrade	N/A
Caveats	N/A
Version number	RS80-A, RS80-H, RS90 and RS92

References

L. Miloshevich, H. Vömel, D.N. Whiteman, T. Leblanc, Accuracy assessment and correction of Vaisala RS92 radiosonde water vapor measurements. J. Geophys. Res. **114**, D11 305 (2009). doi: 10.1029/2008JD011565

L.M. Miloshevich, A. Paukkunen, H. Vomel, S.J. Oltmans, Development and validation of a time lag correction for Vaisala radiosonde humidity measurements. J. Atmos. Oc. Tech. **21**, 1305–1327 (2004)

J. Wang, H.L. Cole, D.J. Carlson, E.R. Miller, K. Beierle, A. Paukkunen, T.K. Laine, Corrections of Humidity Measurement Errors from the Vaisala RS80 Radiosonde - Application to TOGA COARE Data. J. Atmos. Ocean. Tech. **19**, 981–1002 (2002)

A.2.4 Ground-Based FTIR Instruments Contributing to the Project MUSICA (MUlti-platform remote Sensing of Isotopologues for investigating the Cycle of Atmospheric water)[1]

Technique	Ground-based FTIR
Platform	The MUSICA ground-based FTIR sites: Eureka (80.1 °N, 86.4 °W, 610 m a.s.l.); Ny Alesund (78.9 °N, 11.9 °E, 15 m a.s.l.); Kiruna (67.8 °N, 20.4 °E, 419 m a.s.l.); Bremen (53.1 °N, 8.9 °E, 27 m a.s.l.); Karlsruhe (49.1 °N, 8.4 °E, 110 m a.s.l.); Jungfraujoch (46.6 °N; 8.0 °E; 3580 m a.s.l.); Iza na (28.3 °N, 16.5 °W, 2367 m a.s.l.); Addis Ababa (9.0 °N, 38.8 °E, 2324 m a.s.l.); Wollongong (34.5 °S, 150.9 °E, 30 m.a.s.l.); Lauder (45.1 °S, 169.7 °E, 370 m a.s.l.); Arrival Heights (77.8 °S, 166.7 °E, 250 m a.s.l.)
Observation geometry	Solar absorption
Observing frequency/ wavelength/ wave number	750–4250 cm^{-1} (NDACC stations) and 3800–9000 cm^{-1} (TCCON stations)
Units	vmr (ppmV), partial columns/total columns (molec./cm^2)
Vertical resolution	Given as FWHM of the averaging kernels: lower troposphere 3 km; middle troposphere 6 km; upper troposphere/lower stratosphere: 10 km
Horizontal resolution	Measurement are performed in solar absorption geometry, i.e. horizontal resolution depends on solar elevation angle (vertical resolution multiplied by tangens of solar zenith angle)
Temporal resolution	5–10 min
Frequency of operation	2–3 times per week
Vertical range	Sensitive to all H_2O between instrument and sun; Vertical profiling possible from surface up to 10–15 km (upper end depends on H_2O slant column amounts)
Horizontal range	Single point measurement
Stability/ drift	Total column: degradation of optical elements, detectors, instrumental line shape may cause small drifts; Partial columns/Profiles: instrumental line shape degradation may cause drifts
Precision	Total column: 2 %/5 % Partial columns: lower troposphere 10 %/20 %, middle troposphere 10 %/20 %, upper troposphere 10–100 %/30–100 %
Systematic error	Total column: 5–10 % Partial columns: 20 %
Daytime/ nighttime	Daytime
Weather conditions	Needs clear sky conditions; homogeneous transparency
Interferences/ contamination (payload, spectral)	Minor contaminations due to spectroscopic interferences with HNO_3, O_3, CH_4, CO_2
Bottlenecks, limitations	Needs clear sky/homogeneous transparency conditions, large instrument, limited transportability
Absolute or calibration needed?	Self calibrating (differential absorption principle)
Corrections needed?	No a posteriori corrections needed

[1] www.imk-asf.kit.edu/english/musica.

Auxiliary data	daily temperature profiles from pTu sondes and/or Reanalysis (NCEP, ECMWF)
Averaging kernels	An important component of the produced data
A priori information	Data from pTu sondes, or models
Spectroscopic parameters	from spectroscopic databases (e.g. HITRAN)
Vapour pressure equations used	N/A
Transportability/ Suitability for campaign	Limited transportability, there are several mobile ground-based FTIR systems (installed in big shipping containers)
System availability	Continuously since mid/end 1990s
Data set availability	Frank Hase: mail to: frank.hase@kit.edu (for Kiruna); Philippe Demoulin: mail to: demoulin@astro.ulg.ac.be (for Jungfraujoch); Matthias Schneider: mail to: matthias.schneider@kit.edu (for Izaña)
Data processing time	2–3 months
Instrument contributing to networks	NDACC (at Izaña in addition TCCON)
Technical upgrade	N/A
Caveats	Averaging kernels required for interpretation of profiles
Version number	N/A

References

F. Hase, J.W. Hannigan, M.T. Coffey, A. Goldman, M. Hopfner, N.B. Jones, C.P. Rinsland, S.W. Wood, Intercomparison of retrieval codes used for the analysis of high-resolution, ground-based FTIR measurements. J. Quant. Spectrosc. Ra. **87**, 25–52 (2004). doi: 10.1016/j.jqsrt.2003.12.008

M. Schneider, F. Hase, T. Blumenstock, Water vapour profiles by ground-based FTIR spectroscopy: study for an optimised retrieval and its validation. Atmos. Chem. Phys. **6**, 811–830 (2006a)

M. Schneider, G.C. Toon, J.F. Blavier, F. Hase, T. Leblanc, H_2O and δD profiles remotelysensed from ground in different spectral infrared regions. Atmos. Meas. Tech. **3**, 1599–1613 (2010)

A.2.5 Ground-based FTIR at Spitsbergen, Bremen and Polarstern (research ship)

Technique	Ground-based FTIR
Platform	Ground-based, at Spitsbergen (78.9 °N; 11.9 °E; 15 m a.s.l.), Bremen (53.5 °N; 8.8 °E; 30 m a.s.l.), and Polarstern (research ship) (79 °N-60 °S; 20 m a.s.l.)
Observation geometry	Solar absorption
Observing frequency/ wavelength/ wave number	750–4300 cm^{-1}
Units	vmr (ppmV), partial columns/total columns (molec./cm^2)
Vertical resolution	See fact sheet A.2.4 (profile retrievals are performed in the framework of MUSICA)
Horizontal resolution	Measurement are performed in solar absorption geometry, i.e. horizontal resolution depends on solar elevation angle (vertical resolution multiplied by tangens of solar zenith angle)
Temporal resolution	5–10 min

Frequency of operation	2–3 times per week
Verticalrange	Sensitive to all H_2O between instrument and sun; Vertical profiling possible from surface up to 10–15 km (upper end depends on H_2O slant column amounts)
Horizontal range	Single point measurement
Stability/ drift	Total column: degradation of optical elements, detectors, instrumental line shape may cause small drifts; Partial columns/Profiles: instrumental line shape degradation may cause drifts
Precision	Total column: 2 %/5 %; Partial columns: lower troposphere 10 %/20 %, middle troposphere 10 %/20 %, upper troposphere 10–100 %/30–100 %
Systematic error	Total column: 5–10 %; Partial columns: 20 %
Daytime/ nighttime	Daytime, nighttime using the moon as light source (only for Spitsbergen)
Weather conditions	Needs clear sky conditions; homogeneous transparency
Interferences/ contamination (payload, spectral)	Minor contaminations due to spectroscopic interferences with HNO_3, O_3, CH_4, CO_2
Bottlenecks, limitations	Needs clear sky/homogeneous transparency conditions, large instrument, limited transportability
Absolute or calibration needed?	Self calibrating (differential absorption principle)
Corrections needed?	No a posteriori corrections needed
Auxiliary data	Daily temperature profiles from pTu sondes and/or Reanalysis (NCEP, ECMWF)
Averaging kernels	Yes, it is an important component of the produced data
A priori information	Data from pTu sondes, or models
Spectroscopic parameters	From spectroscopic databases (e.g. HITRAN)
Vapour pressure equations used	N/A
Complexity	Expensive and complex instrument and retrieval algorithm
Transportability/ Suitability for campaign	Limited transportability, there are several mobile ground-based FTIR systems (installed in big shipping containers)
System availability	Continuously since 1992 (Spitsbergen), 2002 (Bremen), 1994 (Polarstern)
Data set availability	Dr. Mathias Palm: mail to: mathias@iup.physik.uni-bremen.de
Delivery time	2–3 months
Instrument contributing to networks	NDACC (at Spitsbergen and Bremen in addition TCCON)
Technical upgrade	Retrieval programs are continuously developed
Caveats	Averaging kernels required for interpretation of profiles
Version number	N/A

References

J. Notholt, G.C. Toon, C.P. Rinsland, N.S. Pougatchev, N.B. Jones, B.J. Connor, R. Weller, M. Gautrois, O. Schrems, Latitudinal variations of trace gas concentrations in the free troposphere measured by solar absorption spectroscopy during a ship cruise. J. Geophys. Res. **105**, 1337–1349 (2000). doi: 10.1029/1999JD900940

M. Palm, C. Melsheimer, S. Noël, J. Notholt, J. Burrows, O. Schrems, Integrated water vapor above Ny Ålesund, Spitsbergen: a multisensor intercomparison. Atmos. Chem. Phys. Discss. **8**, 21171–21199 (2008)

A.2.6 Ground-based FTIR at Zugspitze

Technique	Ground-based FTIR
Platform	Ground-based, at Zugspitze (47.4 °N; 11.0 °E; 2964 m a. s. l.)
Observation geometry	Solar absorption
Observing frequency/wavelength/wavenumber	750–4300 cm^{-1}
Units	vmr (ppmV), partial columns/total columns (molec/cm^2)
Vertical resolution	1–2 km; middle troposphere 3–4 km; upper troposphere/lower stratosphere: 5–7 km
Horizontal resolution	Measurements are performed in solar absorption geometry, i.e. horizontal resolution depends on solar elevation angle (vertical resolution multiplied by tan-gens of solar zenith angle)
Temporal resolution	5–10 min
Frequency of operation	2–3 times per week
Vertical range	Sensitive to all H_2O between instrument and sun; Vertical profiling possible from surface up to 10–15 km (upper end depends on H_2O slant column amounts)
Horizontal range	Single point measurement
Stability/drift	Total column: degradation of optical elements, detectors, instrumental line shape may cause small drifts; Partial columns/Profiles: instrumental line shape degradation may cause drifts
Precision	Total column: 2 %/5 % Partial columns: lower troposphere 10 %/20 %, middle troposphere 10 %/20 %, upper troposphere 10–100 %/30–100 %
Systematic error	Total column: 5–10 % Partial columns: 20 %
Daytime/nighttime	Daytime
Weather conditions	Needs clear sky conditions; homogeneous transparency
Interferences/contamination (payload, spectral)	Minor contaminations due to spectroscopic interferences with HNO_3, O_3, CH_4, CO_2
Bottlenecks, limitations	Needs clear sky/homogeneous transparency conditions, large instrument, limited transportability
Absolute or calibration needed?	Self calibrating (differential absorption principle)
Corrections needed?	No a posteriori corrections needed
Auxiliary data	Daily temperature profiles from pTu sondes and/or Reanalysis (NCEP, ECMWF)
Averaging kernels	An important component of the produced data
A priori information	Data from pTu sondes, or models
Spectroscopic parameters	From spectroscopic databases (e.g. HITRAN)
Vapour pressure equations used	N/A
Transportability/Suitability for campaign	Limited transportability, there are several mobile ground-based FTIR systems (installed in big shipping containers)
System availability	Continuously since mid/end 1990s
Data set availability	Ralf Sussmann: ralf.sussmann@kit.edu
Data processing time	2–3 months
Instrument contributing to networks	NDACC
Technical upgrade	Retrieval programs are continuosly developed
Caveats	Averaging kernels required for interpretation of profiles
Version number	N/A

References

R. Sussmann, K. Schäfer, Infrared spectroscopy of tropospheric trace gases: combined analysis of horizontal and vertical column abundances., Appl. optics **36**, 735–741, ISSN 0003–6935 (1997), http://www.ncbi.nlm.nih.gov/pubmed/18250733

R. Sussmann, T. Borsdorff, M. Rettinger, C. Camy-Peyret, P. Demoulin, P. Duchatelet, E. Mahieu, C. Servais, Technical Note: Harmonized retrieval of column-integrated atmospheric water vapor from the FTIR network—first examples for long-term records and station trends. Atmos. Chem. Phys. **9**, 8987–8999 (2009)

H. Vogelmann, R. Sussmann, T. Trickl, T. Borsdorff, Intercomparison of atmospheric water vapor soundings from the differential absorption lidar (DIAL) and the solar FTIR system on Mt. Zugspitze. Atmos. Meas. Tech. **4**, 835–841, ISSN 1867-8548 (2011), doi: 10.5194/amt-4-835-2011, http://www.atmos-meas-tech.net/4/835/2011/

A.2.7 DIAL Zugspitze

Technique	Differential-absorption Lidar(DIAL)
Platform	Schneefernerhaus (47.5 °N 11.1°E, 2765 m a.s.l.)
Observation geometry	Vertically pointing
Observing frequency/ wavelength/ wave number	817 nm
Units	Number density (m^{-3})
Vertical resolution	50–260 m (altitude dependent)
Horizontal resolution	N/A
Temporal resolution	15 min
Frequency of operation	About 2 measurement days per week
Vertical range	3–12 km a.s.l.
Horizontal range	N/A
Stability/ drift	No drift
Precision	N/A
Systematic error	$\approx 5\,\%$(h < 9 km), or 1.5×10^{20} molec m^{-3} in upper troposphere
Daytime/ nighttime	Both
Weather conditions	Clear sky
Interferences/ contamination (payload, spectral)	Aerosol
Bottlenecks, limitations	Currently detection noise
Absolute or calibration needed?	Spectroscopic calibration
Corrections needed?	Occasional aerosol correction
Auxiliary data	N/A
Averaging kernels	Smoothing in intervals adjusted to S/N
A priori information	N/A
Spectroscopic parameters	H_2O line strengths for 817 nm from Ponsardin and Browell 1997
Vapour pressure equations used	N/A
Transportability/ Suitability for campaign	No
System availability	Routine measurements (non automatic, operator required)
Data set availability	contact KIT (mail to: thomas.trickl@kit.edu)
Data processing time	<1 month

Instrument contributing to networks	No, (NDACC candidate)
Technical upgrade	Operates since 2007, reduction of dectection noise and higher laser output planned (2009)
Caveats	N/A
Version number	1

References

H. Vogelmann, T. Trickl, Wide-range sounding of free-tropospheric water vapor with a differential-absorption lidar (DIAL) at a high-altitude station. Appl. Opt. **47**, 2116–2132 (2008). doi: 10.1364/AO.47.002116

A.2.8 JPL—Table Mountain water vapour Raman Lidar (TMW)

Technique	Raman Lidar
Platform	Ground-based, Table Mountain (34.4 °N 117.7 °W 2285 m a.s.l.)
Observation geometry	Looking at zenith
Observing frequency/ wavelength/ wave number	Out 355 nm; back: 387 nm (N_2) and 407 nm (H_2O)
Units	Volume mixing ratio
Vertical resolution	75 m to 2–3 km (altitude dependent)
Horizontal resolution	From 0.2 to 2 m wide (altitude dependent)
Temporal resolution	Typically 5-minutes minimum, 2-hour routine
Frequency of operation	Typically 3–4 times per week; ∼160 measurements per year
Vertical range	3–15 km
Horizontal range	N/A
Stability/ drift	<1 % per year since beginning of the operation (2007)
Precision	From 0.001 % (bottom) to 50 % (top) (altitude dependent)
Systematic error	<10 %
Daytime/ nighttime	Nighttime only
Weather conditions	Clear sky only (thin cirrus OK)
Interferences/ contamination (payload, spectral)	None
Bottlenecks, limitations	Does not reach yet expected accuracy in the UT/LS; Careful calibration needed
Absolute or calibration needed?	Calibration against radiosonde or calibration lamp
Corrections needed?	Yes for raw signals, no for output products
Auxiliary data	N/A
Averaging kernels	Not necessary for retrieval, but used for vertical smoothing (variable f_c Kaiser filter)
A priori information	N/A
Spectroscopic parameters	N/A
Vapour pressure equations used	N/A
Complexity	Simple principle and implementation
Transportability/ Suitability for campaign	Not transportable
System availability	Both routine and campaign-based operation at fixed location

Data set availability	NDACC or contact (leblanc@tmf.jpl.nasa.gov)
Data processing time	Routine: Monthly; On demand: a few hours
Instrument contributing to networks	Yes, NDACC experimental
Technical upgrade	Operates since April 2005; Receiver upgrade in July 2007 and July 2009
Caveats	Need careful calibration approach if measurements are to be used for long-term monitoring
Version number	v6.2 for lidar signal processing; v2.1 for water vapour retrieval

References

T. Leblanc, I.S. McDermid, Accuracy of Raman lidar water vapor calibration and its applicability to long-term measurements. Appl. Opt. **47**, 5592–5603 (2008), http://ao.osa.org/abstract.cfm?URI=ao-47-30-5592

T. Leblanc, I.S. McDermid, a. R. Aspey, First-year operation of a new water vapor raman lidar at the JPL table mountain facility, California. J. Atm. Ocean. Tech. **25**, 1454–1462 (2008). doi: 10.1175/2007JTECHA978.1, http://journals.ametsoc.org/doi/abs/10.1175/2007JTECHA978.1

A.2.9 Onsala Water Vapour Radiometer (OWVR)

Technique	Passive microwave
Platform	Ground-based, Onsala (57 °N 12 °E 50 m a.s.l.)
Observation geometry	Subtraction of zenith measurement from measurement at ∼20° elevation
Observing frequency/ wavelength/ wave number	22.2 GHz
Units	Volume mixing ratio, vmr
Vertical resolution	∼10–15 km
Horizontal resolution	N/A
Temporal resolution	Hours (stratosphere) to ∼ days (middle mesosphere)
Frequency of operation	Continuous
Vertical range	40–80 km
Horizontal range	N/A
Stability/ drift	<0.5 %/year above ∼50 km
Precision	∼5 % based on satellite validation
Systematic error	∼5 % based on satellite validation
Daytime/ nighttime	Both
Weather conditions	All, except when instrument cover is wet or instrument is covered by snow.
Interferences/ contamination (payload, spectral)	Possible interference with communications systems at some sites.
Bottlenecks, limitations	N/A
Absolute or calibration needed?	Skydip measurements and ambient load. Regular liquid nitrogen load calibrations
Corrections needed?	No

Auxiliary data	Temperature profile
Averaging kernels	Yes—contact PI for files
A priori information	Climatological H_2O profile
Spectroscopic parameters	Liebe (1993) for lineshape, JPL(xxx?) catalog for linestrength
Vapour pressure equations used	N/A
Transportability/ Suitability for campaign	Not transportable
System availability	Current systems to remain at current sites for foreseeable future.
Data set availability	Onsala Space Observatory since 2002
Data processing time	?
Instrument contributing to networks	NDACC
Technical upgrade	Converting autocorrelator to FFT?
Caveats	Averaging kernels required for comparison with measurements with much better vertical resolution
Version number	N/A

References

P. Forkman, P. Eriksson, A. Winnberg, The 22 GHz radio-aeronomy reciver at Onsala Space Observatory. J. Quant. Spectrosc. Radiat. Transfer, **77**, 23–42 (2003), doi: 10.1016/S0022-4073(02)00073-0

A. Haefele, E.D. Wachter, K. Hocke, N. Kämpfer, G.E. Nedoluha, R.M. Gomez, P. Eriksson, P. Forkman, A. Lambert, M.J. Schwartz, Validation of ground based microwave radiometers at 22 GHz for stratospheric and mesospheric water vapor. J. of Geophys. Res. **114**, D23 305 (2009). doi:10.1029/2009JD011997

H.J. Liebe, G.A. Hufford, M.G. Cotton, Propagation modeling of moist air and suspended water/ice particles at frequencies below 1000 GHz, in: AGARD 52nd Specialists Meeting of the Electromagnetic Wave Propagation Panel, Palma de Mallorca, Spain; 1993, (1993), ftp://ftp.its.bldrdoc.gov/pub/mpm93

A.2.10 Water Vapour Millimeter-wave Spectrometer (WVMS)

Technique	Passive microwave
Platform	Ground-based, Lauder(NZE)(45 °S 169.7 °E 200 m a.s.l.) and Mauna Loa(Hawaii, USA)(19.5 °N 155.6 °W 3500 m a.s.l.)
Observation geometry	Subtraction of zenith measurement from measurement at ∼20° elevation
Observing frequency/wavelength/wave number	22.2 GHz
Units	Volume mixing ratio, vmr
Vertical resolution	∼10–15 km
Horizontal resolution	N/A
Temporal resolution	Hours (stratosphere) to ∼1 week (middle mesosphere)
Frequency of operation	Continuous
Vertical range	40–80 km
Horizontal range	N/A
Stability/drift	<0.5 %/year above ∼50 km
Precision	∼5 % based on satellite validation

Systematic error	∼5 % based on satellite validation
Daytime/nighttime	Both
Weather conditions	All, except when instrument cover is wet or instrument is covered by snow.
Interferences/contamination (payload, spectral)	Possible interference with communications systems at some sites.
Bottlenecks, limitations	N/A
Absolute or calibration needed?	Ambient and liquid nitrogen loads to calibrate a noise diode
Corrections needed?	No
Auxiliary data	Temperature profile
Averaging kernels	Yes—contact PI for files
A priori information	Climatological a priori H_2O profile
Spectroscopic parameters	Liebe (1993) for lineshape, JPL catalog for linestrength
Vapour pressure equations used	N/A
Transportability/Suitability for campaign	Not transportable
System availability	Current systems to remain at current sites for foreseeable future.
Data set availability	Mauna Loa since 1996, Lauder since 1994
Data processing time	∼1 year
Instrument contributing to networks	NDACC
Technical upgrade	Converting filterbanks to FFTs
Caveats	Averaging kernels required for comparison with measurements with much better vertical resolution
Version number	N/A

References

G.E. Nedoluha, R.M. Bevilacqua, R.M. Gomez, D.L. Thacker, W.B. Waltman, T.A. Pauls, Ground-based measurements of water vapor in the middle atmosphere. J. Geophys. Res., **100**, 2927–2939 (1995)

G.E. Nedoluha, R.M. Bevilacqua, R.M. Gomez, D.E. Siskind, B.C. Hicks, J. Russell III, B.J. Connor, Increases in middle atmospheric water vapor as observed by the Halogen Occultation Experiment and the ground-based Water Vapour Millimeter-wave Spectrometer from 1991 to 1997. J. Geophys. Res. **103**, 3531–3543 (1998)

G.E. Nedoluha, R.M. Gomez, B.C. Hicks, R.M. Bevilacqua, J.M. Russell III, B.J. Connor, A., Lambert, A comparison of middle atmospheric water vapor as measured by WVMS, EOS-MLS, and HALOE. J. Geophys. Res. **112**, D24S39 (2007). doi: 10.1029/2007JD008757

A.2.11 MIAWARA Microwave Radiometer

Technique	Passive microwave radiometry
Platform	Ground based, Zimmerwald, 7.46527 °E, 46.8771°N, 906.55 m.a.s.l.
Observation geometry	Reference signal at 90° elevation, line signal at 20–40° elevation
Observing frequency/wavelength/wave number	22.23508 GHz
Units	Volume mixing ratio, vmr

Vertical resolution	∼10–15 km
Horizontal resolution	N/A
Temporal resolution	Depending on tropospheric humidity, approx. hours at 50 km, days in the mesosphere
Frequency of operation	All time except during rain
Vertical range	35–75 km
Horizontal range	N/A
Stability/drift	N/A
Precision	5 % @50 km, 10 % @65 km
Systematic error	5 % @50 km, 7 % @65 km
Daytime/nighttime	Independent of day- or nighttime
Weather conditions	Not critical, unless rain
Interferences/contamination (payload, spectral)	N/A
Bottlenecks, limitations	N/A
Absolute or calibration needed?	Calibration with liquid nitrogen needed in regular intervals, otherwise internal hot load and cold sky used as reference
Corrections needed?	No
Auxiliary data	Temperature profile
Averaging kernels	Contact PI
A priori information	Climatological mean H_2O profile
Spectroscopic parameters	HITRAN 2006, JPL 2001 (update 2008)
Vapour pressure equations used	N/A
Transportability/Suitability for campaign	A campaign instrument called MIAWARA-C exists
System availability	Working on a permanent basis
Data set availability	Through NDACC (http://www.NDACC.org) or GEOMON
Data processing time	N/A
Instrument contributing to networks	NDACC, GEOMON
Technical upgrade	FFT from Aqiris with 1 GHz BW and spectral resolution of 60 kHz in 03.2007, FFT from Beam with 25 MHz BW and spectral resolution of 12 kHz in 10.2008
Caveats	For comparison with profiles of higher vertical resolution, averaging kernels have to be applied
Version number	

References

B. Deuber, N. Kämpfer, D. Feist, A new 22-GHz Radiometer for Middle Atmospheric Water Vapour Profile Measurements. IEEE Trans. Geosci. Remote Sens. **42**, 974–984 (2004)

B. Deuber, A. Haefele, D.G. Feist, L. Martin, N. Kämpfer, G.E. Nedoluha, V. Yushkov, S. Khaykin, R. Kivi, H. Vömel, Middle Atmospheric Water Vapour Radiometer - MIAWARA: Validation and first results of the LAUTLOS / WAVVAP campaign. emphJ. Geophys. Res. **110**, D13 306 (2005). doi: 10.1029/2004JD005543

A. Haefele, E.D. Wachter, K. Hocke, N. Kämpfer, G.E. Nedoluha, R.M. Gomez, P. Eriksson, P. Forkman, A. Lambert, M.J. Schwartz, Validation of ground based microwave radiometers at 22 GHz for stratospheric and mesospheric water vapor. J. of Geophys. Res. **114**, D23 305 (2009). doi:10.1029/2009JD011997

A.2.12 MOZAIC Humidity Device (MHD)

Technique	Relative Humidity (RH): Capacitive (thin hydro-active polymer film: Humicap-H, Vaisala, Finland); Temperature (T): PT100-thermistor (microprocessor-controlled transmitter unit (HMP233, Vaisala, 1993)
Platform	Instrument is deployed aboard 5 long distance A340 aircraft in the MOZAIC programme
Observation geometry	In-situ sampling through special aeronautic air intake
Observing frequency/ wavelength/ wave number	N/A
Units	Relative humidity in % RH_W, Temperature in K
Vertical resolution	Relative Humidity: 100–200 m @0–2 km, 200–400 m @2–8 km, 400–500 m @8–12 km
Horizontal resolution	15 km
Temporal resolution	RH-time response is temperature dependent $\Delta t \cong 1$ s at T≅300 K, $\Delta t \cong 15$ s at T≅260 K, $\Delta t \cong 30$ s at T≅240 K, $\Delta t \cong 60$ s at T≅220 K, $\Delta t \cong 120$ s at T≅200 K
Frequency of operation	Continuous, ∼20000 flight hours/year
Vertical range	0–12 km
Horizontal range	Along flight route
Stability/ drift	RH: $< \pm 5$ % RH per 500 hours of flight operation; T: No significant drifts observed ($< \pm 0.1$ K)
Precision	RH: ± (0.5–1)% RH @Z = 0–8 km, ± 1 % RH @Z = 8–12 km; T: ±(0.1–0.2)K @Z = 0–12 km
Systematic error	RH: ±(5–6) % RH @Z = 0–12 km; T: ±(0.5–1.0)K @Z = 0–12 km
Daytime/ nighttime	All day
Weather conditions	All weather
Interferences/ contamination (payload, spectral)	Sensitive to sticking aerosols, fractionally evaporation of liquid hydrometeors in warm clouds (T>230 K), no quantitave evaporation of ice crystals
Bottlenecks, limitations	Limited accuracy of RH in lower stratosphere
Absolute or calibration needed?	Relative Humidity: Yes, regular pre-and post flight calibration after 500 flight hours; Temperature: Not necessary, only performance checks every 6 months
Corrections needed?	No
Auxiliary data	N/A
Averaging kernels	N/A
A priori information	N/A
Spectroscopic parameters	N/A
Vapour pressure equations used	Derived using Sonntag (1994)
Transportability/ Suitability for campaign	Specially adaption for use on subsonic aircraft, both commercial and research aircraft
System availability	Since August 1994
Data set availability	MOZAIC Data Base at Meteo France, Toulouse, France (http://mozaic.aero.obs-mip.fr)
Delivery time	About 6–9 months
Instrument contributing to networks	Operational since August 1994 in the MOZAIC-programme: 1994–2002: 5 × A340 long distance subsonic aircraft, since 2006: 3 × A340 aircraft

Technical upgrade	HMT333-transmitter (Vaisala) with Humicap-H sensor to be installed on new passenger aircraft within the IAGOS-programme. Inflight correction for long-term instrumental drift of offset, i.e. regular calibration only every 6 to 12 months
Caveats	N/A
Version number	MHD-Mark I

References

M. Helten, H.G.J. Smit, W. Straeter, D. Kley, P. Nedelec, M. Zöger, R. Busen, Calibration and performance of automatic compact instrumentation for the measurement of relative humidity from passenger aircraft. J. Geophys. Res. **103**, 25643–25652 (1998)

M. Helten, H. Smit, D. Kley, J. Ovarlez, H. Schlager, R. Baumann, U. Schumann, P. Nedelec, A. Marenco, In-flight intercomparison of MOZAIC and POLINAT water vapour measurements. J. Geophys. Res. **104**, 26087–26096 (1999)

A. Marenco, V. Thouret, P. Nedelec, H. Smit, M. Helten, D. Kley, F. Karcher, P. Simon, K. Law, J. Pyle, G. Poschmann, R. V. Wrede, C. Hume, T. Cook, Measurement of ozone and water vapour by Airbus in-service aircraft: The MOZAIC airborne program, An Overview. J. Geophys. Res. **103**, 25631–25642 (1998)

H. Smit, A. Volz-Thomas, M. Helten, H. Pätz, D. Kley, An in-flight calibration method for near real-time humidity measurements with the airborne MOZAIC sensor. J. Atmos. Ocean. Tech. **25**, 656–666 (2008). doi: 10.1175/2007JTECHA975.1

D. Sonntag, Advancements in the field of hygrometry. Meteorol. Z. **N. F.**, 51–66 (1994)

A.2.13 Cryogenic Frostpoint Hygrometer (CFH)

Technique	Frostpoint Hygrometer
Platform	Meteorological radiosondes
Observation geometry	N/A
Observing frequency/ wavelength/ wave number	N/A
Units	K, mPa, vmr, RH_w
Vertical resolution	20–100 m
Horizontal resolution	N/A
Temporal resolution	N/A
Frequency of operation	Monthly or campaign based (∼50? soundings per year since 2002?)
Vertical range	0 to about 25–29 km
Horizontal range	N/A
Stability/ drift	No drift (<<< accuracy)
Precision	<4 %(troposphere) to 9 % (stratosphere)
Accuracy	<4 %(troposphere) to 9 % (stratosphere)
Daytime/ nighttime	Both
Weather conditions	No rain or 'wet' clouds
Interferences/ contamination (payload, spectral)	Balloon contamination limits vertical range, Rain may terminate measurement
Bottlenecks, limitations	None

Absolute or calibration needed?	Absolute
Corrections needed?	No
Auxiliary data	N/A
Averaging kernels	N/A
A priori information	N/A
Spectroscopic parameters	N/A
Vapour pressure equations used	Frostpoint to partial pressure conversion based on Murphy and Koop (2005)
Transportability/ Suitability for campaign	Yes
System availability	N/A
Data set availability	Freely available upon request
Data processing time	N/A
Instrument contributing to networks? (operational or experimental)	Yes (operational and experimental)
Technical upgrade	N/A
Caveats	Possible minor wet bias when operating as dew point hygrometer
Version number	1.5.2.4

References

H. Vömel, D.E. David, K. Smith, Accuracy of tropospheric and stratospheric water vapor measurements by the cryogenic frost point hygrometer: Instrumental details and observations. J. Geophys. Res. **112** (2007). doi: 10.1029/2006JD007224

Appendix B
Equations for Saturation Vapour Pressure[1]

There is a large number of saturation vapour pressure equations used to calculate the pressure of water vapour over a surface of liquid water or ice. This is a brief overview of the most important equations used. Several useful reviews of the existing vapour pressure curves are listed in the references. Please note the updated discussion of the WMO formulation.

B.1 Vapour pressure over liquid water below 0 °C

Goff Gratch equation (Smithsonian Tables (1984), after Goff and Gratch (1946)):

$$\begin{aligned}\log_{10} p_w &= -7.90298\left(\frac{373.16}{T}-1\right)\\ &\quad +5.02808\cdot\log_{10}\left(\frac{373.16}{T}\right)\\ &\quad -1.3816\times10^{-7}\left(10^{11.344\left(1-\frac{T}{373.16}\right)}-1\right)\\ &\quad +8.1328\times10^{-3}\left(10^{-3.49149\left(\frac{373.16}{T}-1\right)}-1\right)\\ &\quad +\log_{10}(1013.246)\end{aligned} \tag{B.1}$$

with T in (K) and p_w in (hPa)

WMO (Goff 1957):

$$\begin{aligned}\log_{10} p_w &= 10.79574\left(1-\frac{273.16}{T}\right)\\ &\quad -5.02800\cdot\log_{10}\left(\frac{T}{273.16}\right)\\ &\quad +1.50475\times10^{-4}\left(1-10^{\left(-8.2969\left(\frac{T}{273.16}-1\right)\right)}\right)\end{aligned}$$

[1] Based on Holger Vömels Webpage, http://cires.colorado.edu/~voemel/vp.html

N. Kämpfer (ed.), *Monitoring Atmospheric Water Vapour,*
ISSI Scientific Report Series 10,
DOI 10.1007/978-1-4614-3909-7, © Springer Science+Business Media, LLC 2013

$$+0.42873 \times 10^{-3} \left(10^{(+4.76955(1-\frac{273.16}{T}))} - 1\right)$$
$$+0.78614 \tag{B.2}$$

with T in (K) and p_w in (hPa)

(Note: WMO based its recommendation on a paper by (Goff 1957), which is shown here. The recommendation published by WMO (WMO 1988) has several typographical errors and cannot be used. A corrigendum (WMO 2000) shows the term $+0.42873 \times 10^{-3} \cdot \left(10^{(-4.76955 \cdot (1-\frac{273.16}{T}))} - 1\right)$ in the fourth line compared to the original publication by (Goff 1957). Note the different sign of the exponent. The earlier 1984 edition shows the correct formula.)

Hyland and Wexler (Hyland and Wexler 1983):

$$\begin{aligned} \log p_w \quad = \quad & -0.58002206 \times 10^4 / T \\ & +0.13914993 \times 10^1 \\ & -0.48640239 \times 10^{-1} \cdot T \\ & +0.41764768 \times 10^{-4} \cdot T^2 \\ & -0.14452093 \times 10^{-7} \cdot T^3 \\ & +0.65459673 \times 10^1 \cdot \log(T) \end{aligned} \tag{B.3}$$

with T in (K) and p_w in (Pa)

Buck (Manuals 1996); updated equation from (Buck 1981):

$$p_w = 6.1121 \cdot \mathrm{e}^{\frac{\left(18.678-\frac{t}{234.5}\right)t}{257.14+t}} \quad [1996] \tag{B.4}$$

$$p_w = 6.1121 \cdot \mathrm{e}^{\frac{17.502t}{240.97+t}} \quad [1981] \tag{B.5}$$

with t in (°C) and p_w in (hPa)

Sonntag (Sonntag 1994)

$$\begin{aligned} \log p_w \quad = \quad & -6096.9385 / T \\ & +16.635794 \\ & -2.711193 \times 10^{-2} \cdot T \\ & +1.673952 \times 10^{-5} \cdot T^2 \\ & +2.433502 \cdot \log(T) \end{aligned} \tag{B.6}$$

with T in (K) and p_w in (hPa)

Magnus Teten (Murray 1967)

$$\log_{10} p_w = \frac{7.5t}{t + 237.3} + 0.7858 \tag{B.7}$$

with t in (°C) and p_w in (hPa)

Bolton (Bolton 1980)

$$p_w = 6.112 \cdot \mathrm{e}^{\frac{17.67t}{t+243.5}} \tag{B.8}$$

with t in (°C) and p_w in (hPa)

Murphy and Koop (Murphy and Koop 2005)

$$\begin{aligned} \log p_w \quad = \quad & 54.842763 \\ & -6763.22/T \\ & -4.21 \log(T) \\ & +0.000367 \cdot T \\ & + \tanh\left(0.0415(T - 218.8)\right) \\ & \cdot (53.878 - \frac{1331.22}{T} - 9.44523 \log(T) + 0.014025T) \end{aligned} \tag{B.9}$$

with T in (K) and p_w in (Pa)

International Association for the Properties of Water and Steam (IAPWS) Formulation 1995

(Wagner and Pruß 2002)

$$\begin{aligned} \log\left(\frac{p_w}{22.064 \times 10^6}\right) \quad = \quad & \frac{647.096}{T} \cdot (-7.85951783 \cdot \nu \\ & +1.84408259 \cdot \nu^{1.5} \\ & -11.7866497 \cdot \nu^3 \\ & +22.6807411 \cdot \nu^{3.5} \\ & -15.9618719 \cdot \nu^4 \\ & +1.80122502 \cdot \nu^{7.5}) \end{aligned} \tag{B.10}$$

with T in (K) and p_w in (Pa) and $\nu = 1 - \frac{T}{647.096}$

At low temperatures most of these are based on theoretical studies and only a small number are based on actual measurements of the vapour pressure. The Goff Gratch Eq. (B.1) for the vapour pressure over liquid water covers a region of −50 to 102 °C (Gibbins 1990). This work is generally considered the reference equation but other equations are in use in the meteorological community (Elliott and Gaffen 1993). There is a very limited number of measurements of the vapour pressure of water over supercooled liquid water at temperatures below −50 °C. Detwiler (1983)

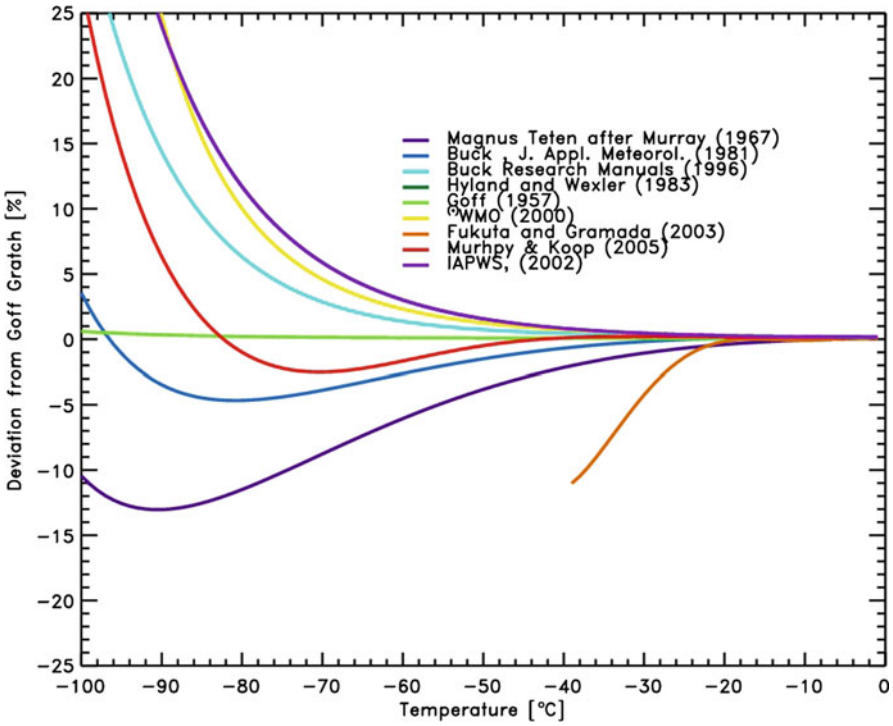

Fig. B.1 Comparison of Eqs. (B.2)–(B.10) with the Goff Gratch equation (B.1) for the saturation pressure of water vapour over liquid water. The measurements by Fukuta and Gramada (2003) are shown as well.
(*)(WMO 2000) is also shown. This is based on Goff (1957) with the different sign of one exponent, likely due to a typographical error.

claims some indirect evidence to support the extrapolation of the Goff-Gratch equation down to temperatures of −60 °C. However, this currently remains an open issue. The Hyland and Wexler formulation is used by Vaisala and is very similar to the formula by Sonntag (B.6). The Magnus Teten formulation (B.7) is widely used in Meteorology and appeals for its simplicity. The comparison for the liquid saturation vapour pressure Eqs. (B.2)–(B.8) with the Goff-Gratch Eq. (B.1) in Fig. B.1 shows that uncertainties at low temperatures become increasingly large and reach the measurement uncertainty claimed by some RH sensors. At −60 °C the deviations range from −6 to +3 % and at −70 °C the deviations range from −9 to +6 %. For RH values reported in the low and mid troposphere the influence of the saturation vapour pressure formula used is small and only significant for climatological studies (Elliott and Gaffen 1993). The WMO recommended formula is a derivative of the Goff-Gratch equation, originally published by Goff (1957). The differences between Goff (1957) and Goff and Gratch (1946) are less than 1 % over the entire temperature range. The formulation published by WMO (1988) cannot be used due to several typographical errors. The corrected formulation (WMO 2000) still differs in the sign

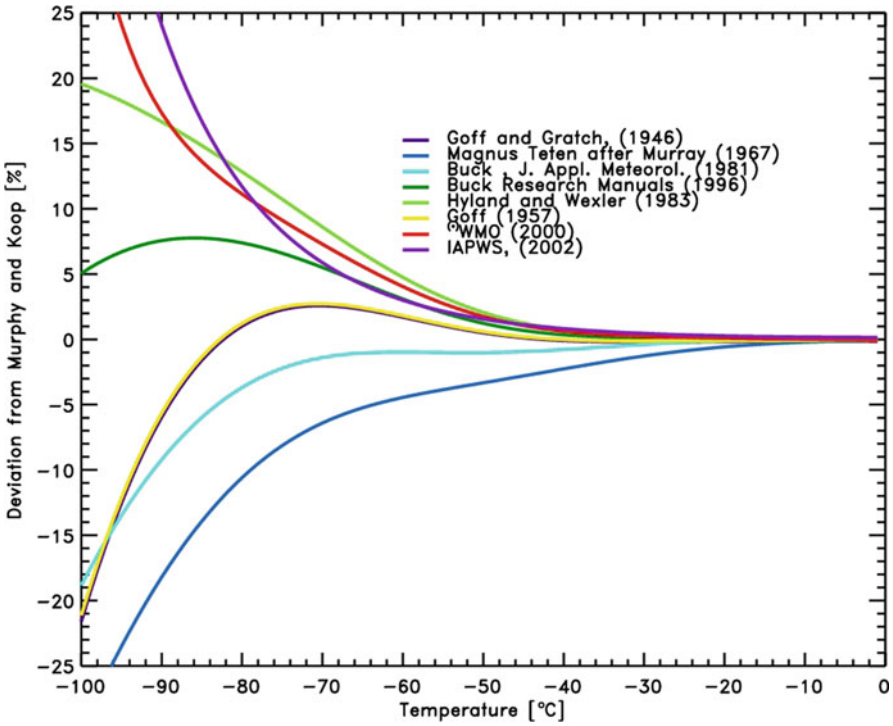

Fig. B.2 Comparison of Eqs. (B.1)–(B.8),(B.10) with the Murphy Koop equation (B.9) for the saturation pressure of water vapour over liquid water
(*)(WMO 2000) is also shown. This is based on Goff (1957) with the different sign of one exponent, likely due to a typographical error.

of one exponent compared to Goff (1957). This incorrect formulation is in closer agreement with the Hyland and Wexler formulation; however, it is to be assumed that Goff (1957) was to be recommended.

The most recent review of vapour pressures of ice and supercooled water by Murphy and Koop (2005) provide a formulation (B.9) based on recent data on the molar heat capacity of supercooled water. The comparison of the vapour pressure Eqs. (B.1)–(B.8) with the formulation by Murphy and Koop (B.9) is shown in Figs. B.2.

The study by Fukuta and Gramada (2003) shows direct measurements of the vapour pressure over liquid water down to −38 °C. Their result indicates that at the lowest temperatures the measured vapour pressure may be as much as 10 % lower than the value given by the Smithsonian Tables (B.1), and as shown in Fig. B.1 lower as any other vapour pressure formulation. However, these data are in conflict with measured molar heat capacity data (Murphy and Koop 2005), which have been measured both for bulk as for small water droplets.

Like most other formulations, the IAPWS formulation 1995 (Wagner and Pruß 2002) are valid only above the triple point. The IAWPS formulation 1995 (Wagner and Pruß 2002) is valid in the temperature range 273.16 K $<$ T $<$ 647.096 K.

It is important to note that in the upper troposphere, water vapour measurements reported in the WMO convention as relative humidity with respect to liquid water depend critically on the saturation vapour pressure equation that was used to calculate the RH value.

B.2 Vapour pressure over ice

Goff Gratch equation (Smithsonian Tables 1984):

$$\begin{aligned} \log_{10} p_i &= -9.09718\left(\frac{273.16}{T}-1\right) \\ &\quad -3.56654\log_{10}\left(\frac{273.16}{T}\right) \\ &\quad +0.876793(1-\frac{T}{273.16}) \\ &\quad +\log_{10}(6.1071) \end{aligned} \tag{B.11}$$

with T in (K) and p_i in (hPa)

Hyland and Wexler (Hyland and Wexler 1983):

$$\begin{aligned} \log p_i &= -0.56745359\times 10^4/T \\ &\quad +0.63925247\times 10^1 \\ &\quad -0.96778430\times 10^{-2}\cdot T \\ &\quad +0.62215701\times 10^{-6}\cdot T^2 \\ &\quad +0.20747825\times 10^{-8}\cdot T^3 \\ &\quad -0.94840240\times 10^{-12}\cdot T^4 \\ &\quad +0.41635019\times 10^1\cdot\log(T) \end{aligned} \tag{B.12}$$

with T in (K) and p_i in (Pa)

Magnus Teten (Murray 1967)

$$\log_{10} p_i = 9.5\frac{t}{t+265.5}+0.7858 \tag{B.13}$$

with t in (°C) and p_i in (hPa)

Buck (Manuals 1996)

$$p_i = 6.1115\cdot \mathrm{e}^{\frac{(23.036-\frac{t}{333.7})t}{279.82+t}} \quad [1996] \tag{B.14}$$

$$p_i = 6.1115\cdot \mathrm{e}^{\frac{22.452t}{272.55+t}} \quad [1981] \tag{B.15}$$

with t in (°C) and p_i in (hPa)

Marti Mauersberger (Marti and Mauersberger 1993)

$$\log_{10} p_i = \frac{-2663.5}{T} + 12.537 \tag{B.16}$$

with T in (K) and p_i in (Pa)

Murphy and Koop (Murphy and Koop 2005)

$$\begin{aligned} \log p_i \;=\; & 9.550426 \\ & -5723.265/T \\ & +3.53068 \log(T) \\ & -0.00728332 \cdot T \end{aligned} \tag{B.17}$$

with T in (K) and p_i in (Pa)

The Goff Gratch Eq. (B.11) for the vapour pressure over ice covers a region of −100 to 0 °C. It is generally considered the reference equation; however, other equations have also been widely used. The equations discussed here are mostly of interest for frost-point measurements using chilled mirror hygrometers, since these instruments directly measure the temperature at which a frost layer and the overlying vapour are in equilibrium. In meteorological practice, relative humidity is given over liquid water (see B.1) and care needs to be taken to consider this difference. Buck Research, which manufactures frost-point hygrometers, uses the Buck formulations in their instruments. These formulations include an enhancement factor, which corrects for the differences between pure vapour and moist air. This enhancement factor is a weak function of temperature and pressure and corrects about 0.5 % at sea level. For the current discussion it has been omitted. The Marti Mauersberger equation is the only equation based on direct measurements of the vapour pressure down to temperatures of 170 K. The comparison of Eqs. (B.12)–(B.17) with the Goff Gratch Equation (Fig. B.3) shows, that with the exception of the Magnus Teten formula, the deviations in the typical meteorological range of −100 to 0 °C are less than 2.5 %, and smaller than typical instrumental errors of frost-point hygrometers of 5–10 %. Not shown is the WMO recommended equation for vapour pressure over ice, since it is nearly identical with the Goff-Gratch Eq. (B.11).

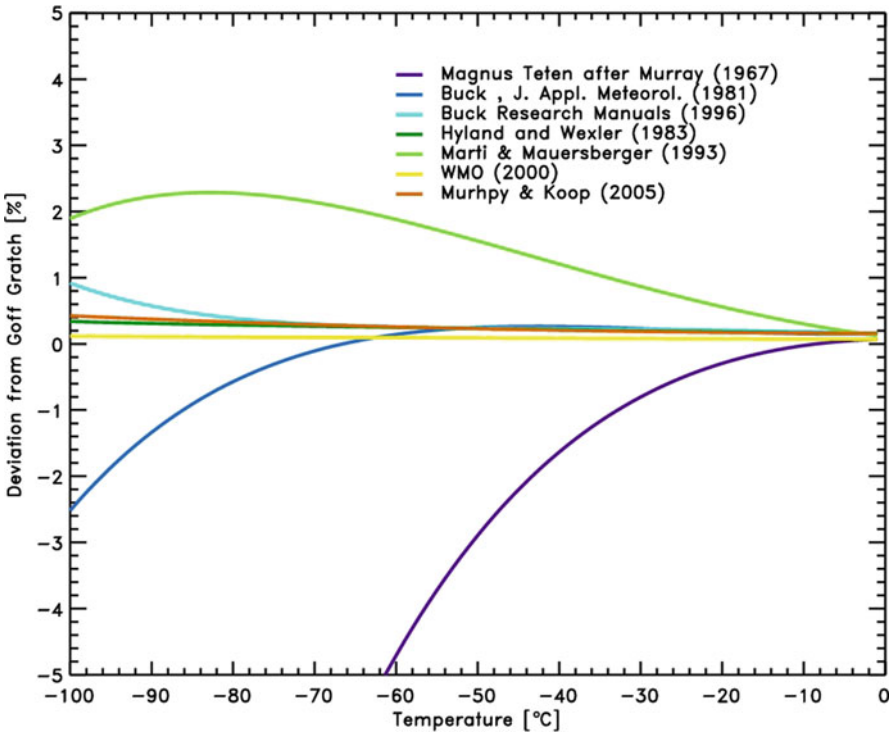

Fig. B.3 Comparison of Eqs. (B.12)–(B.17) with the Goff Gratch Eq. (B.11) for the saturation pressure of water vapour over ice

References

D. Bolton, The computation of equivalent potential temperature. Mon. Weather Rev. **108**, 1046–1053 (1980)

A.L. Buck, New equations for computing vapor pressure and enhancement factor. J. Appl. Meteorol. **20**, 1527–1532 (1981)

A. Detwiler, Extrapolation of the Goff-Gratch formula for vapor pressure over liquid water at temperatures below 0 °C. J. Appl. Meteorol. **22**, 503 (1980)

W.P. Elliott, D.J. Gaffen, Effects of conversion algorithms on reported upper air dewpoint depressions. Bull. Am. Meteorol. Soc. **74**, 11323–1325 (1993)

N. Fukuta, C.M. Gramada, Vapor pressure measurement of supercooled water. J. Atmos. Sci. **60**, 1871–1875 (2003)

C.J. Gibbins, A survey and comparison of relationships for the determination of the saturation vapour pressure over plane surfaces of pure water and of pure ice. Annales Geophys. **8**, 859–886 (1990)

J.A. Goff, Saturation pressure of water on the new Kelvin temperature scale, in *Transactions of the American society of heating and ventilating engineers*, pp. 347–354, presented at the semi-annual meeting of the American society of heating and ventilating engineers, Murray Bay, Que. Canada, 1957

J.A. Goff, S. Gratch, Low-pressure properties of water from −160 to 212 F, in *Transactions of the American society of heating and ventilating engineers*, pp. 95–122, presented at the 52nd annual meeting of the American society of heating and ventilating engineers, New York, 1946

R.W. Hyland, A. Wexler, Formulations for the Thermodynamic Properties of the saturated Phases of H_2O from 173.15 to 473.15 K, *ASHRAE Trans*. **89**, 500–519 (1983)
B.R. Manuals, *Buck Research Manuals* (1996)
J. Marti, K. Mauersberger, A survey and new measurements of ice vapor pressure at temperatures between 170 and 250 K. GRL **20**, 363–366 (1993)
D.M. Murphy, T. Koop, Review of the vapour pressures of ice and supercooled water for atmospheric applications. Quart. J. Royal Met. Soc **131**, 1539–1565 (2005)
F.W. Murray, On the computation of saturation vapor pressure. J. Appl. Meteorol. **6**, 203–204 (1967)
Smithsonian Tables 1984, Smithsonian met. tables, 5th ed.
D. Sonntag, Advancements in the field of hygrometry. Meteorol. Z. **N. F.**, 51–66 (1994)
W. Wagner, A. Pruß, The IAPWS formulation 1995 for the thermodynamic properties of ordinary water substance for general and scientific use. J. Phys. Chem. Ref. Data **31**, 387–535 (2002)
WMO, General meteorological standards and recommended practices, Appendix A, WMO Technical Regulations WMO-No. 49, world meteorological organization (1988)
WMO, General meteorological standards and recommended practices, Appendix A, WMO Technical Regulations WMO-No. 49, world meteorological organization, corrigendum (1998)

Appendix C
List of Acronyms

Networks and Cooperations	
CARIBIC	Civil Aircraft for Regular Investigation of the atmosphere Based on an Instrument Container
COST	European Cooperation in Science and Technology
GAW	Global Atmosphere Watch Programme
GCOS	Global Climate Observing System
GRUAN	GCOS Reference Upper Air Network
IAGOS	In-service aircraft for a Global Observing System
IGACO	Integrated Global Atmospheric Chemistry Observations
IPCC	Intergovernmental Panel on Climate Change
MOZAIC	Measurement of Ozone and Water Vapour by AIRBUS In Service Aircraft
NDACC	Network for the Detection of Atmospheric Composition Change
SPARC	Stratospheric Processes and Their Role in Climate
TCCON	Total Carbon Column Observing Network
Organizations	
AWI	Alfred Wegener Institut (Germany)
CAO	Central Aerological Observatory (Roshydromet, Russia)
CIAI	Izaña Atmospheric Research Centre (Spain)
CMDL	Climate Monitoring and Diagnostics Laboratory (NOAA, USA)
CNES	Centre National d'Études Spatiales (France)
CNRM	Centre National de Recherches Météorologiques (France)
CNRS	Centre National de Recherche Scientifique (France)
DLR	Deutsches Zentrum fur Luft- und Raumfahrt (Germany)
IAP	Institute of Applied Physics (University of Berne, Switzerland)
IMK-ASF	Institute for Meterology and Climate Research â Trace constituents in the Stratosphere and Tropopause Region (KIT, Germany)
ISSI	International Space Science Institute
JPL	Jet Propulsion Laboratory (NASA, USA)
KIT	Karlsruhe Institute of Technology (Germany)
LMD	Laboratoire de Météorologie Dynamique (CNRS, France)
NOAA	National Oceanic and Atmospheric Administration (USA
NRL	Naval Research Laboratory (USA)
WMO	World Meteorological Organization

N. Kämpfer (ed.), *Monitoring Atmospheric Water Vapour,*
ISSI Scientific Report Series 10,
DOI 10.1007/978-1-4614-3909-7, © Springer Science+Business Media, LLC 2013

Instruments	
AOS	Acousto optical spectrometer
CFH	Cryogenic frostpoint hygrometer
CTS	Chirp Transform spectrometer
DIAL	Differential Absorption Lidar
FISH	Fast In situ Stratospheric Hygrometer
FLASH	Flourescence Advanced Stratospheric Hygrometer
FTIR	Fourier Transform Infrared Spectrometry
FTS	Fourier Transform Spectrometer
MHD	MOZAIC humidity device
MIAWARA	Middle Atmospheric Water Vapour Radiometer
SAW	Surface Acoustic Wave frostpoint hygrometer
SRS	Swiss Radiosonde
TMW	Table Mountain Water Vapour Raman Lidar
WVMS	Water vapour millimeter-wave spectrometer
Satellites and Models	
ACE/FTS	Atmospheric Chemistry Experiment Fourier Transform Spectrometer
AIM/SOFIE	Aeronomy of Ice in the Mesosphere - Solar Occultation For Ice Experiment
AMSU	Advanced Microwave Sounding Unit
Aqua/AIRS	Atmospheric Infrared Sounder
ATMOS	Atmospheric Trace Molecule Spectroscopy Experiment
Aura/HIRDLS	High Resolution Dynamics Limb Sounder
Aura/MLS	Microwave Limb Sounder
Aura/TES	Thermal Emission Spectrometer
BASCOE	Belgian Assimilation System of Chemical Observations from Envisat
ECMWF	European Centre for Medium-Range Weather Forecasts
Envisat/GOMOS	Global Ozone Monitoring by Occultation of Stars
Envisat/MIPAS	Michelson Interferometer for Passive Atmospheric Sounding
Envisat/SCIAMACHY	Scanning Imaging Absorption spectroMeter for Atmospheric ChartographY
FORMOSAT/COSMIC	Constelation Observing System for Meteorology, Ionosphere and Climate
GNSS-GPS	Global Navigation Satellite System - Global Positioning System
GOES	Geostationary Operational Environmental Satellite
GOME	Global Ozone Monitoring System
GOSat/TANSO	Greenhouse gases Observing Satellite - Thermal And Near-infrared Sensor for carbon Observation
HIRS	High Resolution Infrared Radiation Sounder
JEM/SMILES	Japanese Experiment module - Japanese Sub-Millimeter Limb Emission Sounder
Meteosat/MVIRI	Meteosat Visible and InfraRed Imager
MetOp/GRAS	GNSS Receiver for Atmospheric Sounding
MetOp/IASI	Infrared Atmospheric Sounding Interferometer
MHS	Microwave humidity sounder
MODIS	Moderate Resolution Imaging Spectroradiometer
MSG/Seviri	Meteosat Secon Generation - Spinning Enhanced Visible and InfraRed Imager
NCEP	National Centers for Environmental Prediction
Odin/SMR	Sub-Millimetre Radiometer
POAM	Polar Ozone and Aerosol Measurement
SAGE	Stratospheric Aerosol and Gas Experiment
TIMED/SABER	Thermosphere, Ionosphere, Mesosphere Energetics and Dynamics - Sounding of the Atmosphere using Broadband Emission Radiometry
UARS/HALOE	Upper Atmosphere Research Satellite - Halogen Occultation Experiment